

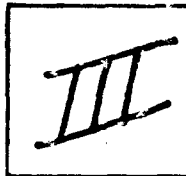
Best Available Copy

PHOTOGRAPH THIS SHEET

AD-E200522

AD A 096097

DTIC ACCESSION NUMBER



LEVEL



INVENTORY

AIR FORCE WEAPONS LAB. KIRTLAND  
AFB, NM

ELECTROMAGNETIC PULSE SENSOR AND SIMULATION  
NOTES -EMP 1-27. FINAL REPT. MAY 80.

DOCUMENT IDENTIFICATION REPT. NO. AFWL-TR-80-401.

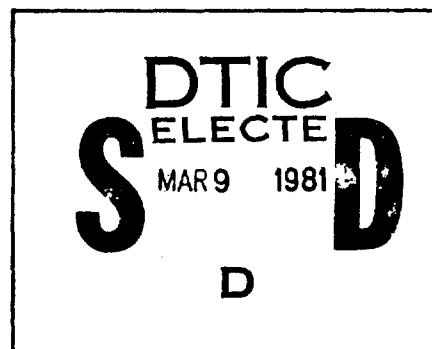
DISTRIBUTION STATEMENT

Approved for public release;  
Distribution Unlimited

DISTRIBUTION STATEMENT

ACCESSION FOR	
NTIS	GRA&I <input checked="" type="checkbox"/>
DTIC	TAB <input type="checkbox"/>
UNANNOUNCED	<input type="checkbox"/>
JUSTIFICATION	
BY	
DISTRIBUTION /	
AVAILABILITY CODES	
DIST	AVAIL AND/OR SPECIAL
A	

DISTRIBUTION STAMP



DATE ACCESSIONED

81 3 09 041

DATE RECEIVED IN DTIC

PHOTOGRAPH THIS SHEET AND RETURN TO DTIC-DDA-2

DTIC FORM 70A  
OCT 79

DOCUMENT PROCESSING SHEET

Best Available Copy

AD-E200522

AFWL-TR-80-401

ELECTROMAGNETIC PULSE SENSOR AND SIMULATION  
NOTES -EMP 1-27

AD A 096097

May 1980

Final Report

Approved for public release; distribution unlimited.

20050118275

AIR FORCE WEAPONS LABORATORY  
Air Force Systems Command  
Kirtland Air Force Base, NM 87117

Best Available Copy

This report is one in the Note Series on EMP and related subjects which is an EMP community-wide series on EMP technology related matters. The editor is Dr C. E. Baum, Air Force Weapons Laboratory (NTM), Kirtland AFB, New Mexico. The editor should be contacted for any matters related to this series.

When US Government drawings, specifications, or other data are used for any purpose other than a definitely related Government procurement operation, the Government thereby incurs no responsibility nor any obligation whatsoever, and the fact that the Government may have formulated, furnished, or in any way supplied the said drawings, specifications, or other data, is not to be regarded by implication or otherwise, as in any manner licensing the holder or any other person or corporation, or conveying any rights or permission to manufacture, use, or sell any patented invention that may in any way be related thereto.

This report has been compiled by an employee of the United States Government. The United States Government retains a nonexclusive, royalty-free license to publish or reproduce the material contained herein, or allow others to do so, for the United States Government purposes.

This report has been reviewed by the Public Affairs Office and is releasable to the National Technical Information Service (NTIS). At NTIS, it will be available to the general public, including foreign nations.

This technical report has been reviewed and is approved for publication.

*Carl E. Baum*

CARL E. BAUM, PhD  
Editor

*Bob L. Francis*

BOB L. FRANCIS  
Colonel, USAF  
Chief, Electromagnetics Division

FOR THE DIRECTOR

*Bruce F. King*

BRUCE F. KING  
Colonel, USAF  
Director of Nuclear Technology

DO NOT RETURN THIS COPY. RETAIN OR DESTROY.

UNCLASSIFIED

SECURITY CLASSIFICATION OF THIS PAGE (When Data Entered)

REPORT DOCUMENTATION PAGE		READ INSTRUCTIONS BEFORE COMPLETING FORM
1. REPORT NUMBER AFWL-TR-80-401	2. GOVT ACCESSION NO. AR-A096 097	3. RECIPIENT'S CATALOG NUMBER
4. TITLE (and Subtitle) ELECTROMAGNETIC PULSE SENSOR AND SIMULATION NOTES - EMP 1-27		5. TYPE OF REPORT & PERIOD COVERED Final Report
7. AUTHOR(s)		6. PERFORMING ORG. REPORT NUMBER
9. PERFORMING ORGANIZATION NAME AND ADDRESS Air Force Weapons Laboratory (NTM) Kirtland AFB, NM 87117		8. CONTRACT OR GRANT NUMBER(s)
11. CONTROLLING OFFICE NAME AND ADDRESS Air Force Weapons Laboratory (NTM) Kirtland AFB, NM 87117		10. PROGRAM ELEMENT, PROJECT, TASK AREA & WORK UNIT NUMBERS 99960002
14. MONITORING AGENCY NAME & ADDRESS (if different from Controlling Office)		12. REPORT DATE May 1980
		13. NUMBER OF PAGES 452
		15. SECURITY CLASS. (of this report) UNCLASSIFIED
		15a. DECLASSIFICATION DOWNGRADING SCHEDULE
16. DISTRIBUTION STATEMENT (of this Report)  Approved for public release; distribution unlimited.		
17. DISTRIBUTION STATEMENT (of the abstract entered in Block 20, if different from Report)		
18. SUPPLEMENTARY NOTES		
19. KEY WORDS (Continue on reverse side if necessary and identify by block number)  EMP		
20. ABSTRACT (Continue on reverse side if necessary and identify by block number) This is a series of ten notes on electromagnetic pulse sensors and simulation. Subjects covered in this volume are: A Study of Waveguide Mode Excitation and Propagation in a Parallel Plate Transmission Line; EMP Simulation and Its Impact on EMP Testing; Electromagnetic Considerations of a Spatial Modal Filter for Suppression of Non-TEM Modes in the Transmission-Line Type of EMP Simulators; An Investigation of Portable EMP Simulators/Alternate Simulators; Electromagnetic Surface Wave Propagation Over a Rectangular Bonded Wire Mesh; over		

DD FORM 1 JAN 73 1473

UNCLASSIFIED

SECURITY CLASSIFICATION OF THIS PAGE (When Data Entered)



UNCLASSIFIED

SECURITY CLASSIFICATION OF THIS PAGE(When Data Entered)

Item 20 continued:

Electromagnetic Wave Propagation Along a Pair of Rectangular Bonded Wire Meshes;  
Surface Wave Propagation on a Rectangular Bonded Wire Mesh Located Over the  
Ground; Equivalent Electromagnetic Properties of a Concentric Wire Cage as  
Compared to a Circular Cylinder; Source Excitation of an Open, Parallel-Plate  
Waveguide; Source Excitation of an Open, Parallel-Plate Waveguide, Numerical  
Results.

UNCLASSIFIED

SECURITY CLASSIFICATION OF THIS PAGE(When Data Entered)

## PREFACE

Much of the existing information on EMP is in the form of notes or semi-formal reports and has not been adequately documented or distributed. In particular, there are several series of notes that act as technical journals for various areas related to EMP and other related subjects. These note series are not exclusively for one organization and are run much as technical journals with an editor, Dr. Carl E. Baum.

The Air Force Weapons Laboratory has undertaken to reissue these existing notes in convenient volume units. The present volume is Volume 27 of the Sensor and Simulation Notes, one of the note series in the Electromagnetic Pulse Note Series. The Sensor and Simulation Notes have the report designation EMP 1 in the EMP group of note series.

Contributions to this volume, EMP 1-27, have been made by the following individuals at the included organizations:

Air Force Weapons Laboratory

Carl E. Baum  
Korada R. Umashankar

Cooperative Institute for Research in Environmental Sciences

James R. Wait

University of Illinois

V. Krichevsky  
R. Mittra

Institute for Telecommunication Sciences

David A. Hill

LuTech, Inc.

D. V. Giri

Mississippi State University

Terry T. Crow  
Kuang Yuh Wu  
Clayborne D. Taylor

NBC Research and Development Institute of the  
Federal Armed Forces Federal Republic of Germany

Hagen Schilling

TDR, Inc.

Maurice I. Sancer  
Scott Siegel  
A.D. Varvatsis

Research for these notes has been funded, in part, by the following agencies:

Defense Nuclear Agency  
United States Air Force

Contributions to the Note Series are encouraged from all organizations actively engaged in related research. Active participation throughout the community will build a collection of information useful to all. Contributions and questions regarding the Note Series should be directed to:

Dr. Carl E. Baum  
Air Force Weapons Laboratory, NTM  
Kirtland Air Force Base, New Mexico 87117.

## TABLE OF CONTENTS

- NOTE 245 A STUDY OF WAVEGUIDE MODE EXCITATION AND PROPAGATION IN A  
PARALLEL PLATE TRANSMISSION LINE  
Terry T. Crow, Kuang Yuh Wu, Clayborne D. Taylor,  
Mississippi State University
- NOTE 246 EMP SIMULATION AND ITS IMPACT ON EMP TESTING  
Carl E. Baum, Air Force Weapons Laboratory
- NOTE 247 ELECTROMAGNETIC CONSIDERATIONS OF A SPATIAL MODAL FILTER FOR  
SUPPRESSION OF NON-TEM MODES IN THE TRANSMISSION-LINE TYPE OF  
EMP SIMULATORS  
D. V. Giri, LuTech, Inc.; Carl E. Baum, Air Force Weapons  
Laboratory; Hagen Schilling, NBC Research and Development  
Institute of the Federal Armed Forces, Federal Republic of  
Germany
- NOTE 248 AN INVESTIGATION OF PORTABLE EMP SIMULATORS/ALTERNATE  
SIMULATORS  
Maurice I. Sancer, Scott Siegel, A. D. Varvatsis, TDR, Inc.
- NOTE 249 ELECTROMAGNETIC SURFACE WAVE PROPAGATION OVER A RECTANGULAR  
BONDED WIRE MESH  
David A. Hill, Institute for Telecommunication Sciences;  
James R. Wait, Cooperative Institute for Research in Environ-  
mental Sciences
- NOTE 250 ELECTROMAGNETIC WAVE PROPAGATION ALONG A PAIR OF RECTANGULAR  
BONDED WIRE MESHES  
David A. Hill, Institute for Telecommunication Sciences
- NOTE 251 SURFACE WAVE PROPAGATION ON A RECTANGULAR BONDED WIRE MESH  
LOCATED OVER THE GROUND  
David A. Hill, Institute for Telecommunication Sciences,  
James R. Wait, Cooperative Institute for Research in Environ-  
mental Sciences
- NOTE 252 EQUIVALENT ELECTROMAGNETIC PROPERTIES OF A CONCENTRIC WIRE  
CAGE AS COMPARED TO A CIRCULAR CYLINDER  
Korada R. Umashankar, Carl E. Baum, Air Force Weapons  
Laboratory
- NOTE 253 SOURCE EXCITATION OF AN OPEN, PARALLEL-PLATE WAVEGUIDE  
V. Krichevsky, R. Mittra, University of Illinois
- NOTE 254 SOURCE EXCITATION OF AN OPEN, PARALLEL-PLATE WAVEGUIDE,  
NUMERICAL RESULTS  
V. Krichevsky, University of Illinois

A STUDY OF WAVEGUIDE MODE EXCITATION  
AND PROPAGATION IN A PARALLEL PLATE TRANSMISSION LINE

ABSTRACT

A study of the waveguide mode excitation and propagation is made for a parallel plate waveguide. Since this configuration is used in the simulation of the nuclear electromagnetic pulse, results appropriate for various simulators are obtained and discussed. The analysis assumes infinitely wide plates, but the question of finite width plates is addressed.

Acknowledgement

The authors wish to express their appreciation to Dr. K. C. Chen of the Air Force Weapons Laboratory for suggesting this work and to Dr. C. E. Baum for reading this paper and offering numerous suggestions for its improvement.

## 1. Introduction

The parallel plate transmission line provides a useful means for measuring the electromagnetic field interaction. In this configuration nearly uniform electric and magnetic fields are produced, and instrumentation can be placed beneath one of the plates. There is, however, a practical problem associated with the design and excitation of the parallel plate transmission line; namely, one must provide a transition section, typically one or two conical transmission line sections, between the source and the parallel plate configuration (see Figures 1 and 2).

Insofar as the transmission line mode is concerned the transition section poses no problems provided the conical line and the parallel plates have approximately the same cross sectional shape at their interface and provided there is a match between the characteristic impedances. However, the spherical wavefront propagating along the conical line does not match the planar wavefront of the TEM mode in the parallel plate region, hence the excitation of TE and TM waveguide modes as well as the TEM mode occurs. Finally, in some situations a single input section is not sufficient to produce the required field strengths. In these cases (usually wide plate separations), dual input sections are used. When using dual input sections one must allow provision in the analysis for the fact that the sources may not fire simultaneously.

In studying the interaction of complex electrical systems with the electromagnetic pulse generated by a nuclear detonation, the parallel plate waveguide can be used to simulate the interaction. The electromagnetic pulse may be simulated by driving the parallel plates from

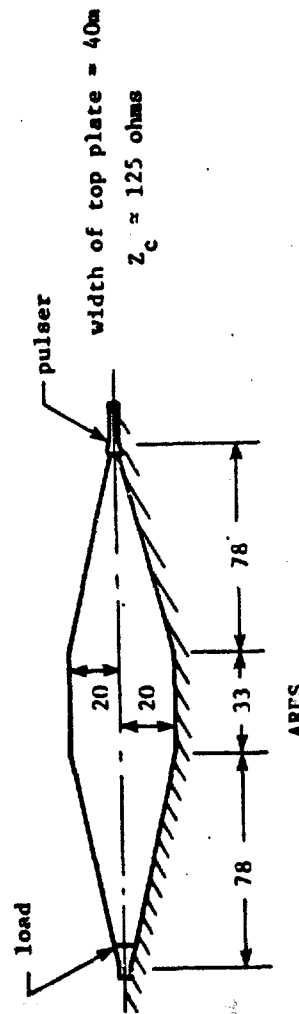
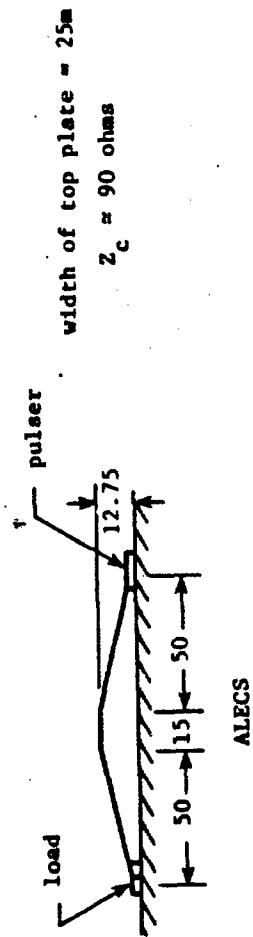
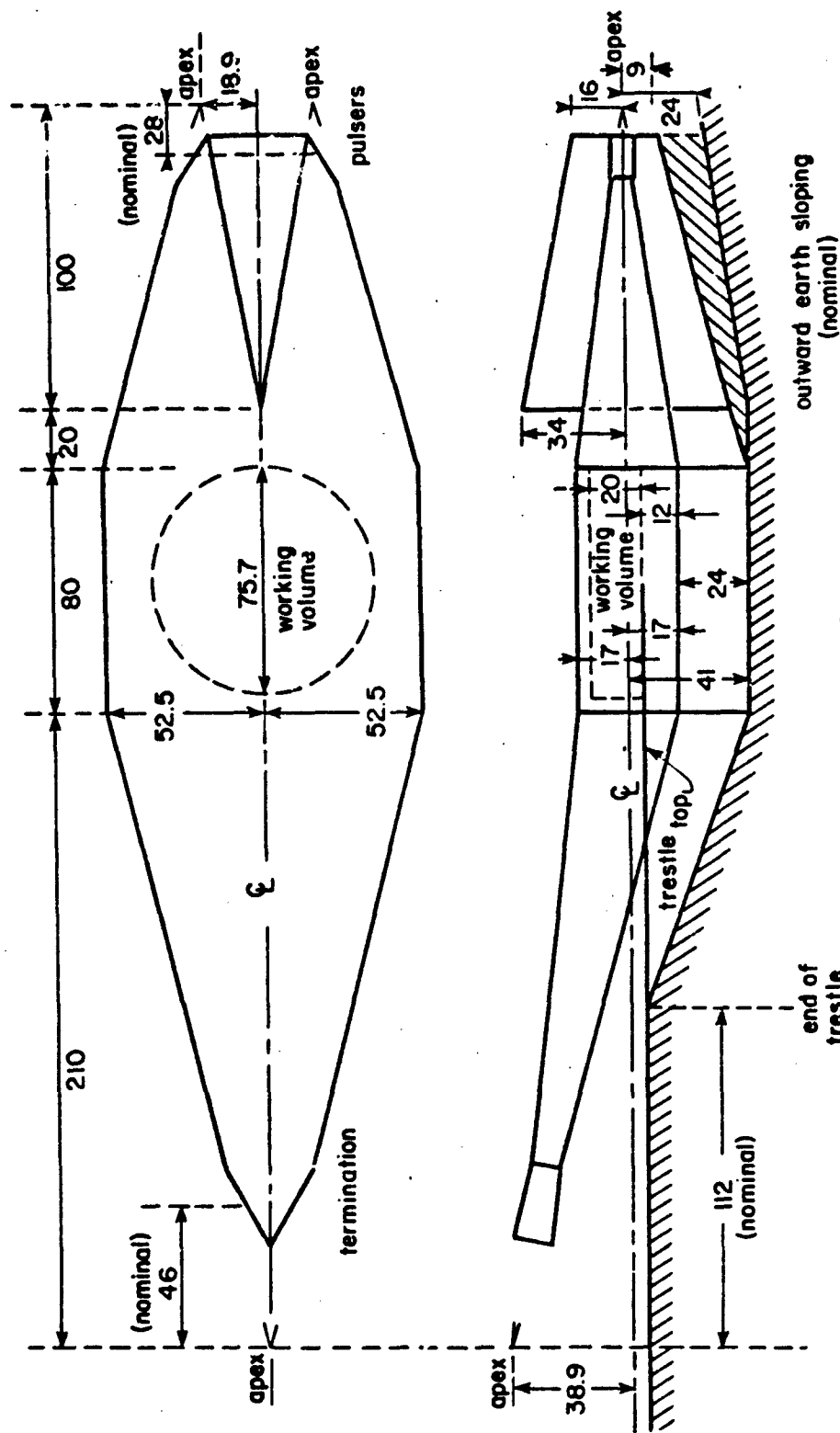


Figure 1. Schematic Diagram of Two Parallel Plate Simulators. Note that all dimensions are in meters and the scale is 1cm = 25m.



ATLAS I: Design 5

Figure 2. Schematic Diagram of a Simulator with Dual Transitions Sections.  
(All dimensions are in meters)



conical input sections with appropriate surge generators. There are a number of these simulation facilities currently in use. Example geometries for single and dual input parallel plate transmission line simulators are shown in Figures 1 and 2.

An additional complicating feature of these simulators is that they are constructed as finite width parallel plate transmission lines. The properties of the TEM mode on such a structure have been studied extensively [1,2]. Other studies [3] have shown that the waveguide modes for open region waveguides differ considerably from the modes of the more familiar closed region waveguides. The excitation coefficients for the modes in an open region structure are obtained by matching boundary conditions at the interface between the conical input section and the parallel plate region as well as on the waveguide walls [3]. Apparently, integral equations must be solved numerically to obtain the coefficients and propagation constants. Due to the complexity of these problems, the finite-width parallel plate configuration is approximated by using infinitely wide plates. However expected differences resulting in the data that are obtained are noted and discussed.

The analysis that is presented is validated by comparisons with measured data and with data obtained by other investigators.

EMP 1-27

245-7

## 2. Electromagnetic Fields in an Infinite, Parallel Plate Waveguide with a Single Conical Input Section

### a. Physical Model

One wishes to obtain the electric and magnetic fields in the parallel plate region of the structure shown in Figure 3 in terms of known quantities in the input section and the physical dimensions of the parallel plates.

Several simplifying assumptions are made. The plates are assumed to be perfectly conducting, the analysis is performed in the plane ASB of Figure 3, the wavefronts are assumed spherical in the conical section and written as

$$\vec{E}(x,z) = V_0 \frac{e^{-jkr}}{r} \hat{\theta} \quad (1)$$

where  $r^2 = x^2 + (z + z_0)^2$  (see Figure 4). Also, it is assumed there are no reflections in the conical section from the parallel plate region, and the electric field in the aperture AMB, Figure 4, is assumed to be a planar section of a spherical wavefront.

### b. Mathematical Model

If one assumes the apex of the conical input pulser generates spherical waves, a magnetic current source  $\vec{M}$  - independent of  $y$  - is located at the plane  $z = 0$  and  $\vec{M}$  is given by [4]

$$\vec{M} = \vec{E}_a \times \hat{n} \quad (2)$$

where  $\vec{E}_a$  is the electric field strength at the aperture or in the plane  $z = 0$ . From the method of images,

$$\vec{M} = 2 \vec{E}_a \times \hat{n} = -2(\vec{E}_a \cdot \hat{x}) \hat{y} = M_y \hat{y} \quad (3)$$

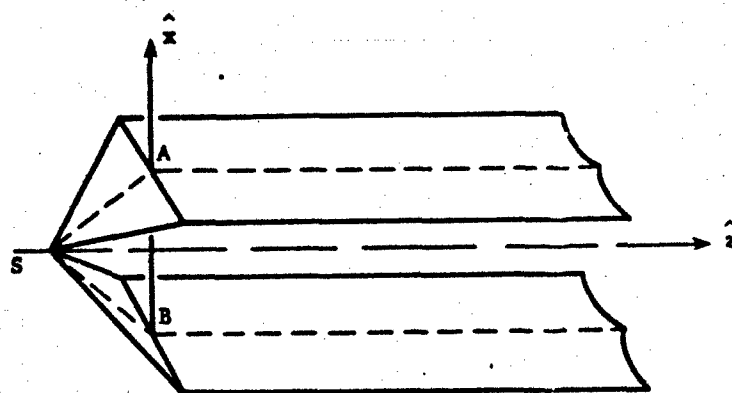


Figure 3. A Parallel-Plate Waveguide with a Single Conical Input Section.

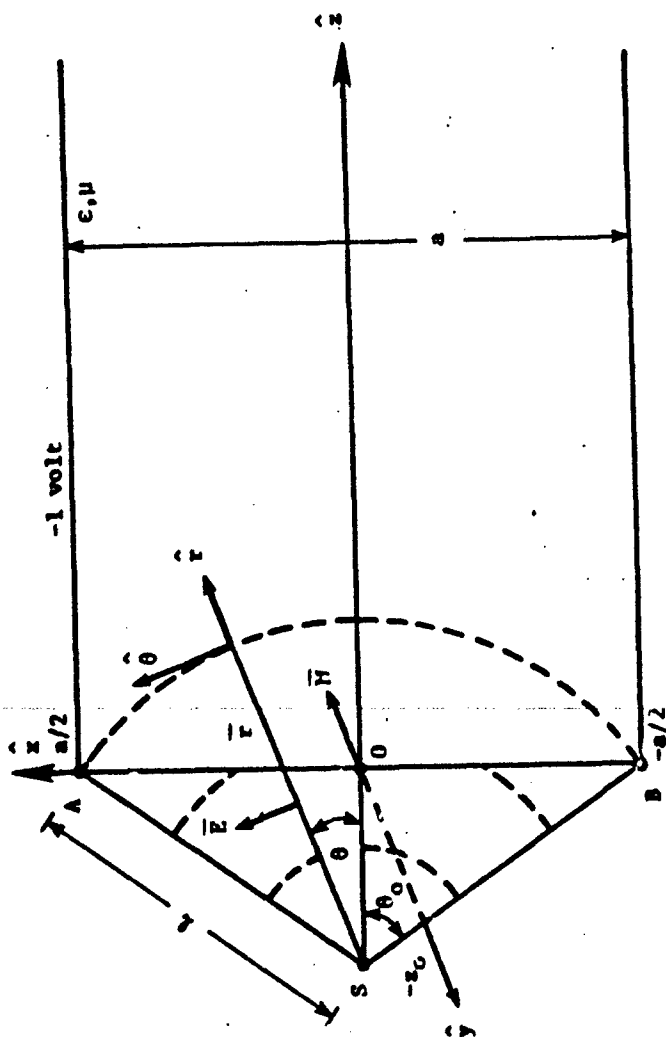


Figure 4. Two-Parallel-Plate Waveguide with a Single Pulse.  
(Longitudinal section through apex S.)

Substitution of (1) into (3) yields

$$M_y = -2V_0 \frac{e^{-jkr_0}}{r_0} \hat{\theta} \cdot \hat{x} \quad (4)$$

Since  $\hat{\theta} \cdot \hat{x} = \cos \theta = z_0/r_0$ , it follows that

$$M_y = -2z_0 V_0 \frac{e^{-jkr_0}}{r_0^2} \quad (5)$$

where  $r_0^2 = x^2 + z_0^2$ . The constant  $V_0$  is defined by normalizing the voltage between the plates to unity: i.e.

$$V_{BA} = - \int_B^A \vec{E}(x,z) \cdot d\vec{s} = -1 \text{ V} \quad (6)$$

Choosing the spherical wavefront through A and B as the path of integration, i.e.,  $r_0 = l$ , one finds

$$V_0 = \frac{e^{jkl}}{2\theta_0} \quad (7)$$

and

$$M_y = \frac{-z_0}{\theta_0(x^2 + z_0^2)} e^{-jk(\sqrt{x^2 + z_0^2} - l)} \text{ V/m} \quad (8)$$

For a charge and current free medium, Maxwell's equations are

$$\begin{aligned} \nabla \cdot \vec{D} &= 0 \\ \nabla \cdot \vec{B} &= 0 \\ \nabla \times \vec{E} &= -j\omega\mu \vec{H} - \vec{M} \\ \nabla \times \vec{H} &= j\omega\epsilon \vec{E} \end{aligned} \quad (9)$$

where  $\epsilon$  and  $\mu$  are the free space values of permittivity and permeability, and the time dependence  $e^{j\omega t}$  is understood but suppressed. Since  $\bar{H}$  is  $y$  independent and the plates are assumed to be infinite in extent in the  $y$  direction, Maxwell's equations must be  $y$  independent. Thus, for TM waves

$$(\nabla_{xz}^2 + k^2) H_y = j\omega\epsilon M_y \quad (10)$$

$$E_x = -\frac{1}{j\omega\epsilon} \frac{\partial H_y}{\partial z} \quad (11)$$

$$E_z = \frac{1}{j\omega\epsilon} \frac{\partial H_y}{\partial x} \quad (12)$$

where  $\nabla_{xz}^2 = \frac{\partial^2}{\partial x^2} + \frac{\partial^2}{\partial z^2}$  and  $k = 2\pi/\lambda = \omega/c$

### c. Frequency Domain

The standard technique for solving (10) is the Green's function method; i.e.,  $H_y$  is replaced by  $G(x, z|x', 0)$  and  $M_y$  is replaced by  $\delta(x-x')\delta(z)$ . Thus, to find  $G$ , one must solve

$$(\nabla_{xz}^2 + k^2) G(x, z|x', 0) = j\omega\epsilon \delta(x-x')\delta(z) \quad (13)$$

Additionally,  $G$  must satisfy the same boundary conditions as  $H_y$ , or

$$(1) \quad \frac{\partial G}{\partial x} = 0 \quad \text{at } x = \pm a/2$$

$$(11) \quad \int_{-\infty}^{\infty} |G|^2 dz < \infty$$

$G$  is assumed to be a Fourier series of even and odd terms

$$G = \sum_{n=0,2,4,\dots} \left(\frac{\epsilon_n}{a}\right)^{\frac{1}{2}} b_n^e(z) \cos \frac{n\pi x}{a} + \sum_{n=1,3,5,\dots} \left(\frac{2}{a}\right)^{\frac{1}{2}} b_n^o(z) \sin \frac{n\pi x}{a} \quad (14)$$

with superscripts  $e$  and  $o$  representing even and odd integers respectively, and

$$\begin{aligned} \epsilon_n &= 1 & \text{if } n &= 0 \\ &= 2 & \text{if } n &\neq 0 \end{aligned}$$

The solution of (13) for the even terms in  $G$  is

$$G^e(x, z | x', 0) = -\frac{\omega \epsilon}{a} \sum_{n=0,2,4,\dots} \frac{\epsilon_n}{2} \cos \frac{n\pi x'}{a} \cos \frac{n\pi x}{a} \frac{e^{-jk_n z}}{k_n} \quad (15)$$

where  $k_n^2 = k^2 - (n\pi/a)^2$ . To obtain  $H_y^e$ , one evaluates the integral

$$H_y^e(x, z) = \int_{-a/2}^{a/2} M_y(x') G^e(x, z | x', 0) dx' \quad (16)$$

It follows that

$$H_y^e(x, z) = \frac{z_0 \omega \epsilon e^{jkz}}{\theta_0 a} \sum_{n=0,2,4,\dots} \left(\frac{\epsilon_n}{2}\right) A_n^e \cos \frac{n\pi x}{a} \frac{e^{-jk_n z}}{k_n} \quad (17)$$

where

$$A_n^e = \int_{-a/2}^{a/2} \cos \frac{n\pi x'}{a} \frac{e^{-jk\sqrt{x'^2 + z_0^2}}}{x'^2 + z_0^2} dx' \quad (18)$$

Similarly, one can solve for the odd terms with the result

$$H_y^o(x, z) = \frac{z_o \omega \epsilon e^{jkl}}{\theta_o a} \sum_{n=1,3,5,\dots} A_n^o \sin \frac{n\pi x}{a} \frac{e^{-jk_n z}}{k_n} \quad (19)$$

and

$$A_n^o = \int_{-a/2}^{a/2} \sin \frac{n\pi x'}{a} \frac{e^{-jk' \sqrt{x'^2 + z_o^2}}}{x'^2 + z_o^2} dx' \quad (20)$$

$A_n^o$  for single cone excitation is identically zero; thus

$$H_y(x, z) = \frac{z_o \omega \epsilon e^{jkl}}{\theta_o a} \sum_{n=0,1,2,3,\dots} \epsilon_n A_n \cos \frac{2n\pi x}{a} \frac{e^{-jk_n z}}{k_n} \quad (21)$$

In (21) it should be observed that the summation is now over all integers,

and

$$A_n = \int_0^{a/2} \cos \frac{2n\pi x'}{a} \frac{e^{-jk' \sqrt{x'^2 + z_o^2}}}{x'^2 + z_o^2} dx' \quad (22)$$

and

$$k_n^2 = k^2 - (2n\pi/a)^2 \quad (23)$$

Use of (11) and (12) in conjunction with (21) leads to

$$E_x(x, z) = \frac{z_o e^{jkl}}{\theta_o a} \sum_{n=0} \epsilon_n A_n \cos \frac{2n\pi x}{a} e^{-jk_n z} \quad (24)$$

$$E_z(x, z) = \frac{2\pi j z_o e^{jkl}}{\theta_o a^2} \sum_{n=0} n A_n \sin \frac{2n\pi x}{a} \frac{e^{-jk_n z}}{k_n} \quad (25)$$



The first terms in (21), (24), and (25) represent the TEM mode and all remaining terms are TM modes. For finite-width parallel plates TE modes also are excited and propagated [3]. Moreover the TE modes are considerably less attenuated than the TM modes. For both sets, the modes are attenuated above cut-off due to the radiation from the open sides of the waveguide. Thus the results that are obtained for the infinitely wide plates must be interpreted carefully.

d. Time Domain, Magnetic Field

Having obtained the frequency domain expressions in section c, one can proceed in several ways to evaluate the time domain results. From (21) [and also (25) though this will not be discussed] one can solve the time domain problem analytically. From (24), one can evaluate the field at various frequencies and by means of numerical inverse Fourier transform [5] determine the behavior in the time domain.

Showing the  $\omega$ -dependence explicitly, one can rewrite (21) as

$$H_y(x, z, \omega) = \frac{z_0}{\theta_0 a \eta} A_0(\omega) e^{j(l-z)\omega/c} + \sum_{n=1}^{\infty} j \frac{2z_0 \epsilon_n}{a \theta_0} \cos \frac{2n\pi x}{a} A_n(\omega) \omega F_n(z, \omega) \quad (26)$$

with

$$A_n(\omega) = \int_0^{a/2} \cos \frac{2n\pi x'}{a} \frac{e^{-j \frac{\omega}{c} \sqrt{x'^2 + z_0^2}}}{x'^2 + z_0^2} dx' \quad (27)$$

$$F_n(z, \omega) = \frac{e^{j\omega l/c} e^{-jz \sqrt{\frac{\omega^2}{c^2} - \left(\frac{2n\pi}{a}\right)^2}}}{j \sqrt{\frac{\omega^2}{c^2} - \left(\frac{2n\pi}{a}\right)^2}} \quad (28)$$

and

$$\eta = \sqrt{\frac{\mu}{\epsilon}}$$

The expression in (26) is the frequency response at a particular  $\omega$  or the response to a  $\delta(t)$  input. The Fourier transform of the step function,  $u(t)$

$$u(t) = \begin{cases} 0 & t < 0 \\ 1 & t \geq 0 \end{cases}$$

is

$$f[u(t)] = \frac{1}{2\pi} \left[ \pi \delta(\omega) + \frac{1}{j\omega} \right] \quad (29)$$

from which it follows that the response to the step function excitation is

$$\begin{aligned} h_y^s(x, z, t) &= \frac{1}{2\pi} \int_{-\infty}^{\infty} \left[ \pi \delta(\omega) + \frac{1}{j\omega} \right] H_y(x, z, \omega) e^{j\omega t} d\omega \\ &= h_y^{so} + \sum_{n=1}^{\infty} h_y^{sn} \end{aligned} \quad (30)$$

where  $o$  and  $n$  refer to the zeroth or  $n$ th term. Rewriting the  $h_y^{so}$  and collecting terms in a convenient manner, one obtains

$$h_y^{so} = \frac{z_o}{\theta_o a \eta} \int_0^{a/2} \frac{1}{x'^2 + z_o^2} \left\{ \frac{1}{2\pi} \int_{-\infty}^{\infty} \left[ \pi \delta(\omega) + \frac{1}{j\omega} \right] e^{j\omega f(t, l, z, x')} d\omega \right\} dx' \quad (31)$$

and

$$f(t, l, z, x') = t + (l - z)/c - \left( \sqrt{x'^2 + z_o^2} \right) / c$$

Thus, (31) becomes

$$h_y^{so} = \frac{z_o}{\theta_o a \eta} \int_0^{a/2} \frac{1}{x'^2 + z_o^2} u \left( t + \frac{l - z}{c} - \frac{\sqrt{x'^2 + z_o^2}}{c} \right) dx' \quad (32)$$

and, since  $l \geq \sqrt{x'^2 + z_0^2}$ , then if  $t \geq z/c$

$$h_y^{so} = \frac{1}{a \eta} \quad t \geq z/c \quad (33)$$

In general one must evaluate (32) subject to the condition that

$$ct \geq \sqrt{x'^2 + z_0^2} + z - l$$

Since  $x'$  varies, this means the integral must be done in one of three ways depending on the time,  $t$ .

1. If  $ct < z_0 + z - l$ , the integral in (32) is identically zero.
2. If  $z_0 + z - l < ct < \sqrt{\left(\frac{a}{2}\right)^2 + z_0^2} + z - l$ , the upper limit on this integral is

$$x_u = \sqrt{(ct + l - z)^2 - z_0^2}$$

3. If  $ct \geq \sqrt{\left(\frac{a}{2}\right)^2 + z_0^2} + z - l$ , the upper limit on the integral is  $a/2$ .

These statements are basically causality conditions.

Using the identity  $\delta(\omega) \phi(\omega) = \delta(\omega) \phi(0)$ , one finds

$$h_y^{sn} = \int_0^{a/c} \frac{\cos \frac{2n\pi x'}{a}}{x'^2 + z_0^2} dx' \cdot \frac{c}{2\pi j} \cdot \int_{-\infty}^{\infty} \frac{e^{-jz \sqrt{\frac{\omega^2}{c^2} - \left(\frac{2n\pi}{a}\right)^2}} e^{j\omega [ct + l - \sqrt{x'^2 + z_0^2}]} d\left(\frac{\omega}{c}\right)}{\sqrt{\frac{\omega^2}{c^2} - \left(\frac{2n\pi}{a}\right)^2}} \quad (34)$$

The second integral in (34) can be transformed analytically [6] using the identity

$$\frac{1}{2\pi j} \int_{-\infty}^{\infty} \frac{e^{-jx\sqrt{\omega^2 - y^2}}}{\sqrt{\omega^2 - y^2}} e^{j\omega t} d\omega = J_0(y\sqrt{t^2 - x^2}) \quad t > x \quad (35)$$

where  $J_0$  is the Bessel function of the first kind. The final result of these manipulations is

$$h_y^s(x, z, t) = \frac{1}{a\eta} f_1 + \frac{2z_0}{\theta_0 a\eta} \sum_{n=1}^{\infty} \cos \frac{2n\pi x}{a} \int_0^{x_u} \cos \frac{2n\pi x'}{a} \frac{1}{x'^2 + z_0^2} J_0 \left\{ \frac{2n\pi}{a} \sqrt{(ct + l - \sqrt{x'^2 + z_0^2})^2 - z^2} \right\} dx' \quad (36)$$

Again, the integral in (36) must be evaluated subject to the same conditions discussed for (32), and  $f_1$  depends on the evaluation of (32) (e.g., if  $ct \geq \sqrt{(\frac{a}{c})^2 + z_0^2} + z - l$ , then  $f_1 = 1$ ). The expression (36), for  $h_y^s$ , must be evaluated numerically. First, define a new function  $\Psi(N)$  which is identical to  $h_y^s$  except the summation runs from one to  $N$  rather than from one to infinity. The function  $\Psi(N)$  versus  $N$  is shown in Figure 5. The function calculated in the program is defined

$$h_y^s(x, z, t) = \frac{\sum_{N=20}^{40} \Psi(N)}{21} \quad (37)$$

One other comment is appropriate. The integrals in (37) are evaluated using a 15 point Gauss-Legendre quadrature formula. As  $n$  increases, the function to be evaluated oscillates more rapidly. Therefore a change of variable is performed such that as  $n$  increases, the number of Gauss-Legendre zones from  $x' = 0$  to  $x' = a/2$  increases proportional to  $n$ .

The  $y$  component of the magnetic field,  $h_y^s(x, z, t)$ , due to a step function excitation is plotted with respect to time ( $t$ ) and shown in

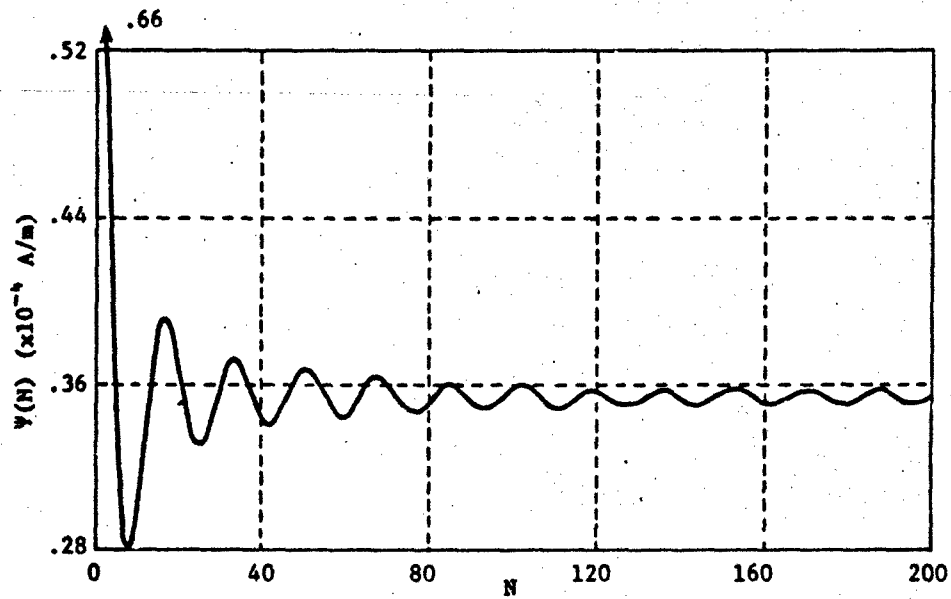


Figure 5. Plots of  $\Psi(N)$  versus  $N$ . (with  $a = 40$  m,  $z_0 = 20$  m at  $x = 0$  and  $z = 50$  m for  $t = 160$  ns)

Figures 6 for several field points in an ALECS\*-type facility, while Figure 7 is appropriate for the ARES\*\* geometry. Note that time is measured from  $t = 0$ , the time at which all the dipoles in the plane  $z = 0$  have turned on. Corresponding frequency domain (Fourier Transforms of  $h_y$ ) are shown in Figures 8 and 9. Note that singularities occur at the cavity resonances of the parallel plates.

e. Time Domain, Electric Field

The electric field calculations in the time domain have been performed using the inverse Fourier transform rather than an analytic solution.  $E_x(x, z, \omega)$ , (24), has been evaluated for 100 different frequencies varying from the d-c term to 100 MHz. The frequencies chosen were as follows:

$f$	$\Delta f$
0	-
.5 - 1 MHz	.1 MHz
1 - 10 MHz	.2 MHz
10 - 100 MHz	2 MHz

$e_x(x, z, t)$  has been evaluated using standard Fourier transform techniques: in this procedure it is assumed that  $E_x(x, z, \omega)$  is a linear function of frequency between the individual calculated field values [5]. Since  $E_x(x, z, \omega)$  as given by (24) is the impulse response then it must be multiplied by the Fourier transform of the actual pulse driving the plates-- in the previous section this pulse was assumed to be a unit step.

---

\*Air Force Weapons Laboratory/Los Alamos Scientific Laboratories  
Electromagnetic Pulse Calibration and Simulation Facility.

\*\*Advanced Research Electromagnetic Pulse Simulation Facility.

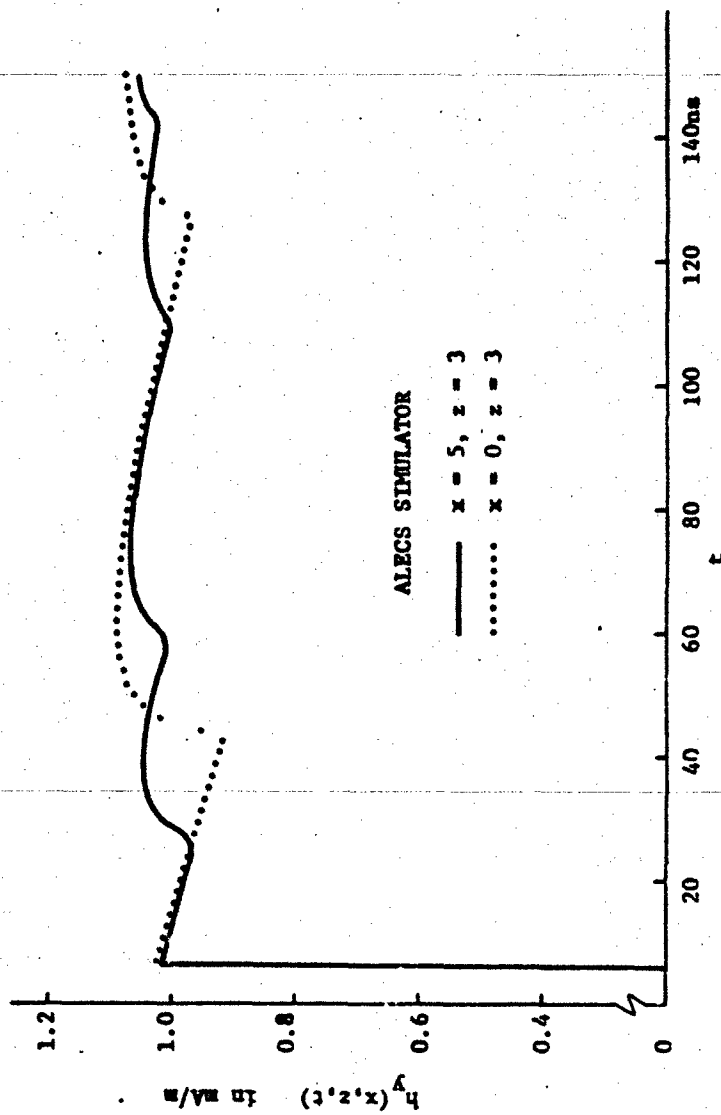


Figure 6: The horizontal magnetic field produced by a unit step excitation of the ALECS simulator.

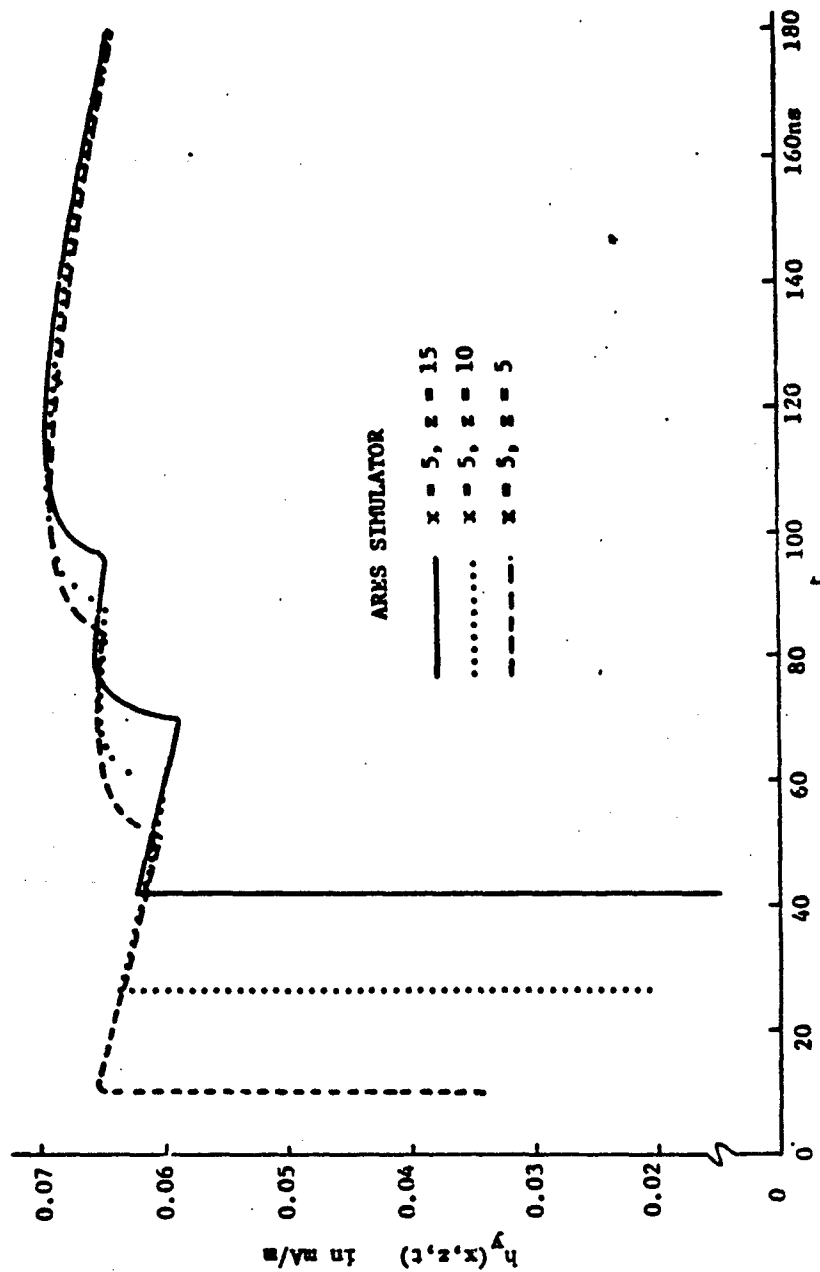


Figure 7: The horizontal magnetic field produced by a unit step excitation of the ARES simulator.



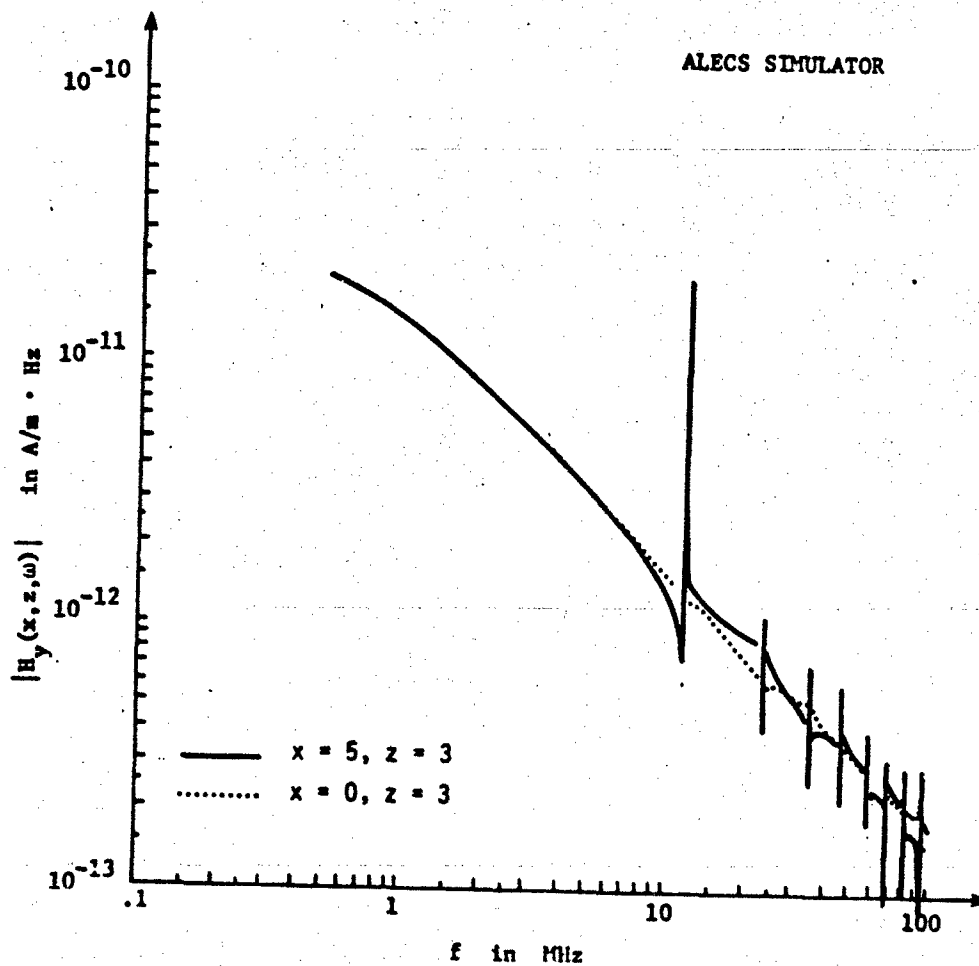


Figure 8: The Fourier transform of the horizontal magnetic field produced by a unit step excitation of the ALECS simulator.

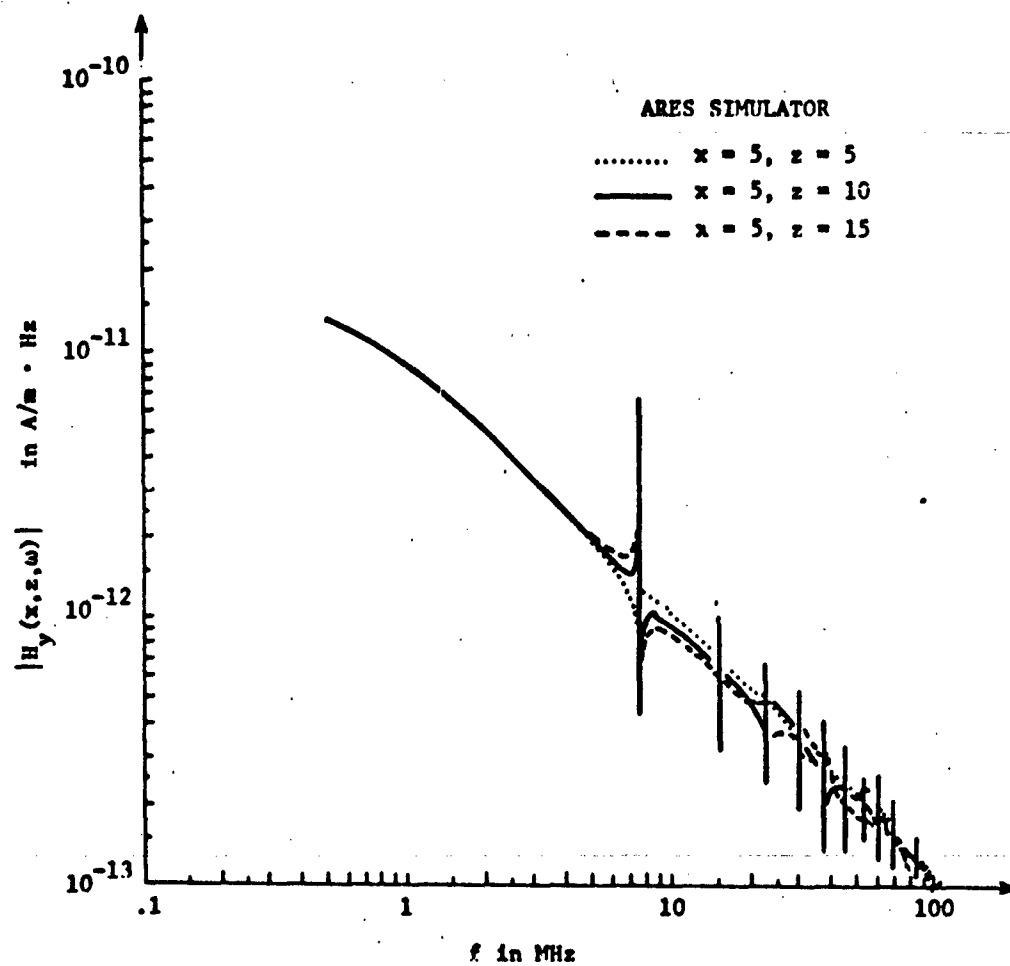


Figure 9: The Fourier transform of the horizontal magnetic field produced by a unit step excitation of the ARES simulator.

However, for convenience in applying the inverse Fourier transform here the unit step with exponential damping is considered, i.e.,  $u(t)e^{-\alpha t}$  where  $\alpha = 4.8 \times 10^3 \text{ s}^{-1}$ .

The complex magnitude of the Fourier transform of the vertical electric field is shown in Figures 10 through 15. In contrast with the results of Figures 8 and 9 the Fourier transform of the vertical electric field does not exhibit singularities at the cavity resonances. Results appropriate for the ALECS and ARES simulators are given. Note that it is only when the frequency is above the lowest cut-off frequency that there is any z-dependence of the fields.

Time domain results for the vertical electric field are shown in Figures 16 through 21. These indicate that the TEM mode contribution is dominant.

f. Comparison of Experimental Data and Theoretical Results  
for the ALECS Facility

In 1974 Giles et.al. [7] evaluated the performance of the ALECS facility in the CW mode. In particular,  $B$  and  $D$  measurements were made versus frequency at the center of the working volume. Figures 22 and 23 shown the results of these measurements. On the same figures one can see the results of the theoretical analysis for CW performance. In order to compare results,  $B_0$  and  $D_0$  were chosen such that the experimental and theoretical results matched at 5 MHz.

Before interpreting the foregoing results, the question of finite width versus infinite width plates should be considered. Marin [8] found that for finite width plates the TE modes were most important, i.e., they exhibited less attenuation above cutoff, and the analysis

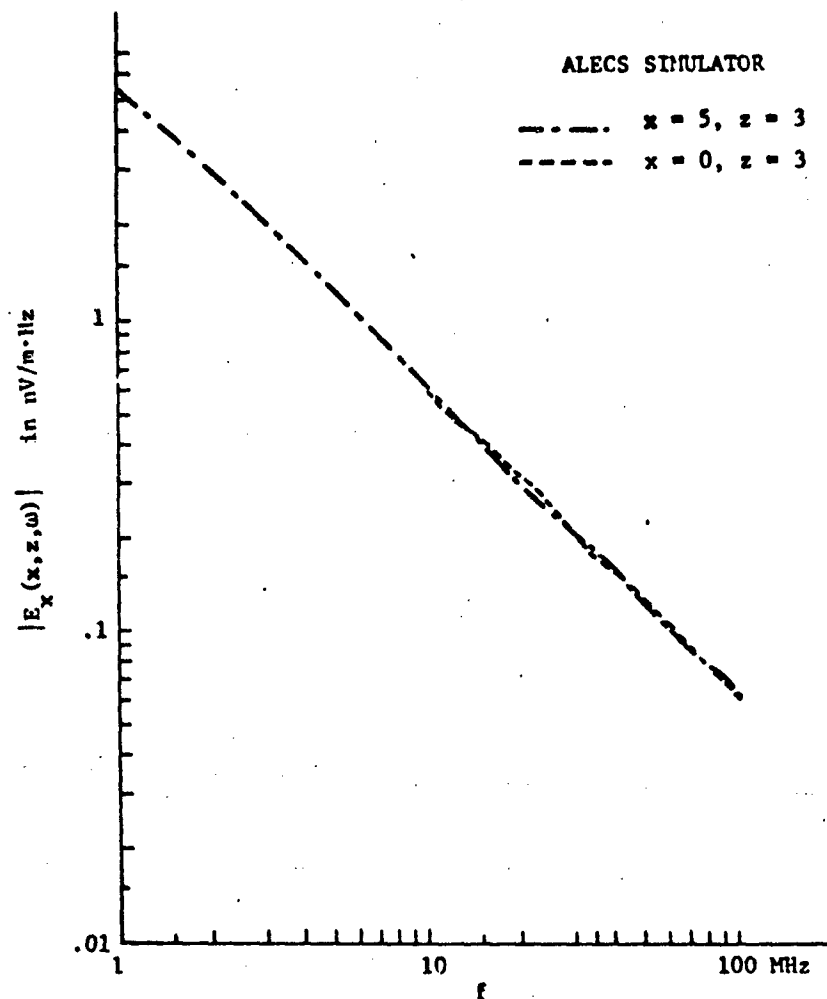


Figure 10: The Fourier transform of the vertical electric field produced by a unit step (with exponential decay) excitation of the ALECS simulator.

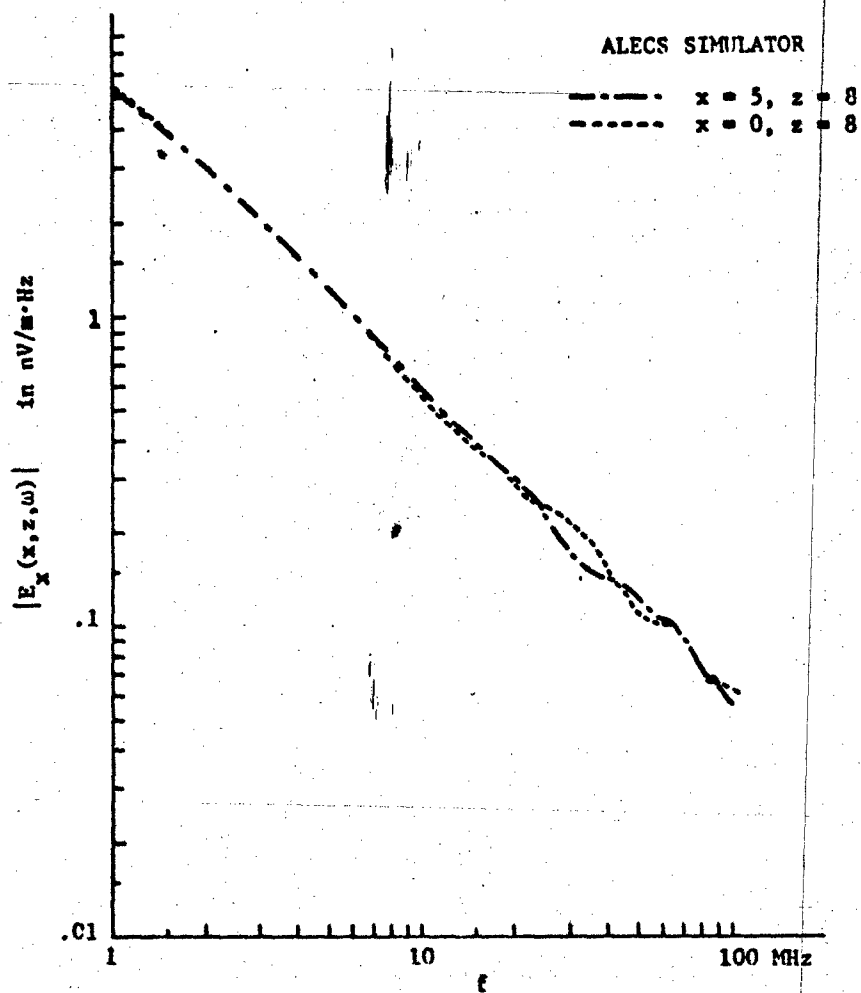


Figure 11: The Fourier transform of the vertical electric field produced by a unit step (with exponential decay) excitation of the ALECS simulator.

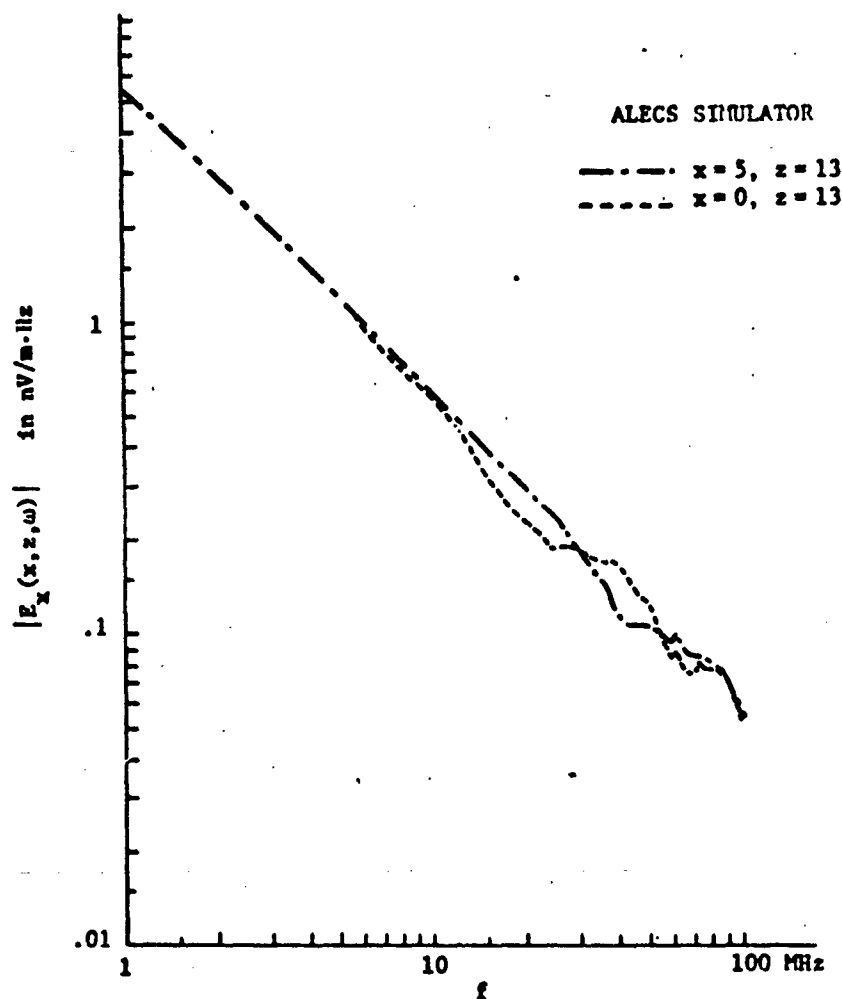


Figure 12: The Fourier transform of the vertical electric field produced by a unit step (with exponential decay) excitation of the ALECS simulator.

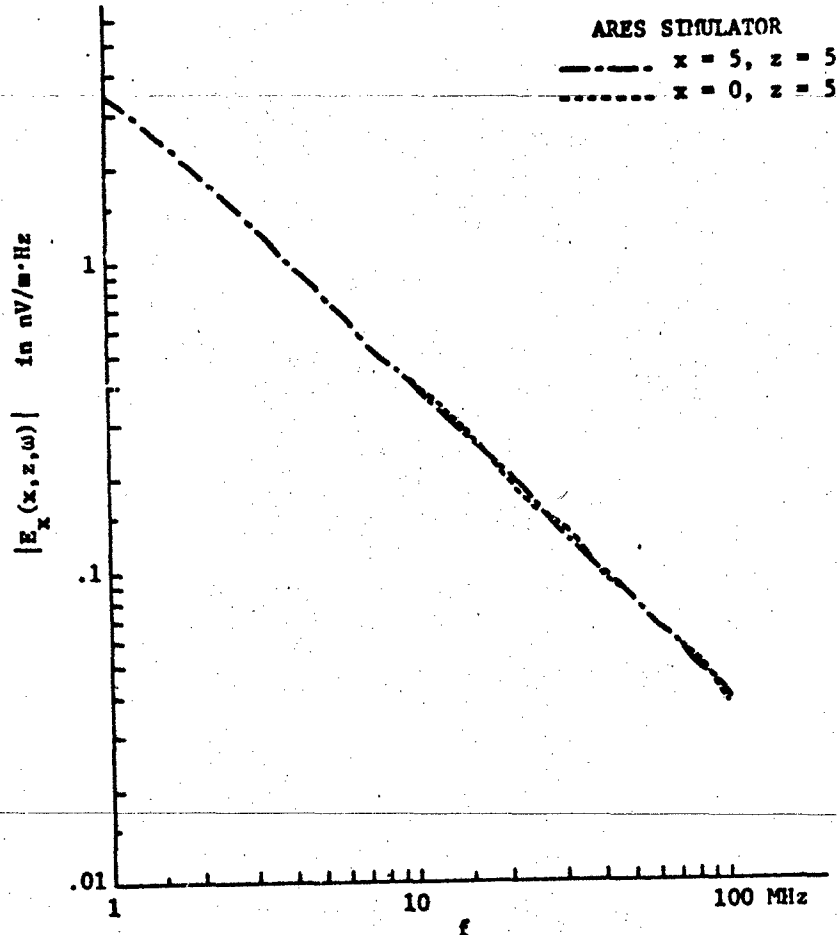


Figure 13: The Fourier transform of the vertical electric field produced by a unit step (with exponential decay) excitation of the ARES simulator.

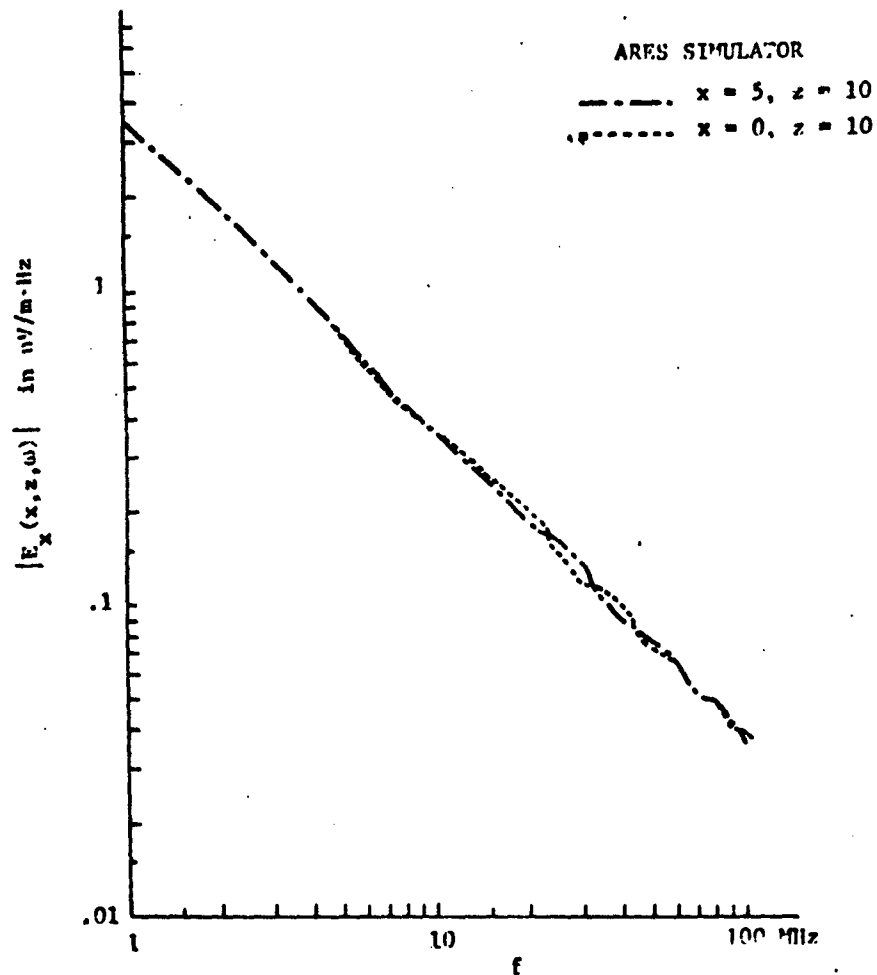


Figure 14: The Fourier transform of the vertical electric field produced by a unit step (with exponential decay) excitation of the ARES simulator.



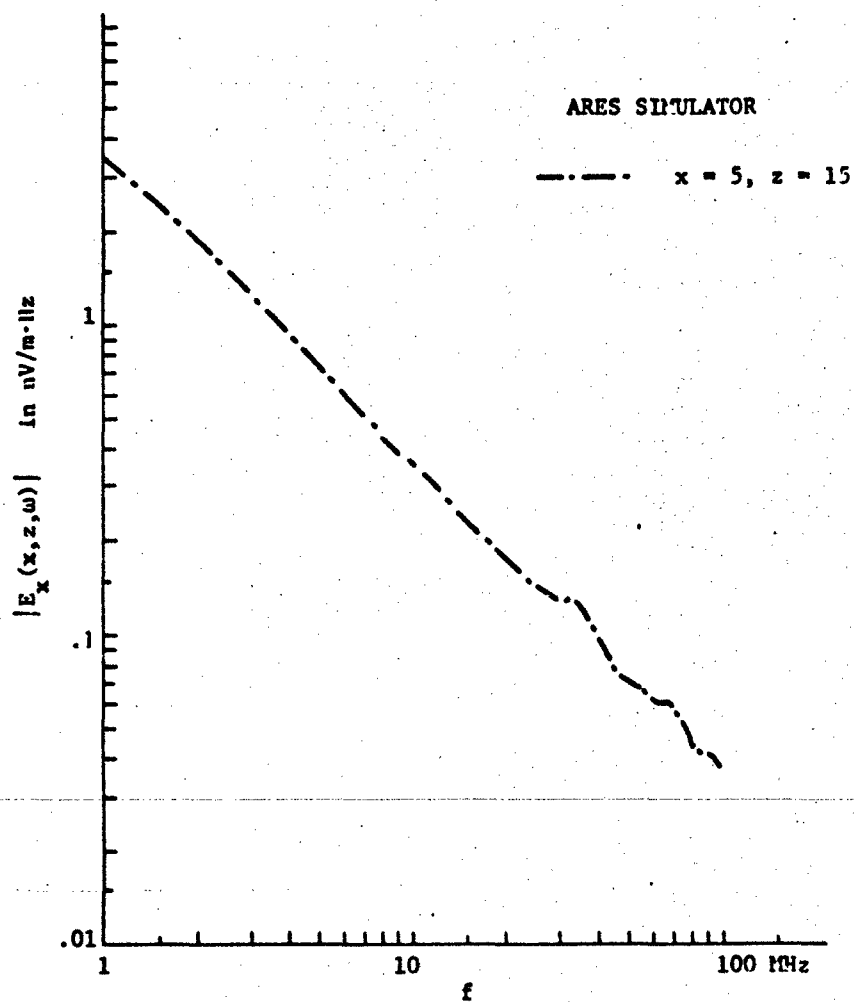


Figure 15: The Fourier transform of the vertical electric field produced by a unit step (with exponential decay) excitation of the ARES simulator.

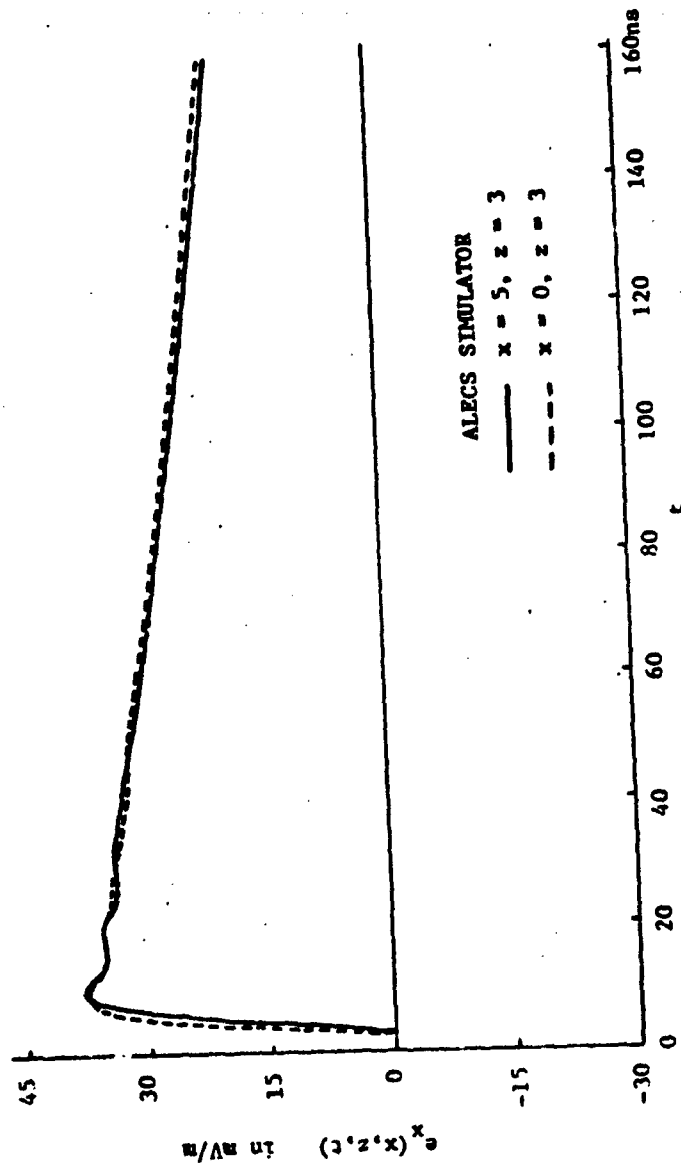


Figure 16: The vertical electric field produced by a unit step (with exponential decay) excitation of the ALECS simulator.

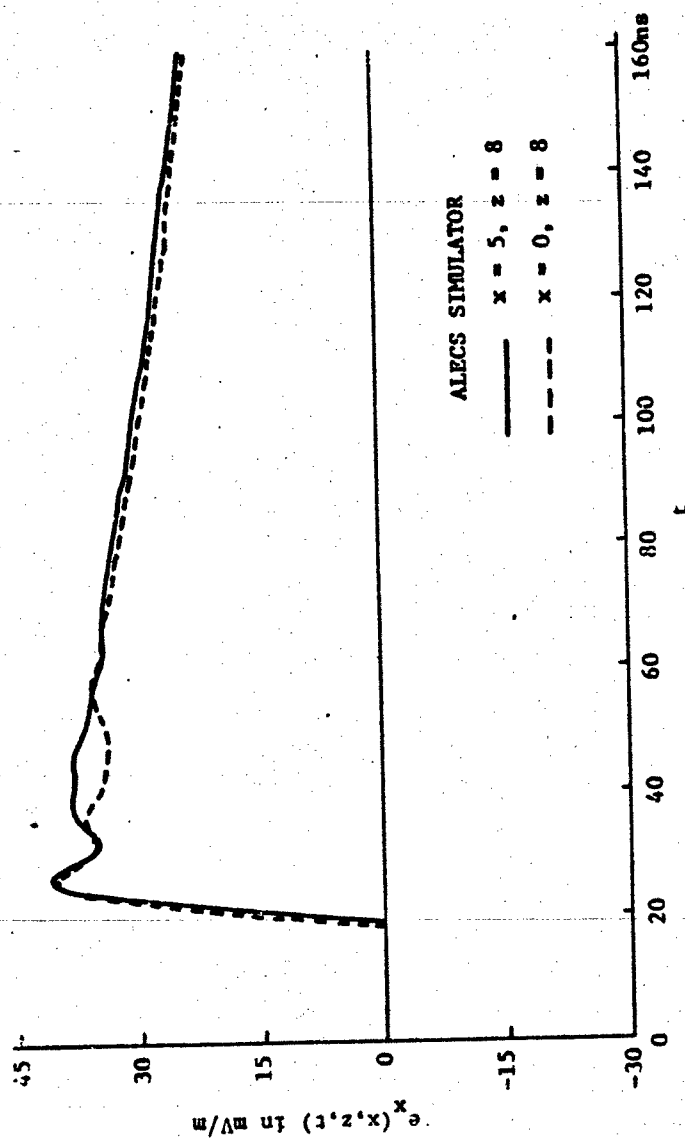


Figure 17: The vertical electric field produced by a unit step (with exponential decay) excitation of the ALECS simulator.

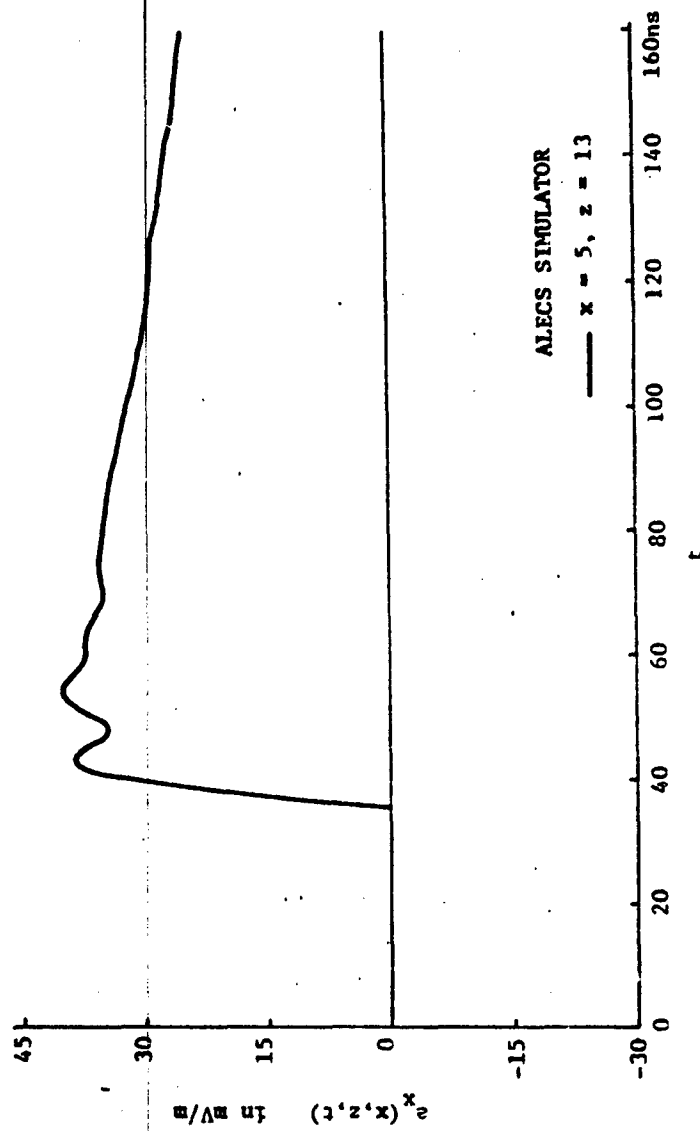


Figure 18: The vertical electric field produced by a unit step (with exponential decay) excitation of the ALECS simulator.

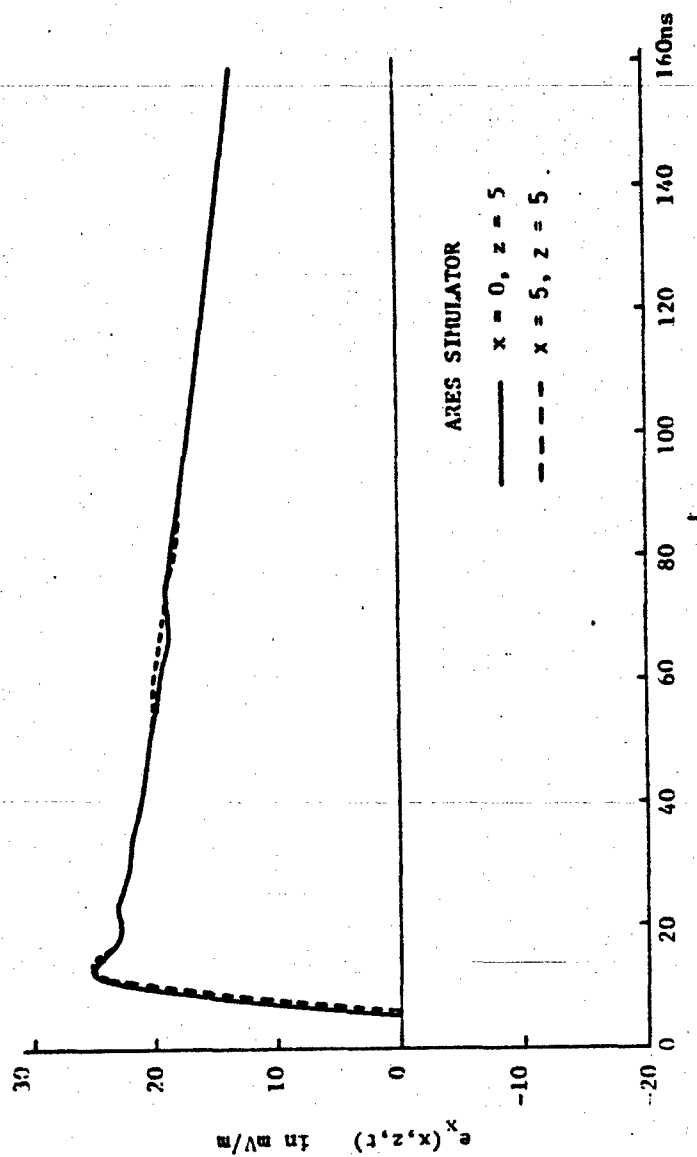


Figure 19: The vertical electric field produced by a unit step (with exponential decay) excitation of the ARES simulator.

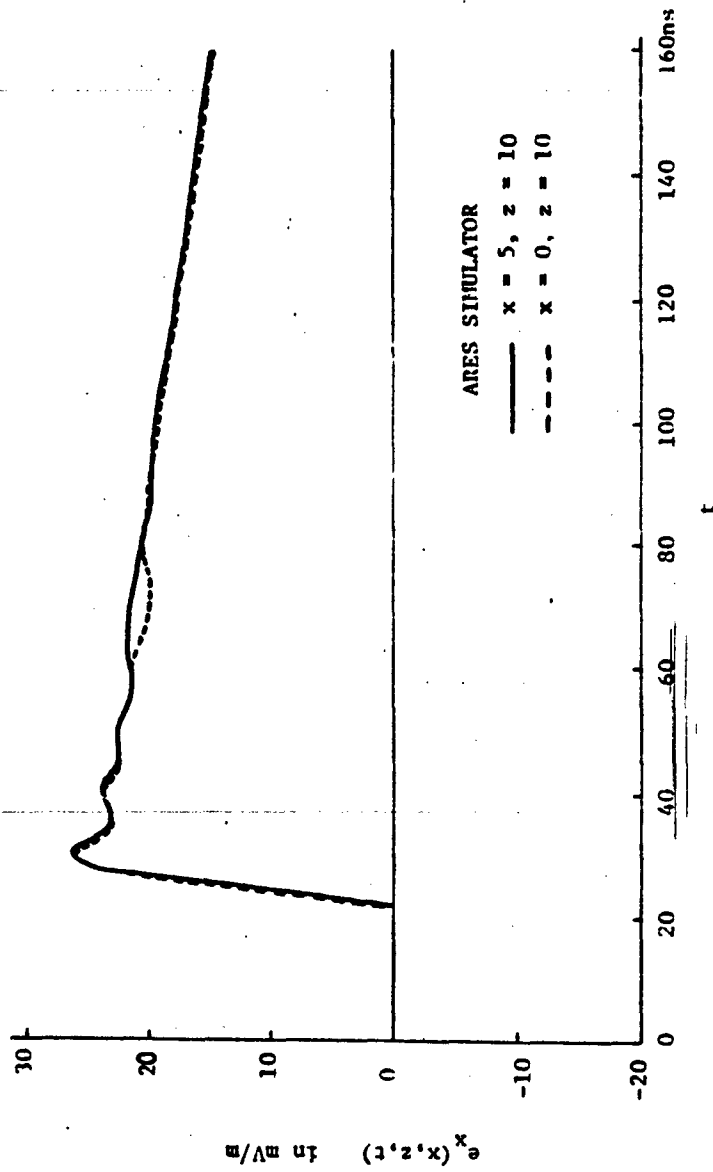


Figure 20: The vertical electric field produced by a unit step (with exponential decay) excitation of the ARES simulator.

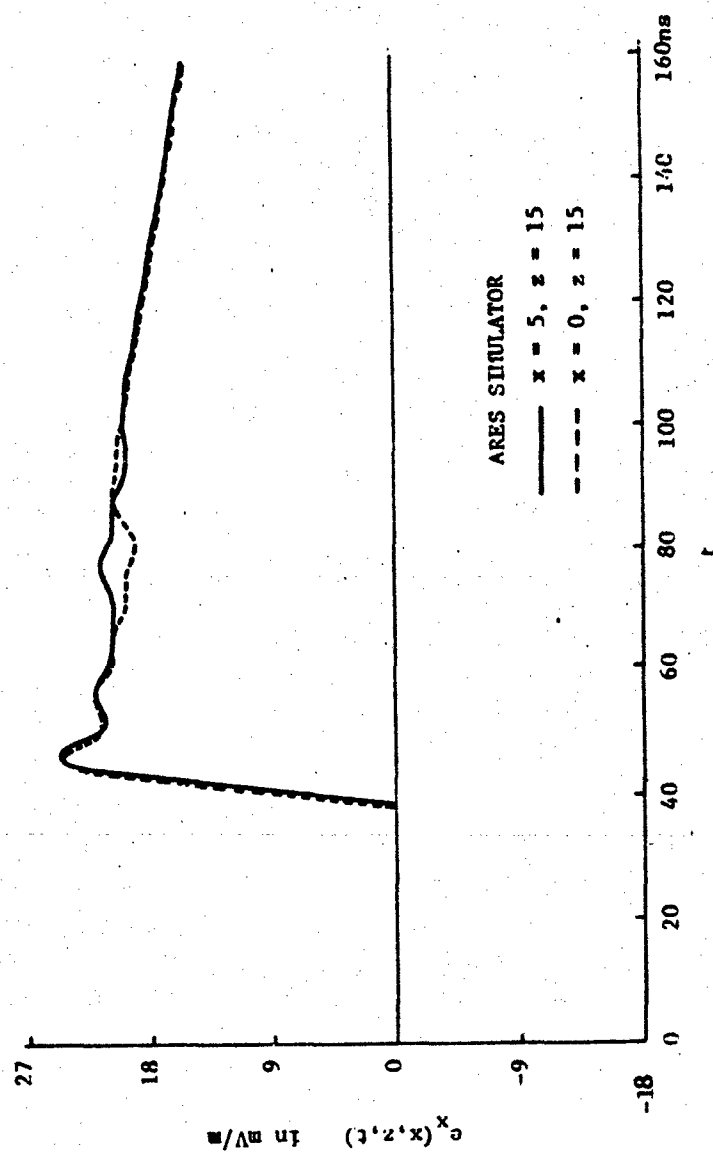


Figure 21: The vertical electric field produced by a unit step (with exponential decay) excitation of the ARES simulator.

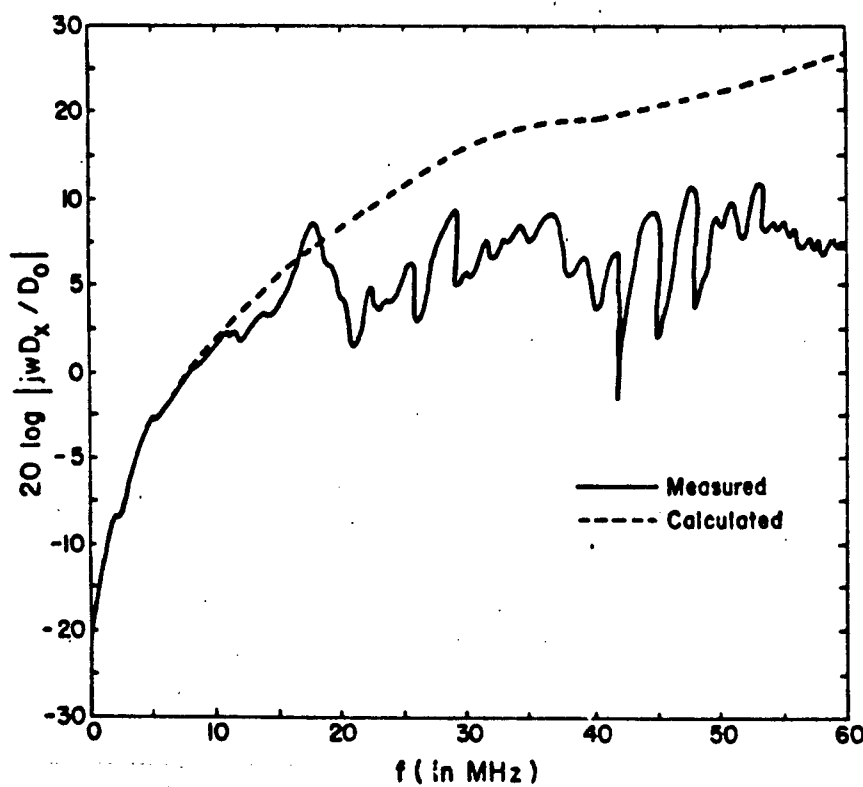


Figure 22: Evaluation of the CW performance of the ALECS facility—electric field determination in the working volume at  $x = 0$ ,  $z = 7.5$ .



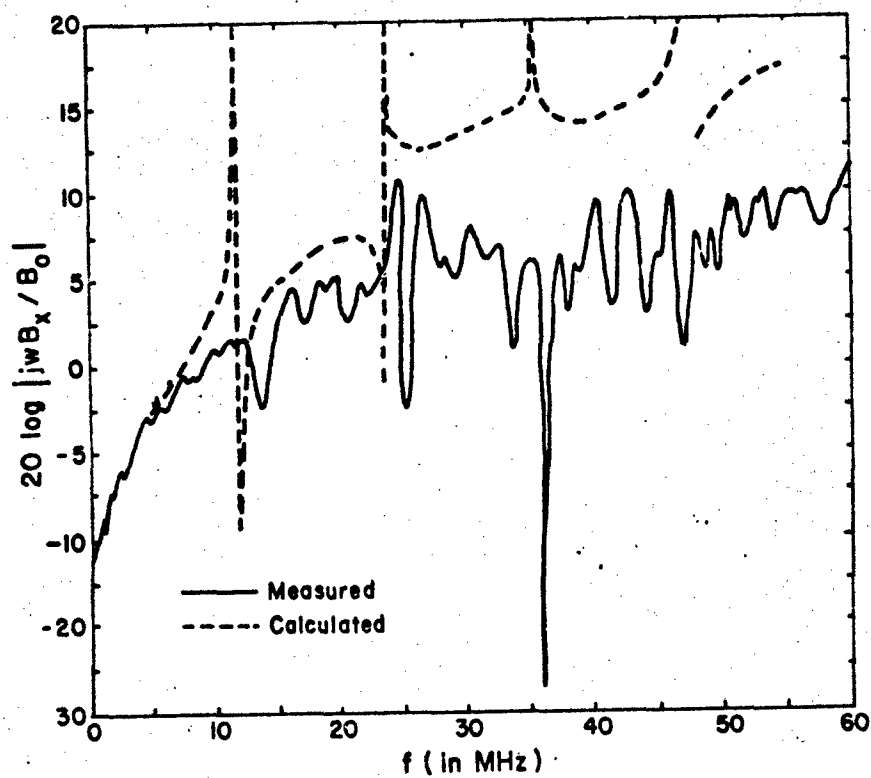


Figure 23: Evaluation of the CW performance of the ALECS facility-magnetic field determination in the working volume at  $x = 0$ ,  $z = 7.5$ .

used here did not include TE modes. But since the TEM mode contributes very significantly to the simulator field there is good agreement between the measured and calculated data as is shown in Figures 22 and 23. The disparity increases significantly at higher frequencies partly because reflections from the termination (not included in the analysis) become more significant and partly because the waveguide modes supported by the actual finite width waveguide have radiation losses. The very sharp variation in the calculated magnetic field may be attributed to the onset of mode propagation, e.g. the cutoff frequency for the TM mode is about 12 MHz.

### 3. Electromagnetic Fields in an Infinite, Parallel Plate Waveguide with a Double Conical Input Section

#### a. Physical Model

In some instances one wishes to obtain field values in the parallel plate region of a simulator that are higher than those attainable from a single pulser. In these situations, one solution is to use two separate pulsers and two input sections, Figure 24. One problem that arises is the nonsimultaneous firing of the sources, and the analysis must take this into account if it is to provide meaningful data.

#### b. Mathematical Model

As in section 2, each source is assumed to generate a spherical wave,  $\bar{E}$

$$\bar{E} = v_0 \frac{e^{-jkr}}{r} \hat{r} \quad (38)$$

where  $r = \sqrt{(x \mp a/4)^2 + (z + z_0)^2}$  for the upper (-) and lower (+) cones.

Again, normalizing each source to 1 volt, one obtains a magnetic source for the upper cone as

$$u_{My} = \frac{-z_0 e^{-jk \left[ \sqrt{(x - a/4)^2 + z_0^2} - l \right]}}{\theta_0 [(x - a/4)^2 + z_0^2]} \quad (39)$$

For the lower cone, the magnetic source becomes

$$u_{My} = \frac{-z_0 e^{-jk \left[ \sqrt{(x + a/4)^2 + z_0^2} - l \right]}}{\theta_0 [(x + a/4)^2 + z_0^2]} \quad (40)$$

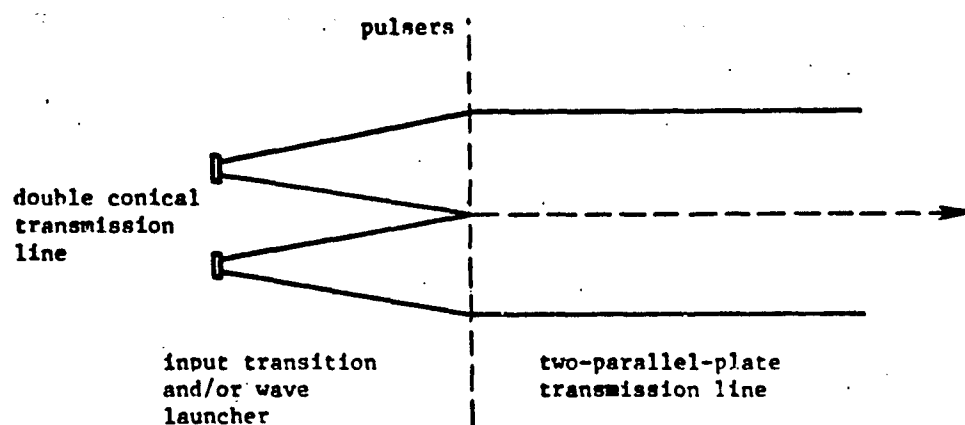


Figure 24: A Design for a Parallel-Plate Transmission Line Simulators. (View parallel to plates and perpendicular to direction of propagation, or z direction.)

Substitution of (39) into (16) [the upper source analysis is performed independently of the lower source] leads to

$$u_{H_y}^e(x, z, \omega) = \frac{z_o \epsilon \omega}{\theta_o a} e^{jkl} \sum_{n=0,2,4,\dots} \frac{\epsilon_n}{2} u_{A_n}^e \cos \frac{n\pi x}{a} \frac{e^{-jk_n z}}{k_n}, \quad z > 0 \quad (41)$$

where

$$u_{A_n}^e = \int_0^{a/2} \frac{\cos \frac{n\pi x'}{a}}{(x' - a/4)^2 + z_o^2} e^{-jk \sqrt{(x' - a/4)^2 + z_o^2}} dx' \quad (42)$$

and

$$u_{H_y}^o(x, z, \omega) = \frac{z_o \omega \epsilon e^{jkl}}{\theta_o a} \sum_{n=1,3,5,\dots} u_{A_n}^o \sin \frac{n\pi x}{a} \frac{e^{-jk_n z}}{k_n}, \quad z > 0 \quad (43)$$

where

$$u_{A_n}^o = \int_0^{a/2} \frac{\sin \frac{n\pi x'}{a}}{(x' - a/4)^2 + z_o^2} e^{-jk \sqrt{(x' - a/4)^2 + z_o^2}} dx' \quad (44)$$

For the lower cone one obtains expressions for  $H_y^e$  and  $H_y^o$  that are identical to (41) and (43) except  $u_{A_n}^e$  and  $u_{A_n}^o$  must be replaced by  $l_{A_n}^e$  and  $l_{A_n}^o$  where

$$l_{A_n}^e = \int_{-a/2}^0 \frac{\cos \frac{n\pi x'}{a}}{(x' + a/4)^2 + z_o^2} e^{-jk \sqrt{(x' + a/4)^2 + z_o^2}} dx' \quad (45)$$

and

$$l_{A_n}^o = \int_{-a/2}^0 \frac{\cos \frac{n\pi x'}{a}}{(x' + a/4)^2 + z_o^2} e^{-jk \sqrt{(x' + a/4)^2 + z_o^2}} dx' \quad (46)$$

For nonsimultaneous firing of the sources, (41) and (43) should be modified so that they differ in phase by  $\omega\tau$  where  $\tau$  is the time duration between the firings.

c. Time Domain, Magnetic Field

The step response for the even terms in the upper cone excitation is obtained as follows. Expression (41) is multiplied by the frequency spectrum of the step function

$$\pi \delta(\omega) + \frac{1}{j\omega}$$

and the Fourier transform is

$$u_{hy}^{se} = \frac{1}{2\pi} \int_{-\infty}^{\infty} \left[ \pi \delta(\omega) + \frac{1}{j\omega} \right] \frac{z_o \epsilon}{a \theta_o} \sum_{n=0,2,4,\dots} \frac{\epsilon_n}{2} \cos \frac{n\pi x}{a} \cdot$$

$$\int_0^{a/2} \frac{\cos \frac{n\pi x'}{a}}{(x' - a/4)^2 + z_o^2} e^{-j \frac{\omega}{c} \sqrt{(x - a/4)^2 + z_o^2}} dx' \cdot$$

$$\omega e^{j l \frac{\omega}{c}} \frac{e^{-j z \sqrt{\frac{\omega^2}{c^2} - \left(\frac{n\pi}{a}\right)^2}}}{\sqrt{\frac{\omega^2}{c^2} - \left(\frac{n\pi}{a}\right)^2}} e^{j \omega t} d\omega \quad (47)$$

As in the single cone case in section 2, the  $\omega$  integral can be performed analytically leading to

$$u_{hy}^{se}(x, z, t) = \frac{1}{a\eta} + \frac{z_o}{a\theta_o \eta} \sum_{n=2,4,\dots} \cos \frac{n\pi x}{a} \int_0^{a/2} \frac{\cos \frac{n\pi x'}{a}}{(x' - a/4)^2 + z_o^2} \cdot$$

$$J_0 \left\{ \frac{n\pi}{a} \left[ \left[ ct + l - \sqrt{(x' - a/4)^2 + z_o^2} \right]^2 - z^2 \right]^{1/2} \right\} dx' \quad (48)$$

with the restriction that  $ct + l - \sqrt{(x' - a/4)^2 + z_0^2} \geq z$ . In a similar fashion odd terms for the upper source,  $u_{hy}^{so}$ , and even and odd terms for the lower source,  $l_{hy}^{se}$  and  $l_{hy}^{so}$  respectively, can be derived. Finally, if one allows the upper source to fire after the lower source by a time interval  $\tau$ , one obtains

$$h_y^s(x, z, t) = u_{hy}^{se}(x, z, t) + u_{hy}^{so}(x, z, t) + l_{hy}^{se}(x, z, \tau_1) + l_{hy}^{so}(x, z, \tau_1) \quad (49)$$

where  $\tau_1 = t + \tau$ . In detail, (49) becomes

$$\begin{aligned} h_y^s(x, z, t) = & \frac{2f_1}{a\eta} + \frac{z_0}{a\theta_0\eta} \sum_{n=2,4,6,\dots} \cos \frac{n\pi x}{a} \int_0^x \frac{\cos \frac{n\pi x'}{a}}{(x' - a/4)^2 + z_0^2} \\ & \left[ J_0 \left\{ \frac{n\pi}{a} \sqrt{(ct + l - \sqrt{(x' - a/4)^2 + z_0^2})^2 - z^2} \right\} \right. \\ & \left. + J_0 \left\{ \frac{n\pi}{a} \sqrt{(c\tau_1 + l - \sqrt{(x' - a/4)^2 + z_0^2})^2 - z^2} \right\} \right] dx' \\ & + \frac{z_0}{a\theta_0\eta} \sum_{n=1,3,5} \sin \frac{n\pi x}{a} \int_0^{a/2} \frac{\sin \frac{n\pi x'}{a}}{(x' - a/4)^2 + z_0^2} \\ & \left[ J_0 \left\{ \frac{n\pi}{a} \sqrt{(ct + l - \sqrt{(x' - a/4)^2 + z_0^2})^2 - z^2} \right\} \right. \\ & \left. - J_0 \left\{ \frac{n\pi}{a} \sqrt{(c\tau_1 + l - \sqrt{(x' - a/4)^2 + z_0^2})^2 - z^2} \right\} \right] dx' \quad (50) \end{aligned}$$

The comments regarding the solution of (36) in section 2 are also applicable to the solution of (50).

d. Time Domain, Electric Field

Having derived  $u_{ly}^s(x, z, \omega)$  and  $\hat{h}_y^s(x, z, \omega)$ , one can obtain the Fourier transform of the vertical electric field  $E_x(x, z, \omega)$  from (24). Then, in exactly the same procedure as that described in section 2e, time domain electric fields may be obtained using the inverse Fourier transform. Also as before the electric field calculation is made for an exponentially-decaying, unit-step excitation.

e. Numerical Results for the ATLAS I\* Simulator

While the ARES simulator can not propagate TE modes, the Atlas I and the ALECS simulators can since the waveguide plates are a wire mesh and hence can support currents transverse to the direction of propagation. Therefore, the results to be presented subsequently are valid only in a qualitative sense since the analysis did not include TE modes. However, the excitation of the TEM mode and the asynchronous firing of the pulses should be treated quite accurately by the analysis. Accordingly a copious amount of data is presented. Since the ATLAS I simulator is still under construction there is no measured data to validate the analysis. For a detailed discussion of the predicted behavior of the ATLAS I simulator the authors defer to references [9] through [12].

First the Fourier transform of the vertical electric field is shown for various positions within the ATLAS I simulator with an assumed typical asynchronous firing of the pulsers. Magnitude plots are given in Figures 25 through 28 for various points within the working volume.

---

\*The horizontally polarized, bounded wave simulator commonly referred to as TRESTLE.



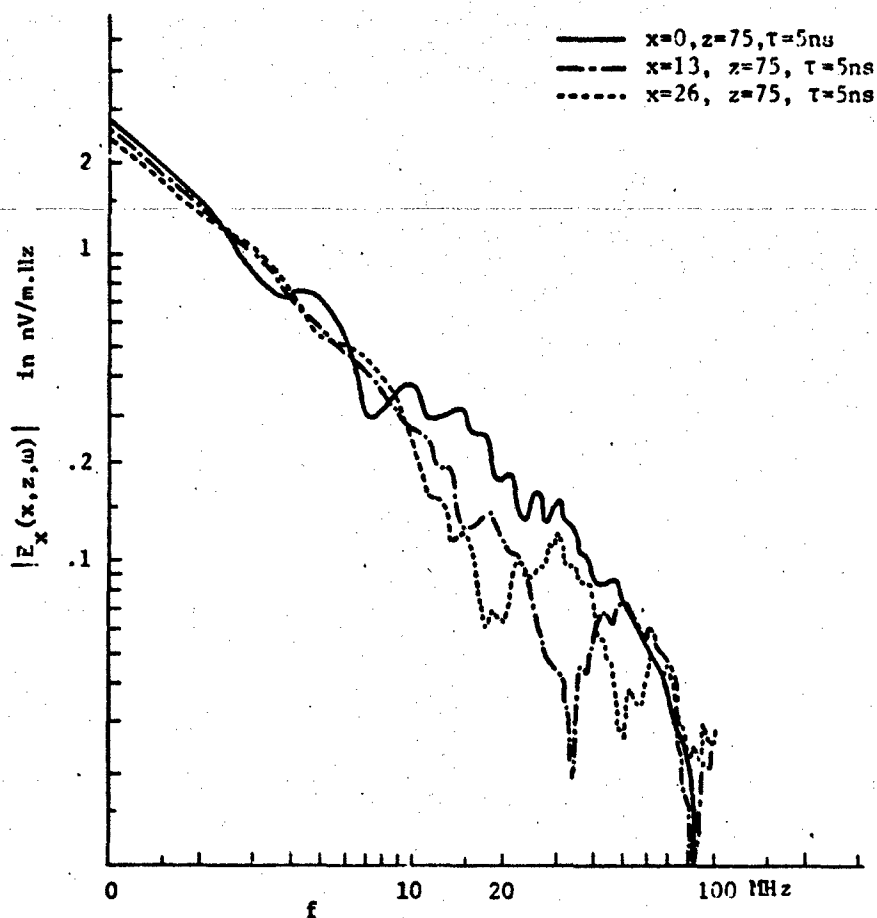


Figure 25: The Fourier transform of the vertical electric field produced by a unit step (with exponential decay) excitation of the ATLAS I simulator.

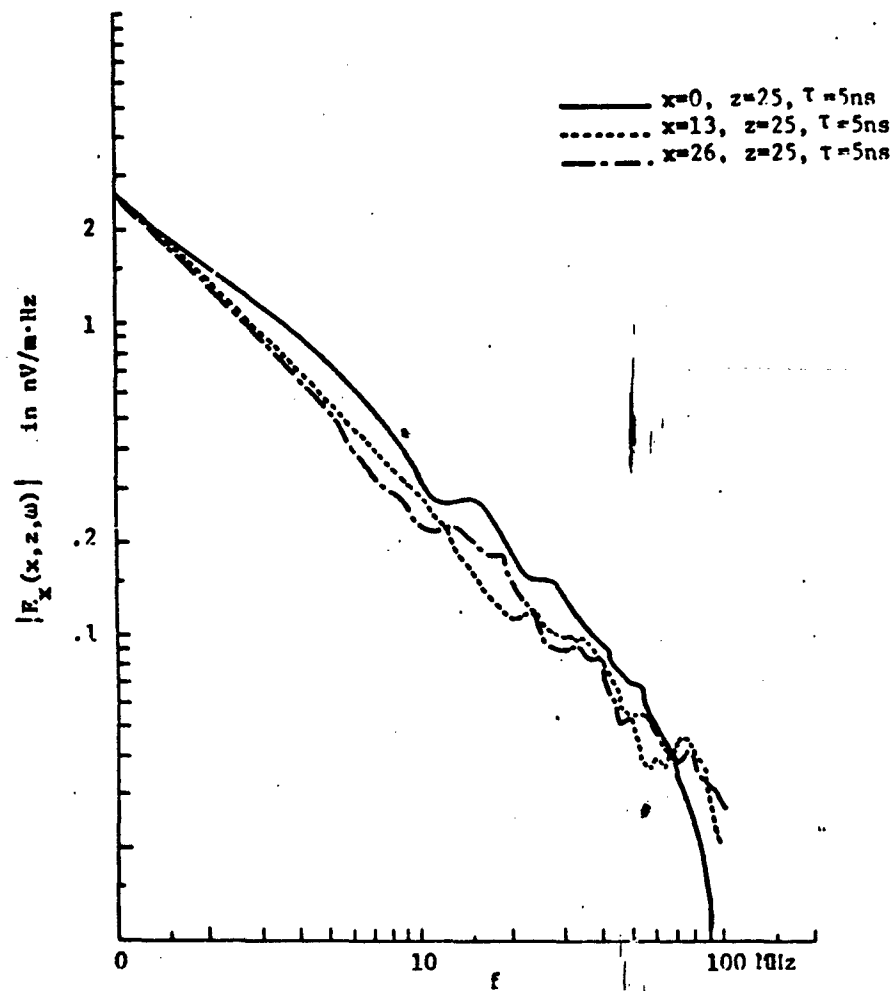


Figure 26: The Fourier transform of the vertical electric field produced by a unit step (with exponential decay) excitation of the ATLAS I simulator.

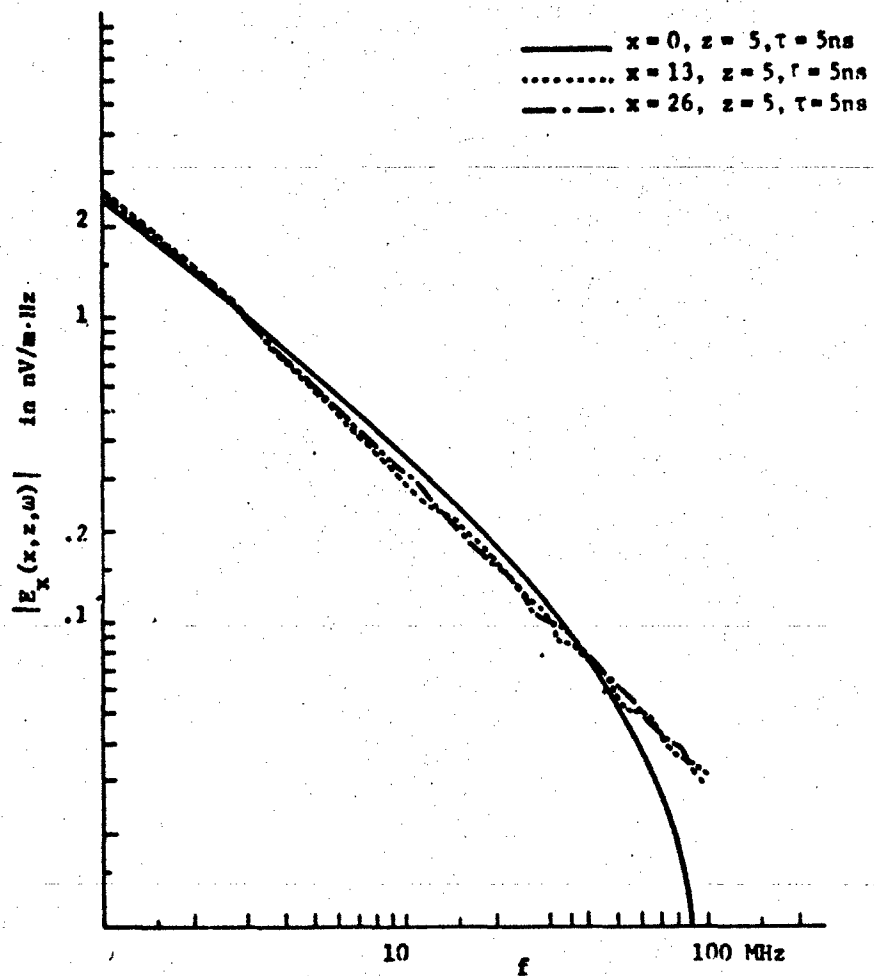


Figure 27: The Fourier transform of the vertical electric field produced by a unit step (with exponential decay) excitation of the ATLAS I simulator.

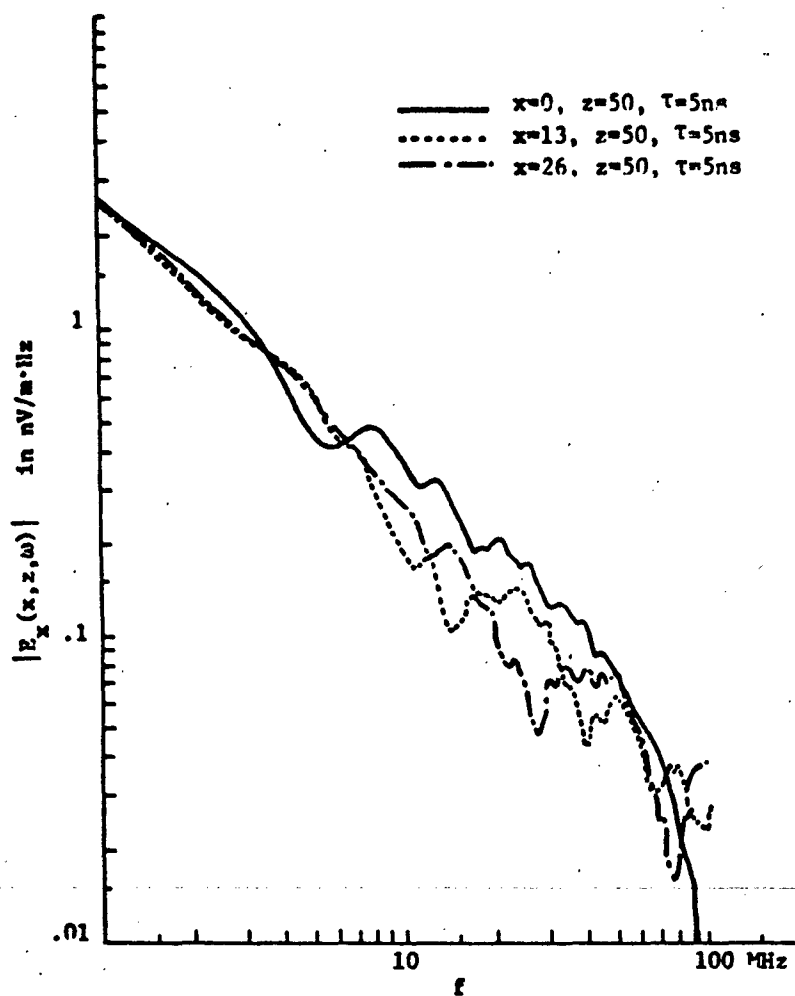


Figure 28: The Fourier transform of the vertical electric field produced by a unit step (with exponential decay) excitation of the ATLAS I simulator.

For a unit step excitation (even with exponential decay), the waveguide modes are much more significant for the ATLAS I simulator than for the ALECS or ARES due to its dual input sections and due to its lowest cut-off frequency for the waveguide modes being only 5.7 MHz. It is readily noted that the higher order modes become increasingly significant with distance from the input transition section. If only a pure TEM mode were excited in the simulator then the magnitude plots of the Fourier transform would be straight lines.

A significant contribution to the excitation of the higher order modes is the asynchronous firing of the pulsers driving the input sections of the ATLAS I simulator. This can be seen from figure 29. However, the deep nulls in the curves at 50 MHz and 100 MHz are due to destructive interference occurring as a result of the phase difference between the two sources of the two input sections.

As mentioned in the foregoing the ATLAS I simulator can support TE modes whereas the analysis includes only TM modes. For finite width plates both the TE and TM modes are evanescent, but for infinite plates the modes do not radiate. Hence the effect of the TM modes is over emphasized by the analysis (as shown in Figures 22 and 23) and the effect of the TE modes under emphasized. One would expect then that the relative importance of the higher order modes as exhibited in Figures 25 through 28 should be representative. But the asynchronous effect as shown in Figure 29 should be quite accurate.

In Figures 30 through 33 the time domain vertical electric field is presented for an exponentially decaying unit step excitation of the dual input sections to the ATLAS I simulator. Note that at the center

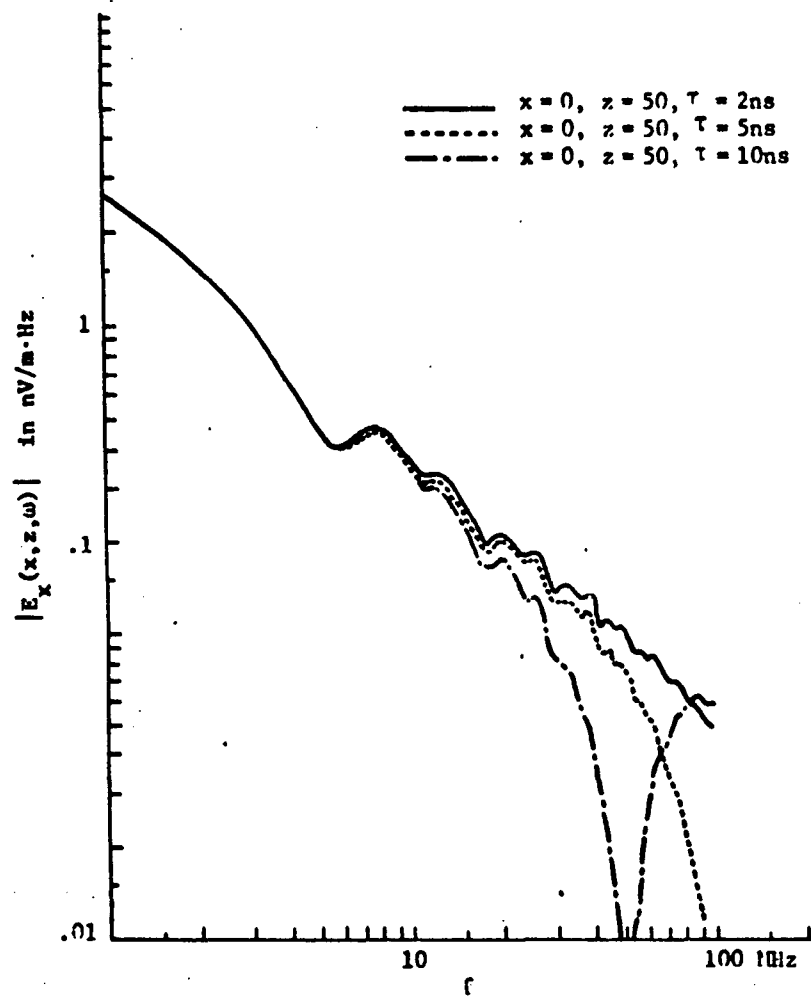


Figure 29: The Fourier transform of the vertical electric field produced by a unit step (with exponential decay) excitation of the ATLAS I simulator.

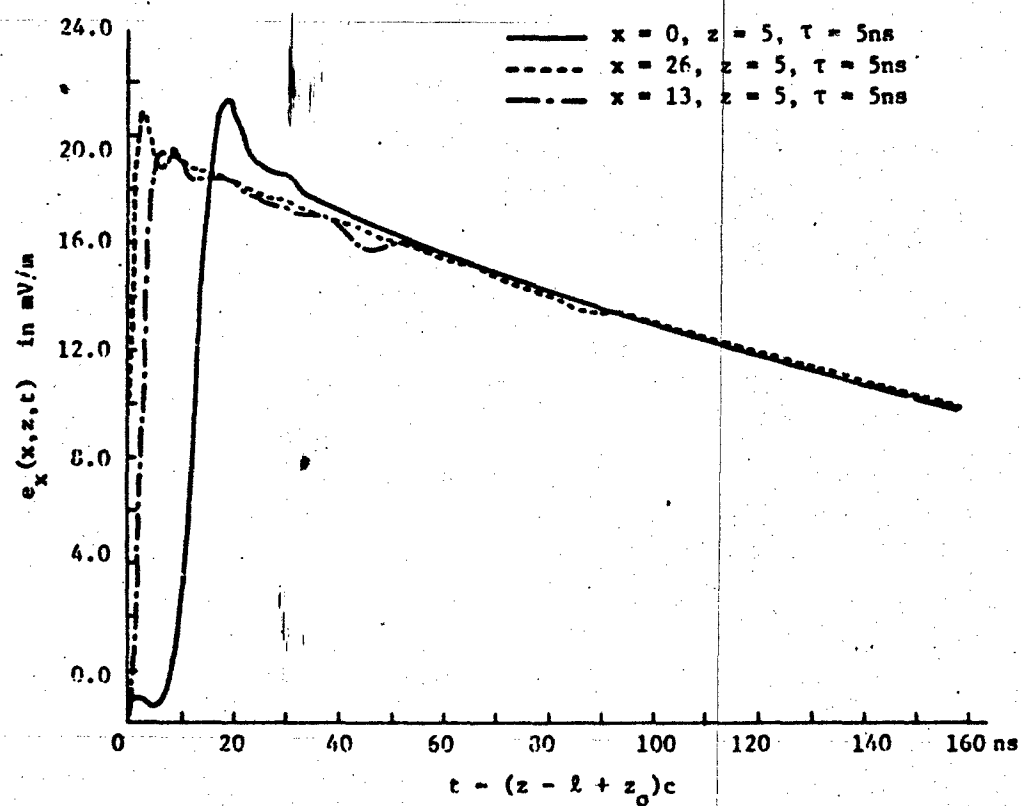


Figure 30: The vertical electric field produced by a unit step (with exponential decay) excitation of the ATLAS I simulator.

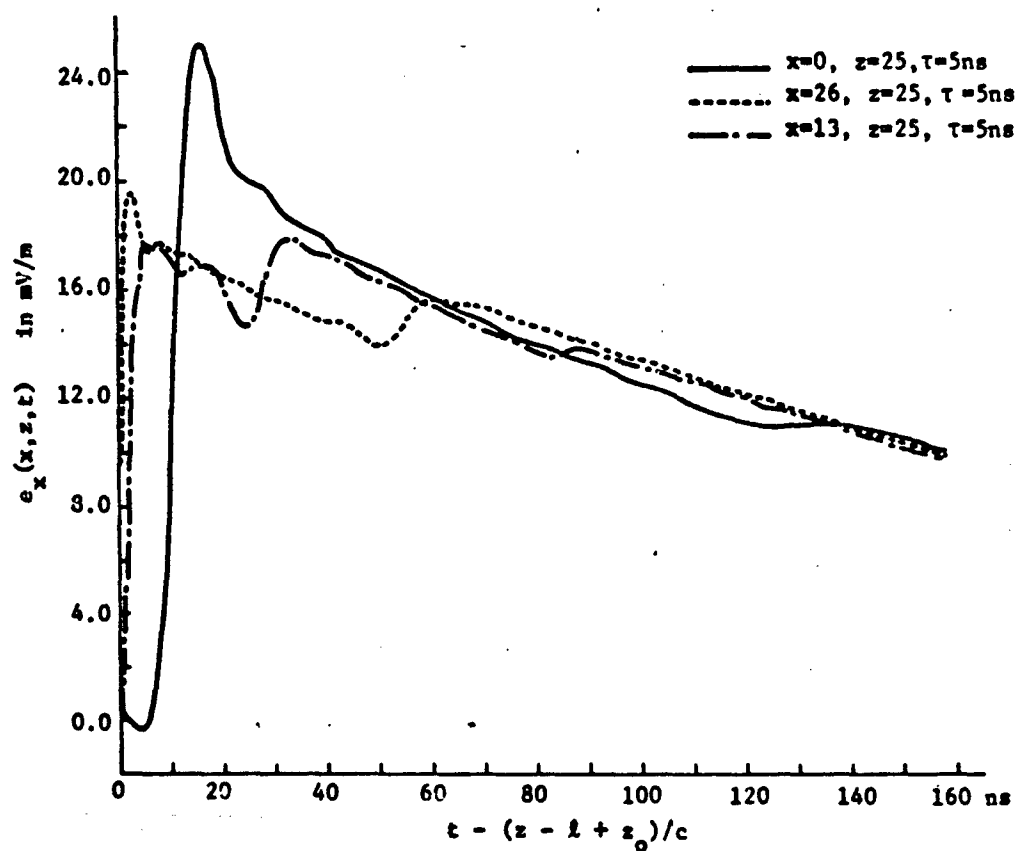


Figure 31: The vertical electric field produced by a unit step (with exponential decay) excitation of the ATLAS 1 simulator.



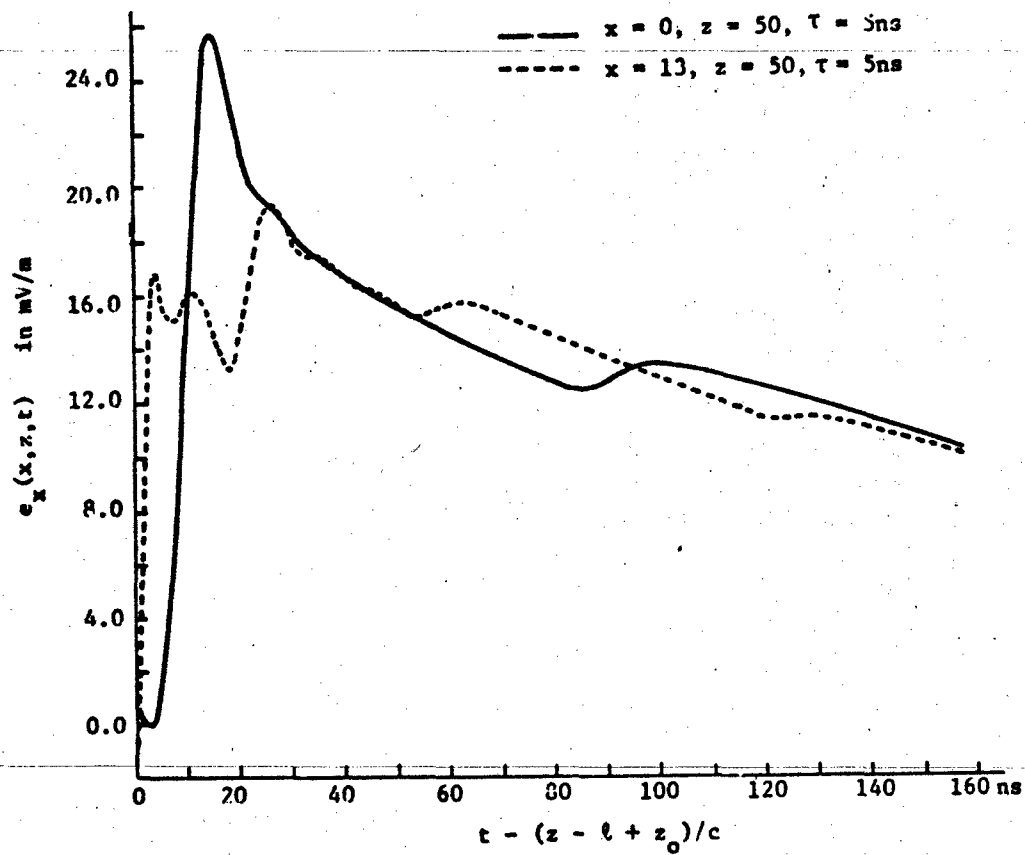


Figure 32: The vertical electric field produced by a unit step (with exponential decay) excitation of the ATLAS I simulator.

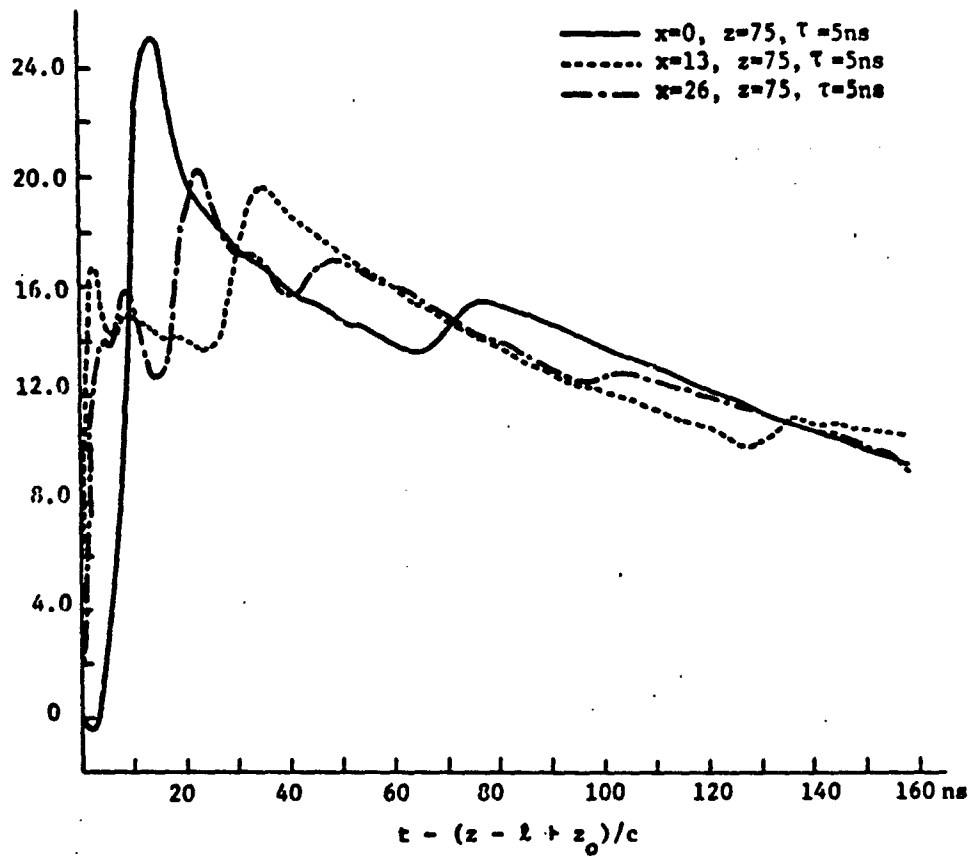


Figure 33: The vertical electric field produced by a unit step (with exponential decay) excitation of the ATLAS I simulator.

of the working volume ( $x=0$ ,  $z=50$ ) the peak electric field is about 26 millivolts/meter. Baum, et al. [12] predict that the value should be about 20 millivolts/meter. In arriving at their result Baum, et al. use ray theory primarily and account for the finite width of the plates. It is further noted that the overall time domain response follows the prediction presented by Baum, et al., considering that their assumed excitation is a unit step. Also the general behavior at  $x=13$ ,  $z=50$  follows the roughly sketched waveform that Baum, et al. predict for their point c. They predict an initial peak of about 11 millivolts/meter whereas the present analysis yields about 17 millivolts/meter, which is quite satisfactory agreement in view of the completely different analyses that are used.

In their predictions of the electric field produced by the ATLAS I simulator Baum, et al. [12] do not consider asynchronous firing of the input pulsed. The effect in the electric field at the center of the working volume due to the nonsimultaneity of the excitations of the dual input sections is exhibited in Figure 34. First there is an increase in the rise time and second if the asynchronous time is sufficiently large, e.g.  $\tau = 10$  ns, a precursor peak occurs. These precursor peaks are even more pronounced in the horizontal magnetic field computations as shown in Figure 35 for the same location in the simulator. The magnitude of the Fourier transform of the horizontal magnetic field is shown in Figure 36 for a typical location in the ATLAS I simulator.

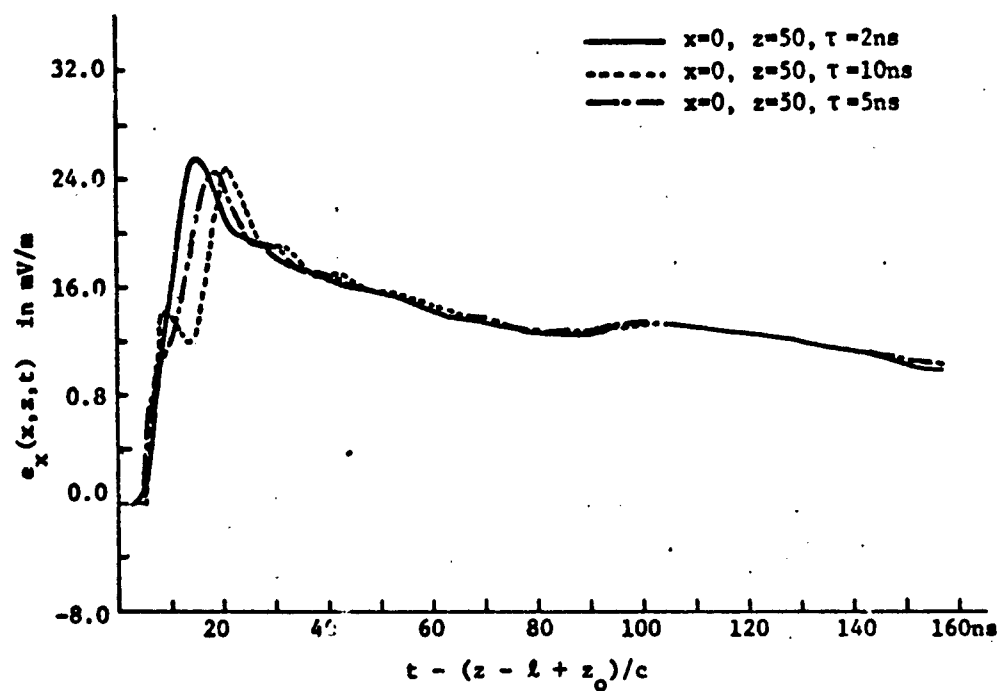


Figure 34: The vertical field produced by a unit step (with exponential decay) excitation of the ATLAS I simulator.

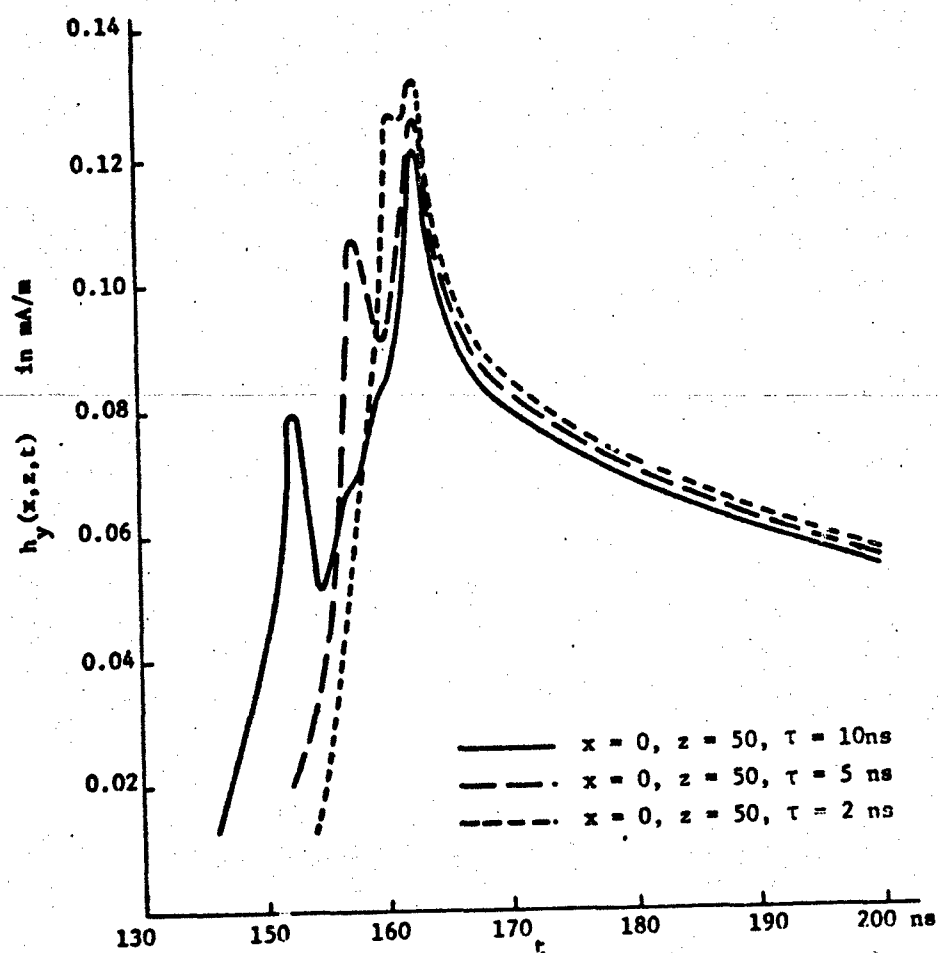


Figure 35: The horizontal magnetic field produced by a unit step excitation of the ATLAS I simulator.

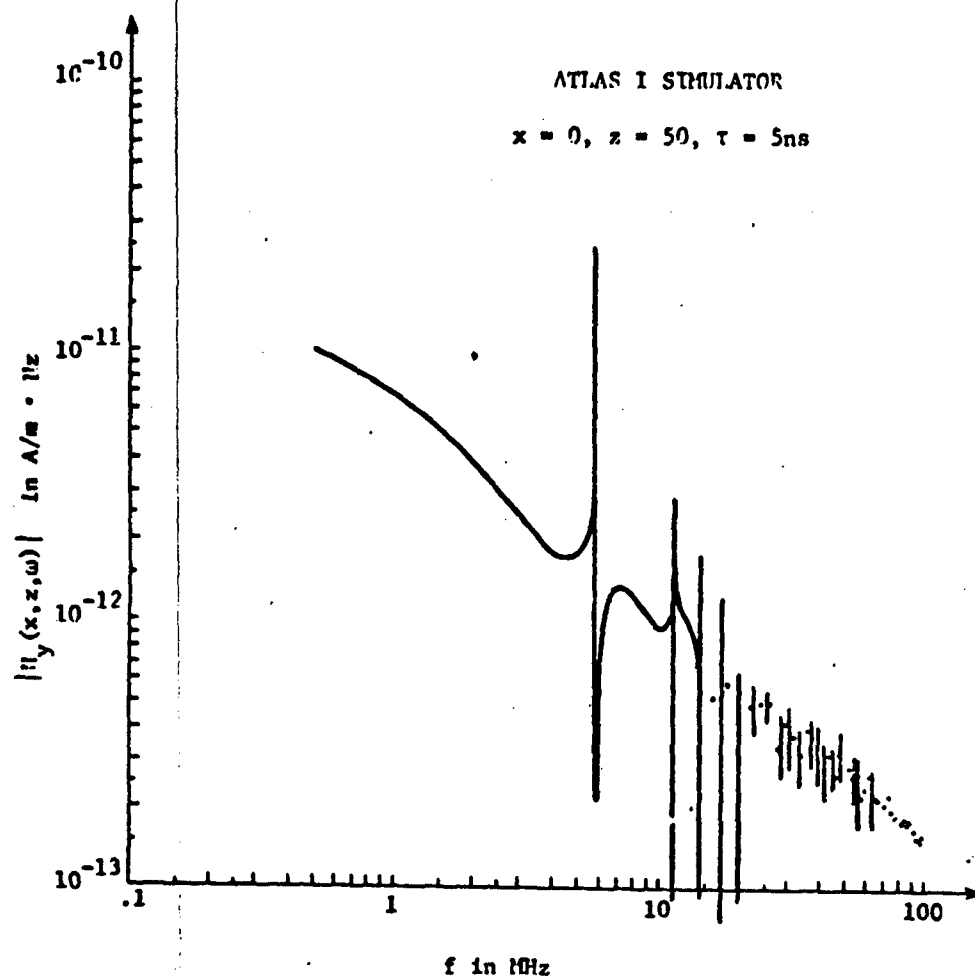


Figure 36: The Fourier transform of the horizontal magnetic field produced by a unit step excitation of the ATLAS I simulator.

## References

1. Baum, C. E., "Impedances and Field Distributions for Parallel Plate Transmission Line Simulators," Sensor and Simulation Note 21, Air Force Weapons Laboratory, Kirtland AFB, N.M., Jan., 1966.
2. Brown, T. L. and K. D. Granzow, "A Parameter Study of Two Parallel Plate Transmission Line Simulators of EMP," Sensor and Simulation Note 52, Air Force Weapons Laboratory, Kirtland AFB, N.M., Apr. 1968.
3. Marin, L., "Modes on a Finite-Width, Parallel-Plate Simulator I Narrow Plates," Sensor and Simulation Note 201, Air Force Weapons Laboratory, Kirtland AFB, N.M., Sept. 1964.
4. Dudley, D. G. and J. P. Quintenz, "Multi-Modal Transient Excitation Effects in an Infinite, Parallel-Plate Wave Guide," Can. Jour. of Physics, 50, 2826 (1972).
5. Taylor, C. D. and T. T. Crow, "Induced Electric Currents on Some Configurations of Wires, Part I, Perpendicular Crossed Wires," Interaction Note 85, Kirtland AFB, N.M., Nov. 1971.
6. Campbell, G. A. and R. M. Foster, Fourier Integrals for Practical Applications, D. Van Nostrand Co., New York, p. 11, 1948.
7. Giles, J. C., M. K. Bumgardner, G. Seely, and J. Furaus, "Evaluation and Improvement of the CW Performance of the ALECS Facility," EG & G Report AL-1085, 29 July 1974.
8. Marin, L., "Modes on a Finite-Width, Parallel-Plate Simulator II. Wide Plates," Sensor and Simulation Note 223, Air Force Weapons Laboratory, Kirtland AFB, N.M., March 1977 (revised September 1977).
9. Higgins, D., "The Diffraction of an Electromagnetic Plane Wave by Interior and Exterior Bends in a Perfectly Conducting Sheet," Sensor and Simulation Note 128, Air Force Weapons Laboratory, Kirtland AFB, N.M., January 1971.
10. Baum, C. E., "General Principles for the Design of ATLAS I and II, Part I: ATLAS: Electromagnetic Design Considerations for Horizontal Version," Sensor and Simulation Note 143, Air Force Weapons Laboratory, Kirtland AFB, N.M., January 1972.
11. Baum, C. E., et al., "Electromagnetic Design Calculations for ATLAS I, Design 1," Sensor and Simulation Note 153, Air Force Weapons Laboratory, Kirtland AFB, N.M., June 1972.
12. Baum, C. E., D. F. Higgins, and D. V. Giri, "Pulser Test Results and Preliminary Estimation of Transient Electric Field Waveforms in ATLAS I," ATLAS Memo 18, Kirtland AFB, N.M., October 1976.

## EMP SIMULATION AND ITS IMPACT ON EMP TESTING

## ABSTRACT

In testing systems for their response to EMP it is necessary to consider the EMP criteria set. Then, having chosen some EMP simulation set, one must consider how closely each simulation approximates the respective criterion, correcting for this difference by extrapolation as necessary. This paper discusses these concepts in the context of currently used techniques.



## I. INTRODUCTION

The interaction of the nuclear electromagnetic pulse (EMP) with a military or civilian electronic system is in general a very complicated process. It is this process which results in the system vulnerability or lack thereof to some EMP criterion or set of such criteria. If one had a perfect quantitative understanding of the EMP interaction process in all cases of interest, then one could presumably predict the system vulnerability or lack of same, i.e., one could perform an assessment by analysis. However, this utopia does not exist in practice.

The problem with the quantitative description of the EMP interaction process is its great complexity. There are typically such a large number of actual and/or potential items of significance to the EMP interaction process in a given system that it becomes impractical to adequately account for them all. This complexity manifests itself in at least two ways:

1. The number of individual items and combinations of items (wires, other conductor paths, impedances, propagation constants, cavities, apertures, conductive penetrations, antennas, interface circuits, filters, etc.) becomes large enough that even a small uncertainty in the analysis of the response of some individual process results in a large uncertainty in the analytically determined EMP response and hardness (or lack of vulnerability) of the system as a whole.

2. Even if the analysis in 1 were perfect (an unlikely circumstance) for a given specified system (say as specified by a "complete" set of blueprints), there is another practical difficulty. Experience has shown that the assumption that one is even aware of the existence of all relevant EMP

penetration paths is often erroneous. There are often items in the real system (for which the analysis is supposed to apply) which are not indicated on the drawings, and which represent important EMP interaction paths.

This can be summarized as: the system is

1. too complicated, and
2. not sufficiently well defined.

The above observations of analysis uncertainty summarize the current state of affairs; this will not necessarily accurately reflect the future state of the art. It is clearly desirable to design new systems in a manner which significantly reduces the above problems. This is obtained in general by greater EMP hardening of the system. If the hardness margins for the individual signals reaching sensitive positions (failure ports) can be significantly increased across the board, then one expects that the probable number of cases with negative hardness margins will be significantly decreased, ideally decreasing to zero in the limit of sufficient individual-failure-port designed hardness. Whether or not (or how often) a practical system can be designed with sufficiently large hardness margins for individual signals such that the overall system hardness margin (smallest individual signal hardness margin) is positive (implying a hard system) is at present uncertain. Some promising concepts for improving the system hardening come under the general heading of electromagnetic topology, in which control is emphasized for all signals passing through defined principal surfaces which are closed surfaces (shields) bounding various volumes in the system [8]; this potentially applies a more structured approach to EMP hardening with various levels of control possible.

In any event, for high confidence that a system is EMP hard, one will have to resort to a full EMP system-level test as a demonstration, at a minimum. Complex systems are normally tested for their performance characteristics. Who commits, for example, a military or civilian aircraft to extensive production without a flight test program? As a reasonable engineering practice why then would one not perform a similar EMP test program on complex electronic systems which are supposed to function after exposure to EMP environments? As the technology evolves and better hardness control is presumably achieved, the extent of the "optimum" EMP test (duration and complexity) will likely also evolve with different parts receiving different emphases to best match the state of the art of EMP hardness understanding.

## II. CRITERIA

Before one has an EMP test, he must know in some sense what EMP is. This paper does not go into a detailed discussion of EMP environments, such being available elsewhere [7]. However, the reader will need at least a simplified version of the EMP environment(s) of concern to be in a position to conduct a meaningful EMP test. A statement of an EMP environment in an appropriate form is referred to as an EMP criterion. Recalling a previous definition [3],

"A(n) (EMP) criterion is:

a quantitative statement of the physical parameters of the (EMP) environment relevant to the (EMP) response of a system of interest in a volume of space and region of time and/or frequency extended to contain all physical parameters having a non-negligible influence on any of the (EMP) response parameters (e.g., as in the case of EMP (plane wave) a particular direction of incidence and a particular polarization and proximity to other scatterers)."

For simplicity and engineering utility this criterion is often expressed in some canonical form involving mathematical expressions (special functions, etc.). This canonical form is best chosen to contain the relevant features of the environment, but in an idealized, somewhat simplified, form. It is important that the simplifications do not remove features of the environment which can contribute to the system vulnerability. For this reason the criteria waveforms are taken to bound the environmental waveforms in relevant aspects such as rate of rise, peak amplitude, time integral (area under the curve), etc. However, to be useful such bounds should be reasonably tight. Such bounds should also

be considered in terms of the magnitude of the Fourier transform, i.e., in frequency domain since system responses are typically frequency selective, or more generally complex-frequency selective in terms of poles of the Laplace transform [9].

While there are many kinds of EMP environments some are of more interest than others for present purposes. The nuclear-source-region EMP environments are rather complex in that they involve current density and conductivity as well as electric and magnetic fields in a non-linear and self-consistent combination [6]. On the other hand, if one goes away from the source region the EMP environment can often be approximated by a plane wave. This is especially the case for what is referred to as the high altitude EMP. In this case with the weapon detonation exoatmospheric, the  $\gamma$  rays interact with the atmosphere to produce compton electrons which spiral in the geomagnetic field in roughly the 20 km to 40 km altitude regime. The resulting fields below this source region (before reflecting from the earth's surface) are approximated as a plane wave with a rise time in the 10 ns regime, a peak for the electric field of the order of  $10^5$  V/m, and a pulse width in the 100 ns ball park.

For this important example of a high-altitude EMP environment canonical forms of the environment have been proposed and employed. Taking a general plane wave in free space as

$$\begin{aligned}\vec{E}(\vec{r}, t) &= E_2 f_2\left(t - \frac{\vec{I}_1 \cdot \vec{r}}{c}\right) \vec{I}_2 + E_3 f_3\left(t - \frac{\vec{I}_1 \cdot \vec{r}}{c}\right) \vec{I}_3 \\ Z_0 \vec{H}(\vec{r}, t) &= -E_3 f_3\left(t - \frac{\vec{I}_1 \cdot \vec{r}}{c}\right) \vec{I}_2 + E_2 f_2\left(t - \frac{\vec{I}_1 \cdot \vec{r}}{c}\right) \vec{I}_3\end{aligned}\quad (1)$$

$$Z_0 = \sqrt{\frac{\mu_0}{\epsilon_0}} \quad (\text{wave impedance of free space})$$

$$c = \frac{1}{\sqrt{\mu_0 \epsilon_0}} \quad (\text{light speed in free space})$$

with orthogonal unit vectors

$$\hat{i}_1 \equiv \text{direction of propagation}$$

$$\hat{i}_2, \hat{i}_3 \equiv \text{orthogonal polarizations} \quad (2)$$

$$\hat{i}_1 \times \hat{i}_2 = \hat{i}_3, \hat{i}_2 \times \hat{i}_3 = \hat{i}_1, \hat{i}_3 \times \hat{i}_1 = \hat{i}_2$$

Since the electric and magnetic fields are very simply related in (1), then in effect only one need be specified. The constants  $E_2$  and  $E_3$  are parameters with dimensions V/m, related to time-domain peaks. The waveforms are  $f_2(t)$  and  $f_3(t)$  shifted into retarded time. For present purposes only one such waveform  $f(t)$  is considered, but in principle polarization can rotate.

The normalized waveform  $f(t)$  is then taken in some convenient analytic form so that its properties in time domain  $f(t)$ , and complex frequency domain  $\tilde{f}(s)$ , appropriately approximate, or better bound (closely), a set of environmental waveforms. Here the two-sided Laplace transform is defined by

$$\begin{aligned} \tilde{f}(s) &\equiv \int_{-\infty}^{\infty} f(t) e^{-st} dt \\ f(t) &= \frac{1}{2\pi j} \int_{\Omega_0 - j\infty}^{\Omega_0 + j\infty} \tilde{f}(s) e^{st} ds \end{aligned} \quad (3)$$

$$s \equiv \Omega + j\omega$$

with  $\Omega_0$  in the strip of convergence. Examples of waveform functions which have been used [5] include

$$\begin{aligned}
 f^{(1)}(t) &= \left[ -e^{-at} + e^{-bt} \right] u(t), \quad a > b > 0 \\
 \tilde{f}^{(1)}(s) &= \frac{a-b}{(s+a)(s+b)} \\
 f^{(2)}(t) &= \left[ e^{-at} + e^{bt} \right]^{-1}, \quad a > 0, \quad b > 0 \\
 \tilde{f}^{(2)}(s) &= \frac{\pi}{a+b} \csc(\pi \frac{a-s}{a+b})
 \end{aligned} \tag{4}$$

In both of these cases  $a$  is chosen to give the desired rise characteristics in time domain and high-frequency characteristics of  $\tilde{f}(j\omega)$ . Typically

$$a \gg b \tag{5}$$

in both examples, corresponding to rise time small compared to decay time. Detailed properties of these canonical waveform functions are discussed in [5].

The plane-wave criterion form in (1) is appropriate for the case of a system in flight below the high-altitude nuclear source region, but at an altitude appreciably above the earth surface, so that the pulse reflected from the earth surface arrives sufficiently later in time that it may be considered a separate event. For a system operating on or near the earth surface such a high-altitude criterion must include the earth reflection, at least implicitly. Furthermore, the proximity of the earth to the system must also be included in the criterion because of the earth effect on the system Green's function (including natural frequencies, etc.).

Having an EMP criterion, such as in (1) we cannot stop there. Such canonical environments still have several parameters to be specified. In (1) the direction of incidence  $\hat{\mathbf{i}}_1$  must be specified; actual EMP environments can have a range of realistic values for  $\hat{\mathbf{i}}_1$ , so one must specify some range or set of  $\hat{\mathbf{i}}_1$ . Similar comments apply to the polarization  $\hat{\mathbf{i}}_2$  and  $\hat{\mathbf{i}}_3$ .

Let us define a statement of a criterion as in (1) and (4), together with a range of the associated parameters (such as the unit vectors  $\hat{\mathbf{i}}_1$ , etc.) as being a criteria set. It is this criteria set which the system is supposed to survive in some defined sense.



### III. SIMULATION

Having some defined EMP criteria set we next must have some kind of EMP simulation set which tests the system of interest in some way which approximates or is quantitatively and experimentally related to the criteria set. As previously defined [1] (EMP) simulation (an individual simulation normally related to a single criterion) is:

"an experiment in which the postulated (EMP) exposure situation is replaced by a physical situation in which:

1. the (EMP) sources are replaced by a set of equivalent sources which to a good approximation produce the same excitation (including reconstruction by superposition to the extent feasible) to the total system under test or some portion thereof as would exist in the postulated nuclear environment, and

2. the system under test is configured so that it reacts to sources (has the same Green's function) in very nearly the same way and to the same degree as it would in the postulated nuclear environment."

"A(n) (EMP) simulator is a device which provides the excitation used for (EMP) simulation without significantly altering the response of the system under test by the simulator presence."

For a given individual criterion and system of interest (including its operational situation to be simulated) one may select an appropriate (EMP) simulator and design the simulation (test); this defines a criterion-simulation pair, abbreviated as a CS pair. A "complete" EMP test program may involve different configurations (including orientations) of the system in a given simulator, and perhaps even several different simulators;

this set is referred to as a simulation set. Now in determining the system response in a simulation test the failure-port response is a most relevant parameter. A failure port [3] "might be some pin on a connector into some black box. This position is of interest because one uses it for referencing signals associated with permanent damage or temporary functional disruption (upset)." This gives two ways to consider a CS pair. First there is a failure-port CS pair concerned with the criterion vs. simulation response at a particular failure port; the best simulation in this sense minimizes the difference between these two at the selected failure port. More interesting is the CS-pair system set which encompasses the failure-port CS pairs throughout the system for a given CS pair.

Now the CS-pair system set defines an individual criterion assessment which is a statement of the system vulnerability or lack thereof to the individual criterion of interest. However, since an EMP criterion set encompasses a range of excitation parameters, and for each selected individual criterion there is in general a separate simulation, then it is the collection of CS-pair system sets, varied over the same set of parameters that determines the criteria set, which determines the assessment of the system to the criteria set of interest; this defines the criteria-set assessment, or system assessment for short. Later there is discussed the use of extrapolated (E) response as an approximation to criterion (C) response. For that case the substitution of extrapolated for criterion, and extrapolated system response set for criteria system response set is appropriate.

For high-altitude EMP simulation various types of EMP simulators are appropriate, the common ones including guided-wave simulators (such as

parallel-plate transmission lines) for simulating in-flight conditions (with the system not actually in-flight), equivalent-electric-dipole simulators (vertically polarized) for testing systems in actual flight, and hybrid simulators for testing systems which are supposed to be on the ground (buildings, parked aircraft, etc.). For other types of EMP, there are other types of simulators. For an extensive discussion of the various types of EMP simulators see [1].

#### IV. EXTRAPOLATION

Simulation is not in general perfect; this should not be a surprise to anyone, considering that simulation is an experiment which is not the "real thing". One would like to have a near perfect simulator, but this is not always possible or practical; it is also generally expensive. Given some particular simulation test, is it possible to quantify the errors and/or correct the results in order to have a more accurate estimate of the system response under criterion conditions? This is the subject of extrapolation as defined and discussed in [3], with the definition:

"Simulator extrapolation is:

an extension of the simulator in which the system undergoing a simulation test is corrected to some degree for differences of its response from those under criterion conditions associated with

1. differences in the simulator environment from the criterion environment, and
2. proximity of the simulator to the system changing its response characteristics (Green's function) from those existing under criterion conditions. (Note that local earth, water, etc., in the context of an EMP simulator is part of the simulator.)"

This can be generalized to simulation extrapolation if one includes

- "3. differences in the system configuration changing its response characteristics from those existing under criterion (operational) conditions."

For present purposes only the first two points are considered.

Figure 1 diagrams the various types of extrapolation discussed in [3] which are summarized here. This extrapolation sequence diagram is a topo-

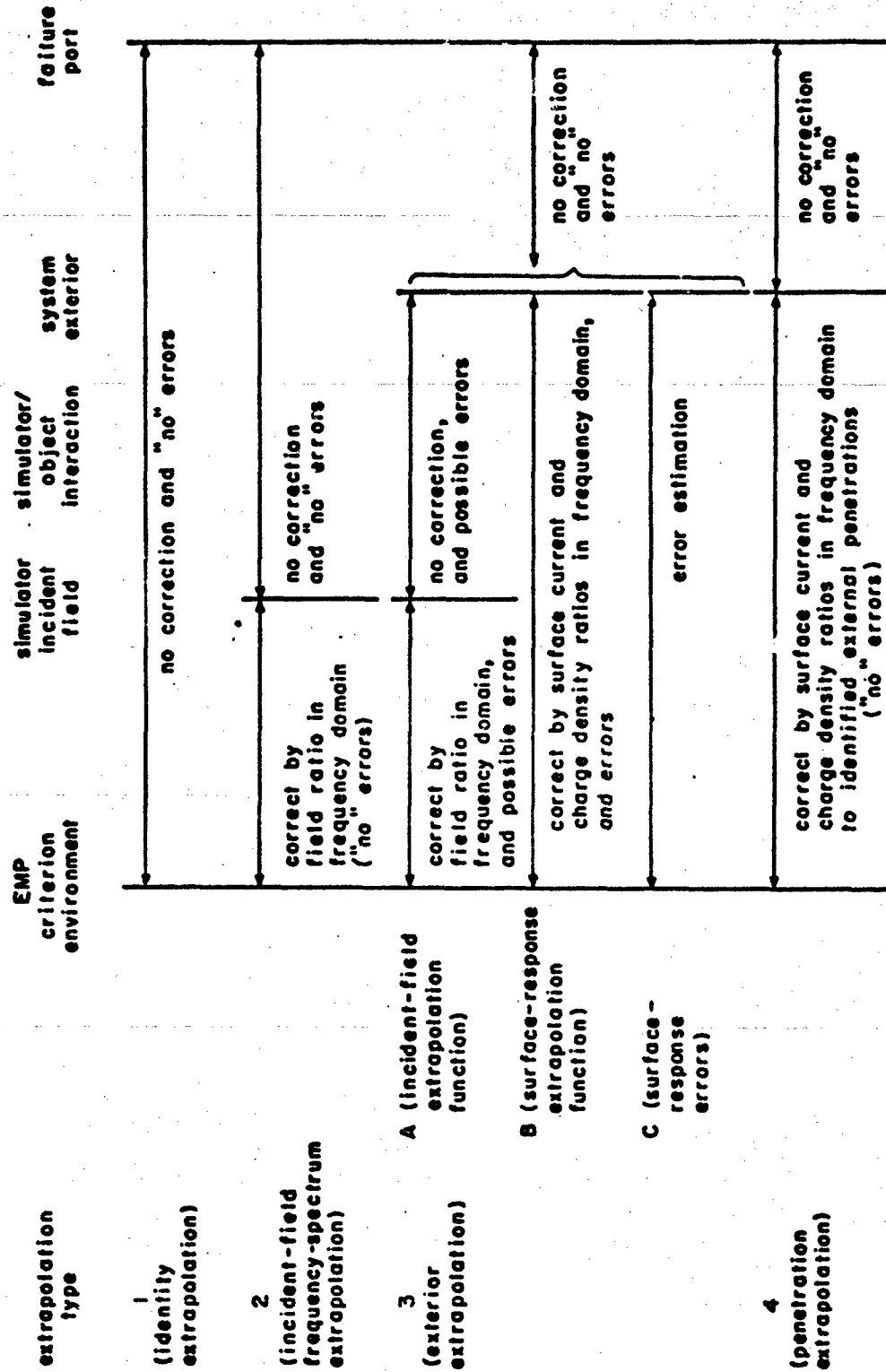


Figure 1 Extrapolation Sequence Diagram

logical diagram similar to the interaction sequence diagram [8] in that it is based on signal flow from the incident wave to the system exterior, through the system exterior, and on to some failure port (such as the input to one of the "black boxes") in the system. Note the inclusion of the simulator/object interaction as a step which can influence the signal flow between the incident field and system in criterion conditions as well as in the simulator. This assumption is often valid but not always; it does, however, significantly simplify the extrapolation problem.

For the extrapolation there is introduced the concept of an extrapolation function, designated in complex frequency domain by  $\tilde{F}_e(s)$ . This function is defined such that it multiplies a response function somewhere to give a corresponding extrapolated response which in some sense approximates the response under criterion conditions. For this purpose we introduce superscripts

$$\begin{aligned} C &\equiv \text{criterion} \\ S &\equiv \text{simulation} \\ E &\equiv \text{extrapolated} \end{aligned} \quad (6)$$

so that we can write

$$\tilde{F}^{(E)}(s) \equiv \tilde{F}_e(s) \tilde{F}^{(S)}(s) \quad (7)$$

where  $\tilde{F}$  refers to some response function of interest with  $\tilde{F}^{(E)}$  approximating (perhaps in a very crude way)  $\tilde{F}^{(C)}$ .

Type 1 extrapolation is (for completeness) identity extrapolation with

$$\tilde{F}_e(s) \equiv 1 \quad (8)$$

i.e., nothing is done to results from the simulation test. Of course this

is accurate only in the limit of the simulation perfectly matching the particular criterion in all relevant aspects.

Type 2 extrapolation corrects for waveform differences, but not different spatial variations of the incident fields or simulator/object interaction, by defining

$$\tilde{P}_e(s) \equiv \frac{P_{inc}^{(C)}(s)}{P_{inc}^{(S)}(s)} \quad (9)$$

with the incident-field function defined in a variety of ways, such as

$$\tilde{P}_{inc}(s) \equiv \tilde{E}_{inc}(\vec{r}_0, s) \cdot \vec{I}_0 \quad (10)$$

where  $\vec{r}_0$  is some selected position in space and  $\vec{I}_0$  a particular direction (polarization) there. This type 2 extrapolation is then an incident-field frequency-spectrum extrapolation. It is particularly appropriate for cases that the simulator spatial distribution of the fields closely matches that of the criterion (e.g., (1)) with a different waveform and field amplitude. An example of such a case is an aircraft flying by an EMP simulator at sufficient range to well simulate in-flight conditions (for perhaps limited choices of direction of incidence and polarization).

Type 3 extrapolation is referred to as exterior extrapolation. As the name implies the electromagnetic response of the system exterior (surface current and charge densities) enters into the extrapolation formulas in the definition of the extrapolation function and/or the estimation of the remaining errors. For this purpose the system is assumed to have an approximately perfectly conducting outer envelope. Of course there are

electrical penetrations through this envelope. For present purposes these penetrations are assumed to be sufficiently small (both electrically and physically) and of not too large a number. Then the transfer function from the incident field (criterion and simulation) to a failure port can be factored into a sum of products with each product having as a factor  $\tilde{F}_{s_m}(\vec{r}_s, s)$  where

$$\tilde{F}_{s_m}(\vec{r}_s, s) = \begin{cases} Z_0 \tilde{J}_s(\vec{r}_s, s) \cdot \vec{I}_{u_m} & \text{for } m = 1, 2 \\ \frac{1}{\epsilon_0} \tilde{\rho}_s(\vec{r}_s, s) & \text{for } m = 3 \end{cases}$$

$$\vec{r}_s \equiv \text{coordinate on surface (envelope)} \quad (11)$$

corresponding to the two components of surface current density and one of the surface charge density. The  $\vec{I}_{u_m}$  are a right-handed set of unit vectors corresponding to an orthogonal  $u_m$  coordinate system with  $u_3 = (\text{some constant})$  corresponding to our system envelope. Furthermore, for developing the error formulas it will be assumed that for a given failure port only one value of  $m$  and one of  $\vec{r}_s$  is dominant, i.e., only one penetration and penetration mode is important for any frequency (or at least most frequencies) of interest, although different frequencies may have different dominant penetrations and/or penetration modes.

As a first step define an extrapolation function. One way (type 3A) is defined as in (9) based on the incident field giving

$$\tilde{F}_e^{(A)}(s) \equiv \frac{\tilde{F}_{inc}^{(C)}(s)}{\tilde{F}_{inc}^{(S)}(s)} \quad (12)$$

Noting from (10) that there is some choice of measurement position  $\vec{r}_0$  and orientation  $\vec{I}_0$  for this type of incident-field extrapolation function, one



might even average the above ratio over various choices of  $\vec{r}_0$  and  $\vec{l}_0$ .

Another way (type 3B) is defined from the surface response quantities as in (11) as

$$\bar{f}_e^{(B)}(s) \equiv \frac{\bar{f}_{s_m}^{(C)}(\vec{r}_{s_0}, s)}{\bar{f}_{s_m}^{(S)}(\vec{r}_{s_0}, s)} \quad (13)$$

for some particular  $\vec{r}_s = \vec{r}_{s_0}$  and choice of  $m$ . Better, an average over the surface and  $m$  is made. Various averages are possible; the one in most common use is a logarithmic average or geometrical mean as

$$\begin{aligned} \bar{f}_e^{(B)}(s) &= \exp \left\{ \sum_{l=1}^{N'_p} \ln \left[ \frac{\bar{f}_{s_l}^{(C)}(s)}{\bar{f}_{s_l}^{(S)}(s)} \right] \frac{1}{N'_p} \right\} \\ &= \left\{ \prod_{l=1}^{N'_p} \frac{\bar{f}_{s_l}^{(C)}(s)}{\bar{f}_{s_l}^{(S)}(s)} \right\}^{1/N'_p} \end{aligned} \quad (14)$$

where  $l = 1, 2, \dots, N'_p$  is an index corresponding to pairs of selected positions ( $\vec{r}_{s_l}$  on the envelope) and orientations ( $\vec{l}_{lm}$ ), perhaps randomly chosen. This latter choice has the property of minimizing the errors (in a ratio sense) which follow.

Now take the surface response quantities to define a set of ratios as

$$\bar{r}_{s_l}(s) \equiv \frac{\bar{f}_{s_l}^{(E)}(s)}{\bar{f}_{s_l}^{(C)}(s)} \equiv \frac{\bar{f}_e(s) \bar{f}_{s_l}^{(S)}(s)}{\bar{f}_{s_l}^{(C)}(s)} \equiv \bar{r}_{s_l}^{-1}(s) \quad (15)$$

where either (A) or (B) can be applied as a superscript on the extrapolation function. If one graphs  $|\bar{r}_{s_l}(j\omega)|$  as a function of  $\omega$  (or  $f = \omega/(2\pi)$ ) for  $l = 1, 2, \dots, N'_p$ , deviation of the magnitudes of the ratios from unity can be

taken as a measure of the (linear) errors remaining after correction of the system response at the failure ports by the extrapolation function. These errors can also be considered in time domain by using individual ratios as in (13) to construct  $N_p$  different extrapolation functions with multiplication as in (7) and inverse Laplace transformation; the spread of the resulting time-domain failure-port waveforms from that using (12) or (14) gives the time-domain errors. Note that as the spatial part of the fields in the simulator is made to match the criterion, and the simulator/object interaction tends to criterion conditions, then all the ratios in (15) become the same. Furthermore if the surface extrapolation function in (13) or (14) is used, then the above ratios all become 1.0. This general kind of error is referred to as type 3C in this extrapolation development.

In order to obtain the surface response quantities above one needs the surface response set under criterion conditions. This can be obtained in various ways. The real system can be used to experimentally determine the criterion surface responses, provided for this purpose a sufficiently pure simulation which requires no more severe than type 2 extrapolation is used. Typically measurements on scale models (of the system exterior envelope, including large antennas) have been used to obtain the criterion surface responses [2, 4].

Finally, type 4 extrapolation attempts to avoid the 3C errors. It does this by experimentally associating the signal at a failure port with the surface response quantities (11) appropriate to the penetrations driving that particular failure port. While this avoids the uncertainty as in (14), it introduces the significant complexity of determining which penetrations and penetration modes are associated with each failure port. In effect, extrapolation functions must be determined for each failure port.

## V. CONCLUSION

This paper has outlined the basics in the process of EMP assessment. Some particular system is designed or defined to operate under exposure to some EMP criteria set. For each particular case under the EMP criteria set (or an appropriate sample of such cases) an individual criterion assessment can be performed. This requires the definition of an appropriate EMP simulation set, an individual simulation corresponding to an individual criterion. However, an individual simulation is in general not perfect, i.e., it has errors. These errors are in general different at each failure port.

The failure-port CS pair concerns the survivability of the individual failure port to the individual criterion. The CS-pair system set extends this consideration to the entire system, and forms the basis for an individual criterion assessment. Extending this to the criteria set with its associated simulation set one can determine the criteria-set assessment or system assessment as a statement (ideally quantitative) of the system vulnerability or lack thereof to the criteria set.

However, simulation is in general imperfect. So one defines a process of extrapolation to correct the signals at failure ports under simulation conditions to a more accurate representation of criterion conditions, i.e., extrapolated conditions. With an appropriate definition of an extrapolation function and associated errors, one can begin to approximate (replace) criterion responses by extrapolated responses. Then simulation (S) in the previous paragraph can be replaced by extrapolated (E). This defines the failure-port CE pair, and the CE-pair system set to give an individual extrapolation assessment. Extending this to the criteria set one has the system assessment in terms of the extrapolation set as an approximation to the criteria set.

The comparison between criteria-set response and extrapolation-set response is a measure of simulation quality. The best simulation (corresponding to some individual criterion) is that which involves in some sense the least extrapolation. The differences of simulation response from criterion response fall into two categories. The first difference concerns the required extrapolation function or functions; the closer this function is to 1.0 for all frequencies the better is the simulation. The second difference concerns the errors after extrapolation; the smaller the errors (or the closer the "exact" individual extrapolation functions approach to some common (or universal) extrapolation function) the better is the simulation.

This comparison of simulation quality to criterion can be turned into an economic question. How much is high-quality simulation worth? One should consider the alternatives. One can have poor simulation (extrapolation functions far from unity and/or large residual errors) with corresponding large uncertainties in system assessment. This can alternately be interpreted as requiring large hardness margins at failure points (ratios of signals for vulnerability to extrapolated signals, including implications of probabilistic distributions of such ratios). While this may be cheap in terms of simulators it requires large hardness margins with appropriate constraints on their distributions. Alternatively one can have better simulation (at greater expense) and tolerate smaller hardness margins (with appropriate attention to distributions). This is perhaps an oversimplified view, but still realistic. There are still state-of-the-art limitations on the technology for determining what the best trade-off is. Note that such trade-offs are still in the context of linear extrapolation; nonlinear effects still require high quality simulation.

## REFERENCES

1. C. E. Baum, "EMP Simulators for Various Types of Nuclear EMP Environments: An Interim Categorization," Sensor and Simulation Note 151, July 1972, and IEEE Trans. Antennas and Propagation, January 1978, and IEEE Trans. Electromagnetic Compatibility, February 1978, and Sensor and Simulation Note 240, January 1978.
2. V. V. Liepa, "Sweep Frequency Surface Field Measurements," Sensor and Simulation Note 210, July 1975.
3. C. E. Baum, "Extrapolation Techniques for Interpreting the Results of Tests in EMP Simulators in Terms of EMP Criteria," Sensor and Simulation Note 222, March 1977.
4. D. E. Merewether, J. F. Prewitt, and C. E. Baum, "Characterization of Errors in Extrapolation of Data from an EMP Simulator to an EMP Criterion," Sensor and Simulation Note 232, October 1977.
5. C. E. Baum, "Some Considerations Concerning Analytic EMP Criteria Waveforms," Theoretical Note 285, October 1976.
6. C. E. Baum, "Electromagnetic Pulse Interaction Close to Nuclear Bursts and Associated EMP Environment Specification," Interaction Note 76, July 1971.
7. C. L. Longmire, "On the Electromagnetic Pulse Produced by Nuclear Explosions," IEEE Trans. Antennas and Propagation, January 1978, and IEEE Trans. Electromagnetic Compatibility, February 1978.
8. C. E. Baum, "The Role of Scattering Theory in Electromagnetic Interference Problems," in P.L.E. Uslenghi (ed.), Electromagnetic Scattering, Academic Press, 1978.
9. C. E. Baum, "Toward an Engineering Theory of Electromagnetic Scattering: The Singularity and Eigenmode Expansion Methods," in P.L.E. Uslenghi (ed.), Electromagnetic Scattering, Academic Press, 1978.

ELECTROMAGNETIC CONSIDERATIONS  
OF A SPATIAL MODAL FILTER FOR SUPPRESSION  
OF NON-TEM MODES IN THE TRANSMISSION-LINE TYPE  
OF EMP SIMULATORS

ABSTRACT

The subject of this note is the suppression or damping of non-TEM modes in the transmission-line type of EMP simulator. This suppression may be accomplished by introducing a spatial modal filter (SMF), initially in the output conical section of the simulator. In this note, we deal with the electromagnetic considerations of the SMF which is essentially decoupled from the principal TEM mode. Although these considerations, in general, apply to any wave guiding structure (open or closed) that can support a dominant TEM mode, attention is currently being focused on the two-parallel-plate transmission-line type of EMP simulator.

Acknowledgement

We are thankful to Mr. Bill Kehrer for his encouragement and interest in this problem. For many useful discussions, tanks are also due Dr. F. M. Tesche.

## I. INTRODUCTION

An important class of EMP simulators is the parallel-plate transmission-line type. This type of an electromagnetic structure is essentially an open waveguide, between the conductors of which a transient pulse with a planar wavefront must travel. In practice, however, the fields obtained in the working volume can depart from the ideal TEM behavior owing to the excitation and propagation of non-TEM modes. It has been known for some time [1 to 5] that a finitely wide parallel-plate transmission line can support and propagate TE and TM modes if they are excited for any reason. Since the chief object of such an EMP simulator is to produce an EMP environment appropriate to a plane wave (outside the source region), it is desirable to suppress the non-TEM modes without disturbing the TEM wave. To successfully accomplish this suppression, a clear understanding of the characteristics of the TEM and non-TEM (i.e., TE and TM) modes is essential. Much detailed work has been done concerning the TEM properties of both the parallel-plate [6 to 9] and the conical [10, 11] transmission lines. References [12,13] have considered the conical transmission line as a launcher and receptor of waves on the cylindrical transmission line by introducing the concept of dispersion distances, or equivalently, dispersion times. Formulas have also been developed [13] for the TEM mode coefficient in terms of the cross-section fields. Detailed calculations of TE and TM modes of propagation are currently available for the two limiting cases of narrow (separation  $\gg$  width) [1] and wide (separation  $\ll$  width) [4,5] plates. A parametric study is presently in progress [14] for the general case where the separation to width ratio is not restricted. This study will consider geometries of the existing (ALECS

and ARES) and future (ATLAS I and II) transmission-line type of EMP simulator facilities at the Air Force Weapons Laboratory, as well as the laboratory model simulator at Harvard University. Comparisons of the electromagnetic field calculations from this study with the available experimentally measured fields in ALECS and Harvard's model simulator is expected to lead to an identification of the effects of the higher order modes. In any case, there exists a need for suppressing or damping the non-TEM modes.

In Section II, the departure of the measured fields in the working volume from the ideal TEM behavior will be considered, and in Section III, available computations of TE and TM modes in the parallel-plate region will be reviewed. Sections IV and V deal with various aspects of the spatial modal filter, and design formulas are developed. The note is concluded with a summary in Section VI.



## II. DEPARTURE FROM THE IDEAL TEM BEHAVIOR

This class of EMP simulators operating in a pulsed mode is a complex electromagnetic structure to analyze. The complexity is partially due to the fact that the input pulse contains a wide range of frequencies and, consequently, the relevant dimensions of the structure ranges from a small fraction of a wavelength to many wavelengths. Because of this, the simulator while operating in a pulsed mode is a transmission line, a radiator and an optical diffracting structure, all for the same pulse. In reference [15], the electromagnetic characteristics of the simulator were qualitatively discussed by categorizing the frequency range of interest into a) low frequencies, b) high-frequency asymptotics, and c) intermediate frequencies.

At low frequencies, one has near-ideal conditions in terms of simulation because quasi-static considerations apply and the TEM mode of propagation is dominant. The main problem here is to minimize the impedance discontinuity and TEM field discontinuity across the junction between the cylindrical and the conical transmission lines. Such a matching of the TEM modes at the input and output "bends" is achieved by reducing the dispersion distance [12,13].

At higher frequencies, the relevant dimensions of the simulator, e.g., width and spacing of the plate become several wavelengths long, and ray-optical considerations apply. Several canonical problems have been defined and solved [16-19], which are useful in estimating the early-time pulsed fields associated with conducting wedges and thus reduce waveform distortion. Some experimentally measured data [20] is available concerning the early-time fields indicating the  $(1/\sqrt{r})$  variation of the spherical

wave launched by the conical line followed by edge diffraction and specular reflections. Some of the problems here are large dispersion times, edge diffractions and excessive ripple in the measured data.

However, it is the intermediate frequencies that present the most serious problems. Relevant distances now become comparable to wavelengths rendering both the quasi-static and the ray-optic considerations inapplicable. In this note, we focus our attention on the behavior of the simulated electromagnetic fields in this frequency regime by taking a superposition of the TEM and non-TEM modes. The non-TEM modes are those supported in a finitely wide two-parallel-plate open waveguiding structure, which are to be contrasted with the familiar propagating modes of a closed rectangular waveguide or a closed circular coaxial transmission line. By taking this view, one can define the problem to be that of damping or suppressing the non-TEM modes without significantly disturbing the desired TEM mode of propagation.

A typical geometry of this class of EMP simulator is shown in Figure 2.1. This figure shows a vertically polarized parallel-plate transmission-line type of simulator. By virtue of symmetry and practicality, it suffices to construct the symmetric half of the structure above the horizontal symmetry plane where a wide conducting plane is placed. Accordingly, Figure 2.1 shows the side view of the simulator comprising the top plate of width  $2a$  at a height  $b$  above the ground plane. The plate-to-plate separation (for a symmetric situation with two identical parallel plates) is then  $2b$  and the lengths of the conical and the parallel-plate transmission lines are designated  $L$  and  $w$  respectively. With reference to this figure, the nonzero components of electric and magnetic fields for the various modes of propagation in the parallel-plate transmission-line region are:



a) TEM mode

$$\tilde{E}_x, \tilde{E}_y, \tilde{H}_x, \tilde{H}_y \quad \text{with } \tilde{E}_z = \tilde{H}_z = 0$$

b) TM mode (E mode)

$$\tilde{E}_z, \tilde{E}_x, \tilde{E}_y, \tilde{H}_x, \tilde{H}_y \quad \text{with } \tilde{H}_z = 0$$

c) TE mode (H mode)

$$\tilde{H}_z, \tilde{H}_x, \tilde{H}_y, \tilde{E}_x, \tilde{E}_y \quad \text{with } \tilde{E}_z = 0$$

All of the above field quantities are functions of position in the transverse plane and frequency. We shall now summarize certain measurements made in the ALECS facility that are relevant in terms of identifying the departure from the ideal TEM behavior. CW measurements [21] made in the working volume of the ALECS facility have detected what has been referred to as the "notch problem". Specifically, the transfer function from the input voltage to the measured fields, when appropriately normalized and plotted as a function of frequency, displays significant notches at certain frequencies. For example, Figure 2.2 shows the magnitude of the normalized transverse magnetic field  $H_x$  measured at the center (0,0,0) and the notch is seen to appear at ~25 MHz, with roughly a  $\pm 30\%$  ripple at higher frequencies. Figure 2.3 is the normalized principal electric field  $E_y$  measured at the same location. It is noted that the principal electric field does not display a notch behavior at the same location, but perhaps a small enhancement. Correspondingly, the experimental measurements in the scale model simulator at Harvard University have reproduced the notch behavior in the field quantities. The description of the experimental setup along with the measured fields

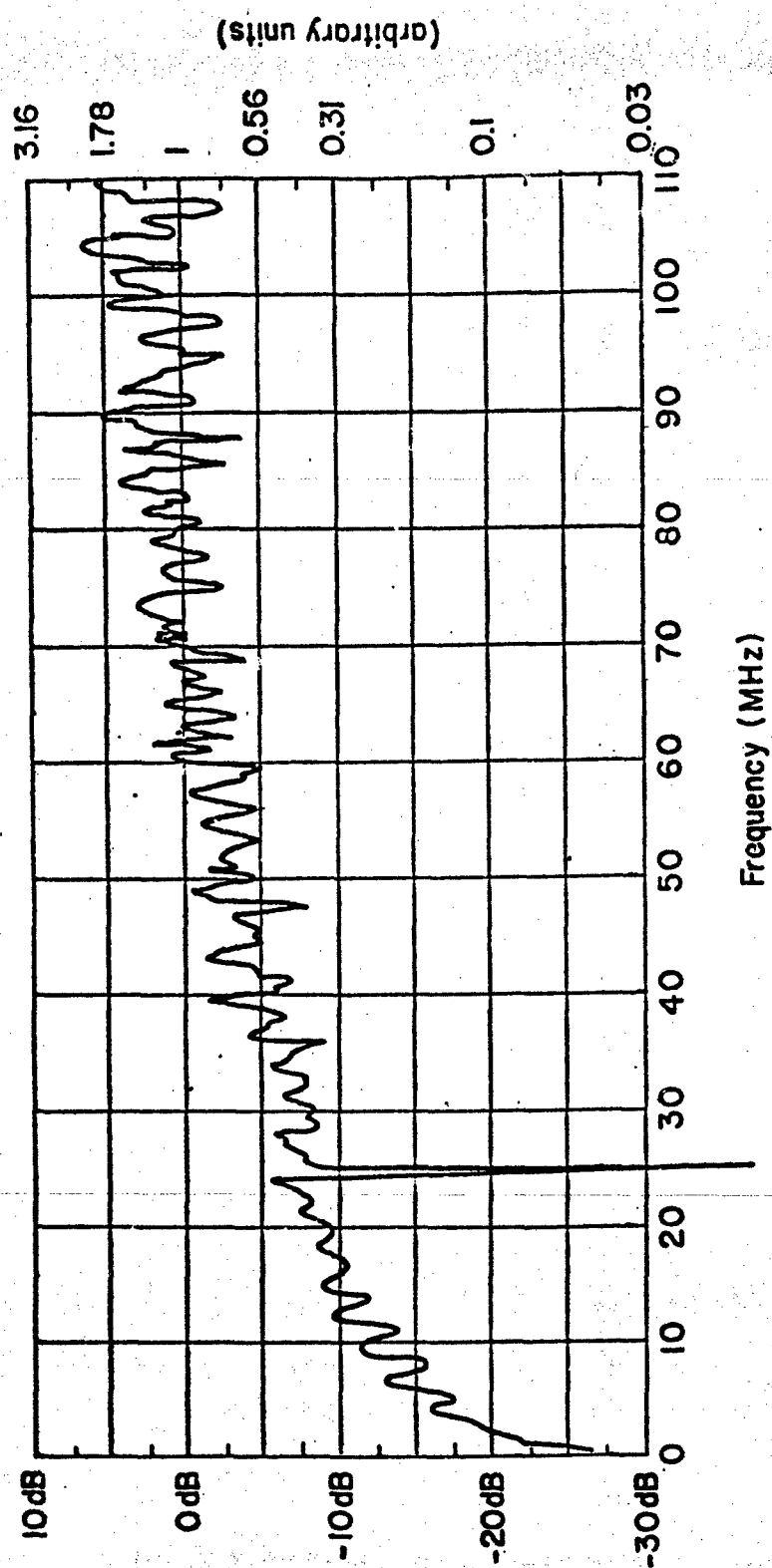


Figure 2.2 Measured  $|B_x/\text{constant}|$  at the center with coordinates (0,0,0) in ALECS facility

(This figure is reproduced here from reference [21].)

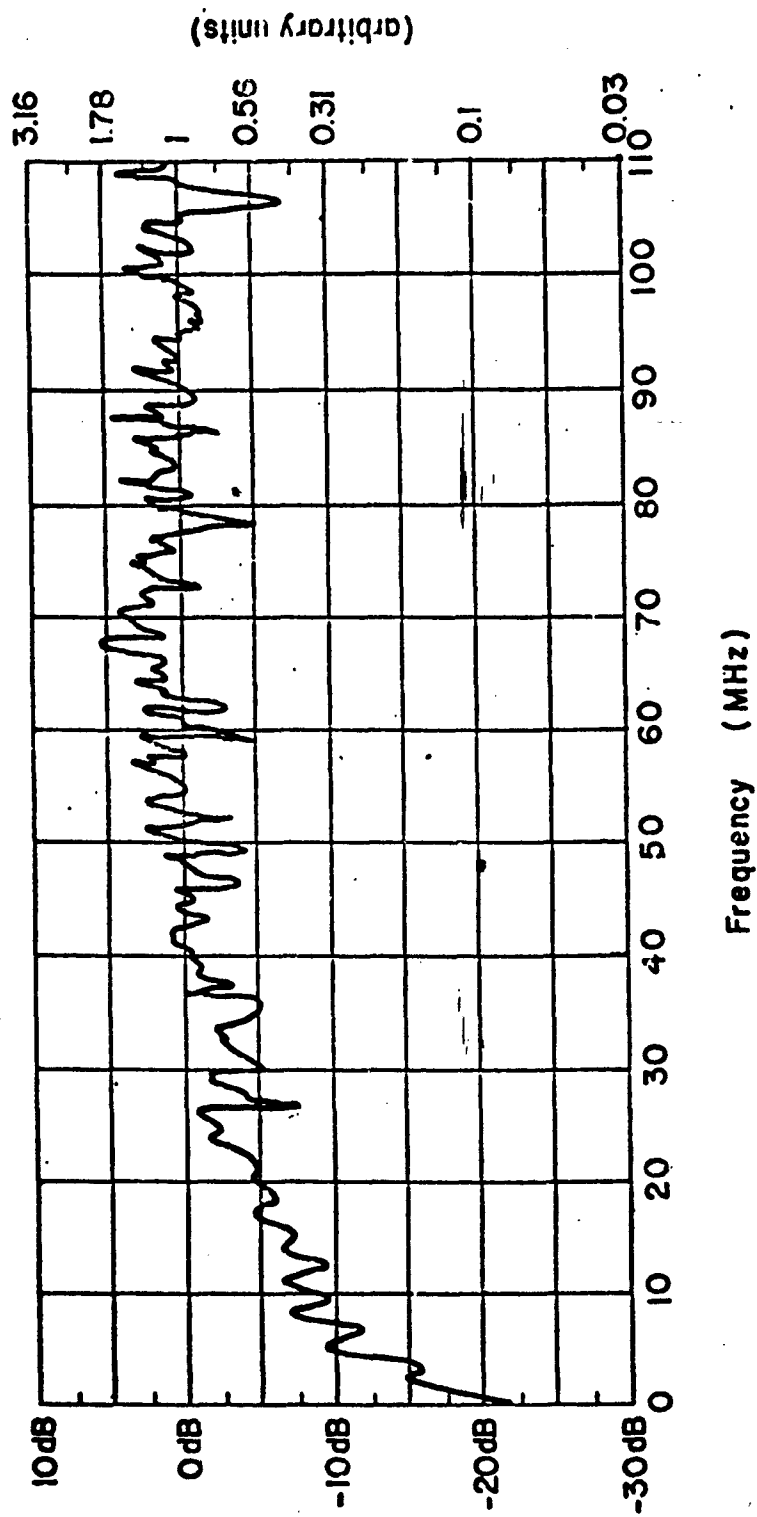


Figure 2.3. Measured  $|\delta_y/\text{constant}|$  at the center with coordinates (0,0,0) in ALECS facility

(This figure is reproduced here from reference [24].)

in the model simulator are well documented in references [22] and [23]. A preliminary measurement of the transverse magnetic field as a function of frequency at a fixed location of (0,0,0) was provided by Blejer [24] and is shown in Figure 2.4. This measurement also displays a sharp null in the magnetic field at ~264 MHz at the measurement location. The null is caused by a cancellation of the transverse magnetic field of the principal TEM mode by that of the first higher TM mode, and the frequency of 264 MHz on the model simulator corresponds very closely to the ~25 MHz notch observed in the ALECS facility. Furthermore, in both configurations (ALECS and the model simulator), the frequencies where one would expect a higher order mode to be excited corresponds approximately to the relevant dispersion distance "d" becoming equal to a half wavelength. Considering a direct path from source apex to load apex and another signal path along the edge of the top plate, d is given by

$$d = \frac{\lambda}{2} \approx 2 \left[ \sqrt{b^2 + a^2 + L^2} - L \right] \quad (2.1)$$

where  $\lambda$  is the wavelength corresponding to a frequency where one may expect a higher order TM mode excitation, and the other variables in Eq. (2.1) are illustrated in Figure 2.1. Substituting the values for the various dimensions, we find that the frequency of expected excitation of higher TM mode is ~25 MHz for ALECS and ~256 MHz for the model simulator at Harvard. These compare well with the experimentally observed values of ~24 MHz for ALECS and ~264 MHz for the model simulator. It can be argued that the notch is due to the superposition of the TEM mode and higher order TM and TE modes. The non-TEM

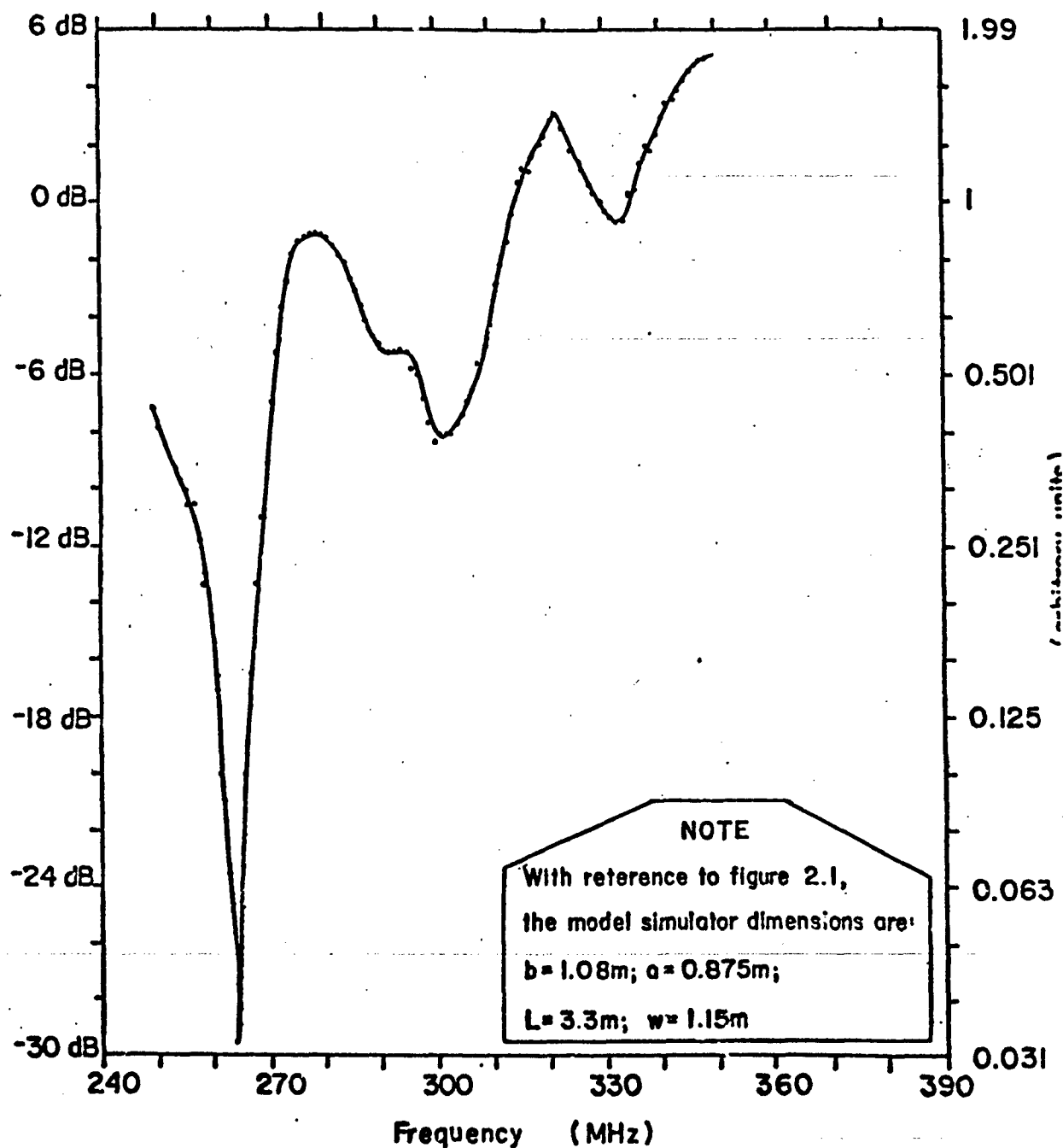


Figure 2.4. Measured  $|\dot{B}_x/\text{constant}|$  at (0,0,0) in the model simulator at Harvard [24]



modes being evanescent at either end of the simulator, as expected, all of the input impedance measurements are dominated by the principal TEM mode. Based on these observations, one may conclude that the notch occurs at the center (0,0,0) due to the symmetry in the simulator as a result of near cancellation of the magnetic field of the TEM mode with its counterpart in the first TM mode. We do not expect a near cancellation in the electric field at the same location for the following reasons. The dominant TEM mode is a traveling wave because of the notched load at the end whereas the TE and TM modes are standing waves owing to reflections. The magnetic field ( $H_x$  component) in the TM modes propagating in the positive and negative  $z$  directions add and their sum cancels the  $H_x$  of the principal TEM mode resulting in the notch behavior. However the electric field in the TM modes propagating in the positive and negative  $z$  directions cancel from each other and thus one does not expect a notch at (0,0,0) in the electric field. This is consistent with the experimentally measured electric field ( $E_y$ ) data shown in Figure 2.3. Furthermore, near the top plate both  $H_x$  and  $E_y$  in the TM mode will have the reversed sign from their values at the ground plane, leading to no cancellation in either of these field quantities with their counterparts in the TEM mode. We also note that the frequency where the notch occurs is also predictable from the dispersion times/distances calculations.

### III. CHARACTERISTICS OF NON-TEM MODES

An open waveguide formed by two perfectly conducting parallel plates of finite width can support, in addition to the dominant TEM mode, higher-order TE and TM modes. These higher modes have suitably complex propagation constants which account for the radiation loss of the modes. Because of radiation, power flow and stored energy are not confined to the inner region of the structure. As the wave (a superposition of modal distributions) propagates, there is a continuous "leaking" of energy from the open waveguiding structure.

In closed waveguides, the higher modes are the solutions of source-free time-harmonic Maxwell's equations characterized by axial field variation of the form  $\exp[j(\omega t - z k_z)]$ . Each one of these modes with real propagation constants ( $k_z$ ) below cutoff satisfies all of the boundary conditions. Above cutoff  $k_z$  is pure imaginary and the modes are evanescent. Also, these modes possess finite energies in a cross section and display orthogonality and completeness properties.

In contrast, the modes on an open waveguide form a discrete spectrum of leaky modes satisfying Maxwell's equations and boundary conditions. However, any cross section extends to infinity and the fields can grow without bounds at large distances from the simulator cross section. These leaky modes on open waveguides do not form a complete orthogonal set and have to be supplemented by a continuous spectrum. The variation of an arbitrary mode can be separated into transverse and longitudinal parts as follows:

$$\tilde{F}(x, y, z, s) = \tilde{f}(x, y, s) e^{-\zeta z} \quad (3.1)$$

where  $\tilde{F}$  denotes an arbitrary field component, and  $\tilde{f}$  denotes variation in the transverse (x-y) plane. The exponential factor displays axial (z coordinate) variation with  $\zeta$  (Laplace transformation variable corresponding to the z coordinate) being the longitudinal complex wavenumber. The complex frequency is denoted by  $s$  and it is the Laplace transformation variable corresponding to the time  $t$ . Setting,

$$p^2 = (s^2/c^2) - \zeta^2 = (\gamma^2 - \zeta^2) \quad (3.2)$$

we have,

$$\zeta = \pm \sqrt{\gamma^2 - p^2} \quad (3.3)$$

To exhibit the cutoff behavior, consider  $s = j\omega$ ,  
 $\gamma = jk$  and  $\zeta = jk_z$

$$\zeta = jk_z = \pm \sqrt{(jk)^2 + (\pm jp)^2} = \pm j \sqrt{k^2 + p^2} \quad (3.4)$$

$$\text{or, } k_z = \pm \sqrt{k^2 + p^2} = (\beta + j\alpha) \quad (3.5)$$

In the integral equation formulation [1], complex  $p$ , multiplied by a factor with linear dimension appears in the argument of special functions. In order to compute the various field quantities, one looks for the roots of transcendental complex functions of  $p$  in the  $p$ -plane. These functions are obtainable in closed form for the limiting cases of narrow and wide plates. Denoting a typical root by  $p_{n,m}$ , the corresponding longitudinal complex wavenumber for this arbitrary mode becomes

$$k_{z,n,m} = \pm \sqrt{k^2 + p_{n,m}^2} = \beta_{n,m} + j\alpha_{n,m} \quad (3.6)$$

$p_{n,m}$  values of interest are approximately pure imaginary with relatively small negative real parts. Let

$$p_{n,m} = u_{n,m} + j v_{n,m} ; \quad (|u_{n,m}| \ll |v_{n,m}|)$$

so that

$$k_{z,n,m} = \pm \sqrt{(k^2 + u_{n,m}^2 - v_{n,m}^2) + 2j u_{n,m} v_{n,m}} \quad (3.7)$$

If  $p_{n,m}$  was pure imaginary (i.e.,  $u_{n,m} = 0$ ), the cutoff behavior is easily exhibited by the factor  $\pm \sqrt{k^2 - v_{n,m}^2}$ . Non-TEM modes are not supported when  $v$  exceeds  $k$  and  $k_z$  becomes pure negative imaginary in the exponential factor,  $\exp(-jk_z z)$ , and the modes are evanescent. The cutoff behavior for the special case when  $[s=j\omega, \gamma=jk \text{ and } p_{n,m}=j v_{nm}]$  can be summarized as follows. For these special conditions, the longitudinal wavenumber  $k_z$  is given by

$$k_{z,n,m} = \begin{cases} \beta_{n,m}; & [\text{with } \beta_{n,m} > 0 \text{ and } \alpha_{n,m} = 0] \text{ for propagation} \\ \beta_{n,m} + j\alpha_{n,m}; & [\text{with } \beta_{n,m} > 0 \text{ and } \alpha_{n,m} < 0] \text{ for evanescence} \end{cases} \quad (3.8)$$

Correspondingly, the longitudinal variation of the fields  $\exp(-jk_{z,n,m} z)$  exhibits the transition from propagation into evanescence. However, the complex singularities ( $p_{n,m}$ ) do have small negative real parts and the transition near cutoff is less abrupt. In the regime of evanescence, the longitudinal wavenumber  $k_{z,n,m}$  becomes largely pure imaginary with a small real part. Consequently, the exponential longitudinal variation  $\exp(-jk_{z,n,m} z)$  exhibits evanescence.

Furthermore, a waveguiding structure formed by two finitely wide plates has two planes ( $x=0$  and  $y=0$ ) about

which the fields can be symmetric or antisymmetric [25]. Such symmetry decomposition can symbolically be represented by indexing the p-plane singularities as

$$p_{n,m}^{(\pm,\pm,E \text{ or } H)}$$

where  $n,m$  correspond to the field variations in  $x$  and  $y$  directions. The two  $\pm$  signs in the superscript indicate symmetry or antisymmetry along the transverse  $x$  and  $y$  directions and  $E$  or  $H$  denote TM or TE mode. Thus, such a representation of the p-plane singularities uniquely specifies a mode and its symmetry properties. Consistent with the above notation, the modes themselves can be denoted by  $E_{n,m}^{(\pm,\pm)}$  (or  $TM_{n,m}^{(\pm,\pm)}$ ) and  $H_{n,m}^{(\pm,\pm)}$  (or  $TE_{n,m}^{(\pm,\pm)}$ ).

These modes in open waveguides formed by a pair of finitely wide parallel plates are found by formulating two different scalar integral equations (of the first kind) for the current and charge densities on the plate. Under certain approximations (separation  $\gg$  width or vice versa), the integral equations can be solved analytically by first transforming them into a Fredholm integral equation of the second kind [1,4,5] and using perturbation techniques.

It is not our intention to show detailed modal distributions of these higher modes in this section, but to point out the methods employed and availability of field plots. Specific calculations of the TM modes in a geometry corresponding to the model EMP simulator at Harvard are currently in progress for later comparisons with the measured data. Such comparisons are expected to lead to unambiguous identification of modes.

#### IV. ELECTROMAGNETIC CONSIDERATIONS OF SPATIAL MODAL FILTERS

The object of introducing a spatial modal filter is to load or damp the non-TEM modes (i.e., TE, TM) without significantly disturbing the TEM modes. One method that has been experimentally implemented in the context of TEM cells [26] with some degree of success is by inserting RF-absorbing material [27,28] along the conducting walls of the waveguiding structure. This technique lacks an analytical basis and also does not fully exploit the uniform characteristics of the dominant TEM mode for damping the non-TEM modes. If we recognize the fact that all propagating modes have spatial properties, one can, hence, take advantage of certain spatial properties to selectively load the modes [29]. In a two-parallel-plate transmission-line type of EMP simulator, all of the important characteristics of the principal TEM mode, both in the parallel-plate region [9] and the conical plate region [10,11], are well known and documented. The quantities of interest are the characteristic impedance, equipotential and field distributions, and field uniformity. Later in this section we shall use a knowledge of these quantities in developing a spatial modal filter. Such filters can take various forms and we dimensionally categorize them below:

##### A. Zero Dimensional

A zero dimensional spatial modal filter will essentially act like a directional coupler in a transmission line that couples to backward propagating modes. In the case of a simulator under consideration, this type of SMF can take the form of two receiving or parasitic antennas (equivalent dipoles, loops) suitably oriented on the top plate or the ground plane so that the TEM mode is uncoupled. The sensitivity of damping of the non-TEM modes is governed by local field ratios.

### B. One Dimensional

One-dimensional spatial modal filters can be implemented by having longitudinal slots both in the top plate and the ground plane. The longitudinal slots (directed along the z-axis of Figure 2.1 in the parallel-plate region and directed along the spherical radial coordinate in the conical region) will be resistively loaded by transverse resistors (x-direction in Figure 2.1). By definition, the only mode with longitudinal component of magnetic field ( $H_z$ ) is the TE mode and, hence, this mode has principally transverse currents ( $J_x$ ) which couple to the transverse resistors. Consequently, this form of SMF is essentially uncoupled from the principal TEM or higher TM modes while loading the higher TE modes.

### C. Two Dimensional

An extension of the one-dimensional SMF is to introduce "loading sheets" that are comprised of a two-dimensional (transverse and longitudinal) array of resistors. In the top plate and the ground plane, one would have only transverse resistors, but in the space away from the simulator plates, the loading sheet will be two dimensional. The sheet will be located along an equipotential surface of the principal TEM mode. This implies that the sheet is electromagnetically invisible to the principal TEM mode while coupling and, hence, damping the non-TEM modes.

### D. Three Dimensional

The two-dimensional loading sheet described above can be repeated to fill some portion of the volume between the top plate and the ground plane resulting in a volumetric suppressor of non-TEM modes.

There are certain constraints to be placed on the choice of the volume of space wherein such a filter can be

placed. For example, the filter should not be close to the working volume of the simulator to avoid any coupling to the test object. Furthermore, the higher-order TE and TM modes become evanescent at a certain distance away from the terminator in the output section. For this reason, little is gained by placing the volumetric SMF near the termination. Such considerations indicate that the SMF should be placed under the output bend extending toward, but not close to, the terminator.

In Section V, we develop an approximate analytical basis for estimating the sheet resistors.



## V. ESTIMATION OF SHEET IMPEDANCES

In this section, we derive relations useful in estimating the longitudinal and transverse resistor values in the individual sheets of a volumetric suppressor. A cross-sectional view of the SMF is sketched in Figure 5.1. Essentially the mode filter would consist of several layers of resistor arrangement, wherein each layer consists of a two-dimensional array of resistors along the axial and transverse directions. Each layer would coincide with a TEM equipotential surface in a conical transmission line. The equipotential and field calculations in a conical transmission line have been reported [10,11], and they are based on stereographically projecting the two-conical-plate line into a cylindrical line of two circular arcs on two different circles. The curved-cylindrical-plate problem is later solved by the method of conformal mapping for the TEM quantities. The physical quantity that is relevant for the SMF design is the TEM equipotential surface, an example of which is shown plotted in Figure 5.2. In this figure, the top plate is held at a potential of  $V_0$  with the ground plane as the reference. The equipotentials (magnetic field lines) are shown in steps of  $0.1 V_0$  and the stream lines (electric field lines) in steps of  $0.1 U_0$ .  $U_0$  is the total current flowing on half of the top plate. The individual resistive sheets of the volumetric suppressor will be made to coincide with the calculated surfaces.

In estimating the values of the transverse ( $R_t$ ) and the longitudinal ( $R_l$ ) resistors, it is useful to view the two-dimensional array of resistors on any given equipotential surface as a resistive sheet with an impedance of  $Z_s$ . We now consider the following two canonical problems useful in estimating  $R_l$  and  $R_t$ . The two problems are posed and analyzed by viewing the mode suppressor sheets as plane wave absorbers.

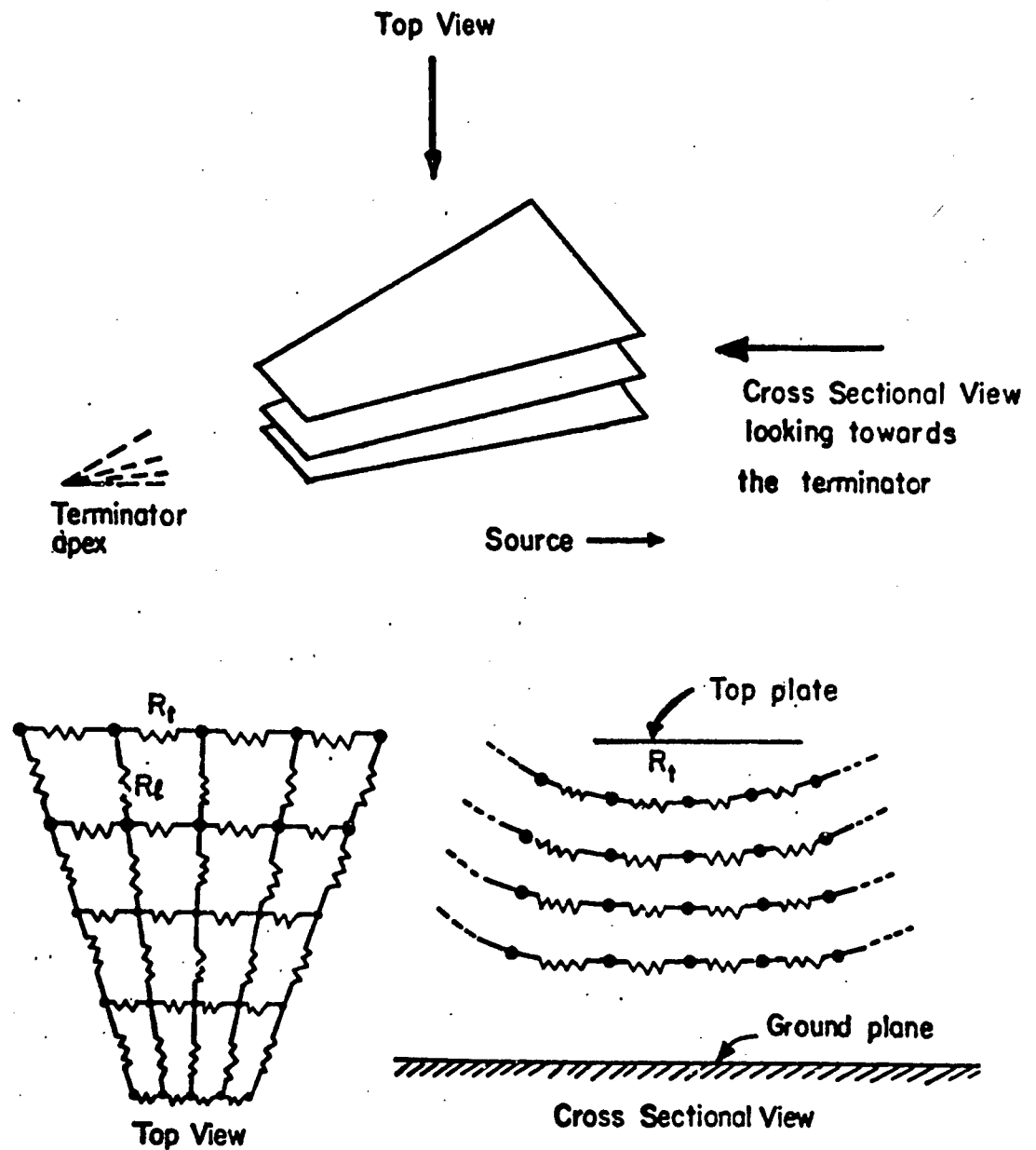


Figure 5.1 Structure of the volumetric spatial modal filter

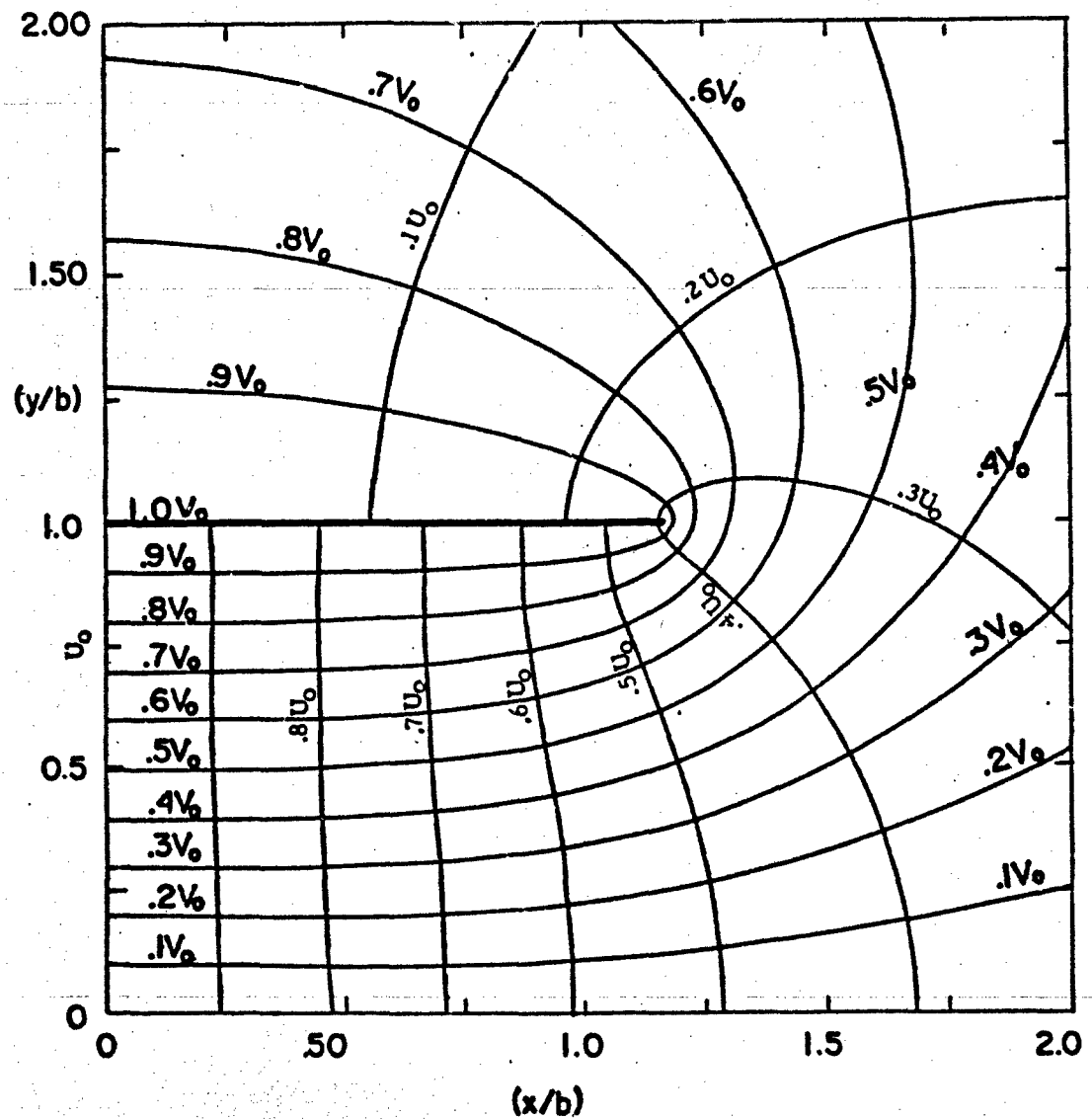


Figure 5.2 A typical TEM equipotential and electric field lines in the conical transmission line [(b/a) = 0.857 and (L/b) = 4.2; scale model simulator with  $z_c^{(TEM)} = 82\Omega$  from top plate to ground plane]

### A. TM Waves Incident on the Resistive Sheet

Consider a TM wave incident on the resistive sheet ( $Z_s$  in  $\Omega$ ), as shown in Figure 5.3a. Denoting the induced surface current density on the sheet by  $J_s$  (A/m), the boundary conditions on the tangential components of the electric and magnetic field lead to

$$E_{\tan} = E_i \sin(\alpha) - E_r \sin(\alpha) = E_t \sin(\alpha) \quad (5.1)$$

The difference in the tangential magnetic field is

$$\Delta H_{\tan} = H_{\text{top}} - H_{\text{bottom}} = H_i + H_r - H_t = J_s = E_{\tan}/Z_s \quad (5.2)$$

$J_s$  is positive and is directed from left to right in Figure 5.3a. Note that the free space characteristic impedance  $Z_0$  is given approximately by

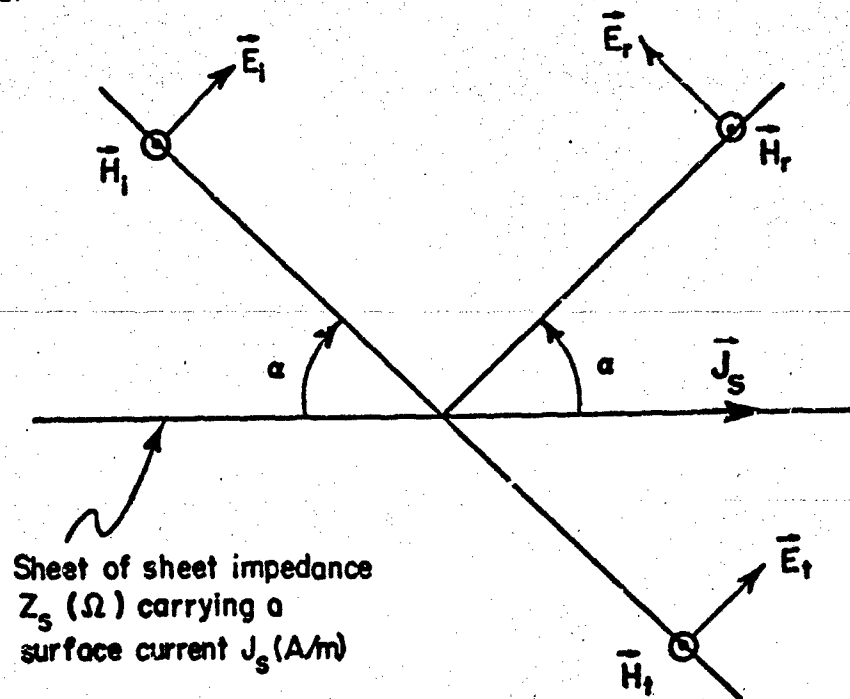
$$Z_0 = \frac{E_i}{H_i} = \frac{E_r}{H_r} = \frac{E_t}{H_t} \approx \sqrt{\frac{\mu_0}{\epsilon_0}} \quad (5.3)$$

Using Eq. (5.3) in Eq. (5.2), and then making use of  $E_r = E_i - E_t$  from Eq. (5.1), we can get

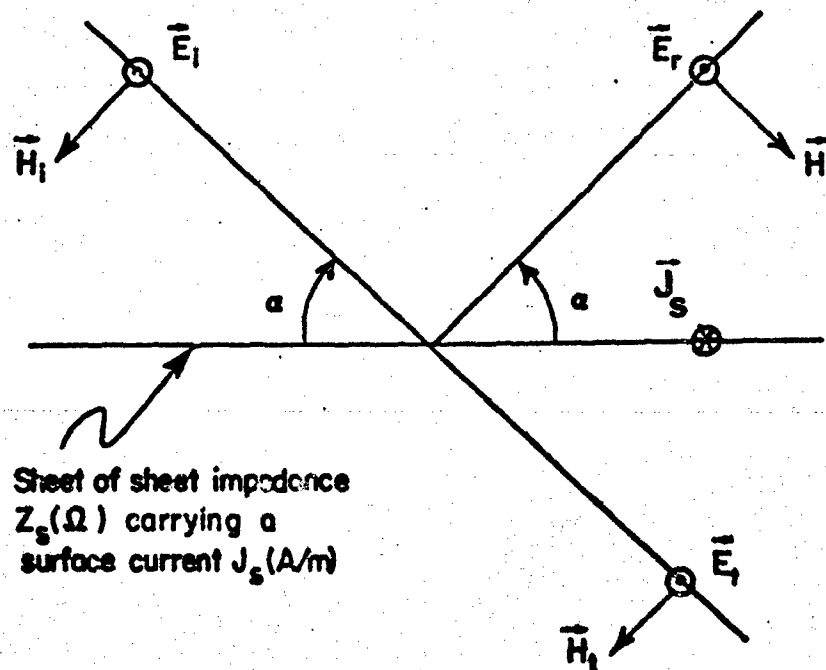
$$\frac{E_t}{E_i} = \frac{2 Z_s}{2 Z_s + Z_0 \sin(\alpha)} \quad (5.4)$$

For fixed values of  $E_i$  and  $\alpha$ , the power dissipated in the sheet per unit area,

$$\begin{aligned} P &= E_{\tan} J_s = (E_{\tan}^2 / Z_s) = (E_t^2 \sin^2(\alpha) / Z_s) \\ &= \frac{E_i^2 \sin^2(\alpha)}{Z_s} \left( \frac{2 Z_s}{2 Z_s + Z_0 \sin(\alpha)} \right)^2 \end{aligned} \quad (5.5)$$



a) TM wave incident on a resistive sheet



b) TE wave incident on a resistive sheet

Figure 5.3 Mode suppressor sheets viewed as plane wave absorbers

Now the power dissipated as heat from the incident wave per unit area normal to the incident wave is

$$P_W = P/\sin(\alpha) = \left( \frac{E_i^2}{Z_0} f \right) \quad (5.6)$$

where  $f$  is the fractional power lost, and is given by

$$f = \frac{Z_0}{E_i^2} \frac{P}{\sin(\alpha)} = \frac{Z_0}{Z_s} \sin(\alpha) \left( \frac{2 Z_s}{2 Z_s + Z_0 \sin(\alpha)} \right)^2 \quad (5.7)$$

Setting

$$\eta = \frac{Z_s}{Z_0 \sin(\alpha)} \quad (5.8)$$

we have

$$f = \frac{1}{\eta} \left[ \frac{2\eta}{1 + 2\eta} \right] \quad (5.9)$$

We may now maximize the fractional power lost by requiring

$$\frac{df}{d\eta} = 0 ; \text{ leading to } \eta_{\text{opt}} = 1/2$$

This give an optimum value for the sheet impedance of

$$Z_s^{(\text{opt})} = \frac{Z_0 \sin(\alpha)}{2} \quad (5.10)$$

Equation (5.10) is now useful in estimating the longitudinal resistors  $R_l$  which carry the current for the TM mode of propagation.

### B. TE Waves Incident on the Resistive Sheet

We can use an entirely similar analysis as in the TM case for the TE case. Consider a TE wave incident on a resistive sheet of impedance  $Z_s$  in  $\Omega$  at an angle  $\alpha$  as shown in Figure 5.3b. Let the induced surface current on the resistive sheet be denoted by  $J_s$  (A/m). The boundary conditions on the tangential fields are

$$E_{\text{tan}} = -E_i - E_r = -E_t \quad (5.11)$$

The difference in the tangential magnetic field is

$$\begin{aligned} \Delta H_{\text{tan}} &= H_{\text{top}} - H_{\text{bottom}} = -H_i \sin(\alpha) + H_r \sin(\alpha) + H_t \sin(\alpha) \\ &= J_s = (E_{\text{tan}}/Z_s) \end{aligned} \quad (5.12)$$

$J_s$  is positive and directed into the plane of the paper in Figure 5.3b. As before, using Eq. (5.3) in (5.12) and later using Eq. (5.11), we can get

$$\frac{E_t}{E_i} = \frac{2 Z_s \sin(\alpha)}{2 Z_s \sin(\alpha) + Z_0} \quad (5.13)$$

Once again, the power dissipated in the sheet per unit area is

$$\begin{aligned} P &= E_{\text{tan}} J_s = (E_{\text{tan}}^2/Z_s) = (E_t^2/Z_s) \\ &= \frac{E_i^2}{Z_s} \left( \frac{2 Z_s \sin(\alpha)}{2 Z_s \sin(\alpha) + Z_0} \right)^2 \end{aligned} \quad (5.14)$$

Using Eq. (5.6), the fractional power lost is now given by

$$f = \frac{Z_o}{E_1^2} \frac{P}{\sin(\alpha)} = \frac{Z_o}{Z_s \sin(\alpha)} \left( \frac{2 Z_s \sin(\alpha)}{2 Z_s \sin(\alpha) + Z_o} \right)^2 \quad (5.15)$$

$$= \frac{1}{v} \left[ \frac{2v}{1 + 2v} \right] \quad (5.16)$$

where  $v = (Z_s \sin(\alpha)/Z_o)$ . We may now maximize the dissipated power by requiring

$$\frac{df}{dv} = 0 ; \quad \text{leading to } v_{\text{opt}} = 1/2 \quad (5.17)$$

This gives an optimum value for the sheet impedance of

$$Z_s^{(\text{opt})} = \frac{Z_o}{2 \sin(\alpha)} \quad (5.18)$$

Once again, we note that for the TE case, only the transverse resistors carry current and, hence, Eq. (5.18) applies to the transverse resistors  $R_t$ .

In either case of TM or TE waves incident on the resistive sheets, the values of the resistors  $R_l$  and  $R_t$  are dependent on the angle of incidence of these waves onto the sheets. In a simulator configuration, this angle ( $\alpha$ ) is, of course, a variable quantity and, consequently, an experimental optimization of the particular values of the resistors is inevitable.

However, at high frequencies, where ray-optic considerations apply, one can estimate the angle  $\alpha$  by considering a typical ray path. It is estimated that the present high frequency ripple of  $\pm 30\%$  can be reduced to within  $\pm 10\%$ . At intermediate frequencies, the angles are harder to estimate, but effective removal of energy from the non-TEM modes results from multiple passes. It is likely that for E modes (TM case), the ratio of  $E_z$  to  $E_x$  or  $E_y$  may define an effective angle  $\alpha$ . A future memo will address these issues specifically.



For the experimental evaluation, initially, a typical angle may be chosen in designing the filter and, later, experimentation around these values will determine the final values.

In successfully implementing these concepts in a given experimental situation, there will be several associated problems and considerations unique to the experiment. For instance, in a model simulator experiment, the power levels are low and, hence, energy dissipation in the resistors is not a serious consideration. However, on a full-scale facility (e.g., ALECS), it may become necessary to place the resistors in plastic tubes filled with oil (if required). Also, in an on-site configuration, the mechanical problems of supporting and holding the sheet along equipotential contours are much more severe. There are questions like how far outward in the cross section should the sheets extend. Such considerations and a detailed design, fabrication and evaluation of the proposed volumetric suppressor will form the subject of a separate report.

## VII. SUMMARY

A two-parallel-plate transmission-line type of EMP simulator has been historically employed to propagate an electromagnetic pulse with a plane wavefront. Since the pulse consists of a wide frequency spectrum, the structures that have been built propagate modes other than the principal TEM mode. Consequently, techniques of non-TEM mode suppression is an important element in the advancement of simulator technology. In this note, we address the problem of mode suppression and, in particular, the electromagnetic considerations of a volumetric suppressor. This suppressor is the result of one of several techniques of mode suppression and believed to be the most efficient. Empirical relations are developed for computing the resistor values required in the fabrication by viewing the suppressor as a plane wave absorber.

An important feature of the SMF is its location. Figure 6.1 shows the side view of a parallel-plate EMP simulator, indicating the approximate locations of two possible SMF. The SMFs have to be located away from the two apexes where the non-TEM modes are evanescent. It is also essential to place the SMF so as to minimize any coupling effects with the test object.

Finally, although our present interest is in EMP simulators, it is recognized that the mode suppression considerations presented here are fairly general and can apply to other types of multimoded structures (e.g., TEM cell) where the non-TEM modes are also undesirable, and due to the lack of radiation losses can cause even more severe problems.

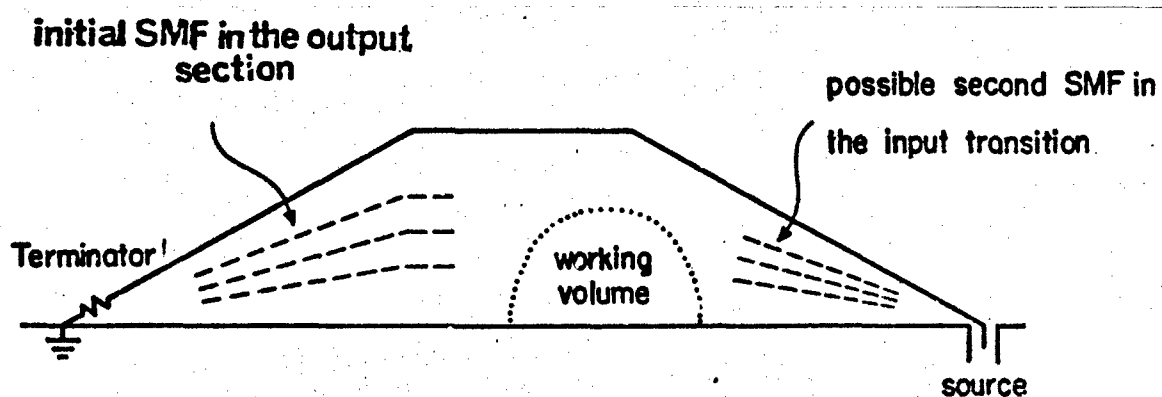


**Figure 6.1** Side view of the simulator showing the approximate locations of two possible spatial modal filters (SMF)

## REFERENCES

1. L. Marin, "Modes on a Finite-Width, Parallel Plate Simulator: I. Narrow Plates", Sensor and Simulation Note 201, September 1974.
2. C-M. Chu, "Mathematics of Guided Wave Propagation in Open Structures", Sensor and Simulation Note 206, May 1974.
3. T. Itoh and R. Mittra, "Analysis of Modes in a Finite Width Parallel-Plate Waveguide", Sensor and Simulation Note 208, January 1975.
4. L. Marin, "Modes on a Finite-Width, Parallel-Plate Simulator: II. Wide Plates", Sensor and Simulation Note 223, March 1977.
5. L. Marin and G.C. Lewis, "Modes on a Finite-Width Parallel-Plate Simulator: III. Numerical Results for Modes on Wide Plates", Sensor and Simulation Note 227, September 1977.
6. A.E.H. Love, "Some Electrostatic Distributions in Two Dimensions", Proc. London Math. Soc., Vol. 22, pp. 337-369, 1923.
7. C.E. Baum, "Impedance and Field Distributions for Parallel Plate Transmission Line Simulators", Sensor and Simulation Note 21, June 1966.
8. T.L. Brown and K.D. Granzow, "A Parameter Study of Two-Parallel-Plate Transmission Line Simulators of EMP Sensor and Simulation Note 21", Sensor and Simulation Note 52, April 1968.
9. C.E. Baum, D.V. Giri and R.D. González, "Electromagnetic Field Distribution of the TEM Mode in a Symmetrical Two-Parallel-Plate Transmission Line", Sensor and Simulation Note 219, 1 April 1976.
10. F.C. Yang and K.S.H. Lee, "Impedance of a Two-Conical-Plate Transmission Line", Sensor and Simulation Note 221, November 1976.
11. F.C. Yang and L. Marin, "Field Distributions on a Two-Conical-Plate and a Curved Cylindrical-Plate Transmission Line", Sensor and Simulation Note 229, September 1977.

12. C.E. Baum, "The Conical Transmission Line as a Wave Launcher and Terminator for a Cylindrical Transmission Line", Sensor and Simulation Note 31, January 1967.
13. C.E. Baum, "General Principles for the Design of ATLAS I and II, Part V: Some Approximate Figures of Merit for Computing the Waveforms Launched by Imperfect Pulser Arrays onto TEM Transmission Lines", Sensor and Simulation Note 148, 9 May 1972.
14. K.S.H. Lee, of Dikewood Industries, Inc., private communication, October 1978.
15. D.V. Giri, C.E. Baum, R.W.P. King, D.J. Blejer and S-K. Wan, "Experimental Investigations into Higher-Order Mode Effects and Simulator/Object Interaction in Parallel-Plate Transmission-Line Geometries", Miscellaneous Simulator Memo 11, 26 May 1977.
16. C.E. Baum, "The Diffraction of an Electromagnetic Plane Wave at a Bend in a Perfectly Conducting Planar Sheet", Sensor and Simulation Note 47, 9 August 1967.
17. J.B. Keller and A. Blank, "Diffraction and Reflection of Pulses by Wedges and Corners", Comm. on Pure and Applied Math., Vol. 4, p. 75, 1951.
18. D.F. Higgins, "The Diffraction of an Electromagnetic Plane Wave by Interior and Exterior Bends in a Perfectly Conducting Sheet", Sensor and Simulation Note 128, January 1971.
19. K.K. Chan, L.B. Felsen, S.T. Peng and J. Shmoys, "Diffraction of the Pulsed Field from an Arbitrarily Oriented Electric or Magnetic Dipole by a Wedge", Sensor and Simulation Note 202, October 1973.
20. D.L. Endsley and D.B. Westenhaver, "Special Report on Field Measurements", ALECS Memo 4, 28 December 1967.
21. J.C. Giles, M.K. Bumgardner, G. Seely and J. Furaus, "Evaluation and Improvement of the CW Performance of the ALECS Facility," ALECS Memo 10, Volume I, Technical Discussion, September 1975.
22. T.T. Wu, R.W.P. King, D.J. Blejer and S-K. Wan, "Laboratory Model Parallel-Plate Transmission Line Type of EMP Simulator (Description of the Set-up and Sample Measurements)," Miscellaneous Simulator Memo 16, 31 July 1977.

23. M. Krook, R.W.P. King, D.J. Blejer, T.K. Sarkar and S-K. Wan, "The Electric Field in a Model Parallel-Plate EMP Simulator at a High CW Frequency," Miscellaneous Simulator Memo 17, July 1978.
24. D.J. Blejer of Harvard University, private communication, November 1978.
25. C.E. Baum, "Interaction of Electromagnetic Fields with an Object Which Has an Electromagnetic Symmetry Plane", Interaction Note 63, 3 March 1971.
26. M.L. Crawford, "Generation of Standard EM Fields Using TEM Transmission Cells", IEEE Trans. on Electromagnetic Compatibility, Vol. EMC-16, pp. 189-195, November 1974.
27. M.L. Crawford, J.L. Workman and C.L. Thomas, "Generation of EM Susceptibility Test Fields Using a Large Absorber-Loaded TEM Cell", IEEE Trans. on Instrumentation and Measurement, Vol. IM-26, No. 3, pp. 225-230, September 1977.
28. M.L. Crawford, J.L. Workman and C.L. Thomas, "Expanding the Bandwidth of TEM Cells for EMC Measurements", IEEE Trans. on Electromagnetic Compatibility, Vol. EMC-20, No. 3, pp. 368-375, August 1978.
29. D.V. Giri and C.E. Baum, "Spatial Modal Filters for Suppression of Non-TEM Modes in Parallel Plate Simulators", presented at the Nuclear EMP Meeting held at the University of New Mexico and sponsored by IEEE Albuquerque Joint Chapters (AP-S, MTT-S, EMC-S) and the Department of Electrical Engineering and Computer Science, University of New Mexico, 6-8 June 1978.

AN INVESTIGATION OF PORTABLE  
EMP SIMULATORS/ALTERMATE SIMULATORS

ABSTRACT

A theory is developed which defines the technical objectives for portable EMP simulator experiments and calculations. It is shown that under certain conditions, a configuration of portable sources need only excite a prescribed external interaction response on a class of systems. Under these conditions, the source configuration will excite the same electrical quantities within the system as would an EMP. Considerable attention is devoted to the demonstration that these conditions must include an accounting for the external environment to the system under test as well as the degree of electromagnetic rigidity of the portable sources. Finally, calculations that were chosen to address the plausibility of achieving the described external interaction objectives are presented and interpreted according to the required conditions.

Acknowledgement

This work was sponsored by the Defense Nuclear Agency under Subtask Code EB200, Work Unit 71.

## PREFACE

Part of the theory presented in this report was developed while one of the authors, Maurice Sancer, was consulting for R & D Associates.

This work sponsored by the Defense Nuclear Agency under: Subtask Code EB200, Work Unit 71.



## SECTION I

## INTRODUCTION

The broad objective of this effort is to guide the experimental investigation of electromagnetic pulse (EMP) simulation by portable simulators. We perform two distinctly different types of analysis directed toward this objective. First, we develop a theory that results in the definition of technical objectives for both experiments and calculations. Finally, we perform calculations to determine whether a very idealized experiment could possibly achieve the required objectives.

The analysis resulting in the technical objectives consists of developing the form of a transfer operator equation in sufficient detail to identify the significance of all terms. Specifically, attention is directed toward clearly identifying the physical quantities related by the transfer operator as well as the physical quantities on which the transfer operator depends. To facilitate the discussion of the physical quantities it is necessary to discuss the type of system we wish to excite with the portable simulators. The class of systems for which this study is applicable are those systems that are, in effect, imperfectly sealed metallic enclosures. Important systems that belong to this class are aircraft, missiles, ships, and tanks. The breaks in these enclosures are referred to as apertures and they might correspond to windows, hatches, or portions of deliberate antennas that are intended to allow energy to flow into the system.

The operator equation relates electrical quantities excited within the actual enclosure (system) to the current density induced on metallic seals placed over all of the apertures of the imperfectly sealed enclosure. The existence of this equation would seem to imply that if a configuration of portable sources excited the same current density on the

seals as did an EMP, then internal electrical quantities within the enclosure of the unsealed system would be identically excited by either the EMP or the portable source configuration. This would be the case under the following conditions; the portable sources must be electromagnetically rigid, i.e., unaffected by the presence of any scatterer, and the external environment of the system must be the same for the portable source configuration as for the EMP. For example, an aircraft having the appropriate seals correctly excited by rigid portable sources when parked on the ground, can only be viewed as having been excited by the corresponding EMP when it is still resting on the ground and in particular is not in free flight.

Even with these limitations, we see that it is possible to assist the alternate simulation program by performing only external interaction measurements or calculations. The initial source configuration can be determined by employing only external interaction considerations. We emphasize that we expect the focus to be on external interaction only in the initial program stages because we anticipate that the local sources will not be capable of exciting exactly the same external interaction quantities on the metallic seals as would an EMP. In order to assess these effects as well as non-rigidity degradation, we expect that internal electrical quantities will have to be measured for excitation by the portable source configuration as well as for excitation by a more orthodox simulator which represents the EMP excitation.

The environment and source rigidity conditions previously discussed result from the dependence of the transfer operator on these factors and not the quantities this operator relates. This source rigidity requirement causes special concern in that any physically realizable portable source is going to

have structure that can interact with the fields reflected from the system under test. This is of particular concern because it is presently anticipated that the configuration of portable sources will be in close proximity to the system under test. The choice of calculations to perform, which represented an idealized experiment, was made with the issue of source rigidity being a distinct factor.

The problem for which we made our calculations was the excitation of a sphere in free space by a plane wave and by various configurations of idealized local sources. These calculations were performed in the frequency domain for a range of frequencies starting at zero and extending to approximately three times the first resonant frequency of the sphere. Well-established plane wave solutions exist for this problem and our method of obtaining our plane wave solution can be verified by comparison of our results to the established results. This is necessary because our method of obtaining the plane wave solution is the same as our method of obtaining the source configuration results and no data is presently available to verify those calculations. As a general conclusion, our calculations indicate that our choice of local source configuration can approximately excite the desired external interaction current density at a shorted point of entry only if at least one local source is in close proximity to the shorting surface. This result increases the need to study the effect of the degree of rigidity of physically realizable sources on the alternate simulation problem.

## SECTION II

## THEORETICAL BACKGROUND

This investigation concerns the local excitation of systems that are predominantly metallic and is valid for those frequencies or times for which the metal can be considered to be perfectly conducting. The equations that form the basis of this investigation of portable EMP simulators is a set of equations that recognizes those essential features of classical aperture coupling analysis that have relevance to complex systems. Since this approach is based on aperture coupling equations, one might be concerned with its relevance to other types of penetrators, e.g., deliberate antennas. Such penetrators have associated apertures or else no energy could penetrate the sealed skin of the system corresponding to that penetrator.

First we will present the general form of the equations that provide the basis of this study and draw all of our theoretical conclusions by referring to properties of this general form. Next we will present a somewhat detailed derivation of these general equations for a complex interaction situation in order to give a more concrete meaning to the general properties on which we based our theoretical conclusions. The form of the underlying equation is as follows

$$LJ_m(\underline{r}') = J_{E.I.}(\underline{r}) \quad (1)$$

where the meaning and significance of each term requires considerable attention. First, we emphasize that equation 1 describes the relationship between electrical quantities on two different physical systems. One system is the actual system of interest and the other system is that original system modified by metallic shorting surfaces covering all apertures (including those associated with antennas). For illustrative purposes

consider the system depicted in figure 1. One system is the aircraft in its environment with the apertures  $S_1$  and  $S_2$  unmodified and the other system needed to give equation 1 meaning is the same aircraft in the same environment with metallic seals covering  $S_1$  and  $S_2$ . In equation 1, the notation  $\underline{J}_m$  was chosen to denote "magnetic current," but it is simply  $\hat{n}(\underline{r}') \times \underline{E}_t(\underline{r}')$  where  $\underline{r}'$  varies over all of the mathematical surfaces corresponding to the open apertures in the original system,  $\hat{n}(\underline{r}')$  is the outward normal at  $\underline{r}'$ , and  $\underline{E}_t(\underline{r}')$  is the tangential component of the electric field induced in the open aperture. The quantity  $\underline{J}_{E.I.}(\underline{r})$  is the "external interaction" current density induced on the shorted system with  $\underline{r}$  ranging only over the shorting surfaces. It is important to note that even though  $\underline{r}$  and  $\underline{r}'$  refer to different physical systems, they mathematically refer to the same set of points. This distinction allows a discussion of the mathematical nature of equation 1 that is not confused by the dual physical nature of the problem. It remains to discuss the meaning of  $L$  in equation 1 to proceed. More specifically,  $L$  is a linear operator that depends on a variety of quantities associated with the system, its environment and certain aspects of its excitation. Just what these quantities are plays an essential role in the underlying theory of portable EMP simulators and we will elaborate on what these quantities are when presenting the details for the system depicted in figure 1.

It is now necessary to introduce an additional equation to augment the information contained in equation 1. This equation also represents a general form and is

$$Q_3 = L_{\beta} \underline{J}_m(\underline{r}') \quad (2)$$

This equation is a mathematical statement of the fact that  $\underline{J}_m(\underline{r}')$  is sufficient to determine a variety of electrical

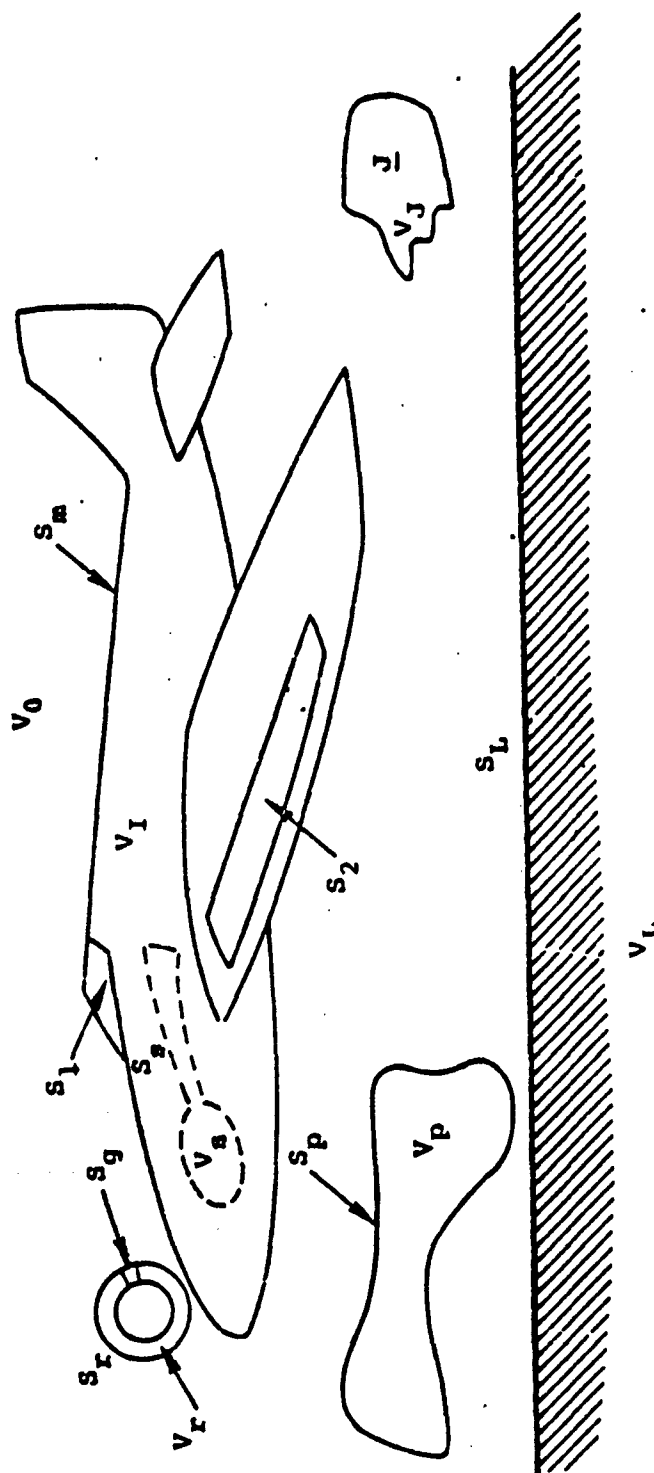


Figure 1. Aircraft and its Environment with Rigid and Non-Rigid Sources

$Q_s$  (e.g.,  $s$  can correspond to a voltage, a current, or a field component) that are excited within the system by fields penetrating through the apertures. In equation 2,  $L_s$  is a linear operator that depends on the internal structure of the system and the choice of the internal electrical quantity that is being determined. Next we introduce a step, the legitimacy of which is currently being studied using a field equivalence point of view. Specifically, it is assumed that the  $L$  appearing in equation 1 has a unique inverse,  $L^{-1}$ , so that from equation 1 we can obtain

$$\underline{J}_m = L^{-1} \underline{J}_{-E.I.} \quad (3)$$

Combining equations 2 and 3 we obtain

$$Q_s = T_s^\alpha \underline{J}_{-E.I.} \quad (4)$$

where

$$T_s^\alpha = L_s L^{-1} \quad (5)$$

and the superscript  $\alpha$  is explicitly introduced to indicate that  $T_s^\alpha$  depends on the environment external to the system. If the same system were placed in two different environments, then the  $\alpha$  designation for each environment could change to accommodate a mathematical representation of the fact that

$$T_s^{\alpha_1} + T_s^{\alpha_2} \quad (6)$$

if the external environments for the same system are sufficiently different. Part of what we shall mean by the external environment is the physical structure of the portable EMP simulators that are being investigated. When we discuss the details

with the system and environment depicted in figure 1, we shall emphasize this source structure dependence and make a crucial distinction between rigid and nonrigid sources.

It is possible to present all of the portable simulator theory on equation 4; however, that equation will be modified to conform to the prevalent notion that both the external interaction current density  $\underline{J}_{E.I.}$  and the external interaction charge density  $\sigma_{E.I.}$  are required for the ultimate determination of the internal quantities  $Q_B$ . For non-zero frequency, it follows from  $\nabla_s \cdot \underline{J}_{E.I.} = i\omega\sigma_{E.I.}$  that  $\underline{J}_{E.I.}$  suffices to determine  $\sigma_{E.I.}$ , so the requirement that  $\sigma_{E.I.}$  be separately determined must be superfluous. There are a number of possibilities why it might be convenient to separately view  $\sigma_{E.I.}$  as a desired input and viewing it as such leads to the following decomposition of equation 4

$$Q_B = T_{JB-E.I.}^{\alpha} \underline{J}_{E.I.} + T_{\sigma B-E.I.}^{\alpha} \sigma_{E.I.} \quad (7)$$

as the basic equation.

At this point we could present the underlying theory of portable EMP simulators by referring to either equation 4 or equation 7 if we did not have to deal with the real physical structure of the portable sources.

The means whereby this aspect enters the consideration is rather complex and is treated by giving a more explicit meaning to these equations. Specifically, this will be accomplished by deriving more explicit representations for equation 1 and equation 2 for the situation depicted in figure 1. First we introduce the following definitions:

- $S_m$ : the surface of the metallic enclosure (aircraft) augmented by the mathematical surfaces  $S_1$  and  $S_2$
- $V_L$ : is the volume of a lossy medium in the proximity of the enclosure (earth, water)



- $S_L$ : the surface bounding  $V_L$   
 $V_P$ : the volume of an object in the proximity of the enclosure (i.e., an aircraft carrier)  
 $S_P$ : the surface bounding  $V_P$   
 $V_S$ : the volume of a subsystem contained within the enclosure  
 $S_S$ : the surface bounding  $V_S$   
 $V_0$ : the volume exterior to  $S_m$  bounded by  $S_m$ ,  $S_P$ ,  $S_L$ ,  $S_r$ , and the hemisphere at infinity  
 $V_I$ : the volume interior to  $S_m$  bounded by  $S_m$  and  $S_S$   
 $V_J$ : the volume of a rigid source of an electromagnetic wave,  $\underline{J}$ , and it is contained in  $V_0$   
 $V_r$ : the volume of the portable radiator  
 $S_r$ : the surface of the portable radiator  
 $S_g$ : the portion of  $S_r$  over which the surface tangential electric field is rigidly specified

The essential equation that this approach is based on is the dyadic identity

$$\begin{aligned}
 & \int_V \left\{ \underline{A}(\underline{r}') \cdot \left[ \nabla' \times \nabla' \times \underline{D}(\underline{r}'; \underline{r}) \right] - \left[ \nabla' \times \nabla' \times \underline{A}(\underline{r}') \right] \cdot \underline{D}(\underline{r}'; \underline{r}) \right\} dV' \\
 & = \int_S \left\{ \underline{A}(\underline{r}') \cdot \left[ \hat{n}(\underline{r}') \times \left[ \nabla' \times \underline{D}(\underline{r}'; \underline{r}) \right] \right] + \left[ \left( \nabla' \times \underline{A}(\underline{r}') \right) \times \hat{n}(\underline{r}') \right] \cdot \underline{D}(\underline{r}'; \underline{r}) \right\} dS'
 \end{aligned}
 \tag{8}$$

where  $\underline{A}(\underline{r}')$  and  $\underline{D}(\underline{r}'; \underline{r})$  are, at this point, a general vector and a general dyadic that must satisfy certain behavior requirements (e.g., differentiability) but not necessarily any equations. In equation 8,  $S$  is the surface bounding  $V$  and  $\hat{n}(\underline{r}')$  is the outward normal to  $V$ . Next, the volume, bounding surface,  $\underline{A}(\underline{r}')$ , and  $\underline{D}(\underline{r}'; \underline{r})$  are specialized.  $V$  is chosen, in turn, as  $V_0$  and  $V_I$  and  $\underline{A}(\underline{r}')$  is chosen as  $\underline{H}_0(\underline{r}')$  and  $\underline{H}_I(\underline{r}')$ . We also choose  $\underline{D}(\underline{r}'; \underline{r})$  as appropriate Green's

dyadics  $(\underline{G}_0(\underline{r}';\underline{r}), \underline{G}_I(\underline{r}';\underline{r}))$  that satisfy the vector wave equation

$$(\nabla' \times \nabla' \times - k_0^2) \underline{G}_\alpha(\underline{r}', \underline{r}) = \underline{I} \delta(\underline{r}' - \underline{r}) \quad \alpha=0, I \quad \underline{r}', \underline{r} \in V_\alpha \quad (9)$$

and subsequently the  $\alpha$  subscript of  $\underline{r}$  and  $\underline{r}'$  will automatically be implied by the subscript on  $\underline{G}_\alpha$  when it is not explicitly indicated. Boundary conditions to be satisfied are

$$\hat{n}(\underline{r}') \times (\nabla' \times \underline{G}_I(\underline{r}', \underline{r})) = 0 \quad \underline{r}' \in S_m \quad (10)$$

$$\hat{n}(\underline{r}') \times (\nabla' \times \underline{G}_0(\underline{r}', \underline{r})) = 0 \quad \underline{r}' \in S_r \cup S_p \cup S_m \quad (11)$$

$$\hat{n}(\underline{r}') \times (\nabla' \times \underline{G}_0(\underline{r}', \underline{r})) = \hat{n}(\underline{r}') \times (\nabla' \times \underline{G}_L(\underline{r}', \underline{r})) \quad \underline{r}' \in S_L \quad (12a)$$

$$\hat{n}(\underline{r}') \times \epsilon_0 \underline{G}_0(\underline{r}', \underline{r}) = \hat{n}(\underline{r}') \times \epsilon \underline{G}_L(\underline{r}', \underline{r}) \quad \underline{r}' \in S_L \quad (12b)$$

The equation satisfied by  $\underline{G}_L(\underline{r}', \underline{r})$  is

$$(\nabla' \times \nabla' \times - \omega^2 \mu_0 \epsilon) \underline{G}_L(\underline{r}', \underline{r}) = 0 \quad \underline{r}' \in V_L, \underline{r} \in V_0 \quad (13)$$

The equations satisfied by the  $\underline{H}_\alpha(\underline{r}')$  are

$$(\nabla' \times \nabla' \times - k_0^2) \underline{H}_\alpha(\underline{r}') = \begin{cases} 0 & \alpha=I \\ \nabla' \times \underline{J}(\underline{r}') & \alpha=0 \end{cases} \quad (14)$$

It also follows from Maxwell's equations

$$\nabla' \times \underline{H}_\alpha(\underline{r}') = -i\omega \epsilon_0 \underline{E}_\alpha(\underline{r}') \quad \underline{r}' \in S_m \quad (15)$$

Substituting equations 9, 14, and 15 into 8 for  $V=V_0$  or  $V_I$  and using the property of the  $\delta$  function, we obtain

$$\begin{aligned} \underline{H}_0(\underline{r}_0) = \underline{I}(\underline{r}_0) + \sum_{q=m,p,r,L} \int_{S_q} \left| \hat{n}_q, \underline{E}_0, \underline{H}_0, \underline{G}_0 \right| dS' \\ + \int_{S_\infty} \left| \hat{a}_r, \underline{E}_0, \underline{H}_0, \underline{G}_0 \right| dS' \end{aligned} \quad (16)$$

$$\underline{H}_I(\underline{r}_I) = \sum_{q=m,s} \int_{S_q} \left| \hat{n}_q, \underline{E}_I, \underline{H}_I, \underline{G}_I \right| dS' \quad (17)$$

where  $\hat{a}_r$  is the unit outward normal to the sphere at infinity  $S_\infty$ .

$$\begin{aligned} \int_S \left| \hat{n}, \underline{E}, \underline{H}, \underline{G} \right| dS' \\ = \int_S \left\{ \underline{H}(\underline{r}') \cdot \left[ \hat{n}(\underline{r}') \times \left[ \nabla' \times \underline{G}(\underline{r}'; \underline{r}) \right] \right] + i\omega\epsilon \left[ \hat{n}(\underline{r}') \times \underline{E}(\underline{r}') \right] \cdot \underline{G}(\underline{r}'; \underline{r}) \right\} dS' \end{aligned} \quad (18)$$

where  $\epsilon$  is the appropriate dielectric permittivity and

$$\underline{I}(\underline{r}_0) = \int_{V_J} \nabla' \times \underline{J}(\underline{r}') \cdot \underline{G}_0(\underline{r}'; \underline{r}_0) dV' \quad (19)$$

Using equations 10 and 11 as well as the fact th

$$\hat{n}(\underline{r}') \times \underline{E}(\underline{r}') = 0 \quad \underline{r}' \in (S_m - S_1 - S_2) \cup S_p \cup (S_r - S_q) \quad (20)$$

we find that

$$\int_{S_p} \left| \hat{n}, \underline{E}_0, \underline{H}_0, \underline{G}_0 \right| dS' = 0 \quad (21)$$

$$\int_{S_r} \left| \hat{n}, \underline{E}_0, \underline{H}_0, \underline{G}_0 \right| dS' = \int_{S_g} i\omega\epsilon_0 \left[ \hat{n}(\underline{r}') \times \underline{E}(\underline{r}') \right] \cdot \underline{G}_0(\underline{r}'; \underline{r}_0) dS'$$

$$\equiv \underline{S}(\underline{r}_0) \quad (22)$$

$$\int_{S_m} \left| \hat{n}_\alpha, \underline{E}_\alpha, \underline{H}_\alpha, \underline{G}_\alpha \right| dS' = i\omega\epsilon_0 \left( \int_{S_1} \left[ \hat{n}_\alpha(\underline{r}') \times \underline{E}_\alpha(\underline{r}') \right] \cdot \underline{G}_\alpha(\underline{r}'; \underline{r}_\alpha) dS' \right.$$

$$\left. + \int_{S_2} \left[ \hat{n}_\alpha(\underline{r}') \times \underline{E}_\alpha(\underline{r}') \right] \cdot \underline{G}_\alpha(\underline{r}'; \underline{r}_\alpha) dS' \right)$$

$$\alpha = 0, I \quad (23)$$

and because  $\underline{E}_0$ ,  $\underline{H}_0$ , and  $\underline{G}_0$  satisfy the radiation condition

$$\int_{S_\infty} \left| \hat{a}_{r'}, \underline{E}_0, \underline{H}_0, \underline{G}_0 \right| dS' = 0 \quad (24)$$

The remaining quantities to evaluate in equations 16 and 17 are the surface integrals over  $S_L$  and  $S_g$ . Substituting the equations appropriate for the lossy half space, that is

$$(\nabla' \times \nabla' \times - \omega^2 \mu_0 \epsilon) \underline{H}_L(\underline{r}') = 0 \quad \underline{r}' \in V_L \quad (25)$$

and

$$\nabla' \times \underline{H}_L(\underline{r}') = -i\omega\epsilon \underline{E}_L(\underline{r}') \quad \underline{r}' \in V_L \quad (26)$$

as well as equation 13 into 8 we obtain

$$\begin{aligned}
& \int_{S_L} \left[ \underline{H}_L(\underline{r}') \cdot \left[ \hat{n}(\underline{r}') \times \left[ \nabla' \times \underline{G}_L(\underline{r}'; \underline{r}) \right] \right] + i\omega\epsilon \left[ \hat{n}(\underline{r}') \times \underline{E}_L(\underline{r}') \right] \underline{G}_L(\underline{r}'; \underline{r}) \right] dS' \\
& + \int_{S_-} \left[ \underline{H}_L(\underline{r}') \cdot \left[ \hat{n}(\underline{r}') \times \left[ \nabla' \times \underline{G}_L(\underline{r}'; \underline{r}) \right] \right] + i\omega\epsilon \left[ \hat{n}(\underline{r}') \times \underline{E}_L(\underline{r}') \right] \underline{G}_L(\underline{r}'; \underline{r}) \right] dS' = 0
\end{aligned}
\tag{27}$$

The second integral in equation 27 is zero due to the losses in  $V_L$  (or the radiation condition if  $V_L$  is lossless). Using the fact that the tangential components of  $\underline{E}$  and  $\underline{H}$  are continuous across  $S_L$  as well the boundary conditions in equation 12a and 12b we see that the integral over  $S_L$  in equation 16 is equal to the integral over  $S_L$  in equation 27 which in turn we have just shown to equal zero. The integral over  $S_g$  will also equal zero and the manner in which this can be seen depends on the physical properties of the subsystem occupying  $V_g$ . If it were totally metallic, the boundary conditions on  $\underline{E}_I$  and  $\underline{G}_I$  would make the surface integral vanish in the same manner they did for the integral over  $S_p$ . If it were a homogeneous dielectric, then the boundary conditions would cause the surface integral over  $S_g$  in the same manner the surface integral over  $S_L$  was caused to vanish. If it were some hybrid of dielectric and metal, a combination of the arguments would be used to cause the surface integral to vanish.

We can now write equations 16 and 17 as

$$\underline{H}_0(\underline{r}_0) = \underline{F}(\underline{r}_0) - K_0 \underline{J}_m(\underline{r}') \tag{28}$$

and

$$\underline{H}_I(\underline{r}_I) = K_I \underline{J}_m(\underline{r}') \tag{29}$$

where

$$\underline{F}(\underline{r}_0) = \underline{I}(\underline{r}_0) + \underline{S}(\underline{r}_0) \quad (30)$$

with  $\underline{I}(\underline{r}_0)$  and  $\underline{S}(\underline{r}_0)$  defined by equations 19 and 22 and the operators  $K_\alpha$  are defined by

$$K_\alpha J_m(\underline{r}') = i\omega\epsilon_0 \left( \int_{S_1} \underline{J}_m(\underline{r}') \cdot \underline{G}_\alpha(\underline{r}', \underline{r}_\alpha) dS' + \int_{S_2} \underline{J}_m(\underline{r}') \cdot \underline{G}_\alpha(\underline{r}', \underline{r}_\alpha) dS' \right)$$

$$\alpha = 0, I \quad (31)$$

and we have made use of the fact that the tangential components of the electric field are continuous through the apertures so that

$$-\hat{n}_0(\underline{r}') \times \underline{E}_0(\underline{r}') = \hat{n}_I(\underline{r}') \times \underline{E}_I(\underline{r}') = \underline{J}_m(\underline{r}') \quad \underline{r}' \in S_1 \cup S_2 \quad (32)$$

Now we focus our attention on  $\underline{F}(\underline{r}_0)$  appearing in equation 28. The meaning of this quantity is an extremely important aspect of the theory behind portable EMP simulators. It would be a very difficult task to evaluate equations 19, 22, and 30 in order to determine the full significance of  $\underline{F}(\underline{r}_0)$ . Instead, we will simply utilize certain key features of those equations as well as equations 28 and 31 to determine what  $\underline{F}(\underline{r}_0)$  must be if all the required equations were evaluated. First, we note according to equation 19 that  $\underline{I}(\underline{r}_0)$  is excited by the rigid (interaction independent) source  $\underline{J}(\underline{r}')$  and that according to equation 22,  $\underline{S}(\underline{r}_0)$  is excited by the rigidly specified  $\hat{n}(\underline{r}') \times \underline{E}(\underline{r}')$  for  $\underline{r}' \in S_g$ . Next, we note that according to these equations, both  $\underline{I}(\underline{r}_0)$  and  $\underline{S}(\underline{r}_0)$  are insensitive to the size

of the apertures  $S_1$  and  $S_2$  and in fact they are insensitive to whether or not these apertures are even present. Using these observations in conjunction with equation 31 as the aperture size becomes zero and using the result in equation 28, we see that  $\underline{F}(\underline{r}_0)$  equals  $\underline{H}_0(\underline{r})$  for the special case where all apertures are sealed (short circuited). Mathematically, we express this evaluation of  $\underline{F}(\underline{r}_0)$  as

$$\underline{F}(\underline{r}_0) = \underline{H}_0^{s.c.}(\underline{r}_0) \quad (33)$$

where the superscript is introduced to indicate "short circuit." We note that  $\underline{F}(\underline{r}_0)$  is the short circuit magnetic field at some point  $\underline{r}_0$  with apertures sealed, but all other aspects of the external environment including the proximity and structure of the radiator,  $S_r$ , unchanged.

Substituting equation 33 into equation 28 we obtain

$$\underline{H}_0(\underline{r}_0) = \underline{H}_0^{s.c.}(\underline{r}_0) - K_0 \underline{J}_m(\underline{r}') \quad (34)$$

Next, we define  $\hat{n}(\underline{r}) = \hat{n}_I(\underline{r}) = -\hat{n}_0(\underline{r})$  for  $\underline{r} \in S_1 \cup S_2$ , use the fact that

$$\hat{n}(\underline{r}) \times \underline{H}_0(\underline{r}) = \hat{n}(\underline{r}) \times \underline{H}_I(\underline{r}) \quad (35)$$

and employ equations 28 and 34 to obtain

$$\lim_{\substack{\underline{r}_0 \rightarrow \underline{r} \\ \underline{r}_I \rightarrow \underline{r}}} \hat{n}(\underline{r}) \times (K_0 + K_I) \underline{J}_m(\underline{r}') = \underline{J}_{E.I.}(\underline{r}) \quad (36)$$

where we have used the definition

$$\hat{n}(\underline{r}) \times \underline{H}_0^{s.c.}(\underline{r}) = \underline{J}_{E.I.}(\underline{r}) \quad (37)$$

and we have the desired result, in that equation 36 is the more detailed representation of equation 1.

Before we can present our theoretical conclusions, we must present our more detailed representation of equation 2. We have, in fact, already a representation of equation 2 for the case where the desired internal electrical quantity is the magnetic field. For that use we might choose the symbol  $\beta$  as  $H$  so that  $Q_H = H$  and  $L_\beta = L_H = K_I$ . Another example where the structure of  $L_\beta$  changes depending on the choice of  $Q_\beta$  is readily demonstrated by considering the case where the desired internal electrical quantity is the electric field  $E$  and we denote  $\beta$  as  $E$  so that  $Q_E = E$ . For this case equation 2 becomes

$$Q_E = L_E J_m(\underline{r}) \quad (38)$$

where

$$L_E = - \frac{1}{i\omega\epsilon_0} \nabla \times K_I \quad (39)$$

Finally, we will discuss the more important case where the desired internal electrical quantity is a current. For this discussion consider that part of the internal subsystem occupying volume  $V_g$  in figure 1 contains a wire and we choose a local cylindrical coordinate system having its axis along the wire and having the local azimuthal vector denoted  $\hat{\phi}_w(l')$  at the point on the wire where we wish to determine the current. The argument of this unit vector,  $l'$ , denotes the circumferential position on the wire. With these definitions, the current on the wire is

$$I = \int dl' \hat{\phi}_w(l') \cdot \underline{H}_I(\underline{r}_I) \quad (40)$$



We see that from equations 29 and 40 that

$$Q_c = L_{c-m} J_m(\underline{r}') \quad (41)$$

where we have denoted  $I = Q_c$  and

$$L_{c-m} J_m(\underline{r}') \equiv \int d\underline{l}' \hat{\phi}_w(\underline{l}') \cdot K_{I-m} J_m(\underline{r}') \quad (42)$$

We have now presented equations 1 and 2 in sufficient detail to draw our desired conclusions. We will base our conclusions on equation 4 which contains exactly the physics as do equations 1 and 2. The specific points we wish to make are i) the external interaction current density,  $J_{E.I.}$ , can be excited by either a rigid source, a non-rigid source, or a combination of the two types ii) the transfer operator,  $T_g^a$ , depends on the external environment to the system iii)  $T_g^a$  depends on the internal environment iv)  $T_g^a$  depends on the internal electrical quantity,  $Q_g$ , being determined v)  $T_g^a$  depends on the rigidity of the source. Equations that specifically illustrate each of these points are identified with the numbered points as follows: i) equations 19, 22, 30, 33, and 37 ii) equations 11 and 12 iii) equation 10 as well as the argument that eliminated the integral over  $S_g$  iv) equations 5, 39, and 42 v) equation 11.

The remaining portion of this report will be devoted to the calculation that represents the idealized experiment.

## SECTION III

## MAGNETIC FIELD INTEGRAL EQUATION FOR A SPHERE

If we impose an orthonormal coordinate system  $\hat{s}, \hat{t}$  on a closed surface possessing continuous curvature such that  $\hat{s} \times \hat{t} = \hat{n}$ , the outward normal to the body, we can write the Magnetic Field Integral Equation (MFIE) as the following system of coupled scalar integral equations

$$\frac{1}{2} J_s(\underline{r}) = -\hat{t}(\underline{r}) \cdot \underline{H}^{inc}(\underline{r}) + \int \left( A(\underline{r}, \underline{r}') J_s(\underline{r}') + B(\underline{r}, \underline{r}') J_t(\underline{r}') \right) dS' \quad (43a)$$

$$\frac{1}{2} J_t(\underline{r}) = \hat{s}(\underline{r}) \cdot \underline{H}^{inc}(\underline{r}) + \int \left( C(\underline{r}, \underline{r}') J_s(\underline{r}') + D(\underline{r}, \underline{r}') J_t(\underline{r}') \right) dS' \quad (43b)$$

where

$$A(\underline{r}, \underline{r}') = -Q(|\underline{r} - \underline{r}'|) \left[ \hat{t}(\underline{r}) \cdot (\underline{r} - \underline{r}') \times \hat{s}(\underline{r}') \right] \quad (44a)$$

$$B(\underline{r}, \underline{r}') = -Q(|\underline{r} - \underline{r}'|) \left[ \hat{t}(\underline{r}) \cdot (\underline{r} - \underline{r}') \times \hat{t}(\underline{r}') \right] \quad (44b)$$

$$C(\underline{r}, \underline{r}') = Q(|\underline{r} - \underline{r}'|) \left[ \hat{s}(\underline{r}) \cdot (\underline{r} - \underline{r}') \times \hat{s}(\underline{r}') \right] \quad (44c)$$

$$D(\underline{r}, \underline{r}') = Q(|\underline{r} - \underline{r}'|) \left[ \hat{s}(\underline{r}) \cdot (\underline{r} - \underline{r}') \times \hat{t}(\underline{r}') \right] \quad (44d)$$

$$Q(R) = (ikR - 1) \frac{e^{ikR}}{4\pi R^3} \quad (45)$$

and  $J_s(\underline{r})$ ,  $J_t(\underline{r})$  are defined through

$$\underline{J}(\underline{r}) = J_s(\underline{r}) \hat{s}(\underline{r}) + J_t(\underline{r}) \hat{t}(\underline{r}) \quad (46)$$

EMP 1-27

For a sphere of radius "a" centered at the origin,  $\hat{n} = (\underline{r}/a)$  for all points on the surface. This permits us to greatly simplify the form of equations 44a - 44d even before specifying our actual choice for  $\hat{s}$  and  $\hat{t}$ . Formal manipulation of the triple products in these equations yield

$$A(\underline{r}, \underline{r}') = -aQ(\underline{r} - \underline{r}') \left[ \hat{s}(\underline{r}) \cdot \hat{s}(\underline{r}') - \hat{t}(\underline{r}) \cdot \hat{t}(\underline{r}') \right] \quad (47a)$$

$$B(\underline{r}, \underline{r}') = -aQ(\underline{r} - \underline{r}') \left[ \hat{s}(\underline{r}) \cdot \hat{t}(\underline{r}') + \hat{t}(\underline{r}) \cdot \hat{s}(\underline{r}') \right] \quad (47b)$$

$$C(\underline{r}, \underline{r}') = aQ(\underline{r} - \underline{r}') \left[ -\hat{t}(\underline{r}) \cdot \hat{s}(\underline{r}') - \hat{s}(\underline{r}) \cdot \hat{t}(\underline{r}') \right] \quad (47c)$$

and

$$D(\underline{r}, \underline{r}') = aQ(\underline{r} - \underline{r}') \left[ -\hat{t}(\underline{r}) \cdot \hat{t}(\underline{r}') + \hat{s}(\underline{r}) \cdot \hat{s}(\underline{r}') \right] \quad (47d)$$

thus showing that  $D(\underline{r}, \underline{r}') = -A(\underline{r}, \underline{r}')$  and  $C(\underline{r}, \underline{r}') = B(\underline{r}, \underline{r}')$ . We also note that  $A(\underline{r}, \underline{r}') = A(\underline{r}', \underline{r})$  and  $B(\underline{r}, \underline{r}') = B(\underline{r}', \underline{r})$ . This latter symmetry property is of considerable importance for analytic treatments of the MFIE on a sphere, but will be lost in the numerical scheme for solving the equations.

A numerical implementation of equations 43a and 43b even with the simplifications of equations 47a - 47d requires that the sphere be imbedded in some coordinate system. We use a spherical coordinate system, i.e., an arbitrary position on the surface of the sphere has cartesian coordinates

$$\underline{r}(\theta, \phi) = a(\cos\phi\sin\theta, \sin\phi\sin\theta, \cos\theta) \quad (48)$$

We may define

$$\hat{t}(\theta, \phi) \equiv -\hat{e}_\theta \equiv -\frac{1}{a} \frac{\partial}{\partial \theta} \underline{r}(\theta, \phi) = (-\cos\phi \cos\theta, -\sin\phi \cos\theta, \sin\theta) \quad (49a)$$

and

$$\hat{s}(\theta, \phi) \equiv \hat{e}_\phi \equiv \frac{1}{a \sin\theta} \frac{\partial}{\partial \phi} \underline{r}(\theta, \phi) = (-\sin\phi, \cos\phi, 0) \quad (49b)$$

obtaining

$$\hat{n}(\theta, \phi) \equiv \hat{s}(\theta, \phi) \times \hat{t}(\theta, \phi) \equiv \frac{1}{a} \underline{r}(\theta, \phi) = (\cos\phi \sin\theta, \sin\phi \sin\theta, \cos\theta) \quad (49c)$$

as it should.

Inserting equations 48, 49a and 49b into equations 47a - 47d and recalling that the element of area on the surface of a sphere is  $a^2 \sin\theta d\theta d\phi$  completes the specification of the MFIE in a spherical coordinate system.

Our procedure for solving the coupled scalar equations of the MFIE is to partition the sphere into zones  $S_j$  by an algorithm which has the maximum separation of any two points of any zone tend to zero as the number of zones tends to infinity. We then approximate both  $J_s$  and  $J_t$  by piecewise constant functions whose discontinuities occur at the zone boundaries. If we pick a representative point from each zone and restrict  $\underline{r}$  to this set of points, we obtain, as a matrix approximation to the MFIE,

$$\begin{aligned} \frac{1}{2} J_s(\underline{r}_i) &= -\hat{t}(\underline{r}_i) \cdot \underline{H}^{inc}(\underline{r}_i) + \sum_j J_s(\underline{r}_i) \int_{S_j} A(\underline{r}_i, \underline{r}') dS' \\ &+ \sum_j J_t(\underline{r}_i) \int_{S_j} B(\underline{r}_i, \underline{r}') dS' \quad (50a) \end{aligned}$$

$$\begin{aligned} \frac{1}{2} J_t(\underline{r}_i) = & \hat{s}(\underline{r}_i) \cdot \underline{H}^{inc}(\underline{r}_i) + \sum_j J_s(\underline{r}_i) \int_{S_j} C(\underline{r}_i, \underline{r}') dS' \\ & + \sum_j J_t(\underline{r}_i) \int_{S_j} D(\underline{r}_i, \underline{r}') dS' \end{aligned} \quad (50b)$$

This method of solution can be viewed as either a method of moments solution or as a product integration method.

We must, however, consider the nature of the integrands in equations 50a and 50b. One can show that for an arbitrary body with everywhere continuous, non-zero, local curvature A, B, C, and D are singular but behave at worst as  $\alpha/|\underline{r}-\underline{r}'|$  as  $\underline{r}'$  approaches  $\underline{r}$  for some finite  $\alpha$ . This will be explicitly shown for the case of a sphere. Since we are dealing with a two-dimensional integral, these integrands are still absolutely integrable, however, these singularities should be treated analytically in order to avoid convergence problems for numerical integration. Our programs for scattering from cylindrical bodies remove this singularity before attempting the numerical integration; experience indicates that such treatment greatly improves the accuracy of both phase calculations and resonant phenomena.

For a sphere, the numerical problem is much simpler. As will be shown by the following analysis, a symmetric integration procedure will permit the singularities to be ignored for sufficiently large zones. By expanding the scalar triple products to second order in  $\theta-\theta'$  and  $\phi-\phi'$  we will show, as we mentioned earlier, that the above mentioned singularity does exist, but numerical techniques exist which avoid the need to treat the singularity analytically.

We start by expanding  $|\underline{r}-\underline{r}'|^2$  in powers of  $(\theta-\theta')$  and  $(\phi-\phi')$ .

$$|\underline{r}-\underline{r}'|^2 = |\underline{r}'|^2 + |\underline{r}|^2 - 2(\underline{r} \cdot \underline{r}') = 2a^2(1-\hat{n} \cdot \hat{n}') \quad (51)$$

which by equation 49c yields

$$\begin{aligned} |\underline{r}-\underline{r}'|^2 &= 2a^2 [1 - \sin\theta \sin\theta' (\cos\phi \cos\phi' + \sin\phi \sin\phi') - \cos\theta \cos\theta'] \\ &= a^2 [\sin^2\theta (\phi - \phi')^2 + (\theta - \theta')^2] + o[(\theta - \theta')^2 + (\phi - \phi')^2] \end{aligned} \quad (52)$$

Similarly, from equations 49a, 49b and 47a we get

$$\begin{aligned} \frac{-A(\underline{r}, \underline{r}')}{aQ} &= \sin\phi \sin\phi' + \cos\phi \cos\phi' \\ &\quad - (\cos\phi \cos\phi' \cos\theta \cos\theta' + \sin\phi \sin\phi' \cos\theta \cos\theta' + \sin\theta \sin\theta') \\ &= \frac{1}{2} [(\theta - \theta')^2 - \sin^2\theta (\phi - \phi')^2] + o[(\phi - \phi')^2 + (\theta - \theta')^2] \end{aligned} \quad (53)$$

while equations 49a, 49b and 47b yield

$$\frac{-B(\underline{r}, \underline{r}')}{aQ} = -a(\phi - \phi')(\theta - \theta') \sin\theta + o[(\phi - \phi')^2 + (\theta - \theta')^2] \quad (54)$$

The above analysis has shown that neither A nor B behaves any worse than  $\alpha/|\underline{r}-\underline{r}'|$  for some finite  $\alpha$ , yet, except at the poles (B is non-singular if  $\theta = 0$ ) there exists directions of approach such that both A and B vary as  $1/|\underline{r}-\underline{r}'|$  as  $\underline{r}'$  approaches  $\underline{r}$ . In addition, we have shown that except at  $\theta=0$  and  $\theta=\pi$  B is antisymmetric in  $(\theta-\theta')$  and  $(\phi-\phi')$  and A is antisymmetric in  $(\theta-\theta') \pm (\phi-\phi') \sin\theta$ . Thus if our integration scheme is symmetric in  $(\theta-\theta')$  and  $(\phi-\phi') \pm (\phi-\phi') \sin\theta$  the singular part effectively vanishes for self term interactions, i.e., when  $i=j$  for equations 50a and 50b. However, neighboring zone interactions do not necessarily have this antisymmetry property. If wavelength considerations force the zones to be small the singularities should be treated analytically.

Our experience has shown that the zoning criteria for accurate solution of the MFIE can be split into wavelength and geometry considerations. As a general rule, between six and ten zones per wavelength are needed to fulfill the wavelength requirements. For this special case we found that we could employ even fewer zones for wavelength. For low frequency, however, geometric considerations dominate the zoning criteria. The adequacy of the geometric requirements can be ascertained by examining the results for magnetostatic excitation. Studying both types of zone requirements, we found that the nearest neighbor zones are far enough removed to permit simple integration schemes for evaluating the integrals of equations 50a and 50b.

## SECTION IV

## PRESENTATION OF SPHERE CALCULATIONS

The coordinate system, incident field description, and zone numbering scheme for this calculation are depicted in figure 2. The boundaries for each zone are determined by allowing 45° increments in  $\theta$  and  $\phi$ . In figures 3 through 11 we present the current density induced by the depicted incident field as well as by selected local excitation. What is meant by the local excitation is that a numbered patch is either considered to be illuminated by the depicted incident field or is considered to receive no incident illumination. A discussion of the relevance of this type of local illumination will be deferred to the next section.

The labeling of the tangential components of the induced current density is as follows

$$J_s = J_\phi \quad (55)$$

$$J_t = -J_\theta \quad (56)$$

and the quantities plotted are the magnitudes of these components of current density normalized to the magnitude of the incident magnetic field,  $H_0$ . The code verification data presented in these figures comes from two sources. For  $ka=0$ , the magnitude of the magnetostatic solution given by

$$J_s = -(3/2)H_0 \cos\phi \cos\theta \quad (57)$$

and

$$J_t = -(3/2)H_0 \sin\phi \quad (58)$$



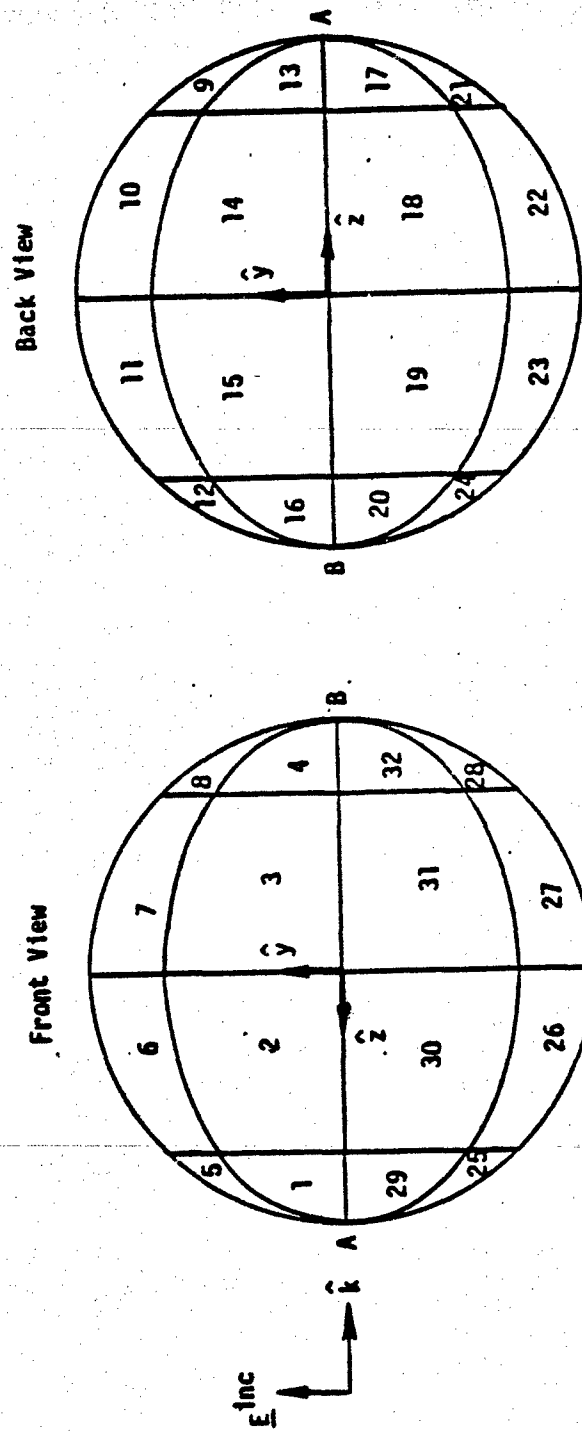


Figure 2. Coordinate System and Zone Numbering Scheme for the Sphere Calculations

is used to obtain the code verification data. For  $k = 1.1, 1.7, 2.3, 2.9$  we use the data presented in figure 66a of reference 1. Specifically, we relate their data,  $K_0$  and  $K_z$ , to the code verification data using the relations

$$\left| \frac{J_s(\theta, \phi)}{H_0} \right| = |K_z(\psi_1) \cos \phi| \quad (59)$$

and

$$\left| \frac{J_t(\theta, \phi)}{H_0} \right| = |K_\theta(\theta_1) \sin \phi| \quad (60)$$

as well as making the identification  $\psi_1 = \theta_1 = \theta$ . The values of  $\theta$  and  $\phi$  which are chosen for the evaluation of equations 57, 58, 59, and 60 for the code verification data correspond to the angular centers of the patches. Finally, we note that we need only present our incident field results for zones 1 through 8 because those results can be translated to the remaining range of  $\phi$  values through the relations

$$\left| \frac{J_s(\theta, \phi)}{H_0} \right| = \left| \frac{J_s(\theta, \phi_p)}{H_0 \cos \phi_p} \cos \phi \right| \quad (61)$$

and

$$\left| \frac{J_t(\theta, \phi)}{H_0} \right| = \left| \frac{J_t(\theta, \phi_p)}{H_0 \sin \phi_p} \sin \phi \right| \quad (62)$$

where  $\phi_p$  corresponds to a value of  $\phi$  in the data presented for zones 1 through 8.

1. King, R.W.P. and T.T. Wu, The Scattering and Diffraction of Waves, Harvard University Press, Cambridge, Massachusetts, 1959.

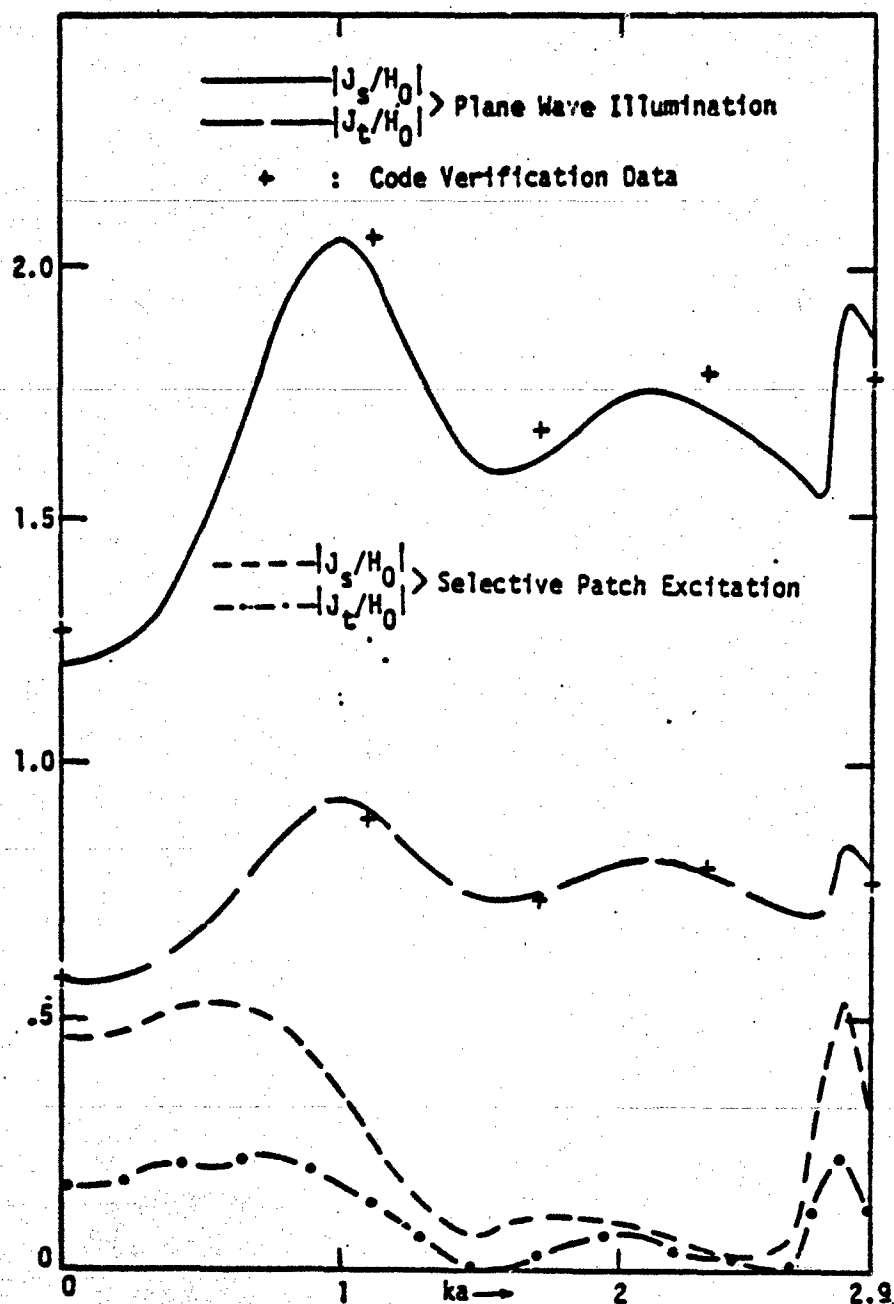


Figure 3. Normalized Current Densities on Patch 1.  
Selective Patch Excitation is Achieved by  
Exciting all Patches but No. 1.

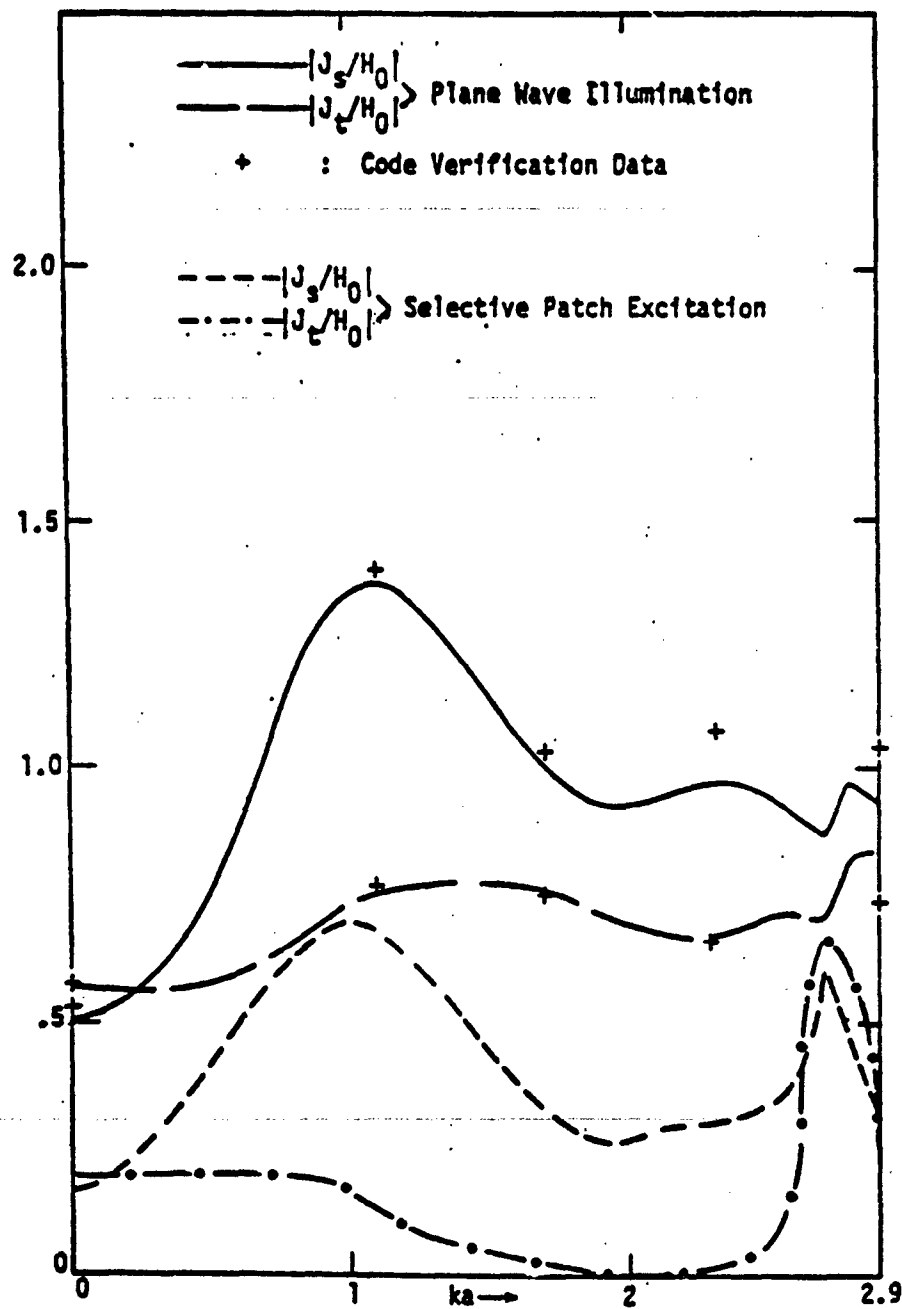


Figure 4. Normalized Current Densities on Patch 2.  
 Selective Patch Excitation is Obtained by  
 Exciting all Patches but No. 2.

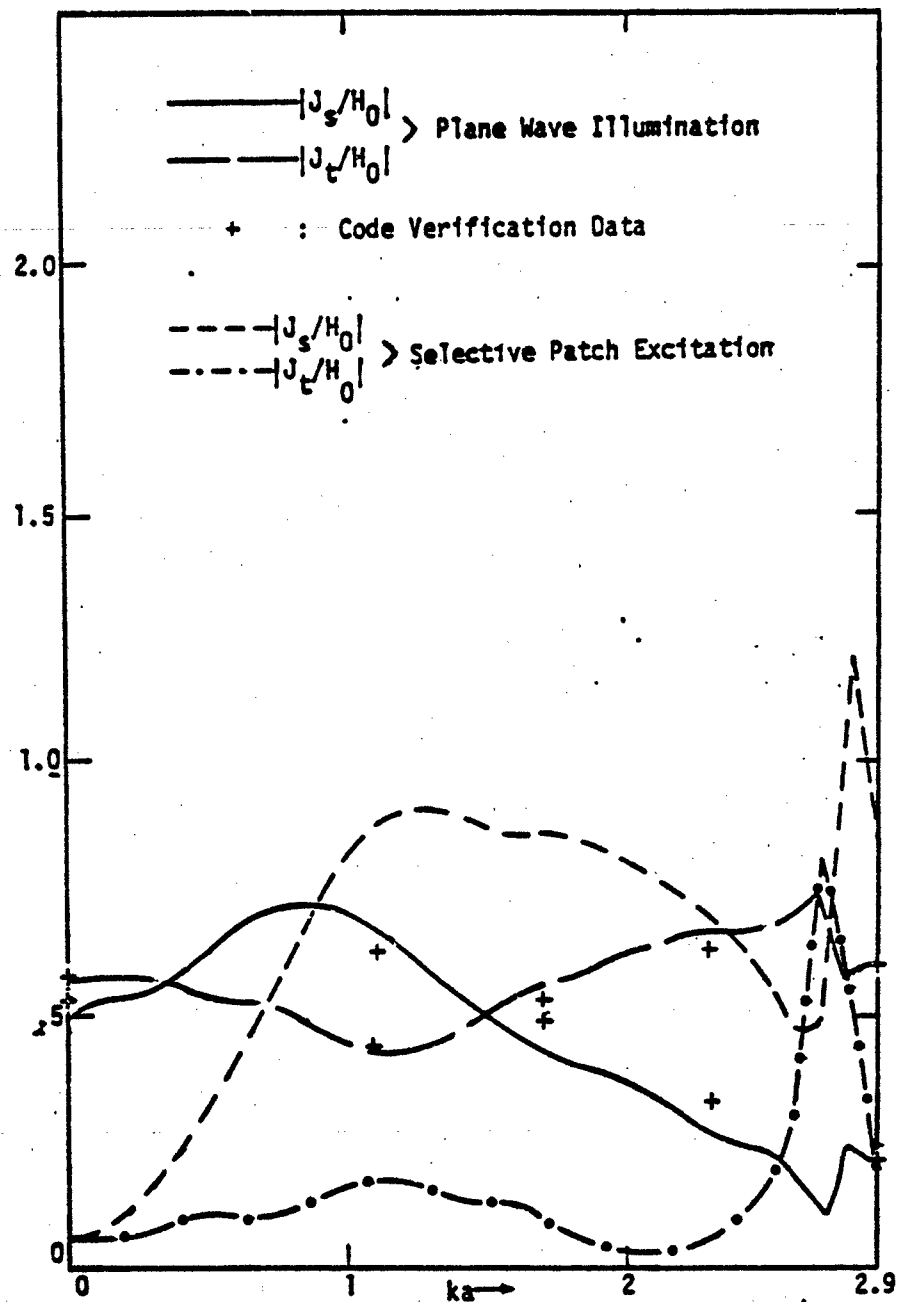


Figure 5. Normalized Current Densities on Patch 3.  
 Selective Patch Excitation is Obtained by  
 Exciting all Patches but  
 Nos. 2, 3, 14, 15, 18, 19, 30, 31.

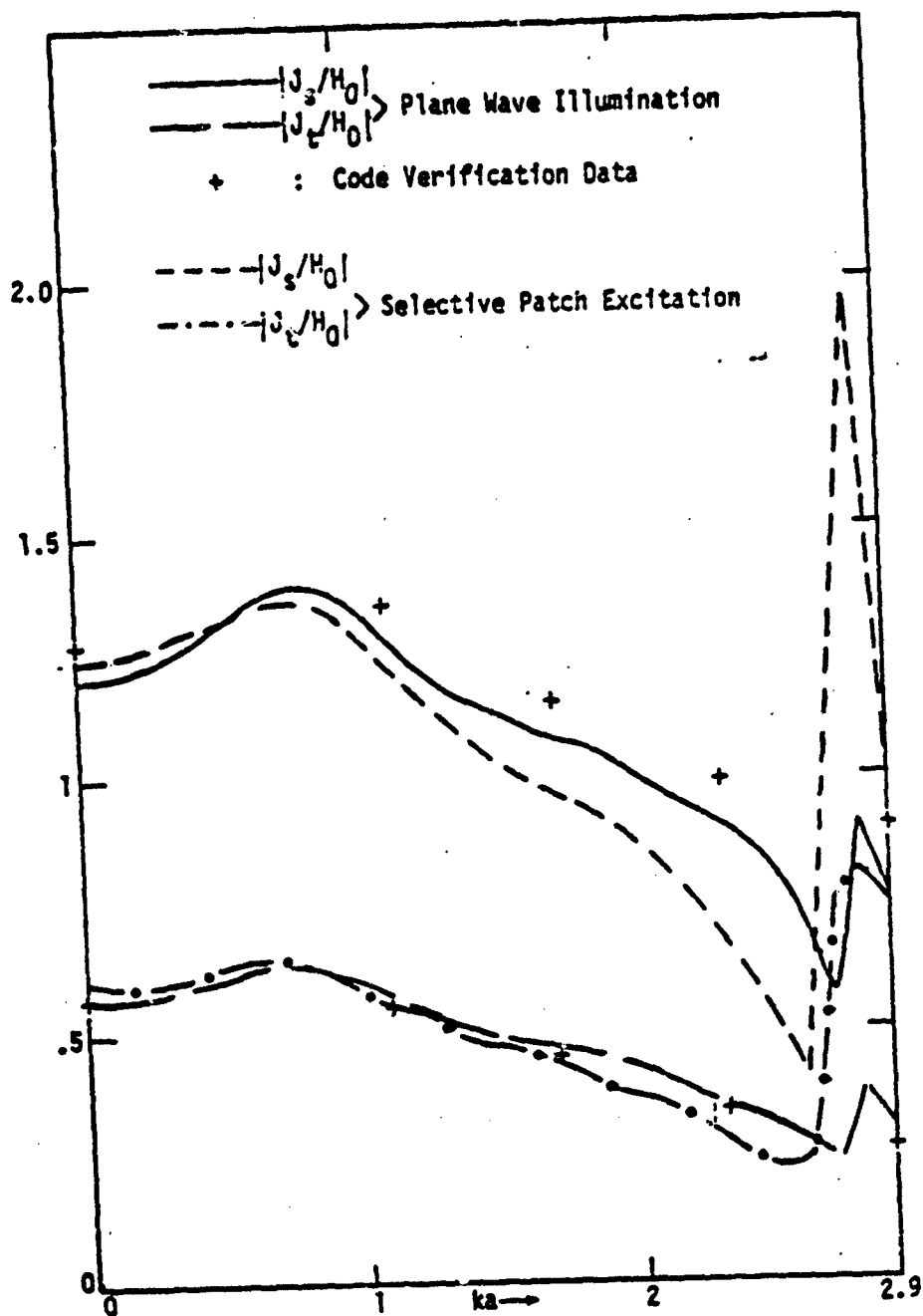


Figure 6. Normalized Current Densities on Patch 4.  
 Selective Patch Excitation is Obtained by  
 Exciting all Patches but  
 Nos. 2, 3, 14, 15, 18, 19, 30, 31.

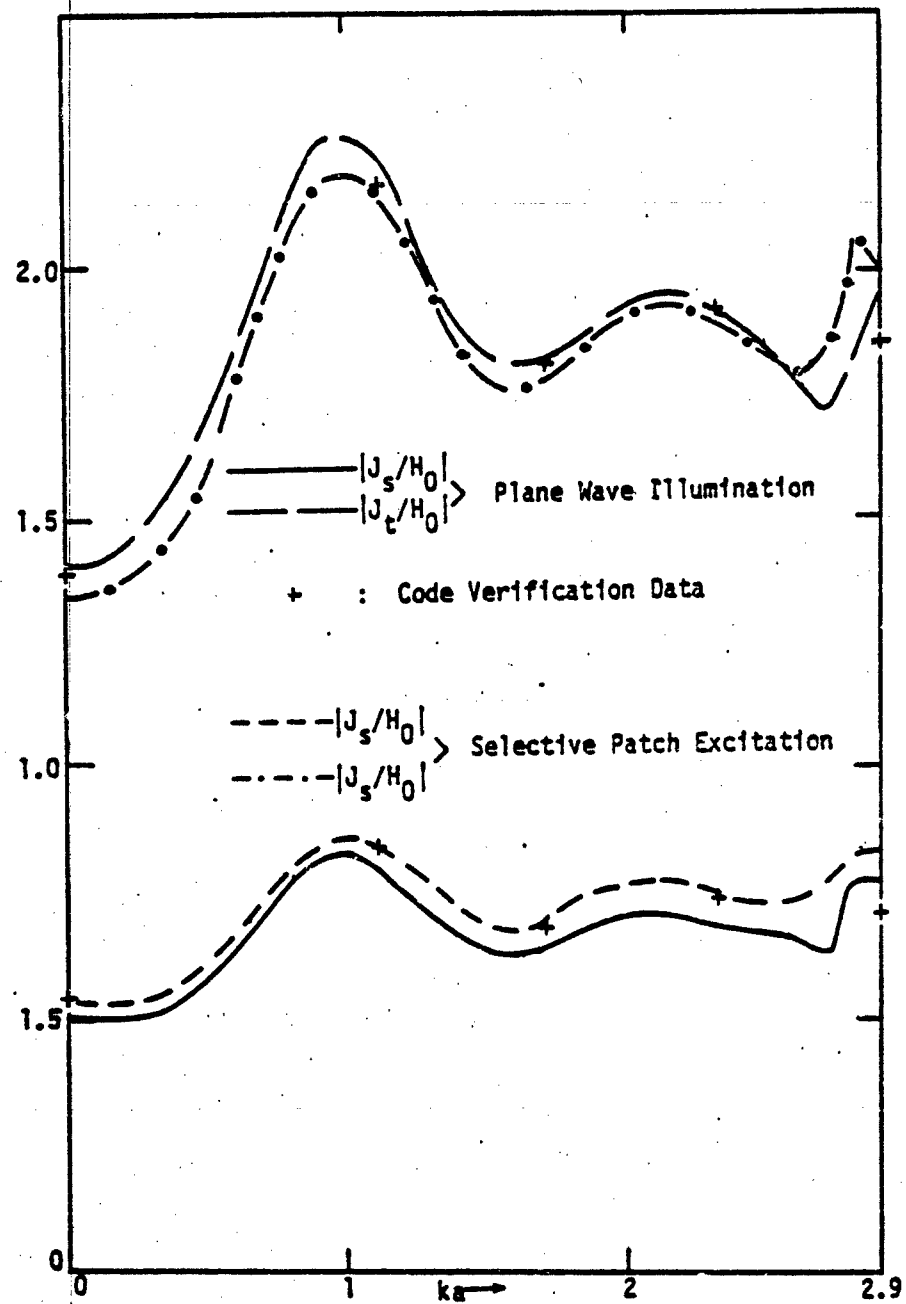


Figure 7. Normalized Current Densities on Patch 5.  
Selective Patch Excitation is Obtained by  
Exciting all Patches but No. 1.

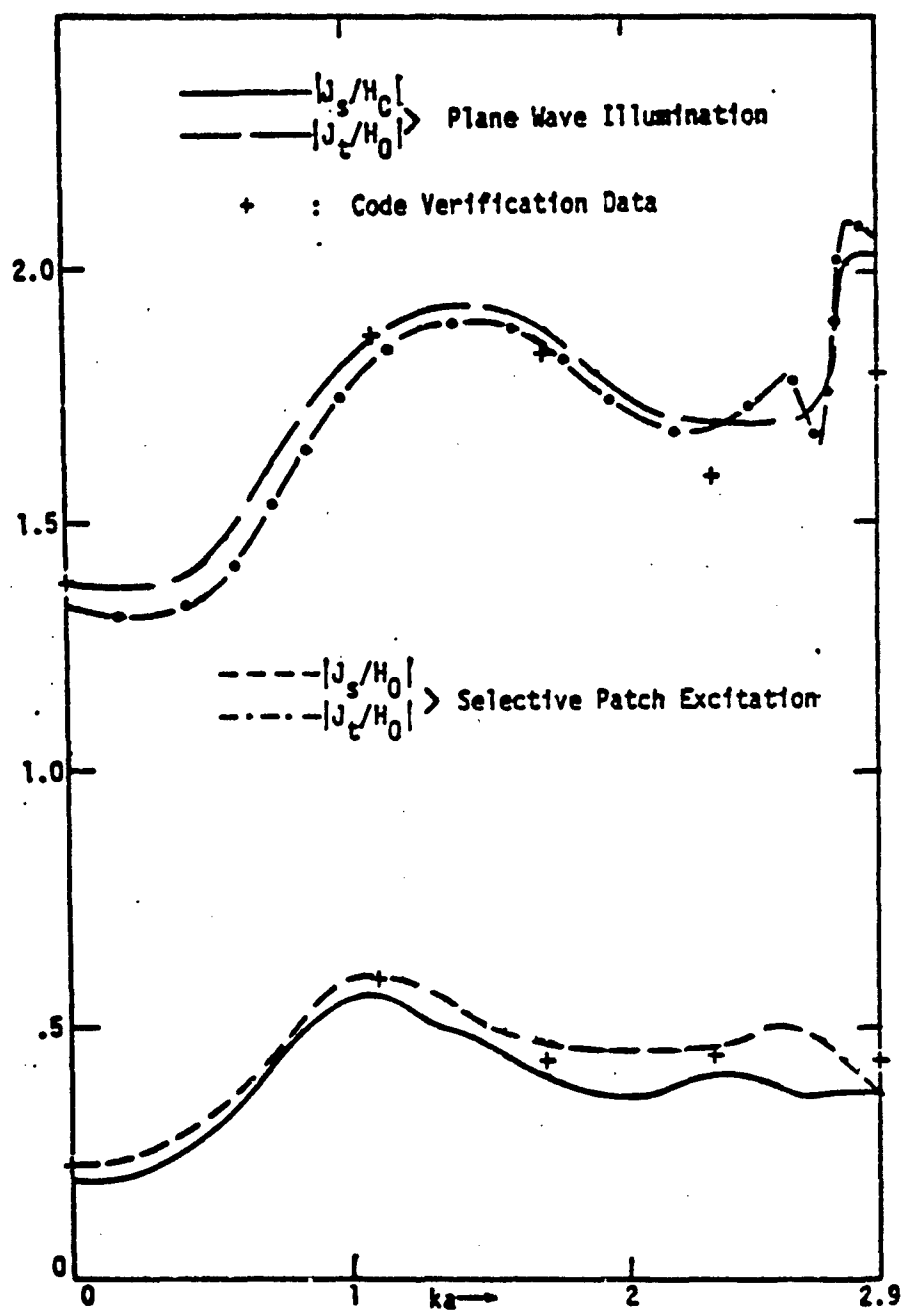


Figure 8. Normalized Current Densities on Patch 6.  
Selective Patch Excitation is Obtained by  
Exciting all Patches but No. 2.



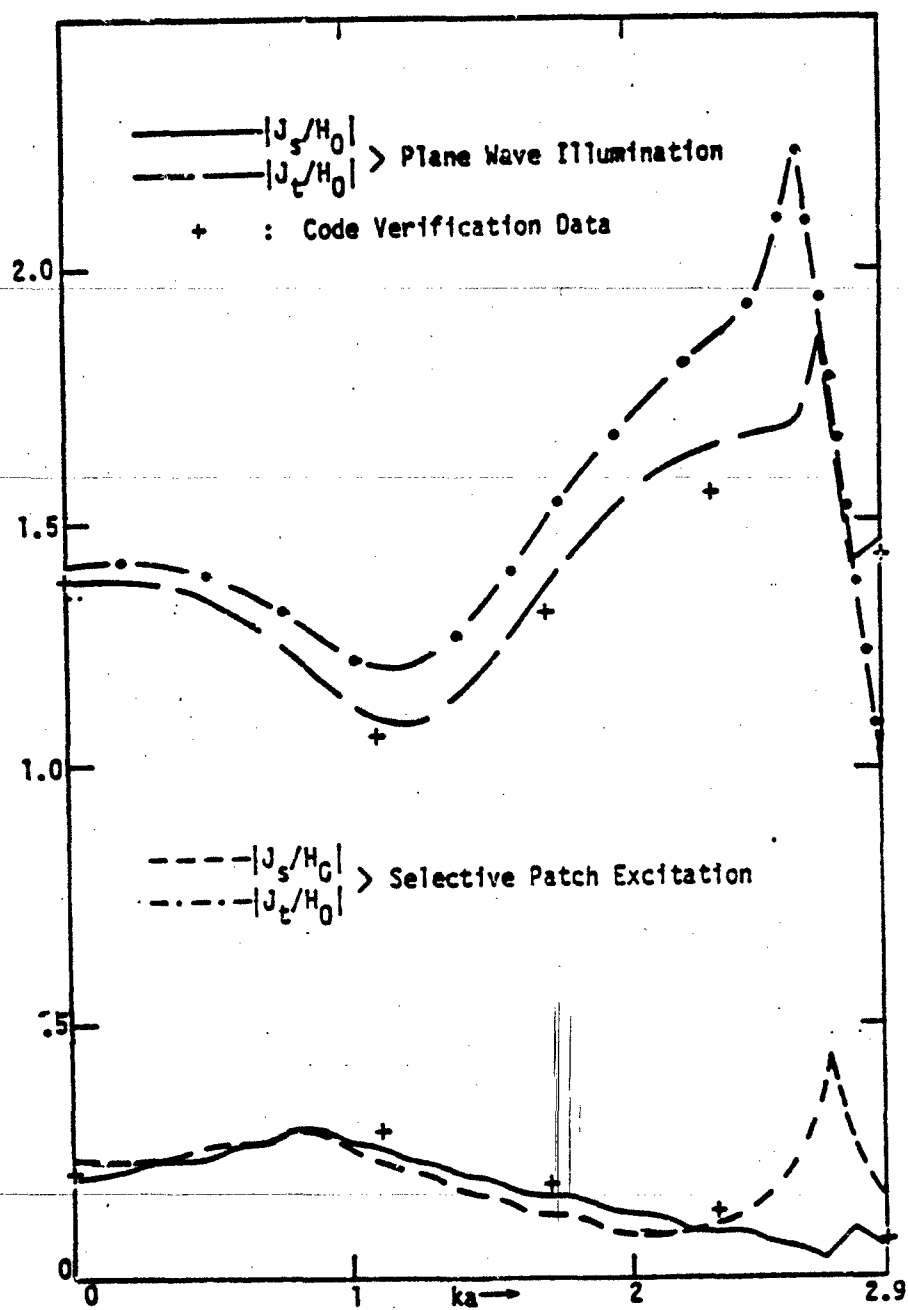


Figure 9. Normalized Current Densities on Patch 7.  
 Selective Patch Excitation is Obtained by  
 Exciting all Patches but  
 Nos. 2, 3, 14, 15, 18, 19, 30, 31.

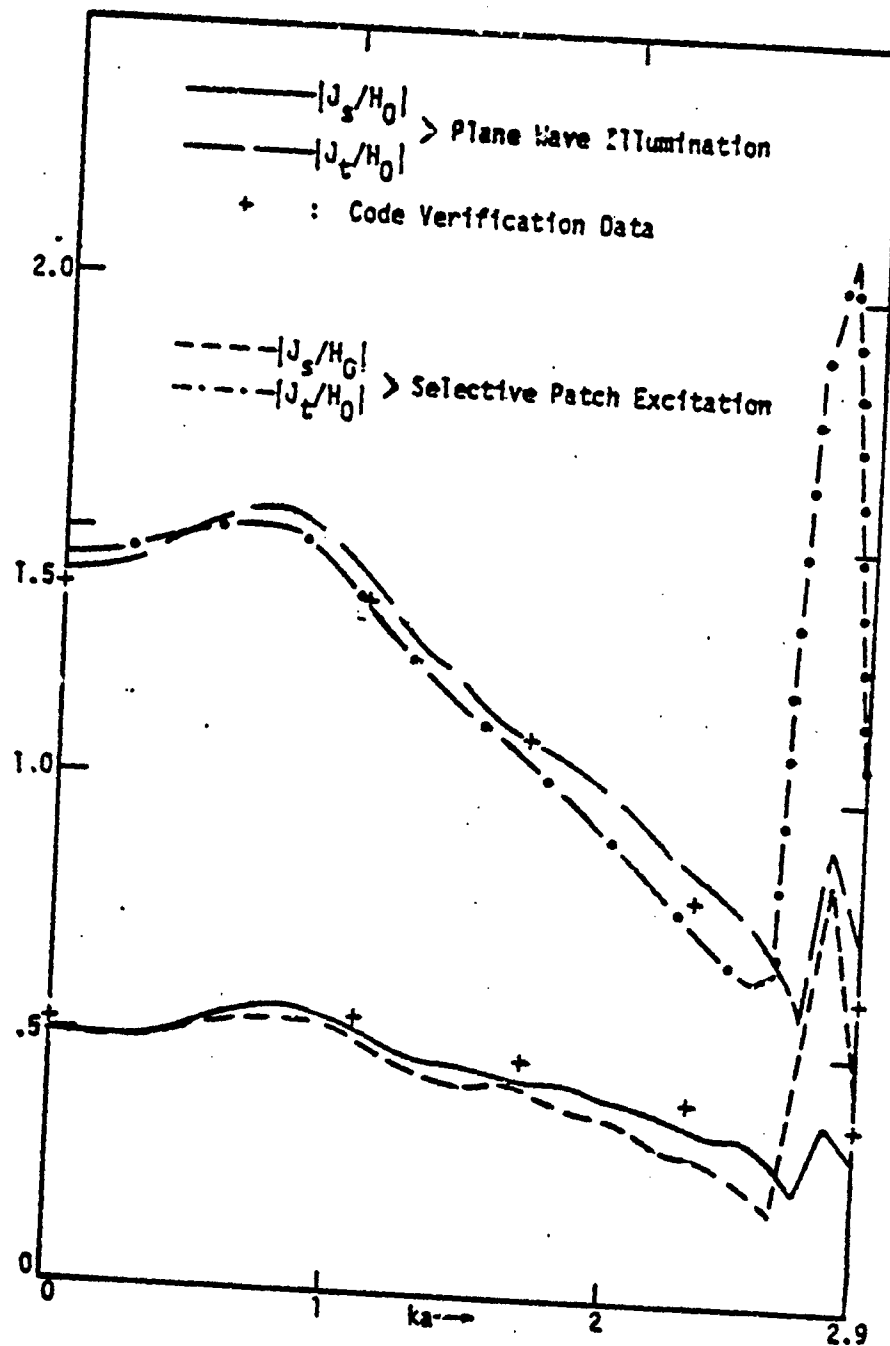


Figure 10. Normalized Current Densities on Patch 8.  
 Selective Patch Excitation is Obtained by  
 Exciting all Patches but  
 Nos. 2, 3, 14, 15, 18, 19, 30, 31.

## SECTION V

## INTERPRETATION OF SPHERE CALCULATIONS

The basis for our choice of the illumination scheme that was used to obtain our data is as follows: i) the objective of each portable simulator was determined only by the incident field ii) it was easy to numerically implement iii) it bore a relation to an identifiable class of real sources iv) it had to succeed as more sources were included. The choice of where to place the sources is related to the source rigidity issue. This is readily seen by interpreting the results presented in figures 3 and 4. In each of these figures, 31 of the 32 patches were illuminated in exactly the same manner that they would be by the incident plane wave. The only patch that wasn't excited is the patch on which we present the data and we see that the induced current density is a very poor approximation to the desired current density which was induced by the incident plane wave. This implies that if the non-illuminated patch corresponds to the shorted POE location, we can obtain good excitation of that POE only by having a source, of the type considered in this report, in close proximity.

This result enhances the importance of source rigidity effects. This is the case because a qualitative examination of the equations that raised the issue of source rigidity indicates that the nonrigidity effect becomes increasingly important as the source location approaches the POE. Determining the quantitative effect of source rigidity appears to be an experimental problem. Figures 7 and 8 show that patches adjacent to the nonexcited patch can be excited in the desired manner for the described 31 out of the 32 patch illumination. This result again, is only meaningful if source rigidity is not found to be a limiting consideration.

The remaining data appearing in figures 5, 6, 9, and 10 correspond to an illumination scheme in which only 24 of the 32 patches are illuminated. The basis for choosing not to illuminate the eight patches is that they correspond to the smallest values of  $\hat{n}xH^{inc}$ . For this more sparse illumination scheme we again see that we obtain good results at a patch that is excited and poor results at a patch that is not excited.

Another conclusion worth noting from all the data presented in figures 3 through 10 is that the plane wave illumination results agree reasonably well with the code verification data for  $ka$  as large as 2.3. In many cases the agreement is still reasonable for  $ka=2.9$ . These results indicate that it is possible to give up a certain measure of accuracy and have fewer zones per wavelength than previously thought. For the data presented, the ratio of the wavelength  $\lambda$  to a zone dimension  $D$  is given by  $\lambda/D=8/ka$  which is 3.5 if we accepted results only up to  $ka=2.3$  and is 2.8 if we accept the results up to  $ka=2.9$ . In either case we see that it is possible to obtain acceptable results with fewer zones than has in general been previously thought. This can impact a scheme for determining a configuration of local sources. The fact that sparse illumination gave good results also provides a rationale for employing fewer sources. Both of these results can assist the choice of a configuration to be employed in an experiment.

At this point, it should be noted that no part of our explicit sphere calculation can be used to infer any experimental information for very early times since our calculation was not appropriate for high frequencies. Another limitation of our calculation should be pointed out. The sphere does not have a sharp resonance and this could contribute to the fact that the patch containing the POE required direct excitation in order for good results to be obtained. For structures having more pronounced resonances, it is possible that near resonance

a given POE can be excited without having the source in as close proximity as indicated by our sphere results. Having elaborated on the limitations of our sphere calculations we would like to emphasize that the general theory presented in this work is valid for all frequencies and consequently all time.

We now address the essential aspects required by our analysis for each local source. In the absence of any other objects and sources, their radiated fields should rapidly decay away from their patch location and at the same time their radiated fields should vary slowly over their own patch location. The simplest source that possesses locality to some extent, is a half-loop placed above the patch. A simple calculation shows that the fields decay rapidly for distances larger than the radius of the loop. Despite its local character which, to a certain degree, satisfies one of our conditions for an allowable source, there are difficulties with the half-loop that we will briefly discuss: i) the field due to a half-loop is slowly varying over a region surrounding the center of the loop but the maximum linear dimension of this region is significantly smaller than the radius of the loop. To remedy this we may either consider a half-loop much larger than the patch or a "solenoid" consisting of many parallel half-loops with its dimensions not significantly larger than the dimensions of the patch. In the case of a large half-loop the incident field will now vary rapidly over other patches, and we have not assessed the effect of this behavior in our calculations. However, the numerical solution is only a convenience for studying selective patch excitation and its inapplicability does not invalidate the potential use of the half-loop as a portable simulator. ii) The "solenoid" is an improvement with regard to the condition of slow variation but it, as well as the large half-loop, may interact with the sphere substantially and this could significantly alter the transfer operator

as explained earlier in connection to non-rigidity of sources. Despite all the described limitations, both the "solenoid" and the half-loop have sufficiently desirable features to be included in an experimental program.

Finally, we discuss the Singularity Expansion Method (SEM) as it relates to alternate simulation. We do this because it offers a hope of determining the global capabilities of a configuration of portable sources. We will now interpret our results as related to SEM. An SEM external interaction solution has the form

$$\underline{J}(\underline{r}, \gamma) = \sum \eta_a(\gamma) \frac{1}{\gamma - \gamma_a} \underline{v}_a(\underline{r})$$

The natural modes  $\underline{v}_a$  and natural frequencies  $\gamma_a c$  are intrinsic properties of the metallic body. The coupling coefficients  $\eta_a$  depend on both the coupling vectors (also an intrinsic property of the body) and the incident field. Thus, once the natural modes, the coupling vectors, and the natural frequencies are known, the responses to various excitations in the SEM prescription are obtained by determining the corresponding coupling coefficients.

Admittedly there is no known recipe for obtaining the coupling coefficients, in general, but at least we know that for the sphere and plane wave illumination the correct coupling coefficients are class 1 given by

$$\eta_{nn'm\sigma}(\gamma) = e^{(\gamma_{nn'} - \gamma)ct_0} \left[ \frac{|\tilde{J}_{nm\sigma}, J_p^{inc}|}{N_{nm\sigma} [d\lambda_n/d\gamma]} \right]_{\gamma=\gamma_{nn'}} \quad (63)$$

where

$$\left| \tilde{\underline{J}}_{nm\sigma}, \underline{J}_p^{inc} \right| = \int_S \tilde{\underline{J}}_{nm\sigma} \cdot \hat{n} \times \underline{J}_p^{inc} dS$$

$$N_{nm\sigma} = \int_S \tilde{\underline{J}}_{nm\sigma} \cdot \hat{n} \times \underline{J}_{nm\sigma} dS$$

$\gamma_{nn}$  are the pole locations ( $\gamma_{nn,c}$  = natural frequencies),  $t_0$  is the instant at which the incident wavefront hits the sphere,  $\underline{J}_p^{inc} = \hat{n} \times \underline{H}_p^{inc}$  and  $p$  stands for polarization,  $\lambda_n$  are the eigenvalues of the Magnetic Field Integral Operator  $L$ , and  $\tilde{\underline{J}}_{nm\sigma}$  are eigenfunctions of  $L$  corresponding to eigenvalue  $1 - \lambda_n$ .

If we were to compare responses to selective patch excitation and plane wave illumination, we could assume that the coupling coefficients for patch excitation are also given by equation 1 and proceed to calculate them. The comparison of the coupling coefficients for the two excitations would allow us then to ascertain how well selective patch excitation simulates plane wave illumination. At this point, however, caution should be exercised. To clarify the point we are trying to emphasize, consider the case whereby we excite all patches on the sphere but one, in the manner that was explained. The MFIE solution shows that the total current induced on the sphere is everywhere approximately equal to the current for plane wave illumination except at the center of the patch that was not excited. However, if we were to use SEM for the comparison of the two types of excitation, the coupling coefficients for the first few modes would be approximately equal and this result might lead one to the false conclusion that the simulation was adequate. Notice, however, that our

patch zoning results provide no information as to any early-time SEM results and/or conclusions.



ELECTROMAGNETIC SURFACE WAVE PROPAGATION  
OVER A RECTANGULAR BONDED WIRE MESH

## ABSTRACT

The electromagnetic surface wave which can propagate over a rectangular wire mesh of infinite extent, is considered. The propagation constant is determined both from a rigorous Floquet formulation and an approximate method using averaged boundary conditions. The agreement is fairly good for sufficiently small mesh dimensions. The rectangular mesh is found to be highly anisotropic, and the possibility of an effective anisotropic transfer inductance representation for the mesh is discussed briefly.

## INTRODUCTION

Wire mesh screens are often employed in electromagnetic shielding applications. Plane wave reflection and transmission coefficients are normally utilized to characterize the shielding effectiveness and, of course, a good shield should have a low transmission coefficient for a wide range of incidence angles for any wave polarization. The method of averaged boundary conditions [1] has been used to analyze the reflecting and transmitting properties of both square [2] and rectangular [3] meshes. The method gives good results for both bonded and unbonded junctions, but is restricted to mesh dimensions which are small compared to a wavelength. General solutions have been given for plane wave scattering from separated wire grids in free space [4] and for unbonded wire grids over a half-space [5] and for bonded wire grids in free space [6]. These solutions generally involve matrix inversion to solve for the wire currents, but fortunately, large matrices are not required.

A major difference between a wire mesh and a continuous metal sheet is the ability of the wire mesh to support a trapped surface wave. When the source and observer are located near the mesh, this surface wave is quite important. For the case of a square bonded mesh, surface wave propagation has been analyzed [7], and the propagation constant of the surface wave is closely related to the shielding effectiveness of the mesh. Here we extend the previous analysis to the more general case of a rectangular bonded mesh. For comparison, the approximate method of averaged boundary conditions is also applied to the rectangular mesh geometry.

## FORMULATION

The geometry of the infinite rectangular bonded mesh in free space (permittivity  $\epsilon_0$  and permeability  $\mu_0$ ) is illustrated in Fig. 1. Arrays of wires parallel to the  $x$  axis with spacing  $b$  and parallel to the  $y$  axis with spacing  $a$  are centered in the plane  $z = 0$ , and perfect contacts are made at the junctions. The wire radius  $c$  is small compared to both the spacings  $a$  and  $b$  and the free space wavelength  $\lambda$ . Consequently, only the axial wire currents are important and the usual thin wire approximations are valid.

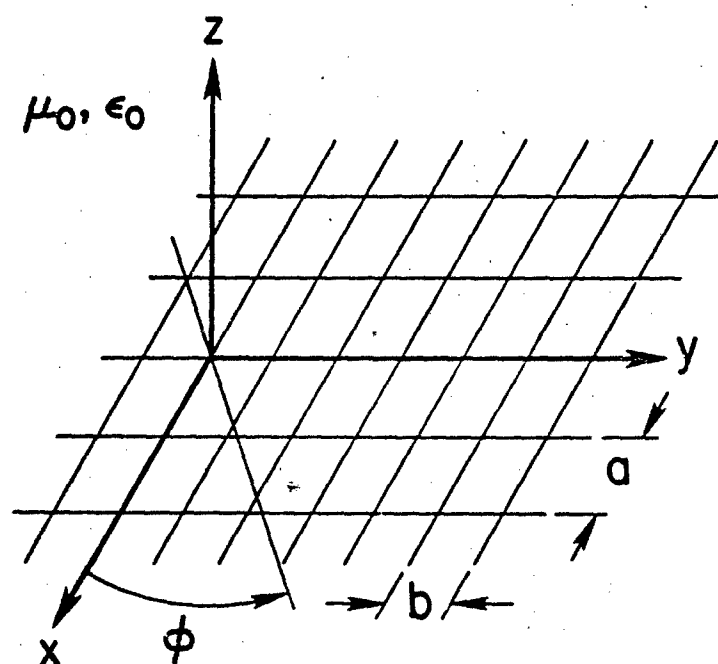


Figure 1. Geometry for a surface wave propagating on a rectangular grid of bonded junctions. Wire radius equals  $c$ .

tions are valid.

Since the mesh structure has a plane of symmetry at  $z = 0$ , the electromagnetic field can be decomposed into symmetric and antisymmetric parts which are uncoupled [8]. The electromagnetic surface wave of interest here is symmetric, and the rectangular components of the electric field satisfy the following [7]:

$$\begin{aligned} E_x(x, y, z) &= E_x(x, y, -z) \\ \text{and} \quad E_y(x, y, z) &= -E_y(x, y, -z). \end{aligned} \quad (1)$$

The analysis closely follows that for the square mesh [7]. Again, we invoke Floquet's theorem [9] in order to express the relevant electromagnetic quantity as an exponential function multiplied by a function which is periodic in  $x$  and  $y$ . Thus, for a surface wave propagating at an angle  $\phi$  to the negative  $x$  axis, the current on the  $q$ th  $x$ -directed wire  $I_{xq}$  and the current on the  $m$ th  $y$ -directed wire  $I_{ym}$  can be written:

$$I_{xq} = \exp[\gamma(x \cos \phi + q b \sin \phi)] \sum_m A_m \exp(i 2 \pi m x / a) \quad (2)$$

and

$$I_{ym} = \exp[\gamma(y \cos \phi + m a \sin \phi)] \sum_q B_q \exp(i 2 \pi q y / b). \quad (3)$$

Here  $A_m$  and  $B_q$  are the unknown Fourier coefficients and  $\gamma$  is the propagation constant which we seek. The  $m$  and  $q$  summations are over all integers including zero from  $-\infty$  to  $\infty$ . The calculation of the fields produced by these currents is straight-forward [5] and will not be repeated here. The thin wire boundary condition for perfectly conducting wires is the following:  $E_x(x, 0, c) = E_y(0, y, c) = 0$ . This

condition need only be applied at the  $m = 0$  and  $q = 0$  wires; the periodic Floquet form of (2) and (3) assures they will be subsequently satisfied at all wires.

Actually, the expressions for the current in (2) and (3) are identical to those in the plane wave scattering case [5] except that  $\gamma$  has replaced  $ikS$  where  $k$  was the free space wave number ( $=2\pi/\lambda$ ) and  $S$  ( $=\sin\theta$ ) was the sine of the incidence angle. Thus the previous equations for  $A_m$  and  $B_q$  [5] can be used with the following modifications: 1) set the incident fields equal to zero (source-free problem), 2) set the grid separation  $h$  equal to zero (bonded grids in the same plane), 3) set the wire impedances equal to zero (perfectly conducting wires), and 4) set the half space parameters equal to those of free space. As a result, equations (24) and (26) in [5] reduce to the following:

$$A_m \frac{(k^2 - k_x^2) P_m}{2ikb} + \frac{ik_x}{2ka} \sum_q B_q k_y \frac{\exp(-\Gamma c)}{\Gamma} = 0, \quad (4)$$

$$B_q \frac{(k^2 - k_y^2) Q_q}{2ika} + \frac{iky}{2kb} \sum_m A_m k_x \frac{\exp(-\Gamma c)}{\Gamma} = 0, \quad (5)$$

where

$$P_m = \frac{b}{\pi} \left\{ -\ln \left[ 1 - \exp \left( \frac{-2\pi c}{b} \right) \right] + \Delta_m \right\} + \frac{\exp(-\Gamma_{mo} c)}{\Gamma_{mo}}, \quad (6)$$

$$\Delta_m = \frac{1}{2} \sum_q' \left[ \frac{2\pi}{b} \frac{\exp(-\Gamma c)}{\Gamma} - \frac{\exp(-2\pi |q| c/b)}{|q|} \right], \quad (7)$$

$$Q_q = \frac{a}{\pi} \left\{ -\ln \left[ 1 - \exp \left( \frac{-2\pi c}{a} \right) \right] + \delta_q \right\} + \frac{\exp(-\Gamma_{oq} c)}{\Gamma_{oq}}, \quad (8)$$

$$\delta_q = \frac{1}{2} \sum_m' \left[ \frac{2\pi}{a} \frac{\exp(-\Gamma c)}{\Gamma} - \frac{\exp(-2\pi |m| c/a)}{|m|} \right], \quad (9)$$

$$\Gamma_{mq}(-\Gamma) = (k_x^2 + k_y^2 - k^2)^{1/2} \quad (10)$$

$$k_x = (2\pi m/a) + kS \cos\phi, \quad (11)$$

and

$$k_y = (2\pi q/b) + kS \sin\phi. \quad (12)$$

A superscripted prime ' over the summation sign indicates omission of the  $q = 0$  (or  $m = 0$ ) term.  $S$  is now defined as  $\gamma/(ik)$ .

The doubly infinite set of linear equations (4) and (5) for  $A_m$  and  $B_q$  is numerically inefficient in the present form because  $A_m$  and  $B_q$  decay slowly for large  $|m|$  and  $|q|$ . The difficulty arises because the cu. expansions in (2) and (3) are slowly convergent for the discontinuous current that occurs at the wire junctions in the bonded meshes. However, we can circumvent this convergence problem by modifying the current expansions to allow for a jump discontinuity at the origin. This procedure was adopted previously for square bonded meshes [6], [7]. As we indicate below, the method requires only slight modifications for rectangular bonded meshes.

We now rewrite the current expressions in (2) and (3) in the following equivalent forms:

$$I_{xq} = \exp[\gamma(x \cos\phi + qb \sin\phi)] \quad (13)$$

$$\cdot [f_{\Delta a}(x) + \sum_m A'_m \exp(i2\pi mx/a)]$$

$$I_{ym} = \exp[\gamma(ma \cos \phi + y \sin \phi)] \quad (14)$$

$$\cdot [-f_{\Delta b}(y) + \sum_q B'_q \exp(i2\pi qy/b)]$$

where  $A'_m$  and  $B'_q$  are the modified coefficients. The sawtooth function  $f_{\Delta a}$  is chosen to have a jump  $\Delta$  at the origin and with a width  $a$ ; it is defined by

$$f_{\Delta a}(x) = \frac{\Delta}{2\pi i} \sum'_n \frac{\exp(i2\pi nx/a)}{n} \quad (15)$$

$$= \Delta \left[ U(x) - \frac{x}{a} - \frac{1}{2} \right]; \quad -\frac{a}{2} < x < \frac{a}{2},$$

where

$$U(x) = \begin{cases} 1; & x > 0 \\ 0; & x < 0 \end{cases}$$

As before, the superscripted prime over the summation sign indicates omission of the  $n = 0$  term. The function  $f_{\Delta b}(y)$  is defined in an exactly analogous manner.

From (2), (3), and (13) - (15), it is clear that  $A_m$ ,  $A'_m$ ,  $B_q$  and  $B'_q$  are related by

$$A_m = A'_m + \frac{\Delta(1-\delta_{m0})}{2\pi i m} \quad (16)$$

and

$$B_q = B'_q - \frac{\Delta(1-\delta_{q0})}{2\pi i q} \quad (17)$$

where

$$\delta_{m0} = \begin{cases} 1; & m = 0 \\ 0; & m \neq 0 \end{cases}$$

Then, by substituting (16) and (17) into (4) and (5), we obtain the following equivalent set of equations for the modified coefficients:

$$A'_m \frac{(k^2 - k_x^2) P_m}{21kb} + \frac{1k_x}{2ka} \sum_q B'_q k_y \frac{\exp(-\Gamma c)}{\Gamma} + \Delta \left\{ \frac{(k^2 - k_x^2) P_m}{2kb} \frac{(\delta_{m0} - 1)}{2\pi m} - \frac{k_x}{2ka} \left[ \frac{P'_m}{b} + \frac{kS \sin \phi}{2\pi} P_{1m} \right] \right\} = 0 \quad (18)$$

and

$$B'_q \frac{(k^2 - k_y^2) Q_q}{21ka} + \frac{1k_y}{2kb} \sum_m A'_m k_x \frac{\exp(-\Gamma c)}{\Gamma} + \Delta \left\{ \frac{k^2 - k_y^2}{2ka} \frac{(1 - \delta_{q0})}{2\pi q} + \frac{k_y}{2kb} \left[ \frac{Q'_q}{a} + \frac{kS \cos \phi}{2\pi} Q_{1q} \right] \right\} = 0 \quad (19)$$

where

$$P_{1m} = \sum_q' \frac{\exp(-\Gamma c)}{q\Gamma} \quad (20)$$

$$P'_m = P_m - \frac{\exp(-\Gamma_{m0} c)}{\Gamma_{m0}} \quad (21)$$

$$Q_{1q} = \sum_m' \frac{\exp(-\Gamma c)}{m\Gamma} \quad (22)$$

and

$$Q'_q = Q_q - \frac{\exp(-\Gamma_{oq} c)}{\Gamma_{oq}} \quad (23)$$

Again, the superscript prime ' on the summation indicates omission of the  $q = 0$  (or  $m = 0$ ) term. Now, all summations are in a rapidly convergent form.

Since we have introduced an unknown  $\Delta$  in the modified current expansions in (13) and (14), another equation is required to have an equal number of equations and unknowns ( $A'_m$ ,  $B'_q$ , and  $\Delta$ ). The most convenient equation is obtained from charge continuity [6]:



$$\frac{1}{2} \left[ \left. \frac{\partial I_{xo}}{\partial x} \right|_{x=0^-} + \left. \frac{\partial I_{xo}}{\partial x} \right|_{x=0^+} \right] = \frac{1}{2} \left[ \left. \frac{\partial I_{yo}}{\partial y} \right|_{y=0^-} + \left. \frac{\partial I_{yo}}{\partial y} \right|_{y=0^+} \right] \quad (24)$$

By substituting (13) and (14) into (24), we obtain the following auxiliary condition:

$$\begin{aligned} & - \frac{\Delta}{2\pi} \left( 1 + \frac{b}{a} \right) + \sum_m A'_m \left( im \frac{b}{a} + \frac{\gamma b}{2\pi} \cos \phi \right) \\ & - \sum_q B'_q \left( iq + \frac{\gamma b}{2\pi} \sin \phi \right) = 0 \end{aligned} \quad (25)$$

Since the current expansions in (13) and (14) are rapidly convergent, the doubly infinite set of equations, (18) and (19), can be truncated with the  $m$  ranging from  $-M$  to  $M$  and  $q$  ranging from  $-Q$  to  $Q$  where  $M$  and  $Q$  are small integers. Thus (18), (19), and (25) yield a set of  $T(=2N+2Q+3)$  linear, homogeneous equations in  $A'_m$ ,  $B'_q$ , and  $\Delta$ :

$$\begin{bmatrix} T \times T \\ \text{coefficient} \\ \text{matrix} \end{bmatrix} \begin{bmatrix} A'_{-M} \\ \vdots \\ A'_0 \\ \vdots \\ A'_M \\ B'_{-Q} \\ \vdots \\ B'_0 \\ \vdots \\ B'_Q \\ \Delta \end{bmatrix} = \begin{bmatrix} 0 \\ \vdots \\ 0 \end{bmatrix} \quad (26)$$

A nontrivial solution to (26) exists only if the determinant, which is a function of  $\gamma(-ikS)$ , vanishes. Thus, the mode equation to be solved for  $\gamma$  is written

$$\begin{vmatrix} T \times T \\ \text{coefficient} \\ \text{matrix} \end{vmatrix} = 0 \quad (27)$$

The  $z$  dependence of the Floquet harmonics is given by the factor  $\exp(-\Gamma_{mq}|z|)$ . For sufficiently small  $ka$  and  $kb$ , there are no grating lobes ( $\Gamma_{mq}$  real) and thus there is no loss mechanism. Consequently,  $\gamma$  is purely imaginary and  $|\gamma| > k$  (or  $S > 1$ ). Equivalently, the equations (18), (19), and (20) can be normalized so that all coefficients are real functions of the real variable  $S$ . This real form has been programmed and (27) has been solved numerically for  $S$  by the bisection method [10].

#### AVERAGED BOUNDARY CONDITIONS

Plane wave scattering from rectangular meshes has been analyzed by Astrakhan [3] by the method of averaged boundary conditions. For a bonded rectangular mesh, Astrakhan derives the following expression for the vertically polarized reflection coefficient,  $R_v^e$ :

$$R_v^e = C\{1 - kC[\gamma_2 \cos^2 \phi + (\delta_2 - \delta_1) \sin \phi \cos \phi - \gamma_1 \sin^2 \phi]\}/I_0 \quad (28)$$

where

$$I_0 = C(1+k^2\delta_1\delta_2-k^2\gamma_1\gamma_2) + kS^2[\gamma_2\cos^2\phi + (\delta_2-\delta_1)\sin\phi\cos\phi - \gamma_1\sin^2\phi] + k(\gamma_1-\gamma_2) \quad (29)$$

$$\gamma_1 = \alpha_1(1 - \frac{a/b}{1+a/b} S^2 \cos^2\phi)$$

$$\gamma_2 = -\alpha_2(1 - \frac{b/a}{1+b/a} S^2 \sin^2\phi)$$

$$\delta_1 = \alpha_1 \frac{a/b}{1+a/b} S^2 \sin\phi\cos\phi$$

$$\delta_2 = -\alpha_2 \frac{b/a}{1+b/a} S^2 \sin\phi\cos\phi$$

$$\alpha_1 = \frac{ib}{\pi} \ln\left(\frac{b}{2\pi c}\right)$$

$$\alpha_2 = \frac{ia}{\pi} \ln\left(\frac{a}{2\pi c}\right)$$

and

$$C = (1-S^2)^{\frac{1}{2}}$$

[Astrakhan's paper contains a misprint, and  $\gamma_2 \sin^2\phi$  should be  $\gamma_1 \sin^2\phi$  in his (14)]. The propagation constant ( $\gamma=ikS$ ) of the surface wave is obtained from the pole of  $R_{11}^e$  in the  $S$  plane. Thus the mode equation for  $S$  is

$$(R_{11}^e)^{-1} = 0 \text{ or } I_0 = 0. \quad (30)$$

Since the averaged boundary condition formulation is valid for only electrically small meshes and does not include the possibility of grating lobes, there is no possible loss mechanism for any values of

the parameters. Thus the solution of (30) for  $S(-\gamma/ik)$  is always real and greater than one. For the general case, no analytical solution for (30) was found, so it was solved numerically by the bisection method [10].

For the special case of propagation along one of the grids ( $\phi = 0^\circ$  or  $90^\circ$ ), the expression for  $R_{\parallel}^e$  in (28) simplifies considerably. For  $\phi = 0^\circ$ , we have

$$R_{\parallel}^e|_{\phi=0^\circ} = \left[ 1 + \frac{k\alpha_1}{C} (1-R_1 S^2) \right]^{-1} \quad (31)$$

where

$$R_1 = \frac{(a/b)}{1 + (a/b)}$$

Thus the mode equation for  $\phi = 0^\circ$  is

$$0 = \left( R_{\parallel}^e \right)^{-1} = 1 + \frac{k\alpha_1}{C} (1-R_1 S^2) \quad (32)$$

By using the quadratic formula, we find

$$S|_{\phi=0^\circ} = \left\{ \frac{2R_1 k^2 \alpha_1^2 - 1 + [1 + 4k^2 \alpha_1^2 (R_1^2 - R_1)]^{1/2}}{2R_1^2 k^2 \alpha_1^2} \right\}^{1/2} \quad (33)$$

For the special case of small  $|k\alpha_1|$ , (33) reduces to

$$S|_{\phi=0^\circ} \approx 1 - \frac{1}{2} k^2 \alpha_1^2 (R_1 - 1)^2 \quad (34)$$

For  $\phi = 90^\circ$ , the results are quite similar.

$$R_{\parallel}^e|_{\phi=90^\circ} = \left[ 1 + \frac{k\alpha_2}{C} (1-R_2 S^2) \right]^{1/2} \quad (35)$$

where

$$R_2 = \frac{b/a}{1 + b/a}$$

$$S|_{\phi=90^\circ} = \left\{ \frac{2R_2 k^2 \alpha_2^2 - 1 + [1 + 4k^2 \alpha_2^2 (R_2^2 - R_2)]^{1/2}}{2R_2^2 k^2 \alpha_2^2} \right\}^{1/2} \quad (36)$$

$$S|_{\phi=90^\circ} = 1 - \frac{1}{2} k^2 \alpha_2^2 (R_2 - 1)^2 \quad (37)$$

For the special case of a square bonded mesh ( $a=b$ ), the results become independent of  $\phi$  and the mesh can be characterized by an isotropic surface transfer impedance which is inductive [7]. The situation is much more complicated for the rectangular mesh as can be seen from the complicated  $\phi$  dependence for  $R_{11}^e$  in (28). However, by noting the simple expressions for  $R_{11}^e$  for  $\phi = 0^\circ$  and  $90^\circ$  in (31) and (34), we can postulate an approximate surface transfer impedance representation for the rectangular mesh which is anisotropic. The anisotropic thin sheet boundary condition has the form [11], [12]:

$$H_{1y} - H_{2y} = -M_x E_x \quad (38)$$

and

$$H_{1x} - H_{2x} = M_y E_y \quad (39)$$

where the subscript 1 denotes the region above the mesh and the subscript 2 denotes the region below. In a similar manner to the square mesh case 7, we can infer  $M_x$  from  $R_{11}^e|_{\phi=0^\circ}$  in (31) and  $M_y$  from  $R_{11}^e|_{\phi=90^\circ}$  in (35) with the following result

$$M_x = \frac{2/\eta}{k\alpha_1(1-R_1 S^2)} \quad (40)$$

and

$$M_y = \frac{2/\eta}{k\alpha_2(1-R_2S^2)} \quad (41)$$

where  $\eta = (\mu_o/\epsilon_o)^{1/2}$ . For angles near grazing, including the surface wave case ( $S=1$ ),  $M_x$  and  $M_y$  can be approximated by

$$M_x = \frac{2/\eta}{k\alpha_1(1-R_1)} \quad (42)$$

and

$$M_y = \frac{2/\eta}{k\alpha_2(1-R_2)} \quad (43)$$

We can also define an effective transfer inductance from

$$M_{\frac{x}{y}} = (i\omega l_{\frac{x}{y}})^{-1} \quad (44)$$

Thus,  $l_x$  and  $l_y$  are given by

$$l_x = \frac{(1-R_1)\mu_o b}{2\pi} \ln\left(\frac{b}{2\pi c}\right) \quad (45)$$

and

$$l_y = \frac{(1-R_2)\mu_o a}{2\pi} \ln\left(\frac{a}{2\pi c}\right) \quad (46)$$

For normal incidence ( $S=0$ ), the surface transfer inductances inferred from (40) and (41) are

$$l_x = \frac{\mu_o b}{2\pi} \ln\left(\frac{b}{2\pi c}\right) \quad (47)$$

and

$$l_y = \frac{\mu_o a}{2\pi} \ln\left(\frac{a}{2\pi c}\right) \quad (48)$$

In this limiting case of normal incidence ( $S=0$ ),  $l_x$  is independent of  $a$  and  $l_y$  is independent of  $b$  because the two grids are uncoupled. Also, we see that (47) and (49) are consistent with the analysis of a single grid for normal incidence [13]. In the grazing case, the factor

$(1-R_1)$  in (45) or  $(1-R_2)$  in (46) represents the coupling between the grids.

### NUMERICAL RESULTS

The mode equation (27) was solved numerically by the bisection method [10], and the convergence was examined by increasing  $M$  and  $Q$  until the value of  $S(=\gamma/ik)$  did not change significantly. Even for the rectangular mesh ( $a \neq b$ ), no advantage was found in making  $M \neq Q$ . Also, for  $M = Q$ , it was found that  $S$  remained essentially constant beyond  $M = Q = 2$  ( $T=11$ ) which is consistent with previous results [6], [7]. All results shown here are for  $M = Q = 2$ , and the required determinant calculation is fairly rapid for the resultant  $11 \times 11$  matrix. For comparison, the approximate results from the method of averaged boundary conditions have been calculated from (30). These results were checked further with the analytical solution in (33) for  $\phi = 0^\circ$  and in (36) for  $\phi = 90^\circ$ .

In Figs. 2-4, we illustrate the  $\phi$  dependence of  $S$  for different values of  $a/b$ . Because of symmetry, only the range of  $\phi$  from  $0^\circ$  to  $90^\circ$  need be shown. As indicated in Fig. 2, the value of  $S$  for the square mesh (i.e.  $a = b$ ), is nearly independent of  $\phi$  for the  $b/\lambda$  values considered. However, when  $a/b$  is increased, as seen clearly in Figs. 2 and 3, the  $\phi$  dependence of  $S$  becomes significant.

As discussed previously [7], the departure of  $S$  from unity is a measure of the degradation of the shielding effectiveness of the mesh for grazing propagation. Also, as expected, the method of averaged boundary conditions tends to underestimate  $S$ , particularly as  $b/\lambda$  is increased [7].

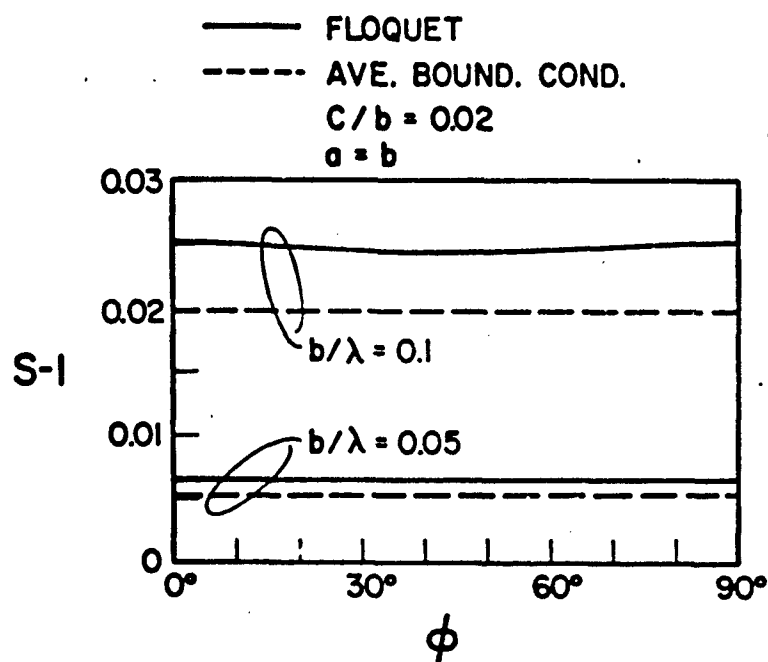


Figure 2. Normalized propagation constant  $S(=\gamma/ik)$  for a square mesh as a function of direction.



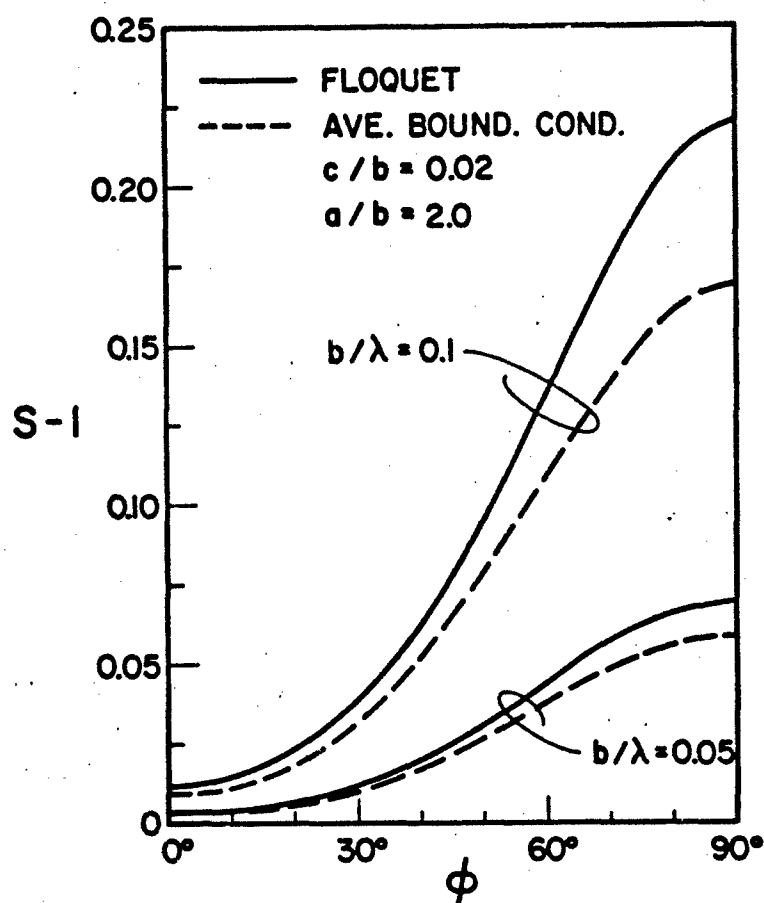


Figure 3. Normalized propagation constant  $S(=\gamma/ik)$  for a 2 to 1 mesh as a function of direction.

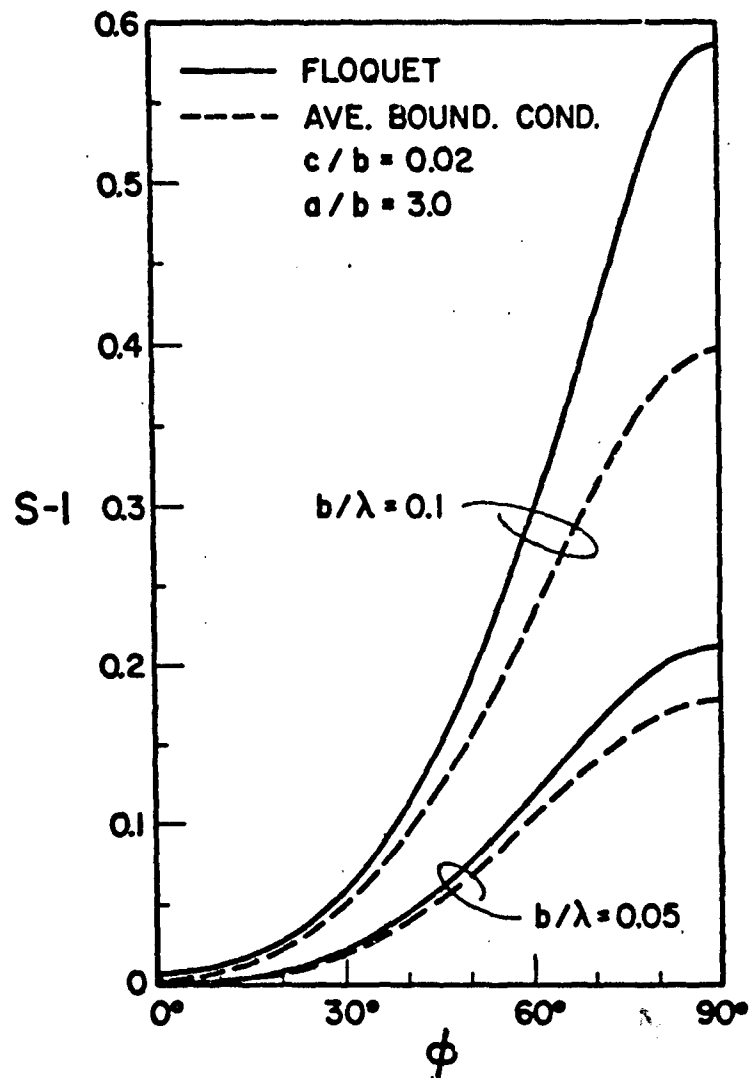


Figure 4. Normalized propagation constant  $S(=\gamma/ik)$  for a 3 to 1 mesh as a function of direction.

In some applications, such as in parallel plate waveguide simulators [14], propagation at  $\phi = 0^\circ$  is of particular interest. In Fig. 5, the frequency dependence for a square mesh and a 3 to 1 mesh is shown. The 3 to 1 ratio has been used in some EMP simulators (private communication, C.E. Baum). Note that  $S$  is smaller for the 3 to 1 mesh than for the square mesh in all cases. In the limit  $a/b = \infty$  (no crossed wires) TEM propagation is possible and  $S$  goes to one. Analytically, the limit of large  $a/b$  is difficult to obtain because for sufficiently large  $a/\lambda$  (or  $b/\lambda$ ),  $\Gamma_{mq}$  in (10) is no longer real and grating lobes can result. The mode equation (27) for  $S$  is still valid, but  $S$  is expected to be complex under such conditions. Then, the mesh would act as a radiator rather than a simple slow-wave structure (i.e.  $S$  is real and greater than one). We have not investigated the grating lobe case because the mesh is not an effective shield under such conditions. Furthermore, the method of averaged boundary conditions does not include the possibility of grating lobes.

#### CONCLUDING REMARKS

The propagation constant of a surface wave propagating along a rectangular mesh in free space has been determined numerically from a general Floquet formulation. For comparison, an approximate solution, from the method of averaged boundary conditions, is also presented. The agreement between the two methods is fairly good for sufficiently small mesh dimensions. In contrast to the square mesh which has a fairly isotropic behavior [7], the rectangular mesh is highly anisotropic.

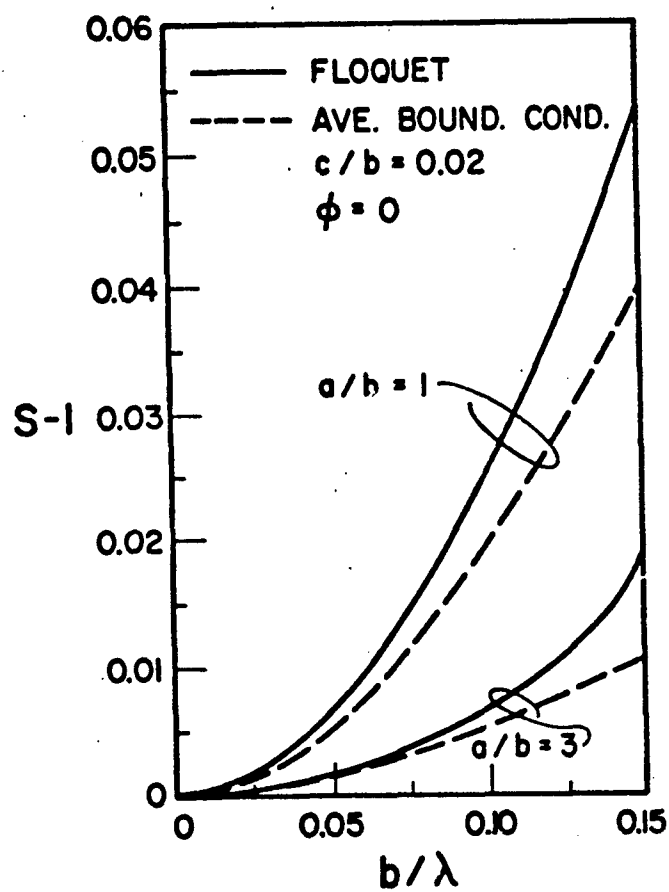


Figure 5. Frequency dependence of propagation constant for propagation along the x-directed wires.

A worthwhile extension is the introduction of imperfect conductivity in the wires by use of an impedance boundary condition at the wire surface rather than imposing zero tangential electric field. The introduction of a lossy half-space [5], [15] would also be useful in modeling ground screens for antennas. Either of the above extensions would introduce a loss mechanism and result in a complex propagation constant  $\gamma$ . Finally, a second mesh (as in a parallel plate waveguide) can be introduced and this configuration has already been treated by the method of averaged boundary conditions [16].

## REFERENCES

- [1] M.I. Kontorovich, "Averaged boundary conditions at the surface of a grating with square mesh", *Radio Engr. Elect. Phys.*, Vol. 8, pp. 1446-1454, 1963.
- [2] M.I. Kontorovich, V. Yu. Petrunkin, N.A. Yesepkina, and M.I. Astrakhan, "The coefficient of reflection of a plane electromagnetic wave from a plane wire mesh", *Radio Engr. Elect. Phys.*, Vol. 7, pp. 222-231, 1962.
- [3] M.I. Astrakhan, "Reflecting and screening properties of plane wire grids", *Telecomm. Radio Engr.*, Vol. 23, pp. 76-83, 1968.
- [4] D.A. Hill and J.R. Wait, "Electromagnetic scattering of an arbitrary plane wave by two nonintersecting perpendicular wire grids", *Can. J. Phys.*, Vol. 52, pp. 227-237, 1974.
- [5] J.R. Wait and D.A. Hill, "Electromagnetic scattering by two perpendicular wire grids over a conducting half-space", *Radio Sci.*, Vol. 11, pp. 725-730, 1976., and Section IV of Sensor and Simulation Note 231, June 1977.
- [6] D.A. Hill and J.R. Wait, "Electromagnetic scattering of an arbitrary plane wave with bonded junctions", *Can. J. Phys.*, Vol. 54, pp. 353-361, 1976., and Section II of Sensor and Simulation Note 231, June 1977.
- [7] D.A. Hill and J.R. Wait, "Electromagnetic surface wave propagation over a bonded wire mesh", *IEEE Trans. Electromag. Compat.*, Vol. EMC-19, pp. 2-7, 1977., and Section III of Sensor and Simulation Note 231, June 1977.
- [8] C.E. Baum, "Interaction of electromagnetic fields with an object which has an electromagnetic symmetry plane", *Interaction Note 63*, Kirtland Air Force Base, NM, March 1971.

- [9] R.E. Collin, *Field Theory of Guided Waves*. New York: McGraw-Hill, 1960, pp. 368-371.
- [10] R.W. Hamming, *Numerical Methods for Scientists and Engineers*. New York: McGraw-Hill, 1973, pp. 62-63.
- [11] J.R. Wait, "The electromagnetic fields of a dipole in the presence of a thin plasma sheet", *Appl. Sci. Res., Sec. B*, Vol. 8, pp. 397-417, 1961.
- [12] J.R. Wait, "Propagation of electromagnetic waves along a thin plasma sheet", *Can. J. Phys.*, Vol. 38, pp. 1586-1595, 1960.
- [13] J.R. Wait, "Reflection at arbitrary incidence from a parallel wire grid", *Appl. Sci. Res.*, Vol. B4, pp. 393-400, 1954.
- [14] L.W. Ricketts, J.E. Bridges, and J. Milletta, *EMP Radiation and Protective Techniques, Appendix C*, New York: John Wiley & Sons, 1976.
- [15] G.A. Otteni, "Plane wave reflection from a rectangular mesh ground screen", *IEEE Trans. Ant. Prop.*, Vol. AP-21, pp. 843-851, 1973.
- [16] M.I. Kontorovich, M.I. Astrakhan, and M.N. Spirina, "Slowing down of electromagnetic waves by wire meshes", *Radio Engr. Elect. Phys.*, Vol. 9, pp. 1242-1245, 1964.

ELECTROMAGNETIC WAVE PROPAGATION ALONG A  
PAIR OF RECTANGULAR BONDED WIRE MESHES

ABSTRACT

A mode equation is derived for propagation between a pair of rectangular wire meshes, and numerical results for the propagation constant of the quasi-TEM mode are presented. An approximate method based on averaged boundary conditions is found to agree if the mesh dimensions are small and the mesh separation is large. The field distributed of the quasi-TEM mode is also examined.



## INTRODUCTION

The electromagnetic properties of wire mesh screens are of interest in numerous shielding and reflecting applications. The relevant plane wave scattering properties have been analyzed both for meshes in free space [1]-[4] and over a lossy earth [5]-[6]. The closely related problem of surface wave propagation on a wire mesh has also been analyzed [7]-[8].

In this paper, we consider propagation of electromagnetic waves between two parallel wire mesh screens. Such a configuration is used in electromagnetic pulse (EMP) parallel plate simulators [9]-[10] which are too large to employ solid metal sheets for the two conducting plates. Similar structures are also useful in cases where a slow-wave behavior is desirable [11]-[13].

## FORMULATION

The geometry of a single rectangular bonded mesh in free space (permittivity  $\epsilon_0$  and permeability  $\mu_0$ ) is illustrated in Fig. 1. Arrays of wires parallel to the x axis with spacing b and parallel to the y axis with spacing a are centered in the plane  $z = 0$ , and perfect contacts are made at the junctions. A second identical mesh is centered in the plane  $z = -2d$  as illustrated in Fig. 2a. The wire radius c is small compared to the spacings a and b, the mesh separation 2d, and the free space wavelength  $\lambda$ . Consequently, only the axial wire currents are important and the usual thin wire approximations are valid.

Since the parallel plate mesh structure in Fig. 2a has a plane of symmetry at  $z = -d$ , the electromagnetic field can be decomposed into symmetric and antisymmetric parts which are uncoupled [14]. The rectangular components of the symmetric part of the electric field satisfy the following:

$$\begin{aligned} E_x(x,y,z) &= E_x(x,y,-z-2d) \\ \text{and} \quad E_y(x,y,z) &= E_y(x,y,-z-2d) \end{aligned} \quad (1)$$

For the symmetric part, it can be shown by image theory that the parallel mesh geometry of Fig. 2a is equivalent to the geometry in Fig. 2b where a perfect magnetic conductor is inserted at  $z = -d$ . Of course the equivalence is valid only for  $z > -d$ .

The rectangular components of the antisymmetric part of the electric field satisfy a similar relationship:

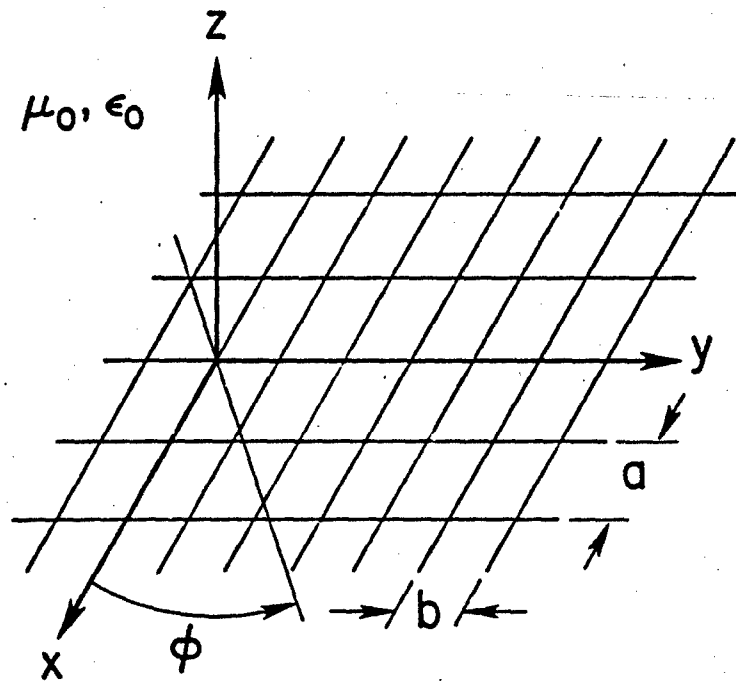


Figure 1. Geometry for a single rectangular wire mesh with bonded junctions. Wire radius equals  $c$ .

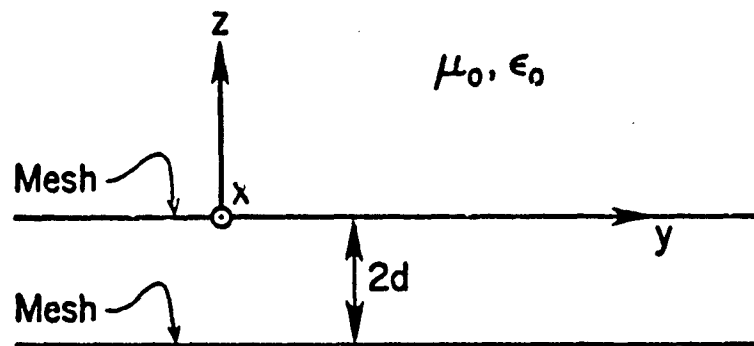


Figure 2a. A pair of identical meshes with separation  $2d$ .

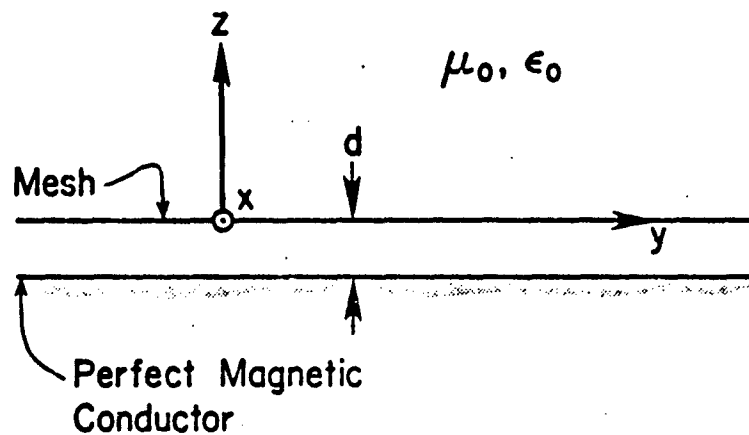


Figure 2b. Equivalent geometry for the symmetric part of the electromagnetic field.

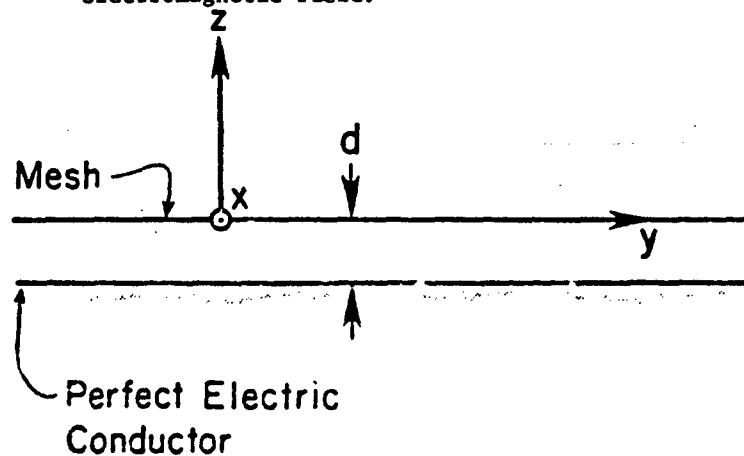


Figure 2c. Equivalent geometry for the antisymmetric part of the electromagnetic field.

$$\begin{aligned}
 &E_x(x, y, z) = -E_x(x, y, -z-2d) \\
 \text{and} \quad &y \quad y \quad (2) \\
 &E_z(x, y, z) = E_z(x, y, -z-2d)
 \end{aligned}$$

In this case, the parallel mesh geometry of Fig. 2a is equivalent (for  $z > -d$ ) to the geometry in Fig. 2c where a perfect electric conductor is inserted at  $z = -d$ . This geometry will support a quasi-TEM mode which has no low frequency cutoff. Since this is the mode of primary interest in parallel plate simulators [9]-[10] and slow-wave structures [11]-[13], from here on we consider only the geometry in Fig. 2c.

The analysis closely follows that for a single rectangular bonded mesh in free space [8]. We seek modes which are propagating in  $x$  and  $y$  but which decay in  $z$  outside the guide ( $z > 0$ ). We invoke Floquet's theorem [15] in order to express the relevant electromagnetic quantity as an exponential function multiplied by a function which is periodic in  $x$  and  $y$ . Thus for a single mode propagating at an angle  $\phi$  to the negative  $x$  axis, the current on the  $q$ th  $x$ -directed wire  $I_{xq}$  and the current on the  $m$ th  $y$ -directed wire  $I_{ym}$  can be written:

$$I_{xq} = \exp[\gamma(x \cos \phi + qb \sin \phi)] \sum_m A_m \exp(i2\pi mx/a) \quad (3)$$

and

$$I_{ym} = \exp[\gamma(ya \cos \phi + y \sin \phi)] \sum_q B_q \exp(i2\pi qy/b) \quad (4)$$

$A_m$  and  $B_q$  are the unknown Fourier coefficients, and  $\gamma$  is the propagation constant of the particular mode which we seek. The  $m$  and  $q$  summations are over all integers including zero from  $-\infty$  to  $\infty$ . The calculation of the fields produced by these currents in the presence of a perfectly conducting half-space is straightforward [6] and will not be

repeated here. The thin wire boundary condition for perfectly conducting wires is the following:

$$E_x(x,0,c) = E_y(0,y,c) = 0 \quad (5)$$

Although (5) is only applied to the  $m = 0$  and  $q = 0$  wires, the periodic Floquet form of (3) and (4) assures that the boundary condition will be satisfied at all wires.

The expressions for the current in (3) and (4) are identical to those in the plane wave scattering case [6] except that  $\gamma$  has replaced  $ikS$  where  $k$  was the free space wave number ( $=2\pi/\lambda$ ) and  $S$  was the sine of the incidence angle. Thus the previous equations for  $A_m$  and  $B_q$  [6] can be used with the following modifications: 1) set the incident fields equal to zero (source-free problem); 2) set the grid separation  $h$  equal to zero (bonded grids in the same plane), 3) set the wire impedances equal to zero (perfectly conducting wires), and 4) set the half-space conductivity equal to infinity. As a result, equations (24) and (26) in [6] reduce to the following:

$$A_m \frac{(k^2 - k_x^2) P_m}{2ikb} + \frac{ik_x}{2ka} \sum_q B_q k_y \left[ \frac{\exp(-\Gamma c) - \exp(-2\Gamma d)}{\Gamma} \right] = 0, \quad (6)$$

$$B_q \frac{(k^2 - k_y^2) Q_q}{2ika} + \frac{ik_y}{2kb} \sum_m A_m k_x \left[ \frac{\exp(-\Gamma c) - \exp(-2\Gamma d)}{\Gamma} \right] = 0, \quad (7)$$

where

$$P_m = \sum_q \left[ \frac{\exp(-\Gamma c) - \exp(-2\Gamma d)}{\Gamma} \right], \quad (8)$$

$$Q_q = \sum_m \left[ \frac{\exp(-\Gamma c) - \exp(-2\Gamma d)}{\Gamma} \right], \quad (9)$$

$$\Gamma_{mq} (= \Gamma) = (k_x^2 + k_y^2 - k^2)^{1/2}, \quad (10)$$

$$k_x = (2\pi m/a) + kS \cos \phi, \quad (11)$$

and

$$k_y = (2\pi q/b) + kS \sin \phi. \quad (12)$$

S is now defined as  $\gamma/(ik)$ . We note in passing that the case of symmetric modes (Fig. 2b) can be obtained from (6)-(9) by simply replacing the image term,  $-\exp(-2\Gamma d)$ , by  $+\exp(-2\Gamma d)$  everywhere that it appears.

The summations involving  $\exp(-\Gamma c)$  in (8) and (9) are rather slowly convergent as they stand. More rapidly convergent forms have been derived previously for  $P_m$  and  $Q_q$  in the free space case [8] and can be applied here to yield

$$P_m = \frac{b}{\pi} \left\{ -\ln \left[ 1 - \exp \left( \frac{-2\pi c}{b} \right) \right] + \Delta_m \right\} + \frac{\exp(-\Gamma_{mo} c)}{\Gamma_{mo}} - \sum_q \frac{\exp(-2\Gamma d)}{\Gamma}, \quad (13)$$

$$Q_q = \frac{a}{\pi} \left\{ -\ln \left[ 1 - \exp \left( \frac{-2\pi c}{b} \right) \right] + \delta_q \right\} + \frac{\exp(-\Gamma_{oq} c)}{\Gamma_{oq}} - \sum_m \frac{\exp(-2\Gamma d)}{\Gamma}, \quad (14)$$

where

$$\Delta_m = \frac{1}{2} \sum_q' \left[ \frac{2\pi}{b} \frac{\exp(-\Gamma c)}{\Gamma} - \frac{\exp(-2\pi |q| c/b)}{|q|} \right] \quad (15)$$

and

$$\delta_q = \frac{1}{2} \sum_m' \left[ \frac{2\pi}{a} \frac{\exp(-\Gamma c)}{\Gamma} - \frac{\exp(-2\pi |m| c/a)}{|m|} \right]. \quad (16)$$

The superscripted prime over the summation sign indicates omission of the  $q = 0$  (or  $m = 0$ ) term.

The doubly infinite set of linear equations (6) and (7) for  $A_m$  and  $B_q$  is numerically inefficient in the present form because  $A_m$  and  $B_q$  decay slowly for large  $|m|$  and  $|q|$ . The difficulty arises because the current expansions in (3) and (4) are slowly convergent for the discontinuous current that occurs at the wire junctions in bonded meshes. We circumvent the convergence problem by modifying the current expansions to allow for a jump discontinuity at the origin. The procedure is nearly identical to that employed for the rectangular bonded mesh in free space [8] and a few of the details are omitted here. The Fourier coefficients of the current  $A_m$  and  $B_q$  are first rewritten [8]:

$$A_m = A'_m + \frac{\Delta(1-\delta_{m0})}{2\pi im} \quad (17)$$

and

$$B_q = B'_q - \frac{\Delta(1-\delta_{q0})}{2\pi iq} \quad (18)$$

where

$$\delta_{m0} = \begin{cases} 1, & m = 0 \\ 0, & m \neq 0 \end{cases}$$

$A'_m$  and  $B'_q$  are modified current coefficients, and  $\Delta$  is an unknown current discontinuity in  $I_{x0}$  at  $x = 0$ . By substituting (17) and (18) into (6) and (7), we obtain the following equivalent set of equations for the modified coefficients:

$$A'_m \frac{(k^2 - k_x^2) P_m}{2ikb} + \frac{ik_x}{2ka} \sum_q B'_q k_y \left[ \frac{\exp(-\Gamma c) - \exp(-2\Gamma d)}{\Gamma} \right] \\ + \Delta \left\{ \frac{(k^2 - k_x^2) P_m}{2kb} \frac{(\delta_{m0} - 1)}{2\pi m} - \frac{k_x}{2ka} \left[ \frac{P'_m}{b} + \frac{kS \sin \phi}{2\pi} P_{1m} \right] \right\} = 0 \quad (19)$$

and



$$B'_q \frac{(k^2 - k_y^2) Q_q}{2ika} + \frac{ik_y}{2kb} \sum_m A'_m k_x \left[ \frac{\exp(-\Gamma c) - \exp(-2\Gamma d)}{\Gamma} \right] \\ + \Delta \left\{ \frac{(k^2 - k_y^2) Q_q}{2ka} - \frac{(1 - \delta_{q0})}{2\pi q} + \frac{k_y}{2kb} \left[ \frac{Q'_q}{a} + \frac{kS \cos \phi}{2\pi} Q_{1q} \right] \right\} = 0 \quad (20)$$

where

$$P_{1m} = \sum_q \left[ \frac{\exp(-\Gamma c) - \exp(-2\Gamma d)}{q\Gamma} \right], \quad (22)$$

$$P'_m = P_m - \left[ \frac{\exp(-\Gamma_{mo} c) - \exp(-2\Gamma_{mo} d)}{\Gamma_{mo}} \right], \quad (22)$$

$$Q_{1q} = \sum_m \left[ \frac{\exp(-\Gamma c) - \exp(-2\Gamma d)}{m\Gamma} \right], \quad (23)$$

and

$$Q'_q = Q_q - \left[ \frac{\exp(-\Gamma_{oq} c) - \exp(-2\Gamma_{oq} d)}{\Gamma_{oq}} \right] \quad (24)$$

Again the superscript prime ' on the summation indicates omission of the  $q = 0$  (or  $m = 0$ ) term. All summations are now in a rapidly convergent form.

Since we have introduced an additional unknown  $\Delta$ , another equation is required to have an equal number of equations and unknowns ( $A'_m$ ,  $B'_q$ , and  $\Delta$ ). The following equation can be obtained from charge continuity [8]:

$$-\frac{\Delta}{2\pi} \left( 1 + \frac{b}{a} \right) + \sum_m A'_m \left( i_m \frac{b}{a} + \frac{ikSb}{2\pi} \cos \phi \right) \\ - \sum_q B'_q \left( i_q + \frac{ikSb}{2\pi} \sin \phi \right) = 0. \quad (25)$$

Since the doubly infinite set of equations, (19) and (20), are rapidly convergent, they can be truncated with  $m$  ranging from  $-M$  to  $M$  and  $q$  ranging from  $-Q$  to  $Q$  where  $M$  and  $Q$  are small integers. Thus (19),

(20), and (25) yield a set of  $T(=2M + 2Q + 3)$  linear, homogeneous equations in  $A'_m$ ,  $B'_q$ , and  $\Delta$ :

$$\begin{bmatrix} \text{T x T} \\ \text{coefficient} \\ \text{matrix} \end{bmatrix} \begin{bmatrix} A'_{-M} \\ \vdots \\ A'_0 \\ \vdots \\ A'_M \\ \vdots \\ B'_{-Q} \\ \vdots \\ B'_0 \\ \vdots \\ B'_Q \\ \Delta \end{bmatrix} = \begin{bmatrix} 0 \\ \vdots \\ \vdots \\ \vdots \\ \vdots \\ \vdots \\ \vdots \\ \vdots \\ \vdots \\ \vdots \\ 0 \end{bmatrix} \quad (26)$$

A nontrivial solution to (26) exists only if the determinant, which is a function of  $S(=\gamma/ik)$ , vanishes. Thus the mode equation to be solved for  $S$  is

$$\begin{vmatrix} \text{T x T} \\ \text{coefficient} \\ \text{matrix} \end{vmatrix} = 0 \quad (27)$$

For modes which are evanescent in the positive  $z$  direction,  $S$  is real and greater than one. For this case equations (19), (20), and (25) can be normalized so that all coefficients are real functions of the real variable  $S$ . This real form has been programmed, and (27) has been solved numerically for  $S$  by the bisection method [15].

#### NUMERICAL RESULTS FOR THE PROPAGATION CONSTANT

Convergence of the mode equation (27) was examined by increasing  $M$  and  $Q$  until the value of  $S(=\gamma/ik)$  did not change significantly. The most rapid convergence was obtained by making  $M = Q$  regardless of

the  $a/b$  ratio. For the cases considered here, convergence was obtained for  $M = Q = 2$  ( $T=11$ ) which is consistent with previous results [7]-[8]. All results shown here are for  $M = Q = 2$ , and the required determinant calculation is fairly rapid for the resultant  $11 \times 11$  matrix. For comparison, some results from the method of averaged boundary conditions [12] have been calculated from (38).

In Fig. 3, we illustrate the  $\phi$  dependence of  $S$  for various values of  $d/b$ . The  $a/b$  ratio of 3 was chosen because a 3 to 1 mesh has been used in some EMP simulators (private communication, C.E. Baum). In all results shown here, the  $c/b$  ratio is  $10^{-2}$ , but the results are only weakly dependent on this ratio. Note that  $S$  always increases as  $\phi$  goes from  $0^\circ$  to  $90^\circ$ . Because of symmetry, only the range of  $\phi$  from  $0^\circ$  to  $90^\circ$  need be shown. As  $d/b$  is increased, the results approach a single mesh in free space ( $d/b = \infty$ ). The dashed results obtained by the method of averaged boundary conditions are in rather poor agreement for  $d/b = 1$ . As the mesh spacing is increased, the agreement improves and is quite good for an isolated mesh ( $d/b = \infty$ ). The reason for poor agreement for small  $d/b$  is probably that the effect of the higher order evanescent terms ( $|m|$  and  $|q| \neq 0$ ) is not accurately included in the method of averaged boundary conditions.

As discussed previously [7], the variation of  $S$  with frequency will result in dispersion when attempting to transmit a pulse. The frequency dependence of  $S$  for  $\phi = 0^\circ$  is shown in Fig. 4 for  $a/b = 1$ . For this square mesh case ( $a/b = 1$ ), the mesh has a nearly isotropic behavior and very little  $\phi$  variation occurs. This is in agreement with an experimental study on a single square mesh by Ulrich and Tacke [16] and a quasi-static analysis by Andreassen and Tanner [17]. Note that the agreement with the method of averaged boundary conditions is again poor for

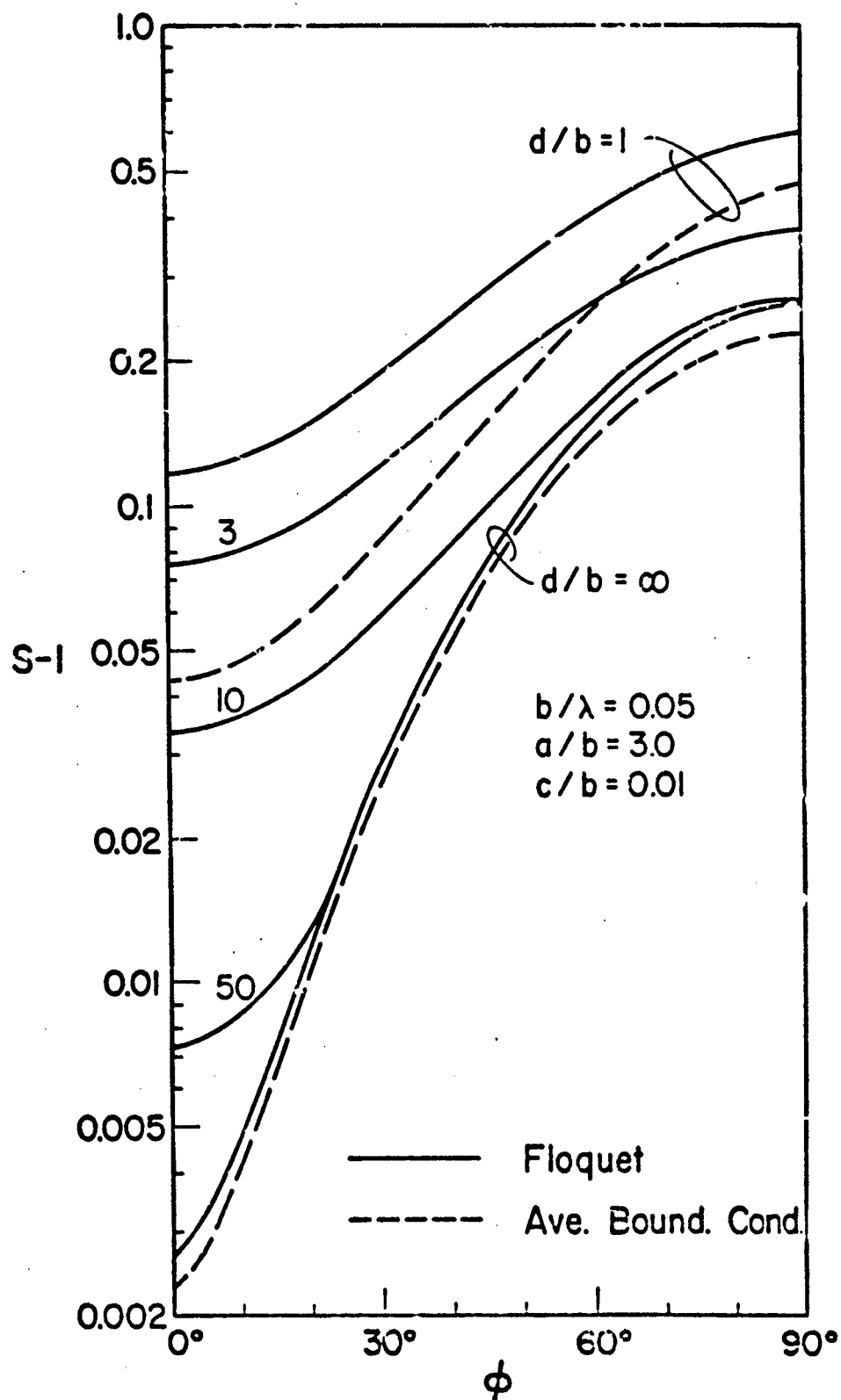


Figure 3. Normalized propagation constant  $S$  for a 3 to 1 mesh as a function of direction

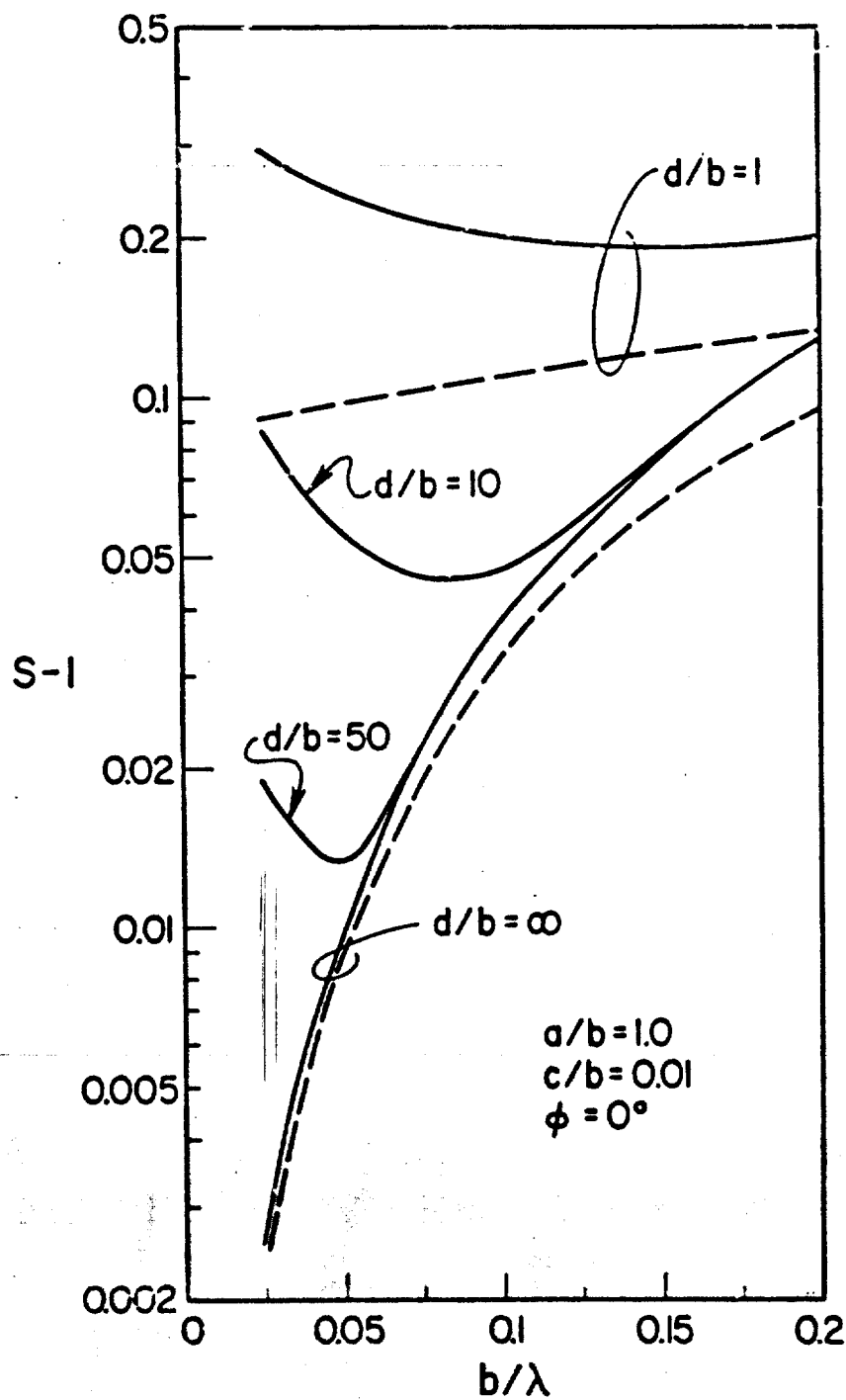


Figure 4. Frequency dependence of the propagation constant for propagation along the x-directed wires of a square mesh.

$d/b = 1$  and good for  $d/b = \infty$ . Also, both methods yield a value of  $S$  greater than one for  $b/\lambda$  approaching zero unless the mesh is completely isolated ( $d/b = \infty$ ).

Similar results for a 3 to 1 mesh are shown in Fig. 5. The trends are similar but the values of  $S$  are smaller. This is due to the fact that there are fewer cross wires to contribute to the slow wave behavior of the guide. The effect of the cross wires has been described qualitatively as a periodic loading [16,17].

### FIELD DISTRIBUTIONS

The field distribution inside a parallel mesh guide is of interest because a uniform plane wave field is desired in the working volume of EMP simulators. Also the field outside the meshes is important because of possible interference problems.

The fields of the currents given by (3) and (4) can be derived from an electric Hertz vector  $\vec{\Pi}$  which has only  $x$  and  $y$  components [6]:

$$\vec{\Pi} = \hat{x}\Pi_x + \hat{y}\Pi_y, \quad (28)$$

where

$$\Pi_x = \frac{-i\eta_0}{2kb} \sum_m \sum_q A_m \left[ \frac{\exp(-\Gamma|z|) - \exp(-\Gamma(z+2d))}{\Gamma} \right] \exp[i(k_x x + k_y y)] \quad (29)$$

$$\Pi_y = \frac{-i\eta_0}{2ka} \sum_m \sum_q B_q \left[ \frac{\exp(-\Gamma|z|) - \exp(-\Gamma(z+2d))}{\Gamma} \right] \exp[i(k_x x + k_y y)], \quad (30)$$

$$\eta_0 = (\mu_0/\epsilon_0)^{1/2},$$

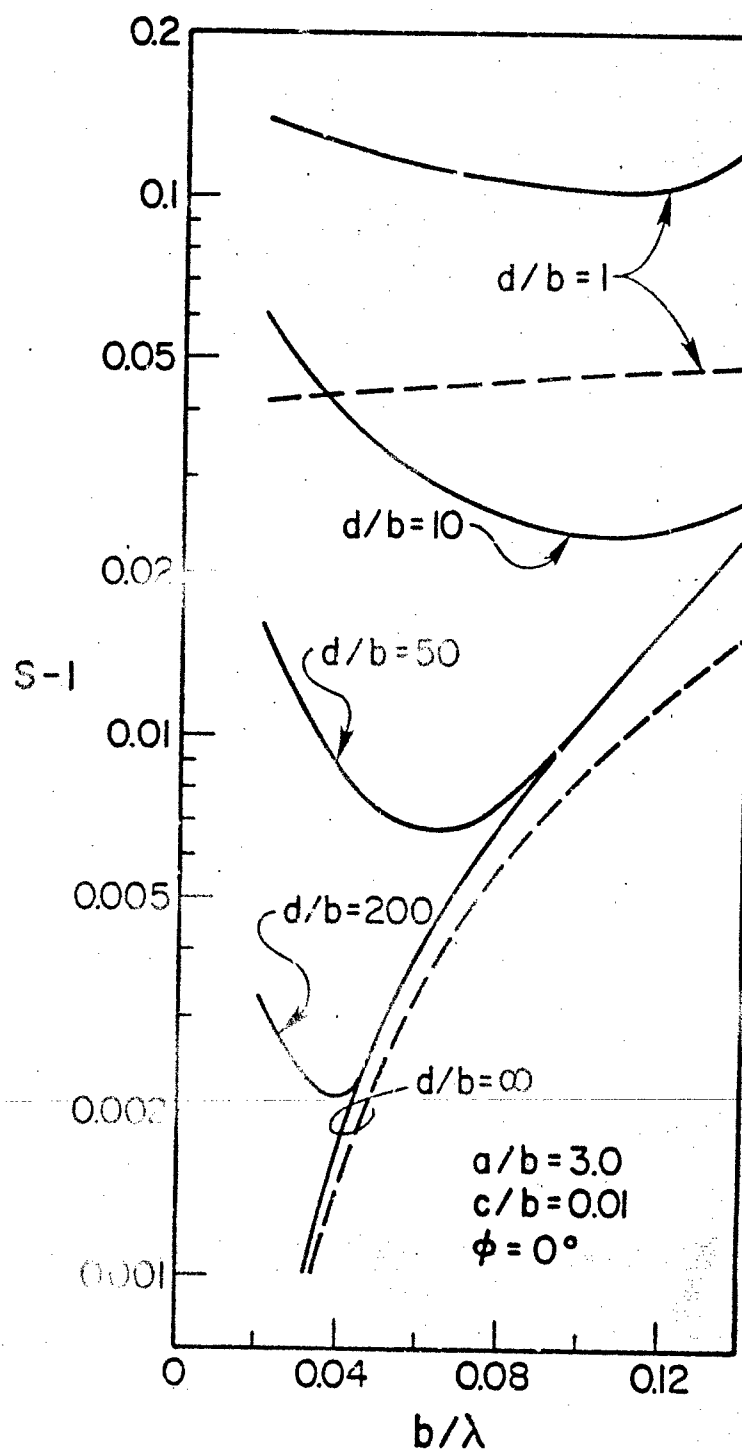


Figure 5. Frequency dependence of the propagation constant for propagation along the x-directed wires of a square mesh.

and  $\hat{x}$  and  $\hat{y}$  are unit vectors. Note that the fields for the symmetric modes (Fig. 2b) could be obtained by replacing the image term,  $-\exp(-\Gamma(z+2d))$ , by  $+\exp(-\Gamma(z+2d))$  in (29) and (30). The electric and magnetic fields are obtained from the following operations on  $\Pi$ :

$$\vec{E} = \nabla \nabla \cdot \Pi + k^2 \Pi \quad (31)$$

and

$$\vec{H} = \frac{ik}{\eta_0} \nabla \times \Pi \quad (32)$$

In general, the expressions for  $\vec{E}$  and  $\vec{H}$  obtained by substituting (28)-(30) into (31) and (32) are rather complicated. However, for sufficiently small  $ka$  and  $kb$  only the constant terms ( $m=q=0$ ) are of significance for observation points more than a cell dimension ( $a$  or  $b$ ) from the mesh. An equivalent interpretation is that we consider the fields averaged over one cell, and only the  $m = q = 0$  terms contribute. The constant terms for the Hertz components  $\Pi_{xo}$  and  $\Pi_{yo}$  are

$$\Pi_{xo} = \frac{-i\eta_0}{2kb} A_0 \left[ \frac{\exp(-\Gamma_0 |z|) - \exp(-\Gamma_0 (z+d))}{\Gamma_0} \right] \exp[i(k_{ox}x + k_{oy}y)] \quad (33)$$

and

$$\Pi_{yo} = \frac{-i\eta_0}{2kb} B_0 \left[ \frac{\exp(-\Gamma_0 |z|) - \exp(-\Gamma_0 (z+d))}{\Gamma_0} \right] \exp[i(k_{ox}x + k_{oy}y)] \quad (34)$$

where  $k_{ox} = kS \cos\phi$ ,  $k_{oy} = kS \sin\phi$ , and  $\Gamma_0 = k(S^2 - 1)^{1/2}$ .

For general angle of propagation  $\phi$ , all three components of the electric and magnetic fields can be non-zero. However, for the important special case of  $\phi = 0^\circ$  (propagation along the  $x$ -directed wires) the fields simplify considerably because  $B_0$  and  $k_{oy}$  are zero. Thus  $\Pi_{xo}$  and  $\Pi_{yo}$  simplify to



$$\Pi_{xo} = \frac{-i\eta_o}{2kb} A_o \left[ \frac{\exp(-\Gamma_o |z|) - \exp(-\Gamma_o (z + 2d))}{\Gamma_o} \right] \exp(ikSx) \quad (35)$$

and

$$\Pi_{yo} = 0.$$

Thus the constant components of the electric and magnetic fields are

$$H_{xo} = H_{zo} = E_{yo} = 0,$$

$$E_{xo} = \left( \frac{\partial^2}{\partial z^2} + k^2 \right) \Pi_{xo}, \quad E_{zo} = \frac{\partial^2 \Pi_{xo}}{\partial z \partial x}, \quad (36)$$

and

$$H_{yo} = \frac{ik}{\eta_o} \frac{\partial \Pi_{xo}}{\partial z}$$

By substituting (35) into (36), we obtain

$$E_{xo} = \frac{i\eta_o A_o}{b} \exp(ikSx) E_{xon},$$

$$E_{zo} = \frac{\eta_o A_o}{b} \exp(ikSx) E_{zon},$$

$$H_{yo} = \frac{A_o}{b} \exp(ikSx) H_{yon},$$

where

$$E_{xon} = (S^2 - 1)^{1/2} [\exp(-\Gamma_o |z|) - \exp(\Gamma_o (z + 2d))]/2, \quad (37)$$

$$E_{zon} = S[-\operatorname{sgn}(z)\exp(-\Gamma_o |z|) + \exp(-\Gamma_o (z + 2d))]/2,$$

$$H_{yon} = [-\operatorname{sgn}(z)\exp(-\Gamma_o |z|) + \exp(-\Gamma_o (z + 2d))]/2$$

and

$$\operatorname{sgn}(z) = \begin{cases} +1, & z > 0 \\ -1, & z < 0 \end{cases}.$$

Note that the normalized fields  $E_{xon}$ ,  $E_{zon}$ , and  $H_{yon}$  are all real and dimensionless. This normalization implies that the mesh carries a fixed current density,  $A_0/b$ .

In Figs. 6-8, we illustrate the  $z$  dependence of  $E_{xon}$ ,  $E_{zon}$ , and  $H_{yon}$  both inside ( $z < 0$ ) and outside ( $z > 0$ ) the guide for various values of  $S$ . Of course, in a specific example  $S$  is determined from the mode equation (27). Here we choose  $d/\lambda = 1$ , but it would be easy to generate results for other values of  $d/\lambda$  from (37). Note that for  $S = 1$ , we have essentially a perfect guide. All fields are zero outside the guide, and  $E_{zon}$  and  $H_{yon}$  are unity inside.  $E_{xon}$  is zero everywhere.

For the extremely slow wave case of  $S = 2$ , the fields are simply those of a slow surface wave on the mesh and decay rapidly on both sides of the mesh. For intermediate values of  $S$ , the values of the desired fields,  $E_{zon}$  and  $H_{yon}$ , decrease toward the center of the guide ( $z = -d$ ) and are nonzero outside the guide. Also,  $E_{xon}$  becomes nonzero. This behavior is consistent with the known fact that the departure of  $S$  from unity is a measure of the shielding degradation for wire meshes [7], [8]. An important design consideration is that  $2\Gamma_0 d (= 2k(S^2 - 1)^{1/2}d)$  must be kept small in order to produce a nearly constant field inside the guide and a small field outside the guide as desired in EMP simulators.

#### CONCLUDING REMARKS

A general formulation has been derived for the propagation modes of a pair of parallel rectangular meshes. The mode equation has been solved numerically for the propagation constant of the quasi-TEM mode. This is a slow-wave mode which has no low frequency cutoff, and it is the dominant mode in parallel mesh EMP simulators. For comparison, results from the method of averaged boundary conditions are also presented. The agreement

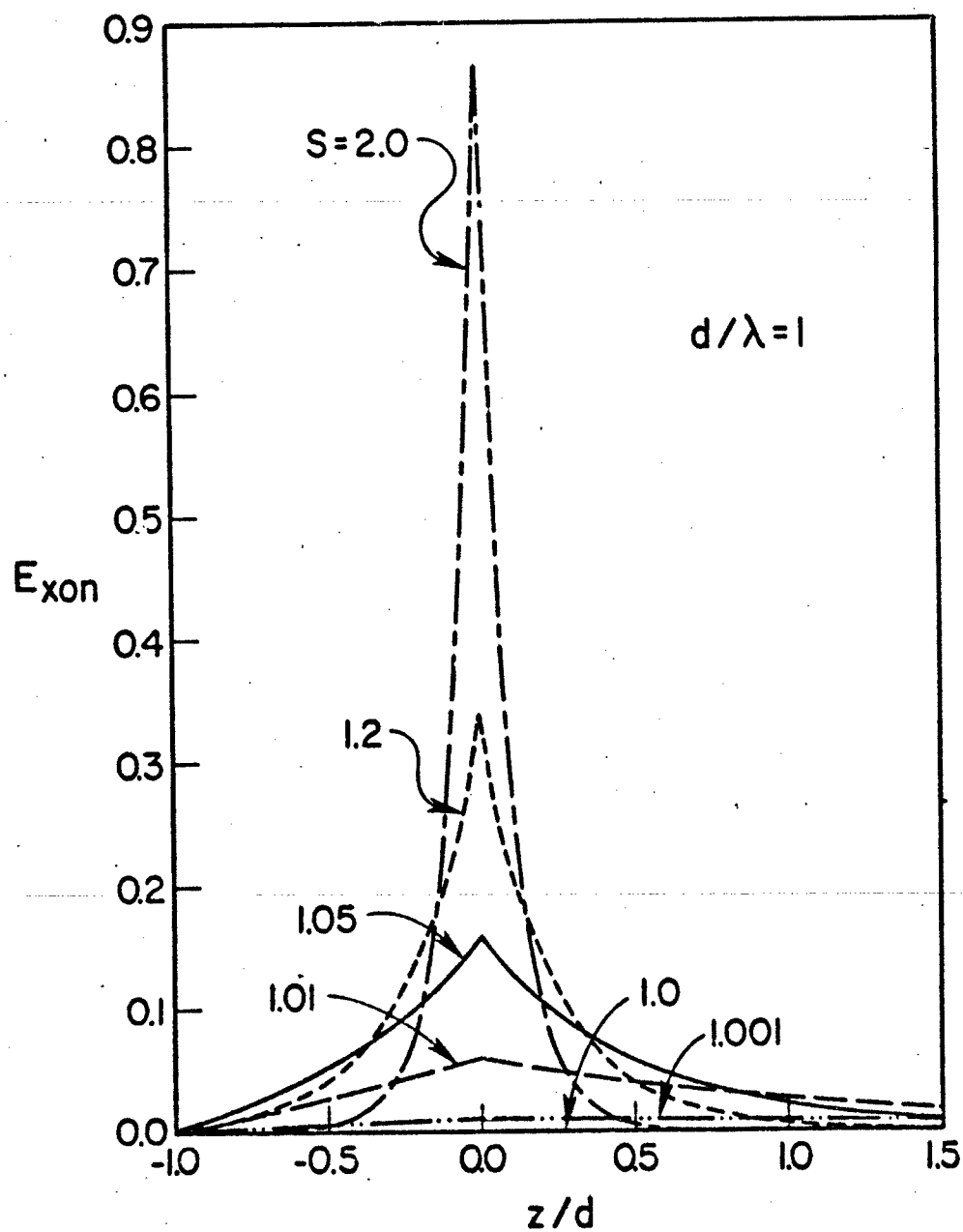


Figure 6. Distribution of the longitudinal electric field  $E_{xon}$  for various values of  $S$ .

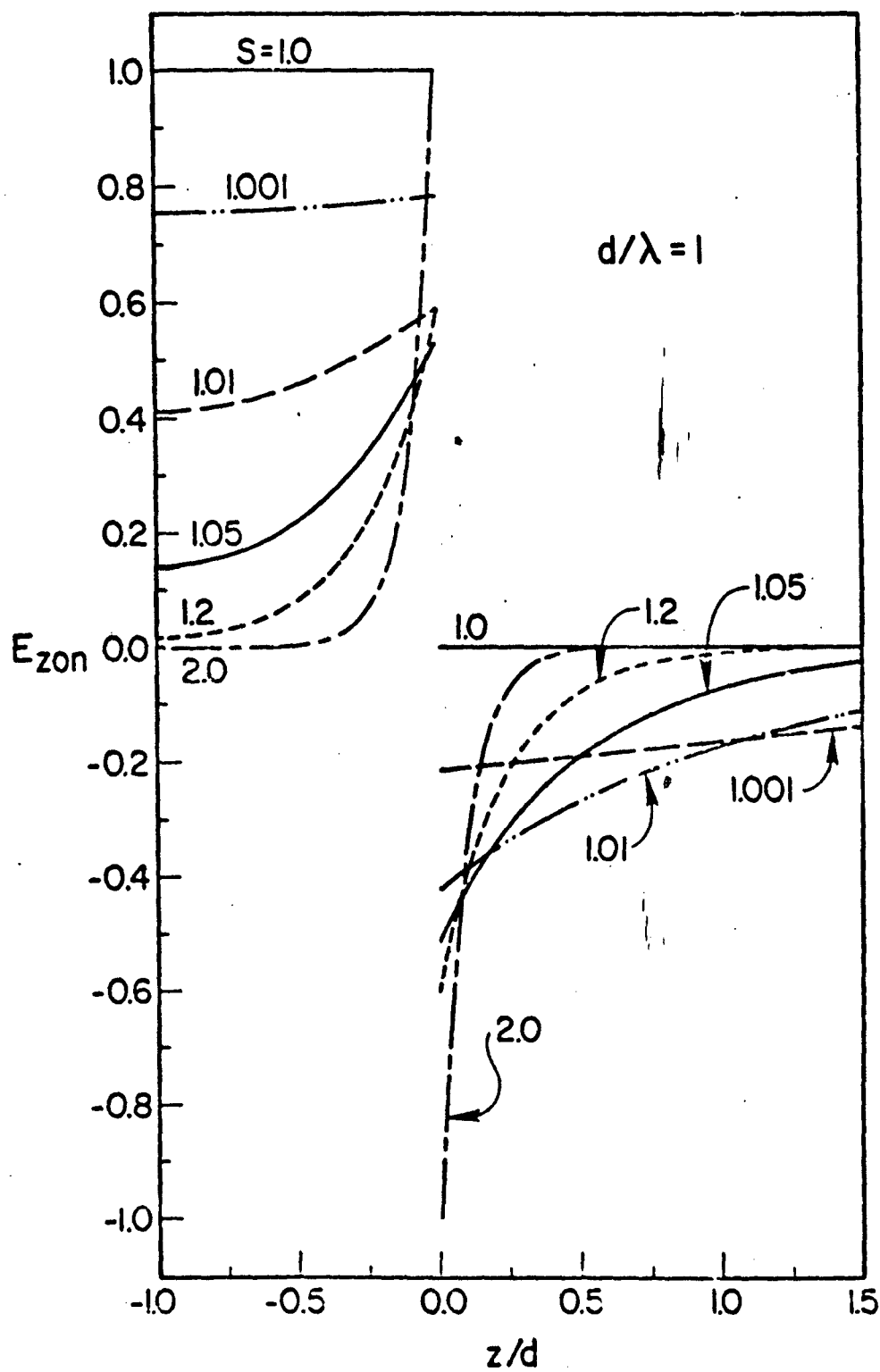


Figure 7. Distribution of the transverse electric field  $E_{zon}$  for various values of  $S$ .

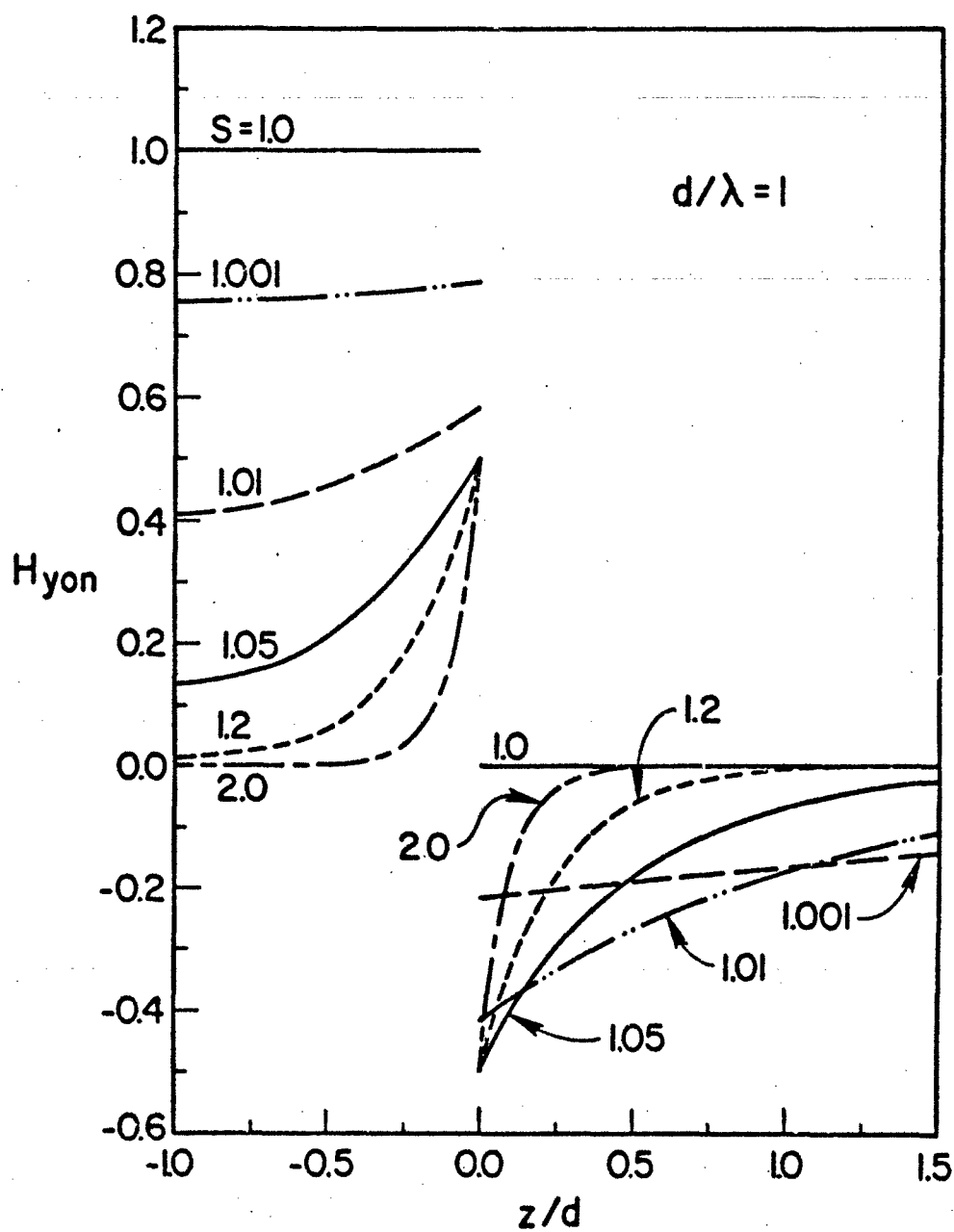


Figure 8. Distribution of the transverse electric field  $E_{zon}$  for various values of  $S$ .

between the two methods is good only when the mesh dimensions are small and the two meshes are widely separated. When the meshes are rectangular ( $a \neq b$ ), the propagation constant is highly dependent on the propagation direction.

Field distributions are also shown for the quasi-TEM mode. When the propagation constant is equal to that of free space (perfect meshes), the interior fields are uniform and transverse, and the exterior fields are zero. As the propagation constant increases (as for realistic meshes), the interior fields decrease toward the center of the guide, and the exterior fields become nonzero.

Several extensions to this work are possible. Although the quasi-TEM mode is of most interest, higher order modes are possible and could be studied from the general mode equation (27) derived here. The introduction of a lossy half-space (rather than the perfect electric and magnetic conductors considered here) would be useful in modeling ground screens for antennas [5], [6]. In general, these extensions would result in complex propagation constants and a numerical search in the complex plane for solution of the mode equation. A final practical problem of interest is the effect of finite mesh width on the propagation constant and field distribution of the modes. Two possible approaches are to model the meshes as sheet impedances [8] or as a finite number of wires [18].

#### ACKNOWLEDGEMENT

The author would like to thank Drs. J.R. Wait and C.E. Baum for useful discussions on this problem and Mrs. L.R. Hope for help in preparing the manuscript.

## APPENDIX - AVERAGED BOUNDARY CONDITIONS

The geometry of Fig. 2c has been treated by the method of averaged boundary conditions [12] which is based on small  $a/\lambda$  and  $b/\lambda$ . The resultant mode equation [12] can be written in the following form:

$$\begin{aligned} & \sin^2\phi \{ (\Gamma_0/k)[1 - \exp(-2\Gamma_0 d)] - X_2[1 - S^2(R_2 \sin^2\phi + R_1 \cos^2\phi)] \} \\ & \cdot \{ [1 - \exp(-2\Gamma_0 d)] + (\Gamma_0/k)X_1[1 - S^2(R_1 - R_2)\cos^2\phi] \} \\ & + \cos^2\phi \{ (\Gamma_0/k)[1 - \exp(-2\Gamma_0 d)] - X_1[1 - S^2(R_1 \cos^2\phi + R_2 \sin^2\phi)] \} \\ & \cdot \{ [1 - \exp(-2\Gamma_0 d)] + (\Gamma_0/k)X_2[1 - S^2(R_2 - R_1)\sin^2\phi] \} = 0 \quad (38) \end{aligned}$$

where

$$R_1 = \frac{a/b}{1 + a/b}, \quad R_2 = \frac{b/a}{1 + b/a},$$

$$X_1 = \frac{2b}{\lambda} \ln\left(\frac{b}{2\pi c}\right),$$

and

$$X_2 = \frac{2a}{\lambda} \ln\left(\frac{a}{2\pi c}\right).$$

This mode equation has been programmed and solved numerically for  $S$  by the bisection method [15].

For the important special case of  $\phi = 0^\circ$ , (38) simplifies to

$$(\Gamma_0/k)[1 - \exp(-2\Gamma_0 d)] - X_1(1 - R_1 S^2) = 0. \quad (39)$$

In the limit of large  $d$ , the exponential term vanishes in (39) for  $\text{Re}(\Gamma_0) > 0$ , and we have:

$$(S^2 - 1)^{1/2} - X_1(1 - R_1 S^2) = 0. \quad (40)$$

This is precisely the mode equation for the rectangular mesh in free space which has an explicit solution for  $S$  [8].

The other limiting case of (39) is for small  $\Gamma_0 d$ . In this case, we can replace  $\exp(-2\Gamma_0 d)$  by  $1 - 2\Gamma_0 d$ . With this approximation (39) can be solved explicitly for  $S$ :

$$S = \left[ \frac{1 + 2kd/X_1}{R_1 + 2kd/X_1} \right]^{1/2} \quad (41)$$

Although the simplicity of (41) is attractive, we find that the method of averaged boundary conditions does not agree well with the rigorous Floquet analysis for closely spaced meshes (small  $d$ ). This poor agreement is illustrated in Figs. 6-8. Consequently, the validity of (41) is questionable.



## REFERENCES

- [1] M.I. Kontorovich, V. Yu. Petrunkin, N.A. Yesepkina, and M.I. Astrakhan, "The coefficient of reflection of a plane electromagnetic wave from a plane wire mesh", *Radio Engr. Elect. Phys.*, Vol. 7, pp. 222-231, 1962.
- [2] M.I. Astrakhan, "Reflecting and screening properties of plane wire grids", *Telecom. Radio Engr.*, Vol. 23, pp. 76-83, 1968.
- [3] D.A. Hill and J.R. Wait, "Electromagnetic scattering of an arbitrary plane wave by two nonintersecting perpendicular wire grids", *Can. J. Phys.*, Vol. 52, pp. 227-237, 1974.
- [4] D.A. Hill and J.R. Wait, "Electromagnetic scattering of an arbitrary plane wave by a wire mesh with bonded junctions", *Can. J. Phys.*, Vol. 54, pp. 354-361, 1976., and Section II of Sensor and Simulation Note 231, June 1977.
- [5] G.A. Otteni, "Plane wave reflection from a rectangular mesh ground screen", *IEEE Trans. Antennas Propagat.*, Vol. AP-21, pp. 843-851, 1973.
- [6] J.R. Wait and D.A. Hill, "Electromagnetic scattering by two perpendicular wire grids over a conducting half-space", *Radio Sci.*, Vol. 11, pp. 725-730, 1976., and Section IV of Sensor and Simulation Note 231, June 1977.
- [7] D.A. Hill and J.R. Wait, "Electromagnetic surface wave propagation over a bonded wire mesh", *IEEE Trans. Electromagn. Compat.*, Vol. EMC-19, pp. 2-7, 1977., and Section III of Sensor and Simulation Note 231, June 1977.
- [8] D.A. Hill and J.R. Wait, "Electromagnetic surface wave propagation over a rectangular bonded wire mesh", submitted to *IEEE Trans. Electromagn. Compat.*, and also Sensor and Simulation Note 249, October 1977.
- [9] C.E. Baum, "General principles for the design of Atlas I and II, Part I: Atlas: Electromagnetic design considerations for horizontal

- version", *Sensor and Simulation Note 143*, Air Force Weapons Laboratory, Jan. 1972.
- [10] L.W. Kicketts, J.E. Bridges, and J. Milletta, *EMP Radiation and Protective Techniques*. Appendix C, New York: John Wiley and Sons, 1976.
- [11] R.K. Arora, "Surface waves on a pair of unidirectional conducting screens", *IEEE Trans. Antennas Propagat.*, Vol. AP-14, pp. 795-798, 1966.
- [12] M.I. Kontorovich, M.I. Astrakhan, and M.N. Spirina, "Slowing down of electromagnetic waves by wire meshes", *Radio Engr. Elect. Phys.*, Vol. 9, pp. 1242-1245, 1964.
- [13] R.K. Arora, B. Bhat, and S. Aditya, "Guided waves on a flattened sheath helix", *IEEE Trans. Microwave Theory Tech.*, Vol. MTT-25, pp. 71-72, 1977.
- [14] C.E. Baum, "Interaction of electromagnetic fields with an object which has an electromagnetic symmetry plane", *Interaction Note 63*, Air Force Weapons Laboratory, March 1971.
- [15] R.W. Hamming, *Numerical Methods for Scientists and Engineers*. New York: McGraw-Hill, 1973, pp. 62-63.
- [16] R. Ulrich and M. Tacke, "Submillimeter waveguiding on periodic metal structure", *Appl. Phys. Lett.*, Vol. 22, pp. 251-253, 1973.
- [17] M.G. Andreassen and R.L. Tanner, "A wire-grid lens antenna of wide application Part II: Wave-propagating properties of a pair of wire grids with square, hexagonal or triangular mesh", *IRE Trans. Ant. Propagat.*, Vol. AP-10, pp. 416-439, 1962.
- [18] J.R. Wait, "Excitation of an ensemble of parallel cables by an external dipole over a layered ground", *AEU*, Vol. 31, pp. 489-493, 1977.

SURFACE WAVE PROPAGATION ON A RECTANGULAR BONDED  
WIRE MESH LOCATED OVER THE GROUND

ABSTRACT

A mode equation is derived for surface wave propagation along a rectangular bonded wire mesh over a lossy half-space. The mode equation is solved numerically for the complex propagation constant of the surface wave. For a sufficiently small mesh size, the attenuation rate of this surface wave is considerably less than that of the Zenneck surface for an isolated half-space or homogeneous ground.

## INTRODUCTION

Wire mesh screens are employed in numerous shielding and reflecting applications. The relevant plane wave scattering properties have been analyzed both for meshes in free space [Kontorovich *et al.*, 1962; Astrakhan, 1968; Hill and Wait, 1974; Hill and Wait, 1976] and over a lossy earth [Ottani, 1973; Wait and Hill, 1976]. The closely related problem of surface wave propagation on a wire mesh in free space has also been analyzed [Hill and Wait, 1977a; Hill and Wait, 1977b] and studied experimentally [Ulrich and Tacke, 1973].

Here we extend our analysis to the case where the rectangular mesh is located at an arbitrary height above a conducting half space. When the height is small, this configuration can be considered as a model to study surface wave propagation over a ground screen. The surface wave contribution to the total field is expected to be significant when the source and observer are located near the ground screen. For example, a conical monopole source over a ground screen has been used to illuminate test objects (also located above the ground screen) with an electromagnetic pulse [Kehrer and Barn, 1975].

Our objective here is to calculate the propagation constant of the surface wave. Due to the lossy earth, the wave suffers attenuation and the propagation constant becomes complex.

#### FORMULATION

The geometry of a rectangular bonded mesh located at a height  $d$  above a conducting half-space is illustrated in Figure 1. Arrays of identical perfectly conducting wires parallel to the  $x$  axis with spacing  $b$  and parallel to the  $y$  axis with spacing  $a$  are contained in the plane  $z = 0$ . This configuration is called a bonded rectangular mesh because the contact between the wire junction is bonded and the interwire spacings  $a$  and  $b$  are not equal in general. Furthermore, the wire radius  $c$  is small compared to the spacings  $a$  and  $b$ , the mesh height  $d$ , and the free space wavelength  $\lambda$ . Consequently, only the axial wire currents are important, and the usual thin wire approximations are valid.

The region  $z > -d$ , external to the wires, is free space with permittivity  $\epsilon_0$  and permeability  $\mu_0$ . The region  $z < -d$  is homogeneous with permittivity  $\epsilon_g$ , conductivity  $\sigma_g$ , and free space permeability  $\mu_0$ .

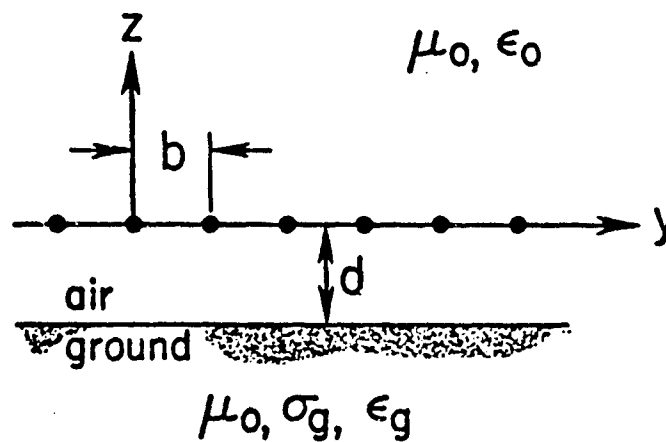
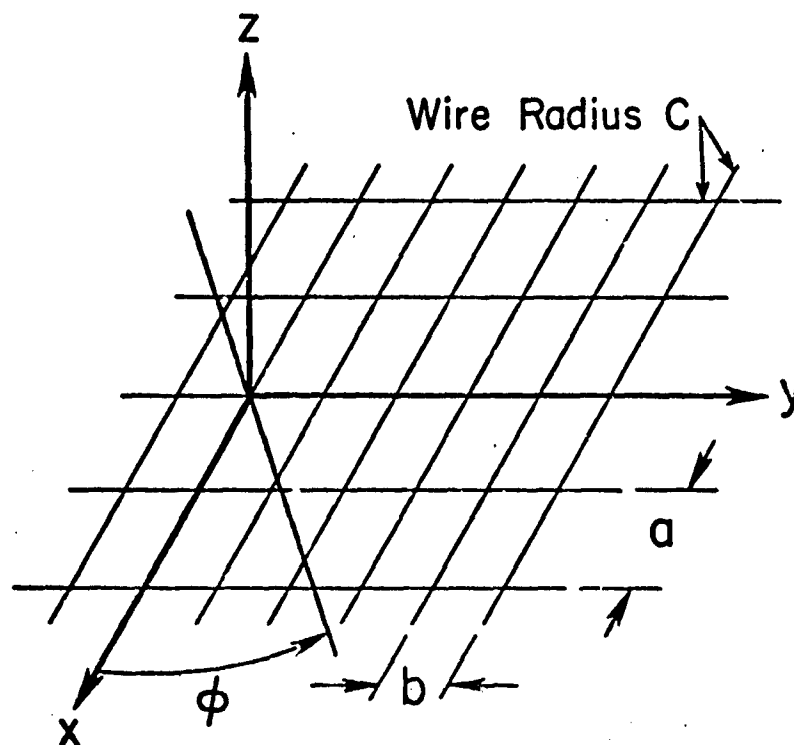


Figure 1. A bonded rectangular wire mesh over a conducting half-space (perspective and side view).

In the following formulation, the mesh is located in free space which means that  $d$  is positive. However, a similar formulation is possible for a buried mesh ( $d < 0$ ).

The formulation closely follows that for a rectangular bonded mesh in free space [Hill and Wait, 1977b]. Thus, we seek modes which are propagating in  $x$  and  $y$  but which decay above the mesh ( $z > 0$ ) and in the earth ( $z < -d$ ). We invoke Floquet's theorem [Collin, 1960] in order to express the relevant electromagnetic quantity as an exponential function multiplied by a function which is periodic in  $x$  and  $y$ . Thus, for a single mode propagating at an angle  $\phi$  to the negative  $x$  axis, the current on the  $q$ th  $x$ -directed wire  $I_{xq}$  and the current on the  $m$ th  $y$ -directed wire  $I_{ym}$  can be written:

$$I_{xq} = \exp[\gamma(x \cos\phi + qb \sin\phi)] \sum_m A_m \exp(i2\pi mx/a) \quad (1)$$

and

$$I_{ym} = \exp[\gamma(ya \cos\phi + y \sin\phi)] \sum_q B_q \exp(i2\pi qy/b) \quad (2)$$

where a time factor  $\exp(i\omega t)$  is assumed. Here  $A_m$  and  $B_q$  are the unknown Fourier coefficients, and  $\gamma$  is the propagation constant of the particular mode which we seek. The  $m$  and  $q$  summations are over all integers including zero from  $-\infty$  to  $\infty$ .

The calculation of the fields produced by the currents given by (1) and (2) in the presence of a conducting half-space is straightforward [Wait and Hill, 1976]. For the present analysis, we employ the following thin wire boundary condition for the assumed perfectly conducting wires:

$$E_x(x, 0, c) = E_y(y, 0, c) = 0. \quad (3)$$

Although (3) is only applied to the  $m = 0$  and  $q = 0$  wires, the periodic Floquet form of (1) and (2) assures that the boundary condition will be satisfied at all wires.

Expressions (1) and (2) for the current are identical to those in the plane wave scattering case except that  $\gamma$  has replaced  $ikS$  where  $k$  is the free space wave number ( $=2\pi/\lambda$ ) and  $S$  is the sine of the incidence angle. Thus the previous equations for  $A_m$  and  $B_q$  can be used with the following modifications: 1) set the incident fields equal to zero (source-free problem), 2) set the grid separation  $h$  equal to zero (bonded grids in the same plane), and 3) set the wire impedance equal to zero perfectly conducting wires. As a result, equations (24) and (26) from the plane wave case [Wait and Hill, 1976] reduce to the following:

$$A_m \frac{(k^2 - k_x^2) P_m}{2ikb} + \frac{ik_x}{2ka} \sum_q B_q k_y \Gamma^{-1} [\exp(-\Gamma c) + (r_{mq} + \frac{ik\eta \Gamma s_{mq}}{k_x k_y}) \exp(-2\Gamma d)] = 0, \quad (4)$$

$$B_q \frac{(k^2 - k_y^2) Q_q}{2ika} + \frac{ik_y}{2ka} \sum_m A_m k_x \Gamma^{-1} [\exp(-\Gamma c) + (R_{mq} - \frac{ik\eta \Gamma s_{mq}}{k_x k_y}) \exp(-2\Gamma d)] = 0, \quad (5)$$

where

$$P_m = \sum_q [\exp(-\Gamma c) + R_{mq} \exp(-2\Gamma d)] \Gamma^{-1}, \quad (6)$$

$$Q_q = \sum_m [\exp(-\Gamma c) + r_{mq} \exp(-2\Gamma d)] \Gamma^{-1} \quad (7)$$

$$\Gamma_{mq}(-\Gamma) = (k_x^2 + k_y^2 - k^2)^{1/2}, \quad (8)$$



$$k_x = (2\pi m/a) + kS \cos\phi, \quad (9)$$

$$k_y = (2\pi q/b) + kS \sin\phi, \quad (10)$$

and  $\eta = (\mu_o/\epsilon_o)^{1/2}$ .  $S$ , being a complex quantity, is now defined as  $\gamma/(ik)$ .

The quantities  $R_{mq}$ ,  $r_{mq}$ ,  $S_{mq}$  and  $s_{mq}$  are functions of the half-space parameters  $\sigma_g$  and  $\epsilon_g$ :

$$R_{mq} = \frac{k^2(\Gamma + \hat{\Gamma}K_x)(\Gamma - \hat{\Gamma}\epsilon_r K_x) + (k_x k_y)^2(1-K_x)^2}{k^2(\Gamma + \hat{\Gamma}K_x)(\Gamma + \hat{\Gamma}\epsilon_r K_x) - (k_x k_y)^2(1-K_x)^2}, \quad (11)$$

$$r_{mq} = \frac{k^2(\Gamma + \hat{\Gamma}K_y)(\Gamma - \hat{\Gamma}\epsilon_r K_y) + (k_x k_y)^2(1-K_y)^2}{k^2(\Gamma + \hat{\Gamma}K_y)(\Gamma + \hat{\Gamma}\epsilon_r K_y) - (k_x k_y)^2(1-K_y)^2}, \quad (12)$$

$$S_{mq} = \frac{-2ik_x k_y \Gamma(1-K_x)/\eta}{k^2(\Gamma + \hat{\Gamma}K_x)(\Gamma + \hat{\Gamma}\epsilon_r K_x) - (k_x k_y)^2(1-K_x)^2}, \quad (13)$$

$$s_{mq} = \frac{2ik_x k_y \Gamma(1-K_y)/\eta}{k^2(\Gamma + \hat{\Gamma}K_y)(\Gamma + \hat{\Gamma}\epsilon_r K_y) - (k_x k_y)^2(1-K_y)^2}, \quad (14)$$

where

$$K_x = (k^2 - k_x^2)/(k_g^2 - k_x^2),$$

$$K_y = (k^2 - k_y^2)/(k_g^2 - k_y^2),$$

$$\hat{\Gamma} = (k_x^2 + k_y^2 - k_g^2)^{1/2},$$

$$k_g^2 = k^2 \epsilon_r,$$

$$\epsilon_r = (\sigma_g + i\omega\epsilon_g)/(i\omega\epsilon_o).$$

For two special cases, we note that (11) - (14) simplify considerably.

When the half space vanishes (i.e.  $\epsilon_r = 1$ ), we have  $R_{mq} = r_{mq} = S_{mq} = s_{mq} = 0$

which is the free space result [Hill and Wait, 1977b]. When the half space

is perfectly conducting (i.e.  $\sigma_g = \infty$ ), we have  $R_{mq} = r_{mq} = -1$  and

$S_{mq} = s_{mq} = 0$ . By image theory, this is the result for a pair of identical meshes [Hill, 1977].

The summations involving  $\exp(-\Gamma c)$  in (6) and (7) are slowly convergent as they stand. More rapidly convergent forms have been derived for  $P_m$  and  $Q_q$  in the free space case [Hill and Wait, 1977b] and they can be applied here to yield

$$P_m = \frac{b}{\pi} \left\{ -\ln[1 - \exp(-2\pi c/b)] + \Delta_m \right\} + \exp(-\Gamma_{mo} c) \Gamma_{mo}^{-1} + \sum_q R_{mq} \exp(-2\Gamma d) \Gamma^{-1}, \quad (15)$$

$$Q_q = \frac{a}{\pi} \left\{ -\ln[1 - \exp(-2\pi c/a)] + \delta_q \right\} + \exp(-\Gamma_{oq} c) \Gamma_{oq}^{-1} + \sum_m r_{mq} \exp(-2\Gamma d) \Gamma^{-1}, \quad (16)$$

where

$$\Delta_m = \frac{1}{2} \sum_q' \left[ \frac{2\pi}{b} \frac{\exp(-\Gamma c)}{\Gamma} - \frac{\exp(-2\pi|q|c/b)}{|q|} \right] \quad (17)$$

and

$$\delta_q = \frac{1}{2} \sum_m' \left[ \frac{2\pi}{a} \frac{\exp(-\Gamma c)}{\Gamma} - \frac{\exp(-2\pi|m|c/a)}{|m|} \right] \quad (18)$$

The superscripted prime over the summation sign indicates omission of the  $q = 0$  (or  $m = 0$ ) term.

The doubly infinite set of linear equations (4) and (5) for  $A_m$  and  $B_q$  is numerically inefficient in the present form because  $A_m$  and  $B_q$  decay slowly for large  $|m|$  and  $|q|$ . The difficulty arises because the current expansions (1) and (2) are slowly convergent for the discontinuous current that occurs at the wire junctions in bonded meshes. We can circumvent the convergence problem by modifying the current expansions to allow for a jump discontinuity at the origin. The procedure is nearly identical

to that employed for the rectangular bonded mesh in free space [Hill and Wait, 1977b]. Thus the Fourier coefficients of the current  $A_m$  and  $B_q$  are rewritten

$$A_m = A'_m + \Delta(1-\delta_{m0})/(2\pi im) \quad (19)$$

and

$$B_q = B'_q - \Delta(1-\delta_{q0})/(2\pi iq) \quad (20)$$

where

$$\delta_{m0} = \begin{cases} 1, & m = 0 \\ 0, & m \neq 0 \end{cases}$$

$A'_m$  and  $B'_q$  are modified current coefficients, and  $\Delta$  is an unknown current discontinuity in  $I_{x0}$  at  $x = 0$ . By substituting (19) and (20) into (4) and (5), we obtain the following equivalent set of linear equations for the modified coefficients:

$$\begin{aligned} A'_m \frac{(k^2 - k_x^2)P_m}{2ikb} + \frac{ik_x}{2ka} \sum_q B'_q k_y \Gamma^{-1} [\exp(-\Gamma c) \\ + \left( r_{mq} + \frac{ik\eta \Gamma s_{mq}}{k_x k_y} \right) \exp(-2\Gamma d)] \\ + \Delta \left\{ \frac{(k^2 - k_x^2)P_m}{2kb} \frac{(\delta_{m0} - 1)}{2\pi m} - \frac{k_x}{2ka} \left[ \frac{P'_m}{b} + \frac{kS \sin \phi}{2\pi} P_{1m} \right] \right\} = 0 \end{aligned} \quad (21)$$

$$\begin{aligned} B'_q \frac{(k^2 - k_y^2)Q_q}{2ika} + \frac{iky}{2ka} \sum_m A'_m k_x \Gamma^{-1} [\exp(-\Gamma c) \\ + \left( R_{mq} - \frac{ik\eta \Gamma s_{mq}}{k_x k_y} \right) \exp(-2\Gamma d)] \\ + \Delta \left\{ \frac{(k^2 - k_y^2)Q_q}{2ka} \frac{(1 - \delta_{q0})}{2\pi q} + \frac{k_y}{2kb} \left[ \frac{Q'_q}{a} + \frac{kS \cos \phi}{2\pi} Q_{1q} \right] \right\} = 0. \end{aligned} \quad (22)$$

where

$$P_{1m} = \sum_q' \left[ \exp(-\Gamma c) + \left( r_{mq} + \frac{ik\eta\Gamma s_{mq}}{k_x k_y} \right) \exp(-2\Gamma d) \right] / (q\Gamma) , \quad (23)$$

$$P_m' = \frac{b}{\pi} \left\{ -\ln[1 - \exp(-2\pi c/b)] + \Delta_m \right\} + \sum_q' \left( r_{mq} + \frac{ik\eta\Gamma s_{mq}}{k_x k_y} \right) \exp(-2\Gamma d) \Gamma^{-1} , \quad (24)$$

$$Q_{1q} = \sum_m' \left[ \exp(-\Gamma c) + \left( R_{mq} - \frac{ik\eta\Gamma s_{mq}}{k_x k_y} \right) \exp(-2\Gamma d) \right] / (m\Gamma) , \quad (25)$$

and

$$Q_q' = \frac{a}{\pi} \left\{ -\ln[1 - \exp(-2\pi c/a)] + \delta_q \right\} + \sum_m' \left( R_{mq} - \frac{ik\eta\Gamma s_{mq}}{k_x k_y} \right) \exp(-2\Gamma d) \Gamma^{-1} \quad (26)$$

Again the superscript prime on the summation indicates omission of the  $q = 0$  (or  $m = 0$ ) term. Note that by setting  $\Delta$  equal to zero in (21) and (22), we could retrieve (4) and (5).

Since we have introduced an additional unknown  $\Delta$ , another equation is required to have an equal number of equations and unknowns ( $A_m'$ ,  $B_q'$ , and  $\Delta$ ). The following equation can be obtained from charge continuity at the junctions [Hill and Wait, 1977b]:

$$-\frac{\Delta}{2\pi} \left( 1 + \frac{b}{a} \right) + \sum_m' A_m' \left( 1 + \frac{b}{a} + \frac{ikSb}{2\pi} \cos\phi \right) - \sum_q' B_q' \left( 1 + \frac{ikSb}{2\pi} \sin\phi \right) = 0 \quad (27)$$

**Δ:**

$$\begin{bmatrix} \text{T X T} \\ \text{coefficient} \\ \text{matrix} \end{bmatrix} = \begin{bmatrix} A_{-M} \\ \vdots \\ A_0 \\ \vdots \\ A_M \\ \vdots \\ B_{-Q} \\ \vdots \\ B_0 \\ \vdots \\ B_Q \\ \vdots \\ \Delta \end{bmatrix}$$

A nontrivial solution to (26) exists only if the determinant, which is a function of  $S(-\gamma/ik)$ , vanishes. Thus the mode equation to be solved for  $S$  is:

T X T  
coefficient - 0  
matrix

The above equation has been programmed and solved numerically for  $S$  by Newton's method.

## NUMERICAL RESULTS

Convergence of the mode equation (29) was examined by increasing  $M$  and  $Q$  until the value of  $S(=\gamma/ik)$  did not change significantly. The most rapid convergence was obtained by making  $M = Q$  for  $a/b$  ratios from 1 to 3. For the cases considered here, convergence was obtained for  $M = Q = 2$  ( $T=11$ ), and all results shown here were computed for  $M = Q = 2$ . The required determinant calculation is fairly rapid for the resultant  $11 \times 11$  matrix. The matrix fill time dominates the determinant calculation time for such cases.

In Fig. 2, we illustrate the  $\phi$  dependence of  $\text{Re}(S)$  for several  $a/b$  ratios. Note that for the mesh in free space,  $\text{Re}(S)$  is always greater than one (slow wave). For the half space environment where  $S$  is complex, this is not always so. The relative dielectric constant  $\epsilon_r = 10 - i1.8$  would correspond to a ground conductivity  $\sigma_g = 10^{-2}$  mho/m and relative permittivity  $\epsilon_g/\epsilon_0 = 10$  at a frequency of 100 MHz. The lack of  $\phi$  dependence for  $a/b = 1$  is to be expected for square bonded meshes which are electrically small (e.g.  $b/\lambda = 0.05$ ). When a preferred direction of propagation exists, a rectangular mesh (i.e. where  $a \neq b$ ) can be useful, and a 3 to 1 mesh has been used in some EMP simulator applications [Baum, 1972; Kehrner and Baum, 1975]. Note that  $\text{Re}(S)$  is closer to unity at  $\phi = 0^\circ$  for the rectangular mesh, but that the  $\phi$  dependence is quite strong. A value of  $c/b = 10^{-2}$  has been used in all calculations shown here, but the results are only weakly dependent on the wire radius  $c$ .

For the same parameters, in Fig. 3 we illustrate the  $\phi$  dependence of  $\text{Im}(S)$  for three  $a/b$  ratios. The actual attenuation rate  $\alpha$  is determined from  $S$  by

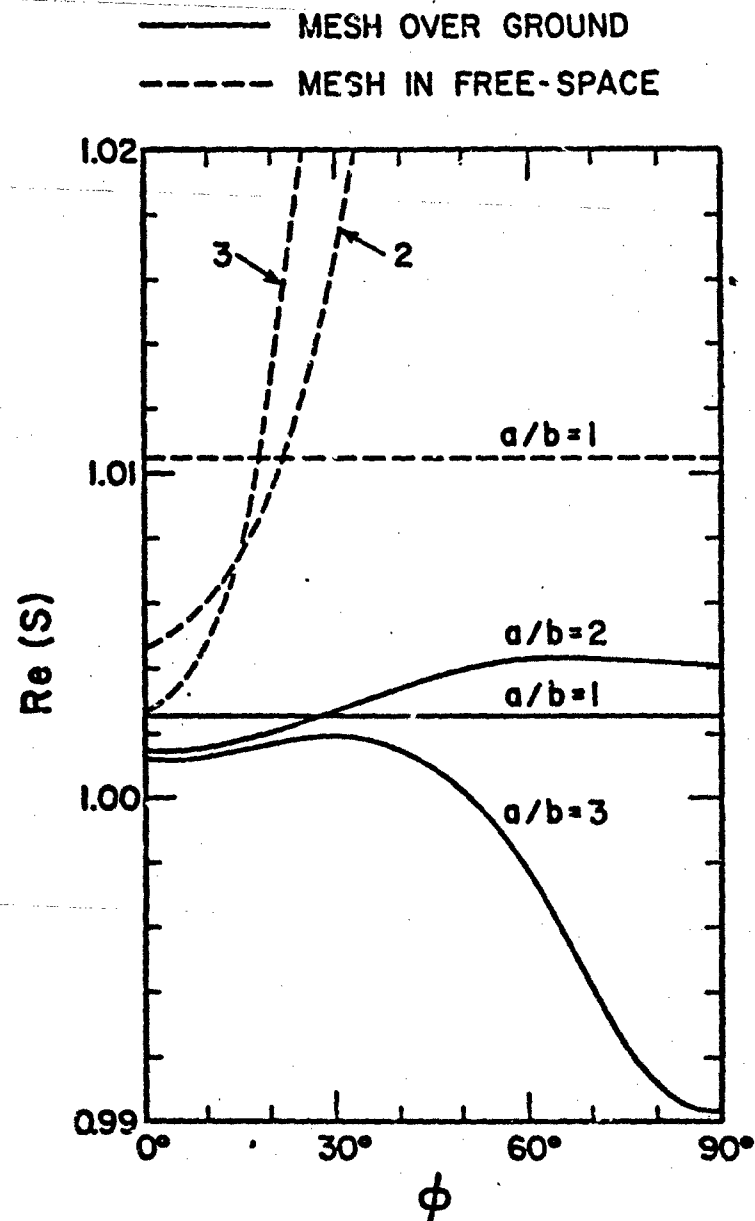


Figure 2. Real part of the normalized propagation constant  $S$  as a function of propagation direction  $\phi$ .  
 Parameters:  $c/b = 10^{-2}$ ,  $d/b = 10^{-1}$ ,  $b/\lambda = 0.05$ ,  
 $\epsilon_r = 10 = 11.8$ .

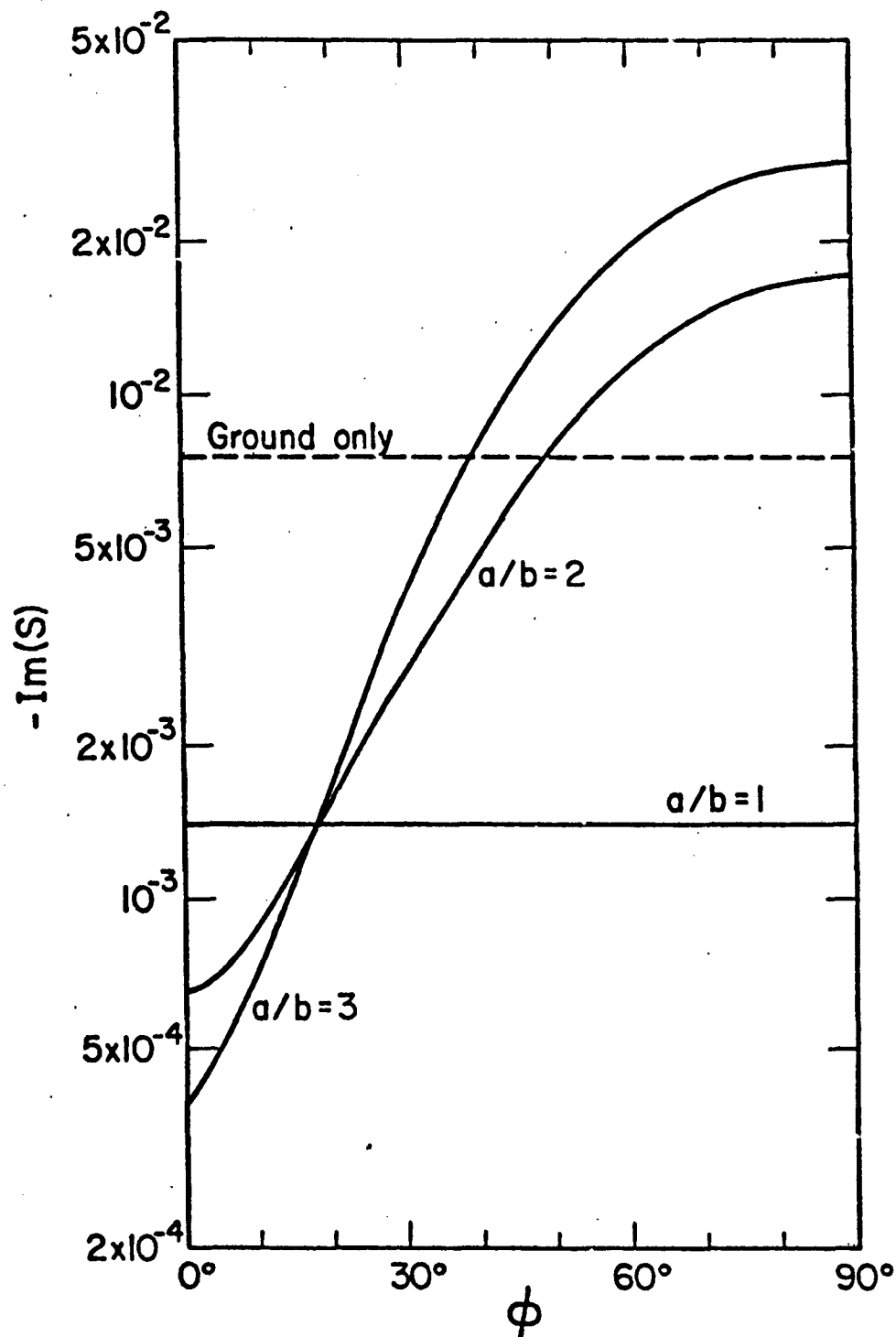


Figure 3. Imaginary part of the normalized propagation constant  $S$  as a function of direction  $\phi$ .



$$\alpha = \text{Re}(\gamma) = -k \text{Im}(S) \text{ (nepers/m)} . \quad (30)$$

No results are shown for the free space comparison because the free space mesh is lossless ( $S$  real). As expected, the square mesh is again isotropic, and the rectangular mesh is highly anisotropic. Also, the attenuation rate is lowest when propagating in the direction of the more closely spaced wires ( $\phi=0^\circ$ ). For comparison, the result for the Zenneck surface wave of the isolated half space is shown. It is computed from [Wait, 1962a; Banos, 1966]:

$$S = [\epsilon_r / (\epsilon_r + 1)]^{1/2} \quad (31)$$

For  $\epsilon_r = 10 - 11.8$ ,  $S$  is approximately 0.9547 - 10.0076. Note the large reduction in attenuation at  $\phi = 0^\circ$  due to the mesh.

In Table 1, we illustrate the dependence of  $S$  on  $b/\lambda$  and  $d/b$  for  $\phi = 0^\circ$ . As before,  $\epsilon_r = 10 - 11.8$  and  $c/b = 10^{-2}$ . Note that the attenuation rate decreases as  $d/b$  is increased from 0.1 to 0.3. This is expected because ground screen performance generally improves as the screen is slightly elevated [Wait, 1962b]. The results for  $d/b = \infty$  are those of the mesh in free space [Hill and Wait, 1977b]. The variation of  $S$  is not necessarily monotonic as  $d/b$  is increased from 0.1 to  $\infty$ . Also note the large increase in both the real and imaginary parts of  $S$  as  $b/\lambda$  is increased from 0.05 to 0.1, particularly for the square mesh.

#### CONCLUDING REMARKS

A general mode equation has been derived for propagation along a bonded rectangular mesh over a lossy earth. The mode equation has been solved numerically for the dominant surface wave mode. This mode suffers attenuation due to the losses in the earth, and for most cases is a slow wave

TABLE 1

Normalized Complex Propagation Constant,  $S$  ( $\epsilon_r = 10 - j1.8$ ,  $c/b = 10^{-2}$ ,  $\phi = 0^\circ$ )

a/b	b/ $\lambda$	d/b	S
1.0	0.05	0.1	1.002485 - j0.001396
"	"	0.3	1.002247 - j0.001161
"	"	1.0	1.002290 - j0.001200
"	"	100.0	1.010513 - j0.000002
"	"	$\infty$	1.010515 - j0.0
"	0.1	0.1	1.510056 - j0.518362
"	"	0.3	1.278652 - j0.338335
"	"	1.0	1.114107 - j0.150493
"	"	100.0	1.038768 - j0.0
"	"	$\infty$	1.038768 - j0.0
3.0	0.05	0.1	1.001114 - j0.000399
"	"	0.3	1.000731 - j0.000197
"	"	1.0	1.000673 - j0.000170
"	"	100.0	1.002683 - j0.000026
"	"	$\infty$	1.002731 - j0.0
"	0.1	0.1	1.003560 - j0.003103
"	"	0.3	1.002708 - j0.001680
"	"	1.0	1.002608 - j0.001471
"	"	100.0	1.010828 - j0.0
"	"	$\infty$	1.010828 - j0.0

(i.e.  $\text{Re}(S) > 1$ ). This is in contrast to the fast surface wave for the lossy earth without a ground screen. For a sufficiently small mesh size, the attenuation rate of the surface wave is considerably less than for the isolated half-space. However, for mesh sizes of  $0.1\lambda$  or greater, the attenuation reduction is not significant and, in fact, the attenuation rate can even increase. For the rectangular mesh ( $a \neq b$ ), the propagation constant is highly dependent on the direction of propagation, and minimum attenuation is obtained for propagation along the more closely spaced wires.

Several extensions to this work would seem worthwhile. The approximate method of averaged boundary conditions which has been applied to single meshes [Astrakhan, 1968] and a pair of meshes [Kontorovich et al., 1964] in free space could be extended to the lossy half-space geometry. Casey [1976] has recently applied this method to a square bonded mesh located at an air-dielectric interface. Since the unbonded mesh has superior reflecting properties [Kontorovich et al., 1962; Hill and Wait, 1976], it could also be analyzed for surface wave propagation in the presence of a lossy half-space. Finally a thorough numerical search for all the modes could be made for the mesh-earth structure. We have examined the expected surface wave mode, but others may be possible. Solution of a source problem (such as vertical dipole excitation) would be useful in assessing the various pole (surface wave, etc.) and branch cut (continuous spectrum) contributions to the total field.

## REFERENCES

- Astrakhan, M.I. (1968), Reflecting and screening properties of plane wire grids, *Telecom. Radio Engr.*, 23, 76-83.
- Banos, A. (1966), *Dipole Radiation in the Presence of a Conducting Half-Space*, Sec. 2.64, Pergamon Press, Oxford.
- Baum, C.E. (1972), General principles for the design of Atlas I and II, Part I: Atlas: Electromagnetic design considerations for horizontal version, Sensor and Simulation, Note 143, Air Force Weapons Laboratory.
- Casey, K.F. (1976), EMP penetration through advanced composite skin panels, *Interaction Note 315*, Air Force Weapons Laboratory.
- Collin, R.E. (1960), *Field Theory of Guided Waves*, pp. 368-371, McGraw-Hill, New York.
- Hill, D.A. (1977), Electromagnetic wave propagation along a pair of rectangular bonded wire meshes, submitted to *IEEE Trans. Electromag. Compat.*, and Sensor and Simulation Note 250, November 1977.
- Hill, D.A. and J.R. Wait (1974), Electromagnetic scattering of an arbitrary plane wave by two nonintersecting perpendicular wire grids, *Can. J. Phys.*, 52(3), 227-237.
- Hill, D.A. and J.R. Wait (1976), Electromagnetic scattering of an arbitrary plane wave by a wire mesh with bonded junctions, *Can. J. Phys.*, 54(4), 353-361., and Section II of Sensor and Simulation Note 231, June 1977.
- Hill, D.A. and J.R. Wait (1977a), Electromagnetic surface wave propagation over a bonded wire mesh, *IEEE Trans. Electromag. Compat.*, EMC-19, 2-7.
- Hill, D.A. and J.R. Wait (1977b), Electromagnetic surface wave propagation over a rectangular bonded wire mesh, submitted to *IEEE Trans. Electromag. Compat.*, and Sensor and Simulation Note 249, October 1977.

- Kehrer, W.S. and C.E. Baum (1975), Electromagnetic design parameters for Athamas II, *Athamas Memo 4, Air Force Weapons Laboratory*.
- Kontorovich, M.I., V.P.Yu. Petrunkin, N.A. Yesepkina, M.I. Astrakhan (1962), The coefficient of reflection of a plane electromagnetic wave from a plane wire mesh, *Radio Eng. Electron. Phys. (USSR)*, 7(2), 222-231.
- Kontorovich, M.I., M.I. Astrakhan, M.N. Spirina (1964), Slowing down of electromagnetic waves by wire meshes, *Radio Engr. Electron. Phys. (USSR)*, 9, 1242-1245.
- Otteni, G.A. (1973), Plane wave reflection from a rectangular mesh ground screen, *IEEE Trans. Antennas Propagat.*, AP-21(6), 843-851.
- Ulrich, R. and M. Tacke (1973), Submillimeter waveguiding on periodic metal structure, *Appl. Phys. Lett.*, 22(5), 251-253.
- Wait, J.R. (1962a), *Electromagnetic Waves in Stratified Media*, Chap. 2, Pergamon Press, Oxford [2nd edition, 1970].
- Wait, J.R. (1962b), Effective impedance of a wire grid parallel to the earth's surface, *IRE Trans. Antennas Propagat.*, AP-10(5), 538-542.
- Wait, J.R. and D.A. Hill (1976), Electromagnetic scattering by two perpendicular wire grids over a conducting half-space, *Radio Sci.*, 11(8,9), 725-730., and Section IV of Sensor and Simulation Note 231, June 1977.

EQUIVALENT ELECTROMAGNETIC PROPERTIES  
OF A CONCENTRIC WIRE CAGE  
AS COMPARED TO A CIRCULAR CYLINDER

ABSTRACT

The electromagnetic equivalence of an infinitely long loaded wire-cage structure and loaded hollow cylindrical geometry is established based on the same radiated fields under identical conditions. Analysis of the canonical infinitely long loaded wire geometries are given by treatment as boundary-value antenna problems. An expression for the equivalent radius of the wire cage and an equivalent impedance-loading function are obtained, including frequency dependence.

## I. INTRODUCTION

The electromagnetic equivalence of radiating objects has been a subject of study for a long time by many investigators.<sup>1-3</sup> This yields a simple equivalence corresponding to a complex radiating structure based on a predefined electromagnetic equivalence criterion. The question of equivalence criterion may be defined according to the same total radiated fields, or the same total current induced, or even the same effective impedance(s) of the geometries under equivalence study. There does not appear as yet to be a unique equivalence criterion one may establish; it entirely depends on the specific need and its application. In this paper, the field radiated by the structure is taken as the basis for comparison and for establishing electromagnetic equivalence.

Even though the question of electromagnetic equivalence is basic in nature, the motivation for the present investigation is to come up with suitable modeling for hybrid EMP simulators.<sup>4</sup> In figures 1.1 and 1.2 are shown examples of wire cage hybrid simulators with complex bicone feed structures.<sup>5,6</sup> A straightforward analysis in a given frequency spectrum is quite complicated. Hence a systematic modeling of the conical feed and generator, wire cage hybrid simulator, and the transition region between the conical feed and the simulator is required.<sup>7</sup>

This note is primarily concerned with the development of a theory for equivalent electromagnetic properties of a wire cage as compared to a hollow conducting cylinder. Wire cage structures have been extensively used in the design of hybrid simulators<sup>5,6</sup> from the practical standpoint of lower structural weight, lower wind resistance, ease of construction and erection at the experimental sites. The exact analysis of the wire cage hybrid simulator is very complicated; one has to suitably model it to simplify the analysis. The reader should note that the wire cage by itself is inadequate to model a hybrid simulator since certain parts of it involve conducting conical, cylindrical, and other transition sections which are physically quite different from a wire cage (and desirably so, for improved performance).

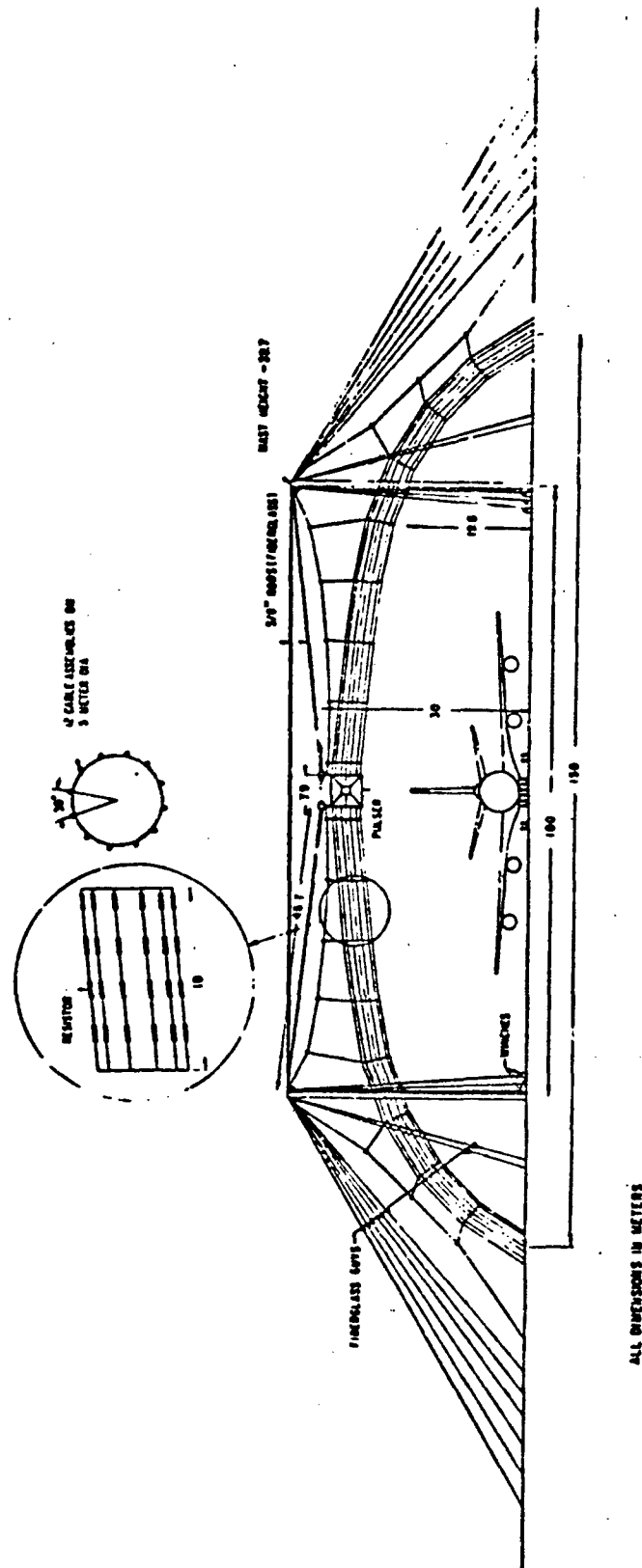


Figure 1.1. Sketch of the ATHAMAS I Simulator Facility at Kirtland AFB, New Mexico



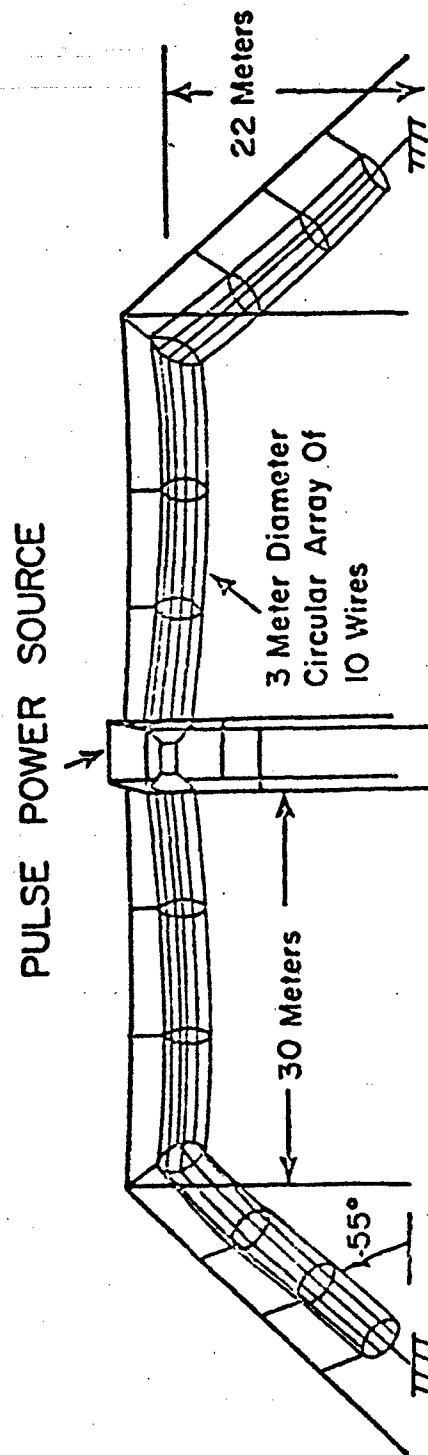


Figure 1.2. Illustration of the Achilles II EMP Simulator Facility, Kirtland AFB, New Mexico

The subject of electromagnetic equivalences as applied to wire cage models is previously studied by Schelkunoff,<sup>1</sup> King,<sup>2</sup> and also recently by Baum,<sup>3</sup> to obtain an equivalent radius. The results obtained<sup>1-3</sup> are in principle applicable to only perfectly conducting wire cages in the limit as frequency approaches zero. In one study<sup>1</sup> a cage consisting of conical wires equally spaced over the surface of a bicone is studied, and compared with respect to a solid cone of same characteristic impedance so that there is only a transmission line mode excited. In the limit as the cone angle becomes small, the result of the effective radius of the cage is the same as the one obtained in reference 3 which is based on conformal transformation; an equivalence between a single charged conductor and a number of equally spaced concentric charged conductors is thereby derived in the static case. A different approach is studied in reference 2 wherein a cage antenna consisting of closely spaced parallel and identical conductors placed around a circle is compared with respect to a single conductor antenna, so that the total axial assumed current distribution is approximately the same in both cases.

This note considers various, but comparatively more accurate, alternative analyses of the impedance loaded, infinitely long cylindrical models which can be used as substitutes to the complex wire cage structure having the same electromagnetic field properties. The question of electromagnetic equivalence of wire cages (both circular cylindrical and circular conical) used in hybrid (and other) simulators as compared to a cylindrical solid wire, a cylindrical cage of strips, or a hollow circular cylinder with complex impedance loading functions is investigated in a larger perspective, based on the detailed analysis of the infinitely long canonical geometries with uniformly loaded impedance functions, treated as boundary value problems. These in general fit into the category of boundary connection supermatrices<sup>8</sup> for the radiated fields.

## II. ANALYSIS OF INFINITELY LONG CANONICAL THIN WIRE ANTENNA GEOMETRIES

An analysis for electromagnetic radiation by two-dimensional uniformly loaded structures is treated as a boundary value problem. The following antenna geometries are considered below:

1. Infinitely long loaded wire antenna (thin)
2. Infinitely long loaded wire cage antenna and its special case of an infinitely long loaded circular cylindrical wire cage antenna
3. Infinitely long loaded hollow circular cylindrical antenna

Integral expressions are derived for the current induced and the corresponding fields radiated for the above canonical problems. Using saddle point integration, the electric and the magnetic far fields and the asymptotic solution for the induced current are evaluated.

### A. Infinitely Long Loaded Wire Antenna

An infinitely long thin wire is oriented along the  $z$  axis in a free space isotropic homogeneous medium. The radius of the cross section of the wire is  $b$  and it is excited by a source generator of voltage  $\tilde{V}(s)$  across a gap of width  $2d$  centered at  $z = 0$  as shown in figure 2.1. The electric and the magnetic fields radiated into the surrounding medium are calculated from the induced electric current  $\tilde{I}(z, s)$  on the wire, which can be obtained by solving the boundary value problem<sup>9</sup> and enforcing the impedance boundary condition on the surface of the wire. Due to the symmetry of the problem and nature of excitation, the radiated electric field  $\tilde{E}(\psi, z, s)$  and magnetic field  $\tilde{H}(\psi, z, s)$  are obtained by

$$\begin{bmatrix} \tilde{E}(\psi, z, s) \\ \tilde{H}(\psi, z, s) \end{bmatrix} = \frac{1}{2\pi j} \int_C \begin{bmatrix} \tilde{E}(\psi, \zeta, s) \\ \tilde{H}(\psi, \zeta, s) \end{bmatrix} \cdot e^{\zeta z} d\zeta \quad (2.1)$$

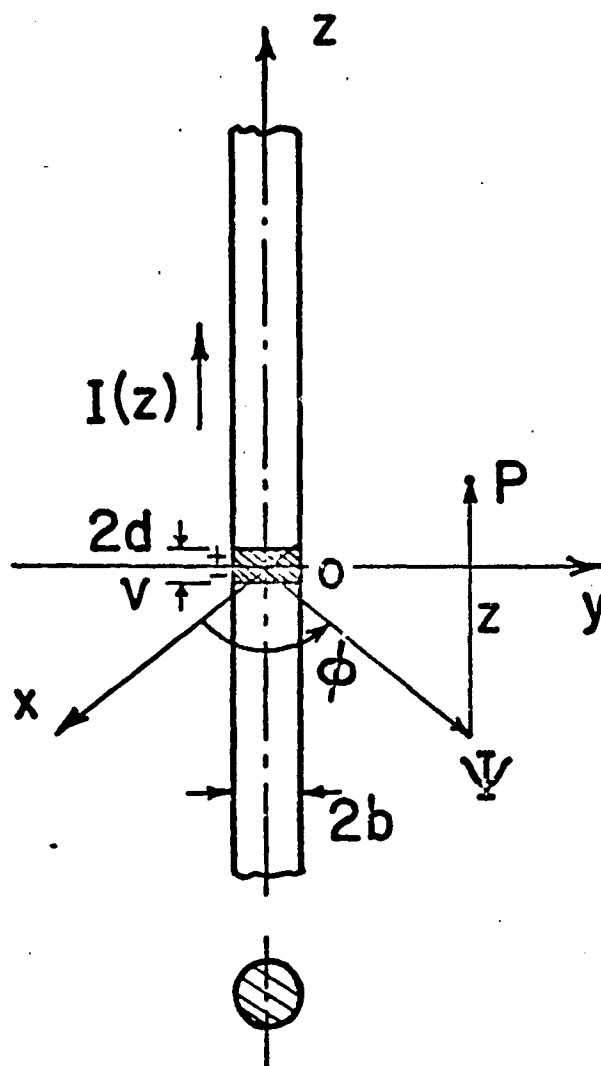


Figure 2.1. Infinitely Long Thin Solid Wire Antenna

where  $\tilde{E}(\Psi, \zeta, s)$  and  $\tilde{H}(\Psi, \zeta, s)$  are the spectral distributions of the corresponding electric and magnetic fields.

In the present analysis, the following Laplace-transform definitions (two-sided) are followed for the time variable  $t$  and the space coordinate variable  $z$ ,

$$\begin{array}{ccc} (t, z) & \xleftrightarrow[\text{Transform}]{} & (s, \zeta) \\ F_1(t) & & \tilde{F}_1(s) \\ F_2(z) & & \tilde{F}_2(\zeta) \\ F_3(t, z) & & \tilde{F}_3(s, \zeta) \end{array}$$

$$\tilde{F}_1(s) = \int_{-\infty}^{\infty} F_1(t) e^{-st} dt \quad (2.2a)$$

$$\tilde{F}_2(\zeta) = \int_{-\infty}^{\infty} F_2(z) e^{-\zeta z} dz \quad (2.2b)$$

which have the corresponding inverse Laplace transforms

$$F_1(t) = \frac{1}{2\pi j} \int_{C_\gamma} \tilde{F}_1(s) e^{st} ds \quad (2.2c)$$

$$F_2(z) = \frac{1}{2\pi j} \int_{C_\zeta} \tilde{F}_2(\zeta) e^{\zeta z} d\zeta \quad (2.2d)$$

where  $C_\gamma$  and  $C_\zeta$  are the contours of integration in the  $s$ - and  $\zeta$ -complex planes as shown in figure 2.2.

At any point P, there exists only the  $z$ -component of the magnetic vector potential,<sup>9,11</sup>

$$\tilde{A}_z(\Psi, z, s) = \frac{1}{2\pi j} \int_{C_\zeta} \tilde{F}(b, \zeta, s) K_0(u\Psi) e^{\zeta z} d\zeta \quad (2.3)$$

from which the radiated electric and the magnetic fields can be obtained as

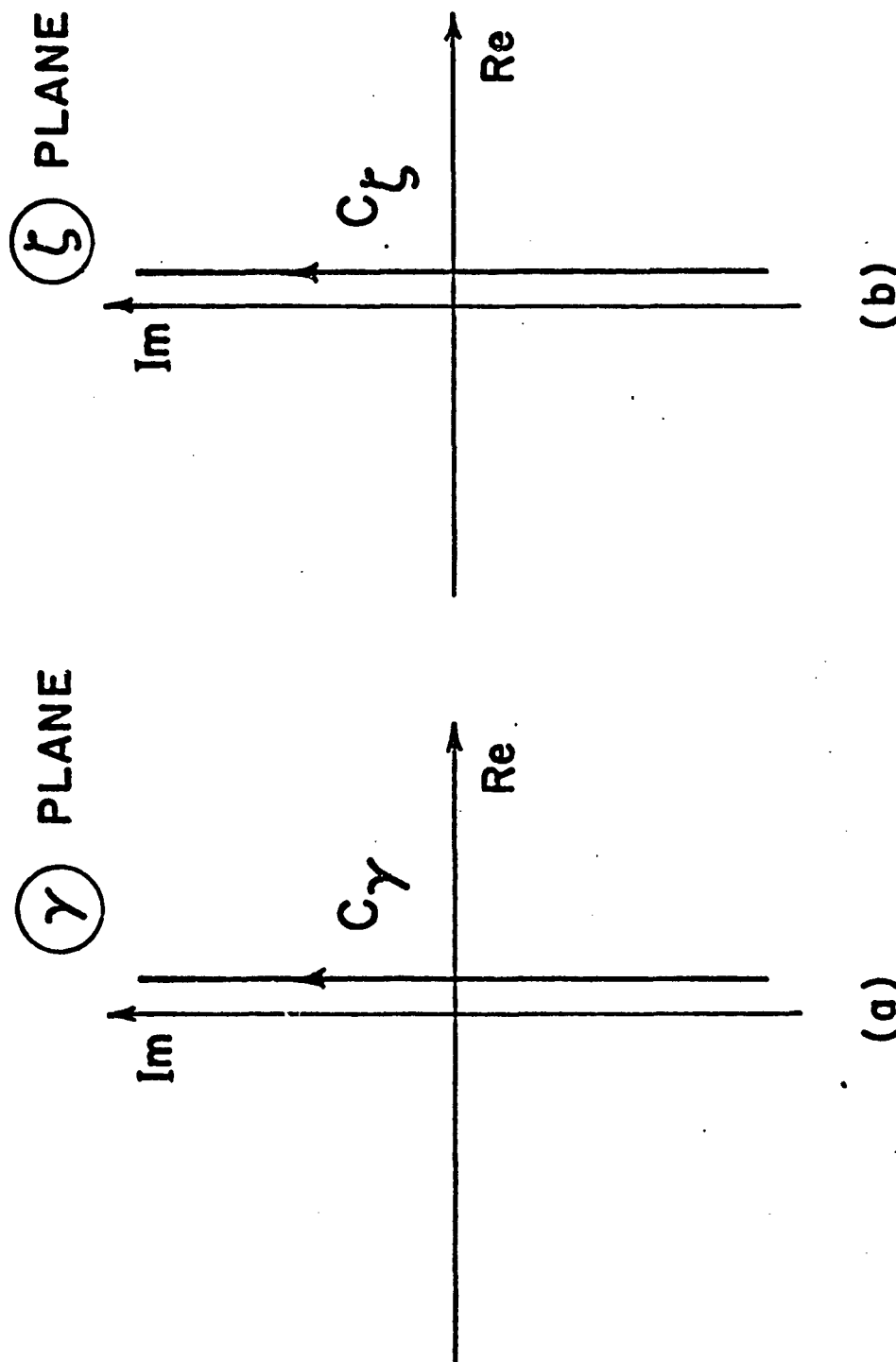


Figure 2.2(a). Integration Contour  $C_\gamma$  in the Complex  $\gamma$  Plane

Figure 2.2(b). Integration Contour  $C_\zeta$  in the Complex  $\zeta$  Plane

$$\tilde{E}(\psi, z, s) = \left[ \frac{s}{\gamma^2} \left( \frac{\partial^2}{\partial z^2} - \gamma^2 \right) \tilde{I}_z + \frac{s}{\gamma^2} \frac{\partial^2}{\partial \psi \partial z} \tilde{I}_\psi \right] \tilde{A}_z(\psi, z, s) \quad (2.4a)$$

$$\tilde{H}(\psi, z, s) = - \frac{1}{\mu} \frac{\partial}{\partial \psi} \tilde{A}_z(\psi, z, s) \tilde{I}_\phi \quad (2.4b)$$

In the expression (2.3),

$$u = [\gamma^2 - \zeta^2]^{\frac{1}{2}} \quad (2.5a)$$

and the cylindrical radial coordinate

$$\psi = [x^2 + y^2]^{\frac{1}{2}} \quad (2.5b)$$

$K_0$  is the modified Bessel function of the second kind, zero order, and the propagation constant is

$$\gamma = [s\mu(\sigma + s\epsilon)]^{\frac{1}{2}} \quad (2.5c)$$

$$= jK \quad (2.5d)$$

where  $\mu$ ,  $\epsilon$ , and  $\sigma$  are the permeability, permittivity, and the conductivity of the homogeneous medium. The spectral term  $\tilde{F}(b, \zeta, s)$  in the expression (2.3), is the term proportional to the Laplace transform of the induced electric current  $\tilde{I}(z, s)$  on the infinitely long wire. In the above spectral representation, an  $e^{st+\zeta z}$  field variation is assumed,  $s$  being the two-sided Laplace transform variable. The infinitely long wire is sufficiently thin to satisfy

$$|\gamma b| \ll 1 \quad (2.6)$$

so that no internal modes are excited.

The spectral term  $\tilde{F}(b, \zeta, s)$  is to be determined based on enforcing the following impedance boundary relationship for the tangential total electric field on the surface of the wire. The infinitely long wire is excited by an ideal source generator of

voltage  $\tilde{V}(s)$  across a gap of width  $2d$ . Within the gap the  $z$  component of the electric field is specified to have the variation  $-\tilde{V}(s)/2d$ . Hence, on the surface of the infinitely long thin wire, the induced electric current  $\tilde{I}(b,z,s)$  and the electric field  $\tilde{E}_z(b,z,s)$  should satisfy,<sup>9</sup>

$$\tilde{E}_z(b,z,s) = \left( -\frac{\tilde{V}(s)}{2d} \right) p_d(z) + \tilde{Z}'_w(s) \tilde{I}(b,z,s) \quad (2.7)$$

where

$$\begin{aligned} p_d(z) &= 1, & |z| < d \\ &= 0, & |z| > d \end{aligned}$$

In the above expression,  $\tilde{Z}'_w(s)$  is the series axial impedance per unit length of the infinitely long loaded wire. In this analysis, the impedance function  $\tilde{Z}'_w(s)$  has the definition of impedance per unit length which is the ratio of the tangential electric field to the total current along the axial direction. This impedance function includes a contribution due to the lossy characteristics of the wire in addition to the externally introduced loading terms. Depending on the cross section of the wire geometry, complex  $s$  dependence may arise at very high frequencies. In Appendix A, the series impedance  $\tilde{Z}'_w(s)$  per unit length is discussed for certain geometries. However, with large external loading, the contribution due to lossy material of the wire can be ignored for all practical purposes.

In terms of the transformed spectral quantities, the boundary relationship (2.7) becomes, with the following source function expansion,<sup>9</sup>

$$\left( \frac{\tilde{V}(s)}{2d} \right) p_d(z) = \frac{\tilde{V}(s)}{2\pi j} \int_{C_\zeta} G(\zeta) e^{\zeta z} d\zeta \quad (2.8a)$$

$$G(\zeta) = \frac{\sinh(\zeta d)}{(\zeta d)} \quad (2.8b)$$

$$\rightarrow 1, \text{ as } |\zeta d| \rightarrow 0$$



and hence,

$$\tilde{E}_z(b, \zeta, s) = -\tilde{V}(s) \tilde{G}(\zeta) + \tilde{Z}'_w(s) \tilde{I}(b, \zeta, s) \quad (2.9)$$

According to the expressions (2.1), (2.2d), (2.3), and (2.4a), the z component of the spectral electric field is

$$\tilde{E}_z(\psi, \zeta, s) = -\frac{s}{\gamma} u^2 K_0(u\psi) \tilde{F}(b, \zeta, s) \quad (2.10)$$

The induced electric current along the infinitely long wire is obtained as a line integral of the  $\phi$  component of the magnetic field (2.4b) evaluated just outside the surface of the infinitely long wire,

$$\tilde{I}(b, z, s) = -\frac{1}{\mu} \int_{\phi=0}^{2\pi} \left[ \psi \frac{\partial \tilde{A}_z(\psi, z, s)}{\partial \psi} \right] \bigg|_{\psi=b} d\phi \quad (2.11)$$

The electric current has no  $\phi$ -angular variation, and using the expressions (2.1), (2.2d), (2.3), and (2.4b), the spectral distribution of the electric current is

$$\tilde{I}(b, \zeta, s) = \frac{1}{\mu} 2\pi b u K_1(ub) \tilde{F}(b, \zeta, s) \quad (2.12)$$

where  $K_1$  is the modified Bessel function of second kind, first order. As pointed out earlier, the term  $\tilde{F}(b, \zeta, s)$  is proportional to the transform of the electric current.

On substituting the expressions (2.10) and (2.12) into the impedance boundary relationship (2.9), the expression for the spectral term  $\tilde{F}(b, \zeta, s)$  is obtained as,

$$\tilde{F}(b, \zeta, s) = \tilde{V}(s) \frac{\gamma}{s} \frac{\tilde{G}(\zeta)}{u \tilde{D}(\zeta, s)} \quad (2.13a)$$

where

$$\tilde{D}(\zeta, s) = u K_0(ub) + 2\pi b \gamma K_1(ub) \frac{\tilde{Z}'_w(s)}{Z_0} \quad (2.13b)$$

and the characteristic impedance of the medium is

$$Z_0 = \left[ \frac{s\mu}{\sigma + s\epsilon} \right]^{\frac{1}{2}} \quad (2.13c)$$

Hence from the expressions (2.2d), (2.12), and (2.13a), the total induced electric current on the infinitely long loaded wire antenna has the distribution,

$$\tilde{I}(z,s) = \frac{\tilde{V}(s)\gamma b}{jZ_0} \int_{C_\zeta} \underline{G}(\zeta) \frac{K_1(ub)}{\tilde{D}(\zeta,s)} e^{\zeta z} d\zeta \quad (2.14)$$

In fact one can verify the expression (2.14) for the special case of a perfectly conducting,  $\tilde{Z}'_w(s) = 0$ , solid cylindrical antenna. Assuming the source to be an ideal slice generator, the electric current on a thin solid perfectly conducting infinitely long antenna<sup>12,13</sup> is given by,

$$\begin{aligned} \tilde{I}^{pc}(z,s) &= \tilde{I}(z,s) \Big|_{\tilde{Z}'_w(s)=0} \\ &= \frac{\tilde{V}(s)\gamma b}{jZ_0} \int_{C_\zeta} \frac{K_1(ub)}{uK_0(ub)} e^{\zeta z} d\zeta \end{aligned} \quad (2.15)$$

Since  $\tilde{F}(b,\zeta,s)$  is known from the expression (2.13a), the  $z$  component of the magnetic vector potential defined in (1.3) takes the form

$$\tilde{A}_z(\psi,z,s) = \frac{\tilde{V}(s)}{2\pi j} \frac{\gamma^2}{s} \int_{C_\zeta} \underline{G}(\zeta) \frac{K_0(u\psi)}{u\tilde{D}(\zeta,s)} e^{\zeta z} d\zeta \quad (2.16)$$

It is now possible to calculate the electric and the magnetic fields as defined in the expressions (2.1) and (2.4), and using the expression (2.13a), we have the spectral fields

$$\begin{bmatrix} \tilde{E}_z(\psi, \zeta, s) \\ Z_0 \tilde{H}_\phi(\psi, \zeta, s) \end{bmatrix} = \begin{bmatrix} \tilde{M}_1 \\ \tilde{M}_2 \end{bmatrix} \quad (2.17a)$$

where  $[\tilde{M}]$  is a vector for the infinitely long thin wire antenna and represents the spectral distribution of the radiated fields,

$$[\tilde{M}] = \begin{bmatrix} \tilde{M}_1 \\ \tilde{M}_2 \end{bmatrix} \quad (2.17b)$$

where the elements of the above vector are,

$$\tilde{M}_1 = -\tilde{V}(s) \underline{G}(\zeta) \frac{uK_0(u\psi)}{\tilde{D}(\zeta, s)} \quad (2.17c)$$

and

$$\tilde{M}_2 = \tilde{V}(s) \underline{G}(\zeta) \frac{\gamma K_1(u\psi)}{\tilde{D}(\zeta, s)} \quad (2.17d)$$

Due to the symmetry of the structure and its excitation, the fields are independent of  $\phi$ -angular variations. The general solution to the radiated fields (2.1) is difficult by direct analytical methods, where the integration is to be performed along the contour  $C_\zeta$  in the complex  $\zeta$ -plane, figure 2.2.

If the far-field distribution is the quantity of interest, it is possible to obtain explicit expressions for the various field components defined in (2.1). A classical approach is based on the saddle point integration,<sup>13</sup> and using this technique, the radiated far fields of the infinitely long perfectly conducting wire antenna are obtained in reference 14, and are extended to infinitely long loaded wire antenna structures conveniently; a summary of the procedure of the saddle point integration method to obtain far field distribution of the  $\tilde{H}_\phi(\psi, z, s)$  as  $\psi \rightarrow \infty$  is given in Appendix B. Hence asymptotically as  $\psi \rightarrow \infty$ , the integral expression (2.1) reduces to the following forms:

$$\tilde{E}_z(r, \alpha, s) \sim - \frac{\tilde{V}(s)}{2} \frac{\cos \alpha}{\tilde{L}_1(\gamma, \alpha)} \frac{e^{-\gamma r}}{r} \quad (2.18a)$$

$$Z_0 \tilde{H}_\phi(r, \alpha, s) \sim \frac{\tilde{V}(s)}{2} \frac{1}{\tilde{L}_1(\gamma, \alpha)} \frac{e^{-\gamma r}}{r} \quad (2.18b)$$

where  $\alpha = 90 - \theta$  and  $\gamma \tilde{L}_1(\gamma, \alpha)$  is defined in Appendix B and repeated below for future usage

$$\tilde{L}_1(\gamma, \alpha) = \cos(\alpha) K_0(\gamma b \cos \alpha) + \tilde{h}_1(s) K_1(\gamma b \cos \alpha) \quad (2.18c)$$

$$\tilde{h}_1(s) = 2\pi b \frac{\tilde{Z}'_w(s)}{Z_0} \quad (2.18d)$$

In the expressions (2.18),  $r$  and  $\theta = 90 - \alpha$  are the spherical coordinate variables, while  $\alpha$  is the angle measured from  $z = 0$  plane, figure B-1.

In a similar way, it is possible to obtain an asymptotic solution for the total axial current  $\tilde{I}(z, s)$  as given in the expression (2.14) or one can evaluate  $\tilde{H}_\phi(\psi, z, s)$  on the surface of the infinitely long wire in the limit as  $z \rightarrow \infty$ ,<sup>14</sup>

$$\tilde{I}(s) \sim 2\pi b \tilde{H}_\phi(\psi, z, s) \Big|_{\psi=b+} \quad \text{as } z \rightarrow \infty \quad (2.19a)$$

To evaluate  $\tilde{H}_\phi(\psi, z, s)$  on the surface of the wire structure  $\psi = b$  for large values of  $z$ , it is necessary to restrict the radial distance  $r$  and angle  $\alpha$  so that  $b = r \cos(\alpha)$ , and we have  $z = r \sin(\alpha)$ . For  $\alpha = \pi/2$ ,  $z = r$  so that in (2.18c) the arguments of the Bessel function can be replaced by  $\gamma b \cos(\alpha) = \gamma b^2/z$ . Hence the expression (2.19a) yields

$$\tilde{I}(s) \sim \frac{\pi \tilde{V}(s)}{Z_0} \frac{e^{-\gamma z}}{K_0(\gamma b^2/z) + [\tilde{h}_1(s)z/b] K_1(\gamma b^2/z)} \quad \text{as } z \rightarrow \infty \quad (2.19b)$$

As  $z$  takes on larger values,  $\gamma b^2/z$  is very small. The modified Bessel functions can be replaced by their small argument approximation,<sup>15</sup>

$$K_0(z) \approx -\ln \frac{\Gamma z}{2} \quad (2.19c)$$

$$K_1(z) \approx \frac{1}{z} \quad (2.19d)$$

$$\Gamma = 0.5772... \quad (2.19e)$$

and (2.19b) simplifies to

$$\begin{aligned} \tilde{I}(s) &\sim \frac{\pi \tilde{V}(s)}{Z_0} \frac{e^{-\gamma z}}{-\ln(\Gamma \gamma b^2/2z) + [\tilde{h}_1(s)\gamma/b](z/\gamma b)^2} \\ &= \frac{\pi \tilde{V}(s)}{Z_0} \frac{e^{-\gamma z}}{-\ln(\Gamma \gamma b^2/2z) + 2\pi[\tilde{Z}'_w(s)/Z_0](z/\gamma b)^2} \end{aligned} \quad (2.19f)$$

as  $z \rightarrow \infty$

#### B. Numerical Results: Far Field

The infinitely long thin-wire loaded antenna has been analyzed in the previous section, and the integral expressions for the induced electric current, and the radiated electric and magnetic fields have been derived. The reader may refer to references 16 and 17 for further discussion and solution of the integral expression (2.15) for the induced electric current. As stated earlier, direct analytical solutions for the radiated fields, expressions (2.1) and (2.17), are complex unless one resorts to numerical techniques.<sup>18</sup> Further, based on the saddle point method, explicit expressions (2.18a, b) have been obtained in the far-field region for the radiated fields.

In figures 2.3 through 2.6 are shown the numerical results of the distribution of the radiated far fields. These are appropriately normalized with respect to  $(e^{-\gamma r}/r)$  and  $\tilde{V}(s) = 1$  is

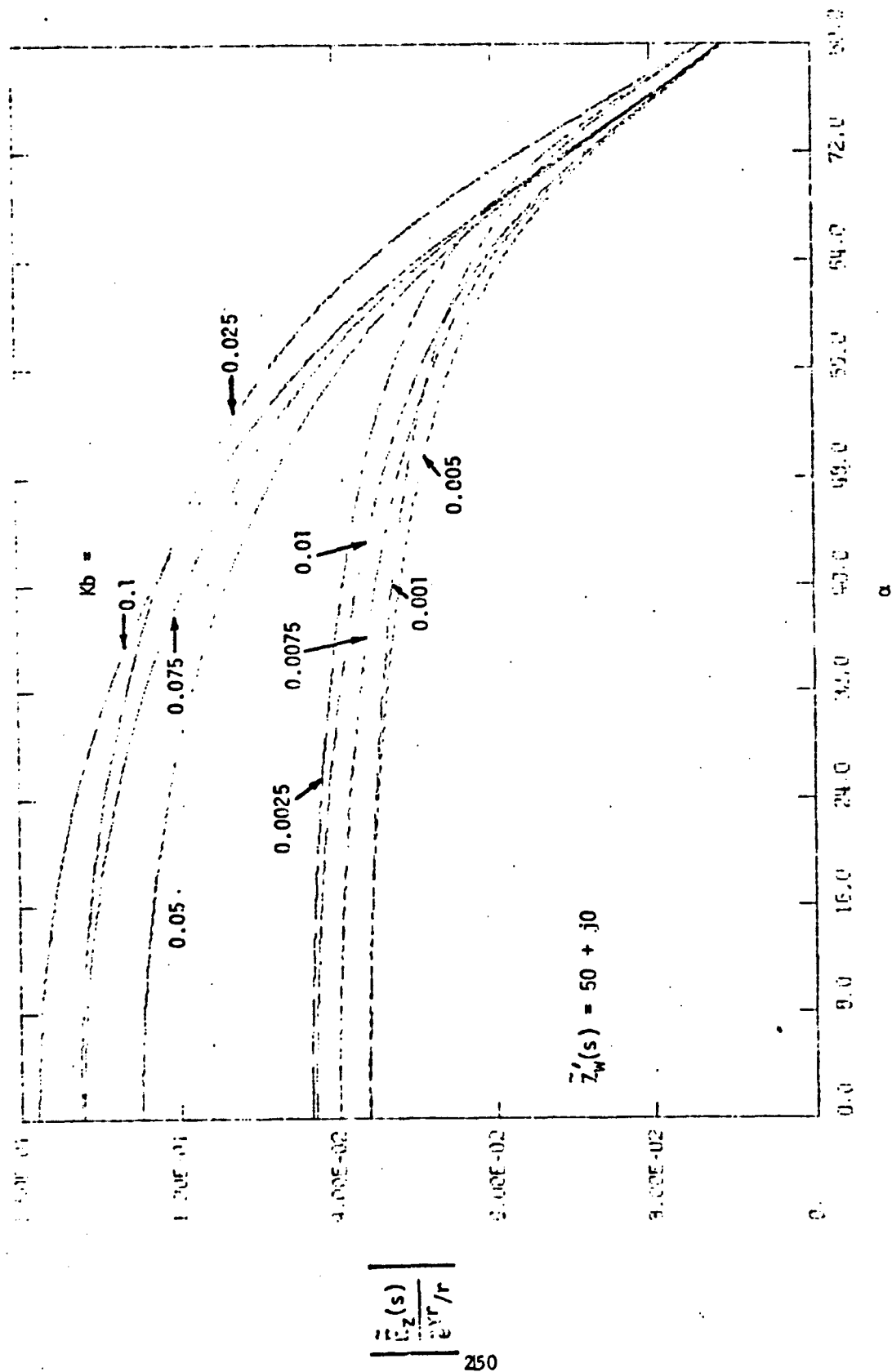


Figure 2.3(a). Magnitude of the Far-Field Distribution, Infinitely Long Thin Wire Loaded Antenna,  $\bar{E}_z$

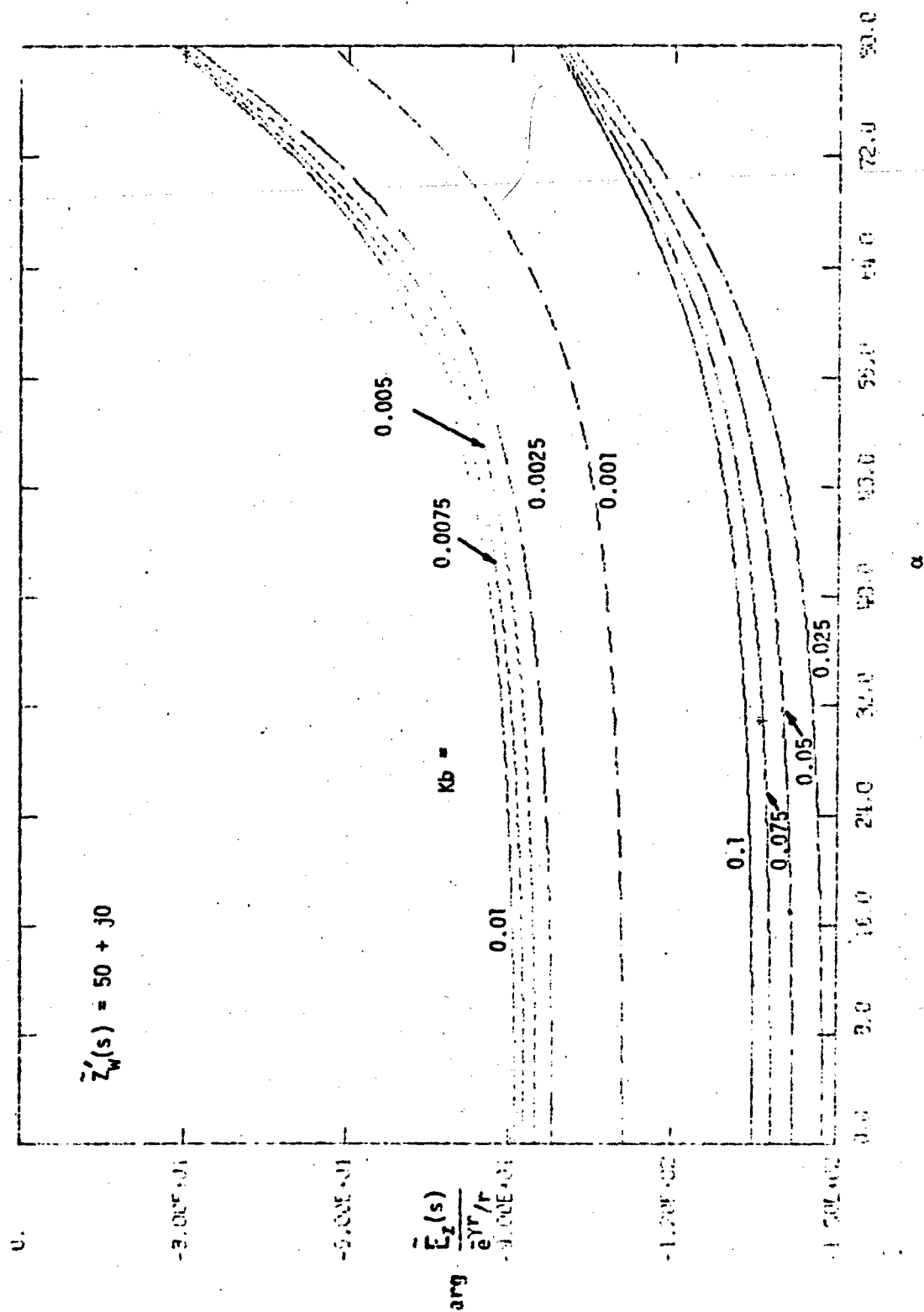


Figure 2.3(b). Phase of the Far-Field Distribution, Infinitely Long Thin Wire Loaded Antenna,  $\bar{E}_z$

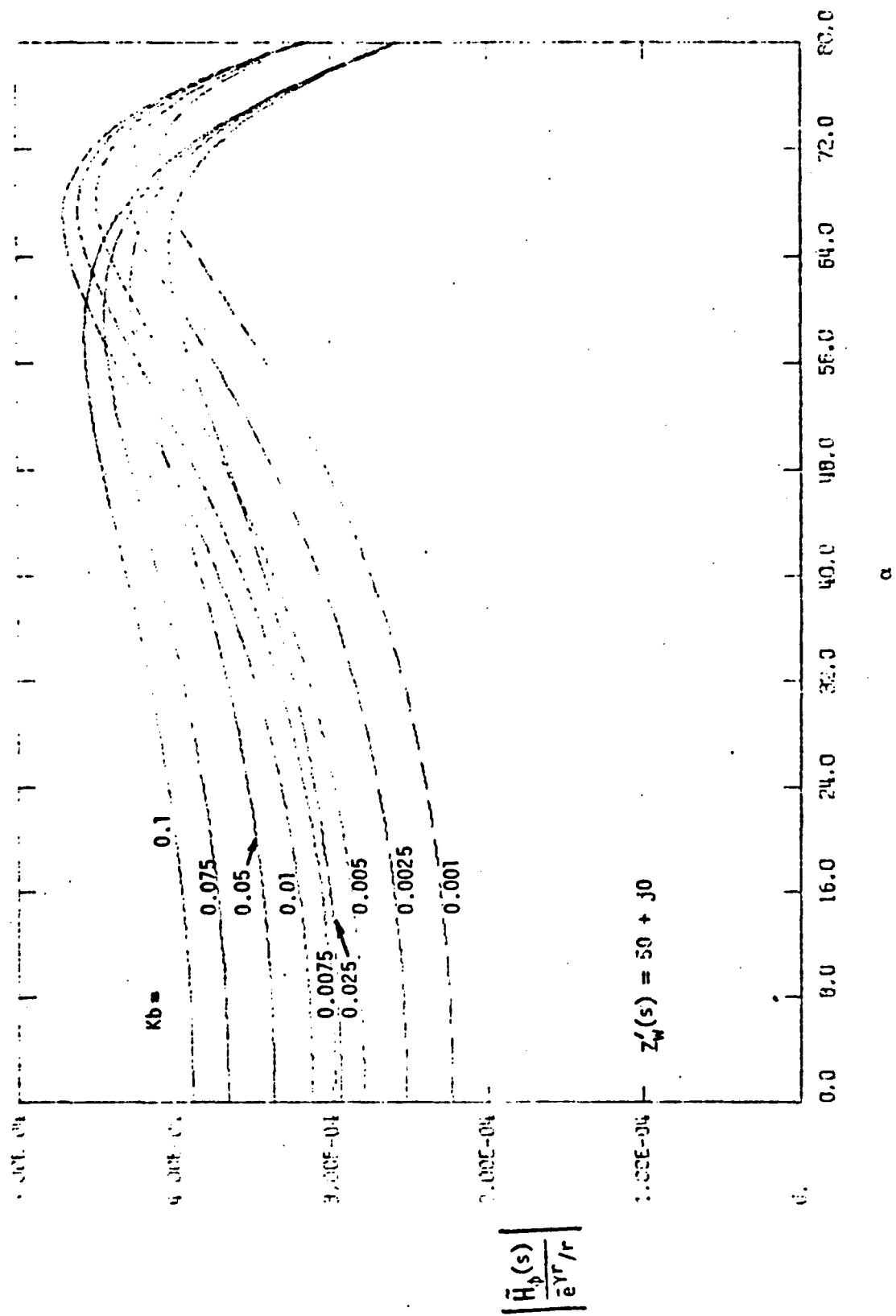


Figure 2.4(a). Magnitude of the Far-Field Distribution, Infinitely Long Thin Wire Loaded Antenna,  $\bar{H}_\phi$



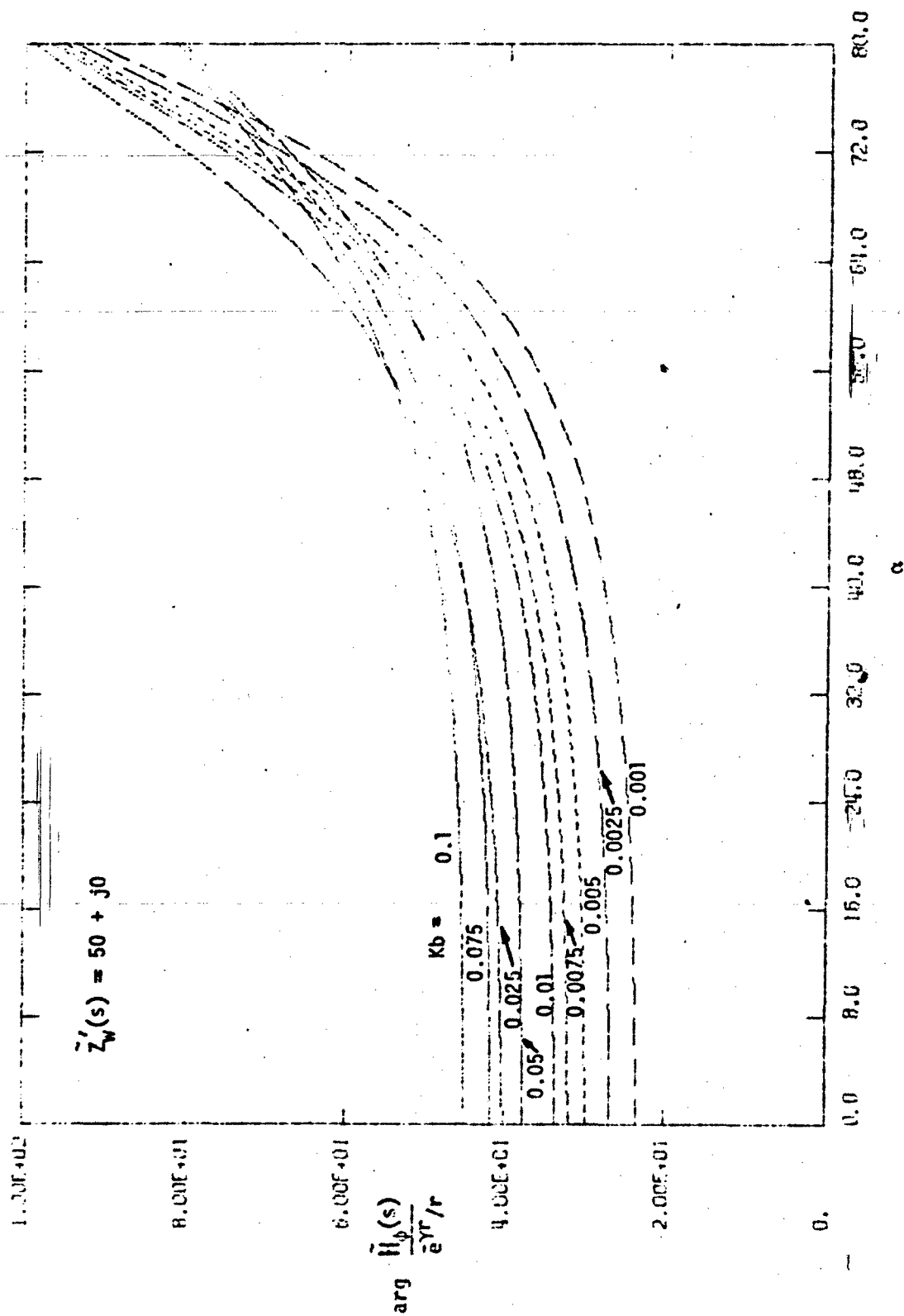


Figure 2.4(b). Phase of the Far-Field Distribution, Infinitely Long Thin Wire Loaded Antenna,  $H_\phi$

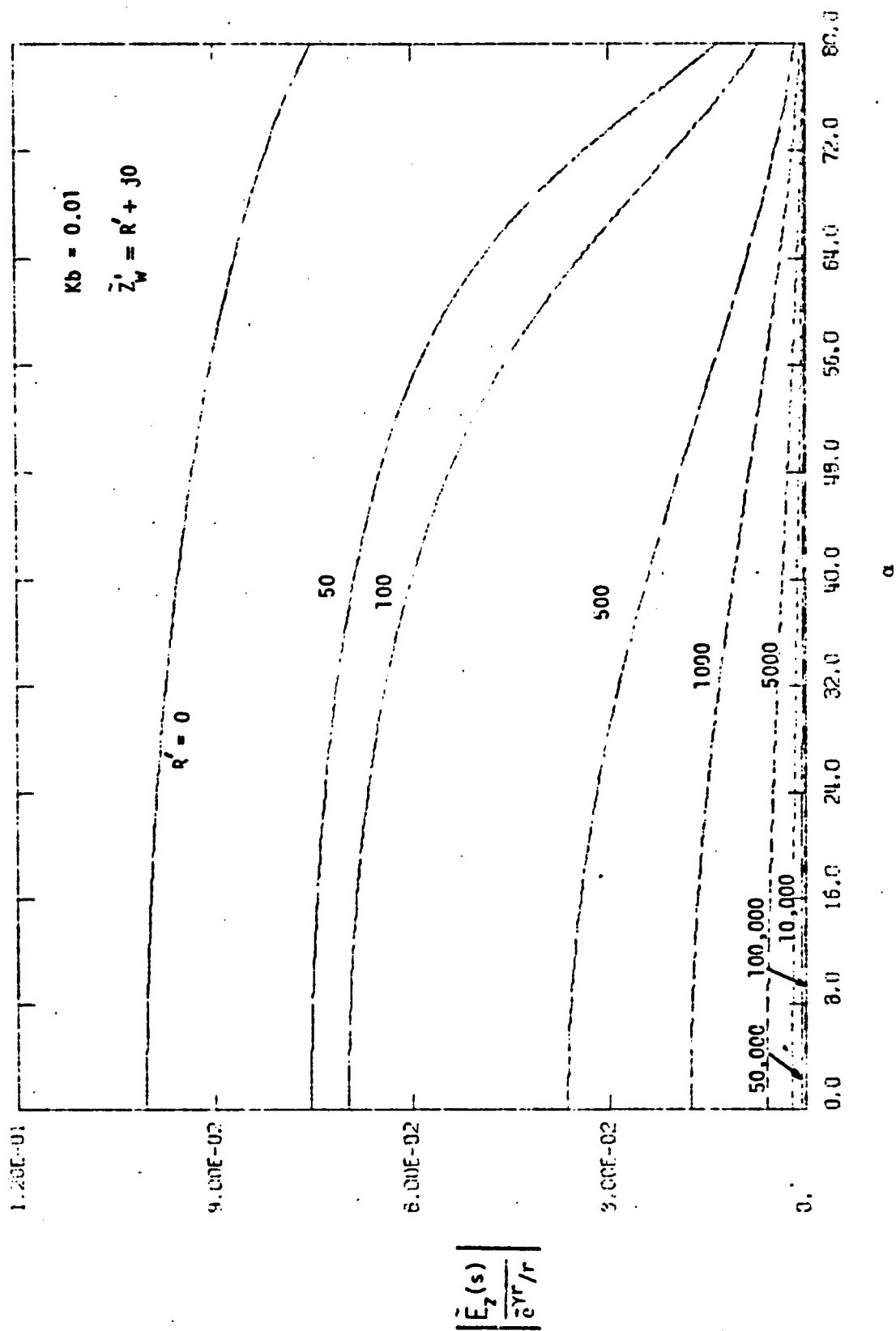


Figure 2.5(a). Magnitude of the Far-Field Distribution, Infinitely Long Thin Wire Loaded Antenna,  $\bar{E}_z$

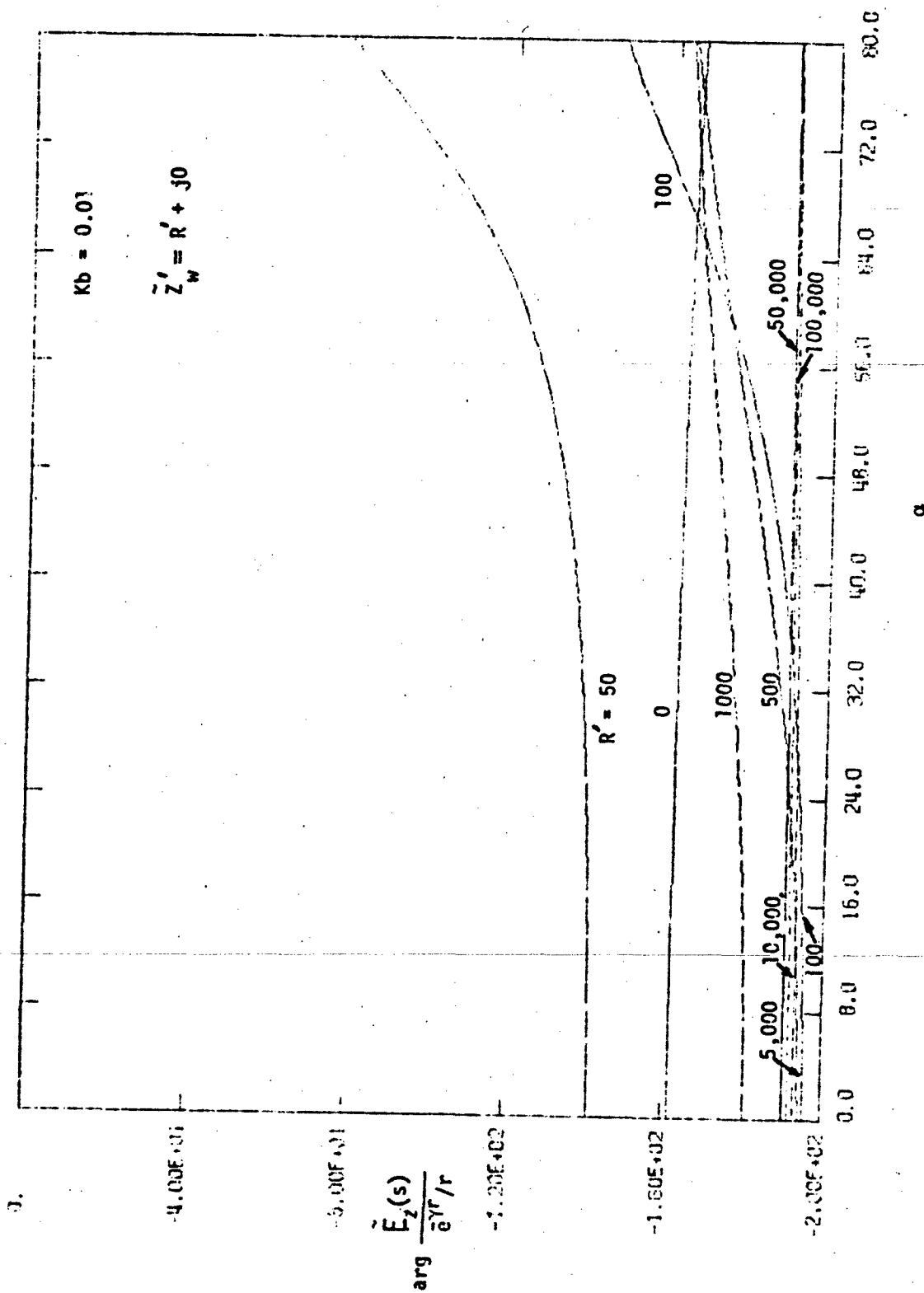


Figure 2.5(b). Phase of the Far-Field Distribution, Infinitely Long Thin Wire Loaded Antenna,  $\tilde{E}_z$

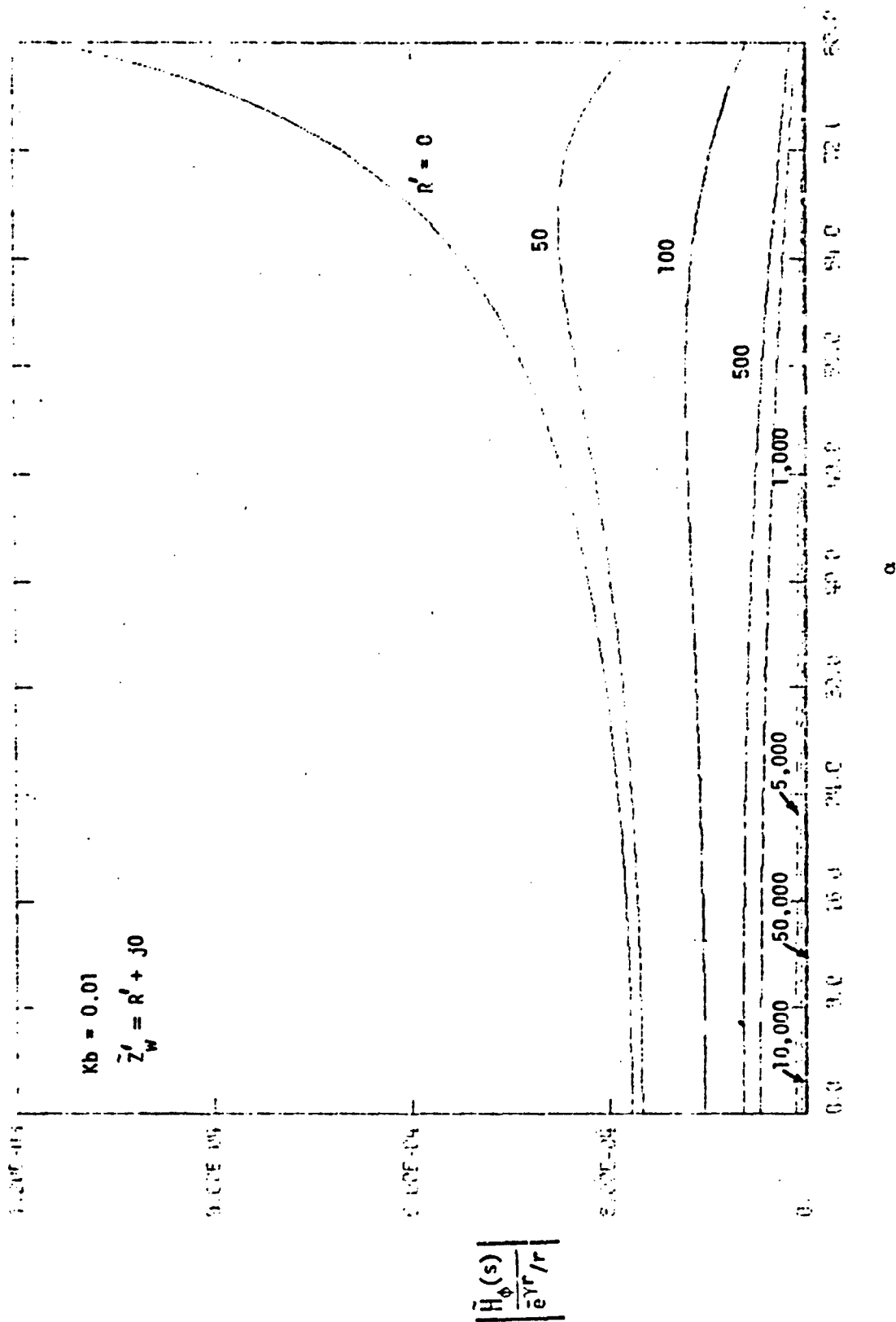


Figure 2.6(a). Magnitude of the Far-Field Distribution, Infinitely Long Thin Wire Loaded Antenna,  $\tilde{H}_\phi$

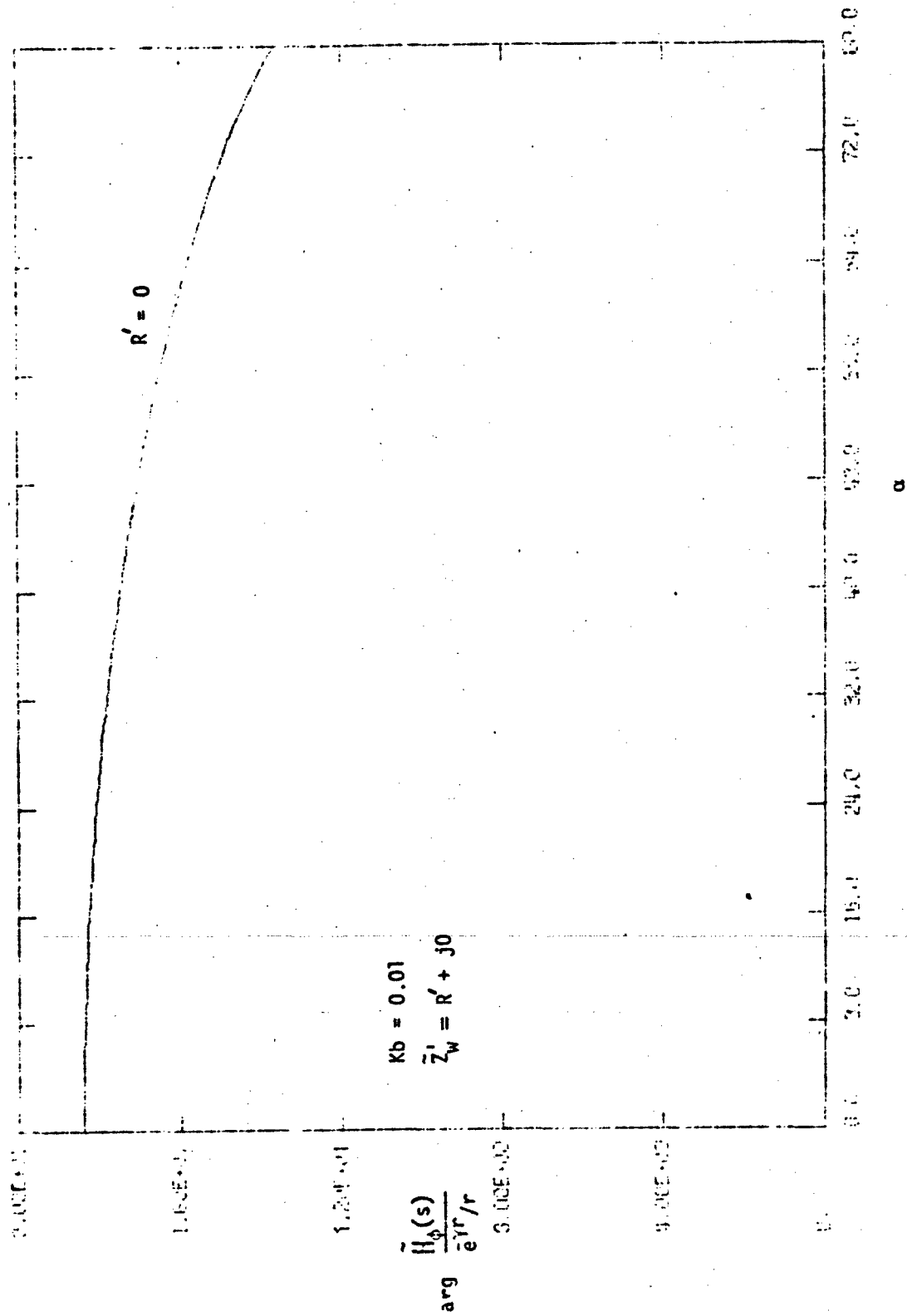


Figure 2.6(b). Phase of the Far-Field Distribution, Infinitely Long Thin Wire Loaded Antenna,  $\tilde{H}_\phi$

assumed. In figures 2.3a and b are shown the magnitude and phase of  $\tilde{E}_z$  far field distribution as a function of observation angle  $\alpha$  for different values of  $|\gamma b| = \frac{\omega b}{c}$  ( $\gamma = jK$ ) and for a fixed value of loading  $\tilde{Z}'_w(s) = 50 + j0$ . The same results are obtained in figures 2.4a and b for  $\tilde{H}_\phi$ . Figures 2.5a and b indicate the magnitude and phase of  $\tilde{E}_z$  far field distribution as a function of  $\alpha$  for different values of the impedance loading  $\tilde{Z}'_w$  for a fixed value of  $|\gamma b| = 0.01$ . The same variations are given in figures 2.6a and b for  $\tilde{H}_\phi$ . The results thus far obtained are useful to analyze infinitely long parallel cage wires.

### C. Infinitely Long Loaded Wire Cage

The analysis of the infinitely long loaded wire antenna as discussed in section II-A, can be similarly extended to infinitely long multiple parallel loaded cage wires. We shall first discuss the general problem and later specialize to a circular cylindrical wire cage.

A set of infinitely long loaded thin wires are all oriented parallel to the  $z$  axis in an isotropic homogeneous medium as shown in figure 2.7. There are  $N$  parallel wires of radius  $a_n$ ,  $n = 1, 2, 3, \dots, N$  which are located at  $(\psi_n, \phi_n)$  with their axes displaced at least a few radii apart. The respective parallel wires are excited by source generators of voltage  $\tilde{V}_n(s)$  across a gap of width  $2d_n$ , all centered at  $z = 0$ . If  $\tilde{I}_n(z, s)$  is the induced axial current on the  $n$ th infinitely long thin cage wire, at any point  $P$  in the medium the  $z$  component of the magnetic vector potential is given by the superposition of the individual wire contributions,<sup>2</sup>

$$\tilde{A}_z^{(c)}(\psi, z, s) = \sum_{n=1}^N \tilde{A}_{z_n}(\psi, z, s) \quad (2.20a)$$

where the superscript  $c$  refers to the cage wires and referring to expression (2.3),

$$\tilde{A}_{z_n}(\psi, z, s) = \frac{1}{2\pi j} \int_{C_\zeta} \tilde{F}_n(a_n, \zeta, s) K_0(u|\tilde{\psi} - \tilde{\psi}_n|) e^{\zeta z} d\zeta \quad (2.20b)$$

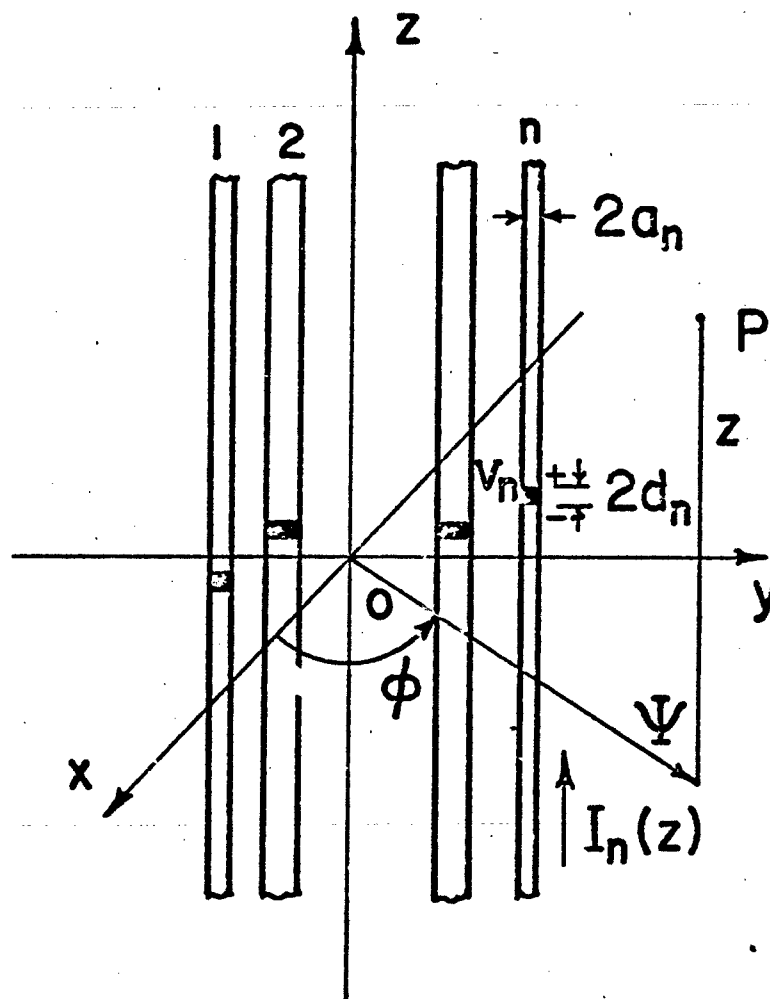


Figure 2.7. Infinitely Long Parallel Loaded Thin Cage Wires

in which

$$|\vec{\psi} - \vec{\psi}_n| = [(x - x_n)^2 + (y - y_n)^2]^{\frac{1}{2}} \quad (2.20c)$$

and the term  $\tilde{F}_n(a_n, z, s)$  is proportional to the Laplace-transform of the corresponding induced electric current on the  $n$ th wire. Again it is assumed  $\tilde{I}_n(z, s)$  has no angular variations and for each of the  $n$  wires

$$|\gamma a_n| \ll 1, \quad n = 1, 2, \dots, N \quad (2.21)$$

so that no modes internal to a wire are excited. The electric and the magnetic fields for the wire cage structure are obtained by the expressions (2.4a,b) with  $\tilde{A}_z$  replaced by  $\tilde{A}_z^{(c)}$ . Since each of the cage wires is excited by an ideal gap of width  $2d_n$ , within each gap the electric field varies approximately as  $-\tilde{V}_n(s)/2d_n$ ; similar to the expression (2.7), the electric current  $\tilde{I}_n(a_n, z, s)$  and the scattered electric field  $\tilde{E}_z^{(c)}(\vec{\psi}, z, s)$  should satisfy the following impedance boundary relationship,

$$\begin{aligned} \tilde{E}_z^{(c)}(\vec{\psi}, z, s) &= \left( -\frac{\tilde{V}_n(s)}{2d_n} \right) p_{d_n}(z) + \tilde{Z}'_{w,n}(s) \tilde{I}_n(a_n, z, s) \\ &\quad \text{at } \vec{\psi} = \vec{\psi}_n \\ &\quad n = 1, 2, 3, \dots, N \end{aligned} \quad (2.22)$$

where

$$\begin{aligned} p_{d_n}(z) &= 1, & |z| < d_n \\ &= 0, & |z| > d_n \end{aligned}$$

and  $\tilde{Z}'_{w,n}(s)$  is the series axial impedance per unit length on the  $n$ th cage wire (Appendix A). In terms of the transformed quantities, the impedance boundary relationship (2.22) becomes



$$\tilde{E}_z^{(c)}(\psi_n, \zeta, s) = -\tilde{V}_n(s) G_n(\zeta) + \tilde{Z}'_{w,n}(s) \tilde{I}_n(a_n, \zeta, s) \quad (2.23)$$

$$n = 1, 2, 3, \dots, N$$

According to the expressions (2.1), (2.2d), (2.4a), and (2.20), the z component of the spectral electric field is

$$\tilde{E}_z(\psi_n, \zeta, s) = \sum_{m=1}^N -\frac{s}{\gamma^2} u^2 K_0(u|\psi_n - \psi_m|) \tilde{F}_m(a_m, \zeta, s) \quad (2.24)$$

Similarly, the induced electric current along the nth infinitely long cage wire is obtained from, referring to expression (2.11),

$$\tilde{I}(a_n, z, s) = -\frac{1}{u} \int_{\phi'=0}^{2\pi} \psi' \frac{\partial \tilde{A}_{zn}(\psi', z, s)}{\partial \psi'} \partial \phi' \bigg|_{\psi'=a_n} \quad (2.25)$$

where  $\psi'$  and  $\phi'$  are the local cylindrical coordinates about the axis of the nth wire. Assuming  $\tilde{I}_n(a_n, z, s)$  has no  $\phi'$  angular variations and the cage wires are placed at least a few radii apart, the expressions (2.1), (2.2d), (2.4b), and (2.20) yield,

$$\tilde{I}(a_n, \zeta, s) = \frac{1}{u} 2\pi a_n u K_1(u a_n) \tilde{F}_n(a_n, \zeta, s) \quad (2.26)$$

On substituting the expressions (2.24) and (2.26) into the impedance boundary relationship (2.23), the following expression is obtained for determining  $\tilde{F}_n(a_n, \zeta, s)$ ,

$$\sum_{m=1}^N -\frac{s}{\gamma^2} u^2 K_0(u|\psi_n - \psi_m|) \tilde{F}_m(a_m, \zeta, s) = -\tilde{V}_n(s) G_n(\zeta) + \tilde{Z}'_{w,n}(s) \left[ \frac{1}{u} 2\pi a_n u K_1(u a_n) \tilde{F}_n(a_n, \zeta, s) \right] \quad (2.27)$$

$$n = 1, 2, 3, \dots, N$$

This forms a set of linear simultaneous equations and the spectral term  $\tilde{F}_n(a_n, \zeta, s)$ ,  $n = 1, 2, 3, \dots, N$  can be determined as the solution to the following matrix equation

$$\begin{bmatrix} \tilde{S}_{nm} \end{bmatrix} \begin{bmatrix} \tilde{F}_m \end{bmatrix} = \begin{bmatrix} \tilde{E}_n \end{bmatrix} \quad (2.28a)$$

where the matrix elements are

$$\tilde{S}_{nm} = u^2 K_0(u|\tilde{\psi}_n - \tilde{\psi}_m|), \quad n \neq m \quad (2.28b)$$

$$\tilde{S}_{nm} = u^2 K_0(ua_n) + 2\pi a_n u \gamma K_1(ua_n) \frac{\tilde{Z}'_{w,n}(s)}{Z_0}, \quad n = m \quad (2.28c)$$

and

$$\tilde{E}_n = \tilde{V}_n(s) \frac{\sinh(\zeta d_n)}{(\zeta d_n)} \frac{\gamma}{s} \quad (2.28d)$$

The matrix equation (2.28a) yields the solution

$$\begin{bmatrix} \tilde{F}_m \end{bmatrix} = \begin{bmatrix} \tilde{S}_{nm} \end{bmatrix}^{-1} \begin{bmatrix} \tilde{E}_n \end{bmatrix} \quad (2.29)$$

The current on each cage wire is obtained from (2.2d) and (2.26), and the magnetic vector potential obtained by substituting the result of (2.28) into the expression (2.20). Thus the radiated fields are obtained from the expressions (2.4) and (2.20).

#### D. Infinitely Long Loaded Circular Cylindrical Wire Cage

The general problem discussed in the previous section is specialized to a circular cylindrical wire cage. Suppose all the  $N$  wires are placed along the circumference of a large circle of diameter  $2A$  and distributed uniformly around the circumference. If the circular wire cage consists of identical wire geometries, figure 2.8, which are fed from identical source generators, the matrix equation (2.9a) simplifies into a diagonal form.

Referring to figures 2.7 and 2.8, let

$$\tilde{V}(s) = \tilde{V}_n(s) \quad \text{source voltage across each gap}$$

$$2d = 2d_n \quad \text{width of each gap}$$

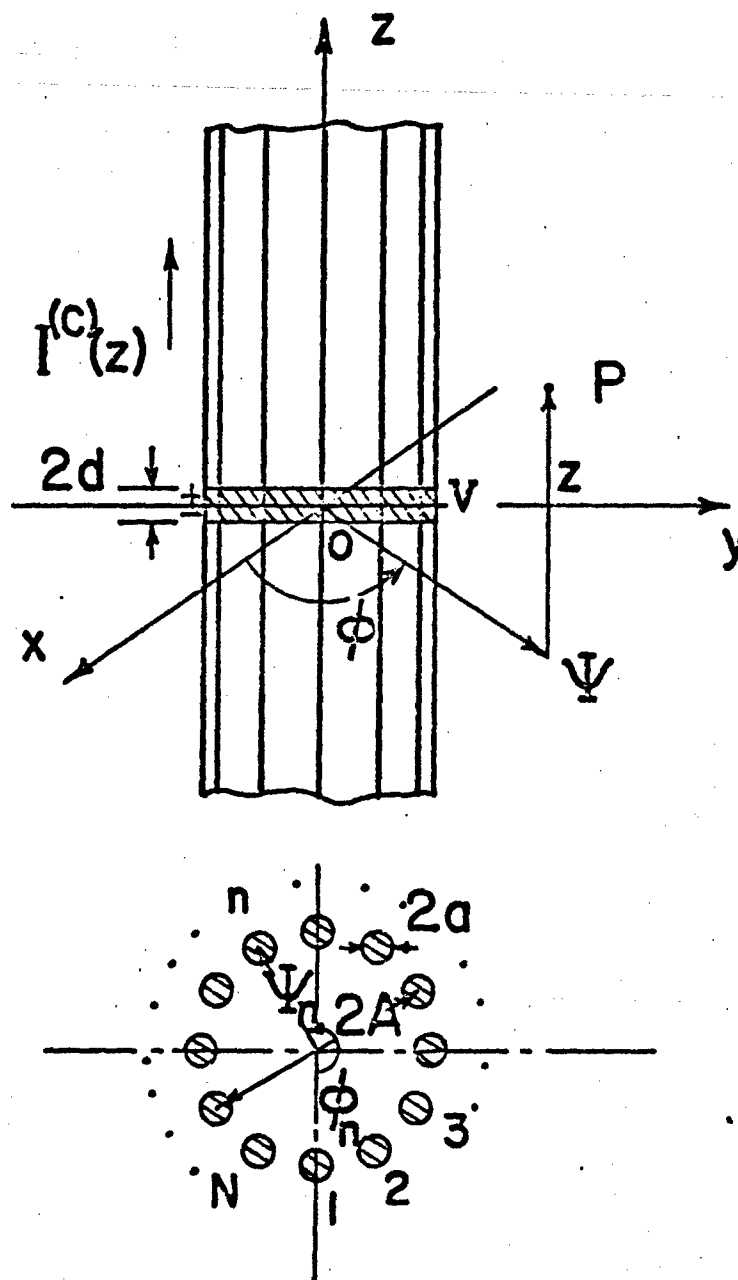


Figure 2.8. Infinitely Long Circular Cylindrical Wire Cage Antenna

$$a = a_n$$

radius of each cage wire

$$\tilde{Z}_w^{(c)'}(s) = \tilde{Z}_{w,n}'(s)/N$$

axial series impedance loading of each cage wire per unit length

$$\text{for } n = 1, 2, 3, \dots, N$$

Under these symmetrical conditions, the spectral functions  $\tilde{F}_n(a_n, \zeta, s)$  are all the same, i.e.,  $\tilde{F}_1 = \tilde{F}_2 = \tilde{F}_3 = \dots = \tilde{F}_N$  ( $= \tilde{F}^{(c)}(a, \zeta, s)$ ). Hence the induced electric current on each of the cage wires is the same,  $\tilde{I}_1(z, s) = \tilde{I}_2(z, s) = \tilde{I}_3(z, s) = \dots = \tilde{I}_N(z, s)$  ( $= \tilde{I}^{(c)}(z, s)/N$ ). Applying these relationships for the concentric wire cage, the expression (2.28) yields the solution,

$$\tilde{F}^{(c)}(a, \zeta, s) = \tilde{V}(s) \frac{\gamma^2}{s} \frac{G(\zeta)}{u\tilde{B}(\zeta, s)} \quad (2.30a)$$

where

$$\tilde{B}(\zeta, s) = \left\{ u \sum_{n=1}^N K_0(uA_{1,n}) \right\} + 2\pi a \gamma K_1(ua) \frac{\tilde{Z}_w^{(c)'}(s)}{Z_0} \quad (2.30b)$$

comparing the expressions (2.13b) and (2.30b), the summation in (2.30b) accounts for various mutual interactions and the factor  $A_{1,n}$  is the inter-chord distance from wire 1 to wire  $n$  given by,

$$A_{1,n} = a, \quad n = 1 \quad (2.30c)$$

$$A_{1,n} = |\vec{\psi}_1 - \vec{\psi}_n|, \quad n = 2, 3, \dots, N \quad (2.30d)$$

Since the angle between any two consecutive wires is  $2\pi/N$ , the inter-chord distances (2.30d) can be written as

$$A_{1,n} = 2A \sin\left[\frac{\pi}{N}(n-1)\right], \quad n = 2, 3, \dots, N \quad (2.30e)$$

Hence the current on each cage wire is obtained from the expressions (2.2d), (2.26), and (2.30a),

$$\frac{1}{N} \tilde{I}^{(c)}(a, z, s) = \frac{\tilde{V}(s) \gamma a}{j Z_0} \int_{C_z} \underline{G}(\zeta) \frac{K_1(ua)}{\tilde{B}(\zeta, s)} e^{\zeta z} d\zeta \quad (2.31)$$

and the corresponding magnetic vector potential is obtained by substituting (2.30a) into the expression (2.20),

$$\tilde{A}_z^{(c)}(\psi, z, s) = \frac{\tilde{V}(s)}{2\pi j} \frac{\gamma^2}{s} \int_{C_z} \underline{G}(\zeta) \left[ \frac{\sum_{m=1}^N K_0(u|\tilde{\psi} - \tilde{\psi}_m|)}{u \tilde{B}(\zeta, s)} \right] e^{\zeta z} d\zeta \quad (2.32)$$

The electric and the magnetic fields can now be written using the expressions (2.1), (2.4), and (2.32) in spectral form as

$$\begin{bmatrix} \tilde{E}_z^{(c)}(\psi, \zeta, s) \\ Z_0 \tilde{H}_\phi^{(c)}(\psi, \zeta, s) \end{bmatrix} = \begin{bmatrix} \tilde{Q}_1 \\ \tilde{Q}_2 \end{bmatrix} \quad (2.33a)$$

where  $[\tilde{Q}]$  is a vector for the circular cylindrical wire cage antenna and is given by

$$[\tilde{Q}] = \begin{bmatrix} \tilde{Q}_1 \\ \tilde{Q}_2 \end{bmatrix} \quad (2.33b)$$

and the elements of the vector are,

$$\tilde{Q}_1 = -\tilde{V}(s) \underline{G}(\zeta) \left\{ \frac{\sum_{m=1}^N u K_0(u|\tilde{\psi} - \tilde{\psi}_m|)}{\tilde{B}(\zeta, s)} \right\} \quad (2.33c)$$

$$\tilde{Q}_2 = \tilde{V}(s) \underline{G}(\zeta) \left\{ \frac{\sum_{m=1}^N \gamma K_1(u|\tilde{\psi} - \tilde{\psi}_m|)}{\tilde{B}(\zeta, s)} \right\} \left[ \frac{d}{d\psi} (|\tilde{\psi} - \tilde{\psi}_m|) \right] \quad (2.33d)$$

Again we have difficulty obtaining general solutions for the fields (2.33a), since the integrations are to be performed along the  $C_z$  contour, figure 2.2. But in the far field region as  $\Psi \rightarrow \infty$ , the expressions (2.33) reduce to simpler forms (Appendix B) based on the saddle-point integration method. Hence for the infinitely long circular wire cage structure, in the far field region the electric and the magnetic field components are obtained as (figure B-1),

$$\tilde{E}_z^{(c)}(r, \alpha, s) \sim - \frac{\tilde{V}(s)}{2} \frac{\cos(\alpha)}{\tilde{L}_2(\gamma, \alpha)} \frac{e^{-\gamma r}}{r} \tilde{C}_f \quad (2.34a)$$

$$Z_0 \tilde{H}_\phi^{(c)}(r, \alpha, s) \sim \frac{\tilde{V}(s)}{2} \frac{1}{\tilde{L}_2(\gamma, \alpha)} \frac{e^{-\gamma r}}{r} \tilde{C}_f \quad (2.34b)$$

where the cage factor is

$$\tilde{C}_f = NI_0(\gamma A \cos(\alpha)) \quad (2.34c)$$

$I_0$  is the modified Bessel function of the first kind, zero order,  $r$  and  $\theta = 90 - \alpha$  are the spherical coordinate variables. In the above expressions

$$\tilde{L}_2(\gamma, \alpha) = \cos \alpha \sum_{n=1}^N K_0(\gamma A_{1,n} \cos \alpha) + \tilde{h}_2(s) K_1(\gamma a \cos \alpha) \quad (2.34d)$$

$$\tilde{h}_2(s) = 2\pi a \frac{\tilde{Z}_w^{(c)'}(s)}{Z_0} \quad (2.34e)$$

#### E. Numerical Results: Far Field

In section II-C the infinitely long loaded wire cage is analyzed, while the specialization to the circular wire cage is given in section II-D along with the expressions for the induced electric current, radiated fields and far-field distributions.

In figures 2.9a and b are shown the magnitude and phase of the  $E_z^{(c)}$  far-field distribution as a function of observation angle  $\alpha$  for different values of the loading  $\tilde{Z}_w^{(c)}$  and for a fixed value of  $KA = 1.0$ ,  $Ka = 0.01$  and number of cage wires  $N = 12$ . The same variations are given in figures 2.10a and b, but for the far-field  $\tilde{H}_\phi^{(c)}$ . Similarly in figures 2.11a and b are shown the magnitude and phase of the  $E_z^{(c)}$  far-field distribution as a function of angle  $\alpha$  for different number of cage wires  $N$  and fixed impedance loadings  $\tilde{Z}_w^{(c)} = (50 + j0) \Omega/m$ . Further, the figures 2.12a and b give the distribution of the corresponding  $\tilde{H}_\phi^{(c)}$  of the far field.

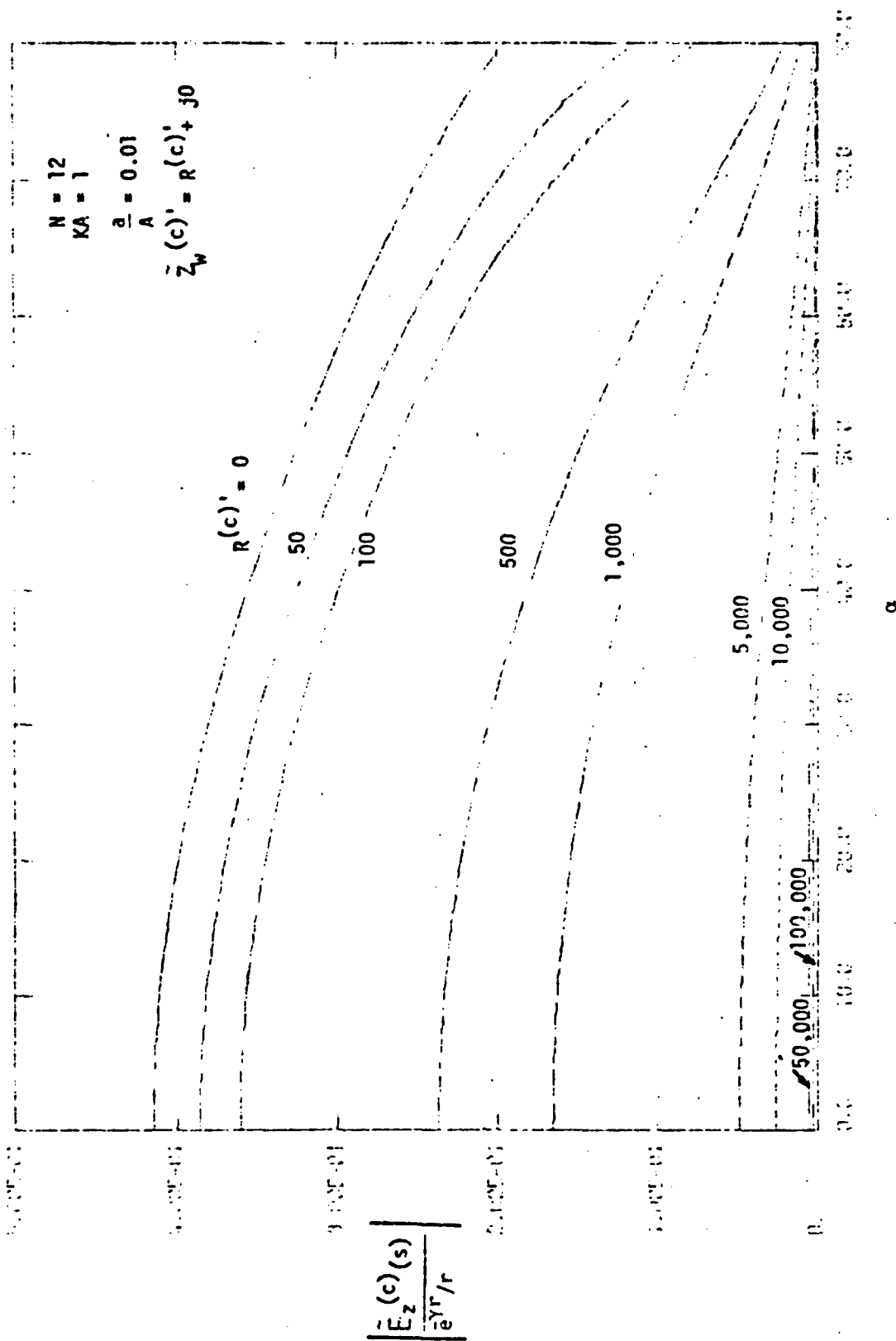


Figure 2.9(a). Magnitude of the Far-Field Distribution, Infinitely Long Loaded Circular Wire Cage Antenna,  $\tilde{E}_z(c)$



### III. INFINITELY LONG LOADED HOLLOW CIRCULAR CYLINDRICAL ANTENNA

The analysis of the hollow cylindrical structure<sup>16,17</sup> is slightly different from the previous cases discussed wherein the wire antenna structure is assumed as thin, so that the fields inside the wire can be completely neglected. This is particularly true with the case of solid thin-wire structures.<sup>13</sup> But when the radius becomes large, one has to analyze both the external and the internal regions separately and enforce the relevant impedance boundary condition on the surface of the hollow cylinder. It is assumed the cylinder wall is very thin and for all the mathematical considerations, the thickness of the wall can be neglected. The material of the wall of the hollow cylinder is lossy and homogeneous and can be characterized in terms of a uniform sheet impedance (Appendix A). Even with an external impedance loading function introduced, the concept of the boundary condition is based on a uniform sheet impedance in contrast to the surface impedance concept utilized in the previous sections.

The infinitely long hollow cylinder is oriented along the  $z$  axis in an isotropic homogeneous medium. The radius of the cylinder is  $C$  and is excited by a source generator of voltage  $\tilde{V}(s)$  across a gap of width  $2d$  centered at  $z = 0$ , as shown in figure 3.1. The medium characteristics  $(\mu, \epsilon, \sigma)$  are the same both for the internal region 1 and the external region 2. The  $z$  component of the magnetic vector potential is given by, in region 1,

$$\tilde{A}_z^{(1)}(\psi, z, s) = \frac{1}{2\pi j} \int_{C_\zeta} \tilde{F}_1(C, \zeta, s) K_0(uC) I_0(u\psi) e^{\zeta z} d\zeta$$

$\psi < C$  (3.1a)

and in region 2,

$$\tilde{A}_z^{(2)}(\psi, z, s) = \frac{1}{2\pi j} \int_{C_\zeta} \tilde{F}_2(C, \zeta, s) I_0(uC) K_0(u\psi) e^{\zeta z} d\zeta$$

$\psi > C$  (3.1b)

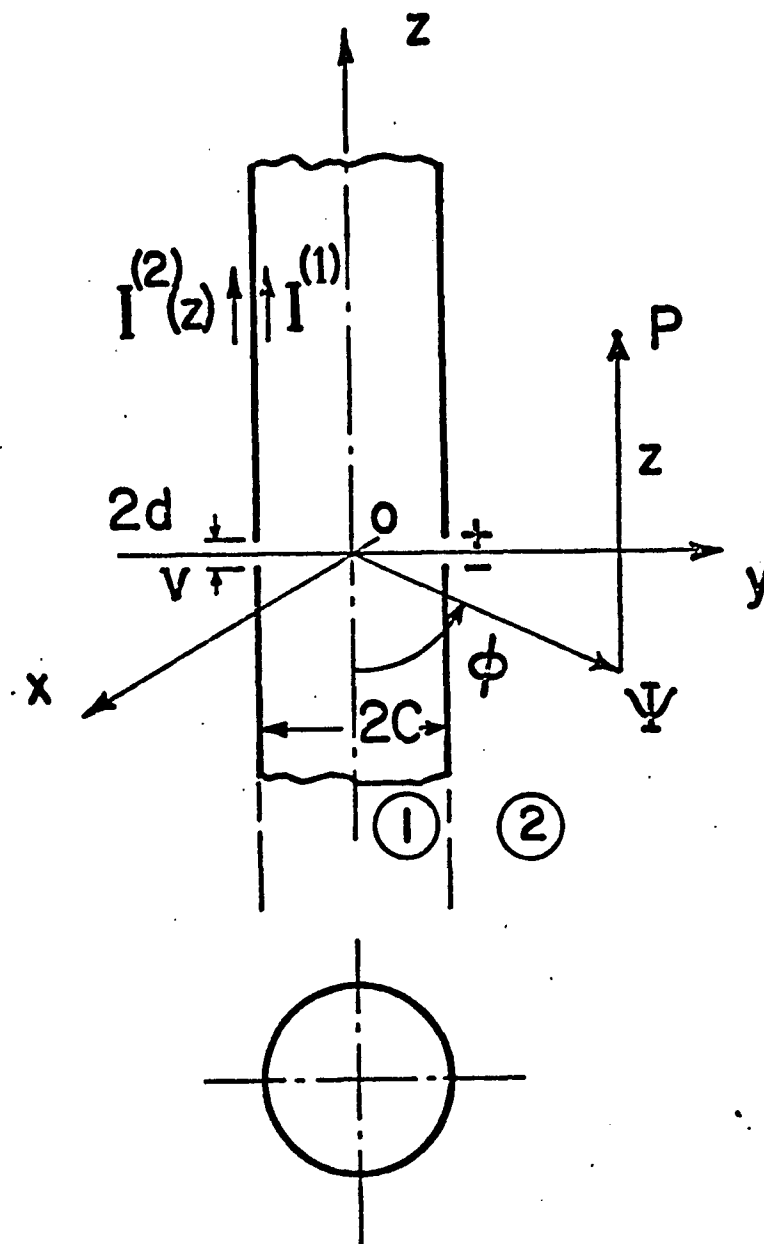


Figure 3.1. Infinitely Long Loaded Hollow Circular Cylindrical Antenna

where  $I_0$  and  $K_0$  are the modified Bessel functions of first and second kind, zero order. The spectral terms  $\tilde{F}_1(C, \zeta, s)$  and  $\tilde{F}_2(C, \zeta, s)$  are proportional to the Laplace transform of the net electric current  $[\tilde{I}_2(C, \zeta, s) + \tilde{I}_1(C, \zeta, s)]$  of the external and internal surface of the hollow cylinder. Again electric and magnetic fields in the regions 1 and 2 are obtained by substituting (3.1) into the expressions (2.1) and (2.4). The tangential electric field  $\tilde{E}_z(\psi, z, s)$  at the wall surface is continuous, while the tangential magnetic field  $\tilde{H}_\phi(\psi, z, s)$  is discontinuous to the extent proportional to the difference of the external and the internal surface currents. Hence we have the following impedance boundary relationship

$$\begin{aligned}\tilde{E}_z^{(1)}(C^-, z, s) &= \tilde{E}_z^{(2)}(C^+, z, s) \\ &= -\frac{\tilde{V}(s)}{2d} p_d(z) + \tilde{Z}'(s) [\tilde{I}^{(2)}(C^+, z, s) + \tilde{I}^{(1)}(C^-, z, s)]\end{aligned}\quad (3.2)$$

where  $\tilde{Z}'(s)$  is the impedance loading function per unit length of the infinitely long hollow cylinder,

$$\tilde{Z}'(s) = \frac{\tilde{Z}_s(s)}{2\pi C} \quad (3.3)$$

and  $\tilde{Z}_s(s)$  is the sheet impedance in ohm of the hollow cylinder (Appendix A). In terms of transformed variables the boundary relationship (3.2) becomes,

$$\begin{aligned}\tilde{E}_z^{(1)}(C^-, \zeta, s) &= \tilde{E}_z^{(2)}(C^+, \zeta, s) \\ &= -\tilde{V}(s) G(\zeta) + \tilde{Z}'(s) [\tilde{I}^{(2)}(C^+, \zeta, s) + \tilde{I}^{(1)}(C^-, \zeta, s)]\end{aligned}\quad (3.4)$$

Referring to the expressions (2.1), (2.2d), (2.4a), and (3.1) the  $z$  component of the electric field is given by,

$$\tilde{E}_z^{(1)}(\psi, \zeta, s) = -\frac{s}{\gamma^2} u^2 K_0(uC) I_0(u\psi) \tilde{F}_1(C, \zeta, s) \quad (3.5a)$$

$$\psi < C$$

and

$$\tilde{E}_z^{(2)}(\psi, \zeta, s) = -\frac{s}{\gamma^2} u^2 I_0(uC) K_0(u\psi) \tilde{F}_2(C, \zeta, s) \quad (3.5b)$$

$$\psi > C$$

Further, the external and the internal currents on the hollow cylinder using the expressions (2.1), (2.2d), (2.4b), and (3.1) are obtained as

$$\tilde{I}^{(2)}(C^+, \zeta, s) = \frac{1}{\mu} 2\pi C u I_0(uC) K_1(uC) \tilde{F}_2(C, \zeta, s) \quad (3.6a)$$

$$\tilde{I}^{(1)}(C^-, \zeta, s) = \frac{1}{\mu} 2\pi C u K_0(uC) I_1(uC) \tilde{F}_1(C, \zeta, s) \quad (3.6b)$$

on substituting the expressions (3.5) and (3.6) into the boundary relationship (3.4), we have

$$\begin{aligned} \tilde{F}_1(C, \zeta, s) &= \tilde{F}_2(C, \zeta, s) \\ &= \tilde{V}(s) \frac{\gamma^2}{s} \frac{G(\zeta)}{u\tilde{P}(\zeta, s)} \end{aligned} \quad (3.7a)$$

where

$$\tilde{P}(\zeta, s) = u I_0(uC) K_0(uC) + 2\pi C \gamma \frac{\tilde{Z}'(s)}{Z_0} \left[ \frac{1}{uC} \right] \quad (3.7b)$$

Hence the electric current on the internal and the external surface of the hollow cylinder is obtained from (2.2d), (3.6), and (3.7) as,

$$\tilde{I}^{(1)}(C, z, s) = \frac{\tilde{V}(s)\gamma C}{jZ_0} \int_{C^-} G(\zeta) \frac{K_0(uC) I_1(uC)}{\tilde{P}(\zeta, s)} e^{\zeta z} d\zeta \quad (3.8a)$$

$$\tilde{I}^{(2)}(C, z, s) = \frac{\tilde{V}(s) \gamma C}{j Z_0} \int_{C_\zeta} G(\zeta) \frac{I_0(uC) K_1(uC)}{\tilde{P}(\zeta, s)} e^{\zeta z} d\zeta \quad (3.8b)$$

The net total current flowing on the hollow cylinder, with the assumption of current flowing in the  $z$  direction as positive, is  $[\tilde{I}^{(2)}(C, z, s) + \tilde{I}^{(1)}(C, z, s)]$ ,

$$\tilde{I}^{(t)}(C, z, s) = \frac{\tilde{V}(s) \gamma}{j Z_0} \int_{C_\zeta} G(\zeta) \frac{1}{u \tilde{P}(\zeta, s)} e^{\zeta z} d\zeta \quad (3.8c)$$

Since the surface current density is independent of  $\phi$ , it is obtained by dividing the expression (3.8c) by the circumferential length  $2\pi C$ . The  $z$  component of the magnetic vector potential in the regions 1 and 2 is obtained by substituting the spectral term (3.7a) in the expressions (3.1a, b),

$$\tilde{A}_z^{(1)}(\psi, z, s) = \frac{\tilde{V}(s)}{2\pi j} \frac{\gamma^2}{s} \int_{C_\zeta} G(\zeta) \frac{K_0(uC) I_0(u\psi)}{u \tilde{P}(\zeta, s)} e^{\zeta z} d\zeta \quad (3.9a)$$

$\psi < C$

$$\tilde{A}_z^{(2)}(\psi, z, s) = \frac{\tilde{V}(s)}{2\pi j} \frac{\gamma^2}{s} \int_{C_\zeta} G(\zeta) \frac{I_0(uC) K_0(u\psi)}{u \tilde{P}(\zeta, s)} e^{\zeta z} d\zeta \quad (3.9b)$$

$\psi > C$

The electric and the magnetic fields radiated are obtained using the expressions (2.1), (2.4), and (3.9b) in the regions 1 and 2 in the spectral form as,

$$\begin{bmatrix} \tilde{E}_z^{(1,2)}(\psi, \zeta, s) \\ Z_0 \tilde{H}_{\phi}^{(1,2)}(\psi, \zeta, s) \end{bmatrix} = \begin{bmatrix} \tilde{W}^{(1,2)} \end{bmatrix} \quad (3.10a)$$

where  $[\tilde{W}^{(1,2)}]$  is the vector for the infinitely long hollow cylindrical antenna,

$$\begin{bmatrix} \tilde{W}^{(1,2)} \end{bmatrix} = \begin{bmatrix} \tilde{W}_1^{(1,2)} \\ \tilde{W}_2^{(1,2)} \end{bmatrix} \quad (3.10b)$$

and the elements of the vector have the form

$$\tilde{W}_1^{(1,2)} = \tilde{V}(s) \underline{G}(\zeta) \frac{\begin{Bmatrix} uK_0(uC) I_0(u\psi) \\ uI_0(uC) K_0(u\psi) \end{Bmatrix}}{\tilde{P}(\zeta, s)} \quad (3.10c)$$

$$\tilde{W}_2^{(1,2)} = \tilde{V}(s) \underline{G}(\zeta) \frac{\begin{Bmatrix} -\gamma K_0(uC) I_1(u\psi) \\ \gamma I_0(uC) K_1(u\psi) \end{Bmatrix}}{\tilde{P}(\zeta, s)} \quad (3.10d)$$

As  $\psi \rightarrow \infty$ , the field expressions can be reduced to simpler forms in the far field region using the saddle point method<sup>14</sup> discussed in Appendix B,

$$\tilde{F}_z^{(2)}(r, \alpha, s) \sim -\frac{\tilde{V}(s)}{2} \frac{\cos \alpha}{\tilde{L}_3(\gamma, \alpha)} \frac{e^{-\gamma r}}{r} \tilde{P}_f \quad (3.11a)$$

$$Z_0 \tilde{H}_\phi^{(2)}(r, \alpha, s) \sim \frac{\tilde{V}(s)}{2} \frac{1}{\tilde{L}_3(\gamma, \alpha)} \frac{e^{-\gamma r}}{r} \tilde{P}_f \quad (3.11b)$$

where the hollow cylinder factors are

$$\tilde{P}_f = I_0(\gamma C \cos \alpha) \quad (3.11c)$$

$$\tilde{L}_3(\gamma, \alpha) = \cos \alpha I_0(\gamma C \cos \alpha) K_0(\gamma C \cos \alpha) + \tilde{h}_3(s) \left[ \frac{1}{\gamma C \cos \alpha} \right] \quad (3.11d)$$

$$\tilde{h}_3(s) = 2\pi C \frac{\tilde{Z}'(s)}{Z_0} \quad (3.11e)$$

### A. Numerical Results: Far Fields

Based on the analytical expressions formulated in the previous section for the induced electric current, radiated fields, and far-field distribution for the case of infinitely long loaded hollow cylinder, numerical results are presented in figures 3.2 through 3.5 for the radiated far-field distribution.

In figures 3.2a and b are shown the magnitude and phase of  $\tilde{E}_z^{(2)}$  of the far-field distribution as a function of the observation angle  $\alpha$  for different values of the radius  $C$  of the hollow cylinder, and for a fixed  $\gamma = j1$  and loading function  $\tilde{Z}' = 50 + j0$ . Figures 3.3a and b indicate the same variations, but for the  $\tilde{H}_\phi^{(2)}$  component. Similarly in figures 3.4a and b are shown the magnitude and phase of the  $\tilde{E}_z^{(2)}$  component far-field as a function of  $\alpha$  for different values of the loading function  $\tilde{Z}'$  and for fixed value of  $|\gamma C| = 1$ . Further the figures 3.5a and b indicate the same variations, but for the  $\tilde{H}_\phi^{(2)}$ .

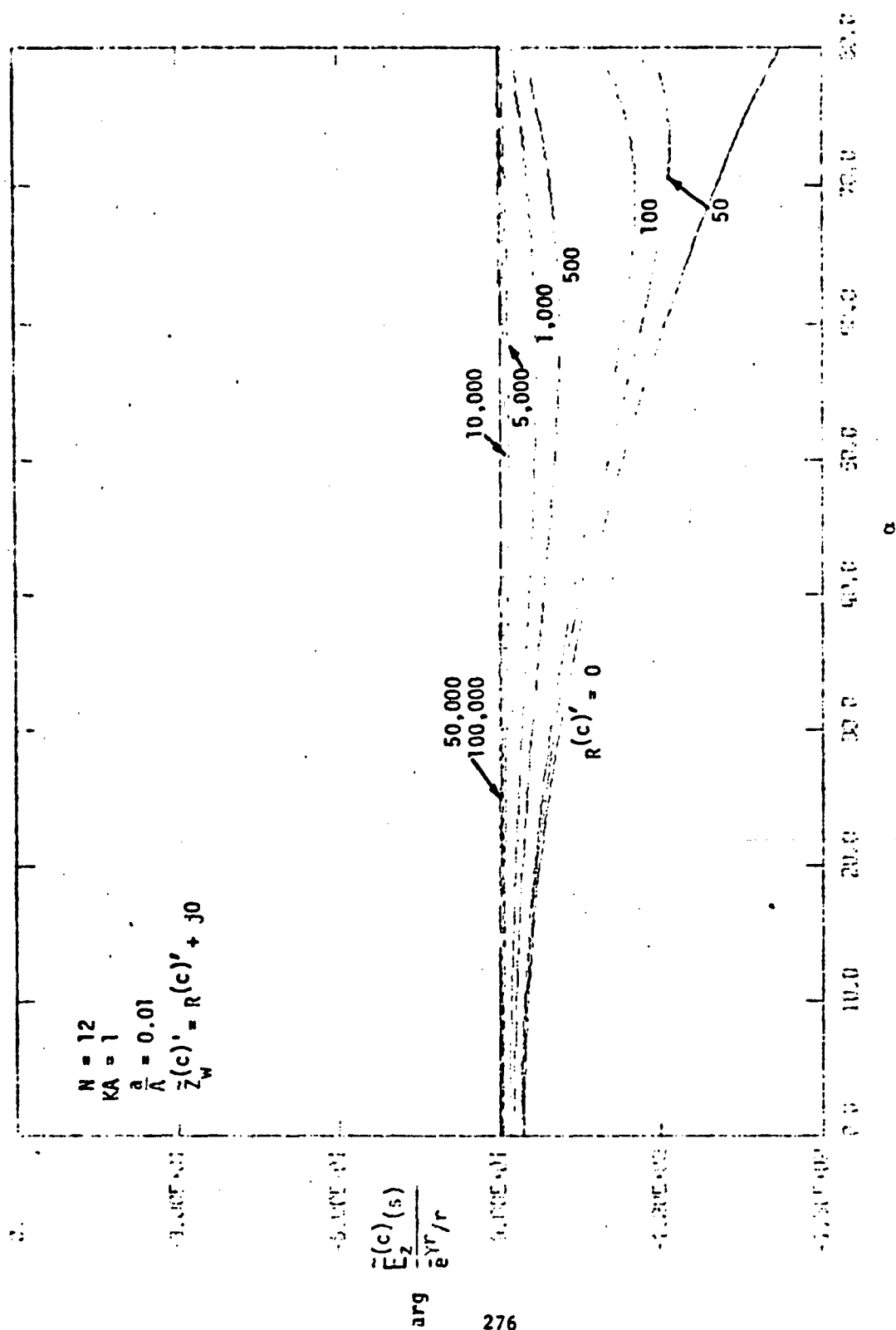


Figure 2.9(b). Phase of the Far-Field Distribution, Infinitely Long Loaded Circular Wire Cage Antenna,  $\bar{E}_z(c)$



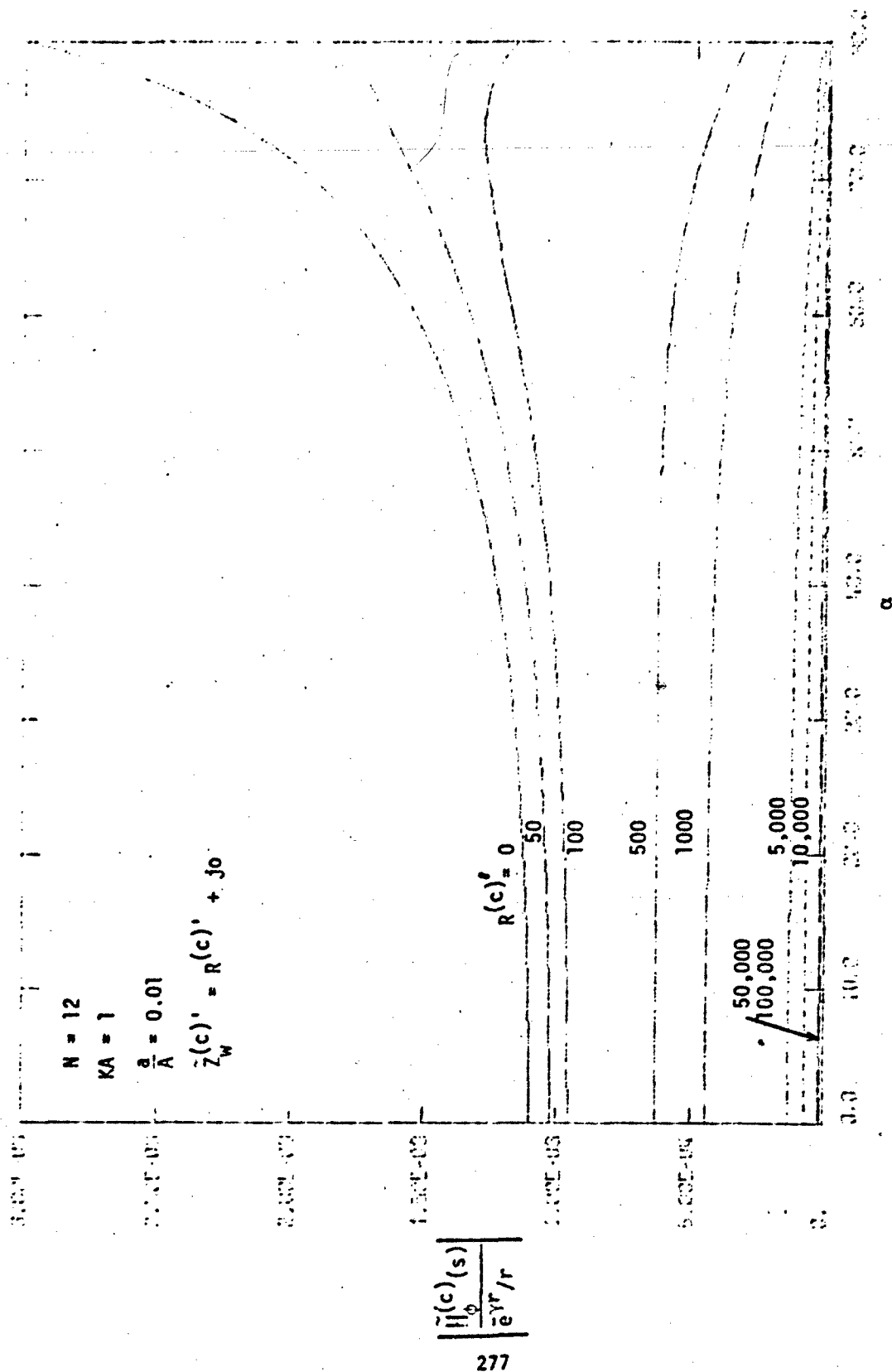


Figure 2.10(a). Magnitude of the Far-Field Distribution, Infinitely Long Loaded Circular Wire Cage Antenna,  $H_\phi^{(c)}$

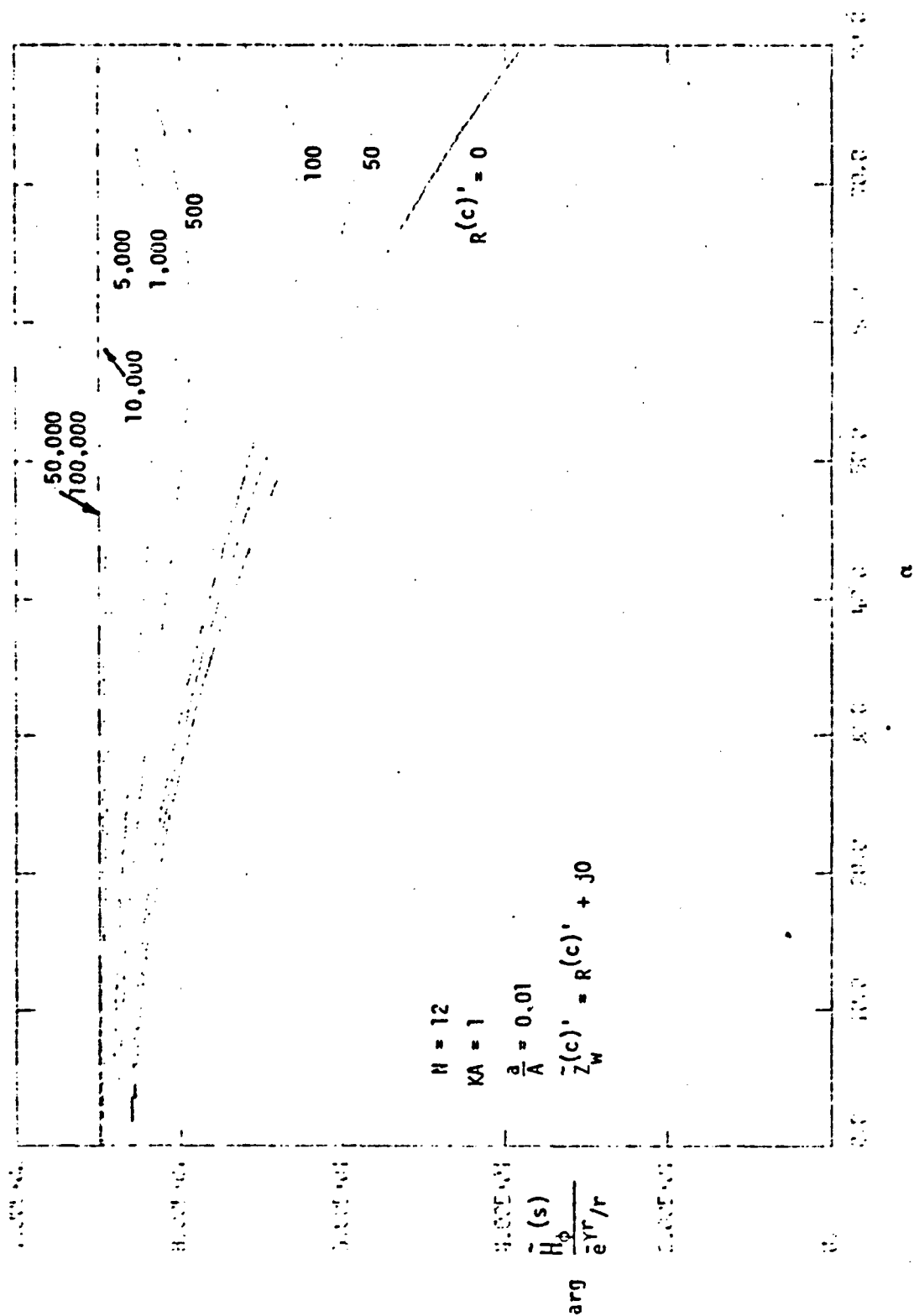


Figure 2.10(b). Phase of the Far-Field Distribution, Infinitely Long Loaded Circular Wire Cage Antenna,  $\tilde{H}_\phi(c)$

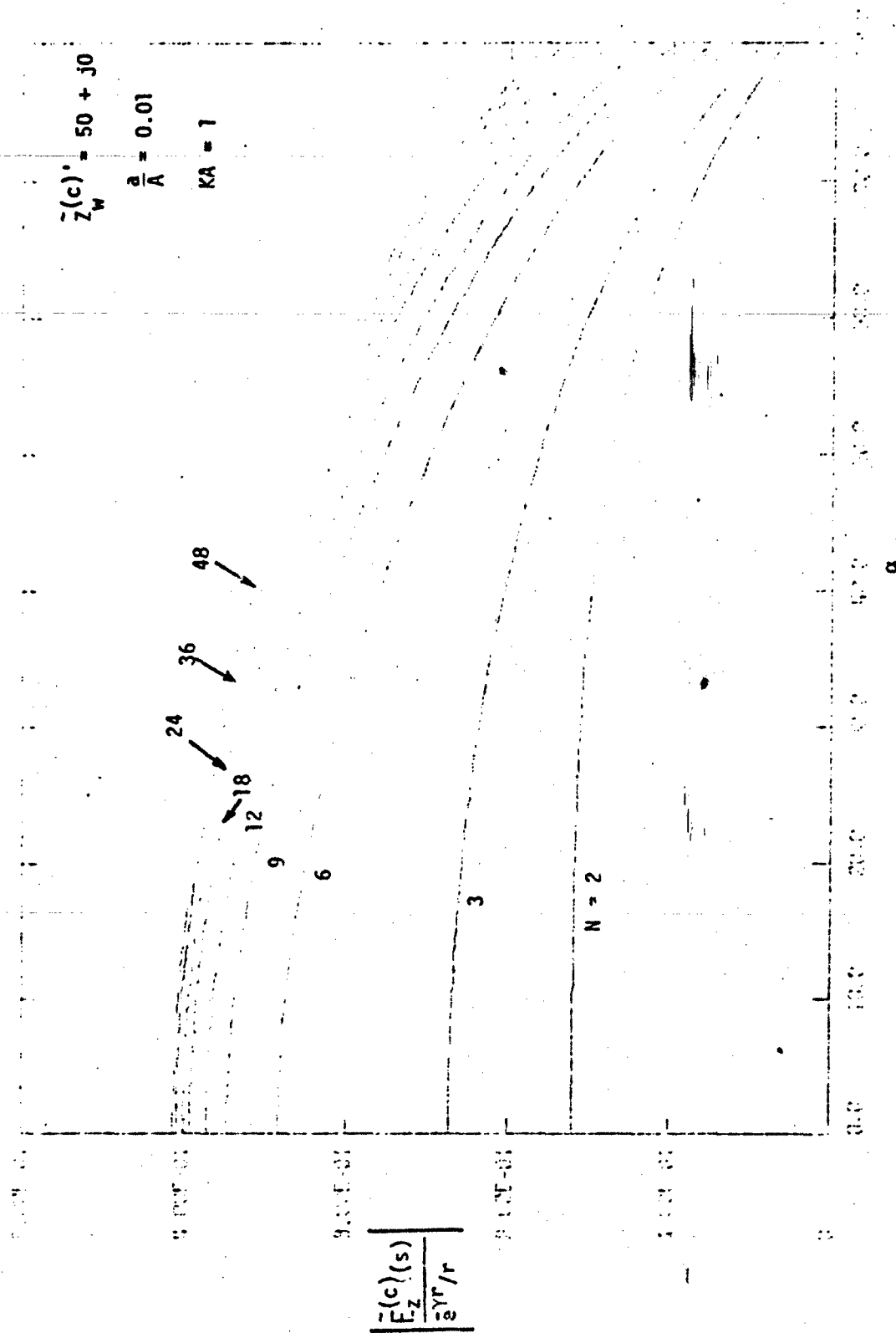


Figure 2.11(a). Magnitude of the Far-Field Distribution, Infinitely Long Loaded Circular Wire Cage Antenna,  $E_z^{(c)}$

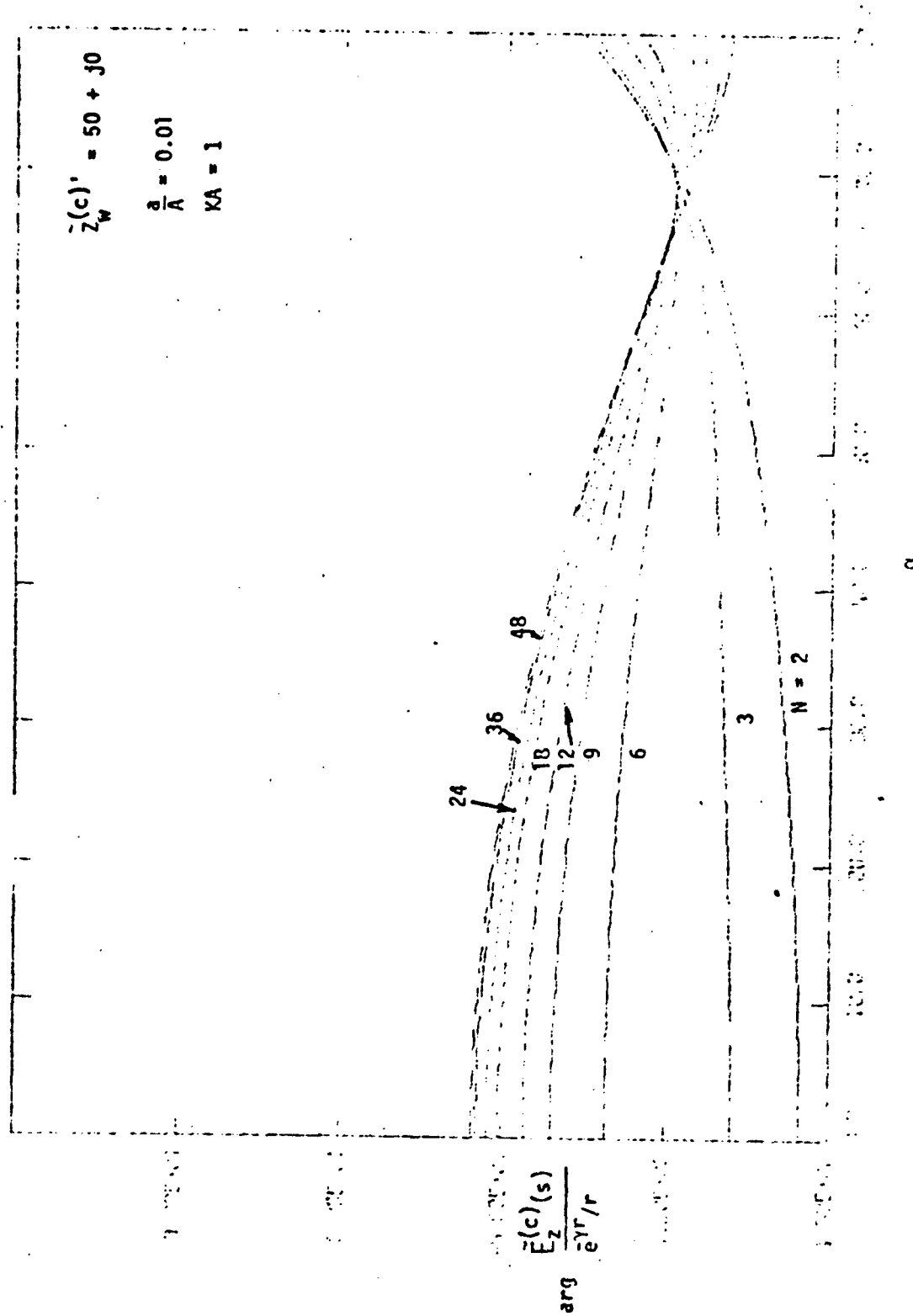


Figure 2.11(b). Phase of the Far-Field Distribution, Infinitely Long Loaded Circular Wire Cage Antenna,  $\tilde{E}_z(c)$

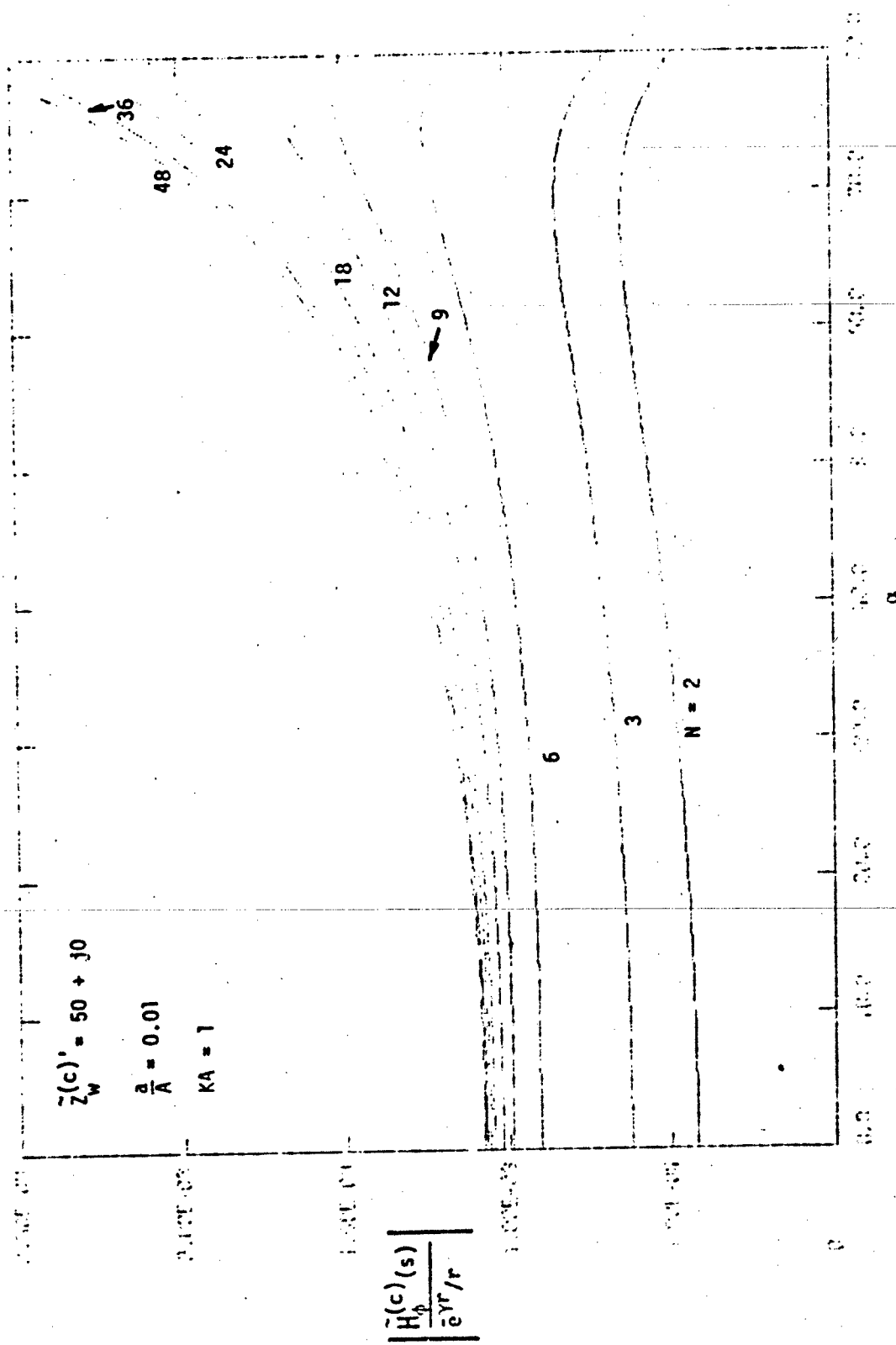


Figure 2.12(a). Magnitude of the Far-Field Distribution, Infinitely Long Loaded Circular Wire Cage Antenna,  $\tilde{H}_0^{(c)}$

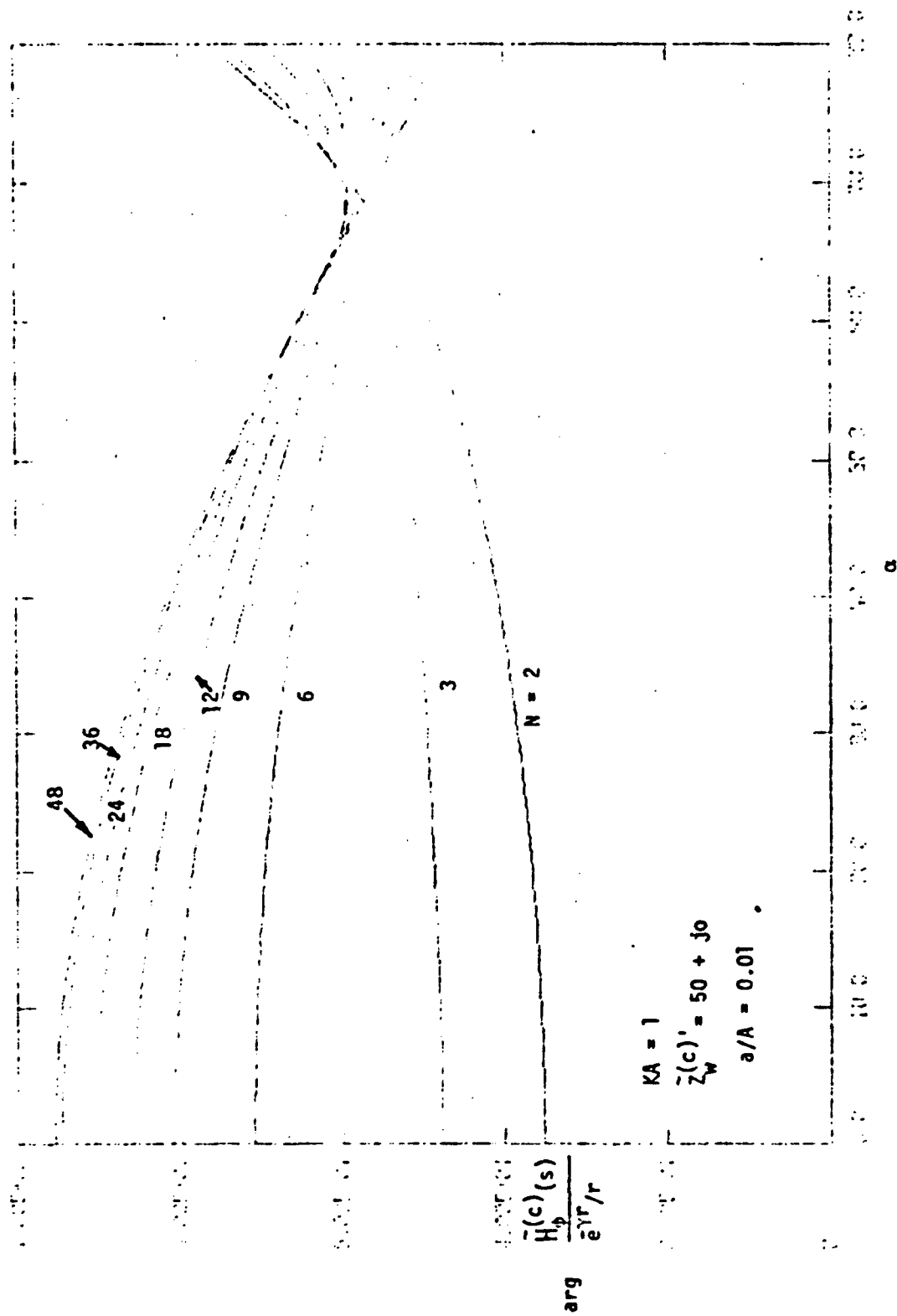


Figure 2.12(b). Phase of the Far-Field Distribution, Infinitely Long Loaded Circular Wire Cage Antenna,  $\tilde{H}_p(c)$

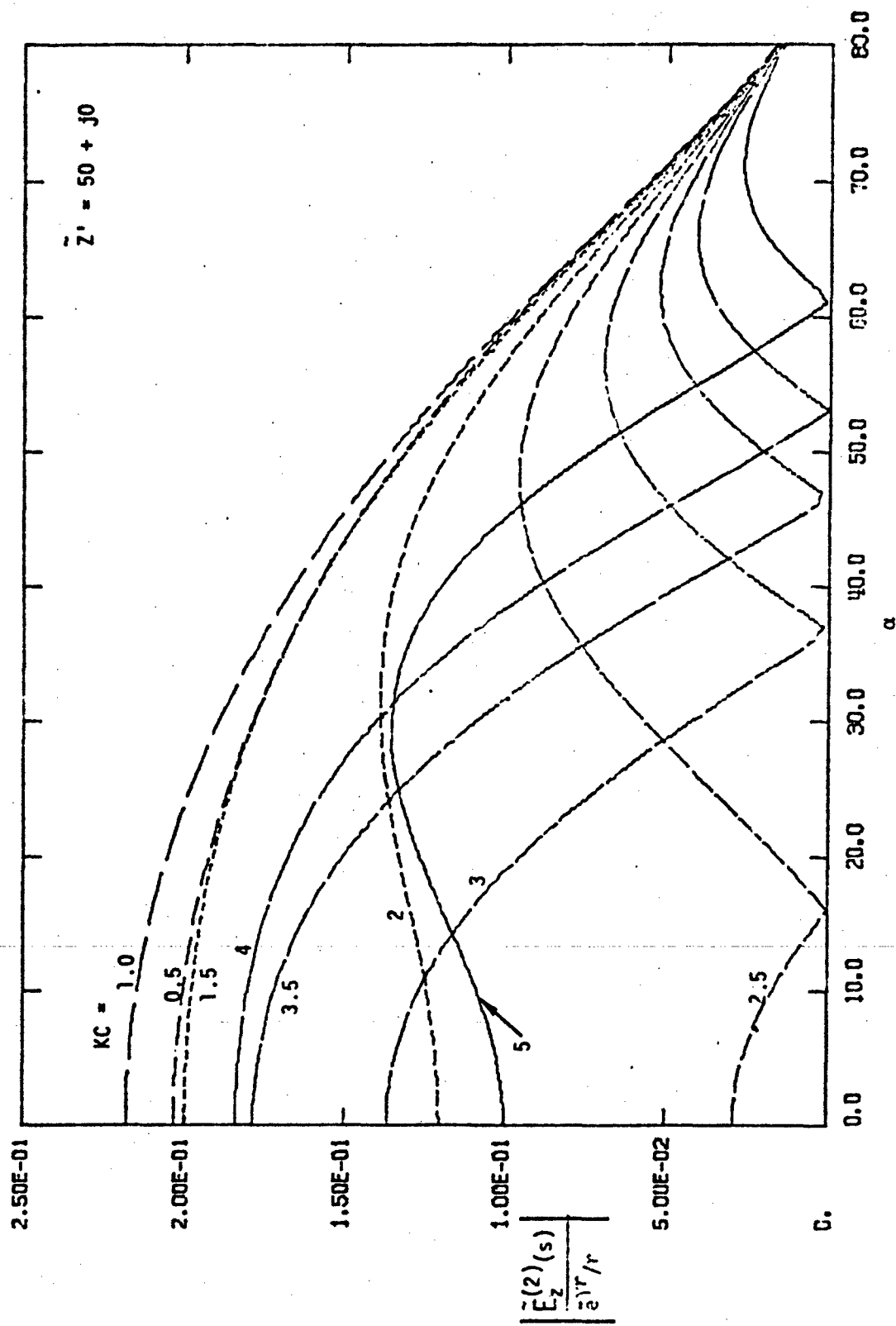


Figure 3.2(a). Magnitude of the Far-Field Distribution, Infinitely Long Loaded Hollow Cylindrical Antenna,  $\tilde{E}_z^{(2)}$

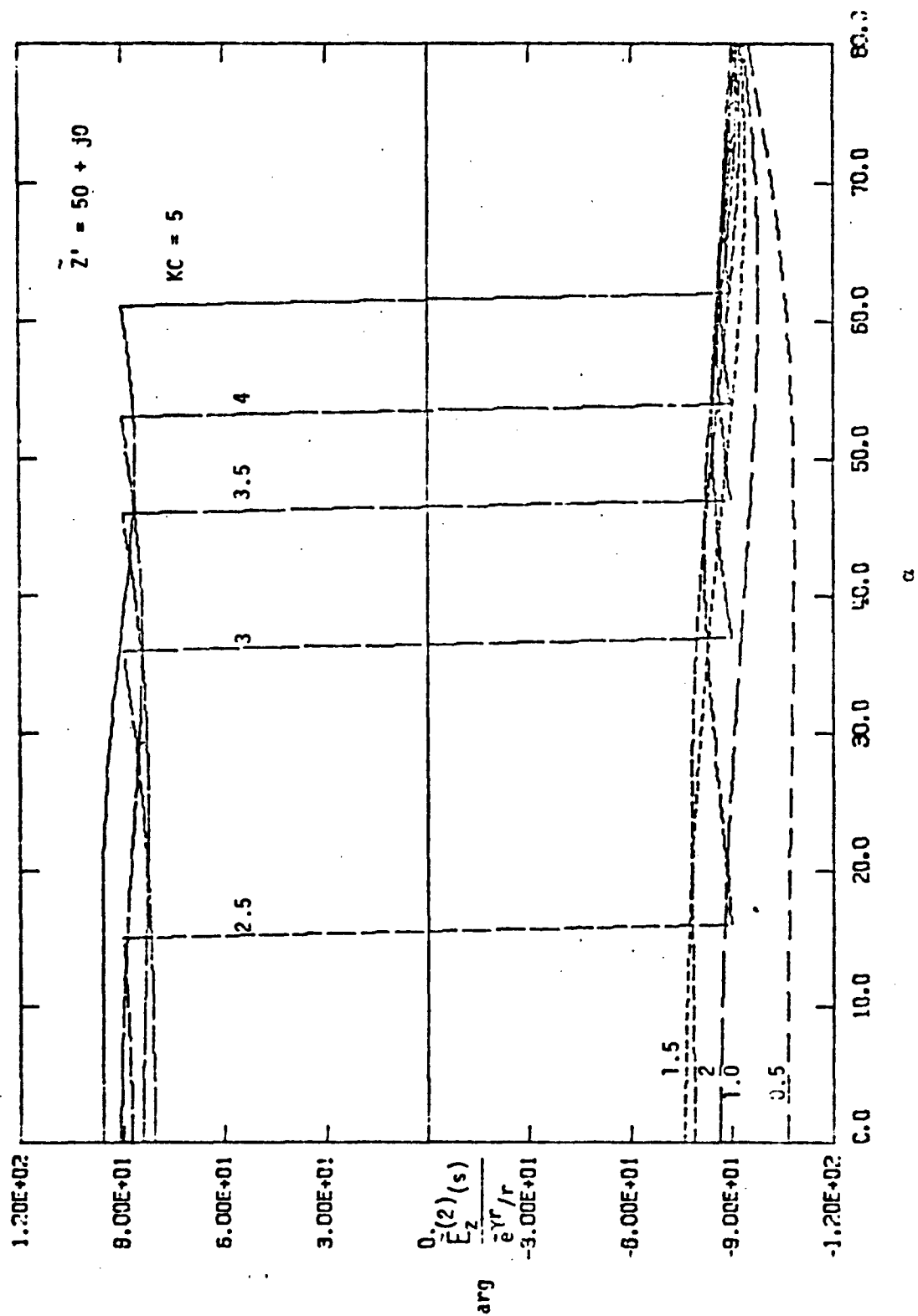


Figure 3.2(b). Phase of the Far-Field Distribution, Infinitely Long Loaded Hollow Cylindrical Antenna,  $\tilde{E}_z(2)$



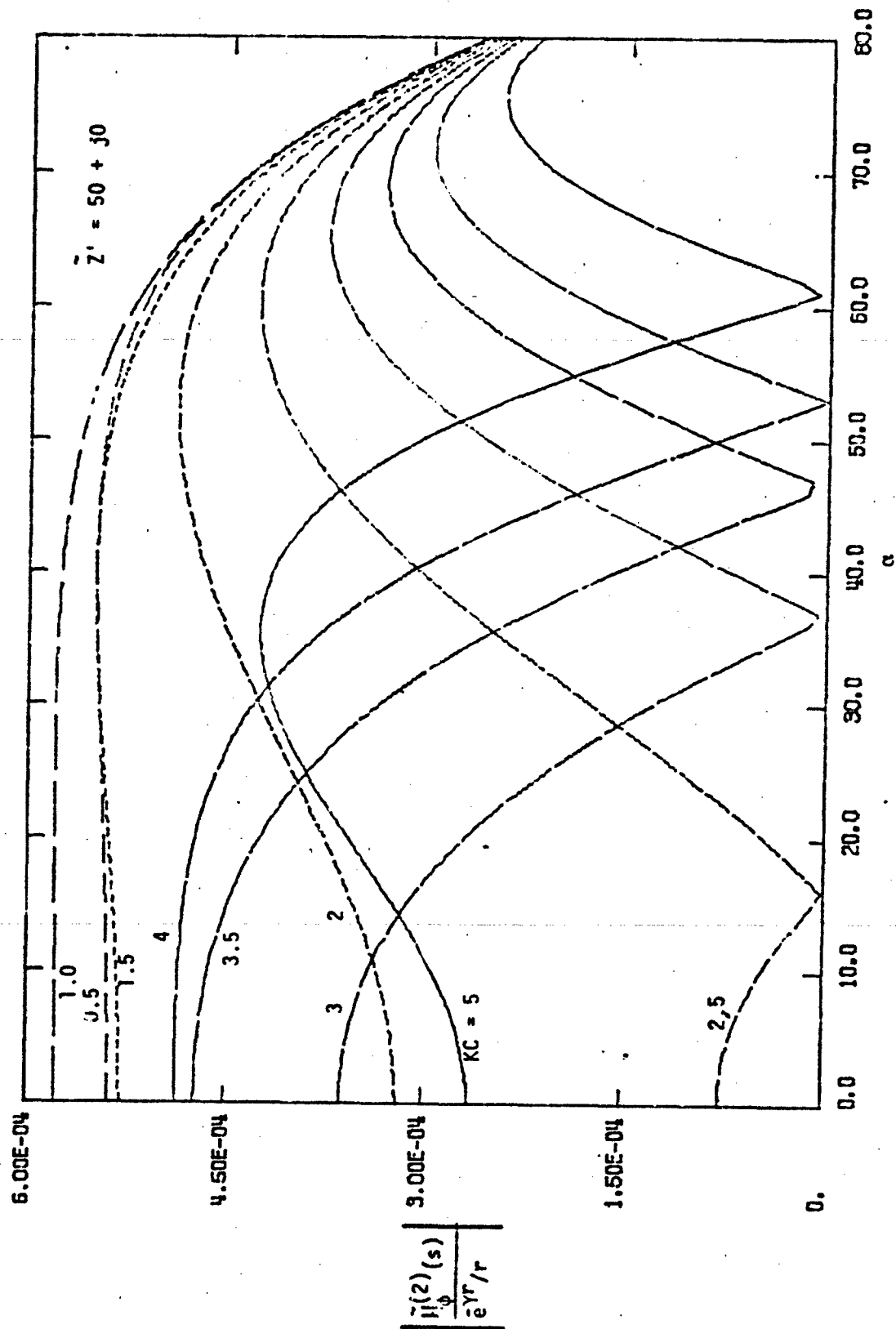


Figure 3.3(a). Magnitude of the Far-Field Distribution, Infinitely Long Loaded Hollow Cylindrical Antenna,  $\tilde{H}_{\phi}^{(2)}$

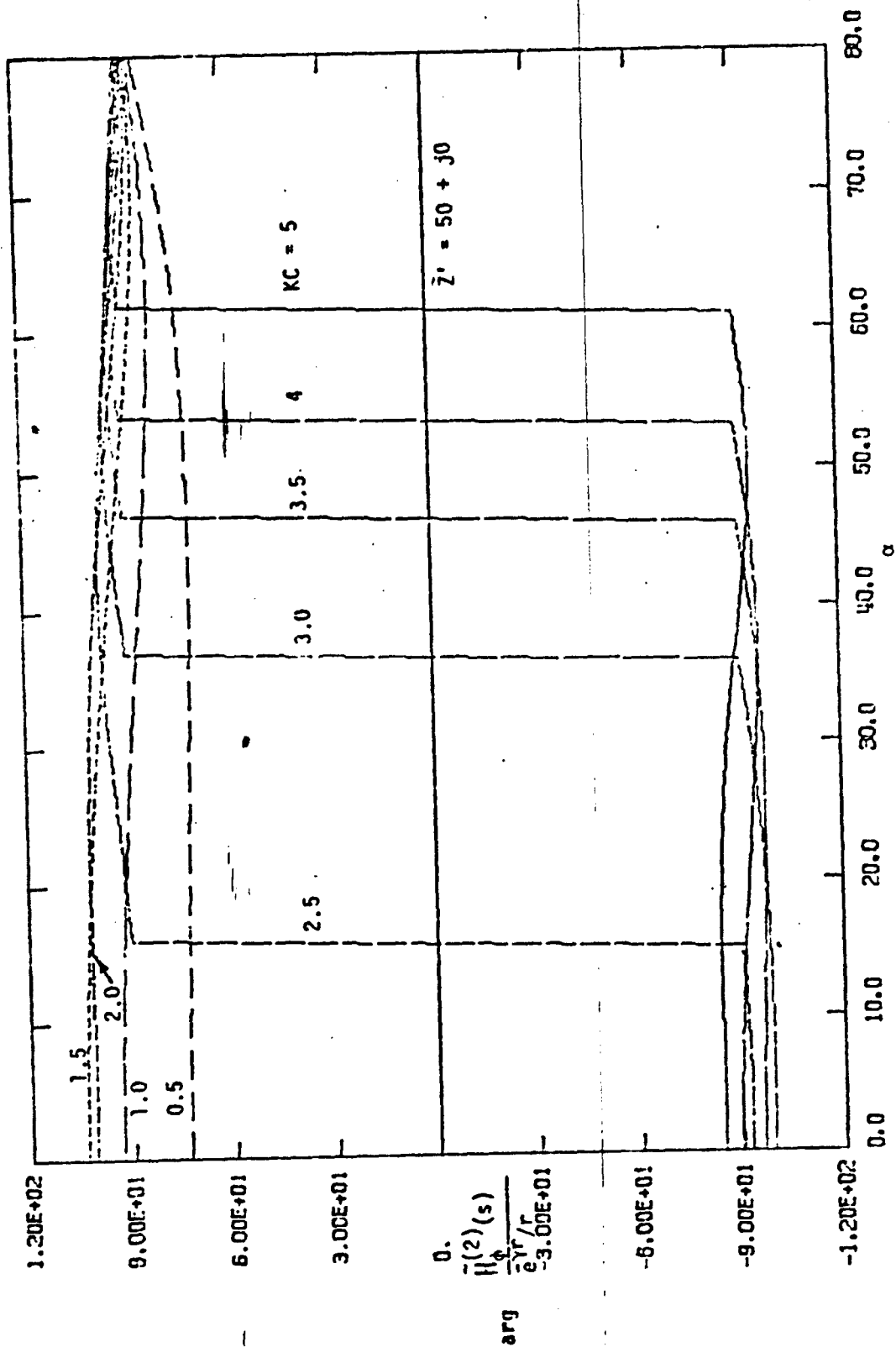


Figure 3.3(b). Phase of the Far-Field Distribution, Infinitely Long Loaded Hollow Cylindrical Antenna,  $H_\phi^{(2)}$

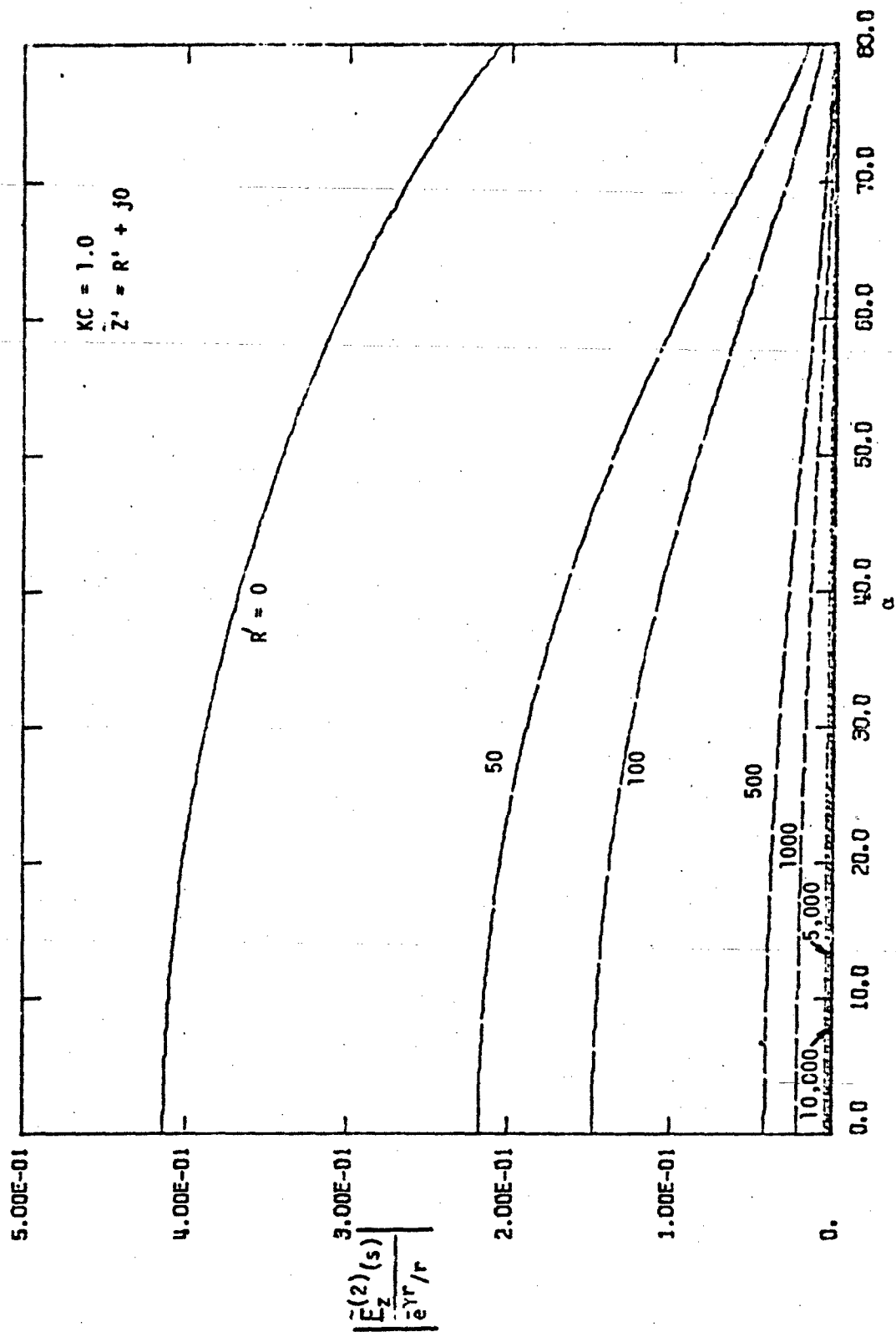


Figure 3.4(a). Magnitude of the Far-Field Distribution, Infinitely Long Loaded Hollow Cylindrical Antenna,  $\tilde{E}_z^{(2)}$

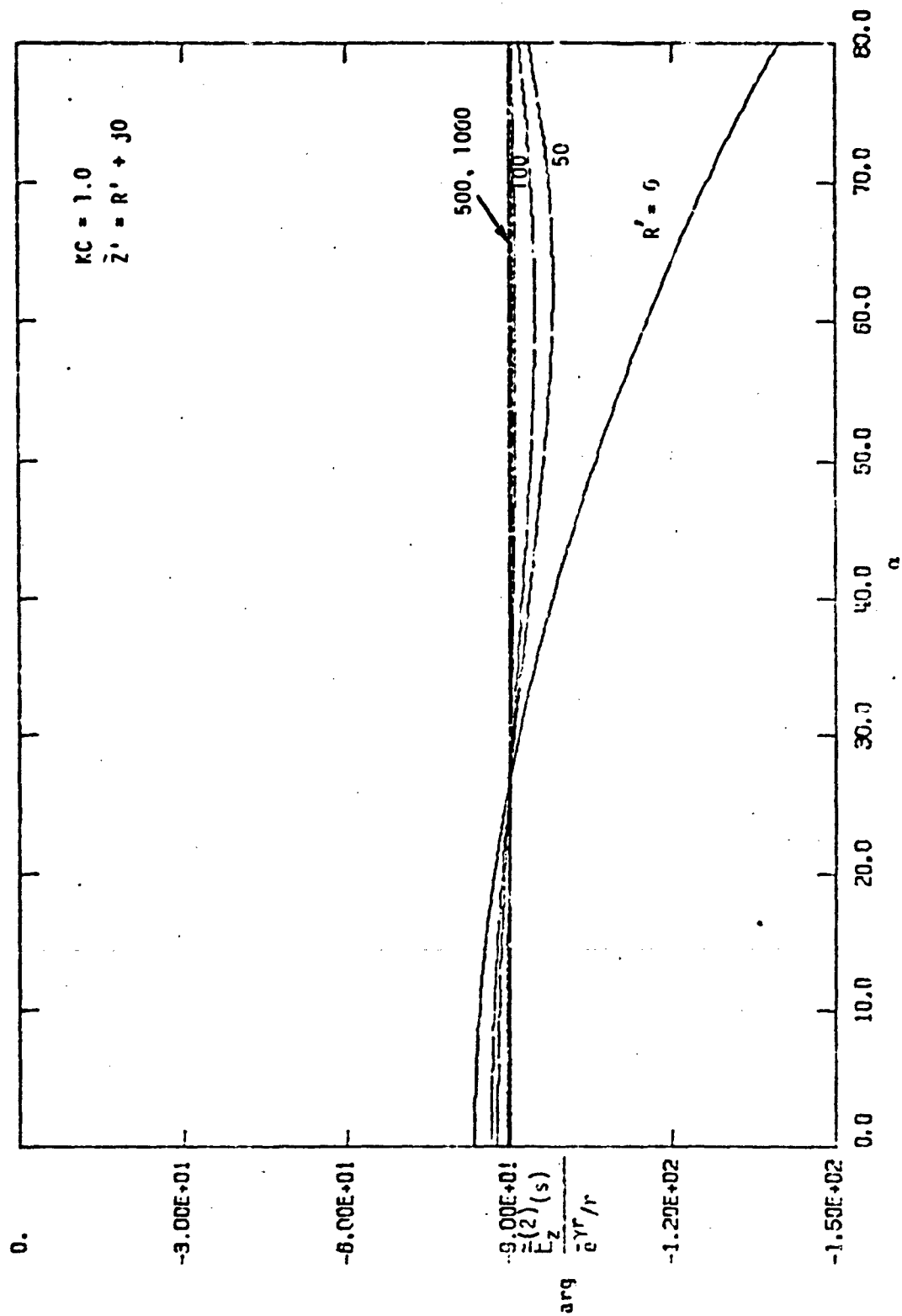


Figure 3.4(b). Phase of the Far-Field Distribution, Infinitely Long Loaded Hollow Cylindrical Antenna,  $\tilde{F}_Z^{(2)}$

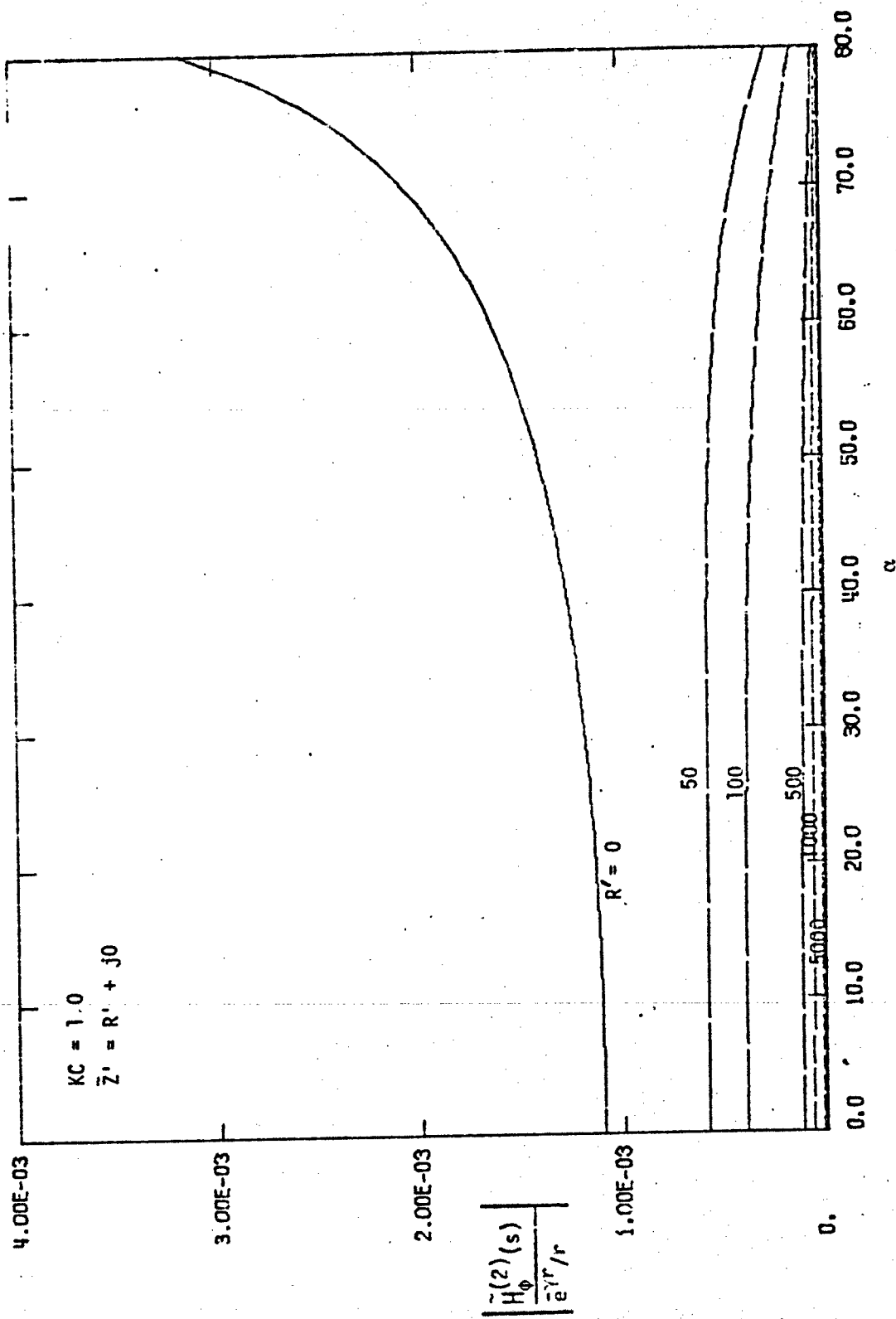


Figure 3.5(a). Magnitude of the Far-Field Distribution, Infinitely Long Loaded Hollow Cylindrical Antenna,  $\tilde{H}_\phi^{(2)}$

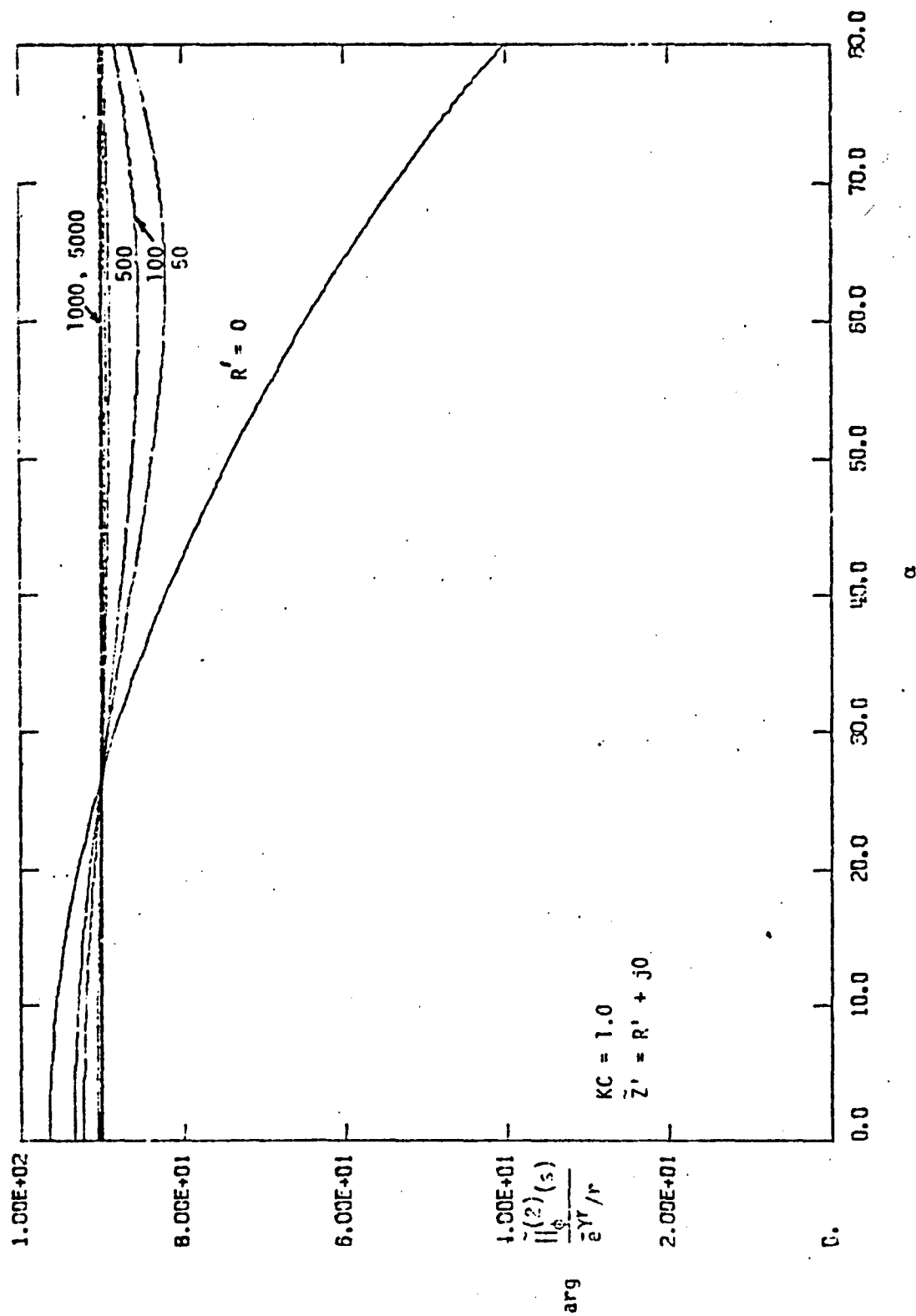


Figure 3.5(b). Phase of the Far-Field Distribution. Infinitely Long Loaded Hollow Cylindrical Antenna,  $\tilde{H}_\phi^{(2)}$

#### IV. ELECTROMAGNETIC EQUIVALENCE BASED ON FAR FIELDS

In the previous sections, three different types of canonical infinitely long antenna geometries are studied viz., (i) the infinitely long loaded solid wire antenna of radius  $b$  and impedance loading function per unit length  $\tilde{Z}'_w(s)$ , (ii) the infinitely long loaded circular wire cage antenna of cage radius  $A$ , radius of each cage wire  $a$ , number of cage wires  $N$  and its corresponding impedance loading function per unit length along each of the cage wires  $\tilde{Z}_w^{(c)'}(s)$ , and (iii) the infinitely long loaded hollow cylindrical antenna of radius  $C$  and sheet impedance loading function  $\tilde{Z}'(s)$ .

For each of the above canonical antenna structures integral expressions for the induced current, and for the radiated electric and magnetic fields are derived. Based on the saddle-point technique, far-field electric and magnetic field components are obtained in a more simplified form. Table II summarizes the results thus far obtained for the far-field distribution.

It is now possible to compare (and thus approximately equate) the distribution of the far-field components of the circular wire cage antenna as against the far-field distribution of a hollow cylindrical antenna. Such a comparison would allow establishing electromagnetic equivalences based on the far-field distributions. Given the circular wire-cage parameters viz., number of cage wires  $N$ , cage radius  $A$ , wire radius  $a$ , and its loading function  $\tilde{Z}_w^{(c)'}(s)$ , the electromagnetic equivalence allows one to pick equivalent radius  $C = \psi_{eq}$  and the corresponding loading function  $\tilde{Z}'(s) = \tilde{Z}'_{eq}(s)$ , so that both the structures radiate the same far-field distributions. The equivalent parameters are in fact a function of the complex frequency  $s$ , and the observation angle  $\alpha$ . The dependence on  $\alpha$  can be eliminated in some cases discussed further.

We shall now consider the electromagnetic equivalence between an infinitely long loaded circular wire cage structure and a loaded hollow circular cylinder based on the same radiated far fields. Columns 2 and 3 in table IIA for the far-field distributions are equated,

Table I

	1	2	3
	Infinitely Long Loaded Thin Wire	Infinitely Long Loaded Wire Cage	Infinitely Long Loaded Hollow Circular Cylinder
Radius	b	Cage A Wire a	C
Axial Impedance Loading	$Z_w'(s)$	$Z_w'(c)'(s)$	$Z'(s)$
Number of Wires	1	N	$\infty$



Table IIA

	1	2	3
Far Fields	Infinitely Long Loaded Thin Wire	Infinitely Long Loaded Wire Cage	Infinitely Long Loaded Hollow Circular Cylinder
$\tilde{E}_z(r, \alpha, s) \sim$	$-\frac{\tilde{V}}{2} \frac{\cos \alpha}{\tilde{L}_1(\gamma, \alpha)} \frac{e^{-\gamma r}}{r}$	$-\frac{\tilde{V}}{2} \frac{\cos \alpha}{\tilde{L}_2(\gamma, \alpha)} \frac{e^{-\gamma r}}{r} \tilde{C}_f$	$-\frac{\tilde{V}}{2} \frac{\cos \alpha}{\tilde{L}_3(\gamma, \alpha)} \frac{e^{-\gamma r}}{r} \tilde{P}_f$
$\tilde{E}_\psi(r, \alpha, s) \sim$	$-\frac{\tilde{V}}{2} \frac{\sin \alpha}{\tilde{L}_1(\gamma, \alpha)} \frac{e^{-\gamma r}}{r}$	$-\frac{\tilde{V}}{2} \frac{\sin \alpha}{\tilde{L}_2(\gamma, \alpha)} \frac{e^{-\gamma r}}{r} \tilde{C}_f$	$-\frac{\tilde{V}}{2} \frac{\sin \alpha}{\tilde{L}_3(\gamma, \alpha)} \frac{e^{-\gamma r}}{r} \tilde{P}_f$
$\tilde{H}_\phi(r, \alpha, s) \sim$	$\frac{\tilde{V}}{2Z_0} \frac{1}{\tilde{L}_1(\gamma, \alpha)} \frac{e^{-\gamma r}}{r}$	$\frac{\tilde{V}}{2Z_0} \frac{1}{\tilde{L}_2(\gamma, \alpha)} \frac{e^{-\gamma r}}{r} \tilde{C}_f$	$\frac{\tilde{V}}{2Z_0} \frac{1}{\tilde{L}_3(\gamma, \alpha)} \frac{e^{-\gamma r}}{r} \tilde{P}_f$

Table IIB

	1 Infinitely Long Loaded Thin Wire	2 Infinitely Long Loaded Wire Cage	3 Infinitely Long Loaded Hollow Circular Cylinder
$\tilde{L}_n(\gamma, \alpha)$	$\tilde{L}_1(\gamma, \alpha) =$ $\cos \alpha K_0(\gamma b \cos \alpha)$ $+ \tilde{h}_1(s) K_1(\gamma b \cos \alpha)$	$\tilde{L}_2(\gamma, \alpha) =$ $\cos \alpha \sum_{n=1}^N K_0(\gamma A_{1,n} \cos \alpha)$ $+ \tilde{h}_2(s) K_1(\gamma a \cos \alpha)$	$\tilde{L}_3(\gamma, \alpha) =$ $\cos \alpha I_0(\gamma C \cos \alpha) \cdot$ $K_0(\gamma C \cos \alpha)$ $+ \tilde{h}_3(s) \frac{1}{(\gamma C \cos \alpha)}$
Loading Factor $\tilde{h}_n(s)$	$\tilde{h}_1(s) = 2\pi b \frac{\tilde{Z}'_w(s)}{Z_0}$	$\tilde{h}_2(s) = 2\pi a \frac{\tilde{Z}'_w(s)}{Z_0}$	$\tilde{h}_3(s) = 2\pi C \frac{\tilde{Z}'(s)}{Z_0}$
Geometric Factor	1	$\tilde{C}_f = NI_0(\gamma A \cos \alpha)$	$\tilde{P}_f = I_0(\gamma C \cos \alpha)$

$$\frac{\tilde{C}_f}{\tilde{L}_2(\gamma, \alpha)} = \frac{\tilde{P}_f}{\tilde{L}_3(\gamma, \alpha)} \bigg|_{\substack{C=\psi_{eq} \\ \tilde{Z}'=\tilde{Z}'_{eq}}} \quad (4.1)$$

where

$\psi_{eq}$  = equivalent radius

$\tilde{Z}'_{eq}$  = equivalent impedance loading

From the expressions (2.34) and (3.11), the expression (4.1) takes the form,

$$\frac{NI_0(\gamma A \cos \alpha)}{\cos \alpha \sum_{n=1}^N K_0(\gamma A_{1,n} \cos \alpha) + \tilde{h}_2(s) K_1(\gamma A \cos \alpha)} = \frac{I_0(\gamma C \cos \alpha)}{\cos \alpha I_0(\gamma C \cos \alpha) K_0(\gamma C \cos \alpha) + \tilde{h}_3(s) \left[ \frac{1}{\gamma C \cos \alpha} \right]} \bigg|_{\substack{C=\psi_{eq} \\ \tilde{Z}'=\tilde{Z}'_{eq}}} \quad (4.2)$$

The expression (4.1) depicts equivalence condition for the loaded cage wire model and the hollow cylinder model, and is a function of the frequency  $\gamma$  and the angle of observation  $\alpha$ . Practically it is impossible to extract both the equivalent radius  $\psi_{eq}$  and equivalent impedance  $\tilde{Z}'_{eq}(s)$  from one equation unless one makes certain choices or forces one more realizable constraint. Some of the alternatives available are discussed in the following.

CASE I: Equivalence of perfectly conducting wire cage and perfectly conducting hollow cylinder

For this we have the impedance loading functions

$$\tilde{Z}'^{(c)}_w(s) = 0 \quad (4.3a)$$

and

$$\tilde{Z}'(s) = 0 \quad (4.3b)$$

the expression (4.2) yields the equivalence condition

$$\sum_{n=1}^N K_0(\gamma A_{1,n} \cos \alpha) - N I_0(\gamma A \cos \alpha) K_0(\gamma \psi_{eq}^{(c)} \cos \alpha) = 0 \quad (4.4)$$

We note  $\psi_{eq}^{(c)}$  is to be determined as the solution to the equation (4.4) and it appears implicitly in the argument of the modified Bessel function. Further

$$\psi_{eq}^{(c)} = \psi_{eq}^{(c)}(\gamma, \cos(\alpha)) \quad (4.5)$$

In the quasi-static case  $|\gamma A| \ll 1$ , the modified Bessel functions can be replaced by their small argument approximations,<sup>15</sup>

$$K_0(z) = -\ln\left(\frac{\Gamma z}{2}\right) \quad (4.6a)$$

$$I_0(z) = 1.0 \quad (4.6b)$$

On substituting the above small argument approximations, the equivalence condition (4.4) simplifies to

$$\psi_{eq_0}^{(c)} = [a A_{1,2} A_{1,3} \dots A_{1,N}]^{1/N} \quad (4.7)$$

where the inter-chord distances  $A_{1,n}$ ,  $n = 2, 3, \dots, N$  are defined in (2.30). It is interesting to note the equivalent radius  $\psi_{eq_0}^{(c)}$  is independent of the variables  $\gamma$  and  $\cos(\alpha)$  in the quasi-static case. The equivalence condition (4.4) yields the same result (4.7) even for the limiting case as  $\alpha \rightarrow \pi/2$  and  $|\gamma \cos \alpha| \ll 1$ . The equivalent radius result (4.7) checks with King's equivalent radius<sup>2</sup> obtained for a perfectly conducting finite circular cage antenna. In fact,  $\psi_{eq_0}^{(c)}$  can be shown also to be identical to the equivalent radius obtained by Baum,<sup>3</sup>

$$\frac{\psi_{eq_0}^{(c)}}{A} = \left[\frac{aN}{A}\right]^{1/N} \quad (4.8)$$

which is based on conformal transformation; an equivalence between a single charged conductor and number of equally spaced concentric charged conductors. Appendix C discusses the two results (4.7) and (4.8) as one and the same.

In figure 4.1 is shown the variation of the normalized equivalent radius  $\psi_{eq_0}^{(c)}/A$  as a function of  $A$  and similarly in figure 4.2 as a function of  $a/A$ ,<sup>3</sup> for different values of number of cage wire  $N$ .

As stated earlier  $\psi_{eq_0}^{(c)}$  is independent of the complex frequency  $\gamma$  and of the variable  $\cos(\alpha)$ , figure B-2, in the quasi-static limit. The first order effect of the complex frequency  $\gamma$  on the equivalent radius  $\psi_{eq}^{(c)}$  can be obtained if higher order terms are included in the series expansion of the modified Bessel functions, and can be written as,<sup>15</sup>

$$K_0(z) = \left[ -\ln\left(\frac{\gamma z}{2}\right) \right] I_0(z) + \frac{\frac{1}{4} z^2}{1!} + \left( 1 + \frac{1}{2} \right) \frac{\left( \frac{1}{4} z^2 \right)^2}{2!} + \dots \quad (4.9a)$$

$$I_0(z) = 1 + \frac{\frac{1}{4} z^2}{1!} + \frac{\left( \frac{1}{4} z^2 \right)^2}{2!} + \dots \quad (4.9b)$$

Picking the first two terms in the above series expansion (4.9) and substituting into the equivalence condition (4.4), it reduces to the following transcendental equation,

$$\left[ \frac{\psi_{eq}^{(c)}}{A} \right]^2 - B_1 \ln \left[ \frac{\psi_{eq}^{(c)}}{A} \right] - B_2 = 0 \quad (4.10a)$$

$$B_1 = \frac{4N}{(\gamma' A)^2} \quad (4.10b)$$

$$B_2 = \left[ \frac{a^2}{A^2} + 2N \right] - \frac{4}{(\gamma' A)^2} \ln \left( \frac{aN}{A} \right) \quad (4.10c)$$

$$\gamma' = \gamma \cos(\alpha) \quad (4.10d)$$

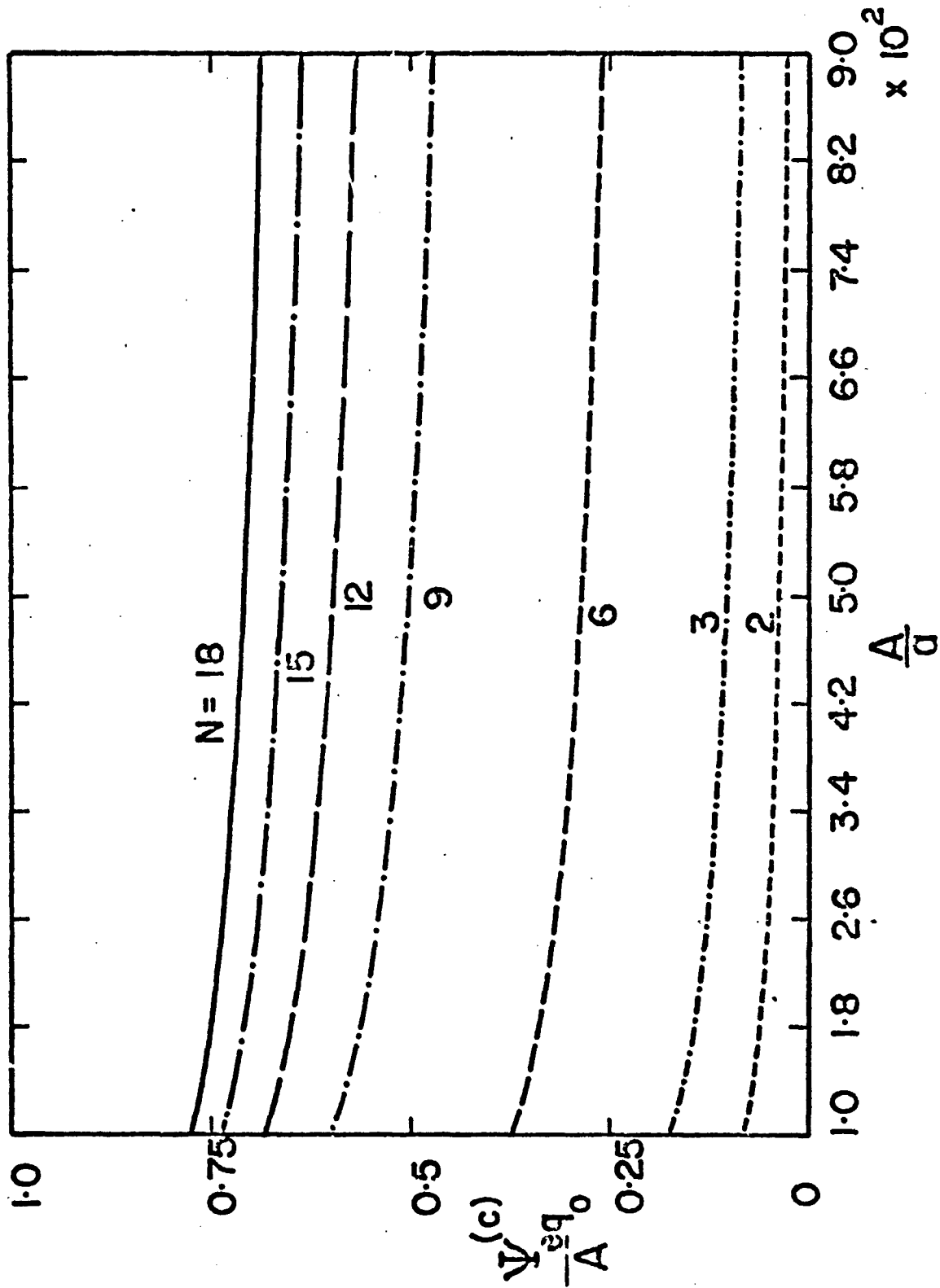
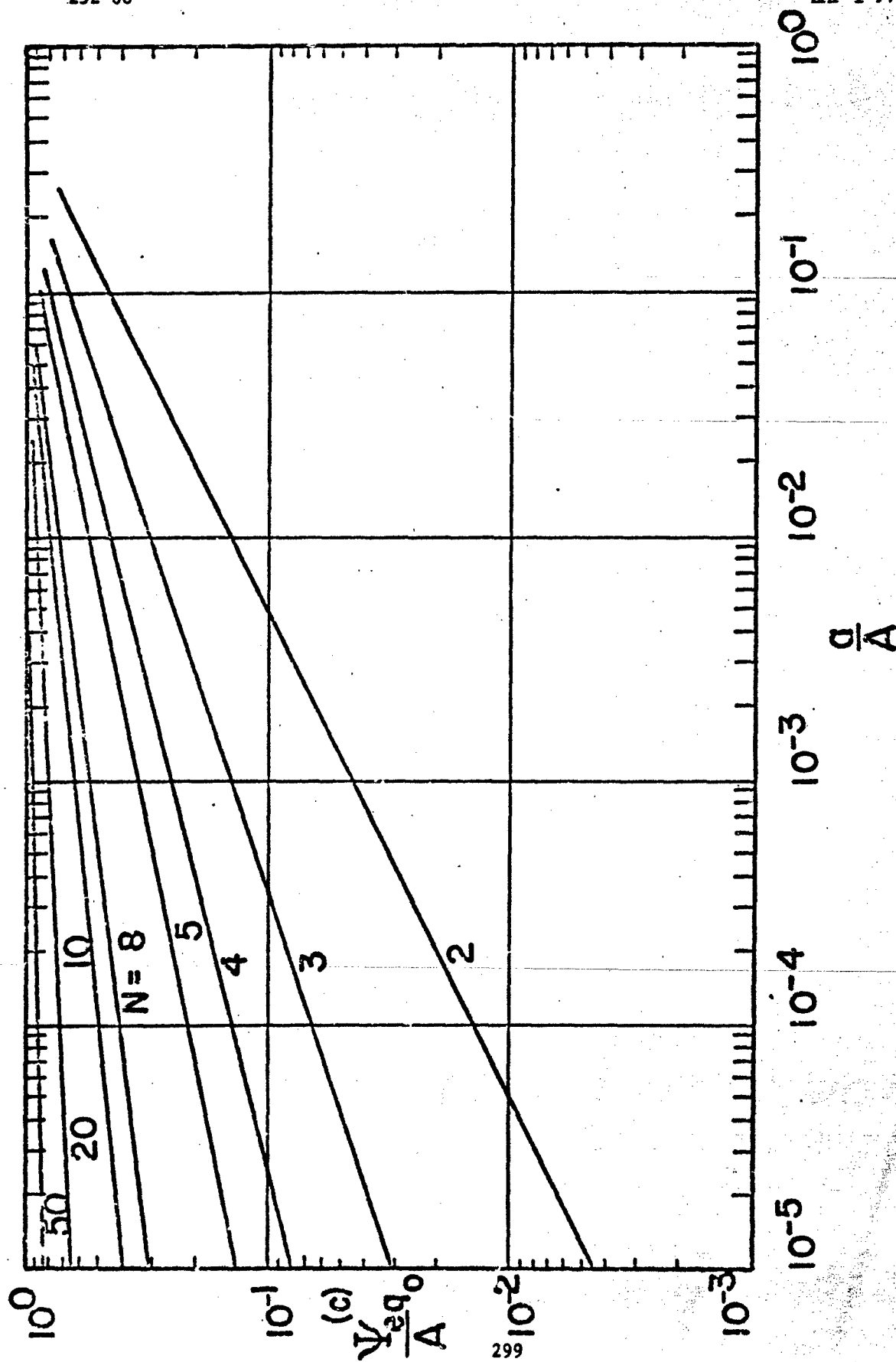


Figure 4.1.1. Equivalent Radius of a Conductor in a Circular Wire Cage in the Quasi-Static Range,  $a = 0.01$

Figure 4.2. Equivalent Radius of a Conducting Circular Wire Cage for Various  $N$

Further, the equation (4.10a) yields the first order solution,

$$\left(\frac{\psi_{eq}^{(c)}}{A}\right) \approx \left(\frac{\psi_{eq_0}^{(c)}}{A}\right) \left[1 - \frac{1}{N} \left(\frac{a^2}{A^2} + 2N\right) \left(\frac{\gamma'A}{2}\right)^2\right], \quad |\gamma'A| < 1 \quad (4.11)$$

The expression (4.4) is also solved numerically<sup>19</sup> to determine the more exact quasi-static frequency range up to which the results of figure 4.1 are valid. Table III gives the lowest first zero solution to the implicit equation (4.4) for a particular set of wire cage parameters. As the frequency approaches large values, the equivalent radius result (4.7) is no longer valid, and  $\psi_{eq}^{(c)}$  should be obtained from the solution to equation (4.4) or equation (4.11) for a given complex frequency  $\gamma$  and observation angle  $\alpha$ . Figure 4.3 indicates the variation of the equivalent radius  $\psi_{eq}^{(c)}$  as a function of  $K'A$ . For very large values of  $|\gamma A \cos(\alpha)|$ , one may substitute asymptotic forms of the modified Bessel function in the expression (4.4) and solve for the equivalent radius  $\psi_{eq}^{(c)}$ .

**CASE II: Equivalence of loaded wire cage and loaded hollow cylinder**

For this general case the equivalence condition (4.2) should be considered leading to the difficulty of one equation and two unknown parameters  $\psi_{eq}$  and  $\tilde{Z}'_{eq}(s)$  to be determined. We can conveniently make a choice of one of the unknown parameters. Suppose the equivalent radius is chosen to be the same as the frequency-dependent equivalent radius  $\psi_{eq}^{(c)}$  (as obtained from (4.4) or approximately from (4.11)) for the perfectly conducting case (case I), we obtain for the equivalent impedance loading function  $\tilde{Z}'_{eq}(s)$ ,

$$\psi_{eq} \equiv \psi_{eq}^{(c)} \quad (4.12a)$$

$$\tilde{Z}'_{eq}(s) = \left(\frac{\tilde{Z}_w^{(c)'}(s)}{N}\right) \gamma a \cos \alpha K_1(\gamma a \cos \alpha) \frac{I_0(\gamma \psi_{eq}^{(c)} \cos(\alpha))}{I_0(\gamma A \cos(\alpha))} \quad (4.12b)$$

As pointed out earlier, the equivalent impedance-per-unit-length function  $\tilde{Z}'_{eq}(s)$  is a function of  $\gamma$  and  $\cos(\alpha)$ . In the quasi-static



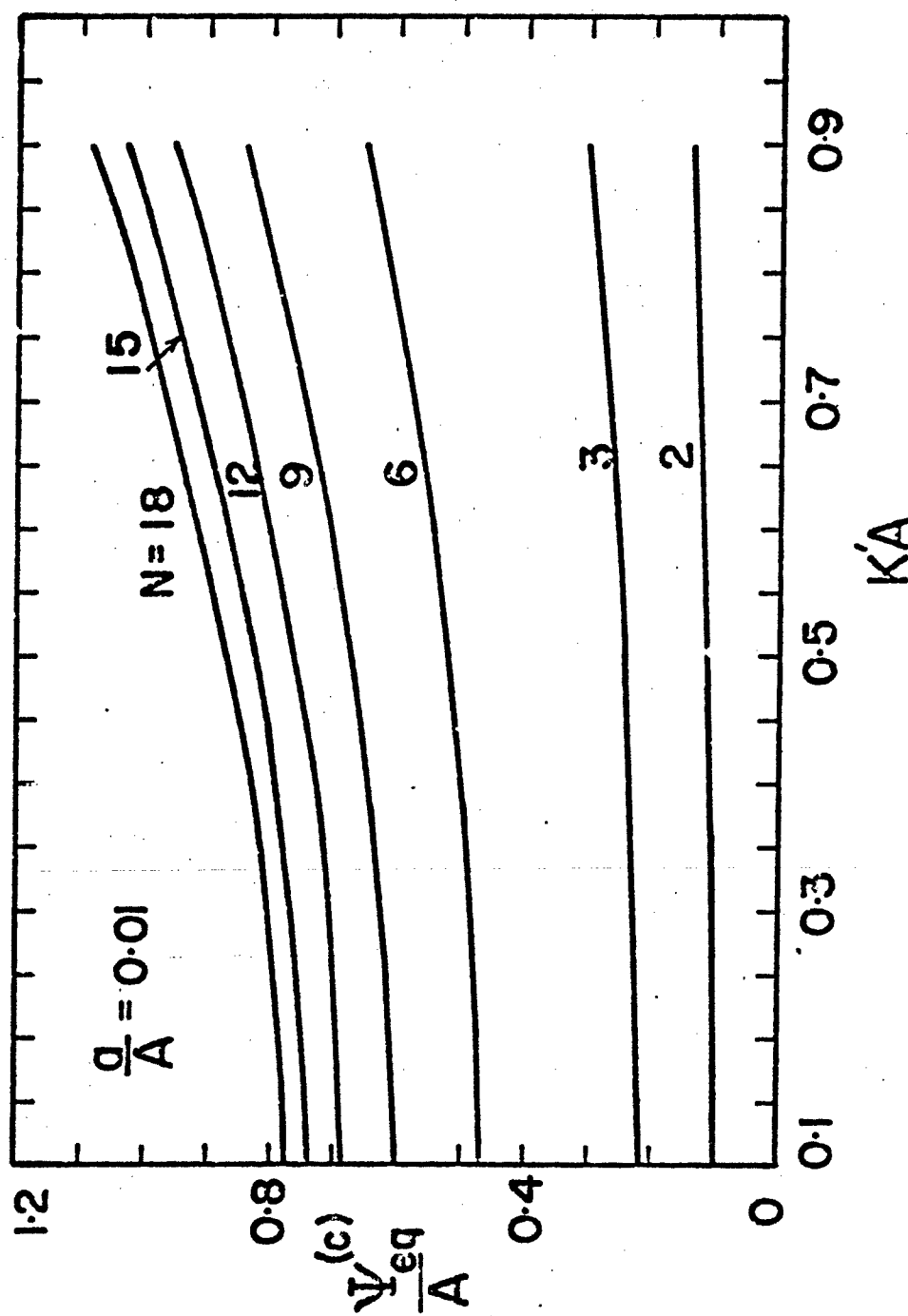


Figure 4.3. Equivalent Radius of a Conducting Circular Wire Cage as a Function of  $K'A$ ,  $\gamma = jK$

Table III

KA cos( $\alpha$ )		$K\psi_{eq}^{(c)} \cos(\alpha)$		$\frac{\psi_{eq}^{(c)}}{A}$	
.1	j 0.0	.08395	j-.00010	.83953	j-.00096
.2	0.0	.16844	-.00074	.84221	-.00370
.3	0.0	.25353	-.00239	.84511	-.00795
.4	0.0	.33913	-.00538	.84783	-.01345
.5	0.0	.42508	-.00999	.85015	-.01999
.6	0.0	.51121	-.01647	.85201	-.02746
.7	0.0	.59736	-.02506	.85337	-.03581
.8	0.0	.68338	-.03605	.85422	-.04507
.9	0.0	.76909	-.04981	.85454	-.05534
1.0	0.0	.85430	-.06681	.85430	-.06681
1.1	0.0	.93877	-.08772	.85343	-.07974
1.2	0.0	1.02218	-.11346	.85182	-.09455
1.3	0.0	1.10405	-.14535	.84927	-.11180
1.4	0.0	1.18360	-.18534	.84543	-.13239
1.5	0.0	1.25953	-.23643	.88969	-.15762
1.6	0.0	1.32939	-.30342	.83087	-.18964
1.7	0.0	1.38810	-.39446	.81653	-.23204
1.8	0.0	1.42353	-.52418	.79085	-.29121
1.9	0.0	1.40057	-.71896	.73714	-.37840
2.0	0.0	1.19554	-.99934	.59777	-.49967

$$\frac{a}{A} = 0.01$$

$$N = 12$$

frequency range  $|\gamma A| \ll 1$ , the above expression (4.12b) simplifies to

$$\tilde{Z}'_{eq}(s) = \frac{\tilde{Z}_w^{(c)'}(s)}{N} \quad (4.12c)$$

which is exactly the equivalent parallel impedance of the  $N$  cage wires. The first order effect of the complex frequency  $\gamma$  on the equivalent sheet impedance per unit length  $\tilde{Z}'_{eq}(s)$  can be obtained by substituting higher order terms for the modified Bessel functions in the expression (4.12b), hence we have

$$\tilde{Z}'_{eq}(s) = \left[ 1 + \frac{1}{2}(\gamma' a)^2 \right] \left[ \frac{4 + (\gamma' \psi_{eq}^{(c)})^2}{4 + (\gamma' A)^2} \right] \frac{\tilde{Z}_w^{(c)'}(s)}{N} \quad (4.13a)$$

$$= \left( \frac{\psi_{eq}^{(c)}}{A} \right)^2 \left[ 1 + \left( \frac{2}{\gamma' \psi_{eq}^{(c)}} \right)^2 - \left( \frac{2}{\gamma' A} \right)^2 - \left( \frac{4}{\gamma' \psi_{eq}^{(c)} \gamma' A} \right)^2 \right] \frac{\tilde{Z}_w^{(c)'}(s)}{N}$$

$$\text{for} \quad \left| \left( \frac{2}{\gamma' A} \right)^4 \right| < 1 \quad (4.13b)$$

### CASE III:

In the above case II, we made a choice for the equivalent radius to be the same as the perfectly conducting case. We can make another practical choice of choosing the equivalent radius  $\psi_{eq}^{(c)} = A$ , the radius of the wire cage, and work out the corresponding appropriate equivalent loading function so that far-field equivalence holds good.

Hence substituting  $\psi_{eq}^{(c)} = A$  in the expression (4.2) yields an expression for the equivalent loading function  $\tilde{Z}'_{eq}(s)$ . In the quasi-static limit as  $|\gamma A| \ll 1$ , we obtain

$$\tilde{Z}'_{eq}(s) = \frac{\tilde{Z}_w^{(c)'}(s)}{N} - \frac{\gamma \cos^2(\alpha) Z_0}{2\pi} \ln \left( \frac{\psi_{eq}^{(c)}}{A} \right) \quad (4.14)$$

which shows an angle dependent ( $\alpha$ ) positive inductance per-unit-length term as

$$\tilde{Z}'_{eq}(s) = \frac{\tilde{Z}_w^{(c)'}(s)}{N} + sL' \quad (4.15)$$

$$L' \equiv \frac{\mu}{2\pi} \cos^2(\alpha) \ln\left(\frac{A}{\psi_{eq}(c)}\right) > 0$$

Note that as  $s \rightarrow 0$  the inductive term is negligible giving the wire loading as the dominant term as one would expect. For higher frequencies, however, the property of having an angle ( $\alpha$ ) dependent impedance per unit length is an undesirable feature because there is then no unique equivalent impedance per unit length; it depends where one looks.

## V. CONCLUSIONS

A preliminary analysis is carried out to aim at suitably modeling hybrid EMP simulators made up of thin wire structures and wire meshes. Canonical infinitely long loaded wire geometries in the form of a thin wire, a circular wire cage and hollow cylindrical structures are analyzed systematically by treating them as boundary value antenna problems. Results of the induced current distribution and the corresponding radiated fields are obtained for each of the canonical geometries.

The radiated fields of the loaded concentric wire cage are compared with the radiated fields of the loaded hollow cylinder to arrive at an electromagnetic equivalence condition. Based on this equivalence, the equivalent radius of the wire cage and the corresponding equivalent sheet impedance per-unit-length loading function are obtained so that both the compared structures radiate the same far fields. In fact the results obtained are a function of the complex frequency. In the low frequency ranges an explicit expression for the equivalent radius of the cage is obtained; one has to solve implicit equations for higher frequencies.

The theory and the concept of the electromagnetic equivalence applied to wire structures, discussed in this note is used in the future work as a foundation to effectively model hybrid simulators including their complex feeding generators.

## APPENDIX A

LONGITUDINAL  $\phi$ -INDEPENDENT IMPEDANCE CHARACTERISTICS  
OF CIRCULAR CYLINDRICAL STRUCTURES

The impedance characteristics of infinitely long circular-cross-section structures are discussed in detail in reference 20. A summary of the expressions utilized in the previous sections is given below.

## 1. Thin Solid Cylindrical Wire

In figure A-1 is shown the geometry of an infinitely long solid circular thin wire of radius  $b$ . The material of the wire has homogeneous characteristics of permeability  $\mu_w$ , permittivity  $\epsilon_w$ , and conductivity  $\sigma_w$ . The structure is oriented along  $z$ -axis in an isotropic homogeneous medium. Only axial electric current  $\tilde{I}(\zeta, s)$  is assumed to exist and hence only the TM (transverse magnetic to  $z$ ) electromagnetic field components  $\tilde{E}_\psi(\zeta, s)$ ,  $\tilde{E}_z(\zeta, s)$  and  $\tilde{H}_\phi(\phi, s)$  are present and are symmetric with respect to  $\phi$ -angular variations.

In the region  $\psi < b$ , the magnetic vector potential is

$$\tilde{A}_z(\psi, \zeta, s) = \tilde{C}(\zeta, s) I_0(u_w \psi) \quad (A.1)$$

where

$$u_w = [\gamma_w^2 - \zeta^2]^{\frac{1}{2}} \quad (A.2)$$

$$\gamma_w = [\mu_w s(\sigma_w + \epsilon_w s)]^{\frac{1}{2}} \quad (A.3)$$

In the expression (A.1),  $\tilde{C}(\zeta, s)$  is a constant which determines the potential distribution. If displacement currents are neglected  $\gamma_w = [\mu_w \sigma_w s]^{\frac{1}{2}}$ . The series axial impedance per unit length of the solid infinitely long wire is given by

$$\tilde{Z}'_w(\zeta, s) = \frac{\tilde{E}_z(\psi, \zeta, s)}{2\pi b \tilde{H}_\phi(\psi, \zeta, s)} \Big|_{\psi=b} \quad (A.4)$$

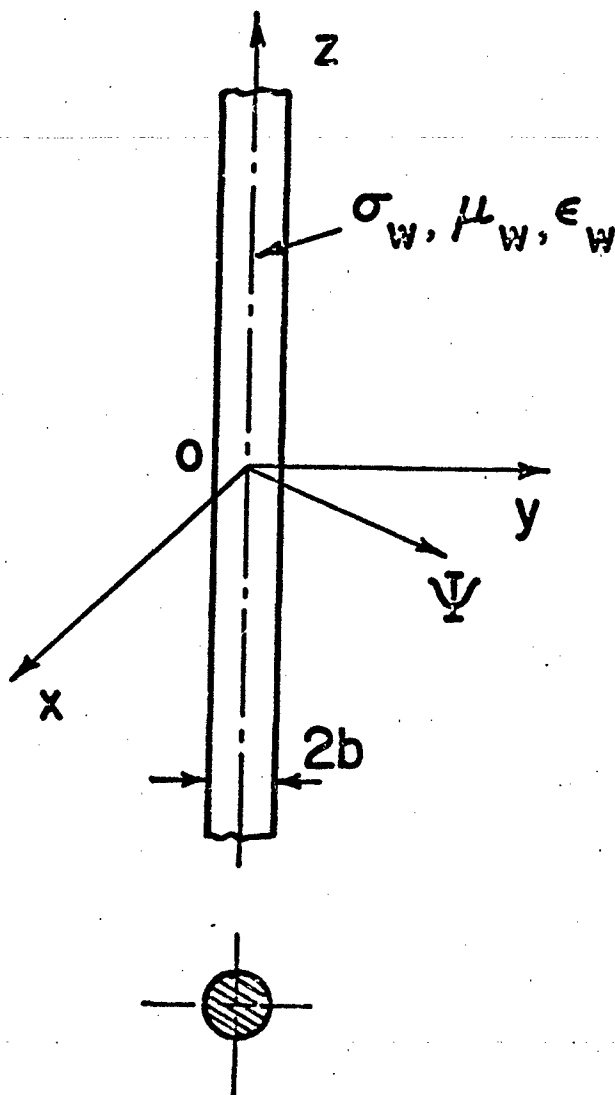


Figure A-1. Thin Solid Cylindrical Wire

which is the ratio of the axial electric field to the total axial current. Using the expressions (2.4a and b)

$$\tilde{Z}'_w(z, s) = \frac{u_w I_0(u_w b)}{2\pi b(\sigma_w + s\epsilon_w) I_1(u_w b)} \quad (A.5)$$

$I_0$  and  $I_1$  are the modified Bessel functions of first kind, zero and first orders, respectively. In the quasi-static range  $|\gamma_w^2| \gg \epsilon^2$ , and the axial impedance per unit length reduces to

$$\tilde{Z}'_w(s) = \frac{\gamma_w I_0(\gamma_w b)}{2\pi b(\sigma_w + s\epsilon_w) I_1(\gamma_w b)} \quad (A.6)$$

For the limiting case of static conditions,  $s \rightarrow 0$ ,

$$I_0(\gamma_w b) \approx 1 \quad (A.7)$$

$$I_1(\gamma_w b) \approx \frac{\gamma_w b}{2} \quad (A.8)$$

$$Z'_w \approx \frac{1}{\pi b^2 \sigma_w} \quad (A.9)$$

The infinitely long thin cable wire characteristics for a typical copper conductor  $\sigma_w = 5.65 \times 10^7$  mho/meter are shown in figures A-2 and A-3, as a function of frequency in the quasi-static range for different radii of the wire. Figure A-1 gives  $\tilde{R}'_w = \text{real}(\tilde{Z}'_w)$ , resistance of the cable wire/meter length and figure A-2 gives  $\tilde{X}'_w = \text{imag.}(\tilde{Z}'_w)$ , self reactance of the cable wire/meter length. As the frequency is increased both  $\tilde{R}'_w$  and  $\tilde{X}'_w$  increase linearly on the logarithmic scale. At very low frequencies  $\tilde{X}'_w$  approaches zero, while  $\tilde{R}'_w$  approaches its static value.

Even if the structure is loaded with extra lumped impedances, it can be included into  $\tilde{Z}'_w(s)$  of (A.6) and characterized as certain uniform impedance per unit length as a function frequency. Whenever external loadings are built into the structure, the



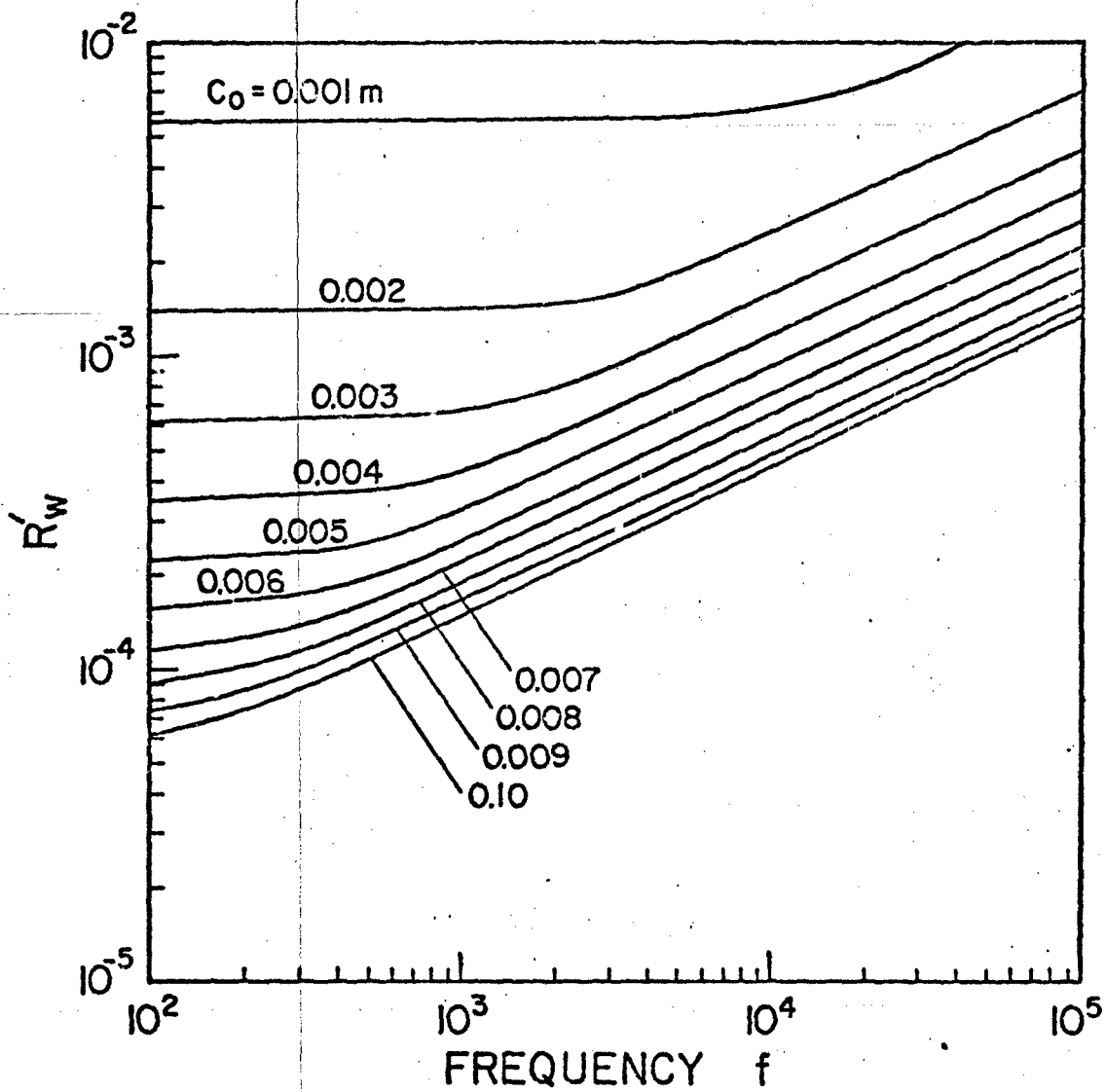


Figure A-2. Resistance per Unit Length for Copper Conductor

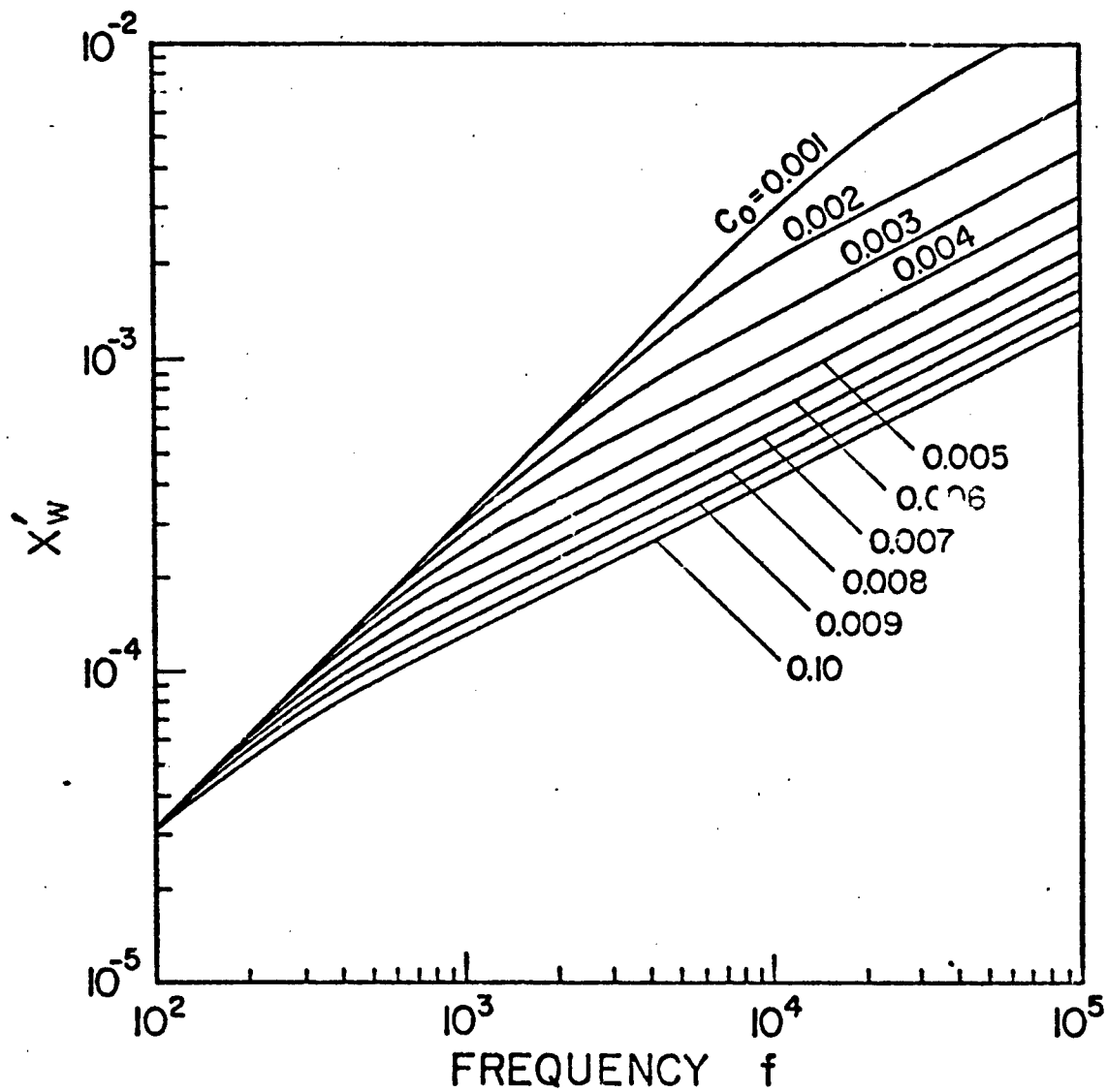


Figure A-3. Reactance per Unit Length for Copper Conductor

impedance loading due to the material characteristics of the wire is a very small percentage of the total loading and hence can be neglected. The concept of the impedance definition is based on the surface impedance in contrast to the sheet impedance definition discussed in the next section.

## 2. Hollow Circular Cylinder

The geometry of the hollow cylindrical tube, having a radius equal to  $C$ , is shown in figure A-4. The thickness of the wall is neglected and the material of the tube has permeability  $\mu_c$ , permittivity  $\epsilon_c$  and conductivity  $\sigma_c$ . The tubular structure is oriented along  $z$  axis in an isotropic, homogeneous medium. Again, only the axial currents are assumed to exist on the outer and inner surface of the hollow cylinder. Similar to the definition (A.4), the impedance per unit length of the hollow circular cylinder is given by the ratio of the axial electric field  $\tilde{E}_z(\zeta, s)$  to the net total current in the axial direction which is obtained by the sum of the outer  $\tilde{I}^{(2)}(\zeta, s)$  and the inner  $\tilde{I}^{(1)}(\zeta, s)$  total currents,

$$\tilde{Z}'(\zeta, s) = \frac{\tilde{E}_z(\zeta, s)}{\tilde{I}^{(2)}(\zeta, s) + \tilde{I}^{(1)}(\zeta, s)} \quad (A.10)$$

evaluated on the surface of the cylinder. According to the expressions (3.5) through (3.8) and (3.10), the expression (A.10) takes the form, after making use of the Wronskin relationship

$$\tilde{Z}'(\zeta) = \frac{Z_{0c}}{2\pi\gamma_c} u_c^2 K_0(u_c C) I_0(u_c C) \quad (A.11)$$

where

$$u_c = [\gamma_c^2 - \zeta^2]^{\frac{1}{2}} \quad (A.12)$$

$$\gamma_c = [\mu_c s(\sigma_c + \epsilon_c s)]^{\frac{1}{2}} \quad (A.13)$$

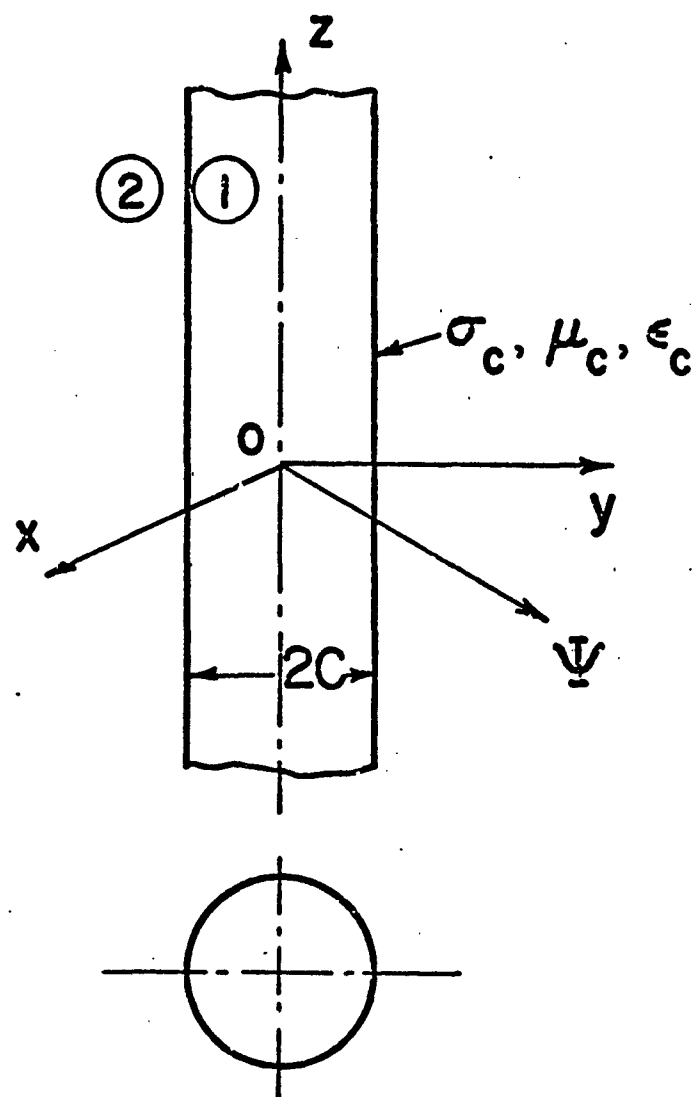


Figure A-4. Hollow Circular Cylinder

and in the quasi-static range  $|\gamma_c^2| \gg \epsilon^2$ , the axial impedance  $\tilde{Z}'(s)$  per unit length of the hollow circular cylinder becomes,

$$\tilde{Z}'(s) = \frac{Z_{oc}}{2\pi} \gamma_c K_0(\gamma_c C) I_0(\gamma_c C) \quad (A.14)$$

where

$$Z_{oc} = \left[ \frac{\mu_c s}{\sigma_c + \epsilon_c s} \right]^{\frac{1}{2}} \quad (A.15)$$

Further, the sheet impedance of the cylinder is given by

$$\tilde{Z}_s(s) = 2\pi C \tilde{Z}'(s) \quad (A.16)$$

### 3. General Solid Cylindrical Wire

In section A-(1), the impedance characteristics of a thin solid cylindrical wire are discussed with the obvious assumption that the current on the surface of the wire is uniform with respect to  $\phi$ -angular variation. Let us consider another case with current density  $\tilde{J}_z(\phi, s)$  on the surface as a function of angle  $\phi$ , but which is independent of the  $z$ -coordinate variable. Then in the region  $\psi < b$ , figure A-1, the electric field distribution is given by,

$$\tilde{E}_z(\psi, \phi, s) = \sum_{m=-\infty}^{\infty} \tilde{C}_m(b, m, s) I_m(\gamma_w \psi) e^{jm\phi} \quad (A.17)$$

where  $\tilde{C}_m$  is the  $m$ th Fourier mode coefficient, so that the representation (A.1) is for the special case of the  $m = 0$  mode. According to the expression (2.4a) and (2.4b) the current density on the surface of the wire is obtained,

$$\begin{aligned} \tilde{J}_z(b, \phi, s) &= \tilde{H}_\phi(b, \phi, s) \\ &= \frac{1}{Z_{ow}} \sum_{m=-\infty}^{\infty} \tilde{C}_m(b, \phi, s) I'_m(\gamma_w b) e^{jm\phi} \end{aligned} \quad (A.18)$$

On the surface of the cylindrical wire, we have the surface impedance boundary relationship,

$$\tilde{E}_z(b, \phi, s) = \tilde{Z}_{sw}(s) \tilde{J}_z(b, \phi, s) \quad (A.19)$$

Substituting (A.17) and (A.18) into (A.19) and enforcing orthogonality of the modes

$$\tilde{Z}_{sw_m}(s) = Z_{ow} \frac{I_m(\gamma_w b)}{I_m'(\gamma_w b)} \quad (A.20)$$

Hence for any given mode excitation  $m$  on the wire, the mode surface impedance  $\tilde{Z}_{sw_m}(s)$  is associated.

#### 4. General Hollow Circular Cylinder

The impedance characteristics of the general solid cylindrical wire can also be extended to the case of a hollow circular cylinder, figure A-2, with the current density  $\tilde{J}_z^{(t)}(C, \phi, s)$  on the surface as a function of angle  $\phi$ , but is independent of  $z$ -coordinate variable. On the surface of the hollow cylinder, we have the sheet-impedance boundary relationship,

$$\tilde{E}_z(C, \phi, s) = \tilde{Z}_s(s) \tilde{J}_z^{(t)}(C, \phi, s) \quad (A.21)$$

where the current density is obtained by the difference in the tangential magnetic field

$$\tilde{J}_z^{(t)}(C, \phi, s) = \tilde{H}_\phi^{(2)}(C, \phi, s) - \tilde{H}_\phi^{(1)}(C, \phi, s) \quad (A.22)$$

Hence for any given mode excitation  $m$  on the hollow cylinder, the associated mode sheet impedance  $\tilde{Z}_{sm}(s)$  is given by

$$\tilde{Z}_{sm}(s) = \gamma_c C Z_{oc} I_m(\gamma_c C) K_m(\gamma_c C) \quad (A.23)$$

# APPENDIX B

## FAR-FIELD EXPRESSION

The  $\phi$ -component of the magnetic field radiated by the infinitely long thin solid wire is given by the expression (2.17a),

$$\tilde{H}_\phi(\psi, z, s) = \frac{\tilde{V}_Y}{j2\pi Z_0} \int_{C_\zeta} G(\zeta) \frac{K_1(u\psi)}{\tilde{D}(\zeta, s)} e^{\zeta z} d\zeta \quad (B.1)$$

In fact the expression (B.1) reduces to the (2.19) for the total axial current  $\tilde{I}(z, s) = 2\pi b \tilde{H}_\phi(\psi, z, s)$  evaluated on the surface of the infinitely long wire  $\psi = b$ . In the expression (B.1), the integration is along a Bromwich contour in the  $\zeta$ -plane, figure 2.2, and

$$u = [\gamma^2 - \zeta^2]^{\frac{1}{2}} \quad (B.2)$$

$$\tilde{D}(\zeta, s) = u K_0(ub) + \tilde{h}_1(s) K_1(ub) \quad (B.3)$$

$$\tilde{h}(s) = 2\pi b(\sigma + s\epsilon) \tilde{Z}'_w(s) \quad (B.4)$$

and  $\tilde{Z}'_w(\zeta, s)$  as given by the expression (A.5) has the form,

$$\tilde{Z}'_w(\zeta, s) = \frac{(\gamma_w^2 - \zeta^2)^{\frac{1}{2}} I_0[b(\gamma_w^2 - \zeta^2)^{\frac{1}{2}}]}{2\pi b(\sigma_w + s\epsilon_w) I_1[b(\gamma_w^2 - \zeta^2)^{\frac{1}{2}}]} \quad (B.5)$$

and  $\tilde{Z}_w(\zeta, s)$  would be independent of  $\zeta$ , (A.6), in the quasi-static region. Assuming an ideal slice generator excitation,  $d \rightarrow 0$  and  $G(\zeta) \rightarrow 1$ .

It is possible to obtain the general solution to the integral (B.1) by closing the contour, figure 2.2, in the left half of the  $\zeta$ -plane for  $z \rightarrow 0$ , but this procedure involves some numerical work. However, as  $\psi \rightarrow \infty$ , in the far-field region, an

explicit expression for  $\tilde{H}_\phi(\Psi, z, s)$  can be obtained based on the saddle-point method of integration.<sup>13,14</sup> With the substitution  $\zeta = \zeta' + j\zeta''$ ,  $\zeta' = 0$  and  $\gamma = jp$ , the integral (B.1) reduces to the form discussed in reference 14 and hence we have for  $z > 0$ ,

$$\tilde{H}_\phi(\Psi, z, s) = \frac{\tilde{V}_\gamma}{2\pi Z_0} \int_{-\infty}^{\infty} \frac{K_1(u\Psi)}{\tilde{D}(\zeta'', s)} e^{-j\zeta''z} d\zeta'' \quad (B.6)$$

and

$$u = jv = j[p^2 - \zeta''^2]^{\frac{1}{2}} \quad (B.7)$$

In the far-field region as  $\Psi \rightarrow \infty$ ,<sup>15</sup>

$$K_1(u\Psi) e^{-j\zeta''z} \sim \left(\frac{\pi}{2u\Psi}\right)^{\frac{1}{2}} e^{-j[v\Psi + \zeta''z]} , \quad |\arg(u\Psi)| < \frac{3\pi}{2} \quad (B.8)$$

The saddle point  $\zeta_0$  is obtained by solving the equation obtained from the exponent of (B.8),

$$\frac{d}{d\zeta''}[v\Psi + \zeta''z]_{\zeta''=\zeta_0} = 0 \quad (B.9)$$

The expression (B.9) yields  $\zeta_0'' = p \sin(\alpha)$ , with the proper substitution  $\Psi = r \cos(\alpha)$ ,  $z = r \sin(\alpha)$  and  $\theta = 90 - \alpha$  where  $r$  and  $\theta$  are the spherical coordinate variables and  $\alpha$  is the angle measured from  $z = 0$  plane, figure B-1. Calling the exponent term in (B.9) as

$$f(\zeta'') = -j[v\Psi + \zeta''z] \quad (B.10)$$

and at  $\zeta'' = \zeta_0''$

$$f(\zeta'') \Big|_{\zeta''=\zeta_0''} = -jp(\Psi \cos(\alpha) + z \sin(\alpha)) \quad (B.11)$$

In the neighborhood of the saddle point  $\zeta'' = \zeta_0''$ ,  $f(\zeta'')$  can be expanded in a Taylor series,



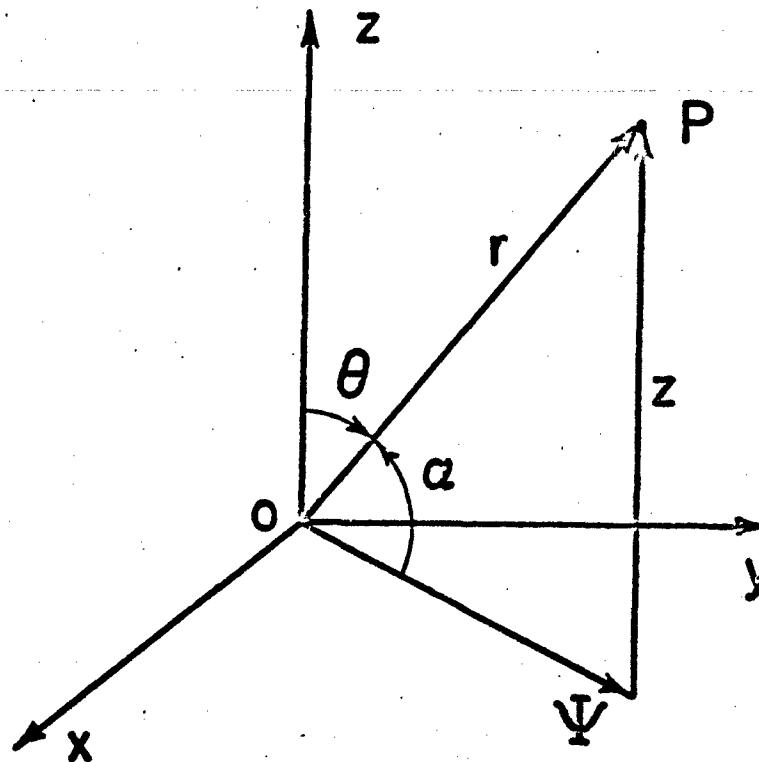


Figure B-1. Coordinates for Far-Field Calculation

$$f(\zeta) \approx -j \left[ p(\psi \cos(\alpha) + z \sin(\alpha)) - \frac{\psi}{p \cos^3(\alpha)} (\zeta'' - \zeta_0'')^2 \right] \quad (\text{B.12})$$

Hence, according to the expression (B.12) the path of the saddle point integration is obtained by forcing the imaginary part of (B.12) to be constant along the path. With the substitution  $\zeta'' - \zeta_0'' = R e^{j\delta_1}$  and  $p = |p| e^{j\delta_2}$ , the path of the saddle point integration is given by the imaginary part (Im) as

$$\text{Im} \left[ -jp \left\{ (\psi \cos(\alpha) + z \sin(\alpha)) - \frac{\psi}{|p| \cos^3(\alpha)} R^2 e^{j2(\delta_1 - \delta_2)} \right\} \right] = \text{constant} \quad (\text{B.13})$$

and (B.13) is satisfied only when

$$\text{Re} \left[ e^{j(\delta_1 - \delta_2)} \right] = 0 \quad (\text{B.14})$$

The expression (B.14) yields  $(\delta_1 - \delta_2) = \pm\pi/4$ . Only the positive value of  $(\delta_1 - \delta_2) = \pi/4$  represents the correct slope of the integration path through the saddle point  $\zeta_0'' = p \sin(\alpha)$ , which is also obvious from the further transformations used in reference 14.

Changing the variable of integration  $\zeta''$  in the expression (B.1) to  $\tau$  by the transformation  $\zeta'' = p \sin \tau$ , and  $\tau = \alpha_1 + j\alpha_2$ , the saddle point is located at  $\alpha_1 = \alpha$  on the real axis of the complex  $\tau$ -plane. The reader may refer to reference 21 for the complete details of the various transformations from  $\zeta''$ -plane to  $\tau$ -plane and the paths of the integration. Hence the expression (B.8) can be written as

$$K_1(u\psi) e^{-j\zeta''z} \sim \left( \frac{\pi}{j2p\psi \cos(\tau)} \right)^{\frac{1}{2}} e^{-j\tau p \cos(\tau - \alpha)} \quad (\text{B.15})$$

In the far-field region, the expression (B.1) for  $\tilde{H}_\phi(\psi, z, s)$  becomes,

$$\tilde{H}_\phi(\psi, z, s) \sim \frac{\tilde{V}_Y}{2\pi Z_0} \int_{\alpha - \frac{\pi}{2} - j\infty}^{\alpha + \frac{\pi}{2} + j\infty} \left( \frac{\pi}{j2p\psi \cos(\tau)} \right)^{\frac{1}{2}} \frac{e^{-j\tau p \cos(\tau - \alpha)}}{\tilde{L}_1(\gamma, \alpha)} p \cos(\tau) d\tau \quad (\text{B.16})$$

Most of the contribution to the integral (B.16) comes from the vicinity of the saddle point  $\tau = \alpha$ , and with the approximation  $\cos x \approx 1 - x^2/2$ , and  $\tau - \alpha = e^{j\pi/4}$ , the expression (B.16) reduces to,

$$\tilde{H}_\phi(\psi, z, s) \sim \frac{\tilde{V}_Y}{2\pi Z_0} \left(\frac{\pi p}{2r}\right)^{\frac{1}{2}} \frac{e^{-Yr}}{\tilde{L}_1(Y, \alpha)} \int_{-\epsilon}^{\epsilon} e^{-\frac{1}{2}pr\eta^2} d\eta \quad (B.17)$$

and the integral in (B.17) as  $r \rightarrow \infty$ ,  $\epsilon \rightarrow \infty$ ,<sup>15</sup>

$$\int_{-\infty}^{\infty} e^{-\frac{1}{2}pr\eta^2} d\eta = \left(\frac{2\pi}{pr}\right)^{\frac{1}{2}} \quad (B.18)$$

Hence  $\tilde{H}_\phi(r, \alpha, s)$  in the far-field region has the form

$$\tilde{H}_\phi(r, \alpha, s) = \frac{\tilde{V}_Y}{2Z_0} \frac{1}{\tilde{L}(Y, \alpha)} \frac{e^{-Yr}}{r} \quad (B.19)$$

where the denominator term is

$$\begin{aligned} \tilde{L}(Y, \alpha) &= \tilde{D}(\zeta'' = \zeta_0'') \\ &= Y \cos \alpha K_0(Yb \cos \alpha) + \tilde{h}(s) K_1(Yb \cos \alpha) \end{aligned} \quad (B.20)$$

where  $\tilde{h}(s)$  is defined in the expression (B.4).

We note that  $\tilde{h}(s)$  in the expression (B.20) holds good only in the quasi-static frequency ranges, or when the wire is loaded uniformly by external impedances. For very large frequencies  $\tilde{h}_1(s)$  in (B.20) should be replaced by  $\tilde{h}(\zeta_0'', s)$  where

$$\begin{aligned} \tilde{h}(\zeta_0'', s) &= \tilde{h}(\zeta'', s) \Big|_{\zeta'' = \zeta_0'' = -jY \sin \alpha} \\ &= 2\pi b(\sigma + s\epsilon) \tilde{Z}_w'(\zeta_0'', s) \end{aligned} \quad (B.21)$$

## APPENDIX C

DIFFERENT FORMS OF THE EQUIVALENT-RADIUS EXPRESSIONS  
IN THE QUASI-STATIC LIMIT

It is interesting to note the different forms of the equivalent radius<sup>1-3</sup> of a circular wire cage derived in quasi-static limit are one and the same, and check with the result obtained in section IV. In the earlier studies,

- (i) a cage consisting of conical wires equally spaced over surface of a cone is studied, and compared with respect to a solid cone of same characteristic impedance so that there is only a transmission line mode excited,<sup>1,10</sup> expression (4.8)
- (ii) an equivalence between a single charged conductor and number of equally spaced concentric charged conductors is studied based on conformal transformation,<sup>3</sup> expression (4.8)
- (iii) a wire cage antenna consisting of closely spaced parallel and identical conductors placed around a circle is compared to a single conductor antenna, so that the total axial assumed current distribution is approximately the same,<sup>2</sup> expression (4.7)
- (iv) far-field equivalence of the canonical infinitely long circular wire cage and hollow cylindrical antenna structure, section IV, expression (4.7).

In the following, the expression (4.7) for the circular wire cage equivalent radius

$$r_{eq_0}^{(c)} = [aA_{1,2}A_{1,3}\dots A_{1,N}]^{1/N} \quad (C.1)$$

is shown to be equivalent to the expression (4.8)

$$\frac{\psi_{eq_0}^{(c)}}{A} = \left(\frac{a_N}{A}\right)^{1/N} \quad (C.2)$$

Normalizing (C.1) with respect to A,

$$\frac{\psi_{eq_0}^{(c)}}{A} = \left[ \frac{aA_{1,2}A_{1,3}\dots A_{1,N}}{A^N} \right]^{1/N} \quad (C.3)$$

$$= \left[ \frac{aR}{A} \right]^{1/N} \quad (C.4)$$

where the mean inter-chord distance is

$$R = \frac{A_{1,2}A_{1,3}\dots A_{1,N}}{A^{N-1}} \quad (C.5)$$

The various inter-chord distances  $A_{1,n}$ ,  $n = 2, 3, \dots, N$ , are defined in (2.30). On substituting  $A_{1,n}$  into (C.5)

$$\begin{aligned} R &= \frac{(2A \sin \frac{\pi}{N})(2A \sin \frac{2\pi}{N})\dots(2A \sin \frac{(N-1)\pi}{N})}{A^{N-1}} \\ &= 2^{N-1} \prod_{n=1}^{N-1} \sin\left(\frac{n\pi}{N}\right) \end{aligned} \quad (C.6)$$

But we have the product expression,<sup>22</sup>

$$\sin(Nx) = 2^{N-1} \prod_{n=1}^{N-1} \sin\left(x + \frac{n\pi}{N}\right) \quad (C.7)$$

Hence, from (C.6) and (C.7)

$$\begin{aligned} R &= \left. \frac{\sin(Nx)}{\sin(x)} \right|_{x \rightarrow 0} \\ &= \left. \frac{N \cos(Nx)}{\cos(x)} \right|_{x \rightarrow 0} \\ &= N \end{aligned} \quad (C.8)$$

## REFERENCES

1. Schelkunoff, S. A., and H. T. Friis, Antennas Theory and Practice, John Wiley and Sons, NY, 1952.
2. King, R.W.P., The Theory of Linear Antennas, Harvard University Press, MA, 1956.
3. Baum, C. E., "Design of a Pulse Radiating Dipole Antenna as Related to High Frequency and Low Frequency Limits," Sensor and Simulation Notes, Note 69, January 1969.
4. Baum, C. E., "EMP Simulators for Various Types of Nuclear EMP Environments: An Interim Categorization," Sensor and Simulation Notes, Note 151, July 1972.
5. Kehrer, W. S., and C. E. Baum, "Summary of Characteristics," ATHAMAS Memos, Memo 1, November 1973.
6. Castillo, J. P., "Some Notes on the Design of ACHILLES II," ACHILLES Memos, Memo 1, August 1973.
7. Blackburn, R. F., and C. D. Taylor, "On the Electromagnetic Fields from a Hybrid Type of EMP Simulator," Sensor and Simulation Notes, Note 211, November 1975.
8. Casey, K. F., "Electromagnetic Shielding by Advanced Composite Materials," Interaction Notes, Note 341, June 1977.
9. Hill, D. A., and J. R. Wait, "Gap Excitation of an Axial Conductor in a Circular Tunnel," Journal of Applied Physics, Vol. 45, No. 11, November 1974.
10. Higgins, D. F., "The Effects of Constructing a Conical Antenna Above a Ground Plane Out of a Number of Thin Wires," Sensor and Simulation Notes, Note 142, January 1972.
11. Jones, D. S., The Theory of Electromagnetism, Pergamon Press, 1964.
12. Latham, R. W., and K.S.H. Lee, "Waveforms Near a Cylindrical Antenna," Sensor and Simulation Notes, Note 89, June 1969.
13. Mittra, R., and S. W. Lee, Analytical Techniques in the Theory of Guided Waves, MacMillan, 1971.
14. Papas, C. H., "On the Infinitely Long Cylindrical Antenna," Journal of Applied Physics, Vol. 20, pp. 437-440, May 1949.

15. Abramowitz, M., and I. A. Segun, Handbook of Mathematical Functions, Dover, NY, 1968.
16. Kunz, K. S., "Asymptotic Behavior of the Current on an Infinite Cylindrical Antenna," Journal of Research of NBS, Vol. 67D, No. 4, July-August 1963.
17. Shen, L. C., T. T. Wu, and R.W.P. King, "A Simple Formula of Current in Dipole Antennas," IEEE Transactions on Antennas and Propagation, Vol. 16, No. 5, September 1968.
18. Hill, D. A., and J. R. Wait, "Coupling between a Dipole Antenna and an Infinite Cable over an Ideal Ground Plane," Radio Science, Vol. 12, No. 2, March-April 1977.
19. Conte, S. D., Elementary Numerical Analysis, McGraw Hill, NY, 1966.
20. King, R.W.P., Fundamental Electromagnetic Theory, Dover, NY, 1963.
21. Tyras, G., Radiation and Propagation of Electromagnetic Waves, Academic Press, NY, 1960.
22. Gradshteyn, I. S., and I. M., Ryzhik, Tables of Integrals, Series and Product, Academic Press, NY, 1965.

SOURCE EXCITATION OF AN  
OPEN, PARALLEL-PLATE WAVEGUIDE

ABSTRACT

In this work, we consider the problem of an open, finite-width, parallel-plate waveguide which is excited by a y-directed current source. The source current is assumed to be confined at  $x = x_0$ , have a  $\sin(N\pi/2H)$  or  $\cos(N\pi/2H)$  variation in the y-direction, and an  $\exp(i\beta z)$  behavior along the longitudinal z-direction. Such an excitation can be interpreted as one spectral component of a transversely confined source. The solution to the longitudinally confined source problem can be subsequently constructed by an appropriate superposition of the spectral solutions derived in this paper. The important question of the excitation or non-excitation of the zero-mode in the guide is examined and the resonance condition for a leaky mode in an open, finite-width waveguide is derived.

Acknowledgement

The authors are thankful to their colleague, Professor S. W. Lee, for critical comments and helpful suggestions during the course of this work. The financial support of the AFOSR-76 Grant 3066B is gratefully acknowledged.



The organization of the report is as follows: Section II presents the statement of the problem we wish to investigate. In Section III we formulate the integral equations and present the solution of these equations in Section IV. Section V is devoted to the calculation of the vector potentials which are useful for the derivation of the fields. In Section VI we investigate the special case when only the zero mode can propagate in the guide and derive the resonance condition for leaky modes. Finally, in Section VII, we discuss the case when more than one mode can propagate in the guide and present a summary of the results in Section VIII.

## II. STATEMENT OF THE PROBLEM

In this work we address ourselves to the problem of source excitation of an open waveguide when the source is located inside the waveguide. The open waveguide is formed by two parallel, perfectly conducting strips:  $-2L < x < 0$ ,  $y = \pm H$  (see Figure 1).

We will investigate two types of sources, viz.,

Case A

$$\bar{J} = \hat{y}\delta(x + x_0) \sin\left(\frac{N\pi y}{2H}\right) e^{i\beta z}, \quad \text{here } N = 1, 2, \dots \quad (2.1)$$

Case B

$$\bar{J} = \hat{y}\delta(x + x_0) \cos\left(\frac{N\pi y}{2H}\right) e^{i\beta z}, \quad \text{here } N = 0, 1, 2, \dots \quad (2.2)$$

where the current  $\bar{J}$  has only a y-component. The time factor  $\exp(-i\omega t)$  is implicit throughout this report. We assume that  $\text{Re}\beta > 0$  and  $\text{Im}\beta = 0$ .

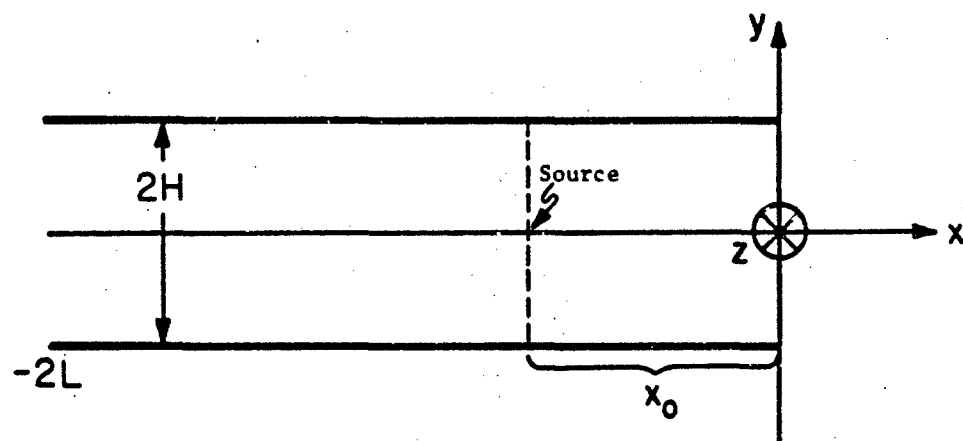


Fig. 1

Geometry of the problem of source excitation  
of a parallel-plate waveguide.

## III. BASIC FORMULATION

We begin with Maxwell's equations:

$$\nabla_1 \times \bar{E} - i\omega\mu\bar{H} = 0 \quad (3.1)$$

$$\nabla_1 \times \bar{H} + i\omega\epsilon\bar{E} = \bar{J} \quad (3.2)$$

where

$$\nabla_1^2 = \frac{\partial^2}{\partial x^2} + \frac{\partial^2}{\partial y^2} + \frac{\partial^2}{\partial z^2} = \nabla^2 + \frac{\partial^2}{\partial z^2}$$

The electromagnetic fields may be expressed in terms of a vector potential function  $\bar{A}^{(1)}$  by means of the following equations:

$$\bar{H} = \frac{1}{\mu} \nabla_1 \times \bar{A}^{(1)} \quad (3.3)$$

$$\bar{E} = i\omega\bar{A}^{(1)} - \frac{1}{i\omega\epsilon\mu} \nabla_1 \nabla_1 \cdot \bar{A}^{(1)} \quad (3.4)$$

where  $\bar{A}^{(1)}$  is a solution to the following inhomogeneous equation:

$$\nabla_1^2 \bar{A}^{(1)} + \omega^2 \epsilon\mu \bar{A}^{(1)} = -\mu\bar{J} \quad (3.5)$$

Since the excitation current has only a y-component, we may let  $\bar{A}^{(1)} = A_y^{(1)} \hat{y}$  and express the various field components in terms of  $A_y^{(1)}$  as:

$$E_x = -\frac{1}{i\omega\epsilon\mu} \cdot \frac{\partial^2 A_y^{(1)}}{\partial x \partial y} \quad (3.6a)$$

$$E_y = i\omega A_y^{(1)} - \frac{1}{i\omega\epsilon\mu} \cdot \frac{\partial^2 A_y^{(1)}}{\partial y^2} \quad (3.6b)$$

$$E_z = -\frac{1}{i\omega\epsilon\mu} \cdot \frac{\partial^2 A_y^{(1)}}{\partial y \partial z} \quad (3.6c)$$

$$H_x = -\frac{\partial A_y^{(1)}}{\partial z} ; H_y = 0 ; H_z = \frac{\partial A_y^{(1)}}{\partial x} \quad (3.6d)$$

$A_y^{(1)}$  satisfies the inhomogeneous wave equation:

$$\nabla_1^2 A_y^{(1)} + \omega^2 \epsilon \mu A_y^{(1)} = -\mu J_y \quad (3.7)$$

We look for the solutions of (3.7) having the form  $A_y^{(1)} = A e^{i\beta z}$ . The reduced potential  $A$  satisfies

$$\nabla^2 A + k^2 A = -\mu I \quad (3.8)$$

where  $k^2 = \omega^2 \epsilon \mu - \beta^2$ , and

$$I = \delta(x + x_0) \begin{cases} \sin\left(\frac{N\pi y}{2H}\right) & \text{for case (A) } N = 1, 2, \dots \\ \cos\left(\frac{N\pi y}{2H}\right) & \text{for case (B) } N = 0, 1, 2, \dots \end{cases}$$

Enforcing the boundary condition on the tangential E-field at the plates, we have

$$\left. \frac{\partial A}{\partial y} \right|_{y = -H, H} = 0, \quad -2L < x < 0 \quad (3.9)$$

For mathematical convenience we initially assume that  $\epsilon$  has a small imaginary part, with  $\text{Im} \epsilon > 0$ , intending to let  $\text{Im} \epsilon \rightarrow 0$  after the derivation of the solution is complete. We then have

$$k = \sqrt{\omega^2 \epsilon \mu - \beta^2} = k_1 + ik_2 \quad (3.10)$$

where  $k_1, k_2 > 0$ .

We next proceed to derive the solution to the problem at hand using the Wiener-Hopf technique. To this end we define the transformed function  $\phi$  as

$$\phi(\alpha, y) = \int_{-\infty}^{\infty} A(x, y) e^{i\alpha x} dx \quad (3.11)$$

where  $\alpha$  is the Fourier transform variable. Since the region  $|y| > H$  is source free, we have  $\phi$  satisfying the differential equation

$$\frac{\partial^2 \phi}{\partial y^2} - \gamma^2 \phi = 0, \quad \gamma = \sqrt{\alpha^2 - k^2}, \quad (3.12)$$

which admits solutions of the form

$$\phi(\alpha) = c_3 e^{\gamma y} \quad \text{for } y < -H \quad (3.13a)$$

$$\phi(\alpha) = c_4 e^{-\gamma y} \quad \text{for } y > H \quad (3.13b)$$

with the requirement that

$$\operatorname{Re} \gamma = \operatorname{Re} \left( \sqrt{\alpha^2 - k^2} \right) \rightarrow +\infty \quad \text{as } \alpha \rightarrow \pm \infty.$$

Figure 2 shows the branch cuts for  $\gamma$  in the complex  $\alpha$ -plane. Taking the principal branch we get

$$\gamma = \sqrt{|\alpha - k| |\alpha + k|} e^{i \frac{\phi + \psi}{2}} \quad \text{and} \quad (3.14)$$

$$\gamma = -i \sqrt{k^2 - \alpha^2} \quad \text{for } |\alpha| < |k|. \quad (3.15)$$

In the region interior to the waveguide, i.e., for  $|y| < H$ , the differential equation for  $\phi$  takes the form

$$\frac{\partial^2 \phi}{\partial y^2} - \gamma^2 \phi = -\mu \begin{cases} \sin \left( \frac{N\pi y}{2H} \right) & \text{Case (A)} \\ \cos \left( \frac{N\pi y}{2H} \right) & \text{Case (B)} \end{cases} e^{-i\alpha x_0} \quad (3.16)$$

and the solution may be written as [see Appendix I]:

$$\phi(y) = c_1 e^{\gamma y} + c_2 e^{-\gamma y} + \tilde{T}_N \begin{cases} \sin \left( \frac{N\pi y}{2H} \right) & \text{Case (A) } N=1,2,\dots \\ \cos \left( \frac{N\pi y}{2H} \right) & \text{Case (B) } N=0,1,2,\dots \end{cases} \quad (3.17)$$

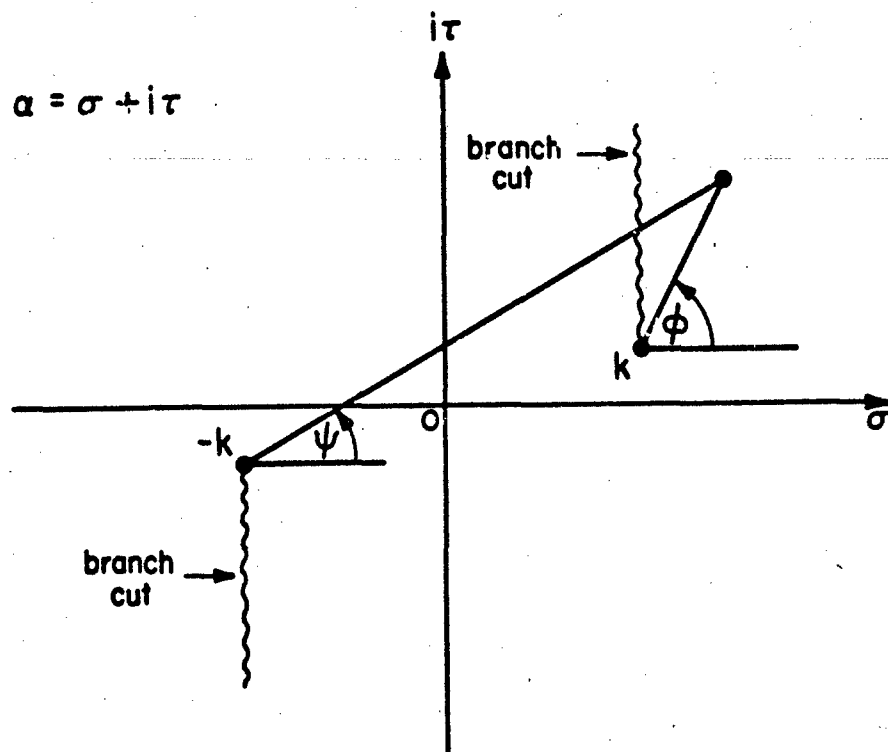


Fig. 2

Branch cuts in the complex  $\alpha$ -plane.

with

$$\tilde{T}_N = \frac{e^{-i\alpha x_0} \mu}{\gamma^2 + \left(\frac{N\pi}{2H}\right)^2} \quad (3.18)$$

The coefficients  $c_1$  and  $c_2$  will, of course, be different for the cases A and B. Since

$$\frac{\partial \Phi}{\partial y} = \int_{-\infty}^{\infty} \frac{\partial A}{\partial y} e^{i\alpha x} dx, \quad (3.19)$$

from (3.13a) and (3.19) we have:

$$\int_{-\infty}^{\infty} \frac{\partial A}{\partial y} \Big|_{y=-H} e^{i\alpha x} dx = c_3 \gamma e^{-\gamma H} \quad (3.20)$$

Let

$$\begin{aligned} \frac{\partial A}{\partial y} \Big|_{y=-H} &= \psi_2; \quad \frac{\partial A}{\partial y} \Big|_{y=H} = \psi_1 \quad \text{for } -\infty < x < -2L \\ \frac{\partial A}{\partial y} \Big|_{y=-H} &= \chi_2; \quad \frac{\partial A}{\partial y} \Big|_{y=H} = \chi_1 \quad \text{for } 0 < x < \infty \end{aligned} \quad (3.21)$$

Then from (3.9), (3.20), (3.21),

$$\int_{-\infty}^{-2L} \psi_2 e^{i\alpha x} dx + \int_0^{\infty} \chi_2 e^{i\alpha x} dx = c_3 \gamma e^{-\gamma H} \quad (3.22)$$

or

$$c_3 = \gamma^{-1} e^{\gamma H} \left[ \int_{-\infty}^{-2L} \psi_2 e^{i\alpha x} dx + \int_0^{\infty} \chi_2 e^{i\alpha x} dx \right] \quad (3.23)$$

Using the inverse Fourier transform, we finally obtain the representation of  $A(x, y)$  for  $y < -H$ :



$$A(x,y) = \frac{1}{2\pi} \int_{-\infty+ib}^{\infty+ib} \gamma^{-1} e^{\gamma H} e^{\gamma y} e^{-i\alpha x} d\alpha \left[ \int_{-\infty}^{-2L} \psi_2 e^{i\alpha \xi} d\xi + \int_0^{\infty} \chi_2 e^{i\alpha \xi} d\xi \right]. \quad (3.24)$$

Similarly for  $y > H$  we have:

$$A(x,y) = -\frac{1}{2\pi} \int_{-\infty+ib}^{\infty+ib} \gamma^{-1} e^{\gamma H} e^{-\gamma y} e^{-i\alpha x} d\alpha \left[ \int_{-\infty}^{-2L} \psi_1 e^{i\alpha \xi} d\xi + \int_0^{\infty} \chi_1 e^{i\alpha \xi} d\xi \right] \quad (3.25)$$

where

$$-k_2 < b < k_2.$$

Letting  $y = \pm H$ , we obtain from (3.9), (3.17), (3.19):

$$I_1 = \gamma c_1 e^{\gamma H} - \gamma c_2 e^{-\gamma H} + \tilde{T}_N \frac{N\pi}{2H} \begin{bmatrix} \cos \left( \frac{N\pi}{2} \right) \\ -\sin \left( \frac{N\pi}{2} \right) \end{bmatrix} \quad (3.26)$$

$$I_2 = \gamma c_1 e^{-\gamma H} - \gamma c_2 e^{\gamma H} + \tilde{T}_N \frac{N\pi}{2H} \begin{bmatrix} \cos \left( \frac{N\pi}{2} \right) \\ \sin \left( \frac{N\pi}{2} \right) \end{bmatrix} \quad (3.27)$$

where

$$I_1 = \int_{-\infty}^{-2L} \psi_1 e^{i\alpha x} dx + \int_0^{\infty} \chi_1 e^{i\alpha x} dx \quad (3.28)$$

$$I_2 = \int_{-\infty}^{-2L} \psi_2 e^{i\alpha x} dx + \int_0^{\infty} \chi_2 e^{i\alpha x} dx \quad (3.29)$$

where  $c_1$  and  $c_2$  are constants, given by [see Appendix II]:

$$c_1 = \frac{1}{2 \sinh(2\gamma H) \gamma} \left\{ I_1 e^{\gamma H} - I_2 e^{-\gamma H} + \tilde{T}_N \frac{N\pi}{2H} 2 \begin{bmatrix} -\cos \left( \frac{N\pi}{2} \right) \sinh(\gamma H) \\ \sin \left( \frac{N\pi}{2} \right) \cosh(\gamma H) \end{bmatrix} \right\} \quad (3.30)$$

$$c_2 = \frac{1}{2 \sinh(2\gamma H) \gamma} \left\{ I_1 e^{-\gamma H} - I_2 e^{\gamma H} + \tilde{T}_N \frac{N\pi}{2H} 2 \begin{bmatrix} \cos(\frac{N\pi}{2}) \sinh(\gamma H) \\ \sin(\frac{N\pi}{2}) \cosh(\gamma H) \end{bmatrix} \right\}. \quad (3.31)$$

In the interior region  $|y| < H$  we have

$$\begin{aligned} A(x, y) &= \frac{1}{2\pi} \int_{-\infty+ib}^{\infty+ib} \phi(a, y) e^{-iax} da \\ &= \frac{1}{2\pi} \int_{-\infty+ib}^{\infty+ib} \left\{ I_1 \cosh[\gamma(y+H)] - I_2 \cosh[(y-H)\gamma] \right\} \frac{e^{-iax}}{\gamma \sinh(2\gamma H)} da \\ &\quad + \frac{1}{2\pi} \cdot \frac{N\pi}{2H} \cdot 2 \int_{-\infty+ib}^{\infty+ib} \begin{bmatrix} -\cos \frac{N\pi}{2} \sinh(\gamma H) \sinh(\gamma y) \\ \sin \frac{N\pi}{2} \cosh(\gamma H) \cosh(\gamma y) \end{bmatrix} \frac{\tilde{T}_N e^{-iax}}{\gamma \sinh(2\gamma H)} da \\ &\quad + \frac{1}{2\pi} \left[ \frac{\sin(\frac{N\pi y}{2H})}{\cos(\frac{N\pi y}{2H})} \right] \int_{-\infty+ib}^{\infty+ib} \tilde{T}_N e^{-iax} da. \end{aligned} \quad (3.32)$$

Imposing the boundary conditions:

$$\begin{aligned} A(x, +H+0) &= A(x, +H-0) \\ A(x, -H+0) &= A(x, -H-0) \end{aligned} \quad \text{for } \begin{cases} -\infty < x < -2L \\ \text{and } 0 < x < \infty \end{cases} \quad (3.33)$$

we derive from (3.24), (3.25), (3.32) [see Appendix III] for  $-\infty < x < -2L$ ,

$0 < x < \infty$ :

$$\begin{aligned} &\int_{-\infty}^{-2L} \psi_1 K_1^{(*)}(k|x-\xi|) d\xi + \int_0^{\infty} \chi_1 K_1^{(*)}(k|x-\xi|) d\xi - \int_{-\infty}^{-2L} \psi_2 K_2^{(*)}(k|x-\xi|) d\xi \\ &\quad - \int_0^{\infty} \chi_2 K_2^{(*)}(k|x-\xi|) d\xi = f_1^{(*)}(x) \end{aligned} \quad (3.34)$$

and

$$\begin{aligned}
 & \int_{-2L}^{-\infty} \phi_1 \kappa_2^{(*)} (k|x - \xi|) d\xi + \int_0^{\infty} \chi_1 \kappa_2^{(*)} (k|x - \xi|) d\xi - \int_{-\infty}^{-2L} \psi_2 \kappa_1^{(*)} (k|x - \xi|) d\xi \\
 & - \int_0^{\infty} \chi_2 \kappa_1^{(*)} (k|x - \xi|) d\xi = f_2^{(*)} (x), \quad (3.35)
 \end{aligned}$$

where

$$\kappa_1^{(*)} (k|x - \xi|) = \frac{1}{2\pi} \int_{-i\infty}^{+i\infty} \frac{e^{2H\gamma}}{\gamma \sinh(2H\gamma)} e^{i\alpha(\xi - x)} d\alpha \quad (3.36)$$

$$\kappa_2^{(*)} (k|x - \xi|) = \frac{1}{2\pi} \int_{-i\infty}^{+i\infty} \frac{1}{\gamma \sinh(2H\gamma)} e^{i\alpha(\xi - x)} d\alpha \quad (3.37)$$

$$\begin{aligned}
 f_1^{(*)} (x) = & -\frac{N}{4H} \int_{-i\infty}^{+i\infty} \begin{bmatrix} -\cos\left(\frac{N\pi}{2}\right) \tanh(\gamma H) \\ \sin\left(\frac{N\pi}{2}\right) \coth(\gamma H) \end{bmatrix} \frac{\tilde{T}_N e^{-i\alpha x}}{\gamma} d\alpha \\
 & - \frac{1}{2\pi} \begin{bmatrix} \sin\left(\frac{N\pi}{2}\right) \\ \cos\left(\frac{N\pi}{2}\right) \end{bmatrix} \int_{-i\infty}^{+i\infty} \tilde{T}_N e^{-i\alpha x} d\alpha \quad (3.38)
 \end{aligned}$$

$$\begin{aligned}
 f_2^{(*)} (x) = & -\frac{N}{4H} \int_{-i\infty}^{+i\infty} \begin{bmatrix} \cos\left(\frac{N\pi}{2}\right) \tanh(\gamma H) \\ \sin\left(\frac{N\pi}{2}\right) \coth(\gamma H) \end{bmatrix} \frac{\tilde{T}_N e^{-i\alpha x}}{\gamma} d\alpha \\
 & - \frac{1}{2\pi} \begin{bmatrix} -\sin\left(\frac{N\pi}{2}\right) \\ \cos\left(\frac{N\pi}{2}\right) \end{bmatrix} \int_{-i\infty}^{+i\infty} \tilde{T}_N e^{-i\alpha x} d\alpha \quad (3.39)
 \end{aligned}$$

Adding (3.34) and (3.35) we obtain

$$\int_{-2L}^{-\infty} Y_1(\xi) K_1(k|x - \xi|) d\xi + \int_0^{\infty} Z_1(\xi) K_1(k|x - \xi|) d\xi = f_1(x) \quad (3.40)$$

where

$$Y_1(\xi) = \psi_1 - \psi_2 \quad (3.41)$$

$$Z_1(\xi) = x_1 - x_2$$

$$K_1(k|x - \xi|) = K_1^{(*)}(k|x - \xi|) + K_2^{(*)}(k|x - \xi|) = \frac{1}{2\pi} \int_{-\infty + ib}^{\infty + ib} \frac{e^{\gamma H}}{\gamma \sinh(\gamma H)} e^{i\alpha(\xi - x)} d\alpha \quad (3.42)$$

$$f_1(x) = \begin{cases} 0 & \text{Case A} \\ F_1^{(N)}(x) & \text{Case B} \end{cases} \quad (3.43)$$

$$F_1^{(N)}(x) = -\frac{N}{2H} \sin\left(\frac{N\pi}{2}\right) \int_{-\infty + ib}^{\infty + ib} \tilde{T}_N \frac{\coth(\gamma H)}{\gamma} e^{-i\alpha x} d\alpha - \frac{1}{\pi} \cos\left(\frac{N\pi}{2}\right) \int_{-\infty + ib}^{\infty + ib} \tilde{T}_N e^{-i\alpha x} d\alpha \quad (3.44)$$

Equation (3.40) represents one of the integral equations we have been seeking to derive. The unknowns in this equation are  $Y_1$  and  $Z_1$  and  $f_1(x)$  is a known function related to the source.

Next we subtract (3.35) from (3.34) to get:

$$\int_{-2L}^{-\infty} Y_2(\xi) K_2(k|x - \xi|) d\xi + \int_0^{\infty} Z_2(\xi) K_2(k|x - \xi|) d\xi = f_2(x) \quad (3.45)$$

where

$$Y_2(\xi) = \psi_1 + \psi_2 \quad (3.46)$$

$$Z_2(\xi) = x_1 + x_2$$

$$\kappa_2(k|x-\xi|) = \kappa_1^{(*)}(k|x-\xi|) - \kappa_2^{(*)}(k|x-\xi|) = \frac{1}{2\pi} \int_{-+ib}^{++ib} \frac{e^{\gamma H} e^{ia(\xi-x)}}{\gamma \cosh(\gamma H)} d\alpha \quad (3.47)$$

$$f_2(x) = \begin{cases} F_2^{(N)}(x) & \text{Case A} \\ 0 & \text{Case B} \end{cases} \quad (3.48)$$

$$F_2^{(N)}(x) = \frac{N}{2H} \cos\left(\frac{N\pi}{2}\right) \int_{-+ib}^{++ib} \tilde{T}_N \frac{\tanh(\gamma H)}{\gamma} e^{-iax} d\alpha - \frac{1}{\pi} \sin\left(\frac{N\pi}{2}\right) \int_{-+ib}^{++ib} \tilde{T}_N e^{-iax} d\alpha \quad (3.49)$$

which is the second integral equation we have been seeking. Thus, in summary, we have reduced the original problem to that of solving a pair of integral equations (3.40) and (3.45) with four unknown functions, viz.,  $\Upsilon_1(\xi)$ ,  $Z_1(\xi)$ ,  $\Upsilon_2(\xi)$ , and  $Z_2(\xi)$ .

## IV. SOLUTION OF THE INTEGRAL EQUATIONS

As a first step we rewrite the integral equations (3.40) and (3.45)

as:

$$\int_{-\infty}^{-2L} Y_1(\xi) K_1(k|x - \xi|) d\xi + \int_0^{\infty} Z_1(\xi) K_1(k|x - \xi|) d\xi = \begin{cases} f_1(x) & -\infty < x < -2L, \quad 0 < x < \infty \\ e_1(x) & -2L < x < 0 \end{cases} \quad (4.1)$$

and

$$\int_{-\infty}^{-2L} Y_2(\xi) K_2(k|x - \xi|) d\xi + \int_0^{\infty} Z_2(\xi) K_2(k|x - \xi|) d\xi = \begin{cases} f_2(x) & -\infty < x < -2L, \quad 0 < x < \infty \\ e_2(x) & -2L < x < 0 \end{cases} \quad (4.2)$$

where we have deliberately introduced two new unknown functions, viz.,  $e_1(x)$ ,  $e_2(x)$ , in order to extend the range of  $x$  from  $-\infty$  to  $+\infty$ . This is important for the next step which is to multiply (4.1) and (4.2) throughout by  $\exp(iax)$  and integrate with respect to  $x$  from  $-\infty$  to  $\infty$ . This gives

$$\begin{aligned} & \int_{-\infty}^{-2L} Y_1(\xi) e^{ia\xi} d\xi \cdot K_3(\alpha) + \int_0^{\infty} Z_1(\xi) e^{ia\xi} d\xi \cdot K_3(\alpha) \\ &= \int_{-\infty}^{-2L} f_1(x) e^{iax} dx + \int_{-2L}^0 e_1(x) e^{iax} dx + \int_0^{\infty} f_1(x) e^{iax} dx \end{aligned} \quad (4.3)$$

and

$$\begin{aligned} & \int_{-\infty}^{-2L} Y_2(\xi) e^{ia\xi} d\xi \cdot K_4(\alpha) + \int_0^{\infty} Z_2(\xi) e^{ia\xi} d\xi \cdot K_4(\alpha) \\ &= \int_{-\infty}^{-2L} f_2(x) e^{iax} dx + \int_{-2L}^0 e_2(x) e^{iax} dx + \int_0^{\infty} f_2(x) e^{iax} dx \end{aligned} \quad (4.4)$$

where

$$K_3(\alpha) = \frac{e^{\gamma H}}{\gamma \sinh(\gamma H)}, \quad K_4(\alpha) = \frac{e^{\gamma H}}{\gamma \cosh(\gamma H)} \quad (4.5)$$

are analytic in the strip  $-k_2 < \text{Im} \alpha < k_2$ .

Defining the transforms of the unknown functions in (4.3) and (4.4) and indicating their domains of analyticity, we have

$$\phi_+(\alpha) = \int_0^\infty z_1(\xi) e^{i\alpha \xi} d\xi, \quad (4.6)$$

$$\phi_-(\alpha) = \int_{-\infty}^{-2L} y_1(\xi) e^{i\alpha(\xi+2L)} d\xi, \quad (4.7)$$

$$\psi_+(\alpha) = \int_0^\infty z_2(\xi) e^{i\alpha \xi} d\xi, \quad (4.8)$$

$$\psi_-(\alpha) = \int_{-\infty}^{-2L} y_2(\xi) e^{i\alpha(\xi+2L)} d\xi, \quad (4.9)$$

where the functions  $\phi_+(\alpha)$ ,  $\psi_+(\alpha)$  are analytic for  $\text{Im} \alpha > -k_2$  and  $\phi_-(\alpha)$ ,  $\psi_-(\alpha)$  are analytic for  $\text{Im} \alpha < k_2$ . We can also write the transforms of the known functions  $f_1(x)$  and  $f_2(x)$  in the range  $-\infty < x < -2L$  as

$$H_j(\alpha) = \int_{-\infty}^{-2L} f_j(x) e^{i\alpha x} dx = e^{-i\alpha 2L} H_{j-}(\alpha) \quad (4.10)$$

where  $j = 1, 2$  and

$$H_{j-}(\alpha) = \int_{-\infty}^{-2L} f_j(x) e^{i\alpha(x+2L)} dx. \quad (4.11)$$

Likewise for the range  $0 < x < \infty$  we have the transform

$$H_{j+}(\alpha) = \int_0^{\infty} f_j(x) e^{i\alpha x} dx \quad (4.12)$$

where

$$H_{1\pm}(\alpha) = \begin{cases} 0 & , \text{ Case A} \\ \tilde{H}_{1\pm}^{(N)}(\alpha) & , \text{ Case B} \end{cases} \quad (4.13)$$

where the superscript (N) is associated with the excitation function and is defined in (2.1) and (2.2). To obtain the expressions for  $H_{1\pm}(\alpha)$ , we have to calculate the functions  $f_1(x)$  for two cases: (a)  $-\infty < x < -2L$  and (b)  $0 < x < \infty$ . We also need to perform these calculations for N both even and odd. For Case (A) we need to close the contour with a semicircle in the upper half plane, whereas the closure for the second case is in the lower half plane. Substituting the results of these calculations in (4.12), we obtain the final expressions for  $\tilde{H}_{1\pm}^{(2l)}$  and  $\tilde{H}_{1\pm}^{(2l-1)}$ , which read:

$$\tilde{H}_{1\pm}^{(2l)}(\alpha) = \pm (-1)^l \mu \frac{1}{\alpha_l(\alpha \pm \alpha_l)} \left\{ \begin{bmatrix} 1 \\ 0 \end{bmatrix} e^{i\alpha_l' x_0} + \begin{bmatrix} 0 \\ 1 \end{bmatrix} e^{i\alpha_l'(2L-x_0)} \right\} \quad (4.14)$$

$$l = 0, 1, \dots$$

$$\begin{aligned} \tilde{H}_{1\pm}^{(2l-1)}(\alpha) = \pm (-1)^{l+1} \frac{(2l-1)\mu}{\pi} & \left\{ \frac{2}{(2l-1)^2} \frac{1}{k(\alpha \pm k)} \begin{bmatrix} 1 \\ 0 \end{bmatrix} e^{i\alpha_l' x_0} \right. \\ & + \left. \begin{bmatrix} 0 \\ 1 \end{bmatrix} e^{i\alpha_l'(2L-x_0)} \right\} - \sum_{n=1}^{n_1} \frac{1}{n^2 \alpha_n \left[ 1 - \left( \frac{l-1/2}{n} \right)^2 \right] (\alpha \pm \alpha_n)} \\ & \cdot \left\{ \begin{bmatrix} 1 \\ 0 \end{bmatrix} e^{i\alpha_n' x_0} + \begin{bmatrix} 0 \\ 1 \end{bmatrix} e^{i\alpha_n'(2L-x_0)} \right\} \end{aligned} \quad (4.15)$$



Note that we have neglected the exponentially decaying terms by retaining only  $n_1$  terms in the summation. The integer  $n_1$  satisfies the conditions:

$$\frac{n_1 \pi}{H} < k, \quad \frac{(n_1 + 1) \pi}{H} > k. \quad (4.16)$$

We can also show that

$$H_{2\pm}(\alpha) = \begin{cases} \tilde{H}_{2\pm}^{(N)}(\alpha) & , \text{ Case A} \\ 0 & , \text{ Case B} \end{cases} \quad (4.17)$$

where

$$\begin{aligned} \tilde{H}_{2\pm}^{(2l)}(\alpha) &= \pm (-1)^l \frac{2\mu}{\pi} \sum_{n=1}^{n_2} \frac{1}{\left(n - \frac{1}{2}\right)^2 \alpha_{n-1/2}^2 \left[1 - \left(\frac{l}{n - 1/2}\right)^2\right]} \left(\alpha \pm \alpha_{n-1/2}\right) \\ l &= 1, 2, \dots \\ &\cdot \left( \begin{bmatrix} 1 \\ 0 \end{bmatrix} e^{i\alpha_{n-1/2} x_0} + \begin{bmatrix} 0 \\ 1 \end{bmatrix} e^{i\alpha_{n-1/2} (2L - x_0)} \right) \end{aligned} \quad (4.18)$$

and  $n_2$  is determined from the condition

$$\frac{(n_2 - 1/2)\pi}{H} < k, \quad \frac{(n_2 + 1/2)\pi}{H} > k \quad (4.19)$$

and

$$\begin{aligned} \tilde{H}_{2\pm}^{(2l-1)}(\alpha) &= \pm (-1)^{l+1} \mu \frac{1}{\alpha_{l-1/2}^2 (\alpha \pm \alpha_{l-1/2})} \left( \begin{bmatrix} 1 \\ 0 \end{bmatrix} e^{i\alpha_{l-1/2} x_0} + \begin{bmatrix} 0 \\ 1 \end{bmatrix} e^{i\alpha_{l-1/2} (2L - x_0)} \right) \\ l &= 1, 2, \dots \end{aligned} \quad (4.20)$$

Utilizing the definition of various transforms, we rewrite (4.3) and

(4.4) as:

$$e^{-i\alpha 2L} \phi_- (\alpha) - \gamma^2 H M_1(\alpha) \phi_1(\alpha) = \left[ e^{-i\alpha 2L} H_{1-}(\alpha) + H_{1+}(\alpha) \right] \gamma^2 H \phi_1(\alpha) \quad (4.21)$$

and

$$e^{-ia2L} \psi_-(\alpha) + \psi_+(\alpha) - \gamma M_2(\alpha) \psi_1(\alpha) = \left[ e^{-ia2L} H_{2-}(\alpha) + H_{2+}(\alpha) \right] \gamma M_2(\alpha) \quad (4.22)$$

where

$$\psi_1(\alpha) = \int_{-2L}^0 e_1(x) e^{iax} dx \quad (4.23)$$

$$\psi_1(\alpha) = \int_{-2L}^0 e_2(x) e^{iax} dx \quad (4.24)$$

$$M_1(\alpha) = e^{-\gamma H} \frac{\sinh(\gamma H)}{\gamma H} \quad (4.25)$$

$$M_2(\alpha) = e^{-\gamma H} \cosh(\gamma H) \quad (4.26)$$

The next step is to factorize the functions  $M_1(\alpha)$  and  $M_2(\alpha)$  in the form of products,

$$M_1(\alpha) = M_{1+}(\alpha) M_{1-}(\alpha) \quad (4.27)$$

$$M_2(\alpha) = M_{2+}(\alpha) M_{2-}(\alpha) \quad (4.28)$$

where  $M_{1+}(\alpha)$ ,  $M_{2+}(\alpha)$  are regular and non-zero in the upper half plane

$\tau > -k_2$ , whereas  $M_{1-}(\alpha)$ ,  $M_{2-}(\alpha)$  are regular and non-zero in the lower half plane  $\tau < k_2$ . Then, multiplication of (4.21) by

$$\frac{e^{+ia2L}}{(\alpha - k) M_{1-}(\alpha)}$$

and (4.22) by

$$\frac{e^{ia2L}}{\sqrt{\alpha - k} M_{2-}(\alpha)}$$

leads to the following coupled equations in the transform domain:

$$\begin{aligned} \frac{\phi_-(\alpha)}{(\alpha-k)H_{1-}(\alpha)} + \frac{\phi_+(\alpha)e^{ia2L}}{(\alpha-k)H_{1-}(\alpha)} - (\alpha+k)HM_{1+}(\alpha)\phi_1(\alpha)e^{ia2L} \\ = (\alpha+k)HM_{1+}(\alpha)H_{1-}(\alpha) + (\alpha+k)HM_{1+}(\alpha)H_{1+}(\alpha)e^{ia2L} \end{aligned} \quad (4.29)$$

and

$$\begin{aligned} \frac{\psi_-(\alpha)}{\sqrt{\alpha-k}M_{2-}(\alpha)} + \frac{\psi_+(\alpha)e^{ia2L}}{\sqrt{\alpha-k}M_{2-}(\alpha)} - \sqrt{\alpha+k}M_{2+}(\alpha)\psi_1(\alpha)e^{ia2L} \\ = \sqrt{\alpha+k}M_{2+}(\alpha)H_{2-}(\alpha) + \sqrt{\alpha+k}M_{2+}(\alpha)H_{2+}(\alpha)e^{ia2L} \end{aligned} \quad (4.30)$$

The first terms on the left-hand side of (4.29) and (4.30) are regular in the lower half plane, whereas the third terms on the left-hand side and the second terms on the right-hand side of (4.29) and (4.30) are regular in the upper half plane.

To solve these equations we carry out the decomposition

$$e^{ia2L} \frac{\phi_+(\alpha)}{(\alpha-k)H_{1-}(\alpha)} = R_+(\alpha) + R_-(\alpha) \quad (4.31)$$

$$(\alpha+k)HM_{1+}(\alpha)H_{1-}(\alpha) = \tilde{S}_{1+}(\alpha) + \tilde{S}_{1-}(\alpha) \quad (4.32)$$

$$e^{ia2L} \frac{\psi_+(\alpha)}{\sqrt{\alpha-k}M_{2-}(\alpha)} = Q_+(\alpha) + Q_-(\alpha) \quad (4.33)$$

$$\sqrt{\alpha+k}M_{2+}(\alpha)H_{2-}(\alpha) = \tilde{S}_{2+}(\alpha) + \tilde{S}_{2-}(\alpha) \quad (4.34)$$

Using the method of factorization we obtain the equations:

$$\frac{\phi_-(\alpha)}{(\alpha-k)H_{1-}(\alpha)} + R_-(\alpha) - \tilde{S}_{1-}(\alpha) = 0 \quad (4.35)$$

$$\frac{\psi_-(\alpha)}{\sqrt{\alpha-k} M_{2-}(\alpha)} + Q_-(\alpha) - \tilde{S}_{2-}(\alpha) = 0 \quad (4.36)$$

where

$$R_-(\alpha) = -\frac{1}{2\pi i} \int_{1d-\infty}^{1d+\infty} \frac{e^{i\zeta 2L} \phi_+(\zeta)}{(\zeta-k) M_{1-}(\zeta) (\zeta-\alpha)} d\zeta \quad (4.37)$$

$$Q_-(\alpha) = -\frac{1}{2\pi i} \int_{1d-\infty}^{1d+\infty} \frac{e^{i\zeta 2L} \psi_+(\zeta)}{\sqrt{\zeta-k} M_{2-}(\zeta) (\zeta-\alpha)} d\zeta \quad (4.38)$$

$$\tilde{S}_{1-}(\alpha) = -\frac{1}{2\pi i} \int_{1d-\infty}^{1d+\infty} \frac{(\zeta+k) H M_{1+}(\zeta) H_{1-}(\zeta)}{\zeta-\alpha} d\zeta \quad (4.39)$$

$$\tilde{S}_{2-}(\alpha) = -\frac{1}{2\pi i} \int_{1d-\infty}^{1d+\infty} \frac{\sqrt{\zeta+k} M_{2+}(\zeta) H_{2-}(\zeta)}{\zeta-\alpha} d\zeta \quad (4.40)$$

$$\tau < d < k_2, \quad \tau = \operatorname{Im} \alpha$$

After multiplying (4.21) by  $1/[(\alpha+k)M_{1+}(\alpha)]$  and (4.22) by  $1/[\sqrt{\alpha+k} M_{2+}(\alpha)]$  we obtain:

$$\begin{aligned} \frac{\phi_+(\alpha)}{(\alpha+k)M_{1+}(\alpha)} + \frac{e^{-i\alpha 2L} \phi_-(\alpha)}{(\alpha+k)M_{1+}(\alpha)} - (\alpha-k) H M_{1-}(\alpha) \phi_1(\alpha) &= e^{-i\alpha 2L} H_{1-}(\alpha) (\alpha-k) H M_{1-}(\alpha) \\ &+ H_{1+}(\alpha) (\alpha-k) H M_{1-}(\alpha) \end{aligned} \quad (4.41)$$

and

$$\begin{aligned} \frac{\psi_+(\alpha)}{\sqrt{\alpha+k} M_{2+}(\alpha)} + \frac{e^{-i\alpha 2L} \psi_-(\alpha)}{\sqrt{\alpha+k} M_{2+}(\alpha)} - \sqrt{\alpha-k} M_{2-}(\alpha) \psi_1(\alpha) \\ = e^{-i\alpha 2L} H_{2-}(\alpha) \sqrt{\alpha-k} M_{2-}(\alpha) + H_{2+}(\alpha) \sqrt{\alpha-k} M_{2-}(\alpha) \end{aligned} \quad (4.42)$$

Note that the first terms on the left-hand side of (4.41) and (4.42) are regular in the upper half plane; the third terms on the left-hand side and the first terms on the right-hand side are regular in the lower half plane.

We now use the decompositions:

$$\frac{e^{-i\alpha 2L} \phi_{-}(\alpha)}{(\alpha + k) M_{1+}(\alpha)} = U_{+}(\alpha) + U_{-}(\alpha) \quad (4.43a)$$

$$\frac{e^{-i\alpha 2L} \psi_{-}(\alpha)}{\sqrt{\alpha + k} M_{2+}(\alpha)} = \theta_{+}(\alpha) + \theta_{-}(\alpha) \quad (4.43b)$$

$$H_{1+}(\alpha)(\alpha - k) H M_{1-}(\alpha) = V_{1+}(\alpha) + V_{1-}(\alpha) \quad (4.43c)$$

$$H_{2+}(\alpha) \sqrt{\alpha - k} M_{2-}(\alpha) = V_{2+}(\alpha) + V_{2-}(\alpha) \quad (4.43d)$$

Substituting (4.43) into (4.41) and (4.42) and using the Wiener-Hopf technique [10,11] result in the equations:

$$\frac{\phi_{+}(\alpha)}{(\alpha + k) M_{1+}(\alpha)} + U_{+}(\alpha) - V_{1+}(\alpha) = 0 \quad (4.44)$$

$$\frac{\psi_{+}(\alpha)}{\sqrt{\alpha + k} M_{2+}(\alpha)} + \theta_{+}(\alpha) - V_{2+}(\alpha) = 0 \quad (4.45)$$

where

$$U_{+}(\alpha) = \frac{1}{2\pi i} \int_{ic-\infty}^{ic+\infty} \frac{e^{-i\zeta 2L} \phi_{-}(\zeta)}{(\zeta + k) M_{1+}(\zeta) (\zeta - \alpha)} d\zeta, \quad (4.46)$$

$$\theta_{+}(\alpha) = \frac{1}{2\pi i} \int_{ic-\infty}^{ic+\infty} \frac{e^{-i\zeta 2L} \psi_{-}(\zeta)}{\sqrt{\zeta + k} M_{2+}(\zeta) (\zeta - \alpha)} d\zeta, \quad (4.47)$$

$$V_{1+}(\alpha) = \frac{1}{2\pi i} \int_{1c-\infty}^{1c+\infty} \frac{H_{1+}(\zeta)(\zeta - k) H M_{1-}(\zeta)}{\zeta - \alpha} d\zeta, \quad (4.48)$$

$$V_{2+}(\alpha) = \frac{1}{2\pi i} \int_{1c-\infty}^{1c+\infty} \frac{H_{2+}(\zeta) \sqrt{\zeta - k} M_{2-}(\zeta)}{\zeta - \alpha} d\zeta, \quad (4.49)$$

$$-k_2 < c < \tau.$$

The above manipulations have resulted in four coupled integral equations (4.35), (4.36), (4.44) and (4.45) each of which contains two unknowns. We now proceed to derive a set of new equations each with only a single unknown. To this end, we replace  $\alpha$  by  $-\alpha$  in (4.35) and (4.36) and  $\zeta$  by  $(-\zeta)$  in (4.46) and (4.47). Using the representations  $\sqrt{-\alpha + k} = i \sqrt{\alpha - k}$ ,  $\sqrt{-\alpha - k} = -i \sqrt{\alpha + k}$ , adding and subtracting the resulting equations and defining

$$\begin{bmatrix} S_{1+}(\alpha) \\ D_{1+}(\alpha) \end{bmatrix} = \Phi_+(\alpha) \pm \Phi_-(-\alpha) \quad (4.50a)$$

$$\begin{bmatrix} S_{2+}(\alpha) \\ D_{2+}(\alpha) \end{bmatrix} = \Psi_+(\alpha) \pm \Psi_-(-\alpha) \quad (4.50b)$$

We obtain the two sets of coupled equations

$$\begin{bmatrix} S_{1+}(\alpha) \\ D_{1+}(\alpha) \end{bmatrix} \cdot \frac{1}{(\alpha + k) M_{1+}(\alpha)} \pm \frac{1}{2\pi i} \int_{1d-\infty}^{1d+\infty} \begin{bmatrix} S_{1+}(\zeta) \\ D_{1+}(\zeta) \end{bmatrix} \frac{e^{i\zeta 2L} d\zeta}{(\zeta - k) M_{1-}(\zeta)(\zeta + \alpha)} - \left[ V_{1+}(\alpha) \pm \tilde{S}_{1-}(-\alpha) \right] = 0 \quad (4.51)$$

$$\begin{bmatrix} S_{2+}(\alpha) \\ D_{2+}(\alpha) \end{bmatrix} \cdot \frac{1}{\sqrt{\alpha + k} M_{2+}(\alpha)} \pm \frac{1}{2\pi i} \int_{1d-\infty}^{1d+\infty} \begin{bmatrix} S_{2+}(\zeta) \\ D_{2+}(\zeta) \end{bmatrix} \frac{e^{i\zeta 2L} d\zeta}{\sqrt{\zeta - k} M_{2-}(\zeta)(\zeta + \alpha)} - \left[ i V_{2+}(\alpha) \pm \tilde{S}_{2-}(-\alpha) \right] = 0 \quad (4.52)$$

It is shown in Appendix IV that for  $k2L \gg 1$  the integrals appearing in (4.51) and (4.52) can be evaluated in a series form as follows:

$$\begin{aligned}
 & \frac{1}{2\pi i} \int_{1d-\infty}^{1d+\infty} \begin{bmatrix} S_{1+}(\zeta) \\ D_{1+}(\zeta) \end{bmatrix} \frac{e^{1\zeta 2L} d\zeta}{(\zeta - k) M_{1-}(\zeta) (\zeta + \alpha)} \\
 &= \begin{bmatrix} S_{1+}(k) \\ D_{1+}(k) \end{bmatrix} \frac{e^{1k 2L} M_{1+}(k)}{(\alpha + k)} \left\{ 1 + \frac{H}{\pi} e^{-13/4\pi} \sqrt{2k} \sqrt{2L} (\alpha + k) W_{-1} \left[ -12L(\alpha + k) \right] \right\} \\
 &+ \sum_{n=1}^{n_1} \begin{bmatrix} S_{1+}(\alpha'_n) \\ D_{1+}(\alpha'_n) \end{bmatrix} \frac{e^{1\alpha'_n 2L} M_{1+}(\alpha'_n) (\alpha'_n + k)}{\alpha'_n (\alpha + \alpha'_n)} \quad (4.53)
 \end{aligned}$$

and

$$\begin{aligned}
 & \frac{1}{2\pi i} \int_{1d-\infty}^{1d+\infty} \begin{bmatrix} S_{2+}(S) \\ D_{2+}(S) \end{bmatrix} \frac{e^{1\zeta 2L} d\zeta}{\sqrt{\zeta - k} M_{2-}(\zeta) (\zeta + \alpha)} \\
 &= \frac{1}{\pi} e^{-13/4\pi} \sqrt{2L} W_{-1} \left[ -12L(\alpha + k) \right] e^{1k 2L} M_{2+}(k) \cdot \begin{bmatrix} S_{2+}(k) \\ D_{2+}(k) \end{bmatrix} \\
 &+ \frac{1}{H} \sum_{n=1}^{n_2} \begin{bmatrix} S_{2+}(\alpha'_{n-1/2}) \\ D_{2+}(\alpha'_{n-1/2}) \end{bmatrix} \frac{e^{1\alpha'_{n-1/2} 2L} M_{2+}(\alpha'_{n-1/2}) \sqrt{\alpha'_{n-1/2} + k}}{(\alpha + \alpha'_{n-1/2}) \alpha'_{n-1/2}} \quad (4.54)
 \end{aligned}$$

Substituting the various series expressions given in (4.53), and (4.54) into (4.51) and (4.52) gives:

$$\begin{aligned}
 & \begin{bmatrix} S_{1+}(\alpha) \\ D_{1+}(\alpha) \end{bmatrix} = \frac{1}{\pi} (\alpha + k) M_{1+}(\alpha) \left\{ \begin{bmatrix} S_{1+}(k) \\ D_{1+}(k) \end{bmatrix} \frac{e^{1k 2L} M_{1+}(k)}{\alpha + k} \right. \\
 & \quad \left. \cdot \left( 1 + \frac{H}{\pi} e^{-13/4\pi} \sqrt{2k} \sqrt{2L} (\alpha + k) W_{-1} \left[ -12L(\alpha + k) \right] \right) \right\}
 \end{aligned}$$

$$\sum_{n=1}^{n_1} \begin{bmatrix} S_{1+}(\alpha'_n) \\ D_{1+}(\alpha'_n) \end{bmatrix} \frac{e^{i\alpha'_n 2L} M_{1+}(\alpha'_n)(\alpha'_n + k)}{\alpha'_n(\alpha + \alpha'_n)} + \left[ \mp V_{1+}(\alpha) + \tilde{S}_{1-}(-\alpha) \right] \quad (4.55)$$

and

$$\begin{aligned} \begin{bmatrix} S_{2+}(\alpha) \\ D_{2+}(\alpha) \end{bmatrix} = & \mp i\sqrt{\alpha + k} M_{2+}(\alpha) \left\{ \frac{1}{\pi} e^{-13/4\pi} \sqrt{2L} W_{-1}[-12L(\alpha + k)] \right. \\ & \cdot e^{ik2L} M_{2+}(k) \cdot \begin{bmatrix} S_{2+}(k) \\ D_{2+}(k) \end{bmatrix} + \frac{1}{H} \sum_{n=1}^{n_2} \begin{bmatrix} S_{2+}(\alpha'_{n-1/2}) \\ D_{2+}(\alpha'_{n-1/2}) \end{bmatrix} \\ & \cdot \left. \frac{e^{i\alpha'_{n-1/2} 2L} M_{2+}(\alpha'_{n-1/2}) \sqrt{\alpha'_{n-1/2} + k}}{\alpha'_{n-1/2}(\alpha + \alpha'_{n-1/2})} + [\pm iV_{2+}(\alpha) + \tilde{S}_{2-}(-\alpha)] \right\}. \end{aligned} \quad (4.56)$$

Our next step is to obtain the expressions for the vector potentials which depend on the unknown functions  $\phi_-(\alpha)$ ,  $\phi_+(\alpha)$ ,  $\psi_+(\alpha)$ ,  $\psi_-(\alpha)$ , and which are in turn expressed in terms of the functions  $S_{1+}(\alpha)$ ,  $D_{1+}(\alpha)$ ,  $S_{2+}(\alpha)$ ,  $D_{2+}(\alpha)$ .

From (4.50) we have

$$\phi_{\pm}(\pm\alpha) = \frac{1}{2} [S_{1+}(\alpha) \pm D_{1+}(\alpha)] \quad (4.57a)$$

$$\psi_{\pm}(\pm\alpha) = \frac{1}{2} [S_{2+}(\alpha) \pm D_{2+}(\alpha)] \quad (4.57b)$$

Changing  $\alpha \rightarrow -\alpha$  in (4.57) yields

$$\phi_-(\alpha) = \frac{1}{2} [S_{1+}(-\alpha) - D_{1+}(-\alpha)] \quad (4.58a)$$

$$\psi_-(\alpha) = \frac{1}{2} [S_{2+}(-\alpha) - D_{2+}(-\alpha)] \quad (4.58b)$$

We can rewrite (4.57) and (4.58) as:

$$\phi_{\pm}(\alpha) = \frac{1}{2} [S_{1+}(\pm\alpha) \pm D_{1+}(\pm\alpha)] \quad (4.59a)$$

$$\psi_{\pm}(\alpha) = \frac{1}{2} [S_{2+}(\pm\alpha) \pm D_{2+}(\pm\alpha)] \quad (4.59b)$$



To obtain the expressions for  $\phi_+(\alpha)$  and  $\psi_+(\alpha)$ , we need to substitute (4.55) and (4.56) into (4.59). Likewise  $\phi_-(\alpha)$  and  $\psi_-(\alpha)$  are obtained by changing  $\alpha \rightarrow -\alpha$  in (4.55) and (4.56) and substituting the results in (4.59).

Following these steps we derive the equations:

$$\begin{aligned} \phi_{\pm}(\alpha) = & \pm \frac{1}{2} (\alpha \pm k) M_{1\pm}(\alpha) \left\{ \frac{[D_{1+}(k) \mp S_{1+}(k)] M_{1+}(k) e^{ik2L}}{\alpha \pm k} \right. \\ & \cdot \left( 1 \pm \frac{H}{\pi} e^{-13/4\pi} \sqrt{2k} \sqrt{2L} (\alpha \pm k) W_{-1}[\mp 12L(\alpha \pm k)] \right) \\ & + \sum_{n=1}^{n_1} \frac{[D_{1+}(\alpha'_n) \mp S_{1+}(\alpha'_n)] e^{i\alpha'_n 2L} M_{1+}(\alpha'_n) (\alpha'_n + k)}{\alpha'_n (\alpha \pm \alpha'_n)} \\ & \left. + 2 \begin{bmatrix} v_{1+}(\alpha) \\ -\tilde{S}_{1-}(\alpha) \end{bmatrix} \right\}. \end{aligned} \quad (4.60)$$

and

$$\begin{aligned} \psi_{\pm}(\alpha) = & \begin{bmatrix} 1 \\ 1 \end{bmatrix} \frac{\sqrt{\alpha \pm k} M_{2\pm}(\alpha)}{2} \left\{ [D_{2+}(k) \mp S_{2+}(k)] \right. \\ & \cdot \frac{1}{\pi} e^{-13/4\pi} \sqrt{2L} W_{-1}[\mp 12L(\alpha \pm k)] e^{ik2L} M_{2+}(k) \\ & - \frac{1}{H} \sum_{n=1}^{n_2} \frac{[\mp D_{2+}(\alpha'_{n-1/2}) + S_{2+}(\alpha'_{n-1/2})] e^{i\alpha'_{n-1/2} 2L} M_{2+}(\alpha'_{n-1/2}) \sqrt{\alpha'_{n-1/2} + k}}{\alpha'_{n-1/2} (\alpha \pm \alpha'_{n-1/2})} \\ & \left. + 2 \begin{bmatrix} -iv_{2+}(\alpha) \\ \tilde{S}_{2-}(\alpha) \end{bmatrix} \right\}. \end{aligned} \quad (4.61)$$

The last two equations provide us with the expressions for the functions  $\phi_{\pm}(\alpha)$  and  $\psi_{\pm}(\alpha)$ . They depend on the group of constants  $[S_{1+}(k), D_{1+}(k), S_{2+}(k), D_{2+}(k)]$  and also on  $[S_{1+}(\alpha'_n), D_{1+}(\alpha'_n), S_{2+}(\alpha'_{n-1/2}), D_{2+}(\alpha'_{n-1/2})]$ .

We can express the first set of four constants in terms of the ones appearing inside the second bracket. This is accomplished by returning to (4.55) and (4.56) and substituting  $\alpha \rightarrow k$ . The resulting relationships can be further simplified for  $2kL \gg 1$ , i.e., for wide plates, by introducing the asymptotic forms

$$W_{-1}(z) = \frac{\sqrt{\pi}}{z} \quad \text{for } z \rightarrow \infty, \quad -\pi < \arg z < \pi. \quad (4.62)$$

We then obtain the following desired equation relating  $S_{1+}(k)$ , and  $D_{1+}(k)$  with  $S_{1+}(\alpha'_n)$ ,  $D_{1+}(\alpha'_n)$ , etc.,

$$\begin{aligned} \begin{bmatrix} S_{1+}(k) \\ D_{1+}(k) \end{bmatrix} &= \frac{2kM_{1+}(k)}{1 \pm T_1} \left\{ \tilde{+} \sum_{n=1}^{n_1} \begin{bmatrix} S_{1+}(\alpha'_n) \\ D_{1+}(\alpha'_n) \end{bmatrix} \frac{e^{i\alpha'_n 2L} M_{1+}(\alpha'_n)}{\alpha'_n} \right. \\ &\quad \left. + [V_{1+}(k) \tilde{+} \tilde{S}_{1-}(-k)] \right\} \end{aligned} \quad (4.63)$$

and

$$\begin{aligned} \begin{bmatrix} S_{2+}(k) \\ D_{2+}(k) \end{bmatrix} &= \tilde{+} \frac{1/\sqrt{2}kM_{2+}(k)}{1 \pm T_2} \left\{ \frac{1}{H} \sum_{n=1}^{n_2} \begin{bmatrix} S_{2+}(\alpha'_{n-1/2}) \\ D_{2+}(\alpha'_{n-1/2}) \end{bmatrix} \frac{e^{i\alpha'_{n-1/2} 2L} M_{2+}(\alpha'_{n-1/2})}{\alpha'_{n-1/2} \sqrt{k + \alpha'_{n-1/2}}} \right. \\ &\quad \left. + [\tilde{S}_{2-}(-k) \pm iV_{2+}(k)] \right\}, \end{aligned} \quad (4.64)$$

where

$$T_1 = [M_{1+}(k)]^2 e^{ik2L} \left[ 1 + \frac{H}{\sqrt{\pi}} e^{-i\pi/4} \sqrt{\frac{2k}{2L}} \right], \quad (4.65)$$

$$T_2 = [M_{2+}(k)]^2 e^{ik2L} \frac{e^{i\pi/4}}{\sqrt{\pi}} \cdot \frac{1}{\sqrt{2k2L}}. \quad (4.66)$$

The constants  $S_{1+}(\alpha'_n)$ ,  $D_{1+}(\alpha'_n)$ ,  $S_{2+}(\alpha'_{n-1/2})$  and  $D_{2+}(\alpha'_{n-1/2})$  satisfy a set of algebraic equations, which is derived by substituting  $\alpha = \alpha'_n$  into (4.55),  $\alpha = \alpha'_{n-1/2}$  into (4.56) and using the asymptotic representation  $W_{-1}(z)$  and

(4.63) through (4.66) [see Appendix V]. These equations take the form:

For  $S_{1+}(\alpha_n^-)$ ,  $D_{1+}(\alpha_n^-)$ :

$$\sum_{n=1}^{n_1} \begin{bmatrix} S_{1+}(\alpha_n^-) \\ D_{1+}(\alpha_n^-) \end{bmatrix} \begin{bmatrix} G_{mn}^{(1)\pm} \\ \delta_m^n \end{bmatrix} = P_m^{(1)\pm} \quad \text{where } m = 1, 2, \dots, n_1 \quad (4.67)$$

where

$$G_{mn}^{(1)\pm} = \frac{e^{i\alpha_n^- 2L} M_{1+}(\alpha_m^-) M_{1+}(\alpha_n^-)}{\alpha_n^-} \left[ \frac{2kT_1}{1 \pm T_1} + \frac{(\alpha_m^- + k)(\alpha_n^- + k)}{\alpha_m^- + \alpha_n^-} \right] \quad (4.68)$$

$$\delta_m^n = \begin{cases} 1 & m = n \\ 0 & m \neq n \end{cases} \quad (4.69)$$

$$P_m^{(1)\pm} = \begin{cases} 0 & \text{Case A} \\ P_{m,N}^{(1)\pm} & \text{Case B} \end{cases} \quad (4.70)$$

(i) for N-even:

$$P_{m,2l}^{(1)\pm} = (-1)^l H_l \frac{M_{1+}(\alpha_m^-) M_{1+}(\alpha_l^-)}{\alpha_l^-} \left[ \frac{2kT_1}{1 \pm T_1} + \frac{(\alpha_m^- + k)(\alpha_l^- + k)}{(\alpha_m^- + \alpha_l^-)} \right] \\ \left[ e^{i\alpha_l^- x_0} \pm e^{i\alpha_l^- (2L-x_0)} \right] \quad l = 0, 1, 2, \dots \quad (4.71)$$

(ii) for N-odd

$$P_{m,2l-1}^{(1)\pm} = (-1)^{l+1} H_l \frac{M_{1+}(\alpha_m^-)(2l-1)}{\pi} \left\{ \frac{1}{1 \pm T_1} \frac{4 M_{1+}(k)}{(2l-1)^2} \right. \\ \cdot \left[ e^{ikx_0} \pm e^{ik(2L-x_0)} \right] - \sum_{n=1}^{n_1} \left[ \frac{2kT_1}{1 \pm T_1} + \frac{(\alpha_m^- + k)(\alpha_n^- + k)}{(\alpha_m^- + \alpha_n^-)} \right] \\ \cdot \frac{M_{1+}(\alpha_n^-)}{n^2 \alpha_n^- [1 - ((l-1/2)/n)^2]} \left[ e^{i\alpha_n^- x_0} \pm e^{i\alpha_n^- (2L-x_0)} \right] \Big\} \quad (4.72) \\ l = 1, 2, \dots$$

For  $S_{2+}(\alpha'_{n-1/2})$ ;  $D_{2+}(\alpha'_{n-1/2})$ ;

$$\sum_{n=1}^{n_2} \left[ \frac{S_{2+}(\alpha'_{n-1/2})}{D_{2+}(\alpha'_{n-1/2})} \right] \cdot \left[ G_{mn}^{(2)\pm} - \delta_m^n \right] = P_m^{(2)\pm}, \quad (4.73)$$

where

$$G_{mn}^{(2)\pm} = \frac{1/\alpha'_{n-1/2} + k}{H\alpha'_{n-1/2}} M_{2+}(\alpha'_{n-1/2}) M_{2+}(\alpha'_{n-1/2}) e^{i\alpha'_{n-1/2} 2L} \cdot \left[ \frac{2kT_2}{(1 \pm T_2)} \cdot \frac{1}{(\alpha'_{n-1/2} + k) \sqrt{\alpha'_{n-1/2} + k}} \mp \frac{\sqrt{\alpha'_{n-1/2} + k}}{(\alpha'_{n-1/2} + \alpha'_{n-1/2})} \right], \quad (4.74)$$

$$P_m^{(2)\pm} = \begin{cases} P_{m,N}^{(2)\pm} & \text{Case A} \\ 0 & \text{Case B} \end{cases}, \quad (4.75)$$

(i) for N-even:

$$P_{m,2\ell}^{(2)\pm} = i(-1)^\ell \frac{2\mu\ell}{\pi} M_{2+}(\alpha'_{m-1/2}) \cdot \sum_{n=1}^{n_2} \frac{M_{2+}(\alpha'_{n-1/2})}{(n-1/2)^2 \alpha'_{n-1/2} [1 - (\ell/(n-1/2))^2]} \cdot \left[ \frac{\sqrt{\alpha'_{m-1/2} + k} \sqrt{\alpha'_{n-1/2} + k}}{(\alpha'_{m-1/2} + \alpha'_{n-1/2})} \mp \frac{2kT_2}{1 \pm T_2} \cdot \frac{1}{\sqrt{\alpha'_{m-1/2} + k} \sqrt{\alpha'_{n-1/2} + k}} \right] \cdot \left[ e^{i\alpha'_{n-1/2} x_0} \pm e^{i\alpha'_{n-1/2} (2L-x_0)} \right], \quad (4.76)$$

(ii) for N-odd:

$$P_{m,2\ell-1}^{(2)\pm} = i(-1)^{\ell+1} \mu \frac{M_{2+}(\alpha'_{m-1/2}) M_{2+}(\alpha'_{\ell-1/2})}{\alpha'_{\ell-1/2}} \left[ \frac{\sqrt{\alpha'_{m-1/2} + k} \sqrt{\alpha'_{\ell-1/2} + k}}{(\alpha'_{m-1/2} + \alpha'_{\ell-1/2})} \mp \frac{2kT_2}{1 \pm T_2} \cdot \frac{1}{\sqrt{\alpha'_{m-1/2} + k} \sqrt{\alpha'_{\ell-1/2} + k}} \right] \cdot \left[ e^{i\alpha'_{\ell-1/2} x_0} \pm e^{i\alpha'_{\ell-1/2} (2L-x_0)} \right]. \quad (4.77)$$

The  $M_{1+}$  and  $M_{2+}$  functions appearing in the last few equations will now be written explicitly. To this end, we return to the definitions of  $M_1$  and  $M_2$ :

$$M_1(\alpha) = e^{-\gamma H} \frac{\sinh(\gamma H)}{\gamma H} = M_{1+}(\alpha) M_{1-}(\alpha) \quad (4.78)$$

$$M_2(\alpha) = e^{-\gamma H} \cosh(\gamma H) = M_{2+}(\alpha) M_{2-}(\alpha) \quad (4.79)$$

where [see [10] pages 131 and 175]

$$M_{1+}(\alpha) = \sqrt{\frac{\sin kH}{kH}} \exp \left\{ \frac{iH\alpha}{\pi} \left[ 1 - C + \ln \left( \frac{2\pi}{kH} \right) + i \frac{\pi}{2} \right] \right\} \\ \cdot \exp \left[ \frac{iH\gamma}{\pi} \ln \left( \frac{\alpha - \gamma}{k} \right) \right] \prod_{n=1}^{\infty} \left( 1 + \frac{\alpha}{\alpha_n'} \right) e^{i \frac{\alpha H}{n\pi}}, \quad (4.80)$$

$$M_{1-}(\alpha) = M_{1+}(-\alpha) \quad (4.81)$$

$$M_{2+}(\alpha) = \sqrt{\cos(kH)} \exp \left\{ \frac{i\alpha H}{\pi} \left[ 1 - C + \ln \left( \frac{\pi}{2kH} \right) + i \frac{\pi}{2} \right] \right\} \\ \cdot \exp \left[ \frac{iH\gamma}{\pi} \ln \frac{\alpha - \gamma}{k} \right] \prod_{n=1}^{\infty} \left( 1 + \frac{\alpha}{\alpha_{n-1/2}'} \right) e^{i \frac{\alpha H}{(n-1/2)\pi}} \quad (4.82)$$

$$M_{2-}(\alpha) = M_{2+}(-\alpha) \quad (4.83)$$

Substituting  $\alpha = k$  and  $\alpha = \alpha_m'$  into (141) and  $\alpha = \alpha_{m-1/2}'$  into (143), we obtain:

$$M_{1+}(k) = \sqrt{\frac{\sin(kH)}{kH}} \exp \left\{ \frac{iHk}{\pi} \left[ 1 - C + \ln \left( \frac{2\pi}{kH} \right) + i \frac{\pi}{2} \right] \right\} \\ \cdot \prod_{n=1}^{\infty} \left( 1 + \frac{k}{\alpha_n'} \right) e^{i \frac{kH}{n\pi}} \quad (4.84)$$

$$M_{1+}(\alpha_m') = \frac{\sqrt{\sin(kH)}}{kH} \exp \left\{ \frac{iH\alpha_m'}{\pi} \left[ 1 - C + \ln \left( \frac{2\pi}{kH} \right) + i \frac{\pi}{2} \right] \right\} \\ \cdot \exp \left[ m \ln \frac{\alpha_m' + i \pi/H}{k} \right] \prod_{n=1}^{\infty} \left( 1 + \frac{\alpha_m'}{\alpha_n'} \right) e^{i \frac{\alpha_n' H}{n\pi}} \quad (4.85)$$

$$M_{2+}(\alpha_{m-1/2}') = \sqrt{\cos(kH)} \exp \left\{ i \frac{\alpha_{m-1/2}' H}{\pi} \left[ 1 - C + \ln \left( \frac{\pi}{2kH} \right) + i \frac{\pi}{2} \right] \right\} \\ \cdot \exp \left[ (m - 1/2) \ln \left( \frac{\alpha_{m-1/2}' + i \frac{(m-1/2)\pi}{H}}{k} \right) \right] \\ \cdot \prod_{n=1}^{\infty} \left( 1 + \frac{\alpha_{m-1/2}'}{\alpha_{n-1/2}'} \right) e^{\frac{i\alpha_{n-1/2}' H}{(n-1/2)\pi}} \quad (4.86)$$

which are the desired expressions for  $M_{1+}(\alpha_m')$  and  $M_{2+}(\alpha_{m-1/2}')$  we were seeking.

## V. CALCULATION OF THE VECTOR POTENTIALS

From (3.41) and (3.46) we have:

$$\left\{ \begin{array}{l} \psi_1 = \frac{1}{2}[Y_2(\xi) + Y_1(\xi)] \\ \psi_2 = \frac{1}{2}[Y_2(\xi) - Y_1(\xi)] \\ x_1 = \frac{1}{2}[Z_2(\xi) + Z_1(\xi)] \\ x_2 = \frac{1}{2}[Z_2(\xi) - Z_1(\xi)] \end{array} \right. \quad \begin{array}{l} (5.1a) \\ (5.1b) \\ (5.1c) \\ (5.1d) \end{array}$$

Substituting (5.1) into (3.28) and (3.29) and using (4.6) through (4.9) we obtain:

$$I_1 = \frac{1}{2} e^{-i\alpha 2L} [\psi_-(\alpha) + \phi_-(\alpha)] + \frac{1}{2} [\psi_+(\alpha) + \phi_+(\alpha)] \quad (5.2a)$$

$$I_2 = \frac{1}{2} e^{-i\alpha 2L} [\psi_-(\alpha) - \phi_-(\alpha)] + \frac{1}{2} [\psi_+(\alpha) - \phi_+(\alpha)] \quad (5.2b)$$

It is known from the theory of the integral equations that if an integral equation  $g(y) = \int_a^b g(x) K(y,x) dx + f(y)$  has a unique solution for every  $f(y)$  then the integral equation  $g(y) = \int_a^b g(x) K(y,x) dx$  has only a trivial solution  $g \equiv 0$ . In view of this, we obtain:

For Case A:

$S_{1+}(\alpha) = 0$ ,  $D_{1+}(\alpha) = 0$  and from (4.50)  $\phi_+(\alpha) = 0$ ,  $\phi_-(-\alpha) = 0$ .

Furthermore, by substituting  $\alpha = -\alpha$  we have  $\phi_-(\alpha) = 0$ .

For Case B:

$S_{2+}(\alpha) = 0$ ,  $D_{2+}(\alpha) = 0$  and from (4.50)  $\psi_+(\alpha) = 0$ ,  $\psi_-(-\alpha) = 0$ .

Again, substituting  $\alpha = -\alpha$  we obtain  $\psi_-(\alpha) = 0$ .

$$I_1 = \begin{cases} \frac{1}{2} e^{-ia2L} \psi_-(a) + \frac{1}{2} \psi_+(a) & , \text{ Case A} \\ \frac{1}{2} e^{-ia2L} \psi_-(a) + \frac{1}{2} \psi_+(a) & , \text{ Case B} \end{cases} \quad (5.3a)$$

$$(5.3b)$$

$$I_2 = \begin{cases} I_1 & , \text{ Case A} \\ -I_1 & , \text{ Case B} \end{cases} \quad (5.4a)$$

$$(5.4b)$$

Next, inserting (5.4) into (3.32), we obtain the expression for the vector potential

$$A(x,y) = \underbrace{\frac{1}{2\pi} \int_{-ib}^{+ib} \left[ \frac{\sinh(\gamma y)}{\cosh(\gamma H)} \right] \cdot I_1 \frac{e^{-iax}}{\gamma} da}_{J_1} + \underbrace{\frac{N}{4H} \int_{-ib}^{+ib} \left[ \frac{-\cos(\frac{N\pi}{2}) \sinh(\gamma y)}{\cosh(\gamma H)} \right] \frac{\tilde{T}_N e^{-iax}}{\gamma} da}_{J_2} + \underbrace{\frac{1}{2\pi} \left[ \frac{\sin(\frac{N\pi y}{2H})}{\cos(\frac{N\pi y}{2H})} \right] \int_{-ib}^{+ib} \tilde{T}_N e^{-iax} da}_{J_3} \quad (5.5)$$

To calculate the integrals in (5.5) we complete the contours by semicircles in the proper half planes. Integrands connected with Case A have poles in  $a = \pm a'_{m-1/2}$ , and integrands connected with Case B have poles in  $a = \pm k, \pm a'_m$ .



The result:

$$A(x,y) = \begin{cases} A_N^{(A)}(x,y) & \text{Case A} \\ A_N^{(B)}(x,y) & \text{Case B} \end{cases} \quad (5.6)$$

where

$$A_N^{(A)}(x,y) = \frac{1}{2H} \sum_{n=1}^{n_2} (-1)^{n+1} \frac{\sin[(2n-1)\pi y/2H]}{\alpha_{n-1/2}'} \quad (5.7)$$

 $N=1,2,\dots$ 

$$\cdot \left[ \psi_+^{(N)}(\alpha_{n-1/2}') e^{-i\alpha_{n-1/2}' x} + \psi_-^{(N)}(-\alpha_{n-1/2}') e^{i\alpha_{n-1/2}'(x+2L)} \right] + Q_N^{(1)}(x,y) \quad (5.7)$$

$$Q_{2l}^{(1)}(x,y) = i\mu(-1)^{l+1} \frac{1}{\pi} \sum_{m=1}^{n_2} (-1)^m \frac{\sin[(2m-1)\pi y/2H] e^{i\alpha_{m-1/2}' |x+x_0|}}{\alpha_{m-1/2}' (m-1/2)^2 [1 - (\ell/(m-1/2))^2]} \quad (5.8a)$$

$$Q_{2l-1}^{(1)}(x,y) = \frac{i\mu}{2\alpha_{l-1/2}'} \sin[(2l-1)\pi y/2H] e^{i\alpha_{l-1/2}' |x+x_0|} \quad (5.8b)$$

and

$$A_N^{(B)}(x,y) = \frac{1}{4kH} \left[ \phi_+^{(N)}(k) e^{-ikx} + \phi_-^{(N)}(-k) e^{ik(x+2L)} \right] + \frac{1}{2H} \sum_{m=1}^{n_1} (-1)^m \frac{\cos((m\pi/H)y)}{\alpha_m'} \left[ \phi_+^{(N)}(\alpha_m') e^{-i\alpha_m' x} + \phi_-^{(N)}(-\alpha_m') e^{i\alpha_m'(x+2L)} \right] + Q_N^{(2)}(x,y) \quad (5.9)$$

where

$$Q_{2l}^{(2)}(x,y) = \frac{i\mu}{2\alpha_l'} \cos(l\pi \frac{y}{H}) e^{i\alpha_l' |x+x_0|} \quad (5.10a)$$

$$Q_{2l-1}^{(2)}(x,y) = i\mu(-1)^{l+1} \frac{1}{\pi} \left\{ \frac{1}{2l-1} \frac{e^{i\alpha_l' |x+x_0|}}{k} - \frac{(2l-1)}{2} \cdot \sum_{m=1}^{n_1} (-1)^m \frac{\cos(\frac{m\pi}{H}y) e^{i\alpha_m' |x+x_0|}}{m^2 [1 - ((l-1/2)/m)^2] \alpha_m'} \right\} \quad (5.10b)$$

The expressions for  $\psi_{\pm}^{(N)}(\alpha) \Big|_{\alpha = \pm \alpha'_{m-1/2}}$  and  $\phi_{\pm}^{(N)}(\alpha) \Big|_{\alpha = \pm k, \pm \alpha'_m}$  are obtained from (4.60) and (4.61) by substituting  $S_{1\pm}(k)$  and  $D_{1\pm}(k)$  from (4.63) and (4.64).

$\alpha = \pm k, \pm \alpha'_m, \pm \alpha'_{m-1/2}$  and using (4.62).

We obtain:

$$\psi_{\pm}^{(N)}(\pm \alpha'_{m-1/2}) = \psi_{\pm 1}^{(N)}(\pm \alpha'_{m-1/2}) + \psi_{\pm 2}^{(N)}(\pm \alpha'_{m-1/2}) \quad (5.11)$$

where

$$\begin{aligned} \psi_{\pm 1}^{(N)}(\pm \alpha'_{m-1/2}) = & \pm \frac{1}{2} \sqrt{\alpha'_{m-1/2} + k} M_{2+}(\alpha'_{m-1/2}) \left\{ \frac{2kT_2}{(\alpha'_{m-1/2} + k)H} \right. \\ & \cdot \left[ \frac{1}{1 - T_2} \sum_{n=1}^{n_2} \frac{e^{i\alpha'_{n-1/2} 2L} D_{2+}^{(N)}(\alpha'_{n-1/2}) M_{2+}(\alpha'_{n-1/2})}{\alpha'_{n-1/2} \sqrt{k + \alpha'_{n-1/2}}} \right. \\ & \left. \pm \frac{1}{(1 + T_2)} \sum_{n=1}^{n_2} \frac{e^{i\alpha'_{n-1/2} 2L} S_{+}^{(N)}(\alpha'_{n-1/2}) M_{2+}(\alpha'_{n-1/2})}{\alpha'_{n-1/2} \sqrt{k + \alpha'_{n-1/2}}} \right] \\ & \left. + \frac{1}{H} \sum_{n=1}^{n_2} \frac{e^{i\alpha'_{n-1/2} 2L} [D_{2+}^{(N)}(\alpha'_{n-1/2}) + S_{2+}^{(N)}(\alpha'_{n-1/2})] M_{2+}(\alpha'_{n-1/2}) \sqrt{\alpha'_{n-1/2} + k}}{\alpha'_{n-1/2} (\alpha'_{m-1/2} + \alpha'_{n-1/2})} \right\} \end{aligned} \quad (5.12)$$

$$\begin{aligned} \psi_{\pm 2}^{(2\ell)}(\pm \alpha'_{m-1/2}) = & \pm \frac{1}{\pi} \sqrt{\alpha'_{m-1/2} + k} M_{2+}(\alpha'_{m-1/2}) (-1)^{2+\ell} 2\nu \ell \\ & \ell = 1, 2, \dots \\ & \cdot \left\{ \frac{2kT_2}{(\alpha'_{m-1/2} + k)(1 - T_2^2)} \sum_{n=1}^{n_2} \frac{M_{2+}(\alpha'_{n-1/2})}{(n-1/2)^2 \alpha'_{n-1/2} [1 - (\ell/(n-1/2))^2] \sqrt{\alpha'_{n-1/2} + k}} \right. \\ & \cdot \left( \begin{bmatrix} T_2 \\ -1 \end{bmatrix} e^{i\alpha'_{n-1/2} x_0} + \begin{bmatrix} -1 \\ +T_2 \end{bmatrix} e^{i\alpha'_{n-1/2} (2L-x_0)} \right) \\ & + \sum_{n=1}^{n_2} \frac{\sqrt{\alpha'_{n-1/2} + k} M_{2+}(\alpha'_{n-1/2})}{(n-1/2)^2 [1 - (\ell/(n-1/2))^2] (\alpha'_{m-1/2} + \alpha'_{n-1/2}) \alpha'_{n-1/2}} \\ & \cdot \left( \begin{bmatrix} 1 \\ 0 \end{bmatrix} e^{i\alpha'_{n-1/2} x_0} + \begin{bmatrix} 0 \\ 1 \end{bmatrix} e^{i\alpha'_{n-1/2} (2L-x_0)} \right) \left. \right\} \end{aligned} \quad (5.13)$$

$$\psi_{\pm 2}^{(2\ell-1)} (\pm \alpha_{m-1/2}') = i\sqrt{\alpha_{m-1/2}' + k} M_{2+}(\alpha_{m-1/2}') (-1)^\ell \mu \frac{M_{2+}(\alpha_{\ell-1/2}')}{\alpha_{\ell-1/2}'} \\ \ell = 1, 2, \dots$$

$$\cdot \left\{ \frac{2kT_2}{(\alpha_{m-1/2}' + k)(1 - T_2^2)\sqrt{\alpha_{\ell-1/2}' + k}} \begin{pmatrix} T_2 \\ -1 \end{pmatrix} e^{i\alpha_{1-1/2}'x_0} \right. \\ \left. + \begin{pmatrix} -1 \\ T_2 \end{pmatrix} e^{i\alpha_{\ell-1/2}'(2L-x_0)} \right\} + \frac{\sqrt{\alpha_{\ell-1/2}' + k}}{\alpha_{m-1/2}' + \alpha_{\ell-1/2}'} \\ \cdot \left( \begin{pmatrix} 1 \\ 0 \end{pmatrix} e^{i\alpha_{\ell-1/2}'x_0} + \begin{pmatrix} 0 \\ 1 \end{pmatrix} e^{i\alpha_{\ell-1/2}'(2L-x_0)} \right) \quad (5.14)$$

$$\phi_{\pm}^{(N)} (\pm k) = \phi_{\pm 1}^{(N)} (\pm k) + \phi_{\pm 2}^{(N)} (\pm k), \quad (5.15)$$

where

$$\phi_{\pm 1}^{(N)} (\pm k) = kM_{1+}(k) \left\{ \pm T_1 \left[ \frac{1}{1 - T_1^2} \sum_{n=1}^{n_1} \frac{e^{i\alpha_n' 2L} D_{1+}^{(N)}(\alpha_n') M_{1+}(\alpha_n')}{\alpha_n'} \pm \frac{1}{1 + T_1} \right. \right. \\ \left. \cdot \sum_{n=1}^{n_1} \frac{e^{i\alpha_n' 2L} S_{1+}^{(N)}(\alpha_n') M_{1+}(\alpha_n')}{\alpha_n'} \right] - \sum_{n=1}^{n_1} \frac{e^{i\alpha_n' 2L} [S_{1+}^{(N)}(\alpha_n') \mp D_{1+}^{(N)}(\alpha_n')] M_{1+}(\alpha_n')}{\alpha_n'} \right\}, \quad (5.16)$$

$$\phi_{\pm 2}^{(2\ell)} (\pm k) = \frac{2k}{(1 - T_1^2)} (-1)^{\ell+1} \mu \frac{M_{1+}(k) M_{1+}(\alpha_{\ell}')}{\alpha_{\ell}'} \begin{pmatrix} 1 \\ -T_1 \end{pmatrix} e^{i\alpha_{\ell}'x_0} \\ \ell = 0, 1, 2, \dots \\ + \begin{pmatrix} -T_1 \\ 1 \end{pmatrix} e^{i\alpha_{\ell}'(2L-x_0)} \quad (5.17)$$

$$\phi_{\pm 2}^{(2\ell-1)} (\pm k) = \frac{2k}{(1 - T_1^2)} (-1)^\ell \mu \frac{(2\ell-1)}{\pi} M_{1+}(k) \left\{ \frac{2}{(2\ell-1)^2} \frac{M_{1+}(k)}{k} \right. \\ \ell = 1, 2, \dots \\ \cdot \left( \begin{pmatrix} 1 \\ -T_1 \end{pmatrix} \cdot e^{ikx_0} + \begin{pmatrix} -T_1 \\ 1 \end{pmatrix} \cdot e^{ik(2L-x_0)} \right) - \sum_{n=1}^{n_1} \frac{M_{1+}(\alpha_n')}{n^2 \alpha_n' [1 - ((\ell-1/2)/n)^2]} \\ \cdot \left( \begin{pmatrix} 1 \\ -T_1 \end{pmatrix} \cdot e^{i\alpha_n'x_0} + \begin{pmatrix} -T_1 \\ 1 \end{pmatrix} \cdot e^{i\alpha_n'(2L-x_0)} \right) \Big\} \quad (5.18)$$

$$\phi_{\pm}^{(N)}(\pm \alpha_m') = \phi_{\pm 1}^{(N)}(\pm \alpha_m') + \phi_{\pm 2}^{(N)}(\pm \alpha_m') \quad (5.19)$$

where

$$\begin{aligned} \phi_{\pm 1}^{(N)}(\pm \alpha_m') = & \frac{1}{2} (\alpha_m' + k) M_{1+}(\alpha_m') \left\{ \pm \frac{2kT_1}{\alpha_m' + k} \left[ \frac{1}{1 - T_1} \sum_{n=1}^{n_1} \frac{e^{i\alpha_n' 2L} D_{1+}^{(N)}(\alpha_n') M_{1+}(\alpha_n')}{\alpha_n'} \right] \right. \\ & \left. \pm \frac{1}{1 + T_1} \sum_{n=1}^{n_1} \frac{e^{i\alpha_n' 2L} S_{1+}^{(N)}(\alpha_n') M_{1+}(\alpha_n')}{\alpha_n'} \right\} \\ & - \sum_{n=1}^{n_1} \frac{e^{i\alpha_n' 2L} [S_{1+}^{(N)}(\alpha_n') \mp D_{1+}^{(N)}(\alpha_n')] M_{1+}(\alpha_n') (\alpha_n' + k)}{\alpha_n' (\alpha_m' + \alpha_n')} \quad (5.20) \end{aligned}$$

$$\begin{aligned} \phi_{\pm 2}^{(2\ell)}(\pm \alpha_m') = & (-1)^{\ell+1} \mu_H \frac{M_{1+}(\alpha_2')}{\alpha_2'} \left\{ \frac{2kT_1}{(\alpha_m' + k)(1 - T_1^2)} \begin{pmatrix} T_1 \\ -1 \end{pmatrix} e^{i\alpha_2' x_0} \right. \\ & + \begin{pmatrix} -1 \\ T_1 \end{pmatrix} e^{i\alpha_2' (2L - x_0)} \left. + \frac{\alpha_2' + k}{(\alpha_m' + \alpha_2')} \begin{pmatrix} 1 \\ 0 \end{pmatrix} e^{i\alpha_2' x_0} \right. \\ & \left. + \begin{pmatrix} 0 \\ 1 \end{pmatrix} e^{i\alpha_2' (2L - x_0)} \right\} \cdot (\alpha_m' + k) M_{1+}(\alpha_m') \quad (5.21) \end{aligned}$$

$2 = 0, 1, \dots$

$$\begin{aligned} \phi_{\pm 2}^{(2\ell-1)}(\pm \alpha_m') = & (-1)^{\ell} \mu_H \frac{(2\ell-1)}{\pi} (\alpha_m' + k) M_{1+}(\alpha_m') \left\{ \frac{2kT_1}{(\alpha_m' + k)(1 - T_1^2)} \right. \\ & \cdot \left[ \frac{2}{(2\ell-1)^2} \frac{M_{1+}(k)}{k} \begin{pmatrix} T_1 \\ -1 \end{pmatrix} e^{ikx_0} + \begin{pmatrix} -1 \\ T_1 \end{pmatrix} e^{ik(2L-x_0)} \right] \\ & \left. - \sum_{n=1}^{n_1} \frac{M_{1+}(\alpha_n')}{n^2 \alpha_n' [1 - ((\ell - 1/2)n)^2]} \begin{pmatrix} T_1 \\ -1 \end{pmatrix} e^{i\alpha_n' x_0} + \begin{pmatrix} -1 \\ T_1 \end{pmatrix} e^{i\alpha_n' (2L-x_0)} \right] \end{aligned}$$

$$\begin{aligned}
& + \frac{4}{(2l-1)^2} \frac{M_{1+}(k)}{(\alpha_m' + k)} \left( \begin{bmatrix} 1 \\ 0 \end{bmatrix} e^{ikx_0} + \begin{bmatrix} 0 \\ 1 \end{bmatrix} e^{ik(2L-x_0)} \right) \\
& - \sum_{n=1}^{n_1} \frac{(\alpha_n' + k) M_{1+}(\alpha_n')}{n^2 \alpha_n' [1 - ((l-1/2)/n)^2] (\alpha_m' + \alpha_n')} \left( \begin{bmatrix} 1 \\ 0 \end{bmatrix} e^{i\alpha_n' x_0} + \begin{bmatrix} 0 \\ 1 \end{bmatrix} e^{i\alpha_n' (2L-x_0)} \right) \Bigg\}
\end{aligned}
\tag{5.22}$$

This completes the derivation of the vector potentials. We now write them explicitly for the two different excitations, viz., Case A and Case B, and for the zero mode as Case A:

$$A_{N,0}^{(A)}(x,y) = 0 \tag{5.23}$$

Case B:

1) N-even

$$\begin{aligned}
A_{2l,0}^{(B)}(x,y) &= \frac{i\mu}{2k} e^{ik|x+x_0|} \delta_l^0 + \frac{1}{4kH} \left[ \phi_+^{(2l)}(k) e^{-ikx} + \phi_-^{(2l)}(-k) e^{ik(x+2L)} \right] \\
l &= 0, 1, 2, \dots
\end{aligned}
\tag{5.24}$$

2) N-odd

$$\begin{aligned}
A_{2l-1,0}^{(B)}(x,y) &= i\mu(-1)^{l+1} \frac{1}{\pi(2l-1)} \frac{e^{ik|x+x_0|}}{k} \\
&+ \frac{1}{4kH} \left[ \phi_+^{(2l-1)}(k) e^{-ikx} + \phi_-^{(2l-1)}(-k) e^{ik(x+2L)} \right] \\
l &= 1, 2, \dots
\end{aligned}
\tag{5.25}$$

where

$$\delta_l^0 = \begin{cases} 1 & l = 0 \\ 0 & l \neq 0 \end{cases}
\tag{5.26}$$

VI. INVESTIGATION OF THE SPECIAL CASE WHEN ONLY THE ZERO MODE  
CAN PROPAGATE IN THE GUIDE AND DERIVATION OF RESONANCE CONDITION

From (5.15) through (5.18) we have

$$A_{0,0}^{(B)}(x,y) = \frac{1u}{2k} e^{ik|x+x_0|} - \frac{1u}{2k} [M_{1+}(k)]^2 e^{ikx_0} L(T_1, x_0, x) \quad (6.1)$$

$$A_{2l,0}^{(B)}(x,y) = 0 \quad l = 1, 2, \dots \quad (6.2)$$

$$A_{2l-1,0}^{(B)}(x,y) = \frac{1u(-1)^{l+1}}{\pi(2l-1)k} e^{ik|x+x_0|} + \frac{1(-1)^l}{\pi(2l-1)k} [M_{1+}(k)]^2 e^{ikx_0} L(T_1, x_0, x) \quad l = 1, 2, \dots \quad (6.3)$$

where

$$L(T_1, x_0, x) = \frac{1}{(1-T_1^2)} \left\{ \left[ 1 - T_1 e^{ik2(L-x_0)} \right] e^{-ikx} + \left[ 1 - T_1 e^{-ik2(L-x_0)} \right] e^{ik2(L-x_0)} e^{ik(x+2L)} \right\} \quad (6.4)$$

If  $k(L - x_0) = n\pi$  where  $n = 0, \pm 1, \pm 2, \dots, \pm n_3$ ;  $n_3$  satisfies inequalities

$$n_3 \frac{\pi}{k} < L \quad (6.5)$$

$$(n_3 + 1) \frac{\pi}{k} > L$$

or

$$x_0 = L - \frac{n\pi}{k}$$

Then

$$L(T_1, x_0, x) \Big|_{x_0 = L - \frac{n\pi}{k}} = \frac{1}{(1+T_1)} \left[ e^{-ikx} + e^{ik(x+2L)} \right] \quad (6.6)$$

and the resonance condition is

$$T_1 = -1 \quad (6.7)$$

$$\text{if } 2k(L-x_0) = (2n+1)\pi$$

or

$$x_0 = L - \frac{(2n+1)\pi}{2k} \quad (6.8)$$

where  $n = 0, \pm 1, \dots, \pm n_4$ ;  $n_4$  satisfies inequalities:

$$\frac{(2n_4+1)\pi}{2k} < L \quad (6.9)$$

$$\frac{(2n_4+3)\pi}{2k} > L$$

$$\text{then } L(T, x_0, x) \Big|_{x_0 = L - \frac{(2n+1)\pi}{2k}} = \frac{1}{(1 - T_1)} \left[ e^{-ikx} - e^{ik(x+2L)} \right] \quad (6.10)$$

and the resonance condition is

$$T_1 = 1 \quad (6.11)$$

Thus, in general, the resonance conditions are given by

$$T_1 = \pm 1 \quad (6.12)$$

We can rewrite (6.12) as

$$[M_{1+}(k)]^2 e^{i2kL} \cdot f = \pm 1 \quad (6.13)$$

where

$$f = 1 + \frac{e^{-i\pi/4}}{\sqrt{\pi}} \frac{Hk}{\sqrt{kL}} \quad (6.14)$$

The expression  $M_{1+}(k)$ , as given in (4.84), can be simplified for the case when only the zero mode can propagate in the guide. For this case we have

$$M_{1+}(k) = \exp \left\{ i \frac{Hk}{\pi} \left[ 1 - C + \ln \left( \frac{2\pi}{kH} \right) + i \frac{\pi}{2} \right] + i \sum_{\ell=1}^{\infty} \left[ \frac{kH}{\ell\pi} - \arcsin \left( \frac{kH}{\ell\pi} \right) \right] \right\} \quad (6.15)$$

Let us investigate the case

$$\left( \frac{Hk}{\sqrt{\pi}} \right)^2 \lesssim \frac{1}{kL} \ll 1 \quad (6.16)$$

returning only the terms with an accuracy  $O\left[\frac{1}{kL}\right]$ . We then have

$$f = 1 + O\left(\frac{1}{kL}\right) \quad (6.17)$$

$$[M_{1+}(k)]^2 = \exp \left\{ i2 \frac{Hk}{\pi} \left[ 1 - C + \ln \left( \frac{2\pi}{kH} \right) + i \frac{\pi}{2} \right] \right\} \left[ 1 + O\left(\frac{1}{kL}\right) \right] \quad (6.18)$$

The resonance conditions for this case reduce to

$$\exp \left\{ i2 \frac{Hk}{\pi} \left[ 1 - C + \ln \left( \frac{2\pi}{kH} \right) + i \frac{\pi}{2} \right] + i2kL \right\} = \pm 1 \quad (6.19)$$



For the choice of a positive sign in the r.h.s. of (6.19) we get

$$\exp \left\{ 12 \frac{Hk}{\pi} \left[ 1 - C + \ln \left( \frac{2\pi}{kH} \right) + i \frac{\pi}{2} \right] + 12kL \right\} = +1 = \exp(12m\pi) \quad (6.20)$$

or

$$2 \frac{Hk}{\pi} \left[ 1 - C + \ln \left( \frac{2\pi}{kH} \right) + i \frac{\pi}{2} \right] + 2kL = 2m\pi \quad (6.21)$$

where  $m$  is an integer. Since (6.21) implies that  $m \gg 1$ , we can rewrite it as

$$\xi = m\pi - \frac{H\xi}{\pi L} \left[ \ln \left( \frac{\pi L}{H\xi} \right) + 1 - C + \ln 2 + i \frac{\pi}{2} \right] \quad (6.22)$$

where

$$\xi = kL \quad (6.23)$$

Solving (6.22) by the iteration method we obtain:

$$\xi_{(+)} = m\pi - \frac{Hm}{L} \ln \left( \frac{L}{Hm} \right) - \frac{Hm}{L} (1 - C + \ln 2 + i \frac{\pi}{2}) + O \left[ \frac{H^2 m}{\pi L^2} \ln^2 \left( \frac{L}{Hm} \right) \right] \quad (6.24)$$

and

$$k_{(+)} = k_{1+} + ik_{2+} \quad (6.25)$$

where

$$k_{1+} = \frac{m\pi}{L} - \frac{Hm}{L^2} \ln \left( \frac{L}{Hm} \right) - \frac{Hm}{L^2} (1 - C + \ln 2) \quad (6.26a)$$

$$k_{2+} = - \frac{Hm}{L^2} \frac{\pi}{2} \quad (6.26b)$$

In a similar manner for the choice of negative sign in (6.19) we obtain

$$\xi_{(-)} = (m + \frac{1}{2})\pi - \frac{Hm}{L} \ln \frac{L}{Hm} - \frac{Hm}{L} (1 - C + \ln 2 + i \frac{\pi}{2}) + O \left[ \frac{H}{L} \ln \left( \frac{Hm}{L} \right) \right] \quad (6.27)$$

and

$$k_{(-)} = k_{1-} + ik_{2-} \quad (6.28)$$

where

$$k_{1-} = \frac{(m+0.5)}{L} \pi - \frac{Hm}{L^2} \ln \left( \frac{L}{Hm} \right) - \frac{Hm}{L^2} (1 - C + \ln 2) \quad (6.29a)$$

$$k_2 = - \frac{Hm}{L^2} \frac{\pi}{2} \quad (6.29b)$$

## VII. INVESTIGATION OF THE GENERAL CASE WHEN MORE THAN ONE MODE CAN PROPAGATE

As a first step we show that the resonance condition is no longer given by the conventional formulas  $T_1 = \pm 1$  when more than one mode can propagate in the guide.

Let us consider the case  $T_1 = -1$ . Then from (4.67) we have

$$\sum_{n=1}^{\infty} \frac{\exp(i\alpha_n^* 2L) \eta_{1n} M_{1+}(\alpha_n^*)}{\alpha_n^*} = - [V_{1+}(k) - \tilde{S}_1(-k)] \quad (7.1)$$

where we have used

$$S_{1+}(\alpha_m^*) = \eta_{1m} + \eta_{2m}(1 + T_1) + \dots \quad (7.2)$$

Inserting (7.1) in the equation for  $\phi_+(k)$ , we obtain

$$\phi_+(k) = 0[(1 + T_1)^0] \quad (7.3)$$

It is possible to show in the same manner that

$$\phi_-(-k) = 0[(1 - T_1)^0] \quad (7.4)$$

The resonance conditions are given by

$$\text{Case A: } \left| G_{mn}^{(2)\pm} - \delta_m^n \right| = 0 \quad (7.5)$$

$$\text{Case B: } \left| G_{mn}^{(1)\pm} - \delta_m^n \right| = 0 \quad (7.6)$$

## VIII. SUMMARY OF RESULTS

In this work we have addressed ourselves to the problem of a finite-width, parallel-plate waveguide excited by a source located in the interior of the guide. Two types of sources have been investigated, viz.:

Case A:

$$\vec{J} = \hat{y} \delta(x+x_0) \sin\left(\frac{N\pi y}{2H}\right) e^{i\beta z}, \quad N = 1, 2, \dots$$

Case B:

$$\vec{J} = \hat{y} \delta(x+x_0) \cos\left(\frac{N\pi y}{2H}\right) e^{i\beta z}, \quad N = 0, 1, 2, \dots$$

We have assumed that the current has only a y-component and that  $\beta$  is real and greater than zero. Using the vector potential approach, we have reduced the original problem to that of solving the inhomogeneous wave equation (3.8) together with the boundary condition stated in (3.9). Next, two coupled equations for four unknowns ( $Y_1$ ,  $Y_2$ ,  $Z_1$  and  $Z_2$ ) have been derived where these unknowns are related to the vector potential at the extensions of the parallel plates. These equations read [same as (3.40) and (3.45)].

$$\int_{-\infty}^{2L} Y_1(\xi) K_1(k|x-\xi|) d\xi + \int_0^{\infty} Z_1(\xi) K_1(k|x-\xi|) d\xi = f_1(x)$$

where the functions  $f_1(x)$  appearing in the r.h.s are related to the prescribed source and are given in (3.43), (3.44), (3.48) and (3.49). The kernel functions  $K_1$  appearing in the integral equation may be found in (3.42) and (3.47).

Our next step was to solve the integral equations using Fourier transforms and the Wiener-Hopf technique. The results for the vector potential constructed in this manner are given in (5.6) through (5.22) for both cases considered. We have shown that there is no zero mode excited in Case A, and in Case B this mode is excited only when  $N < 2Hk/\pi$ , if  $N$  is even. For  $N$  odd, the zero mode is always excited in Case B.

An important result of the analysis presented here is the expression for the resonance condition. We have shown that this is given by

$$T = (M_{1+}(k))^2 e^{12kl} f = \pm 1$$

$$\text{where } f = 1 + e^{-1\pi/4} (\pi)^{-1/2} Hk/\sqrt{kL}$$

and  $M_{1+}(k)$  is given in (4.84).

For  $(\frac{Hk}{\sqrt{\pi}})^2 < \frac{1}{kL} \ll 1$  the function  $f$  above can be replaced by unity and

the resonance condition is correspondingly simplified. It is interesting to note that for the source located at  $x_0 = L - n\pi/k$  the resonance condition is reduced to  $T_1 = -1$  whereas for  $x_0 = L - \frac{(n+\frac{1}{2})\pi}{k}$  the same condition becomes  $T_1 = +1$ . In general both the plus sign and the minus sign are admissible for the resonance condition. Equations (6.25) and (6.29) state the resonance condition under the constraint that only the TEM mode can propagate in the infinite, parallel-plate guide. For the more general case, the condition for resonance is given by (7.5) and (7.6) and an examination of this reveals that  $T = \pm 1$  no longer represents

the resonance condition for this general case. We point out that the resonance condition is useful for solving the complex (leaky) modes in such open waveguides.

We also draw the attention of the reader to the fact that the resonance condition derived herein is in general more accurate than that given by previous workers. We show, however, in Section 6 that when the condition on the waveguide parameters as expressed by (6.16) applies, the resonance equation reduces to that obtainable by multiple reflection method applied to semi-infinite parallel-plate waveguides, a technique that has been used in the past by other workers [7,8].

## APPENDIX I

The general solution of the equation

$$\frac{\partial^2 \phi}{\partial y^2} - \gamma^2 \phi(y) = f(y) \quad (I.1)$$

is

$$\phi(y) = \mathcal{C}_1 e^{\gamma y} + \mathcal{C}_2 e^{-\gamma y} + \frac{1}{\gamma} \int_0^y f(\xi) \sinh[\gamma(y - \xi)] d\xi \quad (I.2)$$

For

$$f(\xi) = -u \begin{bmatrix} \sin\left(\frac{N\pi\xi}{2H}\right) \\ \cos\left(\frac{N\pi\xi}{2H}\right) \end{bmatrix} e^{-i\alpha x_0} \quad (I.3)$$

we have

$$\phi(y) = c_1 e^{\gamma y} + c_2 e^{-\gamma y} + \tilde{T}_N \begin{bmatrix} \sin\left(\frac{N\pi y}{2H}\right) \\ \cos\left(\frac{N\pi y}{2H}\right) \end{bmatrix} \quad (I.4)$$

where

$$\tilde{T}_N = \frac{e^{-i\alpha x_0} u}{\gamma^2 + [N\pi/(2H)]^2} \quad (I.5)$$

## APPENDIX II

Write (3.40) as

$$C_1 \gamma e^{\gamma H} - C_2 \gamma e^{-\gamma H} = I_1 - F_1 \quad (\text{II.1a})$$

$$C_1 \gamma e^{-\gamma H} - C_2 \gamma e^{\gamma H} = I_2 - F_2 \quad (\text{II.1b})$$

where

$$F_{1,2} = \tilde{T}_N \frac{N\pi}{2H} \begin{bmatrix} \cos(\frac{N\pi}{2}) \\ \mp \sin(\frac{N\pi}{2}) \end{bmatrix} \quad (\text{II.2})$$

The solution of the system equations (II.1) is

$$C_1 = \frac{1}{2\sinh(2\gamma H)\gamma} \left\{ I_1 e^{\gamma H} - I_2 e^{-\gamma H} - I_2 e^{-\gamma H} + \tilde{T}_N \frac{N\pi}{H} \begin{bmatrix} -\cos(\frac{N\pi}{2})\sinh(\gamma H) \\ \sin(\frac{N\pi}{2})\cosh(\gamma H) \end{bmatrix} \right\} \quad (\text{II.3})$$

and

$$C_2 = \frac{1}{2\sinh(2\gamma H)\gamma} \left\{ I_1 e^{-\gamma H} - I_2 e^{\gamma H} + \tilde{T}_N \frac{N\pi}{H} \begin{bmatrix} \cos(\frac{N\pi}{2})\sinh(\gamma H) \\ \sin(\frac{N\pi}{2})\cosh(\gamma H) \end{bmatrix} \right\} \quad (\text{II.4})$$



## APPENDIX III

The continuity condition of the vector potential across the boundaries  $-\infty < x < -2L$ ,  $0 < x < \infty$  for  $y = +H$  and  $y = -H$  is given by (3.44). Substituting the expressions for the vector potential for all three fields from (3.38), (3.39) and (3.43) into (3.44) and changing the order of the integrations gives

$$\begin{aligned} & \int_{-\infty}^{-2L} \psi_1 K_{1,2}^{(*)}(k|x-\xi|) d\xi + \int_0^{\infty} h_1 K_{1,2}^{(*)}(k|x-\xi|) d\xi \\ & - \int_{-\infty}^{-2L} \psi_2 K_{2,1}^{(*)}(k|x-\xi|) d\xi - \int_0^{\infty} h_2 K_{2,1}^{(*)}(k|x-\xi|) d\xi = \gamma_{1,2}(x) \end{aligned} \quad (\text{III.1})$$

where

$$K_{1,2}^{(*)}(k|x-\xi|) = \frac{1}{2\pi} \int_{-\infty+ib}^{\infty+ib} \left[ \frac{\exp(2H\gamma)}{1} \right] \frac{e^{ia(\xi-x)}}{\gamma \sinh(2H\gamma)} da \quad (\text{III.2})$$

$$\begin{aligned} \gamma_{1,2}(x) = & -\frac{N}{4H} \int_{-\infty+ib}^{\infty+ib} \left[ \frac{\pm \cos(\frac{N\pi}{2}) \tanh(\gamma H)}{\sin(\frac{N\pi}{2}) \coth(\gamma H)} \right] \frac{\tilde{T}_N e^{-iax}}{\gamma} da \\ & - \frac{1}{2\pi} \left[ \frac{\pm \sin(\frac{N\pi}{2})}{\cos(\frac{N\pi}{2})} \right] \int_{-\infty+ib}^{\infty+ib} \tilde{T}_N e^{-iax} da \end{aligned} \quad (\text{III.3})$$

## APPENDIX IV

We are interested in calculating the integrals:

$$I = \frac{1}{2\pi i} \int_{1d-\infty}^{1d+\infty} \left[ \frac{S_{1+}(\zeta)}{D_{1+}(\zeta)} \right] \frac{e^{i\zeta 2L} d\zeta}{(\zeta - k) M_{1-}(\zeta) (\zeta + \alpha)}$$

Multiplying the numerator and denominator by  $M_{1+}(\zeta)$ , we obtain

$$= \frac{1}{2\pi i} \int_{1d-\infty}^{1d+\infty} \left[ \frac{S_{1+}(\zeta)}{D_{1+}(\zeta)} \right] \frac{e^{i\zeta 2L} e^{\gamma H} M_{1+}(\zeta)}{(\zeta - k) (\zeta + \alpha) \sinh(\gamma H) \gamma H} d\zeta \quad (IV.1)$$

We have branch cuts from  $k$  to  $\text{Re} k + i\infty$  and from  $-k$  to  $-\text{Re} k - i\infty$ .

Closing the contour with a semicircle in the upper half and using the theory of residues, we get.

$$\frac{1}{2\pi i} \int_C \left[ \frac{S_{1+}(\zeta)}{D_{1+}(\zeta)} \right] \frac{e^{i\zeta 2L} e^{\gamma H} M_{1+}(\zeta) d\zeta}{(\zeta - k) (\zeta + \alpha) \sinh(\gamma H) \gamma H} = \sum_{n=1}^{n_1} \left[ \frac{S_{1+}(\alpha_n^-)}{D_{1+}(\alpha_n^-)} \right] \frac{e^{i\alpha_n^- 2L} M_{1+}(\alpha_n^-) (\alpha_n^- + k)}{\alpha_n^- (\alpha + \alpha_n^-)} \quad (IV.2)$$

where

$$\int_C = \int_{C_1} + \int_{C_2} + \int_{C_3} + \int_{C_T} + \int_{C_R} \quad (IV.3)$$

It can be shown that  $\int_{C_R} \rightarrow 0$ , when  $R \rightarrow \infty$ . Calculating  $\int_{C_T}$  when  $\tau \rightarrow 0$  gives

$$\frac{1}{2\pi i} \int_{C_T} = - \left[ \frac{S_{1+}(k)}{D_{1+}(k)} \right] \frac{e^{ik2L} M_{1+}(k)}{\alpha + k} \quad (IV.4)$$

$\tau \rightarrow 0$

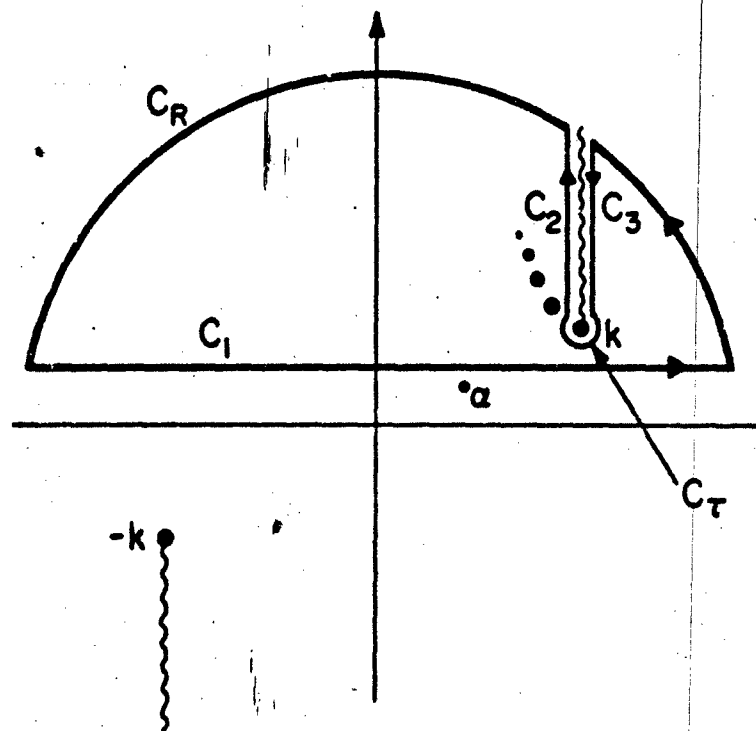


Fig. 3

Contour for integration of the integral  
I in (IV.1)

For  $\int_{c_2} + \int_{c_3}$ , taking note of the fact that  $\sqrt{\zeta^2 - k^2}$  has the + sign on the right-hand side and the - sign on the left-hand side of the cut, respectively, we get

$$\frac{1}{2\pi i} \left[ \int_{c_2} + \int_{c_3} \right] = \frac{H}{\pi i} \int_{\text{Re } k + i\infty}^k \left[ \frac{S_{1+}(\zeta)}{D_{1+}(\zeta)} \right] \frac{e^{i\zeta 2L} M_{1+}(\zeta) \sqrt{\zeta + k}}{\sqrt{\zeta - k} (\zeta + \alpha)} d\zeta \quad (\text{IV.5})$$

To calculate the integral in the r.h.s. of (IV.5) for large guide width, i.e.,  $k2L \gg 1$  we note that the integrand decreases exponentially along the path of integration from  $k$  to  $k + i\infty$ . This allows us to expand

$$\left[ \frac{S_{1+}(\zeta)}{D_{1+}(\zeta)} \right] M_{1+}(\zeta) \sqrt{\zeta + k}$$

in a Taylor's series and retain only the first term for asymptotic evaluation.

This gives the r.h.s. of (IV.5) = I

$$= \frac{H}{\pi i} \left[ \frac{S_{1+}(k)}{D_{1+}(k)} \right] M_{1+}(k) \sqrt{2k} \int_{\text{Re } k + i\infty}^k \frac{e^{i\zeta 2L}}{(\zeta + \alpha) \sqrt{\zeta - k}} d\zeta$$

Introducing a new variable  $u$

$$(\zeta - k)2L = iu, \quad \sqrt{\zeta - k} = \sqrt{\frac{u}{2L}} e^{i\frac{\pi}{4}}$$

$$\zeta 2L = iu + 2kL, \quad d\zeta = \frac{1}{2L} du$$

we obtain

$$I = -\frac{H}{\pi i} \left[ \frac{S_{1+}(k)}{D_{1+}(k)} \right] M_{1+}(k) \sqrt{2k} \sqrt{2L} e^{-i\frac{\pi}{4}} e^{ik2L} W_{-1}[-i2L(\alpha + k)] \quad (\text{IV.6})$$

where

$$W_{-1}[-12L(\alpha + k)] = \int_0^{\infty} \frac{e^{-u}}{\sqrt{u}[u - 12L(\alpha + k)]} du \quad (IV.7)$$

From (IV.2) through (IV.6) we get

$$\begin{aligned} I = & \left[ \frac{S_{1+}(k)}{D_{1+}(k)} \right] \frac{e^{ik2L} M_{1+}(k)}{\alpha + k} \\ & \cdot \left\{ 1 + \frac{H}{\pi} e^{-i\frac{3}{4}\pi} \sqrt{2k} \sqrt{2L} (\alpha + k) W_{-1}[-12L(\alpha + k)] \right\} \\ & + \sum_{n=1}^{n_1} \left[ \frac{S_{1+}(\alpha'_n)}{D_{1+}(\alpha'_n)} \right] \frac{e^{i\alpha'_n 2L} M_{1+}(\alpha'_n)}{\alpha'_n (\alpha + \alpha'_n)} \quad (IV.8) \end{aligned}$$

Note that in (IV.8) we have neglected the exponentially decreasing terms in the summation.

In the same manner we can show:

$$\begin{aligned} & \frac{1}{2\pi i} \int_{id-\infty}^{id+\infty} \left[ \frac{S_{2+}(\zeta)}{D_{2+}(\zeta)} \right] \frac{e^{i\zeta 2L}}{\sqrt{\zeta - k}(\zeta + \alpha) M_{2-}(\zeta)} d\zeta \\ & = \frac{1}{\pi} e^{-i\frac{3}{4}\pi} \sqrt{2L} W_{-1}[-2L(\alpha + k)] e^{ik2L} M_{2+}(k) \left[ \frac{S_{2+}(k)}{D_{2+}(k)} \right] \\ & + \frac{1}{H} \sum_{n=1}^{n_2} \left[ \frac{S_{2+}(\alpha'_{n-1/2})}{D_{2+}(\alpha'_{n-1/2})} \right] \frac{e^{i\alpha'_{n-1/2} 2L} M_{2+}(\alpha'_{n-1/2}) \sqrt{\alpha'_{n-1/2} + k}}{\alpha'_{n-1/2} (\alpha + \alpha'_{n-1/2})} \quad (IV.9) \end{aligned}$$

## APPENDIX V

In this appendix we discuss the problem of deriving the systems of the equations that are satisfied by the constants  $S_{1+}(\alpha'_n)$ ,  $D_{1+}(\alpha'_n)$ ,  $S_{2+}(\alpha'_{n-1/2})$ ,  $D_{2+}(\alpha'_{n-1/2})$ . We present only the calculations for  $S_{1+}(\alpha'_n)$  and  $D_{1+}(\alpha'_n)$  because the same procedure can be followed to solve for the other constants.

After substituting  $\alpha = \alpha'_m$  into (4.55), and using the expression (4.63) together with the asymptotic form of the function  $W_{-1}[-2L(\alpha + k)]$ , we have

$$\sum_{n=1}^{n_1} S_{1+}(\alpha'_n) \left[ G_{mn}^{(1)} - \delta_m^n \right] = P_m^{(1)\pm} \quad m = 1, 2, \dots \quad (V.1)$$

where

$$G_{mn}^{(1)} = \frac{e^{i\alpha'^2 2L} M_{1+}(\alpha'_m) M_{1+}(\alpha'_n)}{\alpha'_n} \left[ \frac{2kT_1}{1 \pm T_1} + \frac{(\alpha'_m + k)(\alpha'_n + k)}{\alpha'_m + \alpha'_n} \right]. \quad (V.2)$$

$$P_m^{(1)\pm} = \pm M_{1+}(\alpha'_m) \left\{ \frac{2kT_1}{1 \pm T_1} [V_{1+}(k) \mp \tilde{S}_{1-}(-k)] \mp (\alpha'_m + k) [V_{1+}(\alpha'_m) \mp S_{1-}(-\alpha'_m)] \right\}. \quad (V.3)$$

To calculate the constants  $V_{1+}(\alpha)|_{\alpha=k, \alpha'_m}$  and  $\tilde{S}_{1-}(-\alpha)|_{\alpha=k, \alpha'_m}$ , we insert the expressions for  $H_{1\pm}(\zeta)$  from (4.13) into (4.39), (4.48) and substitute  $\alpha = k$  and  $\alpha = \alpha'_m$ . This yields certain integrals which we can calculate using the theory of residues. We are interested in examining two cases a) N-even; b) N-odd. Substituting results into (V.3) we obtain the expressions for  $P_m^{(1)\pm}$ . In the same manner we have obtained results for Case A.

REFERENCES

1. C. E. Baum, "General Principles for the Design of ATLAS I and II, Part V: Some Approximate Figures of Merit for Comparing the Waveforms Launched by Imperfect Pulser Arrays onto TEM Transmission Lines." Sensor and Simulation Note 148, May 1972.
2. C. E. Baum, "Impedance and Field Distributions for Parallel Plate Transmission Line Simulators," Sensor and Simulation Note 21, June 1966.
3. T. L. Brown and K. D. Granzone, "A Parameter Study of Two-Parallel-Plate Transmission Line Simulators of EMP Sensor and Simulation Note 21." Sensor and Simulation Note 52 April 1968.
4. C. E. Baum, D. V. Giri, and R. D. Gonzalez, "Electromagnetics Field Distribution of the TEM Mode in a Symmetrical Two-Parallel-Plate Transmission Line," Sensor and Simulation Note 219, April 1976.
5. L. Marin, "Modes on a Finite-Width, Parallel-Plate Simulator. I. Narrow Plates," Sensor and Simulation Note 201, September 1974.
6. L. Marin, "Modes on a Finite Width, Parallel-Plate Simulator. II. Wide Plates," Sensor and Simulation Note 223, March 1977 (revised November 1977).
7. R. Mittra and T. Itoh, "Analysis of Modes in a Finite-Width Parallel-Plate Waveguide," Sensor and Simulation Note 208, January 1975.
8. Ali M. A. Rushdi, R. Menendez and R. Mittra, "A Study of The Leaky Modes in a Finite-Width Parallel-Plate Waveguide", Sensor and Simulation Note 241, July 1977.
9. R. E. Collin, "Field Theory of Guide Waves," McGraw-Hill, New York, 1960.
10. R. Mittra and S. W. Lee, "Analytical Techniques in the Theory of Guided Waves," Macmillan, New York, 1971.
11. B. Noble, "Methods Based on the Wiener-Hopf Technique", Pergamon Press, New York, 1958.

SOURCE EXCITATION OF AN OPEN,  
PARALLEL-PLATE WAVEGUIDE, NUMERICAL RESULTS

ABSTRACT

In this work we investigate numerically the problem of the source excitation of an open, parallel-plate waveguide. The following assumptions are made for the source current 1) the current is oriented in the y-direction, 2) it is located at  $x = 0$ , 3) there is no variation in the y-direction, 4) and the current has  $\exp(i\beta z)$  behavior along the longitudinal z-direction. We provide graphical output for the EM-field components as functions of a longitudinal propagation constant and transverse coordinates and then discuss these results.

Acknowledgement

The author is thankful to Professor R. Mittra for discussion of the problem and for the helpful suggestions during the course of this work. The financial support of AFOSR Grant 76-3066B is gratefully acknowledged.



## I. INTRODUCTION

In the previous report [1], we derived analytical expressions for the source excitation of an open parallel-plate waveguide. However, these formulas were very complicated, and it became necessary to evaluate them numerically. The purpose of this report is to present the numerical results. The computer program contained in Appendix A was written and used to obtain the field distribution as a function of the longitudinal propagation constant and the transverse coordinates. The numerical outputs are presented in graphical forms. The Cyber 175 at the University of Illinois was used for all of the numerical studies.

The organization of the report is as follows: Section II contains a statement of the problem and the basic formulation. Section III presents the real and imaginary parts and the amplitude of the component field distribution as functions of several parameters in graphical form and a detailed discussion of the numerical results. Finally, Section IV is the conclusion.

## II. STATEMENT OF THE PROBLEM AND BASIC FORMULATION

In this section the fields due to a vertical current located inside an open, finite waveguide are investigated. The geometry of the problem considered is shown in Figure 1. This structure consists of two perfectly conducting plates with separation  $2H$  located in a homogeneous and isotropic medium. A Cartesian coordinate system with its  $y$ -axis normal to the plates is erected. Both plates are infinite in the  $z$ -direction and finite in the  $x$ -direction with length  $2L$  as shown in Figure 1. All figures appear at the end of Chapter II. The current is oriented in the  $y$ -direction and is defined as

$$J = \hat{y} \delta(x) \exp(i\beta z) , \quad (1)$$

where  $\beta$  is the propagation constant in the  $z$ -direction, and  $\delta(x)$  is the delta function. In [1] using the vector-potential approach and the Wiener-Hopf technique, we obtained a solution for the problem at hand in a general form for any parameters with one restriction:  $kL$  must be much greater than 1, i.e.,

$$kL \gg 1 , \quad (2)$$

where

$$k = \sqrt{\omega^2 \epsilon \mu - \beta^2} \quad (3)$$

and  $\epsilon$ ,  $\mu$  are the homogeneous media parameters. Using the solution which was obtained in [1], we will perform a numerical calculation for the case:

$$W = \frac{H}{L} = 0.16670 , \quad (4)$$

$$\frac{L}{\lambda_0} = 5 , \quad (5)$$

where

$$\lambda_0 = \frac{2\pi}{\omega \sqrt{\epsilon \mu}} \quad (6)$$

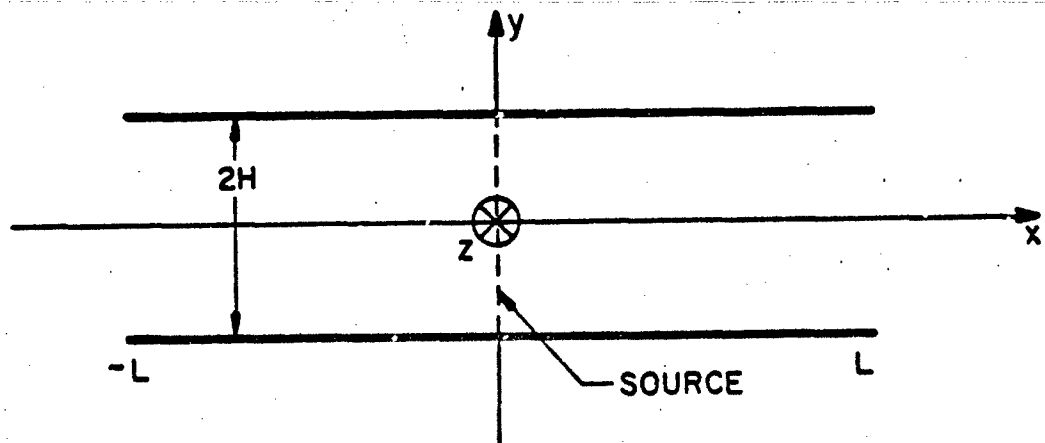


Figure 1. Geometry of the problem of source excitation of a parallel-plate waveguide.

is the free-space wave length. Because of the limitations of Equations (2), (3), and (5) we calculated numerical results for

$$0 < \tilde{\beta} < 0.93 \quad , \quad (7)$$

where  $\tilde{\beta}$  is the normalized propagation constant  $\tilde{\beta} = \frac{\beta}{\omega\sqrt{\epsilon\mu}}$ . It can be

readily proved from Equations (3), (4), and (5) that if  $\tilde{\beta}$  is in the region  $[\tilde{\beta}_0, 0.93]$ , where

$$\tilde{\beta}_0 = 0.80008997 \quad , \quad (8)$$

then only the first mode can propagate in the x-direction; therefore, the electromagnetic field has only three components  $[E_y, H_x, H_z]$ . When  $\tilde{\beta}$  intersects the point  $\tilde{\beta}_0$  and goes to zero, the second mode begins to propagate, and the EM-field consists of five components  $[E_x, E_y, E_z, H_x, H_z]$ . Rewriting the field solution from [1] for the case, when no more than two modes can propagate, we arrive at the EM field:

$$\vec{E}'(x,y,z) = \vec{E}(x,y) \cdot \exp(i\beta z) \quad (9)$$

$$\vec{H}'(x,y,z) = \vec{H}(x,y) \cdot \exp(i\beta z) \quad (10)$$

$$\vec{E}(x,y) = \hat{x}E_x + \hat{y}E_y + \hat{z}E_z \quad (11)$$

$$\vec{H}(x,y) = \hat{x}H_x + \hat{z}H_z \quad (12)$$

$$E_y = \sqrt{\frac{\mu}{\epsilon}} \cdot \frac{0.1 \cdot \theta}{w} \cdot F_2 \sin\left(\frac{\pi y}{H}\right) \sin\left(\theta \cdot \frac{x}{L}\right) \quad (13)$$

$$E_y = \sqrt{\frac{\mu}{\epsilon}} \cdot 10\pi \left[ F_1 \cos\left(a \cdot \frac{x}{L}\right) + \left(1 - \frac{0.01}{w^2}\right) \cdot F_2 \cos\left(\frac{\pi y}{H}\right) \cos\left(\theta \cdot \frac{x}{L}\right) - \frac{1}{2a} \exp\left(-a \left|\frac{x}{L}\right|\right) \right] \quad (14)$$

$$E_z = -1 \sqrt{\frac{\mu}{\epsilon}} \cdot \frac{\beta}{\omega\sqrt{\epsilon\mu}} \cdot \frac{\pi}{w} F_2 \sin\left(\frac{\pi y}{H}\right) \cos\left(\theta \cdot \frac{x}{L}\right) \quad , \quad (15)$$

$$H_x = -u \frac{\beta}{\omega \sqrt{\epsilon \mu}} \cdot 10\pi \left\{ F_1 \cos \left( a \frac{x}{L} \right) + F_2 \cos \left( \pi \cdot \frac{y}{H} \right) \cdot \cos \left( \theta \cdot \frac{x}{L} \right) - \frac{1}{2a} \exp \left( ia \left| \frac{x}{L} \right| \right) \right\}, \quad (16)$$

$$H_z = i\mu a f_1 \sin \left( a \frac{x}{L} \right) + i\theta F_2 \cos \left( \pi \frac{y}{H} \right) \sin \left( \theta \cdot \frac{x}{L} \right) - 0.5 \cdot \exp \left( ia \left| \frac{x}{L} \right| \right) \cdot \frac{x}{L}, \quad (17)$$

where

$$F_1 = \frac{[M_{1+}(k)]^2 \exp(12a)}{(1 + T_1)a} \cdot \left\{ 1 + \frac{2b[M_{1+}(\alpha_1)]^2 \exp(12\frac{a}{b}\alpha_1)}{\theta} \right\}, \quad (18)$$

$$F_2 = \frac{2bM_{1+}(k)M_{1+}(\alpha_1) \exp \left[ ia \left( 1 + \frac{\alpha_1}{b} \right) \right]}{a \cdot Q}, \quad (19)$$

$$Q = (1 + T_1)\alpha_1 \cdot \left\{ \frac{[M_{1+}(\alpha_1)]^2 \exp(12\frac{a}{b}\alpha_1)}{2\alpha_1} \left[ \frac{4T_1b}{1 + T_1} - \frac{(\alpha_1 + b)^2}{\alpha_1} \right] - 1 \right\}, \quad (20)$$

$$M_{1+}(k) = (\alpha_1 + b) \cdot \exp \left\{ i \left[ b(2-C + \ln(\frac{2}{b})) + i\frac{\pi}{2} \right] - \frac{\pi}{2} + \sum_{n=2}^{\infty} \left( \frac{b}{n} - \arcsin \frac{b}{n} \right) \right\}, \quad (21)$$

$$M_{1+}(\alpha_1) = \sqrt{2} \cdot \alpha_1 \cdot \frac{1 - i\alpha_1}{b} \exp \left\{ i \left[ \alpha_1(2-C + \ln(\frac{2}{b})) + i\frac{\pi}{2} \right] + \sum_{n=2}^{\infty} \left( \frac{\alpha_1}{n} - \arcsin \frac{\alpha_1}{\sqrt{n^2 - 1}} \right) \right\}, \quad (22)$$

$$\alpha_1 = \sqrt{b^2 - 1}, \quad (23)$$

$$a = kL = 10\pi \sqrt{1 - \left| \frac{\beta}{\omega \sqrt{\epsilon \mu}} \right|^2}, \quad (24)$$

$$b = a \cdot \frac{W}{\pi}, \quad (25)$$

$$\theta = \frac{\pi \alpha_1}{W}, \quad (26)$$

$$T_1 = [M_{1+}(k)]^2 \exp(i2a) \left[ 1 + \frac{b\sqrt{\pi}}{\sqrt{a}} \exp\left(-1 \frac{\pi}{4}\right) \right] \quad (27)$$

It should be mentioned that we investigated the lossless medium case; therefore, in the region  $\tilde{\beta}_0 < \tilde{\beta} < 0.93$ , the propagation constant for the second mode has only an imaginary part. Because we neglect terms which decrease exponentially, our results for the above mentioned region of  $\tilde{\beta}$  reduce to:

$$1) E_x = E_z = 0 \quad \text{and}$$

$$2) \text{ more simple expressions for the other three components of the field.}$$

We apply numerical analysis only over the regions  $0 \leq y < H$ ,  $0 < x < L$ .

For the remainder of the waveguide, one can obtain results using the correlations:

$$\begin{aligned} E_x(x,y) &= -E_x(-x,y) ; E_x(x,y) = -E_x(x,-y) \\ E_y(x,y) &= E_y(-x,y) ; E_y(x,y) = E_y(x,-y) \\ E_z(x,y) &= E_z(-x,y) ; E_z(x,y) = -E_z(x,-y) \\ H_x(x,y) &= H_x(-x,y) ; H_x(x,y) = H_x(x,-y) \\ H_z(x,y) &= -H_z(-x,y) ; H_z(x,y) = H_z(x,-y) \end{aligned} \quad (28)$$

It is interesting to note that  $E_x$ ,  $H_z$  are continuous and that  $E_y$ ,  $E_z$ ,  $H_x$  are discontinuous when  $\tilde{\beta}$  crosses  $\tilde{\beta}_0$  (or more exactly: they are exponentially decreasing). It is also of interest to determine the character of the behavior of the x-component of Poynting's vector. As one can easily see from the previous expressions for the EM fields, the x-component of Poynting's vector for the second mode is proportional to  $\alpha_1$  and goes to zero when  $\tilde{\beta} \rightarrow \tilde{\beta}_0$ . From this, one finds that the energy flow in the x-direction is continuous when  $\tilde{\beta}$  intersects the point  $\tilde{\beta}_0$ .

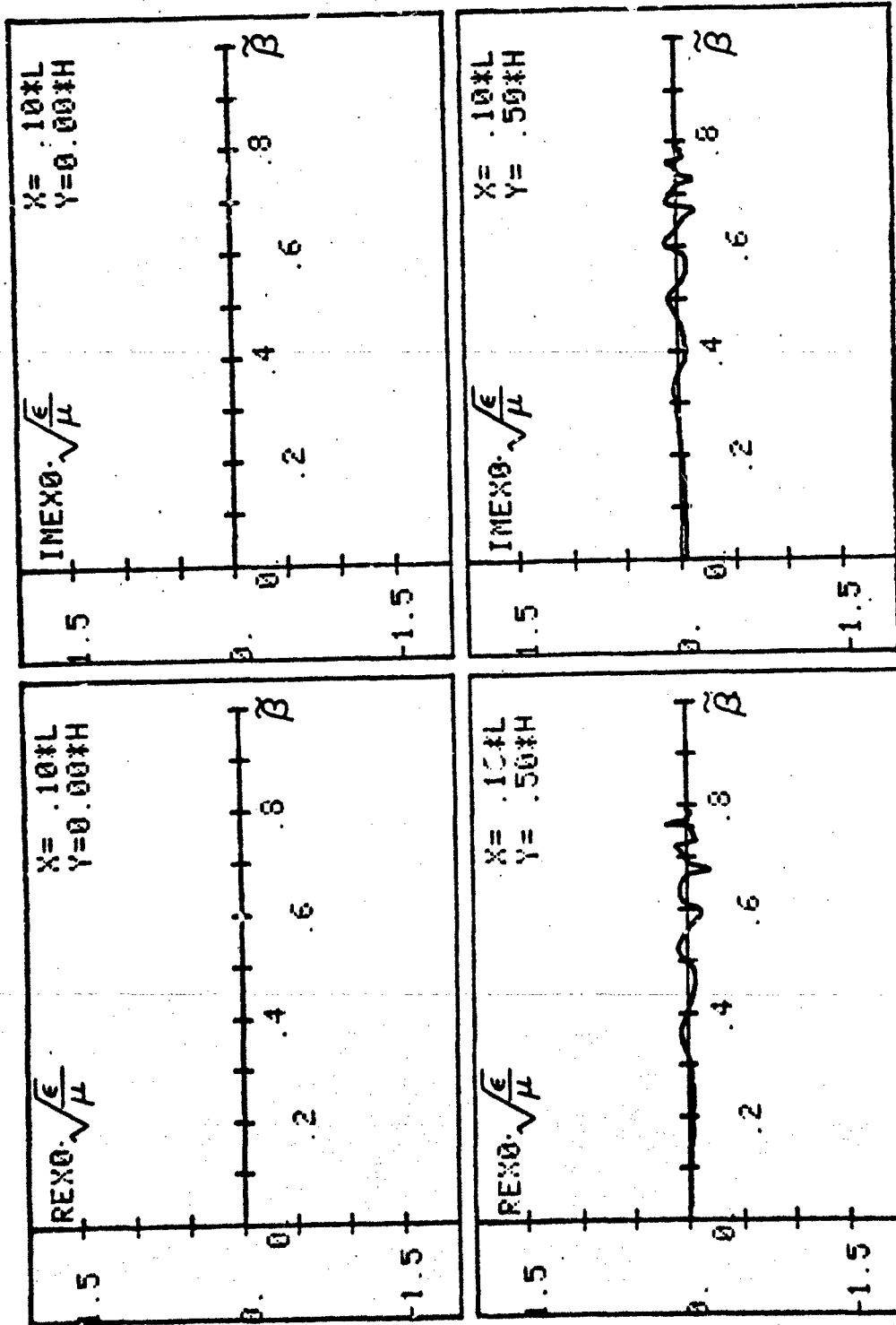


Figure 2. The real and imaginary parts of the electric field asymptotic functions of a longitudinal propagation constant for points of view:  $L = 0.0$ ,  $0.1$ ;  $H = 0.0$ ,  $0.5$ .

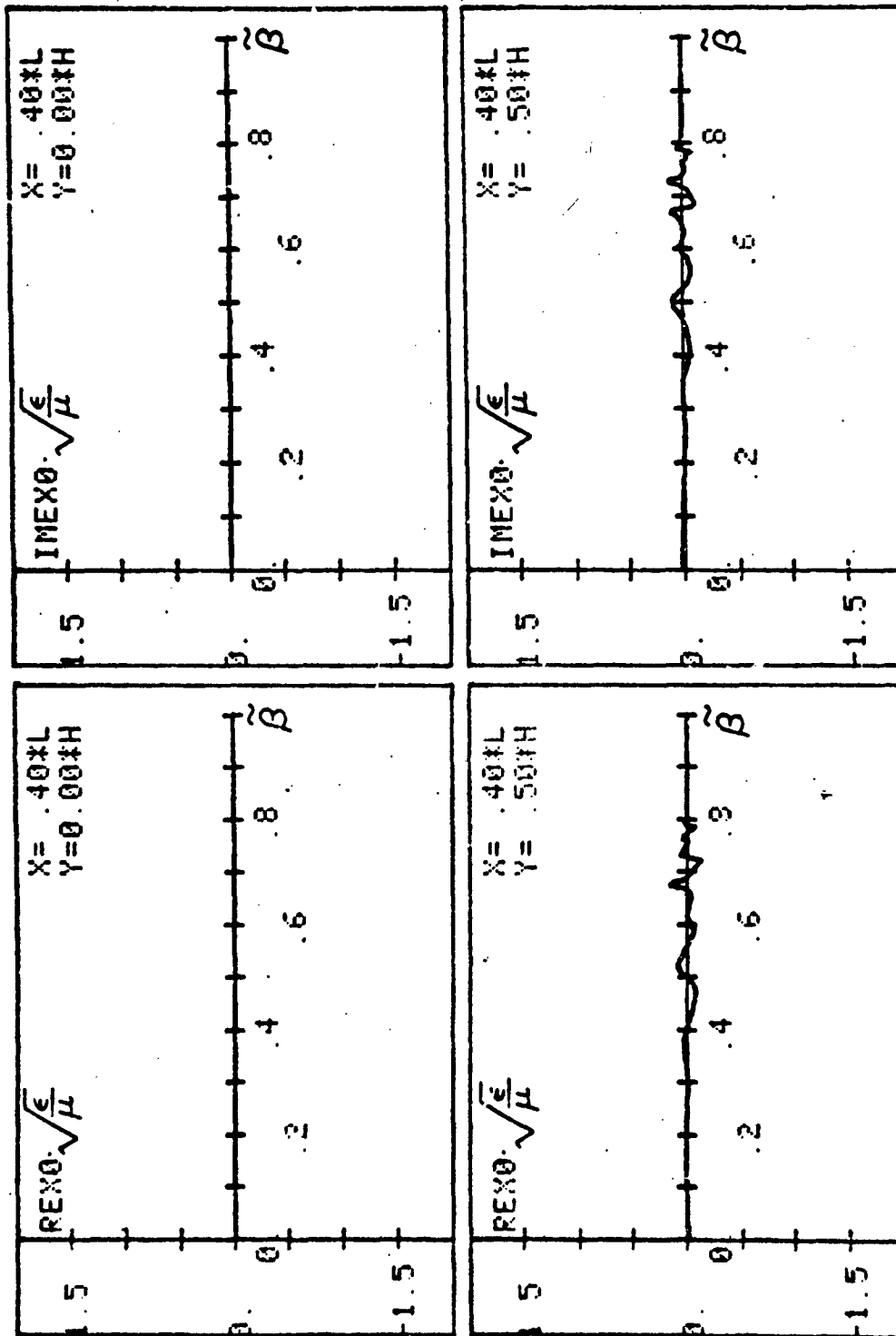


Figure 3. The real and imaginary parts of the electric field as functions of a longitudinal propagation constant for points of view:  $\frac{L}{H} = 0.0, 0.4, 0.5$ .



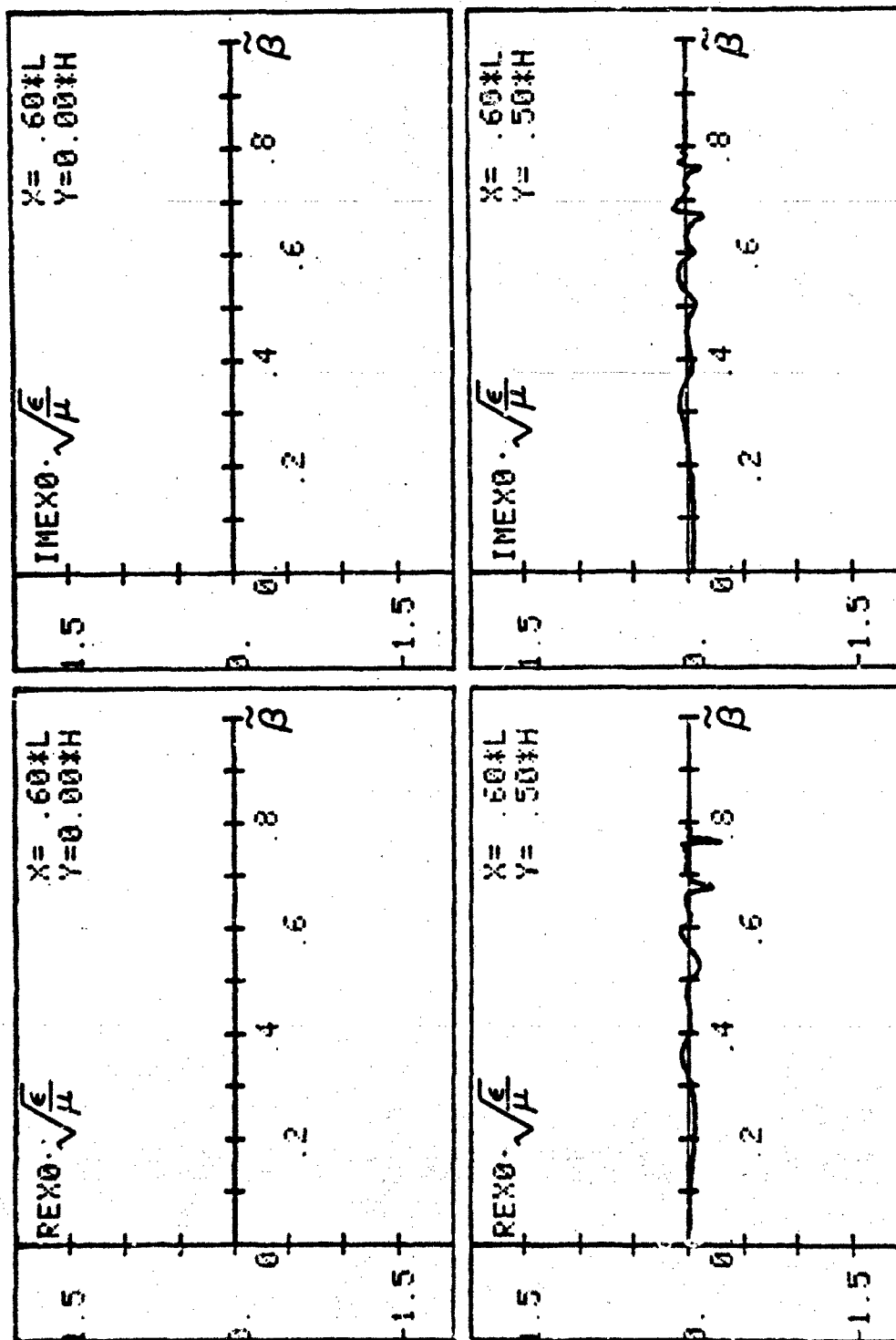


Figure 4. The real and imaginary parts of the electric field as functions of a longitudinal propagation constant for points of view:  $\frac{x}{L} = 0.0, 0.5, 0.6$ ;  $\frac{y}{H} = 0.0, 0.5$ .

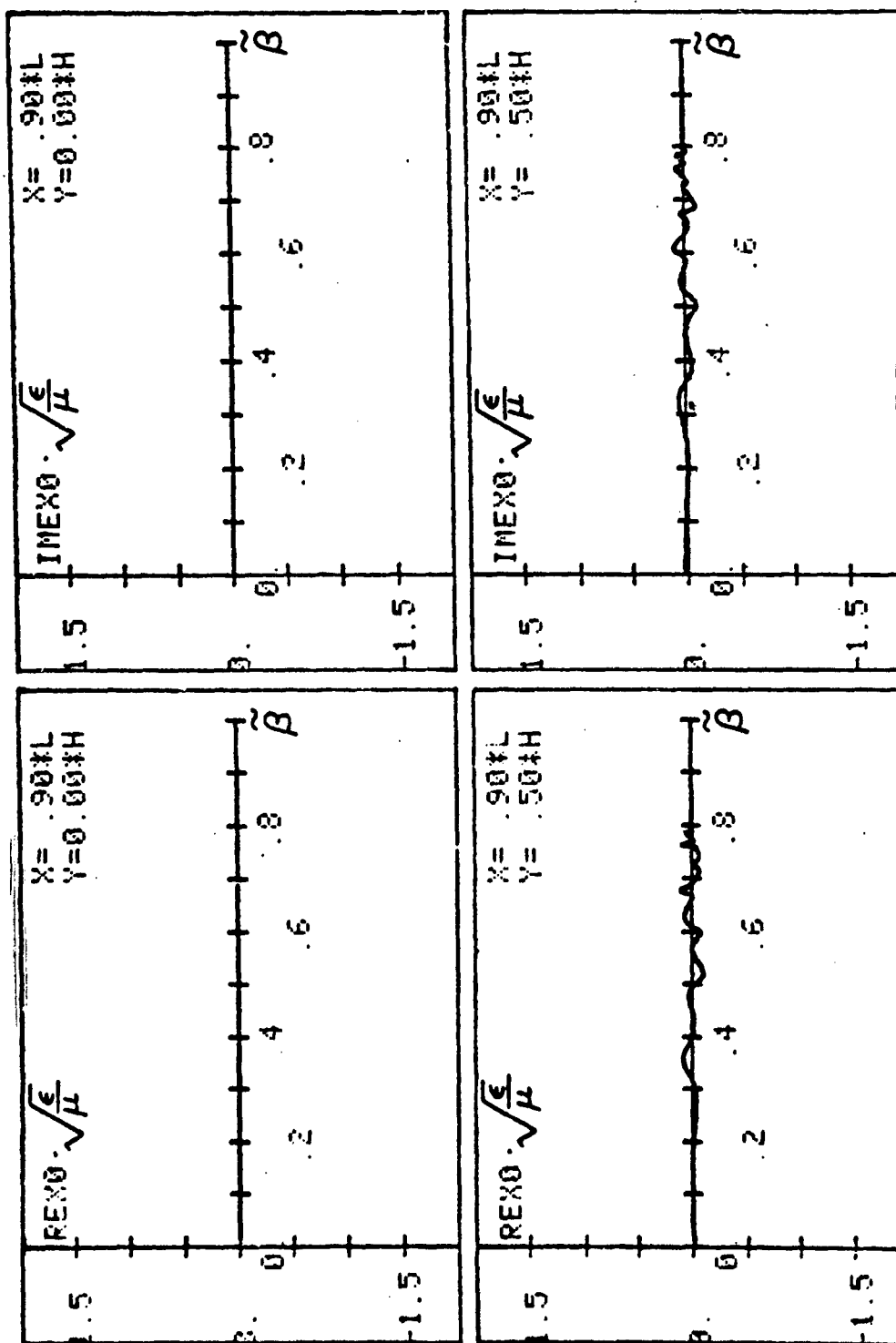


Figure 5. The real and imaginary parts of the electric field as functions of a longitudinal propagation constant for points of view:  $\frac{L}{H} = 0.9, 0.5, 0.0, 0.5$ .

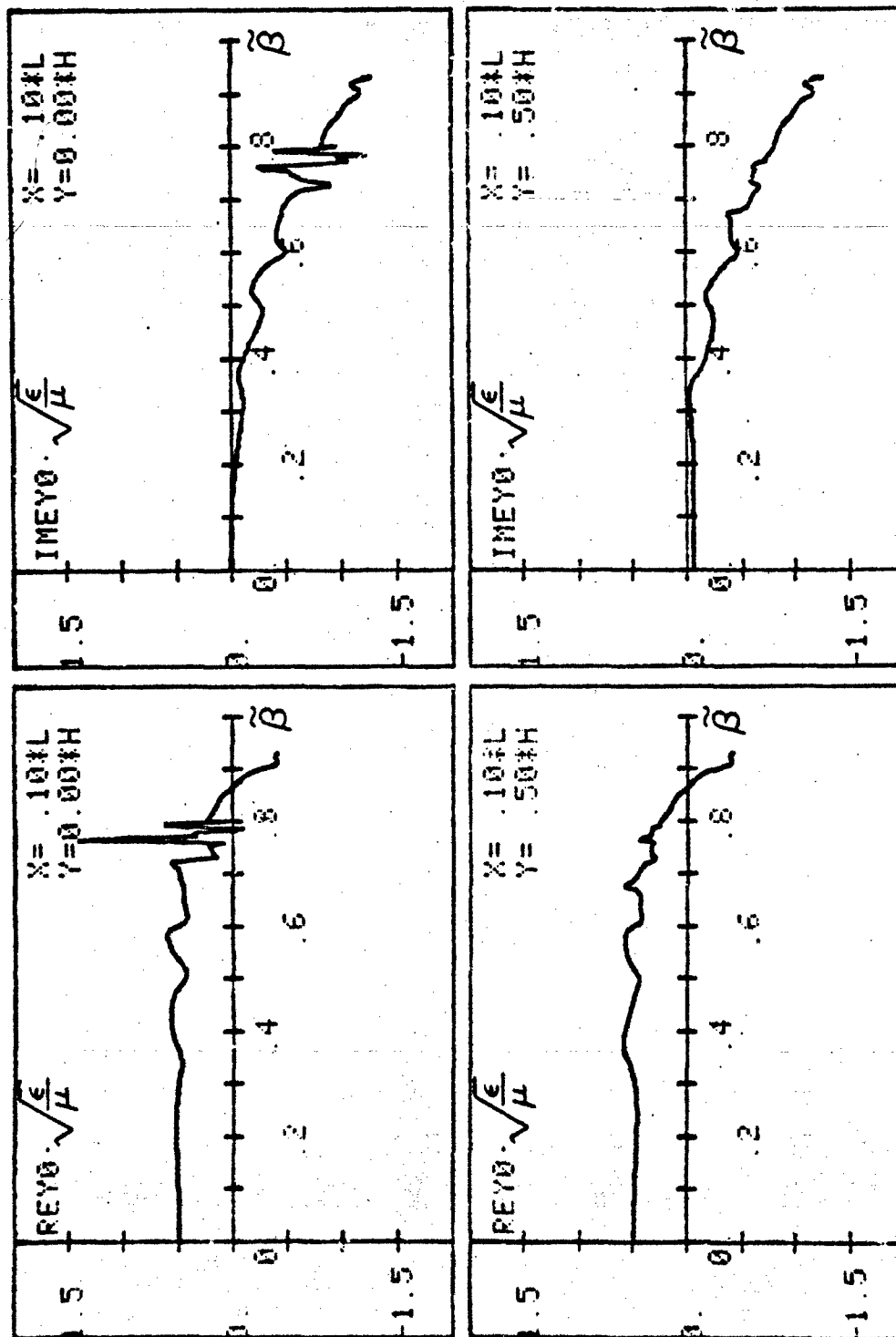


Figure 6. The real and imaginary parts of a y-component of the electric field as functions of a longitudinal propagation constant for points of view:  $\frac{L}{H} = 0.1, 0.5$ .

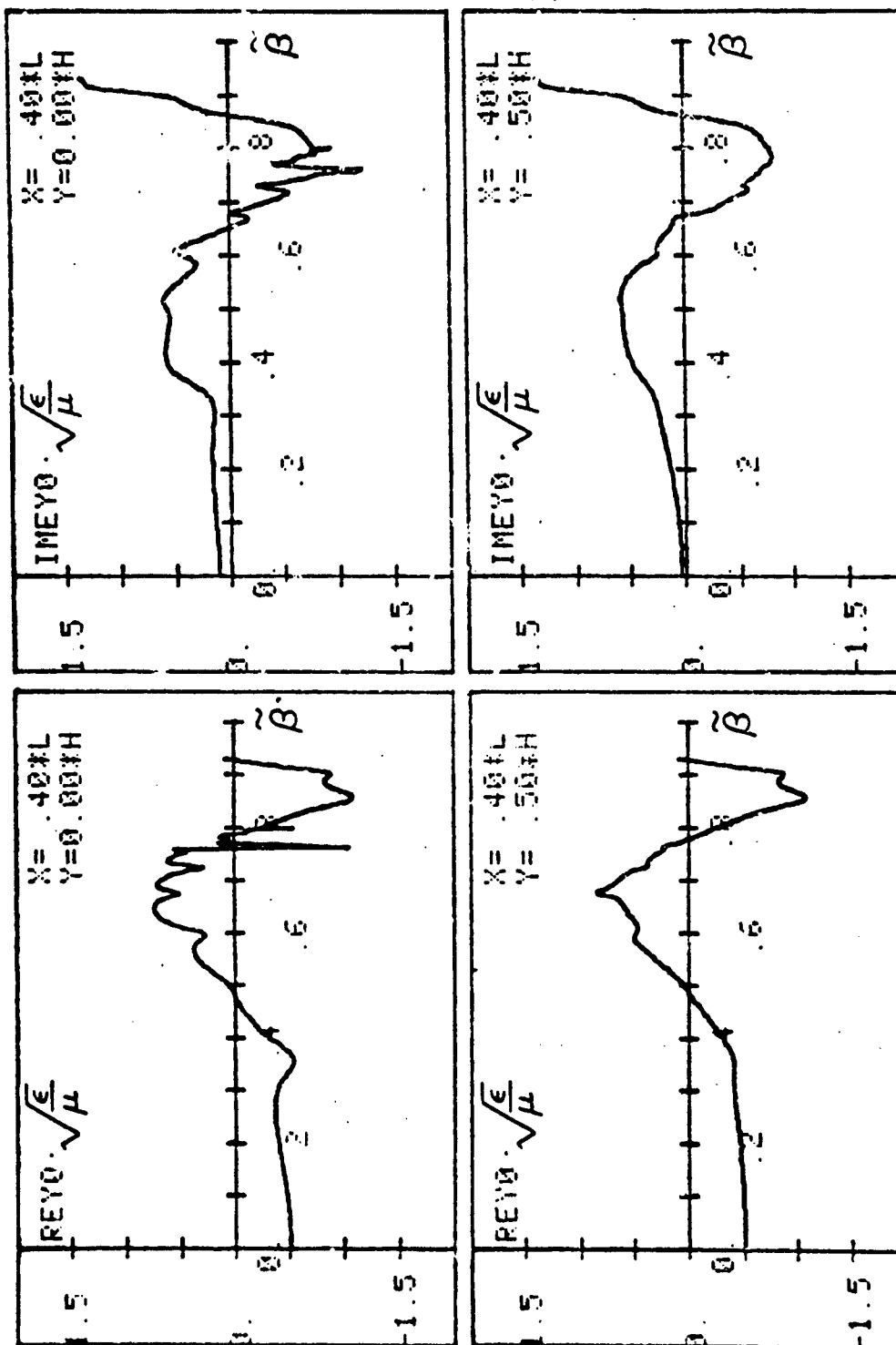


Figure 7. The real and imaginary parts of the electric field as functions of a longitudinal propagation constant for points of view:  $\frac{X}{L} = 0.0, 0.5$ .

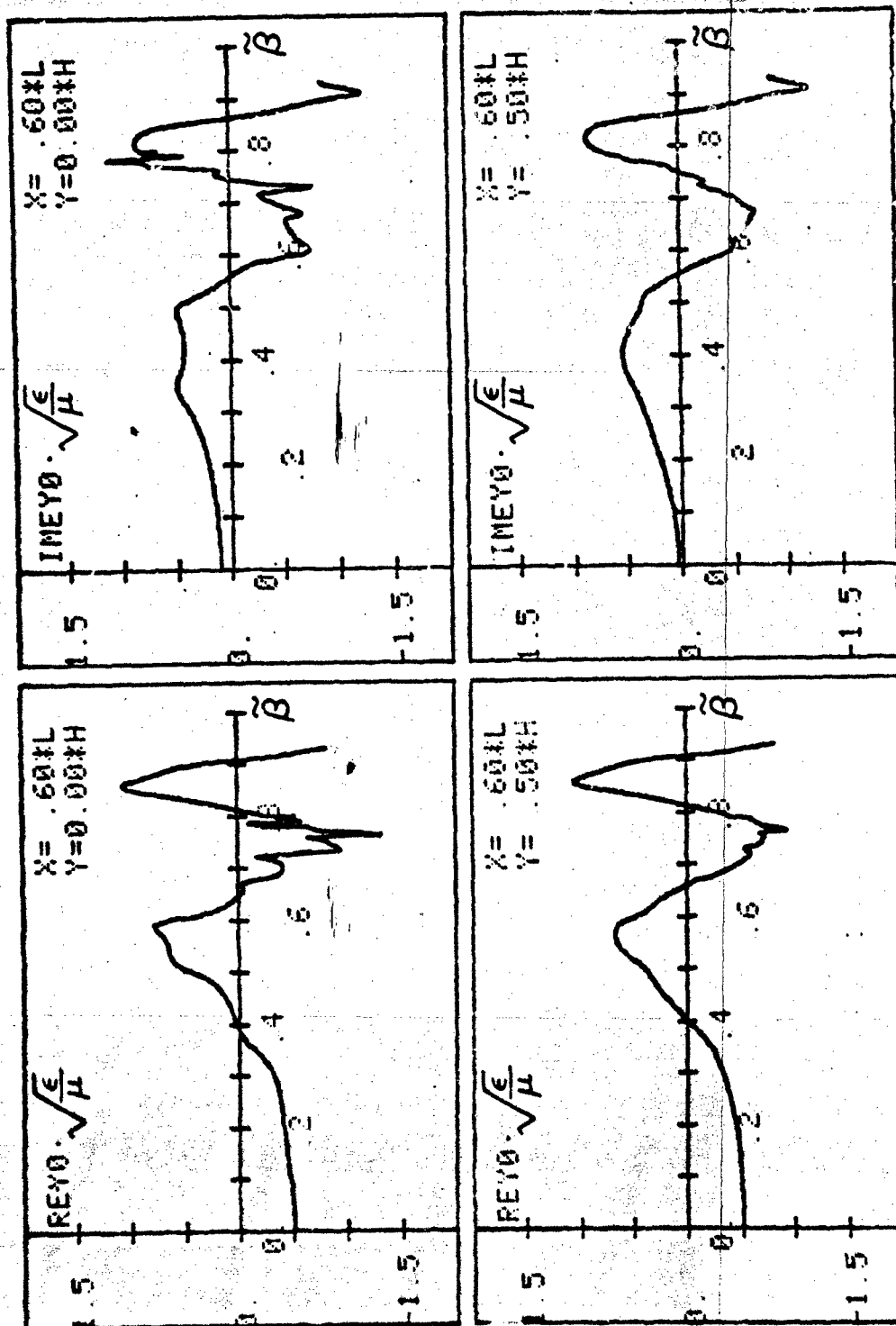


Figure 8. The real and imaginary parts of the electric field as functions of a longitudinal propagation constant for points of view:  $x/L = 0.0, 0.5, 0.6, 0.5$ .

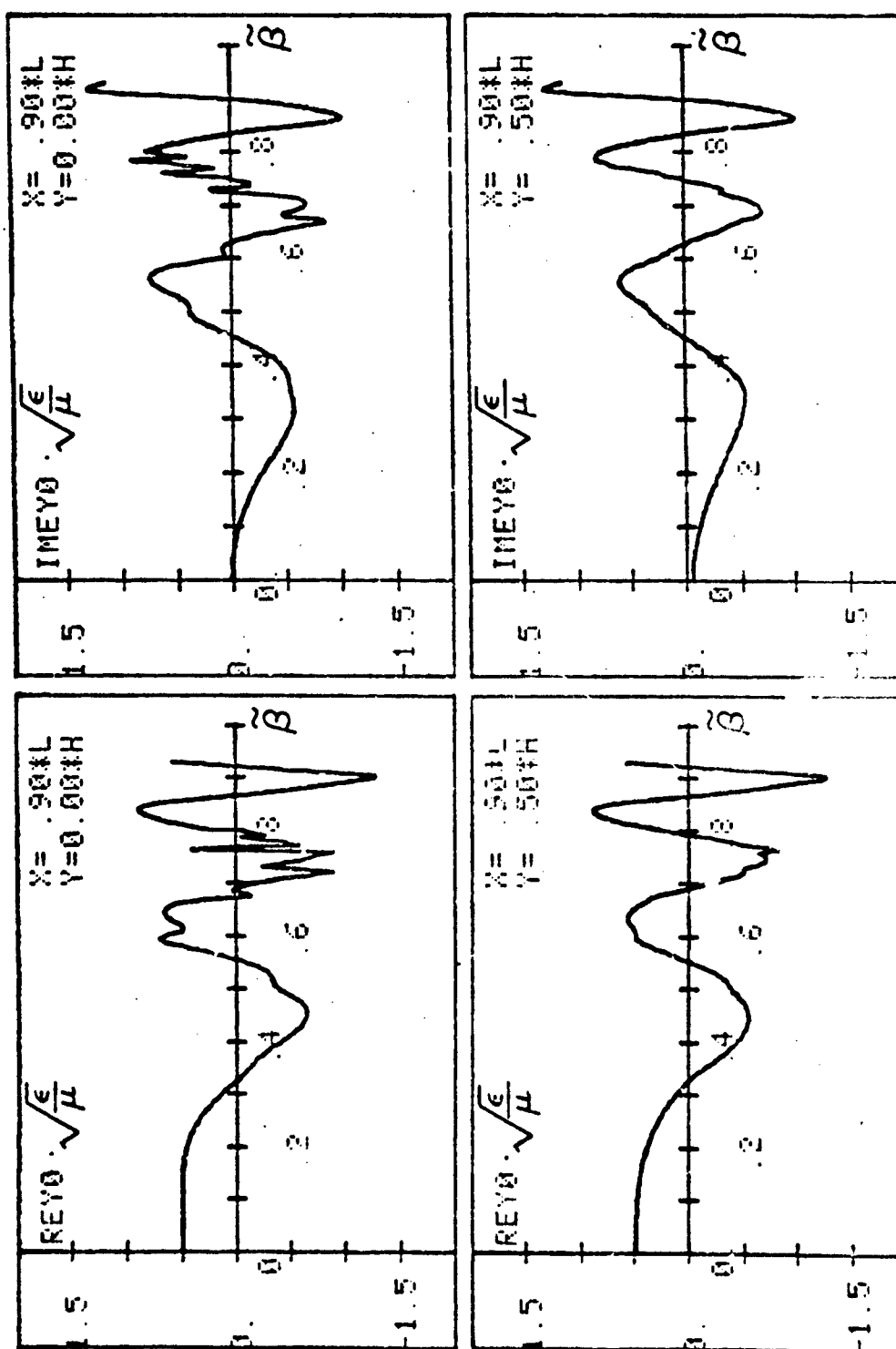


Figure 9. The real and imaginary parts of a y-component of the electric field as functions of a longitudinal propagation constant for values of view:  $\frac{Y}{L} = 0.9$ ;  $\frac{X}{L} = 0.0, 0.5$ .

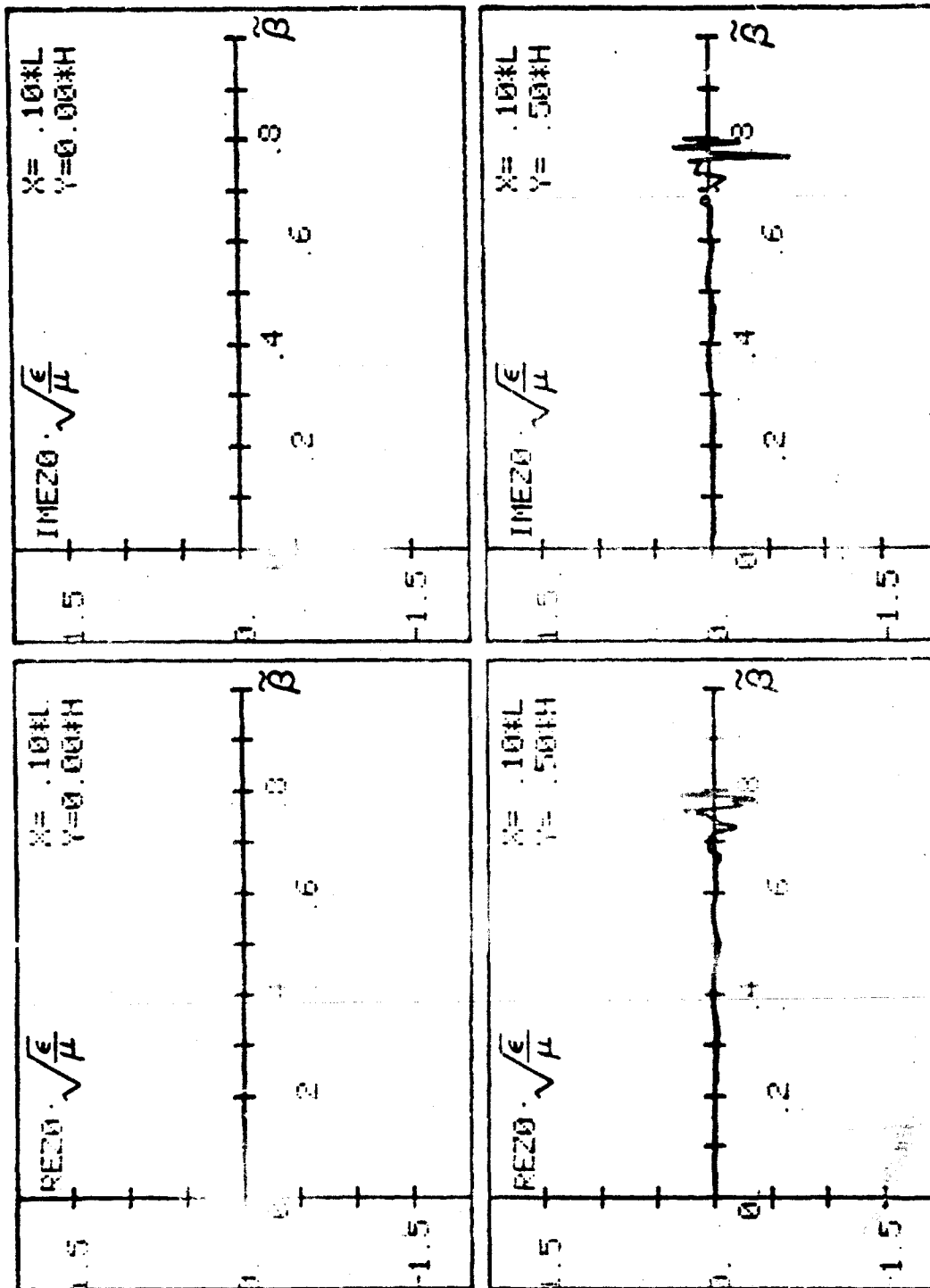


Figure 10. The real and imaginary parts of a z-component of the electric field as functions of a longitudinal propagation constant for points of view:  $\frac{Y}{L} = 0.0, 0.5$ .

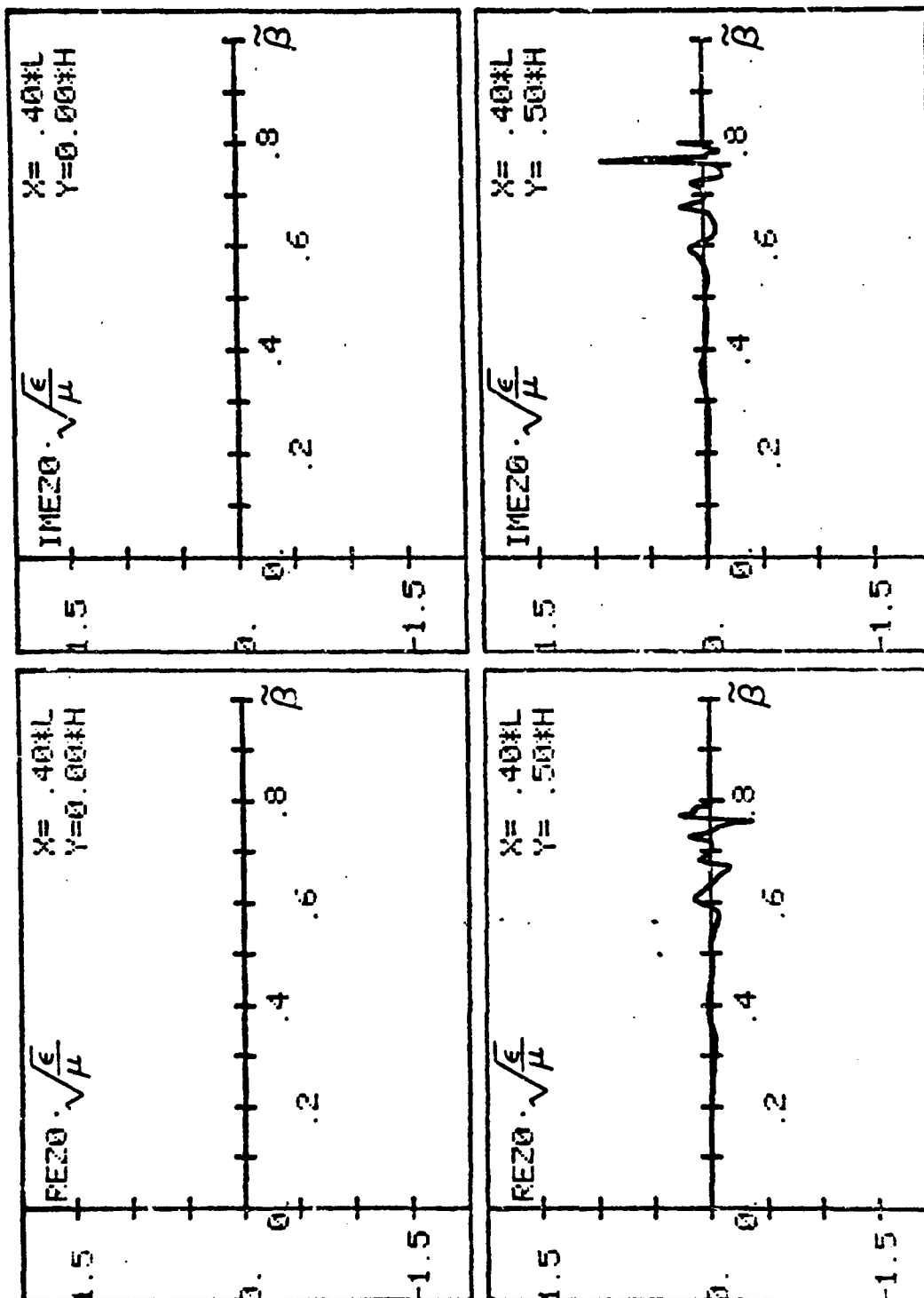


Figure 11. The real and imaginary parts of the electric field as functions of a longitudinal propagation constant for points of view:  $\frac{L}{H} = 0.4$ ;  $\frac{L}{H} = 0.0, 0.5$ .



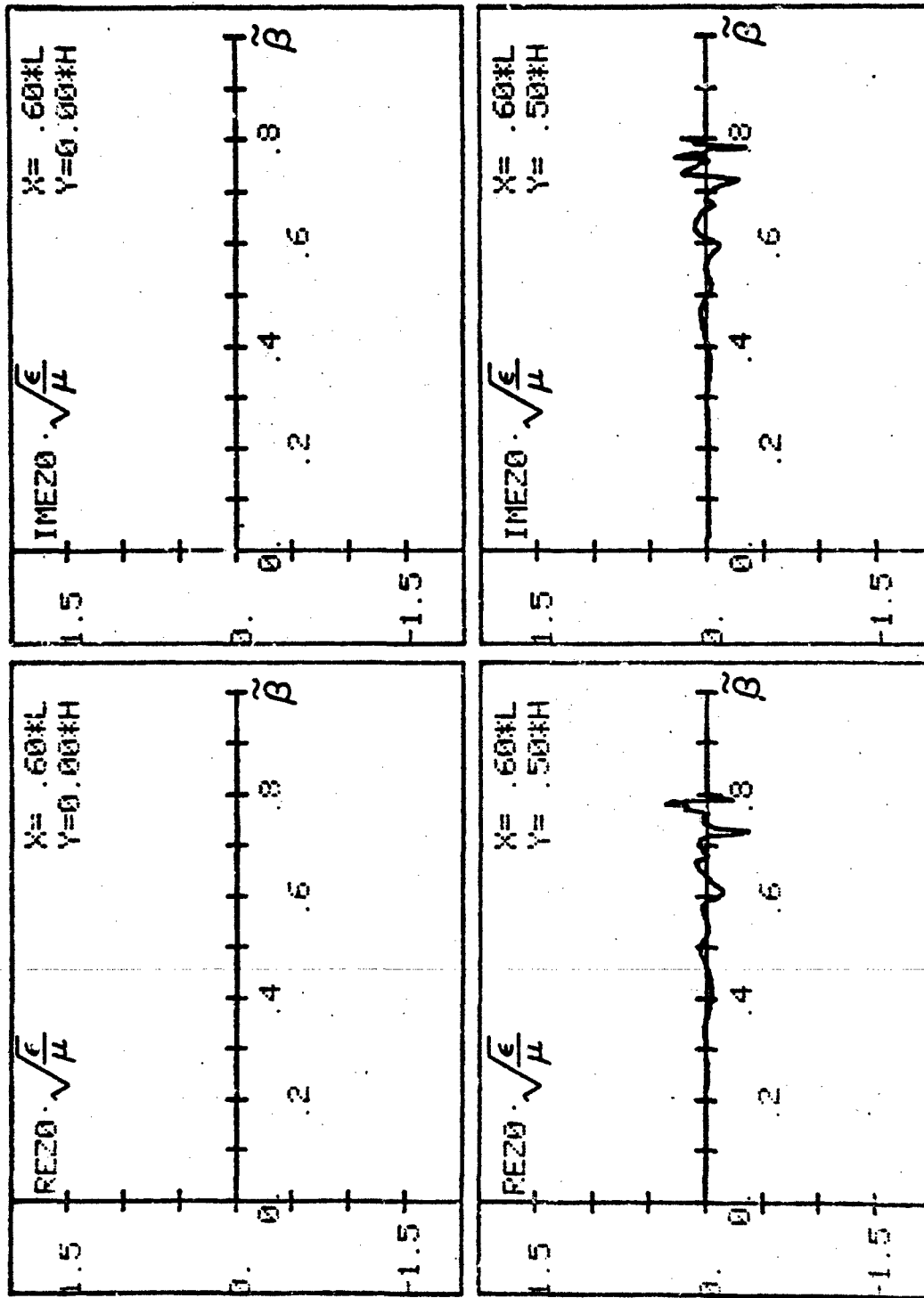


Figure 12. The real and imaginary parts of a z-component of the electric field as functions of a longitudinal propagation constant for points of view:  $\frac{L}{H} = 0.6$ ;  $\frac{Y}{H} = 0.0, 0.5$ .

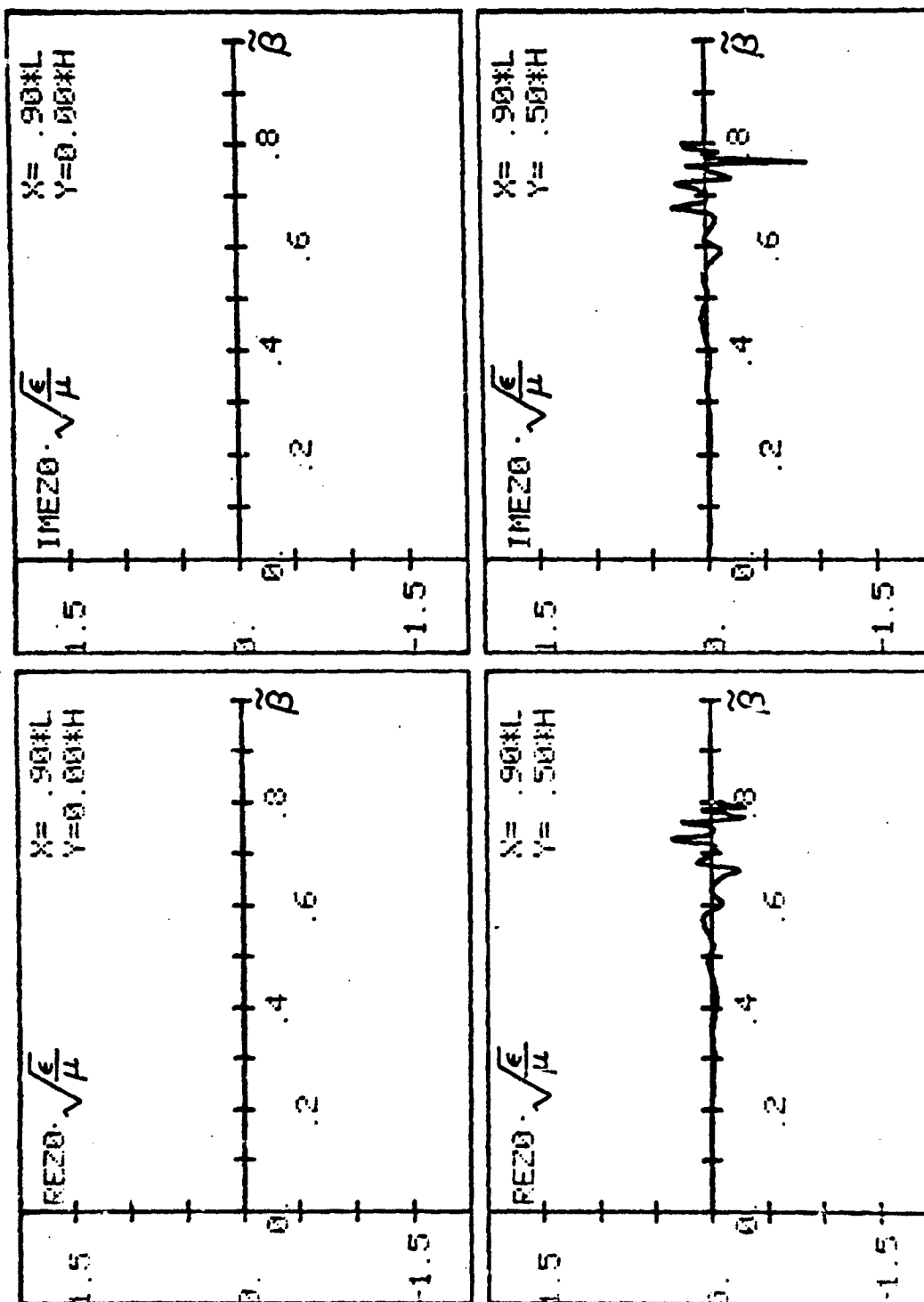


Figure 13. The real and imaginary parts of a z-component of the electric field as functions of a longitudinal propagation constant for points of view:  $\frac{1}{L} = 0.9; \frac{1}{H} = 0.0, 0.5$ .

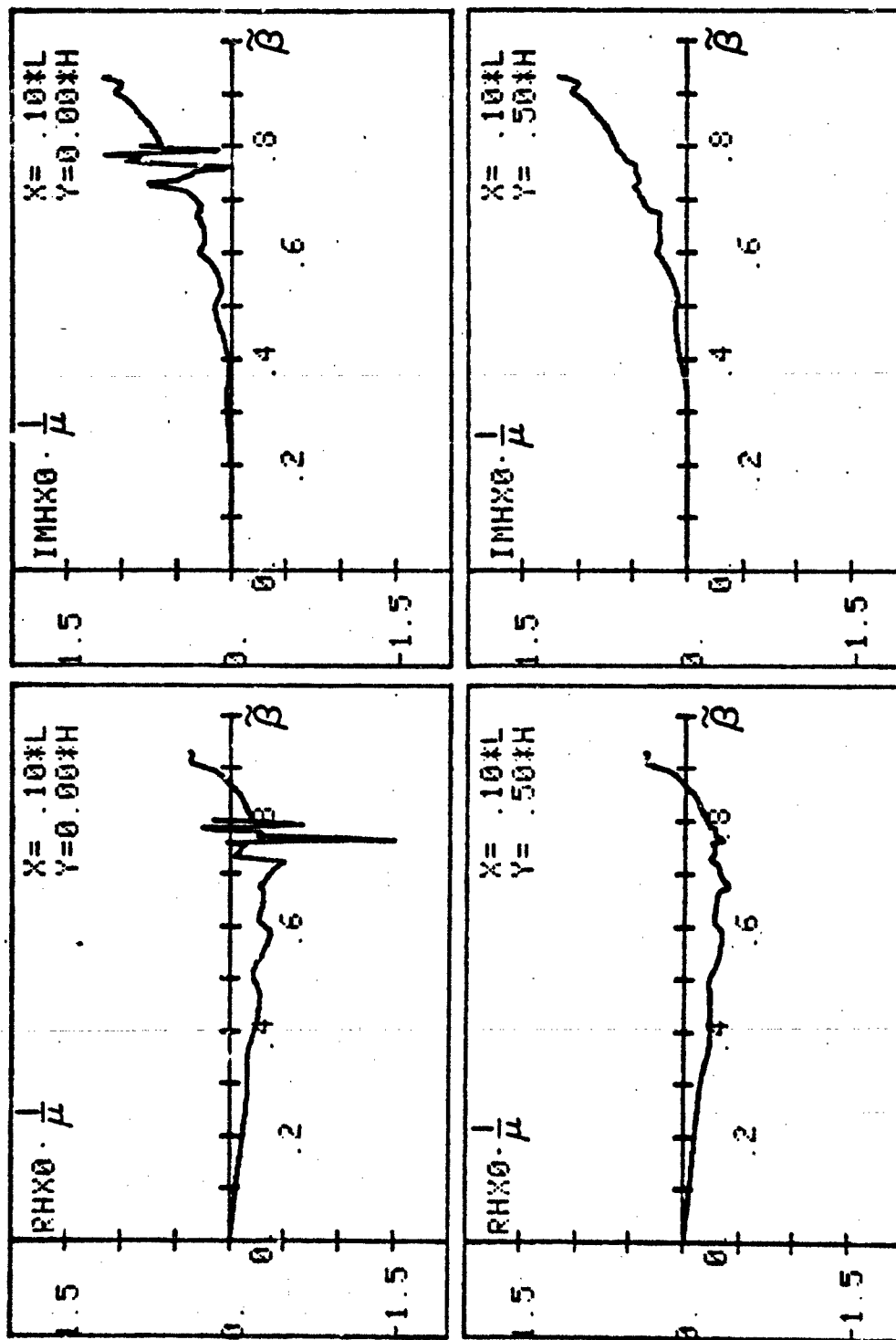


Figure 14. The real and imaginary parts of the magnetic field as functions of a longitudinal propagation constant for points of view:  $\frac{X}{L} = 0.1$ ;  $\frac{Y}{H} = 0.0, 0.5$ .

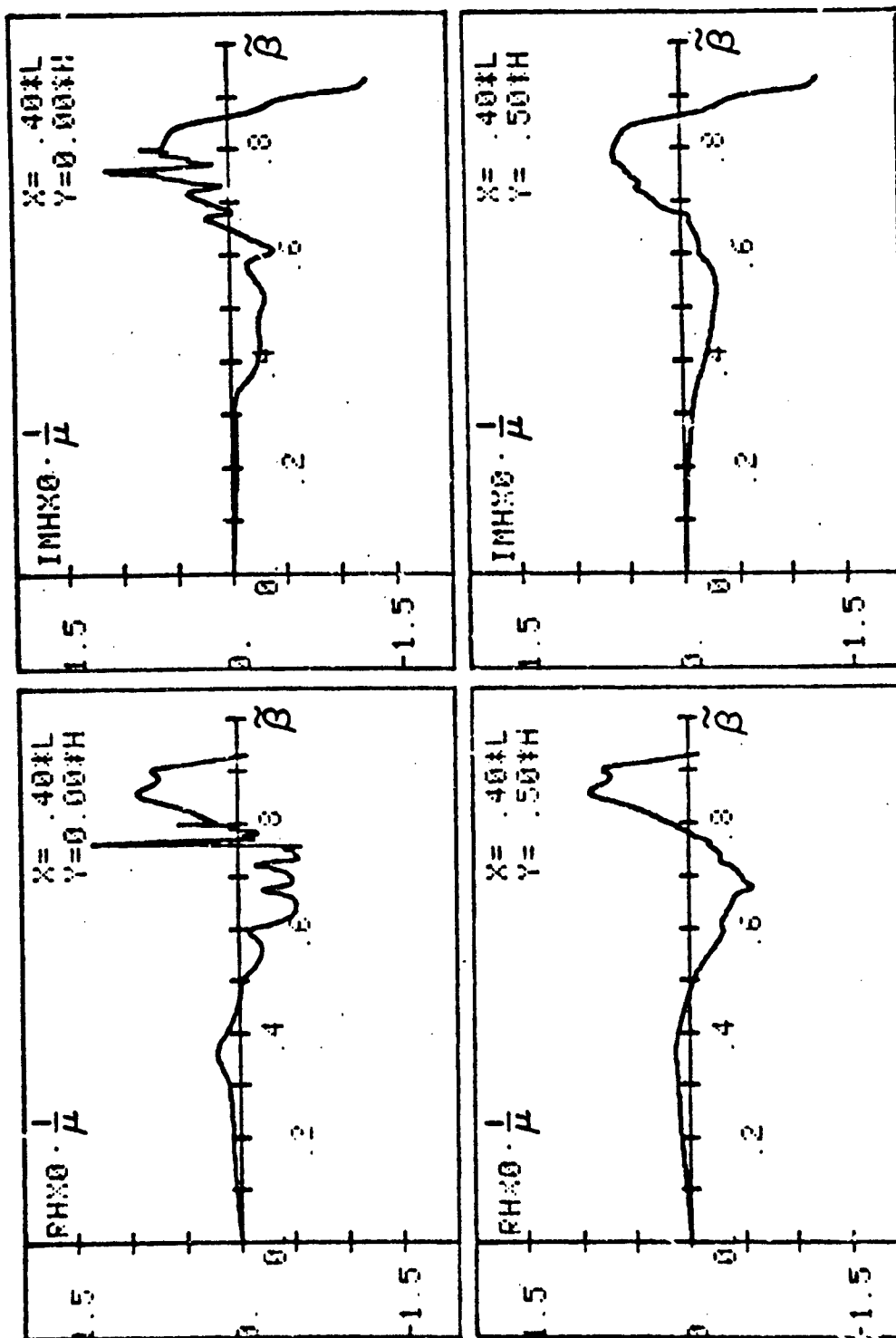


Figure 15. The real and imaginary parts of the magnetic field as functions of a longitudinal propagation constant for points of view:  $\frac{L}{\pi} = 0.0, 0.4, 0.5$ .

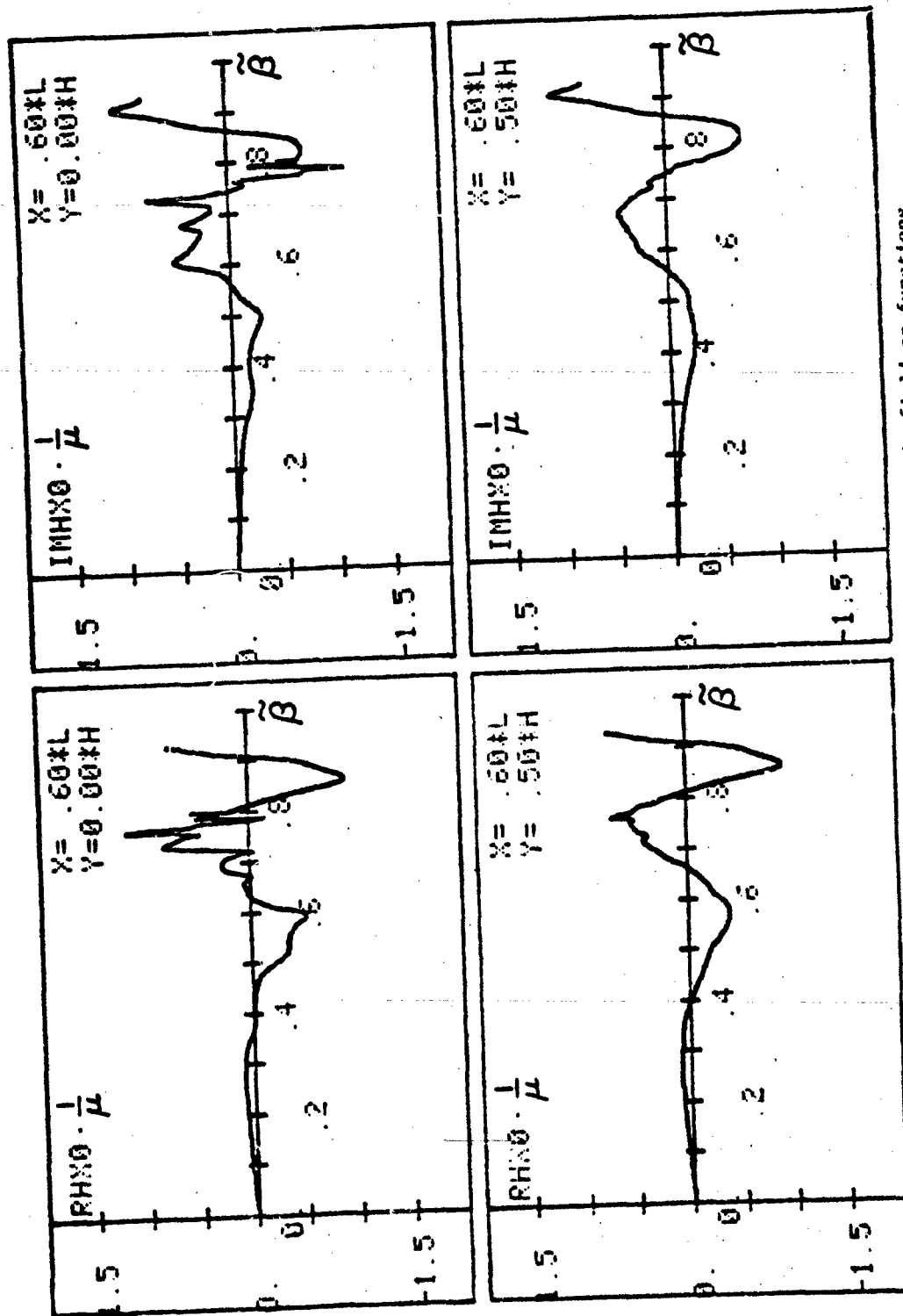


Figure 16. The real and imaginary parts of the magnetic field as functions of a longitudinal propagation constant for points of view: 1, 0.6, 0.5, and 0.0.

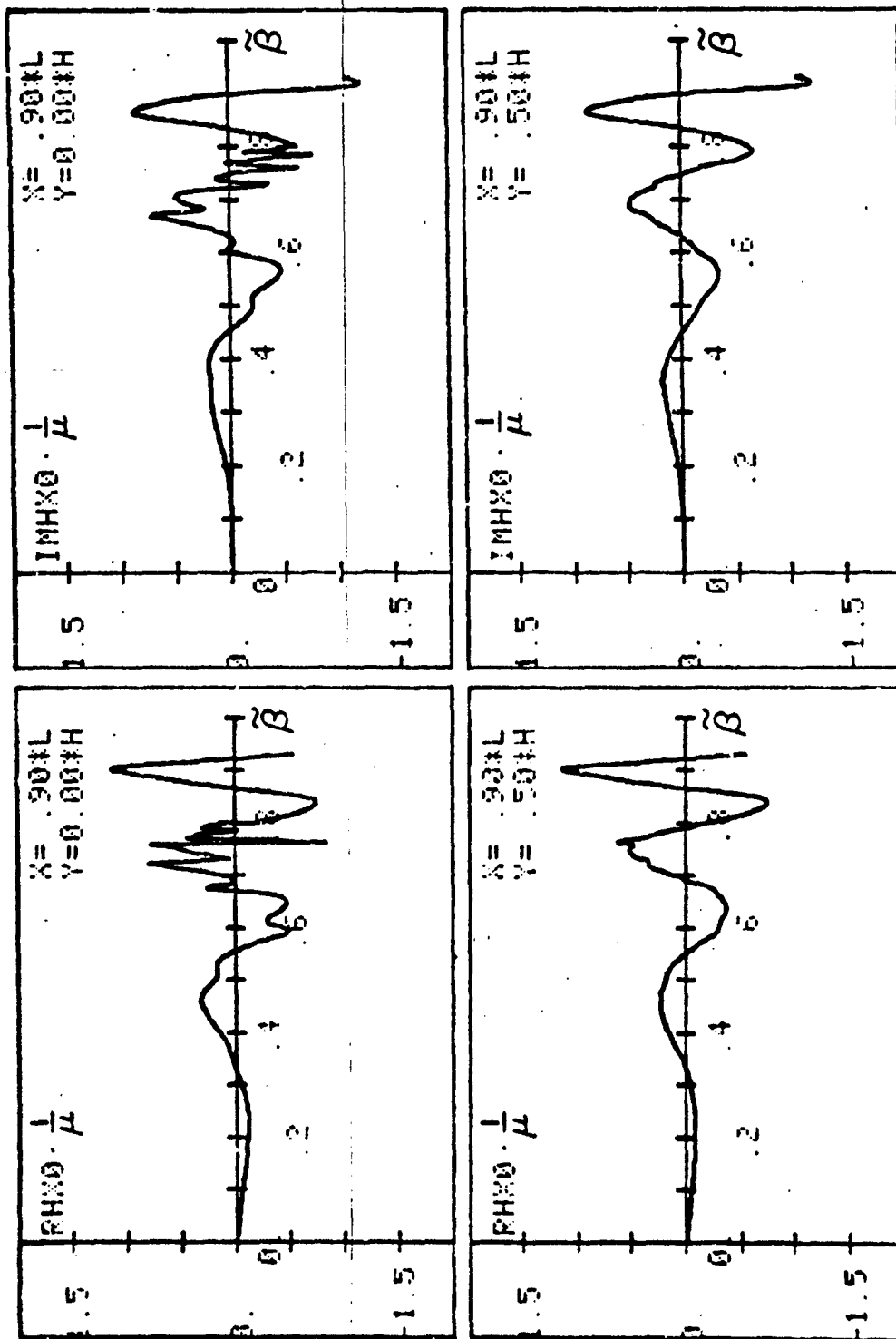


Figure 17. The real and imaginary parts of the magnetic field as functions of a longitudinal propagation constant for points of view:  $\frac{Y}{L} = 0.9$ ;  $\frac{Y}{H} = 0.0, 0.5$ .

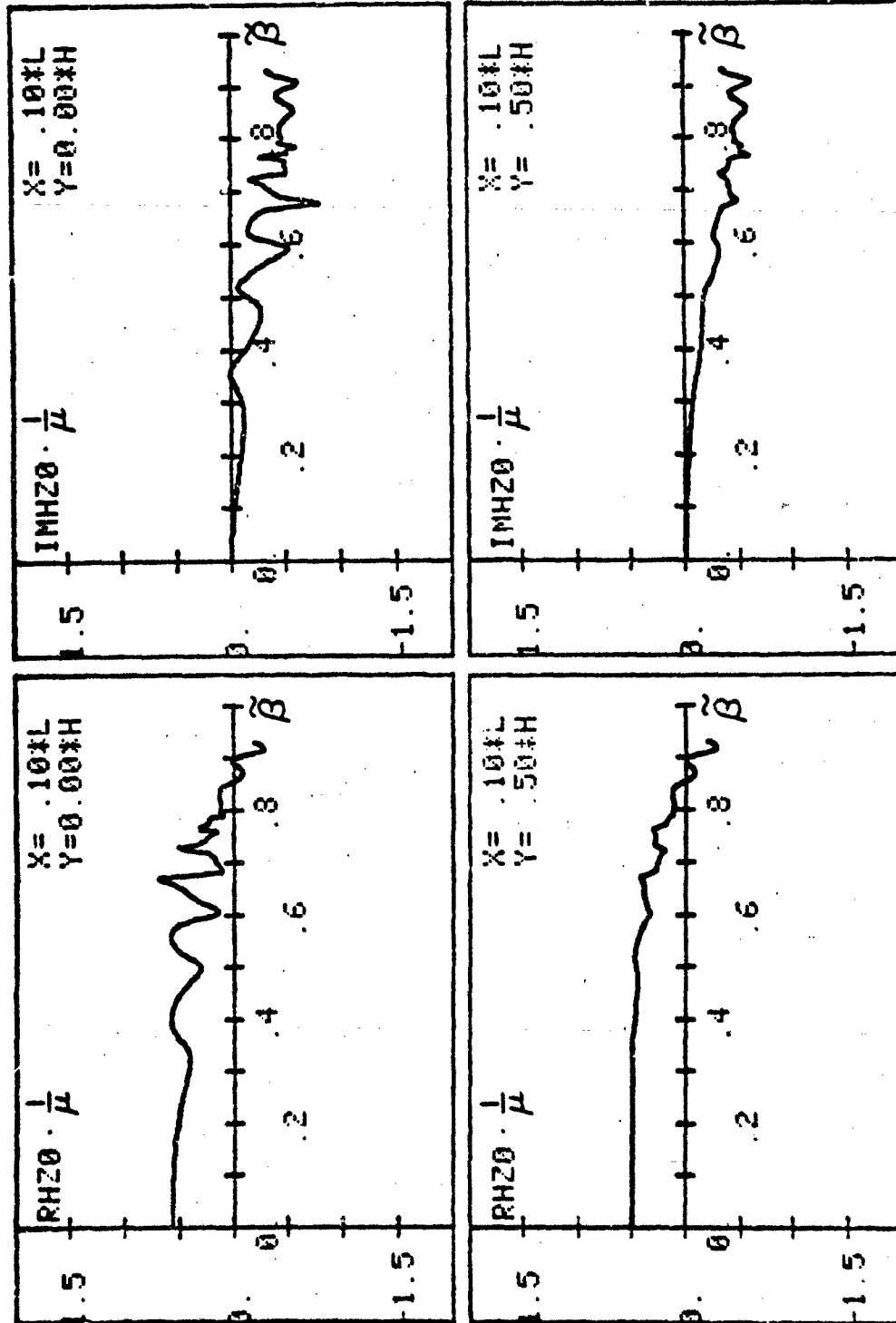


Figure 18. The real and imaginary parts of a z-component of the magnetic field as functions of a longitudinal propagation constant for points of view:  $\frac{L}{k} = 0.1; \frac{L}{k} = 0.0, 0.5$ .

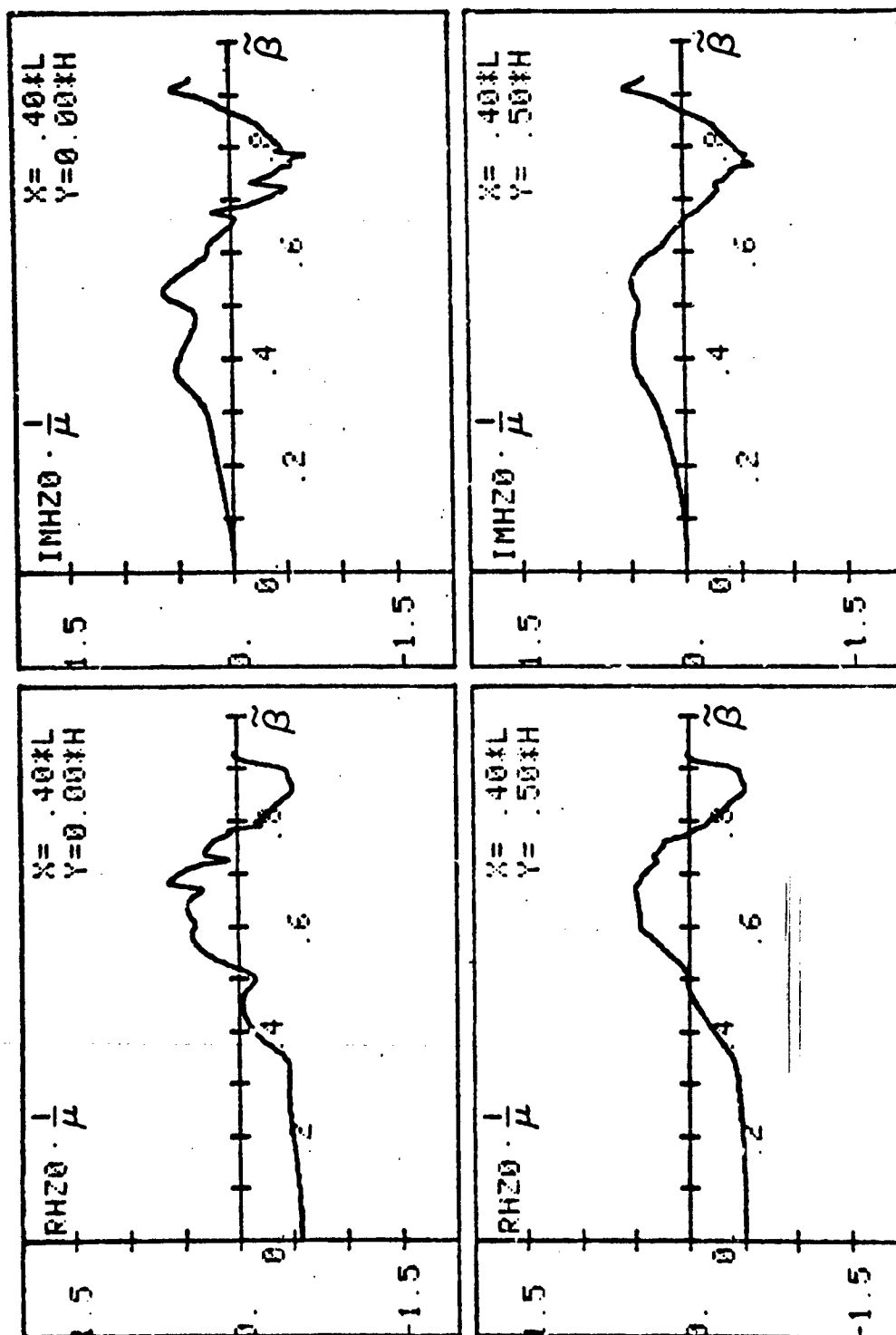


Figure 19. The real and imaginary parts of a z-component of the magnetic field as functions of a longitudinal propagation constant for points of view:  $\frac{1}{l} = 0.4$ ;  $\frac{1}{l} = 0.0, 0.5$ .



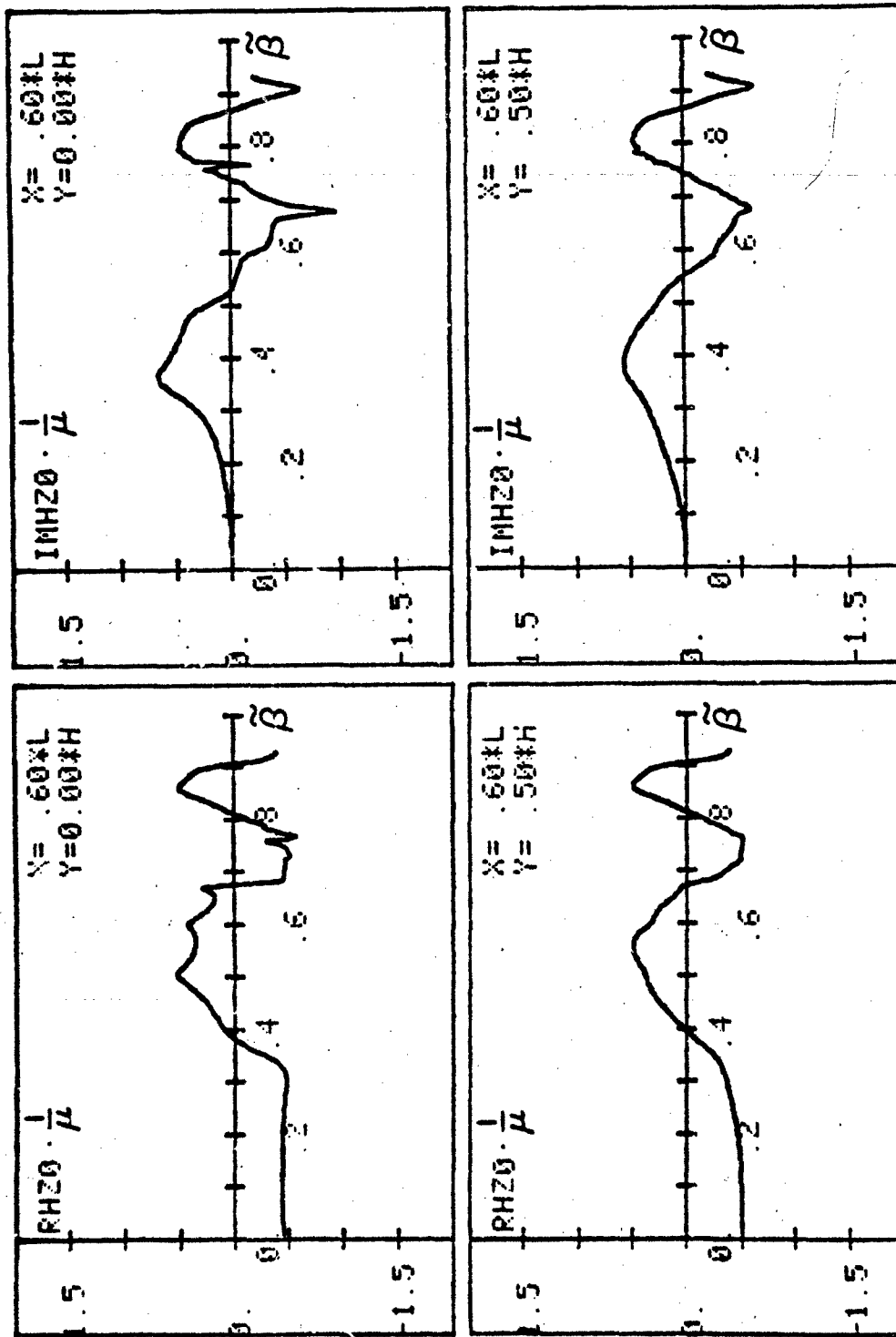


Figure 20. The real and imaginary parts of a 2-component of the magnetic field as functions of a longitudinal propagation constant for points of view:  $\frac{L}{\lambda} = 0.0, 0.5, 0.6, 0.8$ .

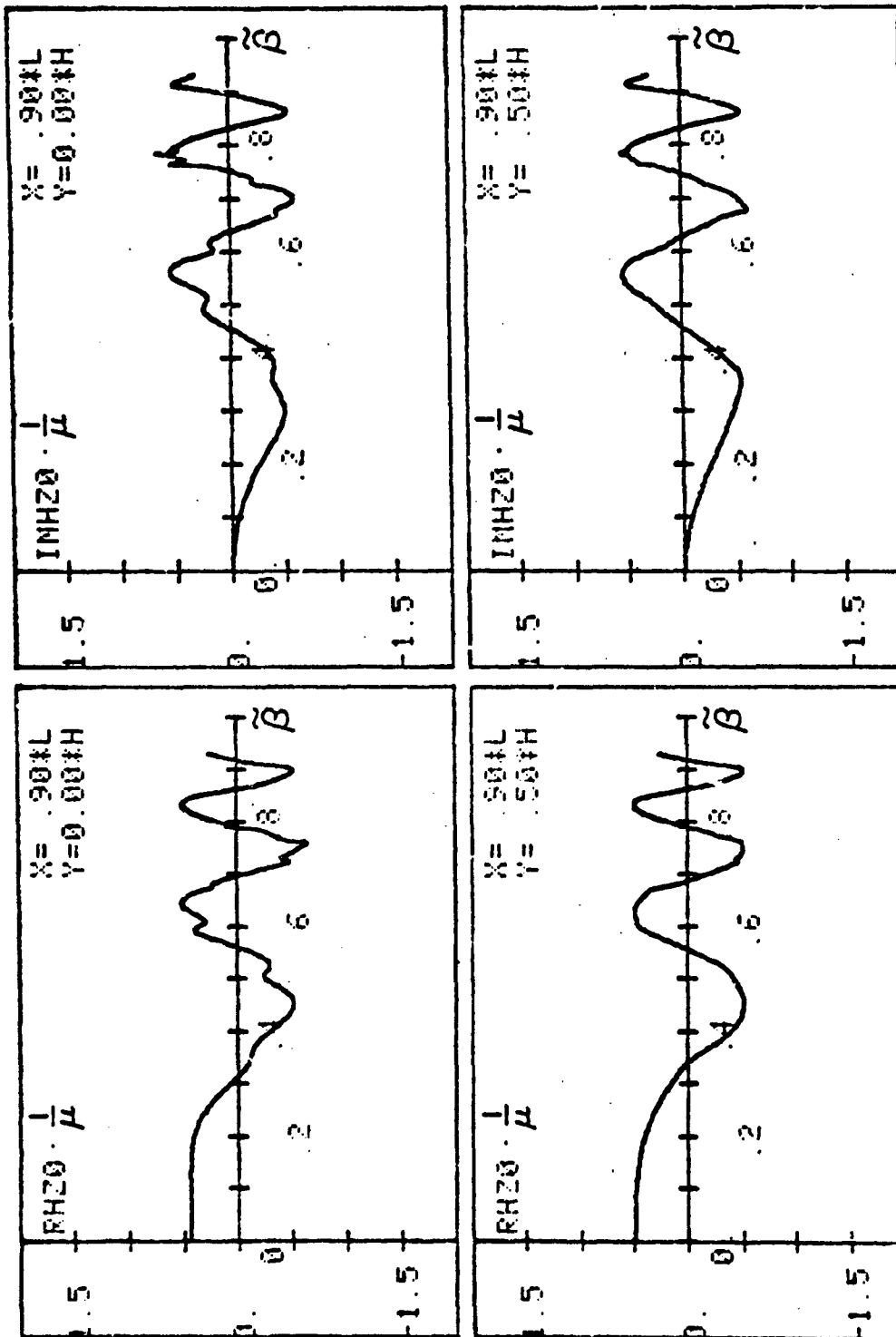


Figure 21. The real and imaginary parts of a z-component of the magnetic field as functions of a longitudinal propagation constant for points of view:  $\frac{Y}{H} = 0.9; \frac{Y}{H} = 0.0, 0.5$ .

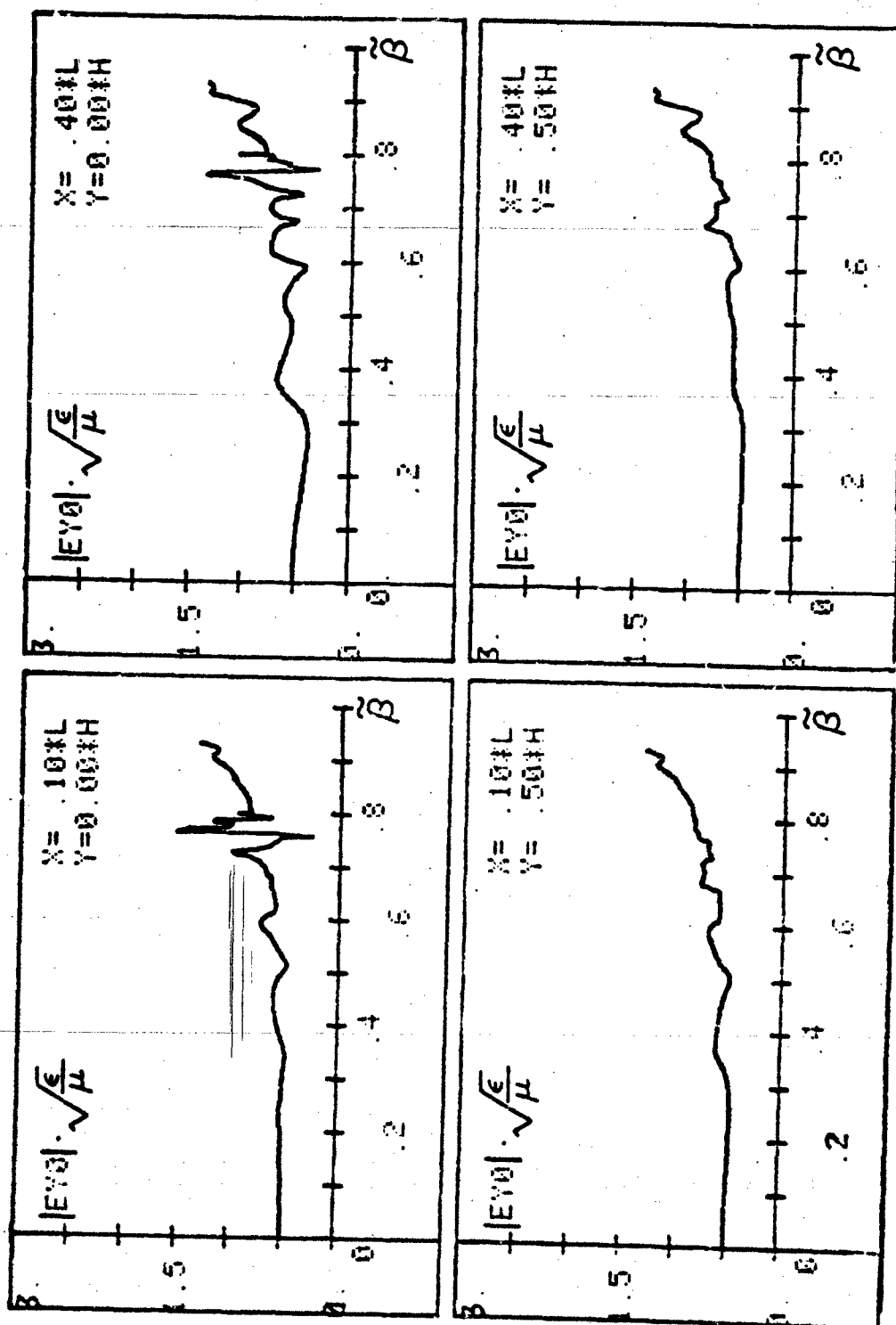


Figure 22. The magnitude of the y-component of the electric field as a function of the longitudinal propagation constant for points of view:  $\frac{Y}{\lambda} = 0.1, 0.4, 0.5$ .

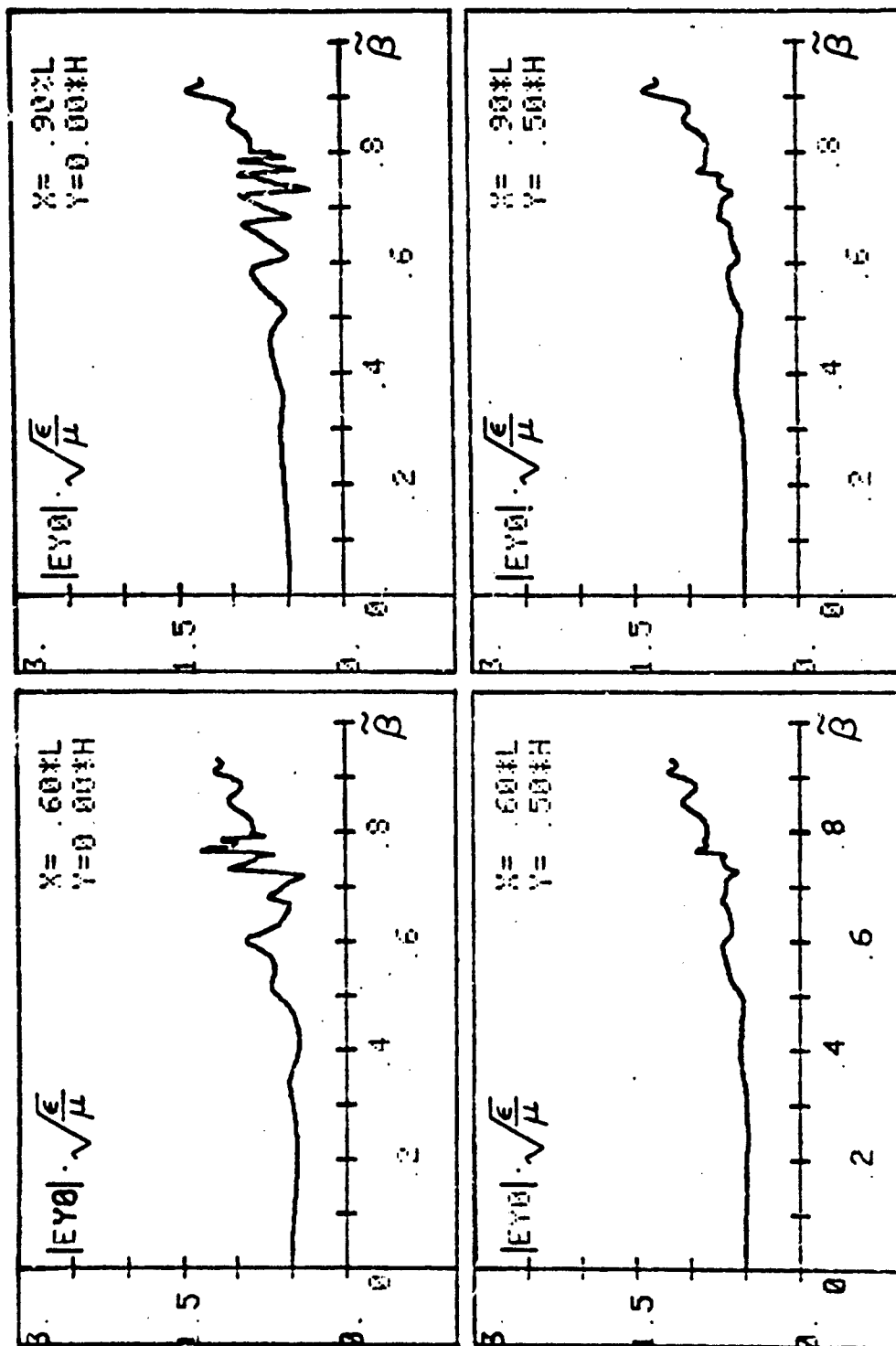


Figure 23. The module of a y-component of the electric field as a function of a  $\tilde{\beta}$  for points of view:  $\frac{X}{L} = 0.6, 0.9$ ;  $\frac{Y}{H} = 0.0, 0.5$ .

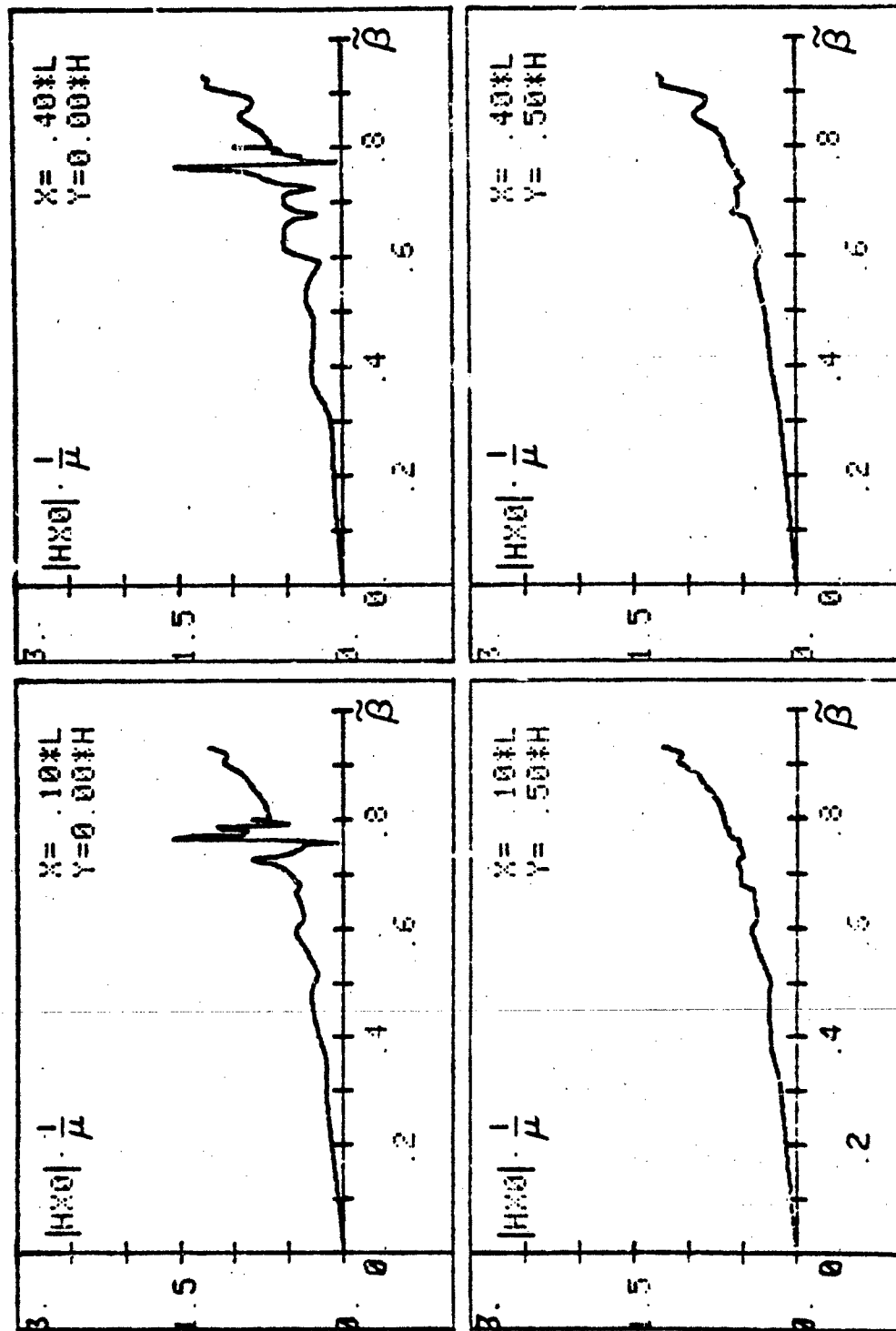


Figure 24. The magnitude of the x-component of the magnetic field as a function of the longitudinal propagation constant for points of view:  $\frac{Y}{H} = 0.1, 0.4; \frac{X}{L} = 0.0, 0.5$ .

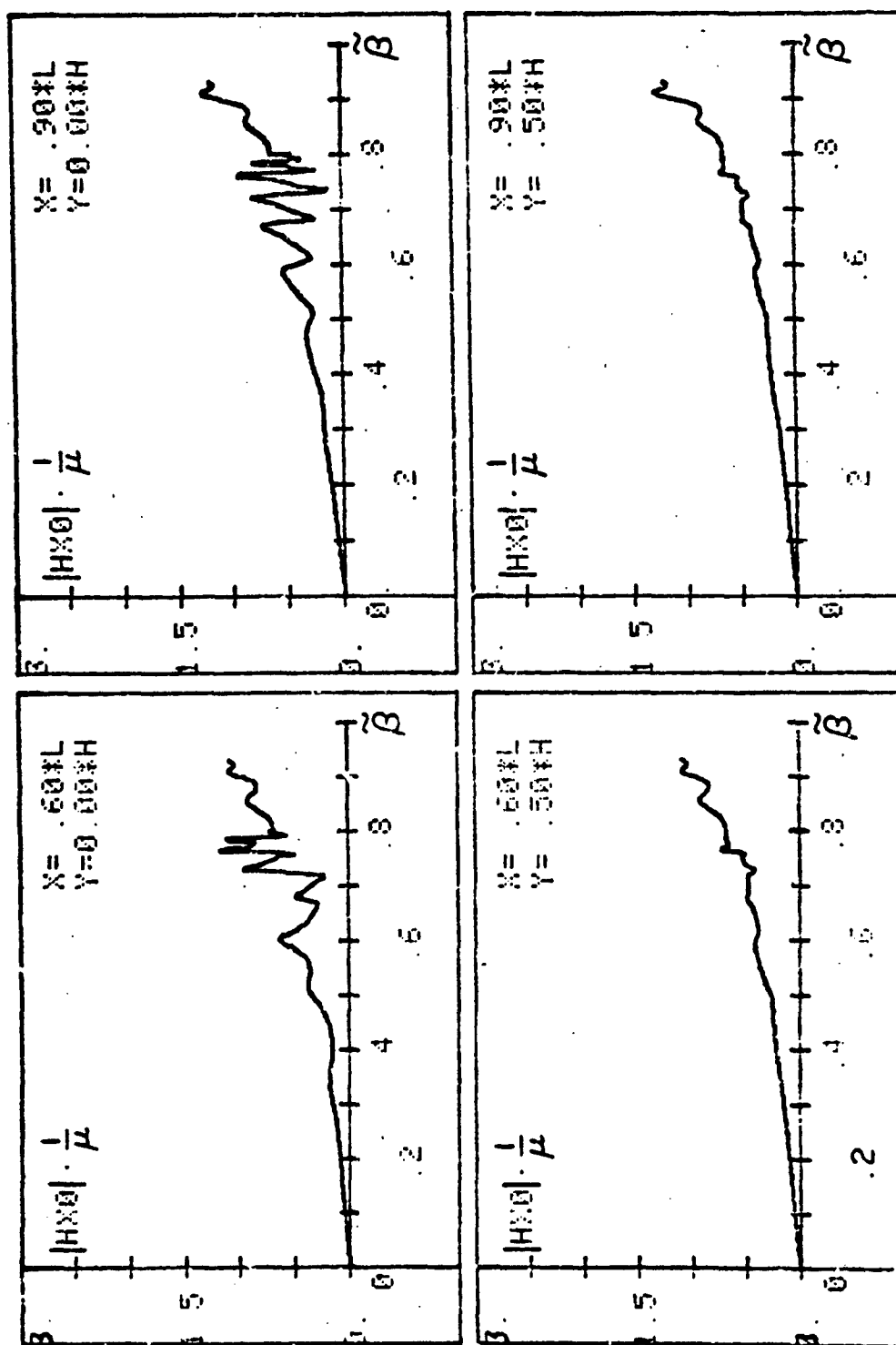


Figure 25. The magnitude of the x-component of the magnetic field as a function of the longitudinal propagation constant for points of view:  $\frac{y}{L} = 0.6, 0.9; \frac{x}{L} = 0.0, 0.5$ .

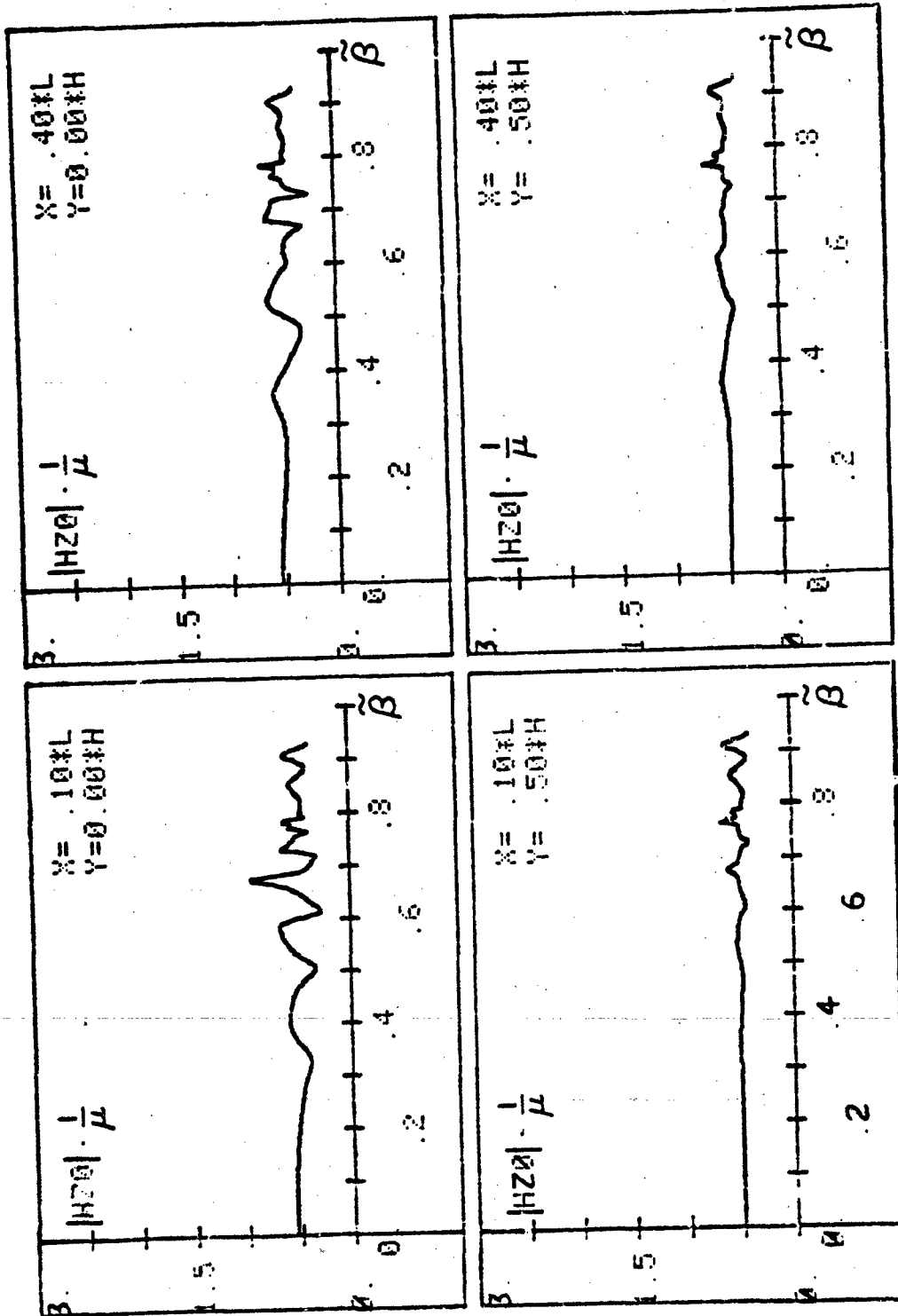


Figure 26. The magnitude of the magnetic field as a function of the longitudinal propagation constant for points of view:  $\frac{X}{L} = 0.1, 0.4$ ;  $\frac{Y}{H} = 0.0, 0.5$ .

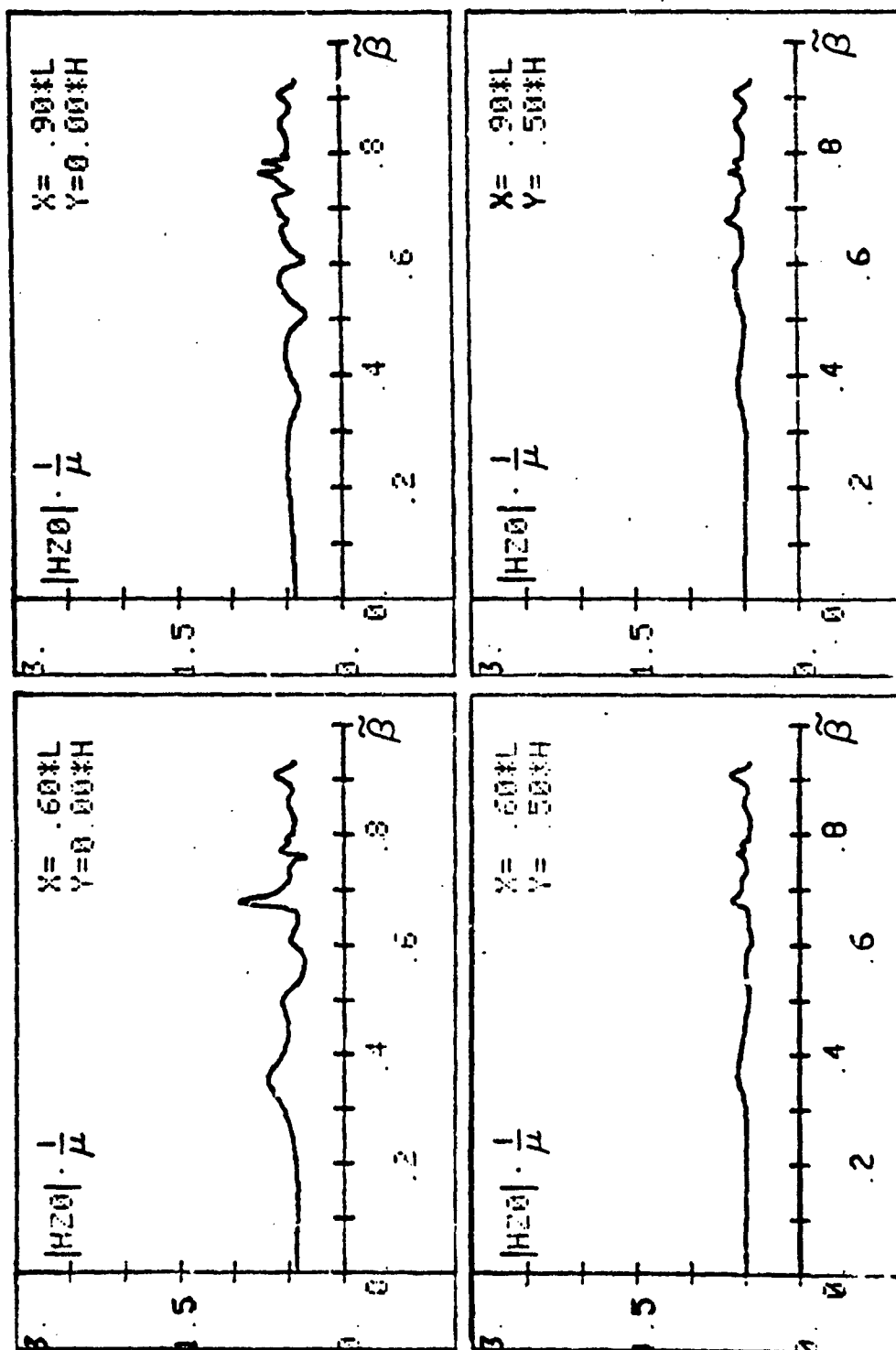


Figure 27. The module of a z-component of the magnetic field as a function of a longitudinal propagation constant for points of view:  $\frac{Y}{L} = 0.6, 0.9; \frac{X}{H} = 0.0, 0.5$ .



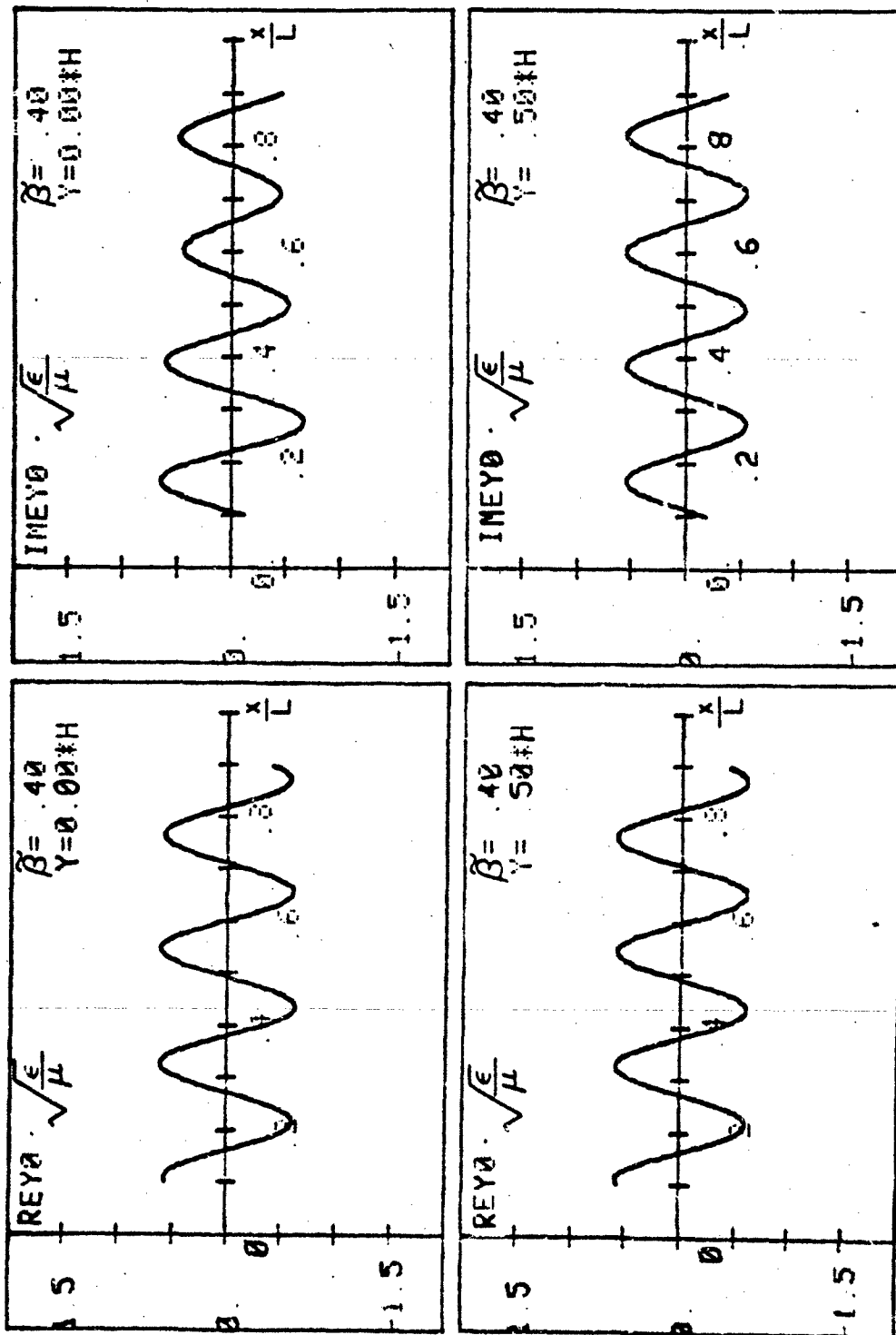


Figure 28. The real and imaginary parts of a y-component of the electric field as functions of an x-coordinate for  $\beta = 0.4$ ;  $\frac{\gamma}{\pi} = 0.0, 0.5$ .

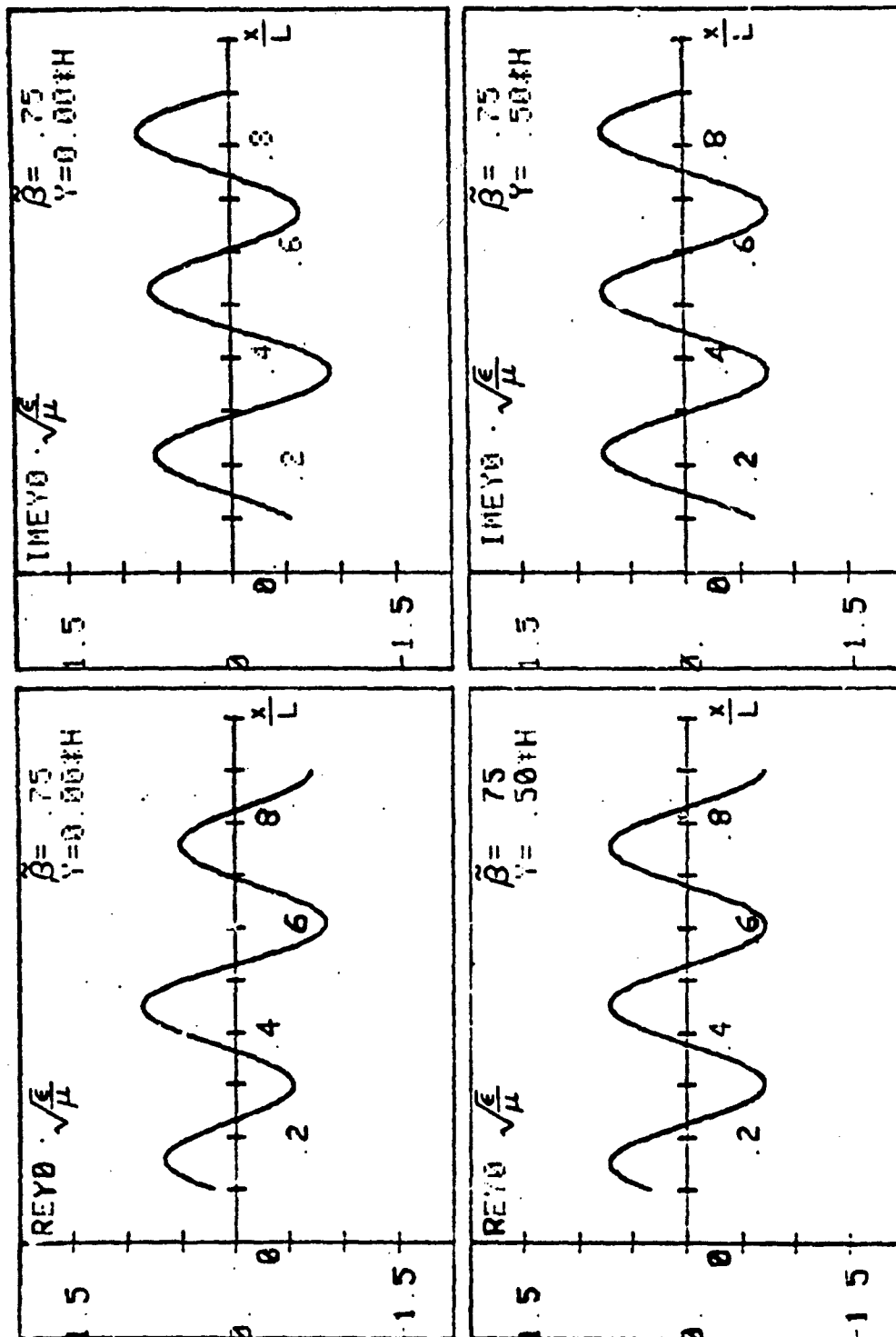


Figure 29. The real and imaginary parts of  $a_y$ -component of the electric field as functions of an x-coordinate for  $\beta = 0.75$ ;  $\gamma = 0.0, 0.5$ .

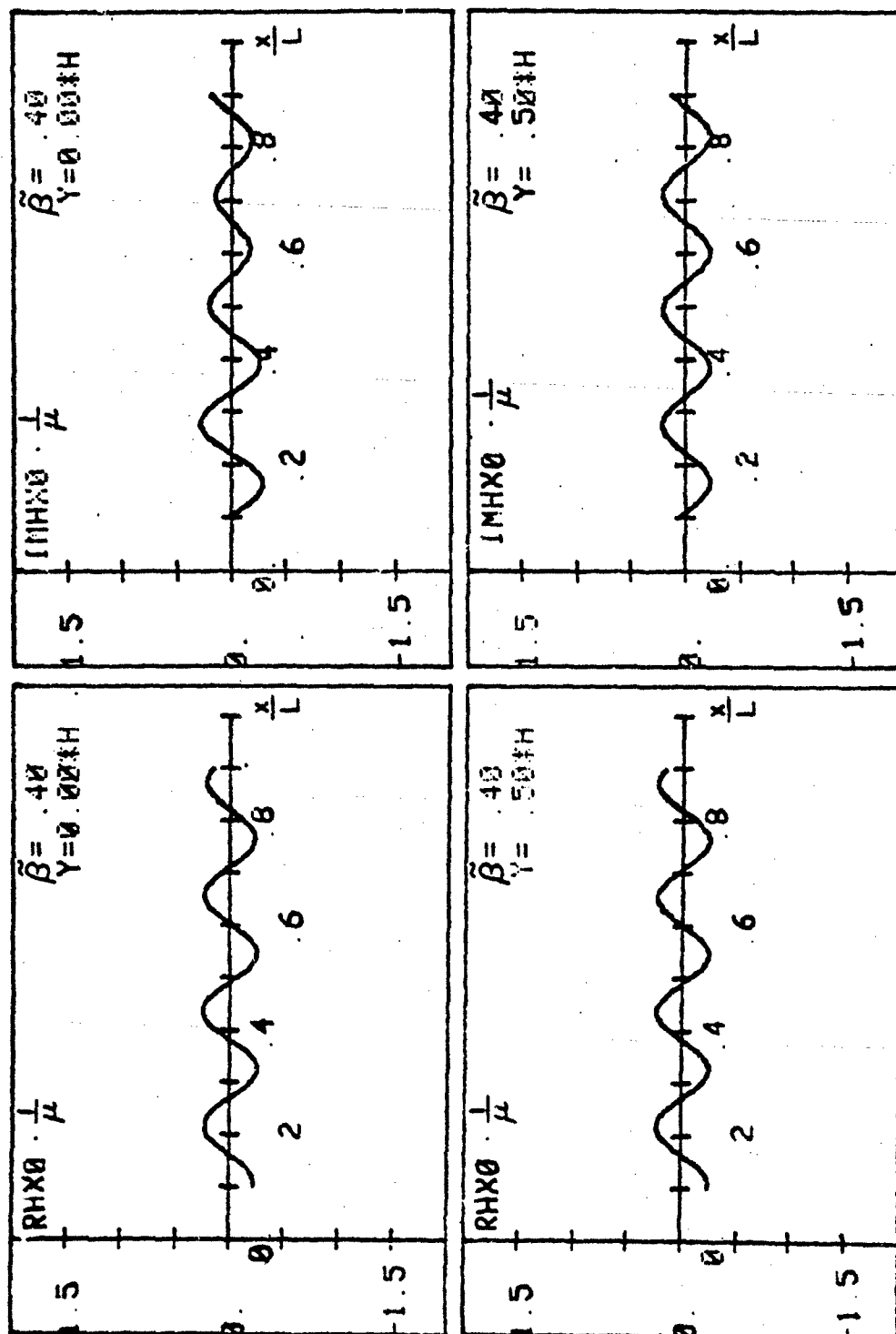


Figure 10. The real and imaginary parts of an  $x$ -component of the magnetic field as functions of an  $x$ -coordinate for  $\beta = 0.4$ ;  $\gamma = 0.0, 0.5$ .

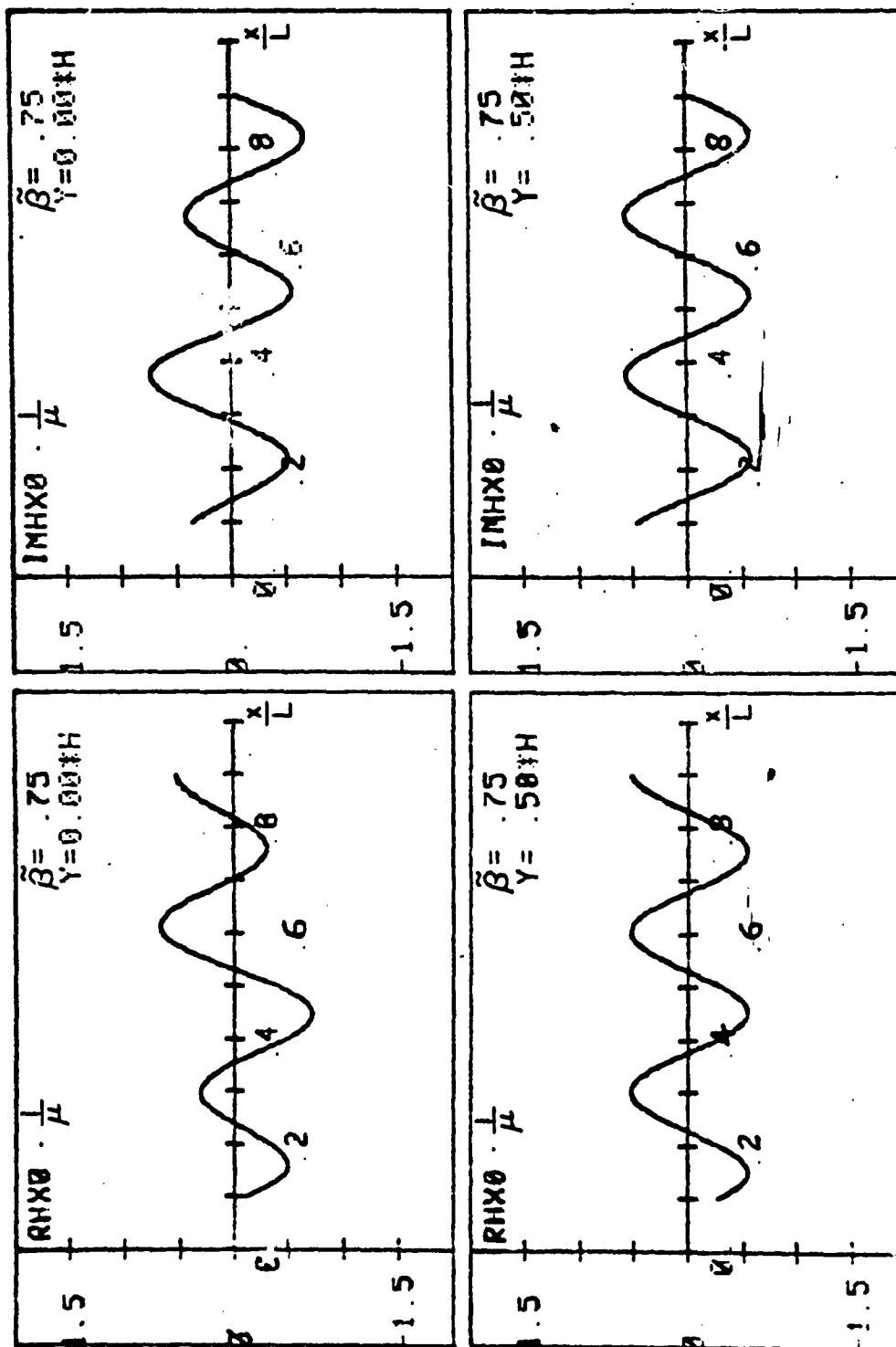


Figure 11. The real and imaginary parts of the magnetic field as functions of an x-coordinate for  $\beta = 0.75$ ;  $\gamma = 0.0, 0.5$ .

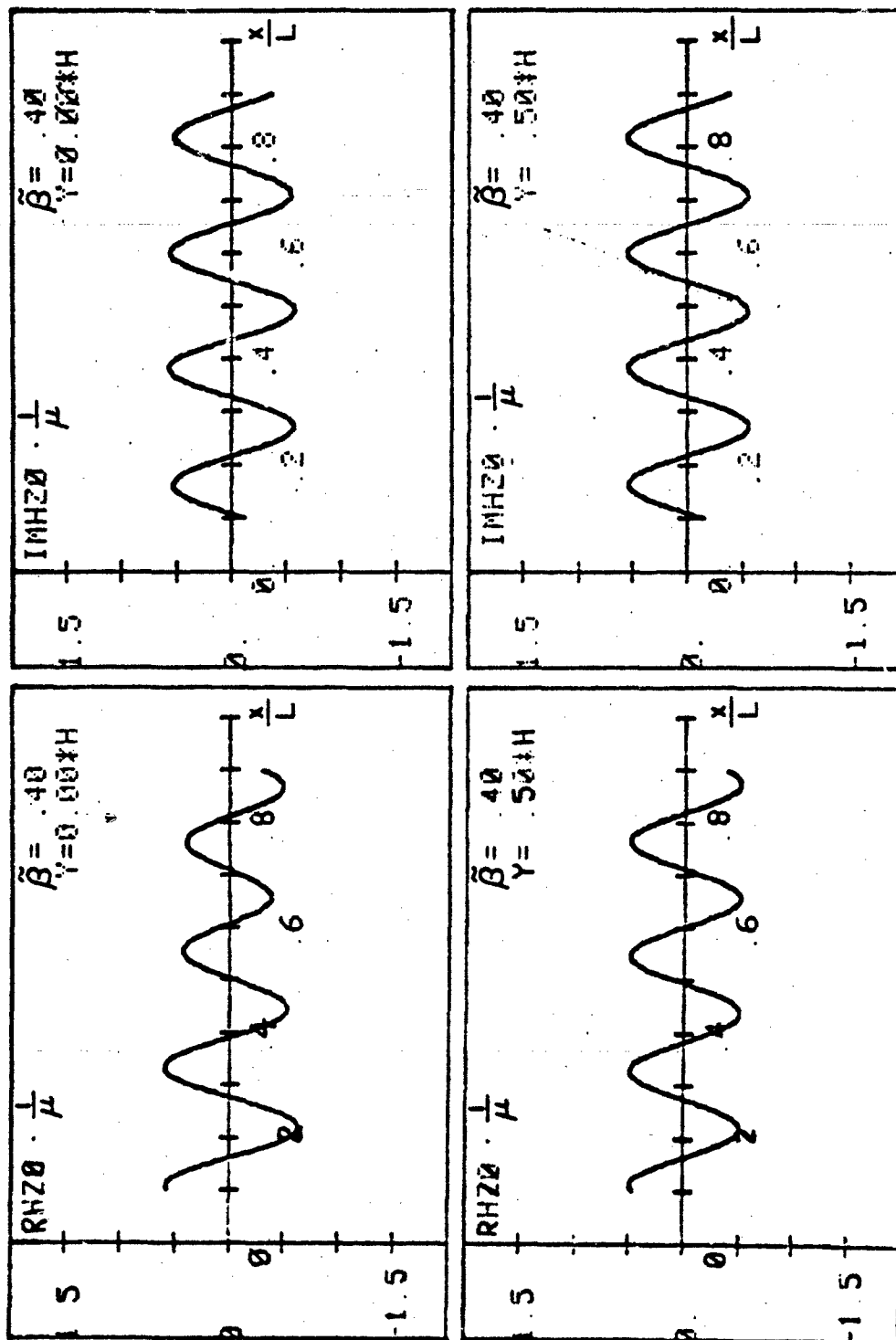


Figure 12. The real and imaginary parts of a  $y$ -component of the magnetic field as functions of an  $x$ -coordinate for  $\beta = 0.4$ ;  $\gamma = 0.0, 0.5$ .

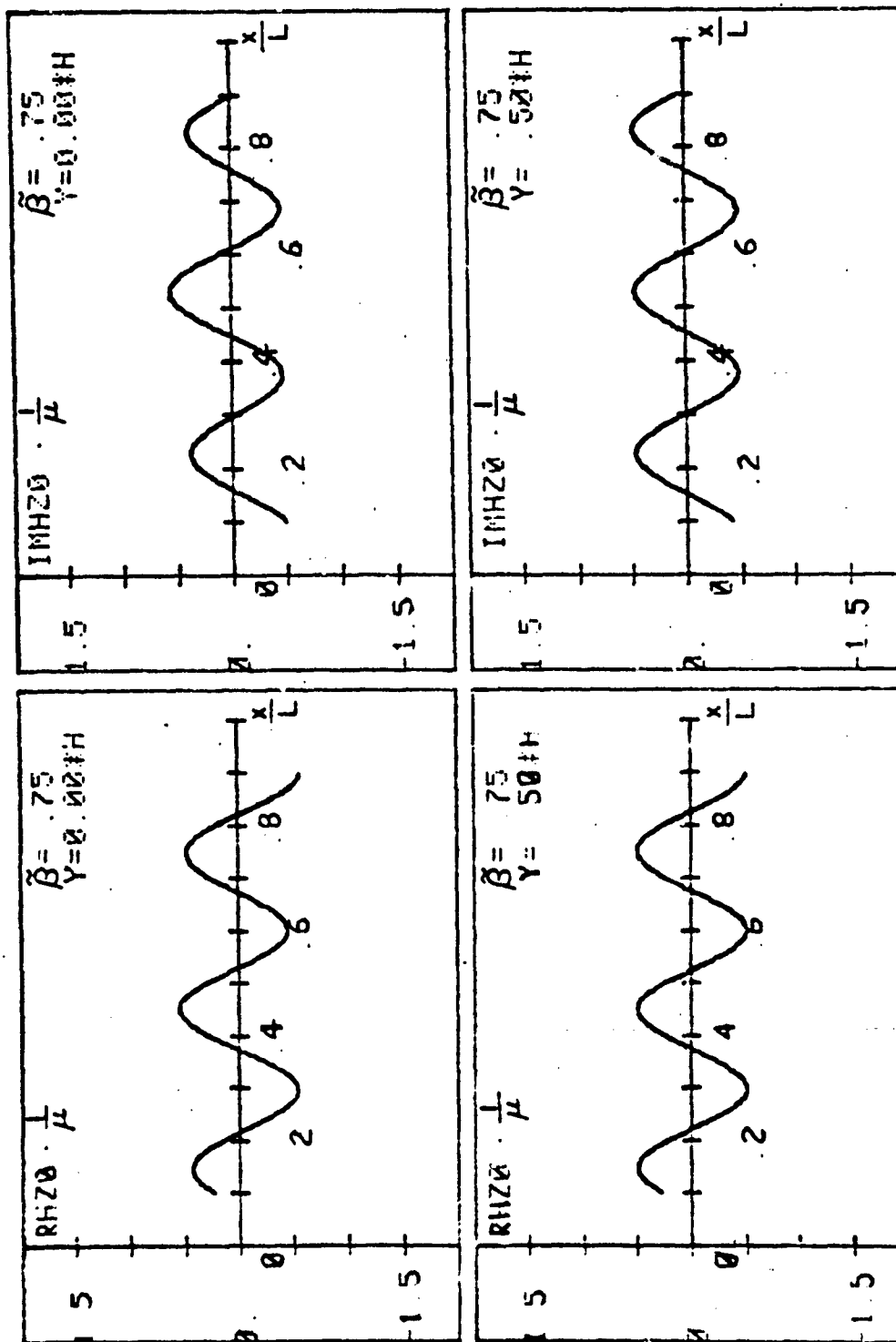


Figure 11. The real and imaginary parts of the magnetic field as functions of an x-coordinate for  $\beta = 0.0, 0.5$ .

### III. NUMERICAL STUDY OF THE PROBLEM

Because the analytical expressions derived in the second section are rather complicated and difficult to analyze, we numerically evaluated the solutions using a digital computer. The results are presented in this section in graphical form. This section consists of two parts: in the first we discuss the field components as functions of the longitudinal propagation constant; in the second - as functions of the transverse coordinates.

#### A. Real and Imaginary Parts and Amplitudes of the Field Components As Functions of the Longitudinal Propagation Constant

The graphics that are supplied in this section were plotted with a step for  $\beta$  equal to 0.005. The point,  $\beta = 0.80009$ , also was used. The figures were plotted using 188 points. The output for the real and imaginary parts and the amplitudes of all five field components for eight observation points:  $\frac{x}{L} = 0.1, 0.4, 0.6, 0.9$  and  $\frac{y}{H} = 0.0, 0.5$  are presented. From the figures it is observed that  $E_y, H_x, H_z$  are dominant components. In Figures 6-9 the real and imaginary parts of  $E_y$  are given. By comparing these results, one can observe for points  $\frac{y}{H} = 0.0$  and  $\frac{y}{H} = 0.5$  that the  $E_y, H_x, H_z$  field behaviors as functions of  $\beta$  are more complicated in the middle of the waveguide. This is hardly surprising in view of the largest contribution of the second mode for the above-mentioned components for  $\frac{y}{H} = 0.0$ . When the point of observation approaches  $\frac{y}{H} = 0.5$ , the contribution of the second mode for those components decreases and has a limiting value equal to zero. In Figures 6-9, 14-17, 22-25 we observe the step changing for the  $E_y, H_x$  components at  $\beta = \beta_0$ . The

second mode is responsible for this misbehavior. When  $\frac{y}{H} \rightarrow 0.5$ , the contribution of that step decreases, and for  $\frac{y}{H} = 0.5$ , it equals zero. One can observe that the curves are smooth at  $\tilde{z} = \tilde{z}_0$ . It should be mentioned that:

(a) The discontinuous behavior is observed because we have neglected the exponentially decreasing terms;

(b) In a lossy medium, the rate of decrease would be less. The  $H_z$ -component (see Figures 18-21, 26) doesn't have the step behavior because the contribution of the second mode is proportional to  $x_1$ , which goes to 0, when  $\tilde{z} \rightarrow \tilde{z}_0$ . The other two components,  $E_x$  and  $E_z$ , are equal to zero on the x-axis and have their largest contribution for  $\frac{y}{H} = 0.5$  (see Figures 2-5, 10-13).  $E_x$  is smooth and  $E_z$  exhibits the step behavior at  $\tilde{z}_0$ . The figures demonstrate that the complexity of the curves occurs approximately in the region  $0.7 < \tilde{z} < 0.8$ , where we observe a sharp peak, which is due to the resonance. In the region  $0 < \tilde{z} < 0.3$  the figures demonstrate the very smooth character of the curves.

### 3. Real and Imaginary Parts of the Field Components as Functions of Transverse Coordinates

In this section we present the real and imaginary parts of the dominant field components  $E_y$ ,  $H_x$ ,  $H_z$  as functions of the x-coordinate for two values of  $\frac{y}{H} = 0.0; 0.5$  and two values of  $\tilde{z} = 0.4; 0.75$ . The graphic output, shown in Figures 28-33, was obtained using the results of calculations for 81 points of  $\frac{x}{L}$  in the region  $[0.1, 0.9]$  (step = 0.01). All the graphs have very smooth characteristics. For  $\tilde{z} = 0.75$  they have slightly more complicated form than for  $\tilde{z} = 0.4$ . As mentioned in the



previous section, for  $\frac{y}{H} = 0.5$  the contribution of the second mode equals zero. We see that the amplitudes of the curves are constant for the entire region of view. For the  $\frac{y}{H} = 0.0$ , the field components are sums of the contributions of two modes. One can observe that the amplitudes of the curves are changing along the x-direction.

## IV. CONCLUSIONS

In this report the problem of a source excitation of an open parallel-plate waveguide was developed. Extensive numerical results for the field components in the waveguide as functions of several parameters of the waveguide and propagation constant were supplied.

## V. REFERENCES

- [1] V. Krichevsky and R. Mittra, "Source excitation of an open parallel-plate waveguide," Sensor and Simulation Note 25, October 1977.

## VI. APPENDIX A

## SOURCE EXCITATION OF AN OPEN, PARALLEL-PLATE WAVEGUIDE PROGRAM

A complete program for source excitation of an open, parallel-plate waveguide program is presented. The computer program provides three-dimensional data-storage for the real and imaginary parts of five components of the EM field. Data were obtained for  $\frac{x}{L}$  between 0.1 - 0.9 with step 0.1;  $\frac{y}{H}$  between 0.0 - 0.9 with step 0.1; and  $\beta$  - propagation constant between 0.0 - 0.93 with step 0.005 plus ( $\cdot$ ) 0.80009. These data were used to plot EM field components as functions of the propagation constant. The program can be readily modified to obtain data for plotting the EM-field component as a function of the  $x$ -coordinate.

```

PROGRAM AFIELD(INPUT,OUTPUT,TAPE3,TAPE1=INPUT)
COMPLEX BBK,BBAL,T1,F1,F2,EX0,EY0,EZ0,HX0,HZ0,CONST,AA,BB
DIMENSION XX(9),YY(10),BETAB(188),REX0(10,9,138),AMEX0(10,9,188),
$REY0(10,9,188),AMEY0(10,9,188),REZO(10,9,188),AMEZO(10,9,188),
$RHX0(10,9,188),AMHX0(10,9,188),RHZO(10,9,188),AMHZO(10,9,188)
READ(1,2)W,YBRI,YBRS,YBRF,XBRI,XBRS,XBRF
2 FORMAT(F7.5,6(F7.3))
M=1000
PI=3.141592654
CONST=CMPLX(0.,1.)
CON=2.11593152
BETAB(1)=0.
DO 70 I=1,160
BETAB(I+1)=BETAB(I)+0.005
70 CONTINUE
BETAB(162)=0.80009
BETAB(163)=0.305
DO 75 I=1,25
75 BETAB(I+163)=BETAB(I+162)+0.005
CONTINUE
DO 98 N=1,161
BETA=BETAB(N)
K=N
A=10.*PI*SQRT(1.-BETA**2)
B=W/PI
ALFA1=SQRT(B**2-1.)
DD=PI*ALFA1/W
CALL BE1(A,B,BBK,PI,M,CON,ALFA1)
CALL BE2(A,B,BBAL,PI,M,CON,ALFA1)
CALL TE1(A,B,T1,BBK,PI)
CALL F12(A,B,T1,ALFA1,BBK,BBAL,F1,F2)
X=XBRI
J=1
30 Y=YBRI
I=1
20 EX0=(PI*ALFA1/(10.*W**2))*F2*SIN(PI*Y)*SIN(DD*X)
EY0=10.*PI*(F1*COS(A*X)+(1.-(1./(100.*W**2)))*F2*COS(PI*Y)*
$COS(DD*X)-CEXP(CMPLX(0.,A*X))/(2.*A))
EZ0=-CONST*BETA*(PI/W)*F2*SIN(PI*Y)*COS(DD*X)
HX0=-BETA*10.*PI*(F1*COS(A*X)+F2*COS(PI*Y)*COS(DD*X)-(1./(2.*A))*
$CEXP(CMPLX(0.,A*X)))
HZ0=CONST*A*F1*SIN(A*X)+CONST*DD*F2*COS(PI*Y)*SIN(DD*X)-
$0.5*CEXP(CMPLX(0.,A*X))
REX0(I,J,K)=REAL(EX0)
AMEX0(I,J,K)=AIMAG(EX0)
REY0(I,J,K)=REAL(EY0)

```

```

AMEYO(I,J,K)=AIMAG(EYO)
REZO(I,J,K)=REAL(EZO)
AMEZO(I,J,K)=AIMAG(EZO)
RHXO(I,J,K)=REAL(HXO)
AMHXO(I,J,K)=AIMAG(HXO)
RHZO(I,J,K)=REAL(HZO)
AMHZO(I,J,K)=AIMAG(HZO)
Y=Y+YBRS
I=I+1
IF(Y.LE.YBRF) GO TO 20
X=X+XBRS
J=J+1
IF(X.LE.XBRF) GO TO 30
98 CONTINUE
DO 99 L=162,188
  BETAB=BETAB(L)
  K=L
  A=10.*PI*SQRT(1.-BETAB**2)
  X=XBRI
  J=1
  B=A*W/PI
  CALL BE(A,B,BB,PI,M)
  X=XBRI
17 AA=CEXP(CMPLX(0.,A*X))
  EYO=-0.5*(AA-BB*COS(A*X))/SQRT(1.-BETAB**2)
  HXO=-BETAB*EYO
  HZO=0.5*(-SIGN(1.,X)*AA+CONST*BB*SIN(A*X))
  DO 18 I=1,10
    REXO(I,J,K)=0.
    AMEXO(I,J,K)=0.
    REZO(I,J,K)=0.
    AMEZO(I,J,K)=0.
    REYO(I,J,K)=REAL(EYO)
    AMEYO(I,J,K)=AIMAG(EYO)
    RHXO(I,J,K)=REAL(HXO)
    AMHXO(I,J,K)=AIMAG(HXO)
    RHZO(I,J,K)=REAL(HZO)
    AMHZO(I,J,K)=AIMAG(HZO)
18 AMHZO(I,J,K)=AIMAG(HZO)
  X=X+XBRS
  J=J+1
  IF(X.LE.XBRF) GO TO 17
99 CONTINUE
WRITE(3,101) REXO,AMEXO,REYO,AMEYO,REZO,AMEZO,RHXO,AMHXO,RHZO,AM
$HZO
101 FORMAT(10F9.5)
  DY=0.1
  DX=0.1
  YY(1)=0.
  DO 50 I=1,9
    YY(I+1)=YY(I)+DY
30 CONTINUE

```

```

      XX(1)=0.1
      DO 60 I=1,8
      XX(I+1)=XX(I)+DX
60  CONTINUE
      WRITE(3,101) YY,XX,BETAB
      STOP
      END
      SUBROUTINE BE1(A,B,BBK,PI,M,CON,ALFA1)
      COMPLEX F,BBK
      AM1=0.
      DO 10 I=2,M
      AM1=AM1+B/I-ASIN(B/I)
10  CONTINUE
      F=CEXP(CMPLX(-B*PI/2.,B*(CON-ALOG(B))-PI/2.+A+AM1))
      BBK=(ALFA1+B)*F
      RETURN
      END
      SUBROUTINE BE2(A,B,BBAL,PI,M,CON,ALFA1)
      COMPLEX F,BBAL,D
      AM1=0.
      DO 10 I=2,M
      AM1=AM1+ALFA1/I-ASIN(ALFA1/SQRT(I**2-1.))
10  CONTINUE
      F=CEXP(CMPLX(-ALFA1*PI/2.,ALFA1*(CON-ALOG(B))+AM1+ALFA1*A/B))
      D=CMPLX(1.,-ALFA1)
      BBAL=F*D*SQRT(2.)*ALFA1/B
      RETURN
      END
      SUBROUTINE TE1(A,B,T1,BBK,PI)
      COMPLEX T1,BBK,D1
      D=B*SQRT(PI)/SQRT(A*2.)
      D1=CMPLX(1.+D,-D)
      T1=BBK**2*D1
      RETURN
      END
      SUBROUTINE F12(A,B,T1,ALFA1,BBK,BBAL,F1,F2)
      COMPLEX T1,BBK,BBAL,F1,F2,D1
      D1=ALFA1*(1.+T1)*(BBAL**2*(4.*T1*B/(1.+T1)-(ALFA1+B)**2/ALFA1)/
      *(2.*ALFA1)-1.)
      F1=(BBK**2/((1.+T1)*A))*(1.+2.*B*BBK**2/D1)
      F2=2.*B*BBK*BBAL/(A*D1)
      RETURN
      END
      SUBROUTINE BE(A,B,BB,PI,M)
      COMPLEX T,F,BB
      CONST=1.115931516
      AM1=0.
      DO 10 I=1,M
      AM1=AM1+B/I-ASIN(B/I)
10  CONTINUE
      T=CEXP(CMPLX(-B*PI,2.*(B*(CONST-ALOG(B))+A+AM1)))
      F1=SQRT(PI)*B/SQRT(2.*A)
      F=CMPLX(1.+F1,-F1)
      BB=2.*T/(1.+T*F)
      RETURN
      END

```

# VII. APPENDIX B

## ADDITIONAL NUMERICAL RESULTS

In Section III of this report, we have calculated the electromagnetic fields as functions of  $\beta$ , the normalized propagation constant in the  $z$ -direction. The parameters chosen for the computation in the report were:

$$\frac{H}{L} = 0.16670, \quad \frac{L}{\lambda_0} = 5, \quad \text{where } \lambda_0 = \frac{2\pi}{\omega\sqrt{\epsilon\mu}}.$$

At the request of Dr. D. Giri of SAI\*, we have now derived additional numerical results for the following choice of parameters, which correspond to those of the experimental parallel-plate structure being investigated at Harvard.

$$L = 12.5 \text{ m}$$

$$H = 12.75 \text{ m}$$

$$f = 25 \text{ Mhz } (\lambda_0 = 12\text{m})$$

$$\frac{H}{L} = 1.020; \quad \frac{L}{\lambda_0} = 1.041667$$

\*presently with LuTech, Inc., Berkeley, CA



The propagation constant in the x-direction can be written in the form:

$$\alpha_m = \frac{\pi}{H} \frac{kH}{\pi} - m^2 \quad m = 0, 1, 2, \dots$$

$$\text{where } k = k_0 \sqrt{1 - \beta^2}, \quad k_0 = \frac{2\pi}{\lambda_0}$$

$$kL \leq k_0 L = 2\pi \frac{L}{\lambda} = 6.544985.$$

The asymptotic analysis presented in this report was based on the assumption ( $kL \gg 1$ ). Consequently, great care should be exercised when the range of application of these formulas is extended below  $kL = 10$ .

It is not difficult to prove that in the range  $0 < \beta < 0.337916$ , only three modes are above cut-off in the x-direction. Furthermore, two modes are propagating in the range  $0.337916 < \beta < 0.882353$  and only one mode can propagate in the range  $\beta > 0.882353$ . The application of the formulas and computer programs developed in this report, though not the theory itself, is restricted to the range where two modes can propagate in the x-direction. For this reason, we develop the numerical results only for the region  $\beta \geq 0.34$ , and specifically for the range

$$0.34 \leq \beta \leq 0.9.$$

We would like to mention that it is possible to develop the necessary formulas and numerical results for the region  $0 < \beta < 0.34$  using the theory given in a previous report [1].

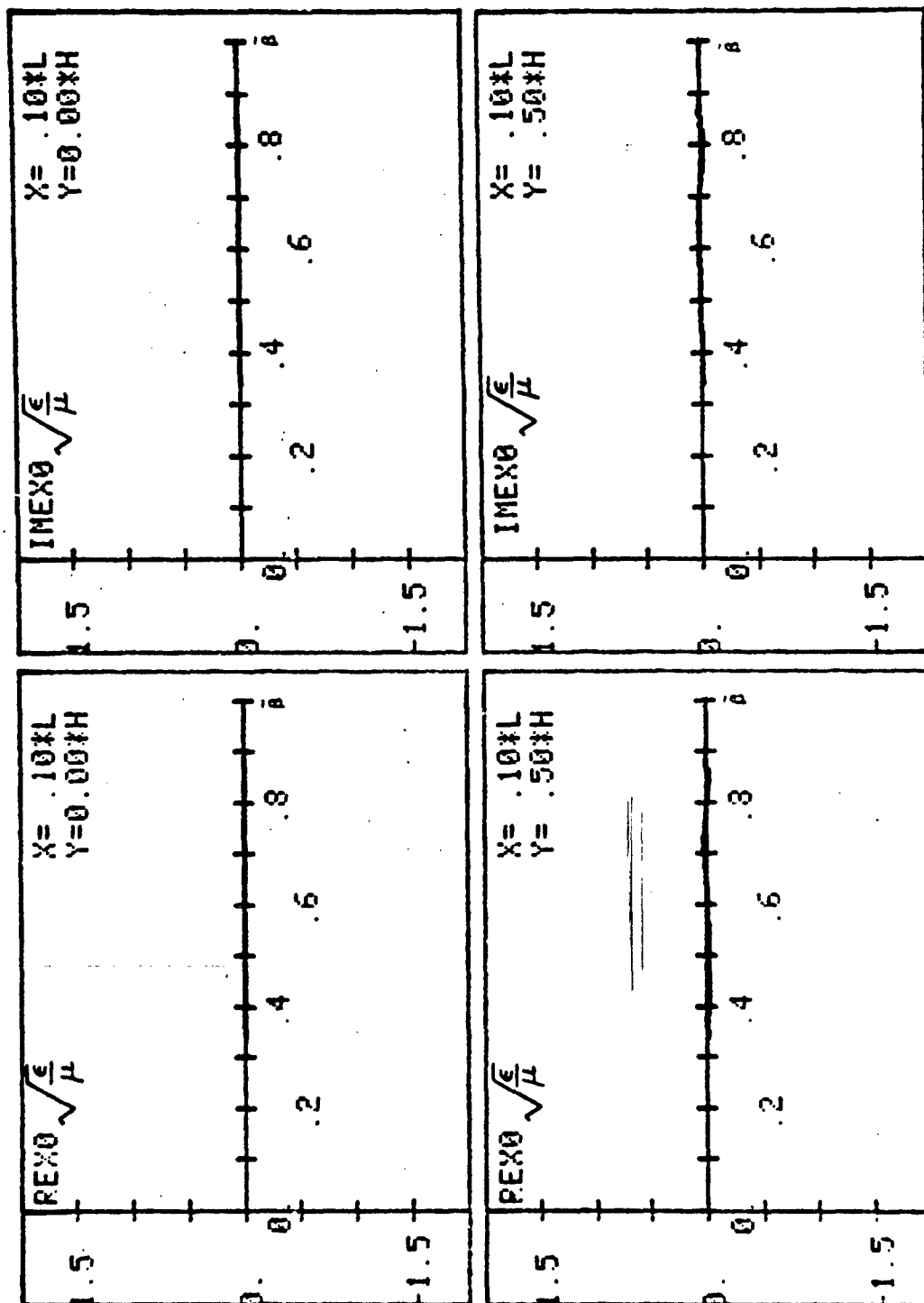


Figure 1. Real and imaginary parts of  $E_x$  as functions of  $\bar{\beta}$  for parameters given in the lower half of Page 1. The x,y values of the observation point are shown in the inset.

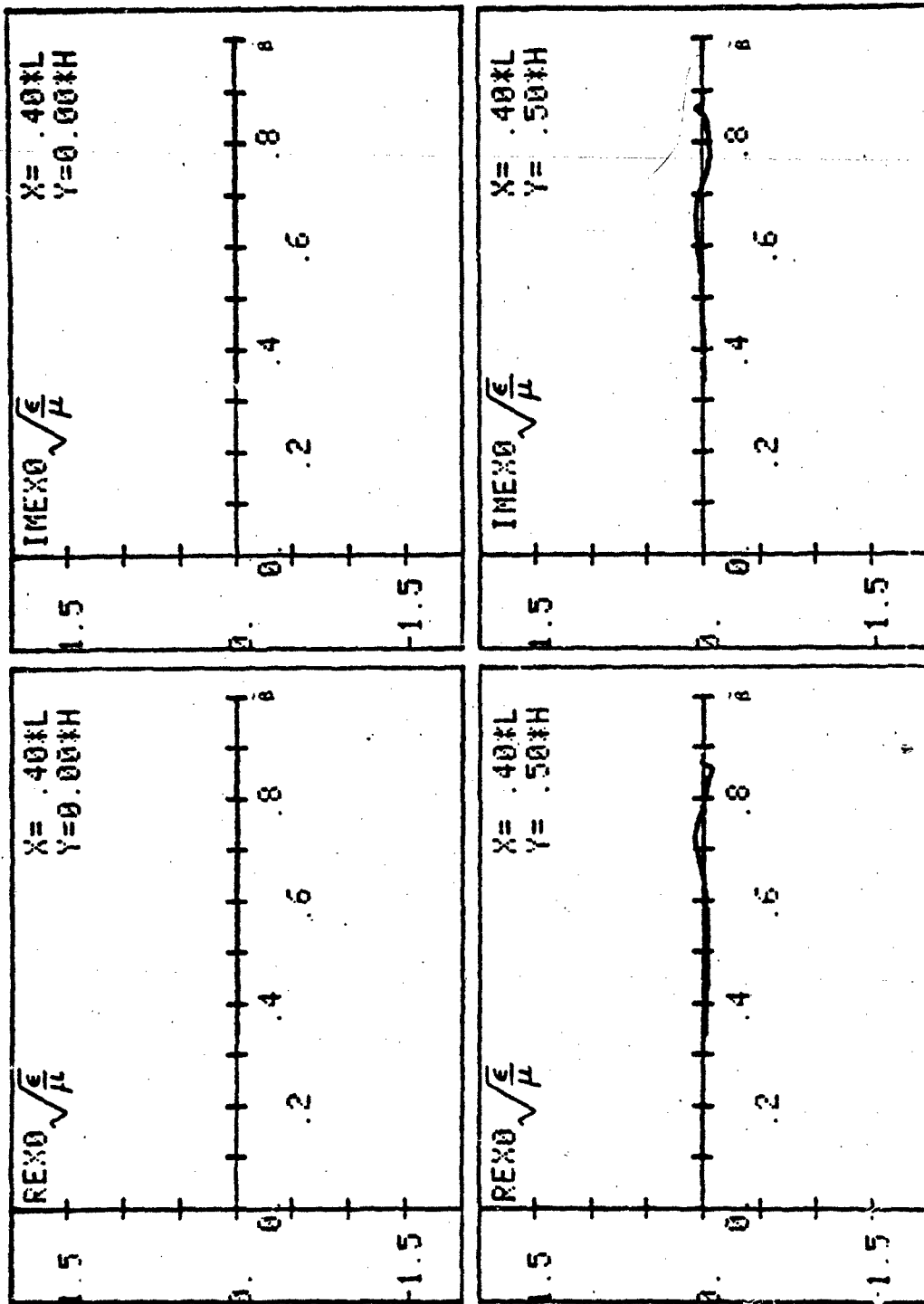


Figure 2. Real and imaginary parts of  $E$  as functions of  $B$  for parameters given in the lower half of Page 1. The  $x, y$  values of the observation point are shown in the inset.

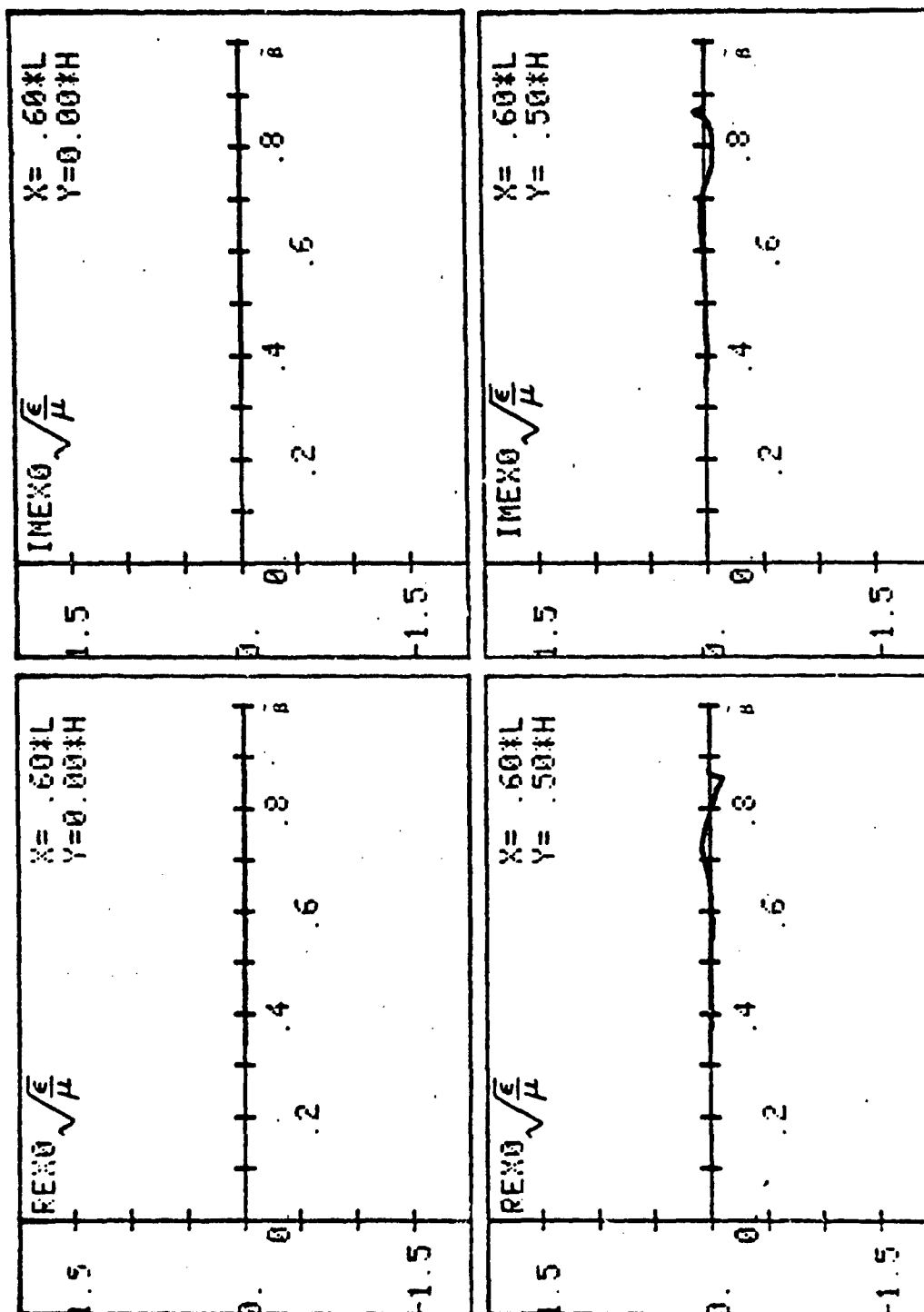


Figure 1. Real and imaginary parts of  $E_x$  as functions of  $B$  for parameters given in the lower half of Page 1. The  $x, y$  values of the observation point are shown in the inset.

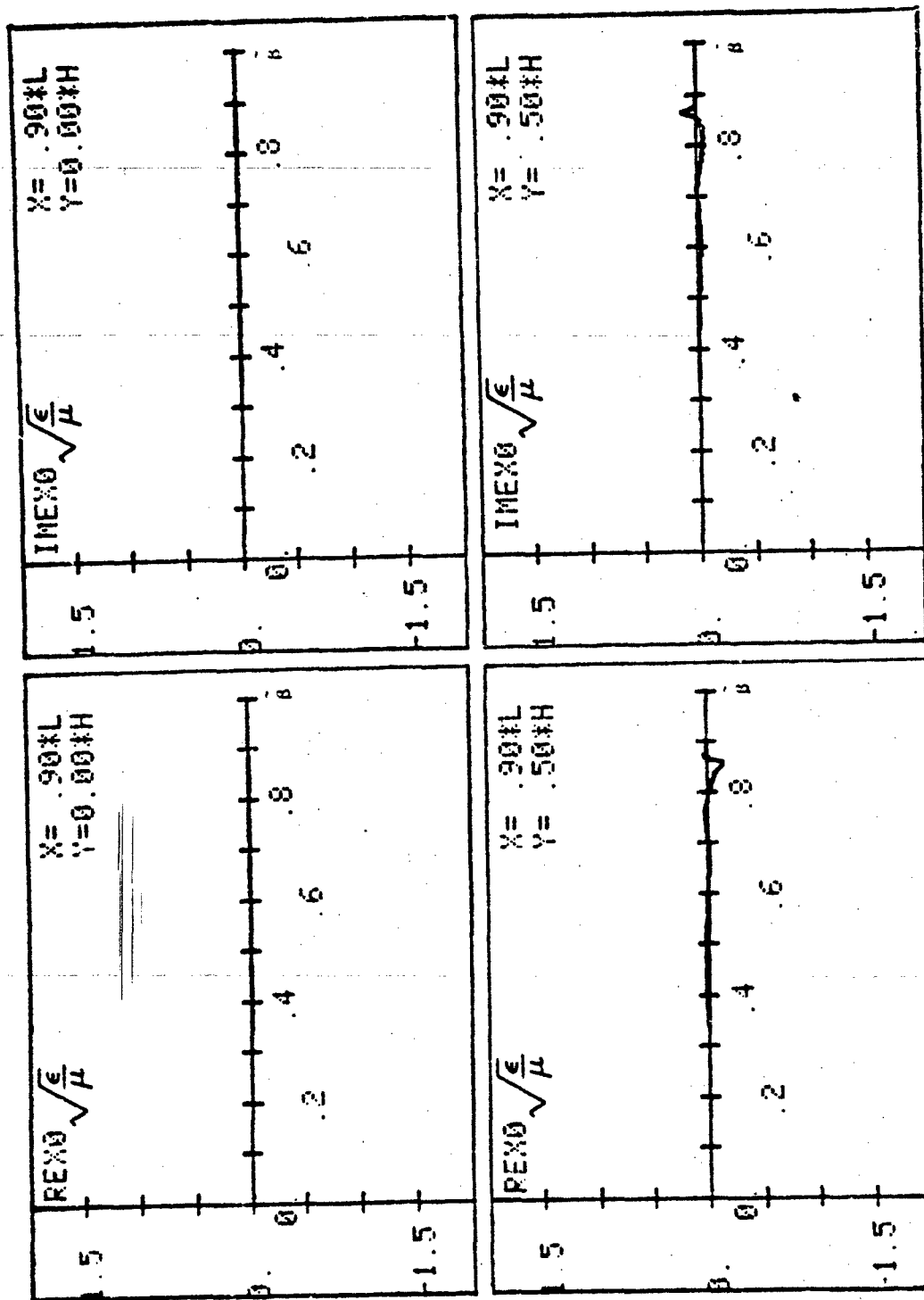


Figure 4. Real and imaginary parts of  $\epsilon$  as functions of  $\beta$  for parameters given in the lower half of Page 1. The x, y values of the observation point are shown in the inset.

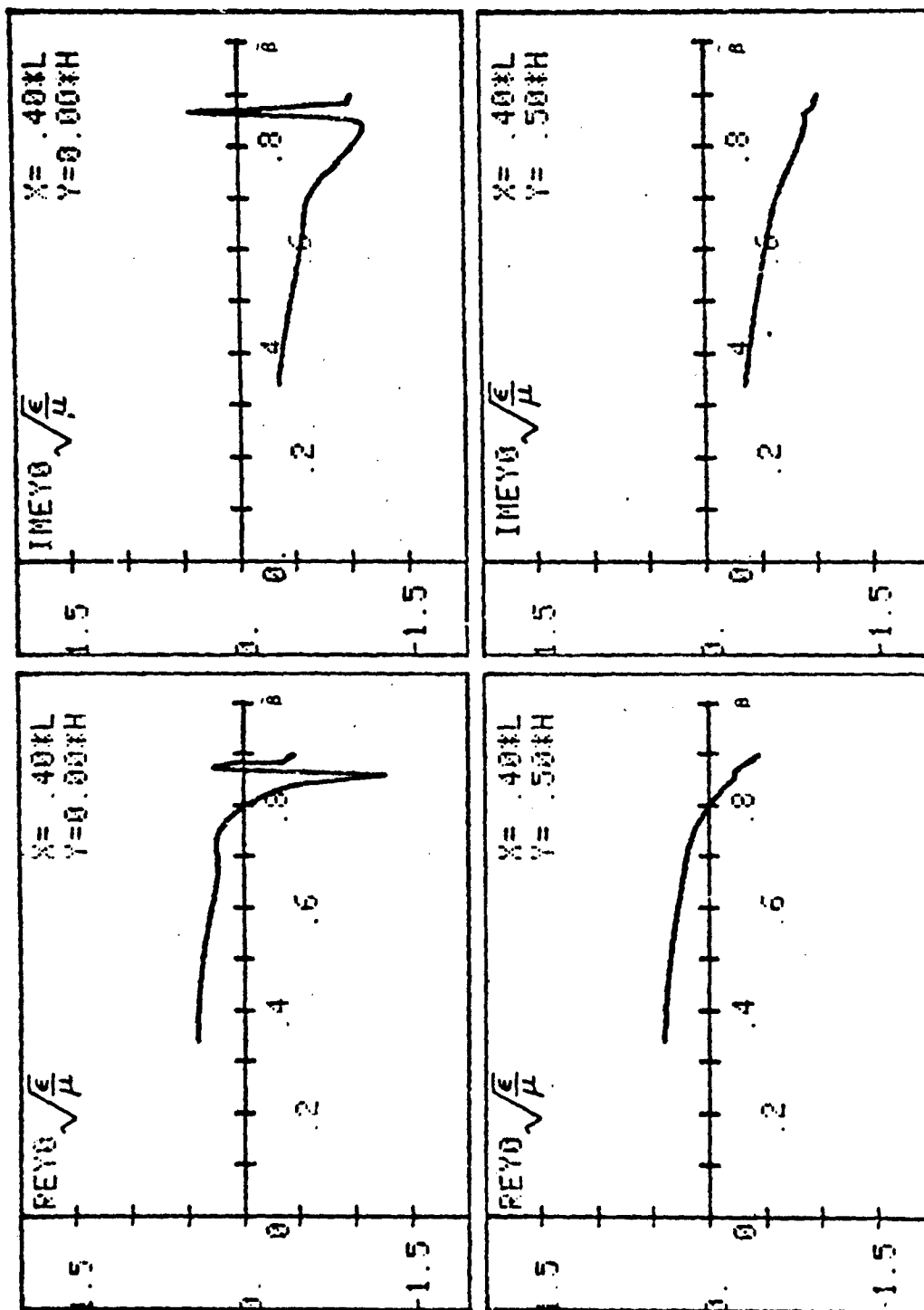


Figure 6. Real and imaginary parts of  $E$  as functions of  $\beta$  for parameters given in the lower half of Page 1. The  $x, y$  values of the observation point are shown in the inset.

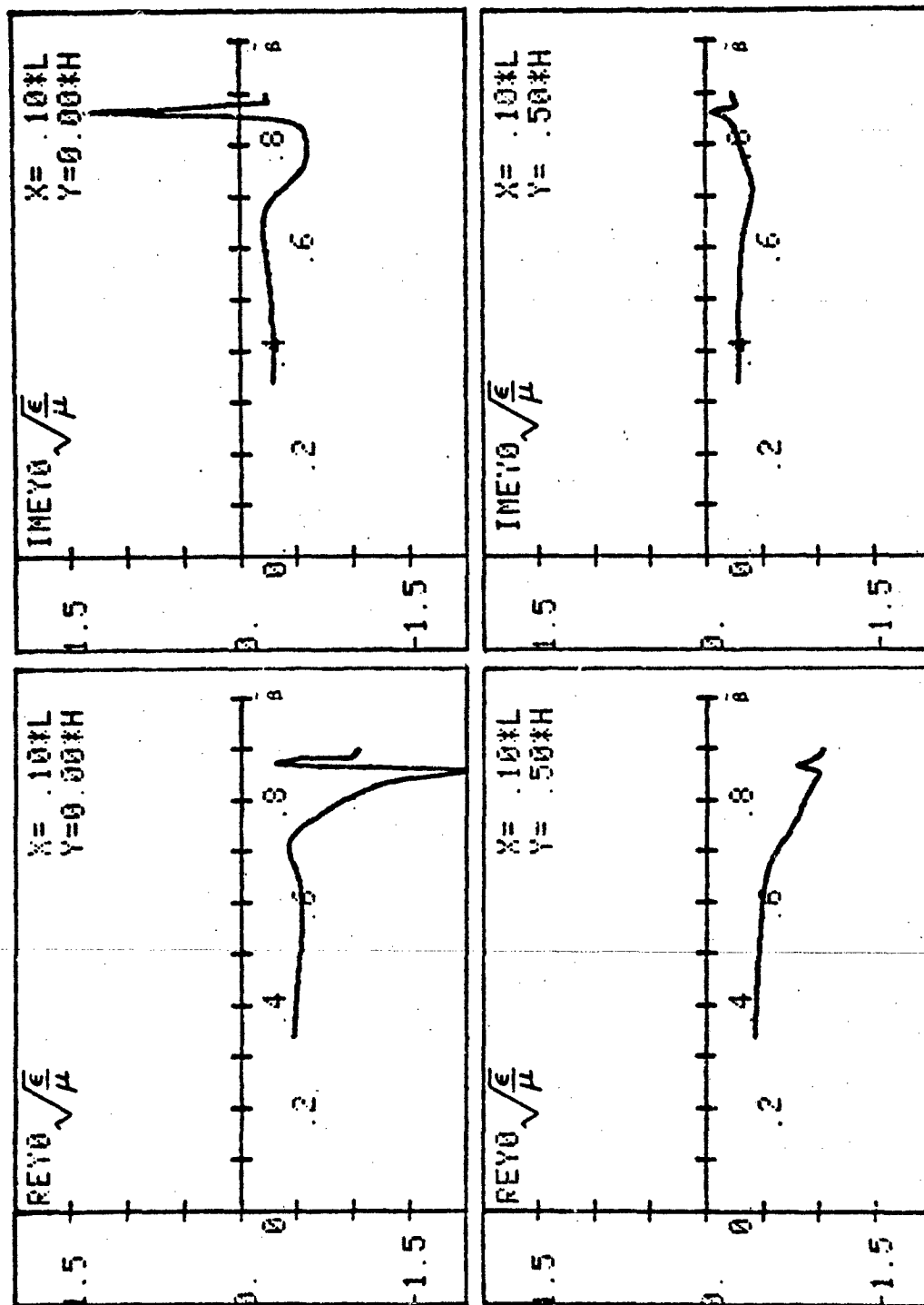


Figure 5. Real and imaginary parts of  $E$  as functions of  $\beta$  for parameters given in the lower half of Page 1. The  $x, y$  values of the observation point are shown in the inset.

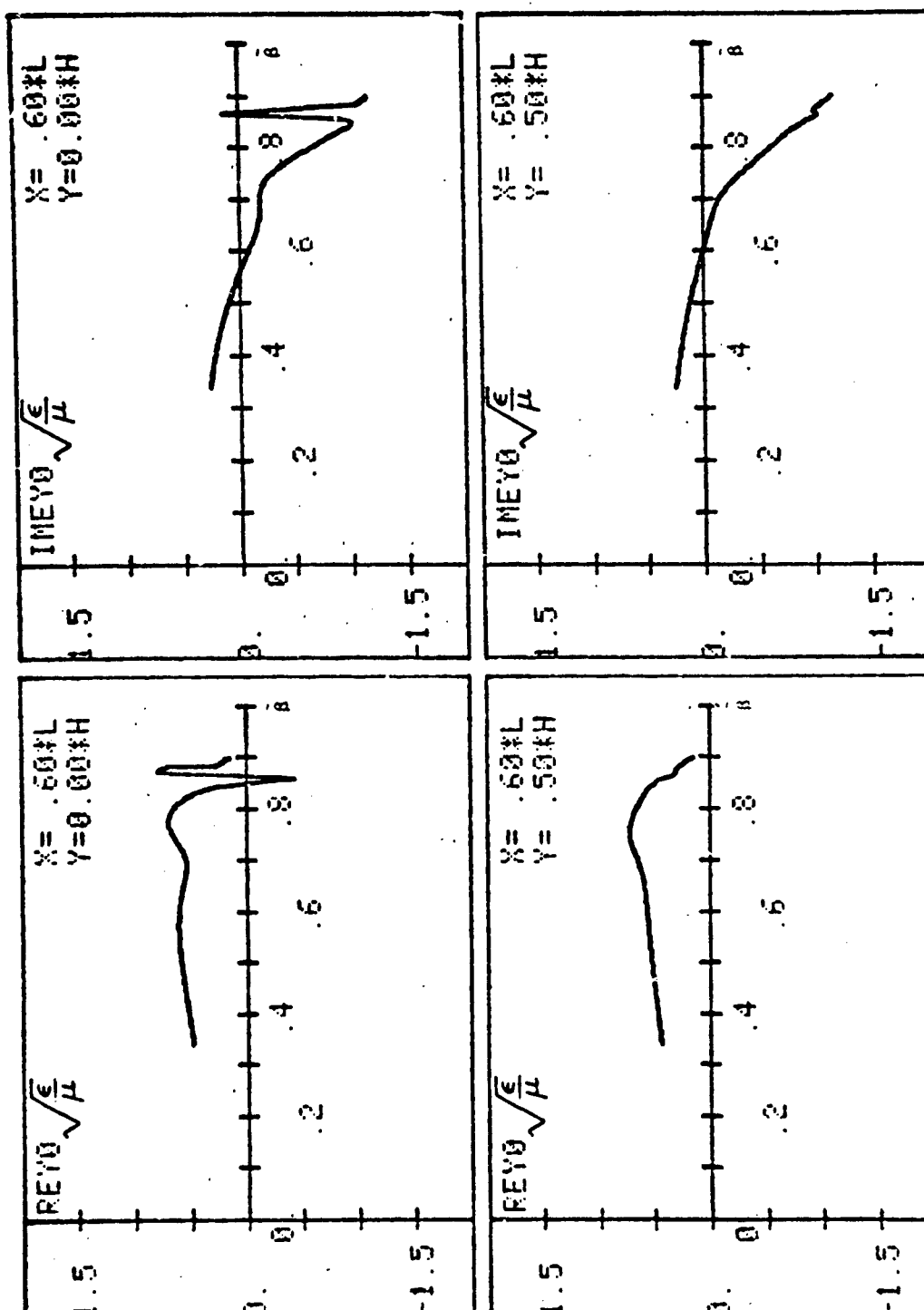


Figure 7. Real and imaginary parts of  $E$  as functions of  $\beta$  for parameters given in the lower half of page 1. The  $x, y$  values of the observation point are shown in the inset.



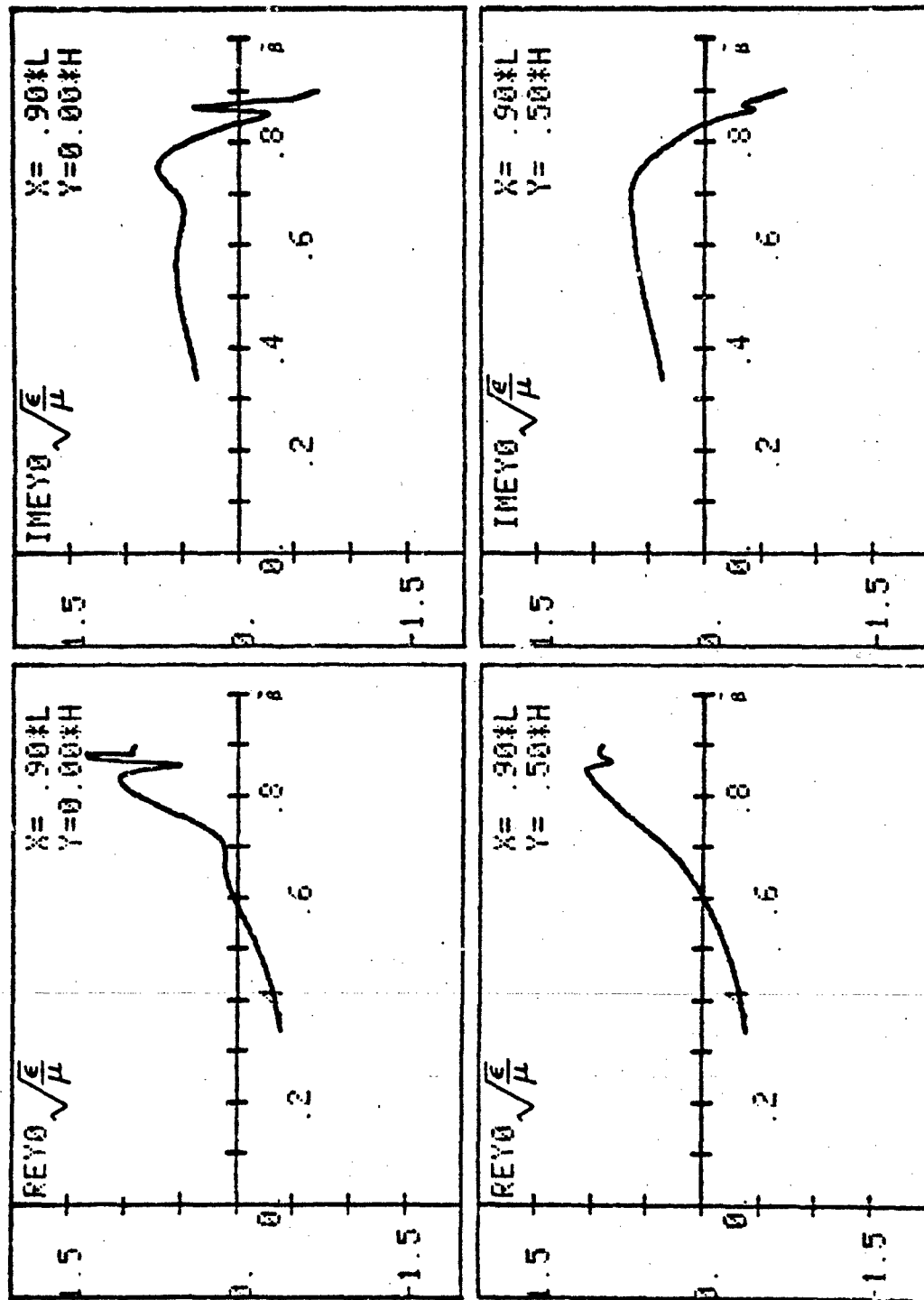


Figure 8. Real and imaginary parts of  $E_x$  as functions of  $\beta$  for parameters given in the lower half of Page 1. The  $x, y$  values of the observation point are shown in the inset.

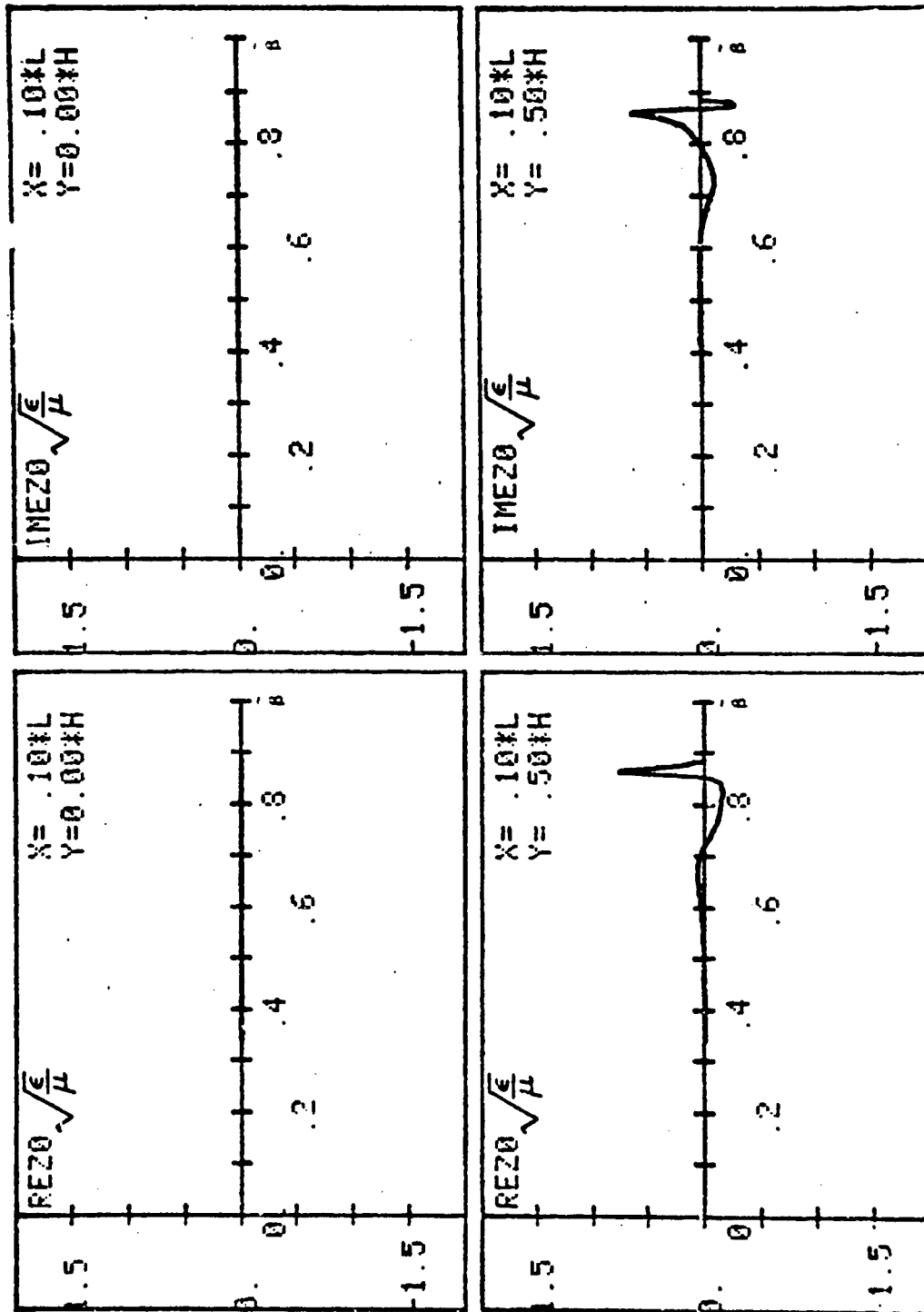


Figure 9. Real and Imaginary parts of  $E_x$  as functions of  $\beta$  for parameters given in the lower half of Page 1. The  $x, y$  values of the observation point are shown in the inset.

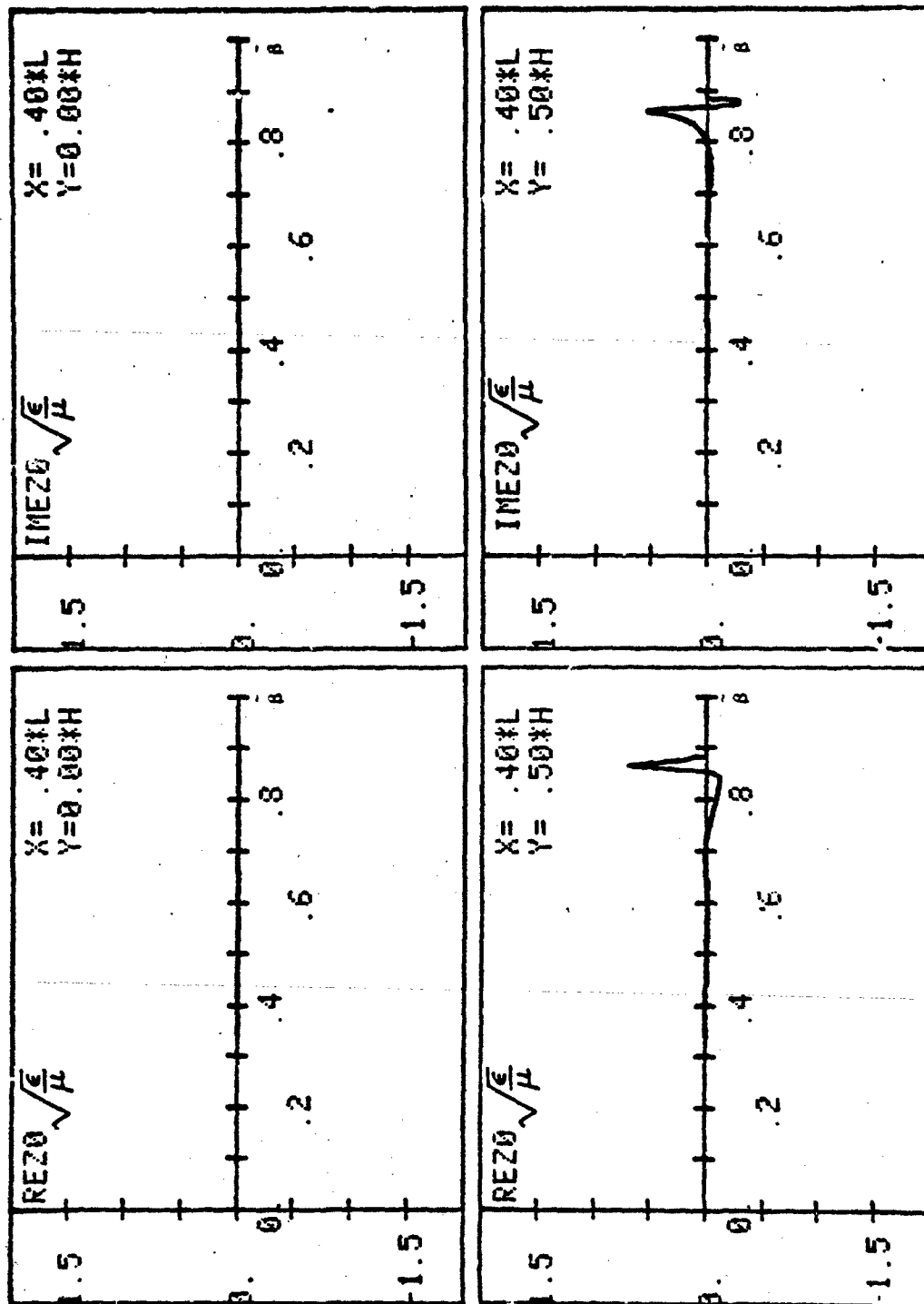


Figure 10. Real and imaginary parts of  $E_x$  as functions of  $\beta$  for parameters given in the lower half of Page 1. The  $x, y$  values of the observation point are shown in the inset.

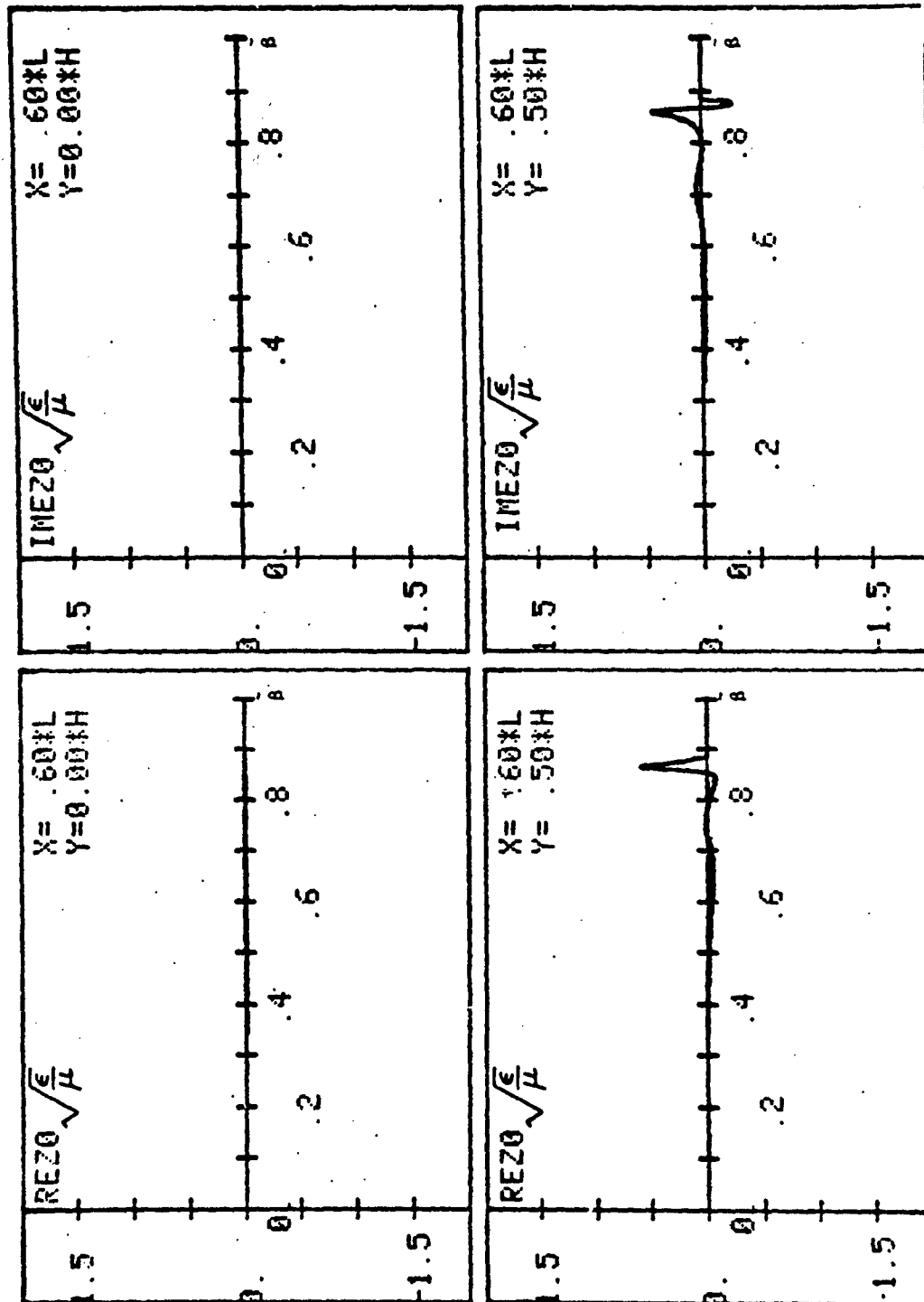


Figure 11. Real and imaginary parts of  $\beta$  as functions of  $\beta$  for parameters given in the lower half of Page 1. The  $x, y$  values of the observation point are shown in the inset.

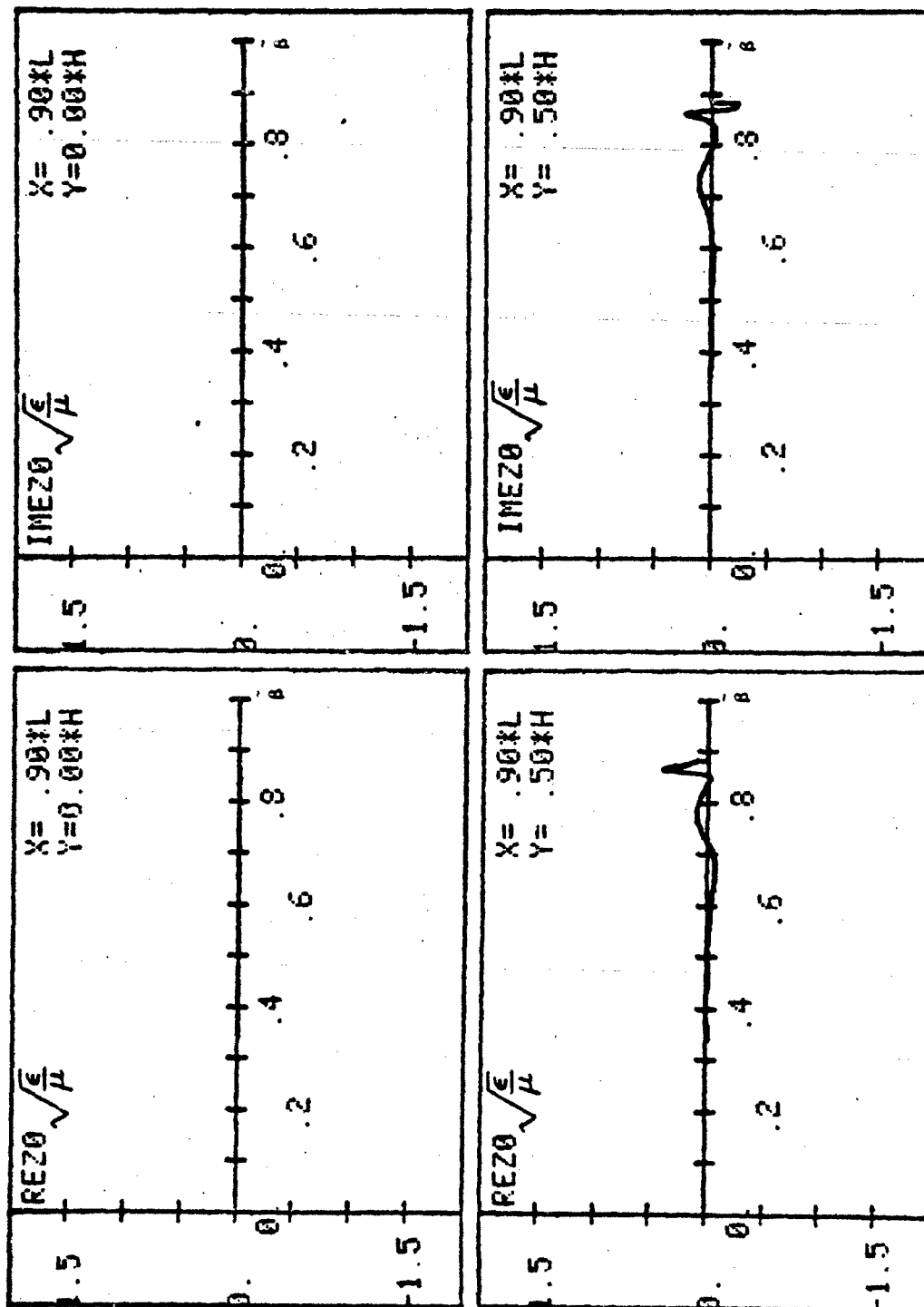


Figure 12. Real and imaginary parts of  $E_x$  as functions of  $\beta$  for parameters given in the lower half of page 1. The  $x, y$  values of the observation point are shown in the inset.

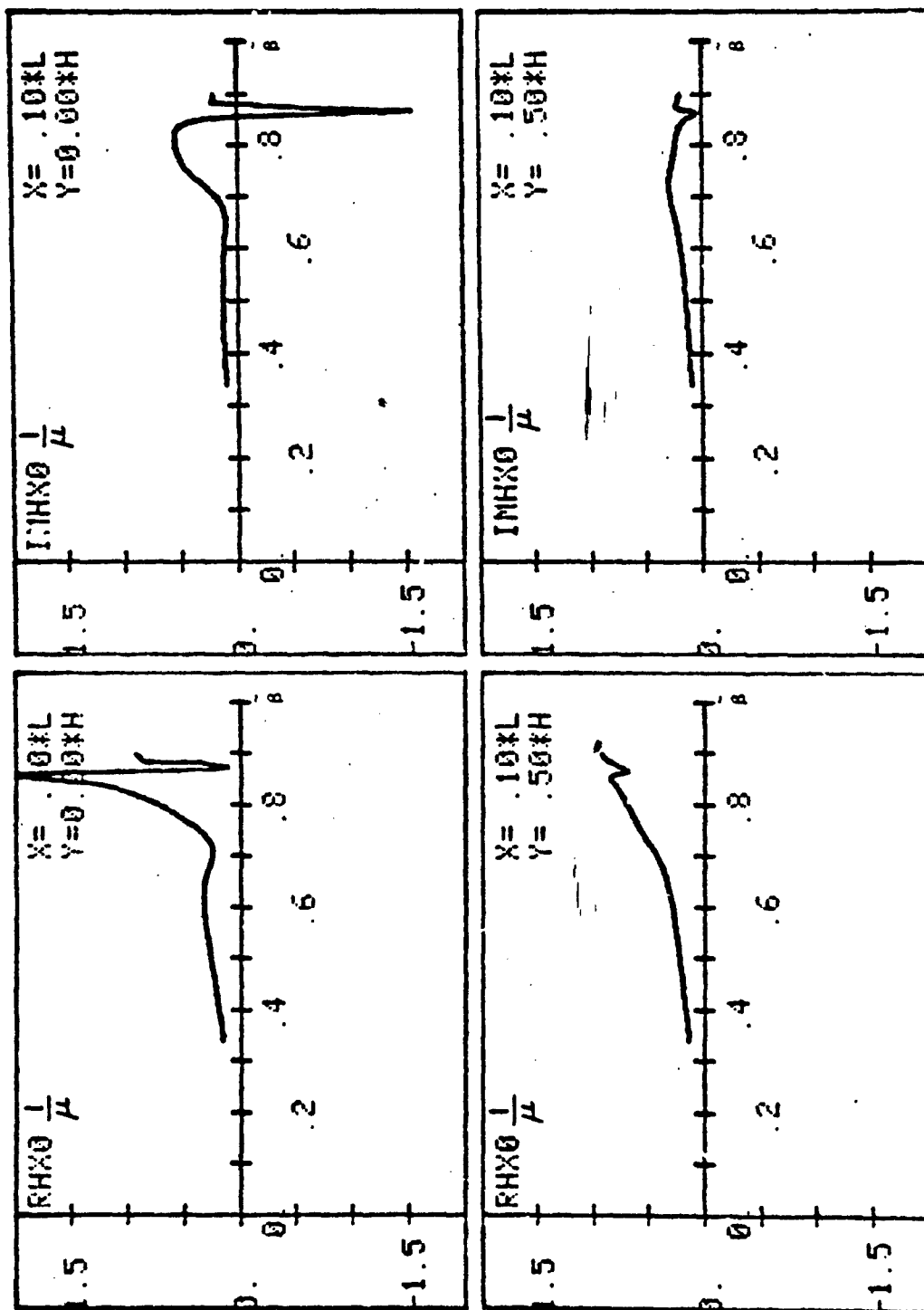


Figure 13. Real and imaginary parts of  $E_x$  as functions of  $B$  for parameters given in the lower half of Page 1. The  $x, y$  values of the observation point are shown in the inset.

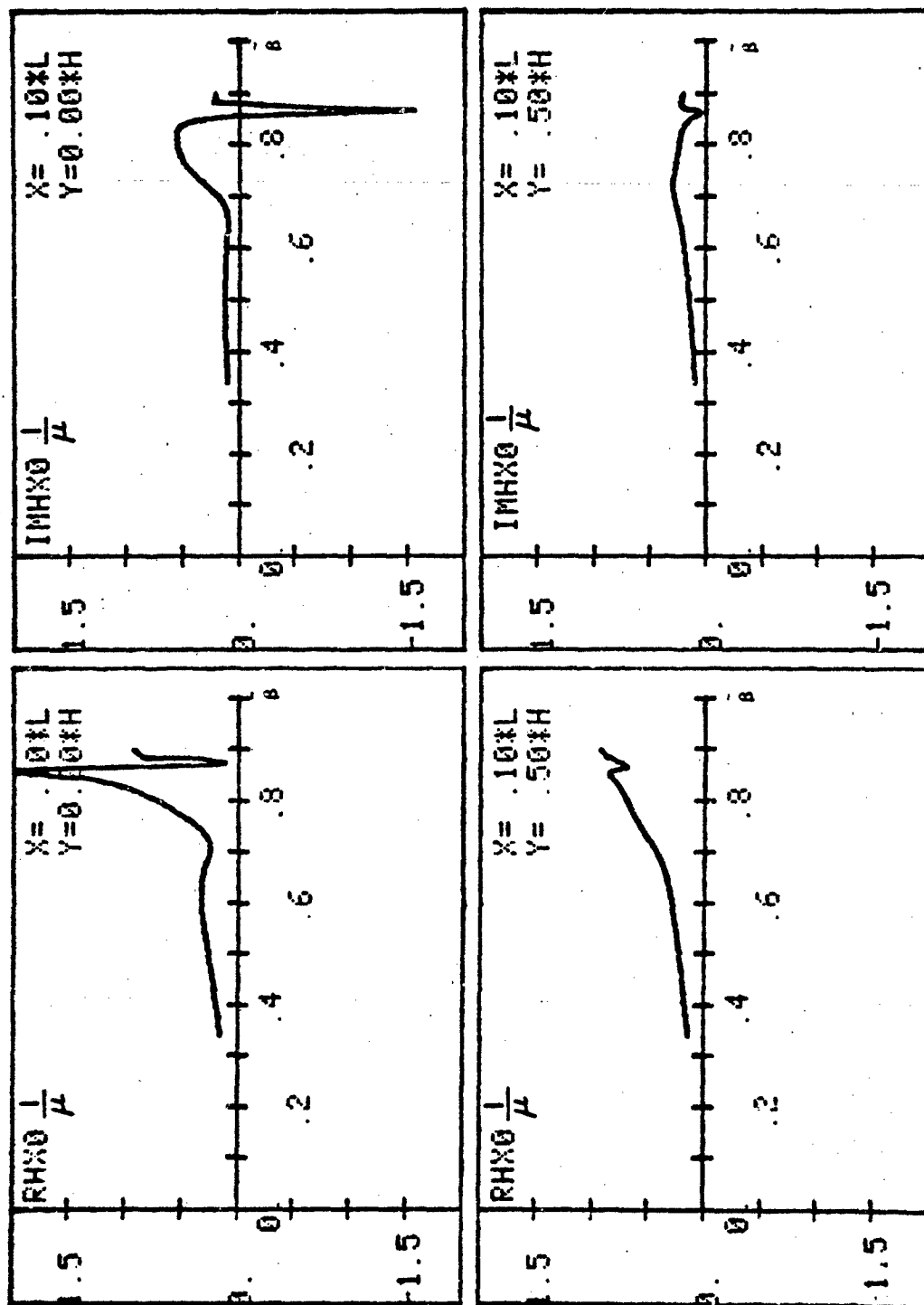


Figure 14. Real and imaginary parts of  $L$  as functions of  $B$  for parameters given in the lower half of Page 1. The  $x, y$  values of the observation point are shown in the inset.

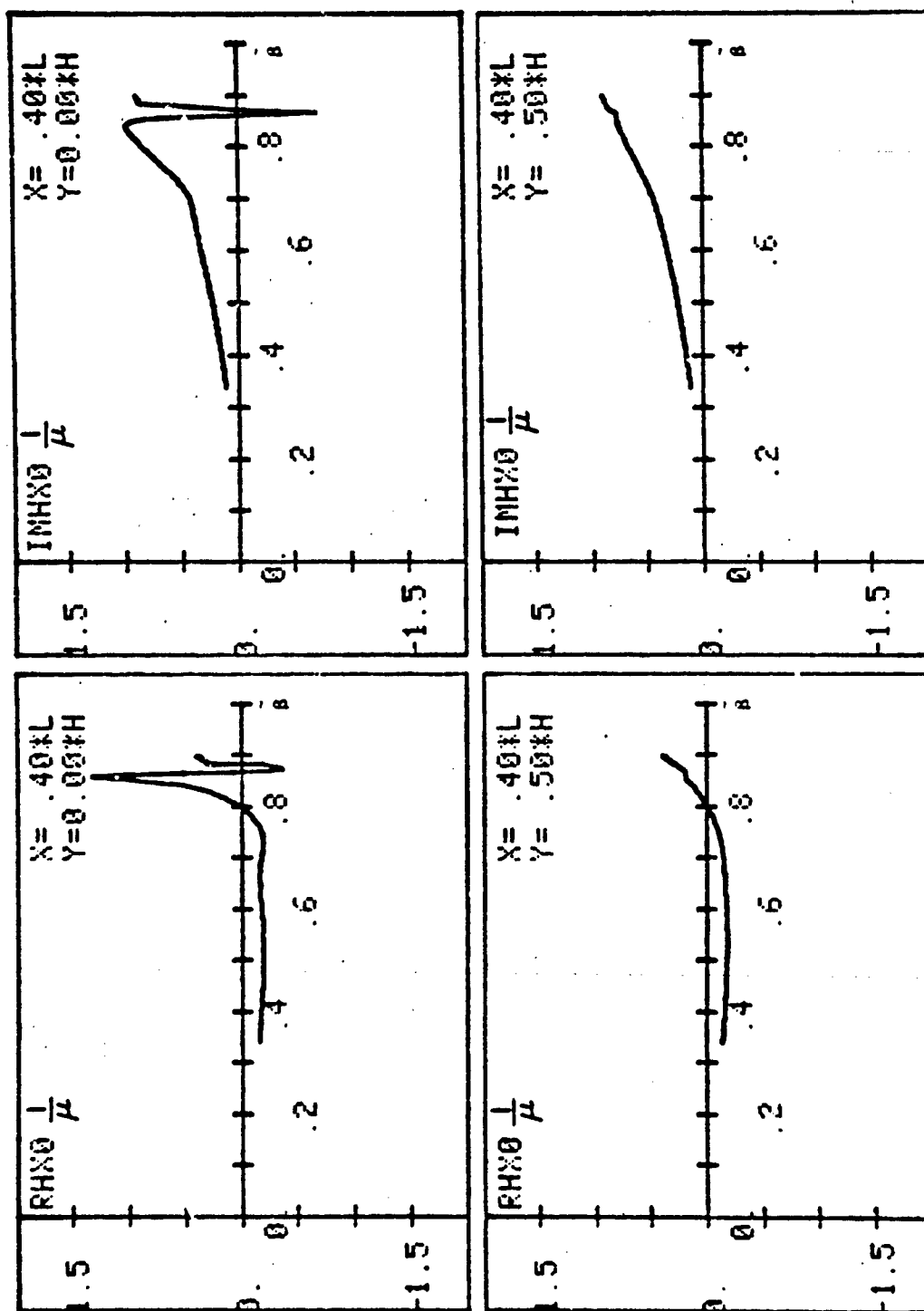


Figure 15. Real and imaginary parts of  $E_x$  as functions of  $\beta$  for parameters given in the lower half of Page 1. The  $x, y$  values of the observation point are shown in the inset.



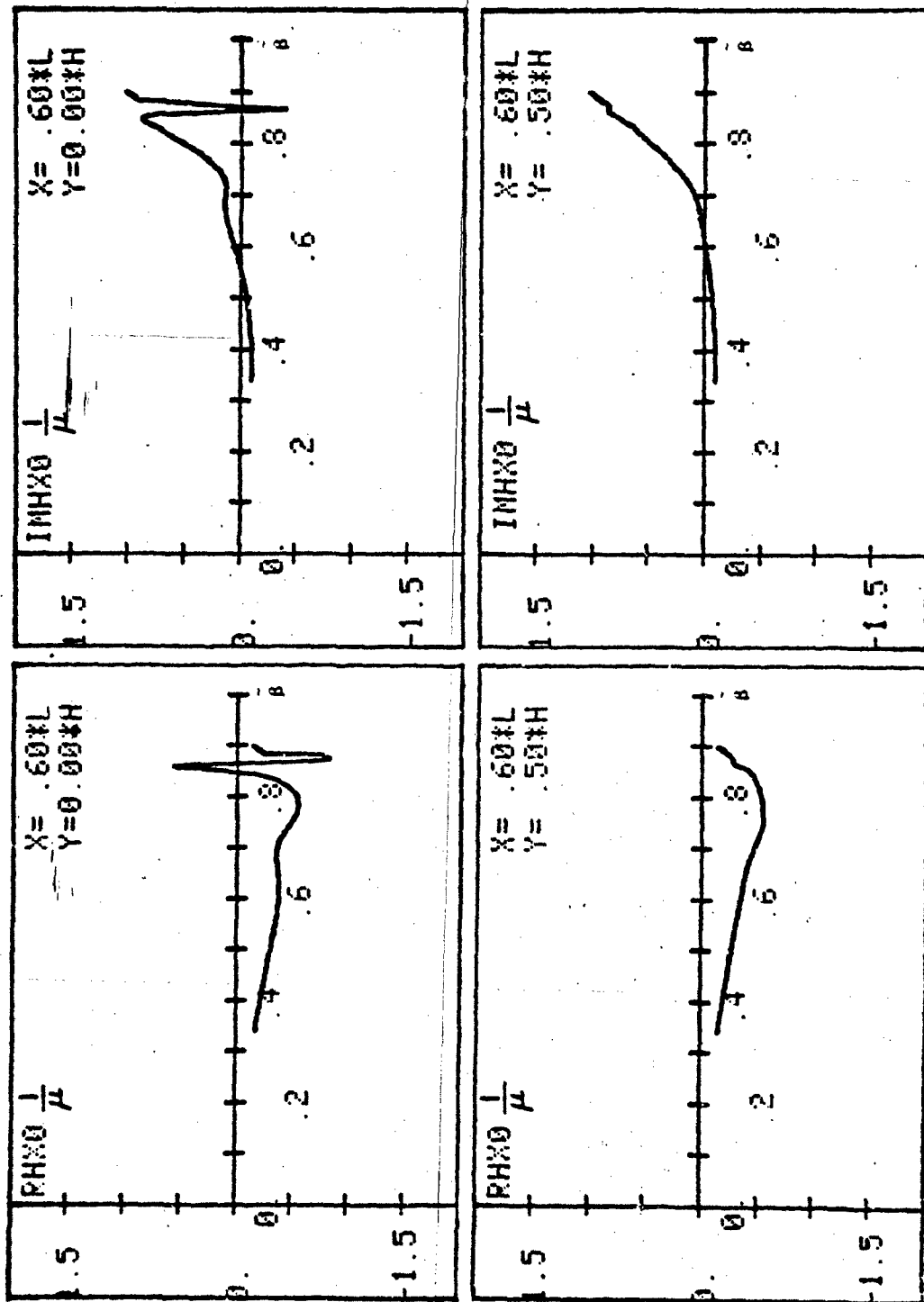


Figure 16. Real and imaginary parts of  $E_x$  as functions of  $\beta$  for parameters given in the lower half of Page 1. The  $x, y$  values of the observation point are shown in the inset.

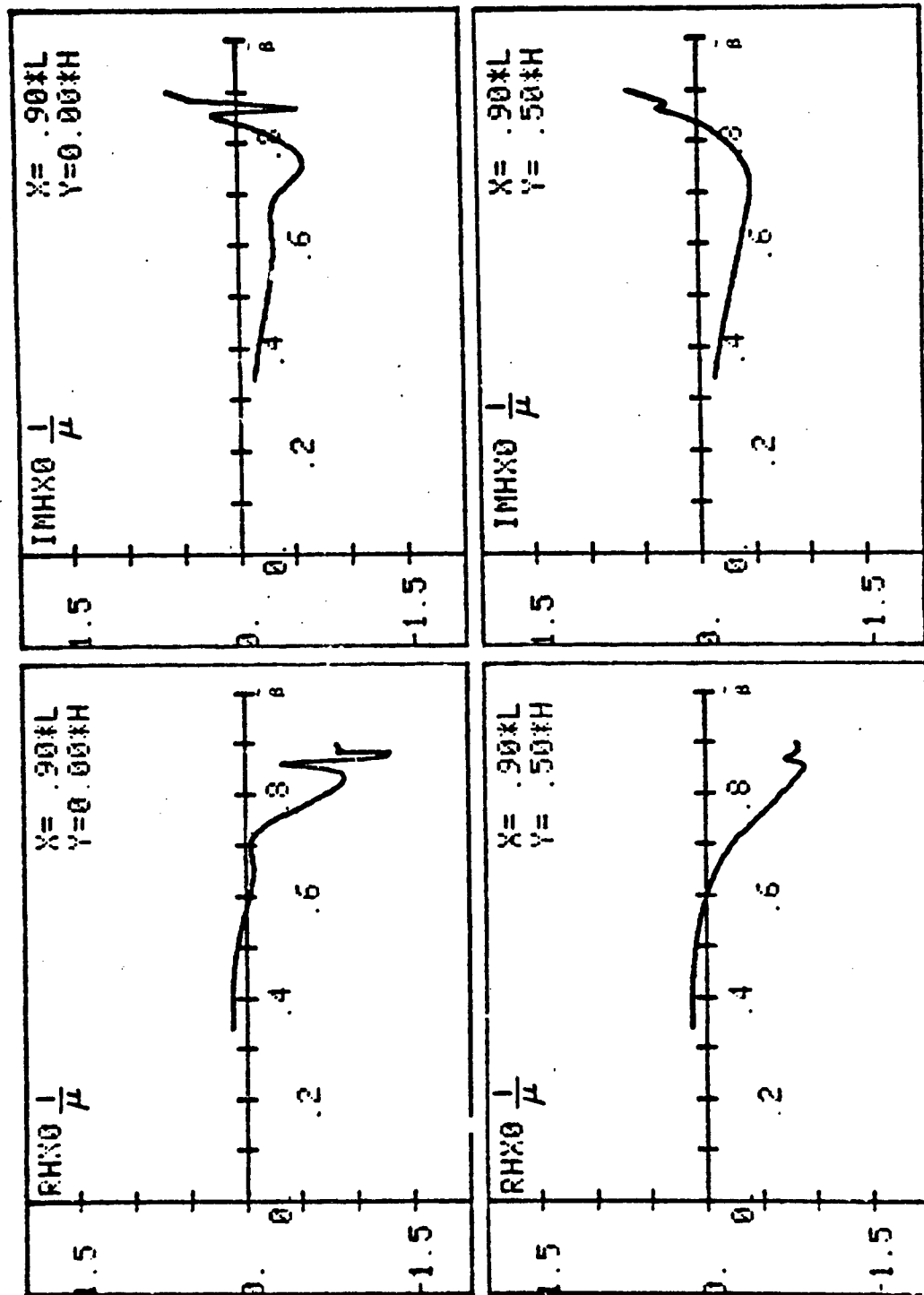


Figure 17. Real and imaginary parts of  $E_x$  as functions of  $\beta$  for parameters given in the lower half of Page 1. The  $x, y$  values of the observation point are shown in the inset.

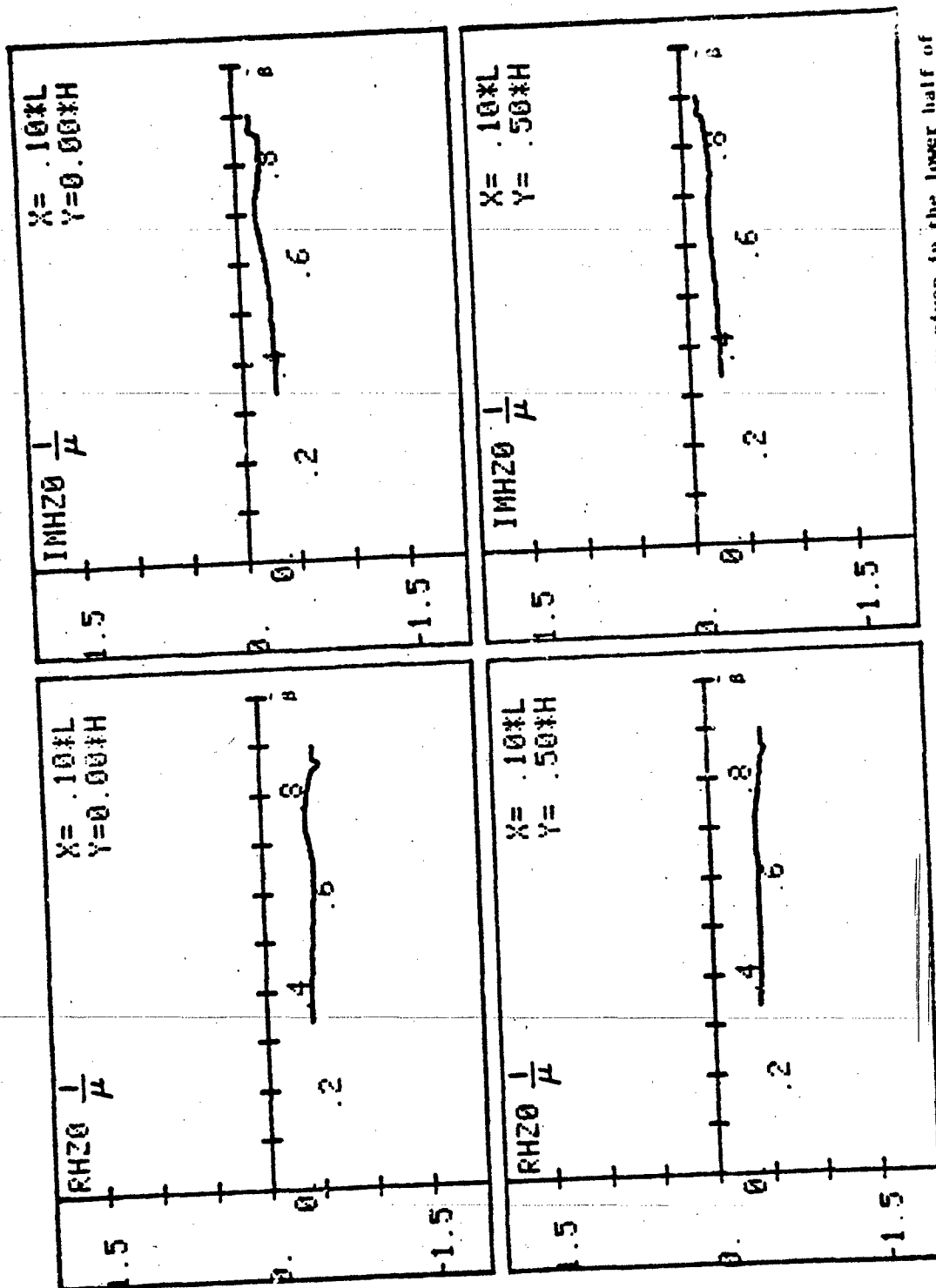


Figure 18. Real and imaginary parts of  $E$  as functions of  $\beta$  for parameters given in the lower half of page 1. The  $x, y$  values of the observation point are shown in the inset.

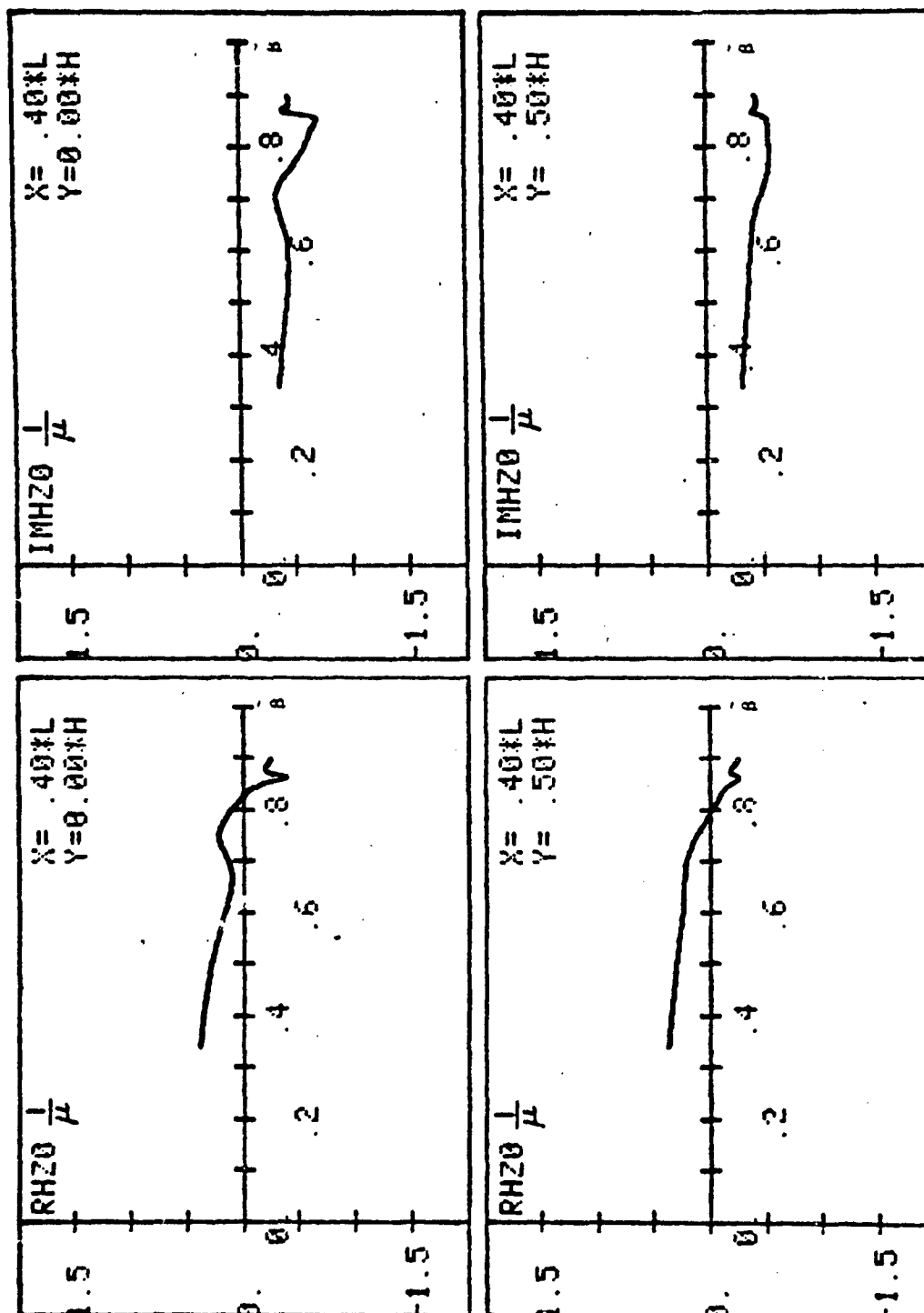


Figure 19. Real and imaginary parts of  $E_x$  as functions of  $\beta$  for parameters given in the lower half of Page 1. The  $x, y$  values of the observation point are shown in the inset.

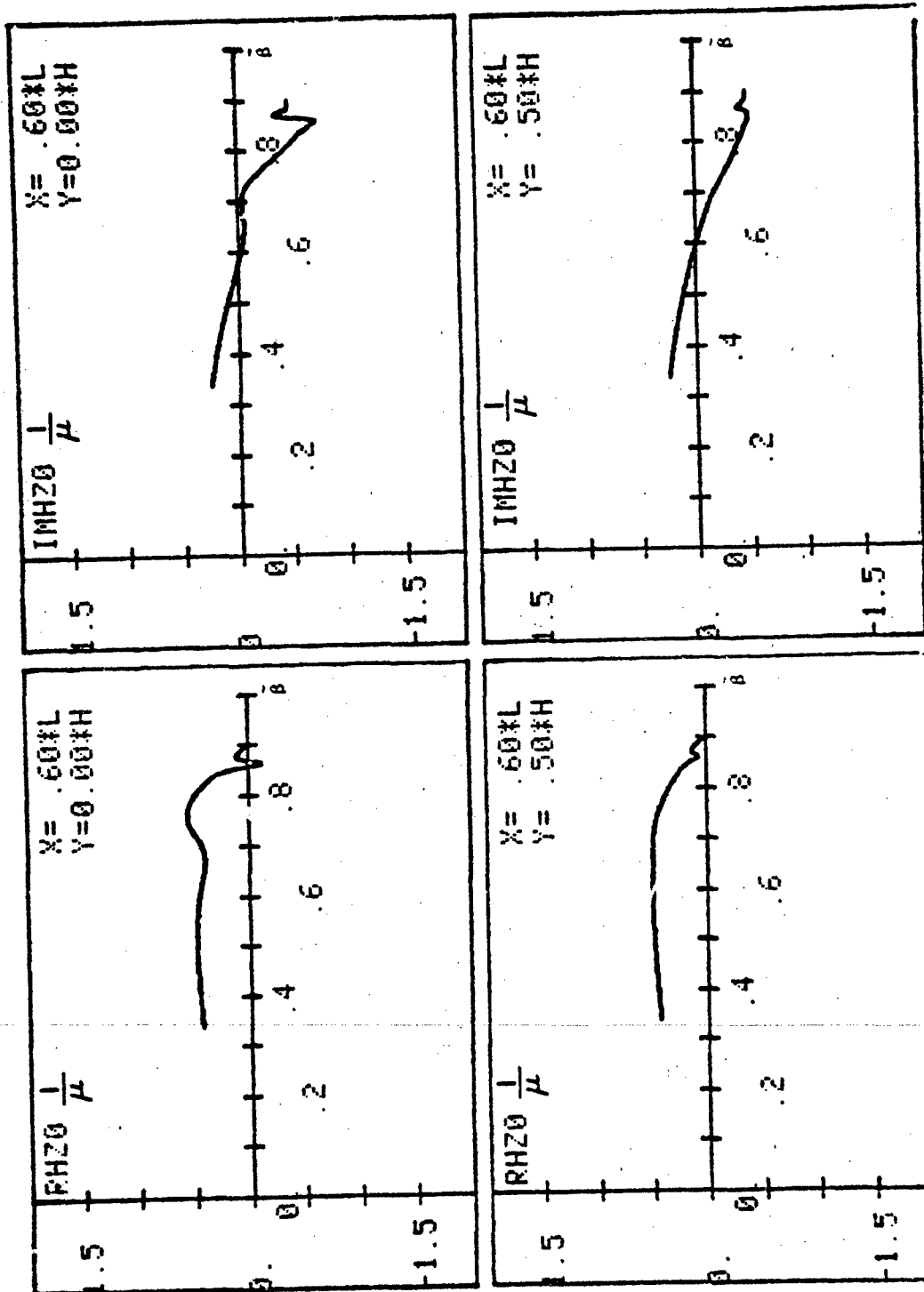


Figure 20. Real and imaginary parts of  $E_x$  as functions of  $\beta$  for parameters given in the lower half of Page 1. The  $x, y$  values of the observation point are shown in the inset.

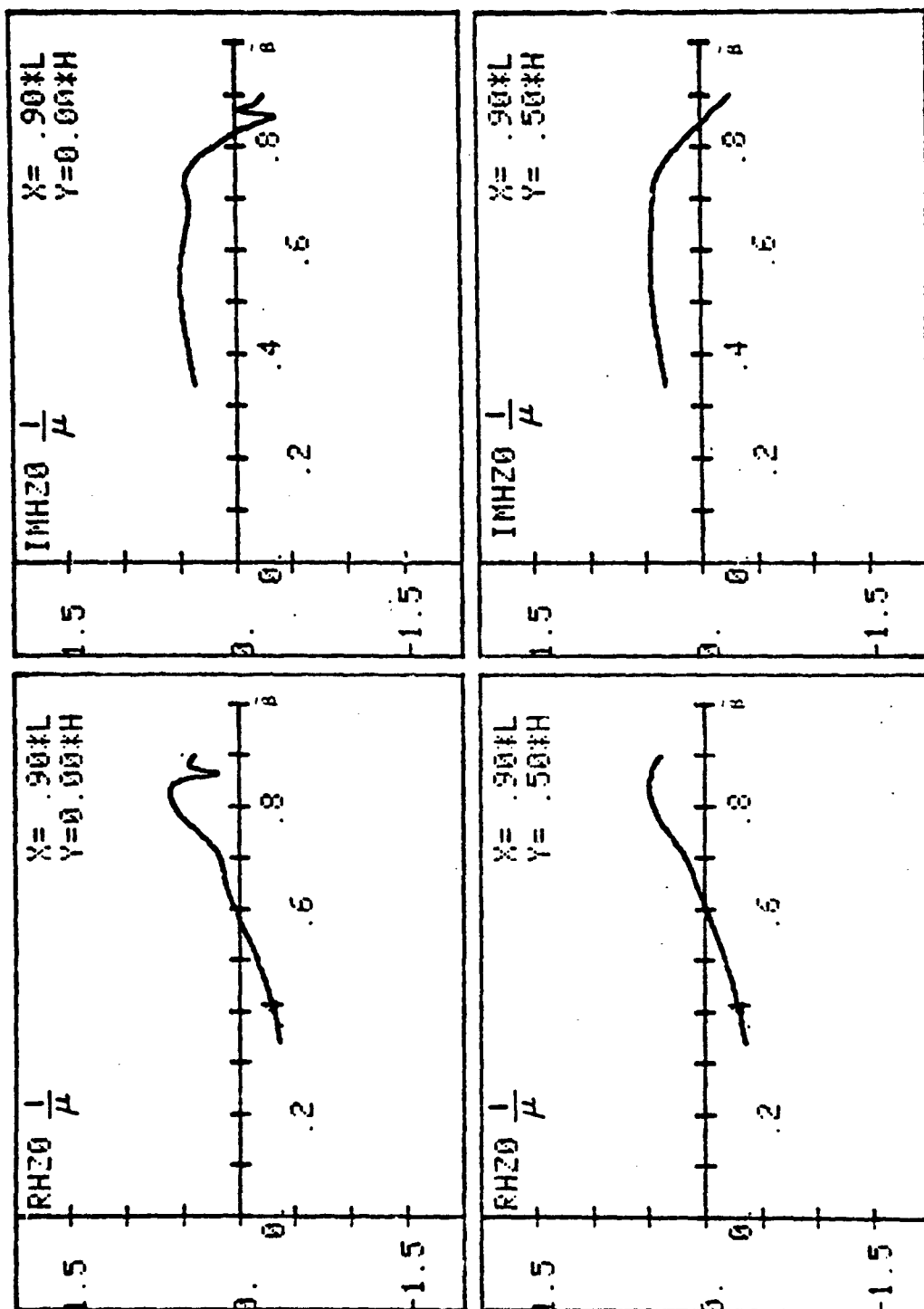


Figure 21. Real and imaginary parts of  $E$  as functions of  $\beta$  for parameters given in the lower half of Page 1. The  $x, y$  values of the observation point are shown in the inset.

AFWL-TR-80-401

DISTRIBUTION

AUL/LDE/Maxwell AFB

DTIC/DDA/Alexandria

AFSC/DLW/Andrews

AFWL, Kirtland AFB

(SUL)

(HO)

Official Record Copy (AFWL/NTMT/Dr Baum)